A Radiogenic Background Model for the Majorana Demonstrator

Micah Buuck

A dissertation
submitted in partial fulfillment of the
requirements for the degree of

Doctor of Philosophy

University of Washington

2019

Reading Committee:

Jason A. Detwiler, Chair

David Hertzog

R. G. Hamish Robertson

Program Authorized to Offer Degree:
Physics

University of Washington

Abstract

A Radiogenic Background Model
for the MAJORANA DEMONSTRATOR

Micah Buuck

Chair of the Supervisory Committee:
Associate Professor Jason A. Detwiler
Physics

Neutrinoless double-beta decay ($0\nu\beta\beta$) is a lepton-number-violating process whose existence would indicate that neutrinos are Majorana fermions. The MAJORANA collaboration is searching for $0\nu\beta\beta$ in germanium-76 using a modular array of high-purity germanium (HPGe) detectors with support and shielding constructed from low-background materials and housed at the 4850' level of the Sanford Underground Research Facility in Lead, South Dakota. The two modules of the experiment contain 44.8 kg of p-type point-contact high-purity germanium detectors, 29.7 kg of which are enriched in germanium-76. Both modules have been in operation since August 2016, and with 26 kg-yr of exposure have achieved a limit of $2.7 * 10^{25}$ yr on the decay half life. The DEMONSTRATOR has achieved an excellent energy resolution of 0.1% FWHM at the 2039 keV region-of-interest (ROI), and has among the lowest ROI backgrounds of current generation $0\nu\beta\beta$ searches.

Although the MAJORANA DEMONSTRATOR has achieved these low backgrounds, trace amounts of radioactivity remain detectable in the array. This work will present the results of an in-depth study of the backgrounds visible to the array, and the details behind a model for the remaining radiogenic backgrounds. The background model is a simultaneous fit of simulated energy spectra to groups of detectors and data sets, and has been validated with

comparisons to Monte Carlo generated and detector calibration data.

TABLE OF CONTENTS

LIST OF FIGURES

LIST OF TABLES

GLOSSARY

Majorana: Ettore Majorana (5 August 1906 – 1959??) was an Italian theoretical physicist most famous for deriving Majorana statistics for neutral fermions. Due to their potential invariance under charge conjugation, neutral fermions do not necessarily require antiparticles to be described theoretically and can obey Majorana statistics instead of the Dirac statistics typical of all charged fermions. Majorana dissappeared under mysterious circumstances in 1938 and was long thought to have perished at sea, but photographic evidence uncovered in 2011 suggests that he in fact escaped to South America and was still alive in Venezuela as late as 1959 [1].

MAJORANA FERMION: A Majorana fermion is a particle with half-integer spin and no electric charge that obeys Majorana statistics. Among the known fundamental particles, neutrinos are the only candidates to be Majorana fermions, as all other fundamental fermions carry nonzero electric charge. Recently, evidence for multi-particle systems obeying Majorana statistics has been discovered [2] in the field of condensed matter physics and was the first observance of Majorana particles in nature.

MAJORANA: The MAJORANA collaboration was formed in 2004 [3] to construct and operate the MAJORANA DEMONSTRATOR. The collaboration consists of over 60 scientists from 6 countries across 3 continents.

MAJORANA DEMONSTRATOR: The MAJORANA DEMONSTRATOR is the eponymous experiment of the MAJORANA collaboration. It is an array of p-type point-contact high-purity germanium detectors, most of which are enriched in the isotope ^{76}Ge designed to search for evidence of neutrinoless double-beta decay.

NEUTRINOLESS DOUBLE-BETA DECAY: Neutrinoless double-beta ($0\nu\beta\beta$) decay is a theoretical process whereby an atomic nucleus decays by the emission of two electrons and zero neutrinos. This stands in contrast to the rare but experimentally measured process of two-neutrino double-beta ($2\nu\beta\beta$) decay which includes the emission of two neutrinos in addition to the two electrons. The process of $0\nu\beta\beta$ decay is possible if and only if neutrinos contain a Majorana component to their mass. Therefore, its detection would provide conclusive proof that neutrinos are Majorana particles. In the

MAJORANA detectors, this process would be observed at a specific energy: the Q-value of the $2\nu\beta\beta$ decay at 2039 keV ($Q_{\beta\beta}$).

GERMANIUM: Germanium is a semiconductor that is used to create particle detectors with extremely good energy resolution. There also happens to be an isotope of germanium that undergoes $2\nu\beta\beta$ decay, and is therefore a candidate for detection of $0\nu\beta\beta$ decay. Due to their superb energy resolution and well-developed existing technology, germanium detectors enriched in the double-beta decay isotope ^{76}Ge are a very attractive option for searches for $0\nu\beta\beta$ decay.

HPGe: The detectors used by the MAJORANA collaboration are made from high-purity germanium. In the context of germanium detector manufacturing, this means that the input material must have a resistivity exceeding 47 Ω·cm, or equivalently fewer than 10^{13} electrical impurities/cm^3 [4].

PPC: The detectors used in the MAJORANA DEMONSTRATOR are p-type point-contact detectors. This means that the main bulk of the detector is a p-type semiconductor instead of an n-type as is usual in most germanium detectors. The words point-contact refer to the geometrical design of the detectors. One of the two electrical contacts (the one kept at ground) is a very small — effectively point-like — surface on one of the flat sides of the detector. It is made from implanted boron. The other contact covers most of the surface area of the detector, and is made from drifted lithium. The part of the surface between the two contacts is passivated and insulates the contacts from each other.

DETECTOR DEAD LAYER: Germanium detectors have a region of some depth into the surface that does not give full charge collection. This is due to the fact that the electrical contacts (in the case of the MAJORANA detectors, primarily the outer lithium contact) are conductive and penetrate some depth into the detector. The effect of the dead layer is that for some region of the detector bulk, the correct energy of a deposition is not recovered which can affect the shape of the detected energy spectrum. Because $0\nu\beta\beta$ decay occurs at a characteristic energy, the thickness of this layer also affects the effective mass of the detectors that is sensitive to $0\nu\beta\beta$ decay.

REGION OF INTEREST: The region of interest, or ROI, refers generically to the region in the energy spectrum of radiation detected by the MAJORANA DEMONSTRATOR near the expected energy of $0\nu\beta\beta$ decay at 2039 keV. Typically, this will refer to an energy window equal to the full-width-half-maximum (FWHM) of the measured peak

shape of the DEMONSTRATOR. While the DEMONSTRATOR was being designed and constructed, a conservative estimate of 4 keV was used as the FWHM, and is the value that is used in the assay results presented in [5] and in section 2.2. After construction, the DEMONSTRATOR achieved a FWHM of 2.53 keV at 2039 keV. The ROI width used in all results is set to maximize sentivity, and varies from data set to data set. Specific ROI widths for each data set can be seen in table 2.5.

`MaGe`: Standing for MAJORANA-GERDA, `MaGe` is a software package developed by the MAJORANA and GERDA collaborations for the purpose of simulating ^{76}Ge $0\nu\beta\beta$ decay experiments. It is built on Geant4, and is capable of simulating interactions from first principles of energetic particles like electrons, photons, and alpha particles with the MAJORANA germanium detectors. It does not apply any detector resolution effects.

`GAT`: Standing for Germanium Analysis Toolkit, `GAT` is a software package developed by the MAJORANA collaboration for processing the output of the MAJORANA DEMONSTRATOR. It contains routines to estimate the energy of detected waveforms, analyze the waveform shapes, and convert the data to a more digestable ROOT format. It also contains a framework to process the output of `MaGe`, simulating all of the detector effects like the energy resolution and dead-layer correction.

`siggen`: `siggen` is a computer code developed by David Radford of Oak Ridge National Laboratory that simulates the generation of waveforms in germanium detectors given a crystal geometry, an energy deposition and location, and some other configuration parameters.

WAVEFORM: This refers to the trace that is recorded by the MAJORANA data acquisition system when an energy deposition is detected. A MAJORANA waveform appears roughly as a step function multiplied by an exponential decay, with the height of the step is more-or-less proportional to the energy of the pulse. The x-axis has units of time (sampled at 100 MHz), and the y-axis has arbitrary units that are proportional to the voltage difference across the detector. Further information about the event can be extracted from the shape of the pulse.

ROOT: ROOT is a data analysis framework widely used in the field of high-energy physics. It contains a variety of very useful features, chief among them its ability to efficiently store and access large arrays of numerical data like those acquired in a modern physics

experiment like the MAJORANA DEMONSTRATOR. It also contains a number of easy-to-use tools for creating plots of physics data, and was used to generate many of the plots in this document.

GEANT4: Standing for GEometry ANd Tracking, Geant4 is a software package use for simulating the interactions of particles in matter that is widely used in the physics community and beyond. It provides the fundamental subroutines that `MaGe` uses to simulate the MAJORANA DEMONSTRATOR.

PYTHON: Python is a high-level programming language that has become quite popular for scientific analysis in recent years, due to its ease of use and extensive community of scientific users. Several well-supported packages, like NumPy [6], SciPy [7], and Matplotlib [8] make computation, analysis, and figure generation quick and effient. Much of the work presented in this document is written in Python and makes use of these packages, as well as several others mentioned in the text.

ACKNOWLEDGMENTS

Throughout history, humans have been curious about the natural world. The urge to understand the world around us seems to be one of the things that can unite people across the globe, and the progress of science, especially in the modern era, is exhilirating and sometimes a bit terrifying. There have been many scientists across time, each one with their own set of unique experiences that drove them to choose that path in life. Some, like Isaac Newton or Charles Darwin, are born at the right time in the right place with the right connections, and have insights that fundamentally alter the way people understand the natural world. Most other scientists do not or will not have such glamorous legacies. But the beauty of the project of scientific discovery — what makes it worthwhile to me personally — is that really this does not matter. Because science is not (or at least should not be) about personal glory. It is a collective endeavor where everyone who participates, who takes themselves and others seriously, who does not quit in the face of adversity, and who finds the right balance between self-doubt and self-assurance, can be a meaningful part of the whole. Because we trust and learn from each other, we can achieve things that are impossible for a single person.

I find great comfort and meaning in the belief that, after I am gone, humanity will still be working together to continue to expand our knowledge of world around us. But this optimistic future is far from guaranteed. We must never forget that science is done by people, and people are flawed. The era of peacefulness that has existed since the end of the second world war (at least relative to the first half of the 20th century) is a large part of what has enabled international scientific cooperation to flourish so dramatically. This

peace is a historical anomaly, and we must guard it jealously. We also benefit today from a quality of life that is historically unmatched. But the same technologies that allow us to live so comfortably are also often the seeds of our own destruction [9] [10]. We cannot expect our collective voyage of discovery to simply continue unaided in a positive direction. If we are to exist as a society (and maybe even a species) indefinitely into the future, we have to learn to account for the consequences of our choices. And we must remember that we are all connected to each other, through the only planet known to support life in the entire universe. After all, what is the point of understanding the universe if we do not do it together?

On that note, I must acknowledge a number of people and organizations, without whom this work would not have been possible. Thank you to Jim Fox for providing the LaTeX template for UW theses. My fellow co-workers Ian Guinn, Julieta Gruszko, Clara Cuesta, Walter Pettus, Clint Wiseman, Nick Ruof, Alexander Hostiuc, Zhenghao Fu, and everyone else at UW and CENPA have been instrumental. Outside of UW, I want to specifically thank Matthew Green at NCSU, who as the head of the simuations working group has worked with and taught me so much about how to do this work correctly. Everyone in the Majorana collaboration who helped to build the Majorana Demonstrator over the years also deserves a mention. Without the experiment operating successfully, none of this would have been possible! I would also like to say a special thank you to my PhD advisor, Jason Detwiler. He is one of the most impressive people I have ever had the pleasure to work with, both in his intellectual abilities and in his perpetually undaunted outlook on life and research. I hope to be as resilient and optimistic of a scientist as he is.

The constant support from my parents, sister, and parents- and brothers-in-law has made it easier to get through the tough times on the way to finishing my PhD these past few years. There are times where I don't know if I would have been able to finish without their support and encouragement. And finally, thank you to my wife, Cecilia Noecker, who has been right

there with me the entire time. I love you, and I don't know what I'd do without you.

This material is based upon work supported by the U.S. Department of Energy, Office of Science, Office of Nuclear Physics, the Particle Astrophysics and Nuclear Physics Programs of the National Science Foundation, and the Sanford Underground Research Facility.

DEDICATION

for Cecilia

Chapter 1

INTRODUCTION AND THEORETICAL MOTIVATION

Contrary to the impression you might get from watching *Star Trek*, we actually know quite a lot about neutrinos. We know how they relate to most of the other known particles, and as far as we can tell they cannot be used to build wormholes, stable or unstable. But even though our knowledge of neutrinos has continuously expanded over the past 90 years, they are still one of the most mysterious particles in the Standard Model of particle physics.

1.1 Historical Overview of Neutrinos

The neutrino as a concept was first proposed in 1930 by Wolfgang Pauli to explain the process of beta decay [11]. At the time, it was known that quantities like energy, angular momentum, and spin should be conserved in physical processes. But the process of beta decay, where apparently only an electron was emitted from an atomic nucleus, presented a problem. If the electron were the only particle emitted from the nucleus in beta decay, it would have to be emitted monoenergetically to conserve energy. But the beta-decay spectrum was continuous in energy, unlike the spectra of the other primary nuclear decay processes of alpha and gamma decay.

Two primary explanations for this behavior were put forth. Niels Bohr suggested that perhaps at the subatomic level, quantities such as energy and angular momentum were only conserved in a statistical ensemble, but not necessarily in any individual interaction. Alternatively, Pauli suggested that all of these quantities were in fact conserved in every beta

decay, but that there was an additional particle — which he called the neutron — emitted along with the electron that carried away the balance of the conserved quantities. Later, the particle we now know as the neutron would be discovered [12]. The particle originally proposed by Pauli underwent a name change to "neutrino", and was a critical component of the theory of beta decay published by Fermi in 1934 [13].

Fermi's theory of beta decay rapidly became widely accepted, but it wasn't until the Cowan-Reines experiment at the Savannah River nuclear power plant in South Carolina that neutrinos were definitively and directly observed for the first time [14]. Cowan and Reines were the first to make use of the process of inverse beta decay, whereby a high-energy anti-electron neutrino combines with a proton to produce a neutron and a positron in the final state:

$$\bar{\nu}_e + p \rightarrow n + e^+ \tag{1.1}$$

After the positron is emitted, it promptly annihilates with a nearby electron, producing two photons which can be detected. An additional signal can be detected from the capture of the neutron on a material with a high neutron-capture cross-section, typically after a few hundred microseconds. In the case of the Cowan-Reines experiment, cadmium was used as the neutron absorbing material. This multi-event signal is quite specific, and with a high enough neutrino flux and a low enough background rate from cosmic ray interactions it can be and was detected for the first time in 1954, some 20 years after the publication of Fermi's theory of beta decay. The process of inverse beta decay is still the primary detection signature for reactor neutrino experiments [15] [16] [17] [18].

1.2 Neutrino Mass

Even though it has now been 65 years since they were first proven to exist, neutrinos are still one of the most poorly understood components of the standard model of particle physics. When they were initially proposed in the 1930s, the question of whether or not neutrinos had

a small mass or were in fact massless was not particularly important. Initially, Pauli believed that they must be much ligher than the proton, because otherwise their emission would cause a noticeable change in the mass of the nucleus they were emitted from. An upper limit on the neutrino mass can in principle be derived by measuring the difference between the endpoint of a beta decay spectrum and the total energy released in the decay (Q-value). This would imply just from a beta decay spectrum that the neutrino mass could be at most on the order of 1 keV, which would make it several orders of magnitude smaller than the electron mass. Current limits on the mass of the electron neutrino place it at 2.2 eV or lower [19] [20], with the upcoming KATRIN experiment projected to have sensitivity to 0.2 eV electron neutrino mass [21]. Since all of the other known fermions have masses between 500 keV and 200 GeV, it was assumed for some time that the neutrino might very well be completely massless.

The first hint that neutrinos had mass came from the Homestake experiment, which began taking data in 1970 in the Homestake gold mine in Lead, South Dakota. The Homestake experiment was performed by Ray Davis, John Bahcall, and collaborators [22], and its purpose was to test Bahcall's theory of solar fusion by measuring the neutrino flux from the sun. Electron neutrinos are produced during solar fusion and immediately escape from the sun, whereas the rest of the particles produced interact with each other and are not directly detectable on Earth. The fluxes and energy spectra of electron neutrinos thus give a unique window into the details of solar fusion processes.

When the Homestake experiment turned on, however, Davis *et. al.* only detected approximately 1/3 of the electron neutrino flux expected by Bahcall's solar model. At the time it was not known if this meant the solar model was wrong, or if the Homestake experiment had an unaccounted for systematic uncertainty. The experiment relied on the detection of just a handful of argon atoms that had been converted from chlorine via interaction with solar neutrinos, so experimental error was a reasonable hypothesis. But over time, the evidence of a disagreement grew more significant.

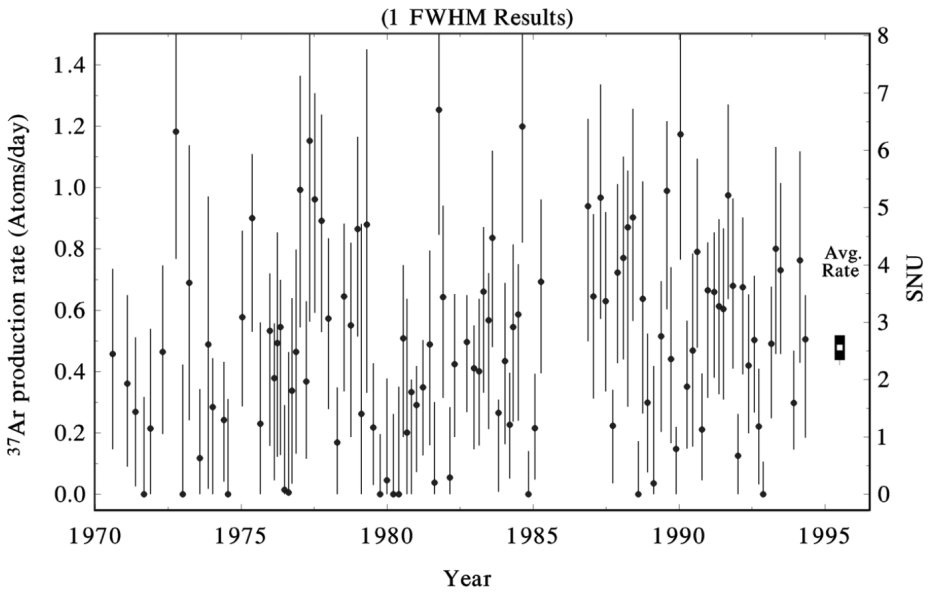

Figure 1.1: Results for 108 individual solar neutrino observations made with the Homestake chlorine detector. The production rate of ^{37}Ar shown has already had all known sources of nonsolar ^{37}Ar production subtracted from it. The errors shown for individual measurements are statistical errors only and are significantly non-Gaussian for results near zero. The error shown for the cumulative result is the combination of the statistical and systematic errors in quadrature. (Caption and figure from [22]) The expected flux from theory was between 6.36 and 9.3 SNUs.

Bruno Pontecorvo had previously shown [23] that if neutrinos had mass, and if the mass states were not aligned with the flavor states (i.e. the three types of electron, muon, and tau neutrinos), then neutrinos of a particular mass state would be expected to transform flavors as they propagated through space. This was capable of producing a result like that seen in the Homestake experiment.

The solar neutrino problem, as it came to be known, was a major avenue of inquiry into neutrino physics for several decades. A number of experiments around the world were

constructed to measure more precisely the solar neutrino flux, and eventually to be sensitive to other types of neutrinos besides just electron neutrinos. Neutrino flavor transformation was definitively identified as the solution to the problem in the early 2000s, with the measurement of the full solar neutrino flux (i.e. all 3 active flavors) by the SNO experiment [24]. SNO was the first experiment able to measure both the flux of electron neutrinos and the full flux of all neutrino flavors, and found that electron neutrinos comprised only 34% of the total solar neutrino flux. Since the sun was only capable of producing electron neutrinos, this result proved that neutrinos were changing flavor after they were produced. Results from atmospheric and reactor neutrino detectors such as Super-Kamiokande [25] and KamLAND [18] definitively proved that the theory of neutrino oscillation established by Maki, Nakagawa, Sakata [26], Gribov, and Pontecorvo [27] (and extended to 3 generations of neutrinos by Mann and Primakoff [28]) accurately described the behavior of neutrinos.

1.3 Majorana Neutrinos

The discovery of neutrino mass reignited interest in the question of whether neutrinos had a Majorana component to their mass. In the 1920s, when quantum mechanics was still a brand new field, Paul Dirac devised the Dirac equation to describe how fermions — particles with a half-integer spin — propagate through space [29] [30]. The Dirac equation requires 4-component spinors to describe the state of a fermion. A spin 1/2 particle like an electron has two possible spin states: spin up and spin down. The additional two components of a Dirac spinor correspond to the anti-particle partners of the two spin states. When Dirac formulated his equation, antimatter had not been experimentally observed, but would be 4 years later by Carl D. Anderson [31]. Dirac's prediction of the existence of antimatter and its subsequent discovery is one of the most impressive results in the history of modern physics.

The spinors that describe the fermion state in the Dirac equation are not invariant under an operation called charge conjugation, which represents flipping the electric charge of the

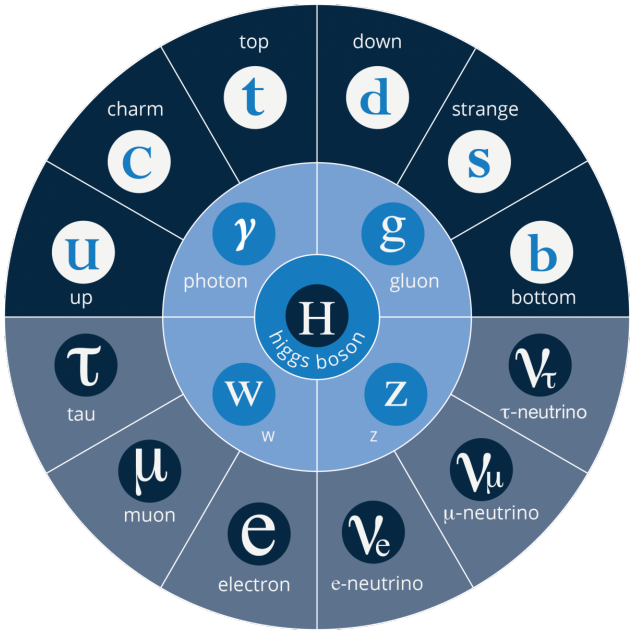

Figure 1.2: The particles of the standard model, with fermions in the outer ring and bosons in the middle. Neutrinos are the only chargeless particles with half integer spin. Credit: ATLAS Collaboration

state. Instead, the charge conjugation operation flips particles to anti-particles and vice-versa. However, if one supposes an uncharged fermion, then in principle it is possible to describe that state in a way that is invariant under charge conjugation, since flipping the sign of an uncharged particle still gives the same uncharged particle. This means that a theory of neutral fermions could be built with just 2-component spinors, as was realized and formalized by Ettore Majorana in 1937 [32].

Currently, every fermion in the standard model, with the possible exception of neutrinos, is a Dirac particle because they all have electric charge. Neutrinos, however, are uncharged and could be Majorana particles, which would mean that there is no distinction between neutrinos and anti-neutrinos. But the fact that neutrinos might be Majorana is more than

just an academic curiosity. Majorana neutrinos are connected to two important open questions in physics, namely: Why is the neutrino mass so small? and How is the asymmetry between matter and antimatter in the universe generated? Theorized explanations to both of those questions predict the existence of Majorana neutrinos, giving us good reason to look for them.

1.3.1 The Seesaw Mechanism and Neutrino Mass

As was mentioned in Section 1.2, current limits on the neutrino mass mean that it is several orders of magnitude less massive than the other standard model fermions. There isn't necessarily anything wrong with this fact, but searching for parsimonious models has been generally quite fruitful for physicists over time, so there is a desire to see if the small neutrino mass can be explained through a more "natural" mechanism. The seesaw mechanism is one example in which the addition to the Standard Model of a heavy Majorana mass term M associated with a non-interacting right-handed neutrino (mass $\approx 10^{15}$ GeV) contributes to the neutrino mass along with a Dirac neutrino mass term D that is on the same scale as the other massive fermions (mass ≈ 100 GeV). The mass matrix associated with these mass terms is:

$$\begin{pmatrix} 0 & D \\ D & M \end{pmatrix} \tag{1.2}$$

Its eigenvalues correspond to the physical masses of the heavy non-interacting neutrino and the interacting left-handed neutrino, and they are $M \approx 10^{15}$ GeV and $D^2/M \approx 0.01$ eV, which is right in line with current limits on the neutrino mass. The seesaw name refers to the fact that increasing the mass of the heavy neutrino directly causes a smaller physical left-handed neutrino mass.

1.3.2 Matter/antimatter Asymmetry

Measurements of the universe indicate that it is virtually entirely made of matter. But the laws of physics as they are currently understood are not capable of explaining the imbalance between matter and antimatter entirely. The standard way of thinking about the matter/antimatter asymmetry of the universe, and what it would take to explain it, was formulated by Andrei Sakharov in 1967 [33]. He listed three conditions that are necessary to produce the observed asymmetry today:

- Baryon number violation
- C- and CP-symmetry violation
- Interactions out of thermal equilibrium

If the previously discussed seesaw mechanism for generating neutrino masses is true, then decays of the new heavy Majorana neutrino in the early universe can be incorporated into a theoretical explanation of the matter/antimatter asymmetry that satisfies all of Sakharov's conditions [34]. The ability of these heavy Majorana neutrinos and the seesaw mechanism to explain several currently unexplained pheonomena (neutrino mass, and matter/antimatter asymmetry) makes the search for evidence of a Majorana nature of standard model neutrinos through neutrinoless double-beta decay extremely interesting. Lepton number violation and CP-symmetry violation can also be observed directly in the neutrino sector, with lepton number violation appearing in the form of Majorana neutrinos, and CP-symmetry violation through the three CP-violating phases δ, α, and β.

Lepton and Baryon Number Violation

A Majorana component to the neutrino mass would very likely generate the process of neutrinoless double-beta decay, the search for which is the focus of the MAJORANA DEMON-

STRATOR and this dissertation. Neutrinoless double-beta decay would be the first process observed that does not conserve lepton number, i.e. the number of leptons going into the process does not equal the number coming out. Under the standard model process of double-beta decay, which was first directly observed in 1987 [35], an atomic nucleus decays and produces two electrons and two anti-electron neutrinos:

$$(A, Z) \rightarrow (A, Z + 2) + e^- + e^- + \bar{\nu}_e + \bar{\nu}_e \tag{1.3}$$

However, Majorana neutrinos being their own antiparticles opens up the additional channel of neutrinoless double-beta decay:

$$(A, Z) \rightarrow (A, Z + 2) + e^- + e^- \tag{1.4}$$

This lepton-number violating process can then be used to generate a baryon number asymmetry [34].

CP Violation

CP symmetry refers to charge-parity symmetry. A process that is invariant under CP symmetry looks the same if you convert all its particles to anti-particles, and left-handed particles to right-handed particles, and vice versa. Most known physical processes conserve CP symmetry, but there are some that do not. Most well known are CP violating processes in the quark sector, via complex phases in the Cabibbo-Kobayashi-Maskawa (CKM) matrix [36] that determines how quarks interact in the weak interaction. Although there are some sources of CP violation in that matrix, as currently understood they are not sufficient to explain the observed matter/antimatter asymmetry. The neutrino sector is capable of providing additional sources of CP violation through the Pontecorvo-Maki–Nakagawa–Sakata (PMNS) matrix which, similar to the CKM matrix, describes how the neutrino flavor and mass states ($\nu_e/\nu_\mu/\nu_\tau$ and $\nu_1/\nu_2/\nu_3$ respectively) mix with each other. The PMNS matrix can be expressed in terms of 3 mixing angles (θ_{12}, θ_{13}, and θ_{23}) and 3 phases (δ, α, and β), as

is shown in equation 1.5, but the phases α and β are not physically observable if neutrinos are Dirac particles. The potential sources of CP violation in the PMNS matrix are quite a bit larger than in the CKM matrix, as is shown in Figure 1.3 from [37].

$$\begin{pmatrix} 1 & 0 & 0 \\ 0 & \cos\theta_{23} & \sin\theta_{23} \\ 0 & -\sin\theta_{23} & \cos\theta_{23} \end{pmatrix} \begin{pmatrix} \cos\theta_{13} & 0 & \sin\theta_{13}e^{-i\delta} \\ 0 & 1 & 0 \\ -\sin\theta_{13}e^{i\delta} & 0 & \cos\theta_{13} \end{pmatrix} \begin{pmatrix} \cos\theta_{12} & \sin\theta_{12} & 0 \\ -\sin\theta_{12} & \cos\theta_{12} & 0 \\ 0 & 0 & 1 \end{pmatrix} \begin{pmatrix} 1 & 0 & 0 \\ 0 & e^{i\alpha} & 0 \\ 0 & 0 & e^{i\beta} \end{pmatrix} \begin{pmatrix} \nu_1 \\ \nu_2 \\ \nu_3 \end{pmatrix} \tag{1.5}$$

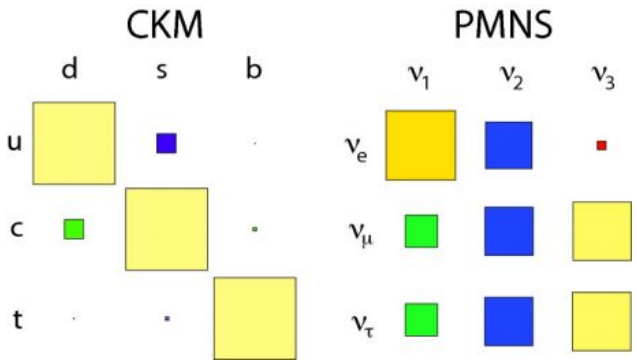

Figure 1.3: (left) Sizes of the the CKM matrix elements for quark mixing, and (right) the PMNS matrix elements for neutrino mixing. The area of the squares represents the square of the matrix element. (Caption and figure from [37]). The upper limit on possible CP violation is related to the sizes of particular matrix elements, which are all off-diagonal except for (2, 2). If neutrinos are Majorana, then all matrix elements in the PMNS matrix except for (1, 1) can in principle contribute to CP violation.

1.4 Overview of the Theory of Neutrinoless Double-Beta Decay

Given the strong theoretical motivations for its existence, many experiments have been designed to search for evidence of a Majorana component to neutrino mass. The most straightforward way to do this experimentally is to search for the process of neutrinoless double-beta decay, which was briefly described in Section 1.3.2. Neutrinoless double-beta

decay is a heretofore unobserved version of the standard model process of double-beta decay, which is the emission of two electrons and two anti-electron neutrinos from an atomic nucleus simultaneously.

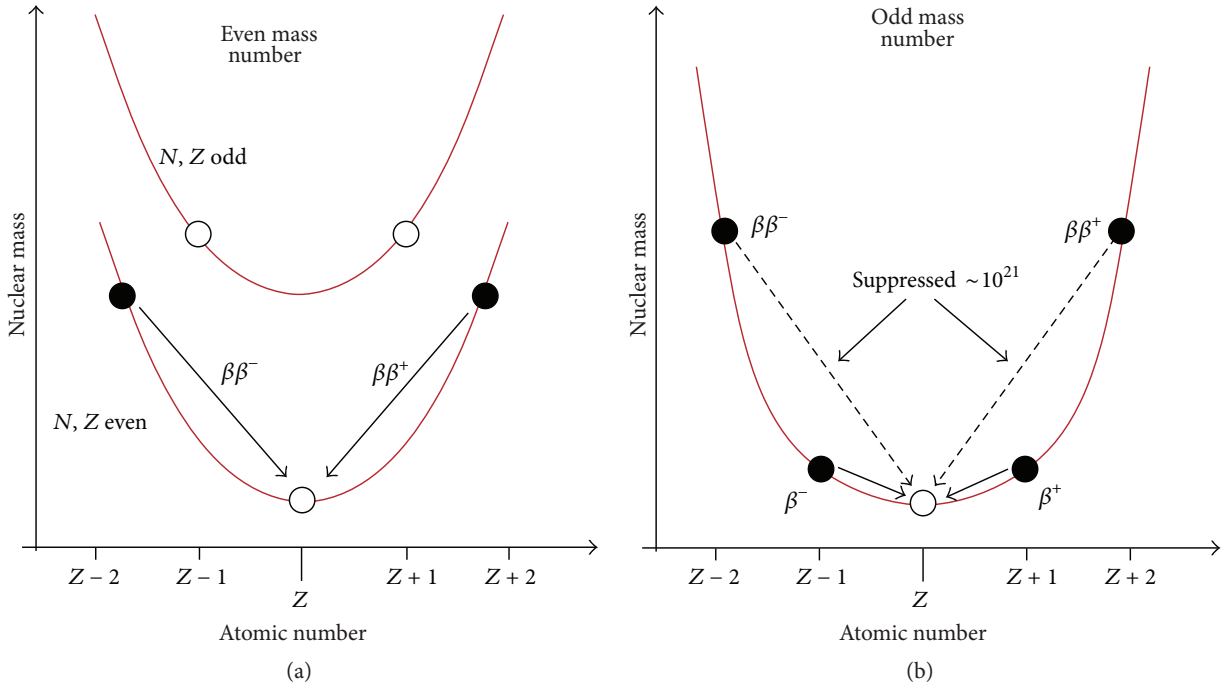

Figure 1.4: Nuclear mass as a function of the atomic number Z in the case of an isobar candidate with A even (a) and A odd (b). (Caption and image from [38])

Double-beta decay is observable in some nuclei where the more common single-beta decay process is prohibited by conservation of energy. The pairing forces of nucleons in a nucleus can cause nuclei with an even number of both protons and neutrons to have a lower energy ground state than the nucleus they would decay to under normal beta decay. However, the neighboring state with $Z + 2$ protons and $N - 2$ neutrons is still even-even, and can be a lower energy than the parent state. For nuclei where this is true, double-beta decay can be observed. Figure 1.4 illustrates this effect.

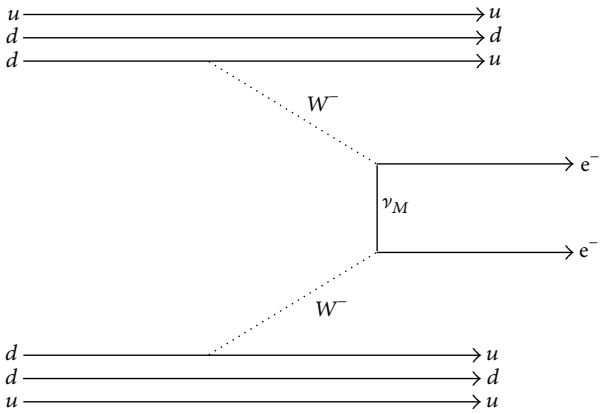

Figure 1.5: Diagram of the $0\nu\beta\beta$ process due to the exchange of massive Majorana neutrinos, here denoted generically by ν_M. (Caption and image from [38])

Any nucleus capable of undergoing double-beta decay is a candidate for neutrinoless double-beta decay. Since what defines a reaction as neutrinoless double-beta decay is only that it produce two electrons and no neutrinos from an atomic nucleus, there are a variety of candidate processes that describe the particle physics happening inside the nucleus during the process. The one that requires the fewest novel particles and processes is light Majorana neutrino exchange (LMνE), which is diagrammed in Figure 1.5. In standard two-neutrino double-beta decay, two protons are converted via the weak interaction into two electrons and two anti-electron neutrinos. With LMνE, those two neutrinos can be instead described as a single virtual particle with an insertion of the Majorana mass. The Majorana mass represents the contribution of particle physics processes to the strength of this interaction, and is given in terms of elements from the PMNS matrix:

$$m_{\beta\beta} = \left| \sum_{i=1,2,3} U_{ei}^2 m_i \right| \tag{1.6}$$

where e refers to the first (electron) row of the PMNS matrix and i iterates over the mass states (columns). This relationship can be motivated by noticing that a calculation of the

tree-level diagram shown in Figure 1.5 requires an insertion of the interaction term between an electron and a neutrino mass eigenstate (U_{ei}) for each electron vertex, as well as an additional factor of the neutrino mass representing the required helicity flip m_i. Since all neutrino mass states can participate in the interaction, we sum over them and obtain the above expression for $m_{\beta\beta}$.

Under the assumption of LMνE, the rate of $0\nu\beta\beta$ decay can be written as:

$$\left[T^{0\nu}_{1/2}\right]^{-1} = G^{0\nu} \left|\mathcal{M}^{0\nu}\right| m^2_{\beta\beta} \tag{1.7}$$

where $G^{0\nu}$ is a phase-space factor and $\mathcal{M}^{0\nu}$ is the nuclear matrix element for $0\nu\beta\beta$ decay.

The sources of uncertainty in $T^{0\nu}_{1/2}$ come nearly entirely from $\mathcal{M}^{0\nu}$ and $m_{\beta\beta}$. While $G^{0\nu}$ can be calculated with a relatively high degree of precision, $\mathcal{M}^{0\nu}$ is difficult to calculate (see Figure 1.6) and $m_{\beta\beta}$ is only constrained by measurements of the parameters of the PMNS matrix and the neutrino masses, some of which are still completely unmeasured. Since this dissertation is focused on the experimental side of the $0\nu\beta\beta$ decay search, it will not cover the state of calculations of nuclear matrix elements in detail. A relatively recent review of the field can be found in [39].

The phase space available to the parameter $m_{\beta\beta}$ is most easily visualized in a 2-dimensional plot, where one dimension is given by $m_{\beta\beta}$ and the other is given usually by either the lightest neutrino mass state (m_{lightest}) or the sum of the active neutrino masses (Σ), which is deduced from measurements of cosmological data. The regions of available phase space depend on whether the three neutrino mass states are ordered such that the smaller of the two known mass splittings separates the two lightest (normal ordering/hierarchy) or the two heaviest (inverted ordering/hierarchy) mass states. Current generation $0\nu\beta\beta$ decay experiments are sensitive to the degenerate region above ~50 meV in $m_{\beta\beta}$, with next-generation experiments currently being designed with sensitivities extending down to ~15 meV.

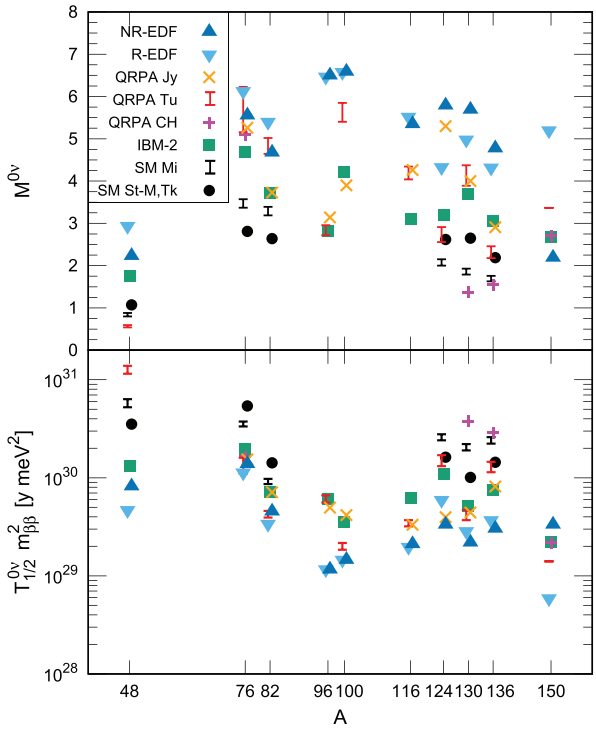

Figure 1.6: Top panel: Long-range nuclear matrix elements ($\mathcal{M}^{0\nu}$) for $0\nu\beta\beta$ decay candidates as a function of mass number A and a variety of calculation techniques. Bottom panel: Associated $0\nu\beta\beta$ decay half-lives, scaled by the square of the unknown parameter $m_{\beta\beta}$. (Caption and image from [39]) Recently a short-range "contact term" of unknown amplitude has been identified to be of importance for the calculation of $\mathcal{M}^{0\nu}$, which is described in [40].

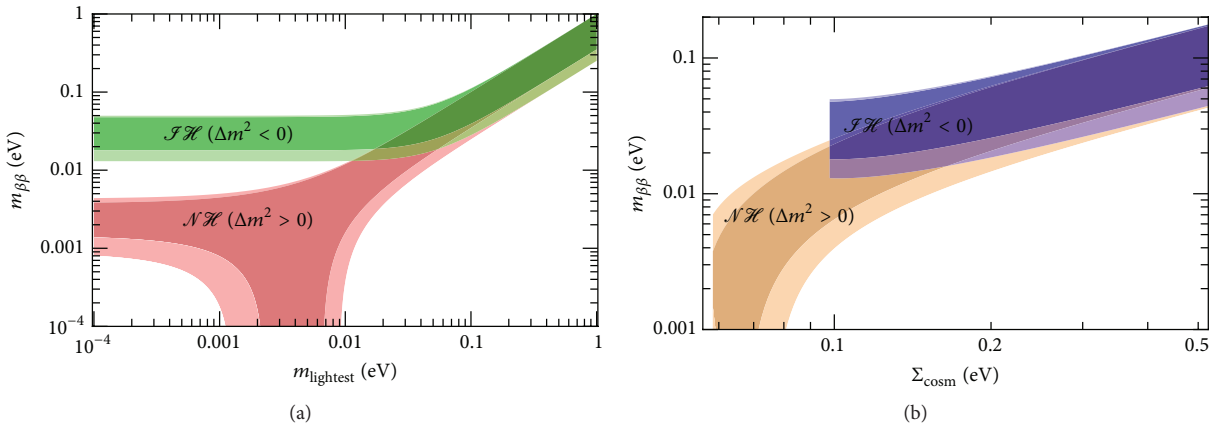

Figure 1.7: Allowed regions for $m_{\beta\beta}$ derived from neutrino oscillation experiments as a function of the lightest neutrino mass (a) and of the sum of the neutrino masses (b). The available phase space depends on whether the neutrino mass hierarchy is normal (two light states and one heavy state) or inverted (one light state and two heavy states). The shaded areas correspond to the 3σ regions due to error propagation of the uncertainties on the oscillation parameters. (Caption and image from [38])

1.5 Neutrinoless Double-Beta Decay Experimental Design

All experiments searching for $0\nu\beta\beta$ decay look for essentially the same signature: a sharp peak at the high end of the energy spectrum of an isotope that decays via $2\nu\beta\beta$ decay. A detector that detects $0\nu\beta\beta$ decay would produce an energy spectrum similar to that shown in Figure 1.8. The specific energy of the decay depends on the isotope, and is known as the Q-value, which is a generic term referring to the total amount of energy released in a decay. When referring to the Q-value specifically for double-beta decay, the symbol $Q_{\beta\beta}$ is often used.

There are a large number of experiments searching for evidence of neutrinoless double-beta decay around the world, employing a variety of different techniques and using many different isotopes. This necessitates using some kind of figure of merit to compare them, often the sensitivity $S_{0\nu}$, defined in Appendix B of [41] as "the value of $T^{0\nu}_{1/2}$ or $m_{\beta\beta}$ for which an experiment has a 50% chance to measure a signal above background with a significance of at least 3σ". I will present a brief derivation of the definition of sensitivity given there.

This formulation of the sensitivity to a half-life of $T^{0\nu}_{1/2}$ is given by

$$S_{0\nu} = T^{0\nu}_{1/2} = \ln 2 T N_{\beta\beta}\epsilon / S_{3\sigma}(B) \tag{1.8}$$

where T is the live time of the experiment, $N_{\beta\beta}$ the number of $0\nu\beta\beta$ decay candidate nuclei in the sample, ϵ the detection efficiency, B the expected number of background counts in the signal region-of-interest, and $S_{3\sigma}(B)$ refers to the Poisson signal expectation at which 50% of the measurements in an ensemble of identical experiments would report a 3σ positive fluctuation above background counts B. In the limit of high backgrounds, we have $S_{3\sigma}(B) \to 3\sqrt{B}$. If B scales with the sensitive exposure ($\mathcal{E} = TN_{\beta\beta}\epsilon$) of the experiment (true for most background sources, which typically produce background counts at a constant rate), then $B = bTN_{\beta\beta}\epsilon$ and the formula for sensitivity is:

$$S_{0\nu} = \frac{1}{3}\ln 2\sqrt{TN_{\beta\beta}\epsilon/b} \tag{1.9}$$

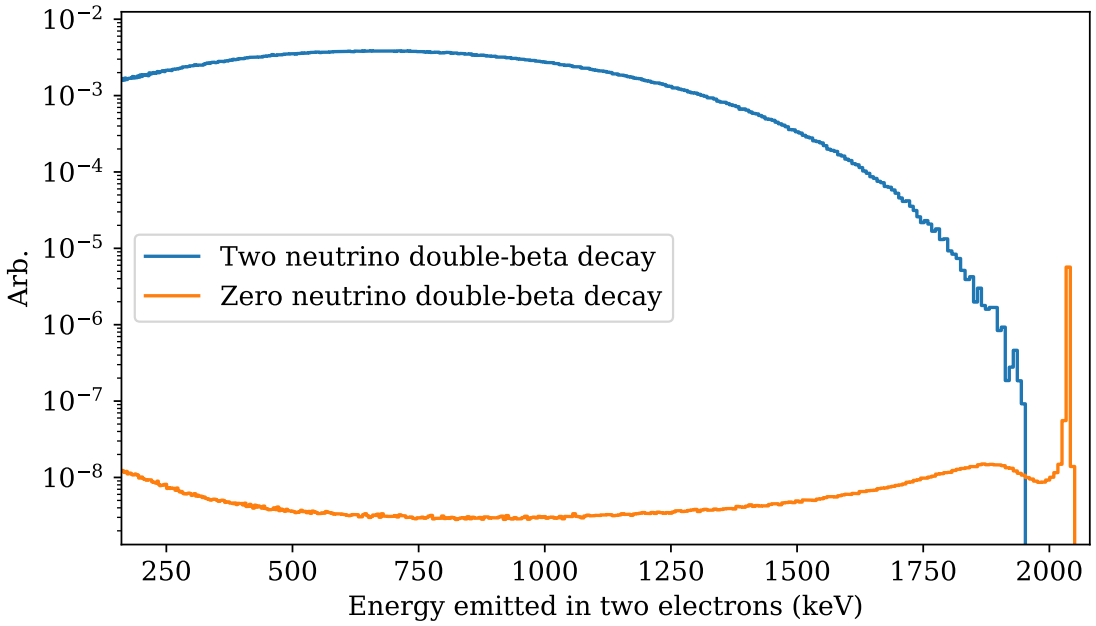

Figure 1.8: An isotope that decays via $0\nu\beta\beta$ decay would produce an energy spectrum similar to that seen here. The spectra plotted are simulations of $2\nu\beta\beta$ (blue) and $0\nu\beta\beta$ (orange) decay in the MAJORANA DEMONSTRATOR. Nearly all $0\nu\beta\beta$-decay events occur in the peak at $Q_{\beta\beta} = 2039$ keV, with a few percent of $0\nu\beta\beta$-decay electrons losing some energy due to bremsstrahlung. The relative heights of the spectra are set to approximate the current limits on $0\nu\beta\beta$ decay relative to the measured rate of $2\nu\beta\beta$ decay in ^{76}Ge. The sum of the bin values for the $2\nu\beta\beta$-decay spectrum is set to 1.

In the limit of zero background, $S_{3\sigma}(B)$ is a constant, and the sensitivity becomes

$$S_{0\nu} \propto \ln 2TN_{\beta\beta}\epsilon \tag{1.10}$$

There is a smooth transition between these two regimes which can be calculated numerically. The details of this calculation are presented in [41], but are not necessary to point

out that in either case presented here, the most important goals of a $0\nu\beta\beta$ decay experiment should be to maximize sensitive exposure and to minimize backgrounds that mimic the signal. In fact, because the sensitivity increases faster with exposure the lower the background is, achieving low backgrounds is arguably the single most important objective of a $0\nu\beta\beta$ decay experiment.

1.5.1 Maximizing Sensitive Exposure

These considerations drive the design of most $0\nu\beta\beta$ decay experiments, and lead to a number of similarities between the many different detectors. For starters, it helps a lot in maximizing ϵ to construct the detectors out of the source material. Nearly all $0\nu\beta\beta$ detectors make this design choice, with only a few exceptions (e.g. the SuperNEMO Demonstrator [42] [43]). This choice also helps maximize the total number of atoms available for $0\nu\beta\beta$ decay, since the emitted electrons do not have to be transported to a detector. If an experiment has a separate source and detector, the source must be made either very thin or very diffuse, since electrons cannot travel more than a few millimeters through most solid materials. This of course makes it more difficult to field large source masses, and is the main reason most $0\nu\beta\beta$-decay experiments use detectors that are built from the $0\nu\beta\beta$-decay isotope. It is also important that the fraction of the $0\nu\beta\beta$-decay isotope where the $0\nu\beta\beta$ signal can actually be detected is as close to 1 as possible. Some experiments fiducialize their sensitive mass in order to achieve lower backgrounds, but that tradeoff should be optimized to achieve maximum sensitivity to $0\nu\beta\beta$ decay. It is also important that achieving low background does not come at the cost of analysis cuts that decimate the detection efficiency. Finally, it is important that any $0\nu\beta\beta$-decay experiment run efficiently with minimal downtime, so as to maximize T.

1.5.2 Sources of Background Events

A large exposure is made much more effective if signal-mimicking background events are minimized in a $0\nu\beta\beta$-decay experiment. If, for example, one were to instrument a germanium detector enriched in ^{76}Ge with off-the-shelf components in a lab on the Earth's surface, they would have no hope of detecting $0\nu\beta\beta$ decay. Cosmic rays constantly bathe the surface of the Earth in radiation, and would produce many events in the detector, as well as generate radioactive isotopes like ^{68}Ge in the detector itself through cosmogenic activation. Because of this, all current leading $0\nu\beta\beta$-decay experiments are located in underground labs where the cosmic ray flux is completely shielded (except for a low rate of high-energy muons), and work very hard during the design and construction phases to ensure that all materials used in the detector are as radioactively clean as possible. The undertaking to source and assay clean materials can often be as significant as the construction and operation of the experiment itself [5].

In an underground lab, the detector is protected from cosmic rays and cosmogenic activation, but must still be shielded from the lab environment. Several long-lived radioactive isotopes are common in rock and metal, and can produce events in the detector at energies high enough to mimic the $0\nu\beta\beta$ signal. In particular, ^{238}U and ^{232}Th are abundant with half-lives on the order of or exceeding the age of the Earth, and can produce high-energy photons. In the ^{232}Th decay chain, ^{208}Tl produces a photon with an energy of 2614.5 keV and a Compton continuum that extends up to 2380 keV. Because of this peak in particular, it is advantageous to choose a $0\nu\beta\beta$-decay candidate isotope with a value of $Q_{\beta\beta}$ that is at least above 2380 keV. As we will see, two of the three currently most popular isotopes share this characteristic, with ^{76}Ge being the exception. Because germanium detectors have a much higher energy resolution than detectors made from ^{136}Xe or ^{130}Te (the other two popular isotopes) — and therefore are better able to distinguish the correct energy of $Q_{\beta\beta}$ — they are able to compensate for their higher sensitivity to environmental backgrounds. Because

of this, the lowest backgrounds for $0\nu\beta\beta$ decay when normalized by the energy resolution have been achieved by ^{76}Ge experiments [44] [45].

^{238}U and ^{232}Th are present at low levels in most metals, many other materials used to construct experiments (plastics, etc.), and generally in the lab environment. ^{222}Rn is a gaseous daughter of ^{238}U which is constantly emanated from the rock in any underground lab, and can be a major source of backgrounds. Although it has a half-life of less than 4 days, it decays to ^{210}Pb, which has a much longer half-life of 22.2 years. Immediately after decaying, the resulting ^{210}Pb atom is an ion, and can be attracted to charged surfaces (such as plastics used to instrument detectors). ^{210}Pb decays eventually to ^{206}Pb, passing through ^{210}Po on its way there which produces an alpha particle with an energy of 5.3 MeV, higher than any $0\nu\beta\beta$ isotope's $Q_{\beta\beta}$. Although they generally cannot penetrate more than a few microns, any alphas that do manage to get through to the sensitive region of a detector are often degraded in energy and can appear at or near $Q_{\beta\beta}$.

Although cosmogenic activation is negligible underground, materials used to construct $0\nu\beta\beta$-decay experiments typically are fabricated above ground, and experience some cosmogenic activation. In the case of an experiment using ^{76}Ge detectors, cosmogenic activation can produce small amounts of ^{68}Ge (HL = 271 days), which decays first to ^{68}Ga (HL = 68 minutes) and then to ^{68}Zn (stable). The decay of ^{68}Ga produces a β^+ (positron) with a maximum energy of 1.9 MeV. When one of the 511 keV photons produced from the subsequent annihilation of the positron deposits enough of its energy inside the same detector, it can exceed $Q_{\beta\beta}$ for ^{76}Ge (2039 keV), producing a background event. The other primary cosmogenic isotope of concern is ^{60}Co, easily produced in copper which is often used to construct and shield $0\nu\beta\beta$ detectors due to its low levels of other radioactive contaminants compared to other common structural metals like steel. ^{60}Co beta-decays with a half-life of 5.3 years to the stable isotope ^{60}Ni, and nearly always produces two photons at 1173 and 1332 keV. If these two photons are detected together, the sum of their energies (2506 keV) can be higher

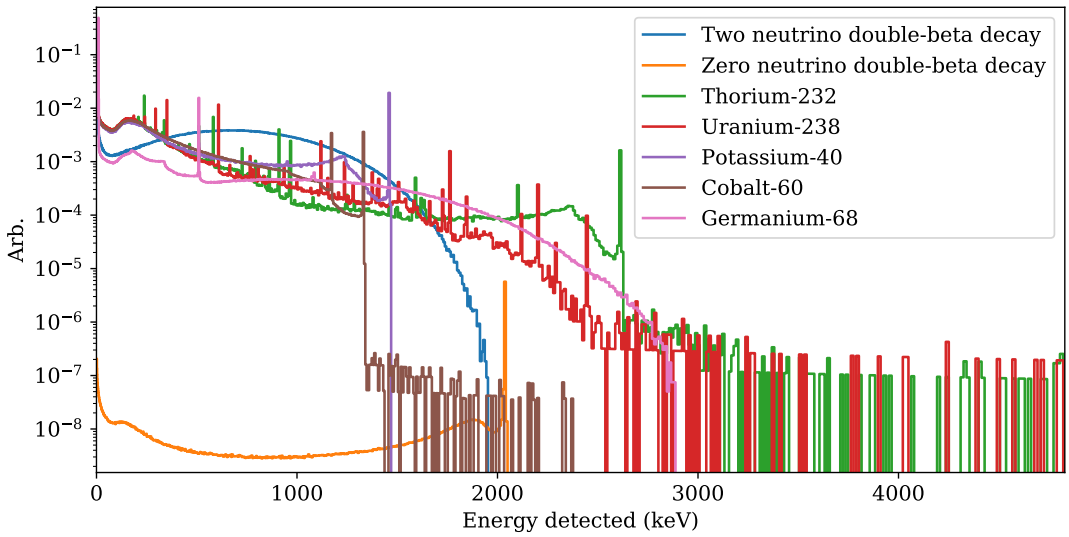

Figure 1.9: Shown are again the same spectra for $0\nu\beta\beta$ and $2\nu\beta\beta$ decay as in Figure 1.8, but this time with possible sources of background overlaid. All of these are simulations done with `MaGe` for the MAJORANA DEMONSTRATOR, and are scaled such that the sums of their bin values are 1, with the exception of the line for $0\nu\beta\beta$ decay which has been normalized to a relative intensity equal to the measurement of $2\nu\beta\beta$ decay and limit on $0\nu\beta\beta$ decay set by the GERDA experiment. ^{210}Pb decays were generated in the DEMONSTRATOR lead shield, ^{40}K, ^{238}U, and ^{232}Th decays were generated in the signal connectors, ^{60}Co decays were generated in the thermosyphon and shield copper, and ^{68}Ge decays were generated in the natural germanium detectors.

than $Q_{\beta\beta}$. ^{60}Co can also be produced in germanium, but since germanium is much further on the chart of nuclides from ^{60}Co than copper is, its activation rate to ^{60}Co is correspondingly lower.

Some additional processes can produce $0\nu\beta\beta$-decay mimicking events, but are likely to

be subdominant to sources already mentioned. The muon flux in a lab thousands of feet underground is quite small, but direct hits of the detectors still happen with some regularity. Therefore, $0\nu\beta\beta$-decay experiments are often outfitted with a muon veto system, and any muon events are removed from the analysis. Muons can also produce energetic neutrons in the shielding of the detector or the rock surrounding the experimental hall. Neutrons from the environment outside the shield can be effectively blocked with neutron-arresting material such as polyethlyene panels, and captured by a substance with a high cross-section for neutron capture such as boron. Neutrons produced in the shielding itself of course cannot be mitigated in this way. However, since they are created by a muon they can also be excluded by removing a period of time from the data after a muon detection sufficient to allow any neutrons generated to be captured or exit the system.

One final common isotope that usually must be accounted for is ^{40}K. ^{40}K is present in the natural environment with an abundance of 0.012% and a half-life of 1.2×10^9 years. Because potassium is an essential element for a wide variety of biological processes, it is pretty much unavoidable in an experiment built by humans. Luckily, ^{40}K decays are not capable of producing photons with an energies above 1461 keV, which is too low in energy to be a source of background for most $0\nu\beta\beta$-decay experiments. However, most $0\nu\beta\beta$-decay experiments are also sensitive to other novel physical processes that have signals lower in energy, so minimizing exposure to ^{40}K is worthwhile. Furthermore, many cleanliness protocols designed to eliminate ^{232}Th and ^{238}U from the lab environment will also help to reduce sources of ^{40}K.

1.5.3 Isotope Choices

There are quite a few possible candidate isotopes, but current experiments primarily use one of the following three isotopes: ^{136}Xe, ^{130}Te, and ^{76}Ge. Each of these isotopes excels in a particular experimental parameter, so the choice of isotope has a large impact on the overall

design of the experiment.

Being a noble gas, ^{136}Xe can be used in a double-beta decay experiment in either a liquid [46] or gas [47] phase, or be dissolved in another substance [48]. Xenon experiments in general are not able to match the energy resolution of germanium experiments, but they are easier to construct and operate with a large mass, as only a single volume needs to be instrumented and operated. It is also possible to continuously purify the xenon and achieve extremely low backgrounds. If a detector is massive enough, it can also be fiducialized, which can significantly reduce backgrounds from the containment vessel [49]. The most stringent limit on the process of $0\nu\beta\beta$ decay as of this writing is $T^{0\nu}_{1/2} = 1.07 \times 10^{26}$ yrs and comes from the ^{136}Xe experiment KamLAND-Zen [48]. The EXO-200 collaboration has also set competitive limits on $0\nu\beta\beta$ decay [46], and the NEXT experiment [47] is pioneering a gaseous ^{136}Xe approach that should have some sensitivity to the kinematics of any observed $0\nu\beta\beta$ decays, which would help to determine the physical mechanism of the process.

^{130}Te has the major advantage of a relatively high natural abundance of 34%. This means that a reasonably-sized detector can be built from natural tellurium, saving the cost of enrichment which can be a major expense, especially as $0\nu\beta\beta$-decay detectors approach the ton scale. The most sensitive tellurium experiment currently operating is the CUORE experiment at the Laboratori Nazionali del Gran Sasso in Italy, which published a lower limit on the half-life of $0\nu\beta\beta$ decay in ^{130}Te of $1.3 \times 10^2 5$ yrs (90% C.L.) in 2018 [50]. The SNO+ experiment is also planning to use ^{130}Te in their detector [51].

Finally, germanium detectors are a well established technology with the best energy resolution available, which greatly improves background rejection. Their major drawbacks are their relatively low $Q_{\beta\beta}$ of 2039 keV, the low abundance of the double-beta decay isotope (^{76}Ge) in natural germanium (~8%) which requires expensive isotopic enrichment, and the difficulty and cost in operating a large mass of germanium, since it must be fashioned into crystals no larger than a few kilograms each. The detector fabrication process is quite

expensive, and the loss of a single electronics channel can lead directly to a reduction in sensitive mass, as has been seen with the MAJORANA DEMONSTRATOR. In general, ^{76}Ge experiments are capable of reaching extremely low backgrounds, but have some trouble in maximizing sensitive exposure. The best sensitivity to neutrinoless double-beta decay is $T^{0\nu}_{1/2} = 5.8 \times 10^{25}$ yrs (90% C.L.) and comes from the ^{76}Ge experiment GERDA [44], while the MAJORANA DEMONSTRATOR has achieved a competitive limit of 2.7×10^{25} yrs (90% C.L.), and the best energy resolution for a $0\nu\beta\beta$-decay experiment[45]. The MAJORANA DEMONSTRATOR will be the focus of the rest of this thesis.

Chapter 2
THE MAJORANA DEMONSTRATOR

Neutrinoless double-beta decay is a rare, never-before-seen process. The sensitivity of an experiment designed to detect it is affected by a variety of factors (see Section 1.5), the most important of which are a large sensitive exposure to the process, and a minimal amount of signal-mimicking backgrounds. The MAJORANA DEMONSTRATOR was designed with three primary goals in mind: to search for $0\nu\beta\beta$-decay in ^{76}Ge (and in particular to test the claim of $0\nu\beta\beta$-decay detection made in [52]), to prove the feasibility of the successful construction and operation of a much larger ^{76}Ge $0\nu\beta\beta$-decay experiment, and to search for other beyond-the-standard-model physics [53] [54] [55].

The MAJORANA DEMONSTRATOR is a low-background array of approximately 44 kg of germanium detectors, approximately 30 kg of which are enriched to 88% in the double-beta decay isotope of ^{76}Ge. The DEMONSTRATOR is located at the 4850' level at the Sanford Underground Research Facility in Lead, SD [56]. It began taking data in 2015 and has been operating continuously (brief periods of downtime notwithstanding) since then. As of June 2019, the best limit on neutrinoless double-beta decay in ^{76}Ge set by the MAJORANA collaboration is 2.7×10^{25} yrs (90% CL) [45] with a median sensitivity of 4.8×10^{25} yrs (90% CL). Figures 2.1 and 2.2 show a cross-section of an early computer rendering of the experiment and a photo of the as-built array.

2.1 Design and Construction of the MAJORANA DEMONSTRATOR

As we saw in Section 1.5, the most important considerations in designing and building a successful $0\nu\beta\beta$-decay experiment are the achievement of a large senstive exposure and the

minimization of signal-mimicking backgrounds. Equations 1.9 and 1.10 show that the sensitivity of any experiment increases with $TN_{\beta\beta}\epsilon$ (the sensitive exposure) and b the background rate (in units of counts per unit of sensitive exposure). As was mentioned in Section 1.5.3, ^{76}Ge $0\nu\beta\beta$-decay experiments excel in the achievement of low backgrounds, in large part due to their extremely good energy resolution, which makes it easier to distinguish events happening at the correct energy from events happening at a nearby energy.

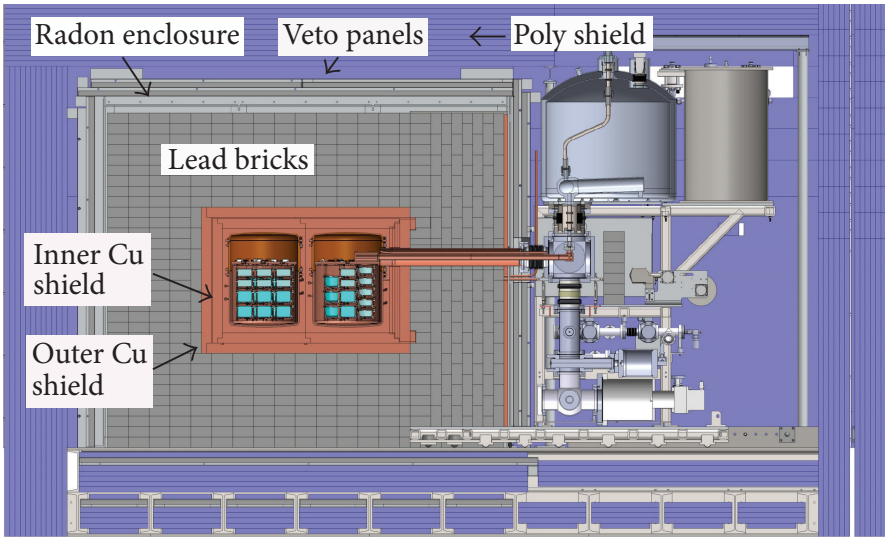

Figure 2.1: A CAD rendering of the Majorana Demonstrator design.

The Demonstrator is fielded as an array of high-purity germanium (HPGe) P-type point-contact detectors arranged into two ultra-clean underground electroformed copper (UGEFCu) vacuum cryostats. The detectors are mounted with UGEFCu, PTFE, and vespel components, as can be seen in Figure 2.2. The detectors themselves are arranged into strings of 3-5 detectors, and affixed to the bottom of a cold plate made from electroformed copper. Custom front-end boards, cables, and connectors were all fabricated by the collaboration and instrument each detector. The strings are then sealed into the UGEFCu vacuum ves-

Figure 2.2: A photo of module 1 under construction in the glove box. A scientist is visible tightening the tie rods that hold the strings in place to the cold plate, which is hidden behind the copper hoop. Photo and copyright by Matthew Kapust (SURF) and distributed under the Creative Commons license.

sels, which are inserted into the shield using a HovAir™ air-bearing table.

The shield is, by mass, comprised nearly entirely of lead bricks arranged to minimize shine paths through the shield. The total mass of lead bricks in the shield is approximately 49,000 kg. For comparison, an empty Boeing 737-800 weighs approximately 41,000 kg. Outside the

lead shielding is the sealed radon-exclusion box, which is constantly purged with boil-off from the liquid nitrogen used to cool the DEMONSTRATOR, and a neutron-arresting polyethylene layer with a borated inner layer designed for neutron capture. Outside of that are muon veto panels which reject signals from the approximately 5 muons/($m^2 \cdot d$) that reach the DEMONSTRATOR [57]. Virtually no radiogenic sources outside the lead shield are capable of creating events in the germanium detectors, but the lead shield itself is a possible source of ^{232}Th, ^{238}U, and ^{210}Pb. To mitigate the lead backgrounds, a 2-in thick layer of oxygen-free commercial copper (OFCu) sits directly inside the lead shield. This is the cleanest commercially available grade of copper, which is still not clean enough to be used for all of the copper needs of the DEMONSTRATOR. Inside the OFCu layer there is another 2-in thick layer of copper shielding, this time made from the ultra-clean UGEFCu, which provides extra shielding from trace amounts of ^{232}Th, ^{238}U, and ^{60}Co that might exist in the OFCu outer copper shield, as well as the lead-originating backgrounds.

Great care was taken during the fabrication and transportation of the enriched germanium detectors to minimize surface exposure and the cosmogenic backgrounds that result from it. A paper was recently published by the collaboration [4] which goes into detail about the procedures set up to ensure minimal cosmogenic activaiton of the detector material during fabrication, as well as the results of reprocessing of the excess material from the initial round of detector fabrication. The reprocessing enabled MAJORANA to produce an additional ~4 detectors (~4 kg) beyond what were made with standard techniques during the initial round of detector manufacturing. Since germanium enriched in ^{76}Ge is quite expensive, maximizing the yield from the original source of natural germanium is an important cost reduction measure (or alternatively, an important exposure maximization measure) that should be taken during any future large-scale ^{76}Ge $0\nu\beta\beta$-decay experiment. The success of this effort is visible in the results obtained in [55], which focuses on processes detectable at low energy (i.e. < 100 keV). The low backgrounds at low energies in the enriched germanium

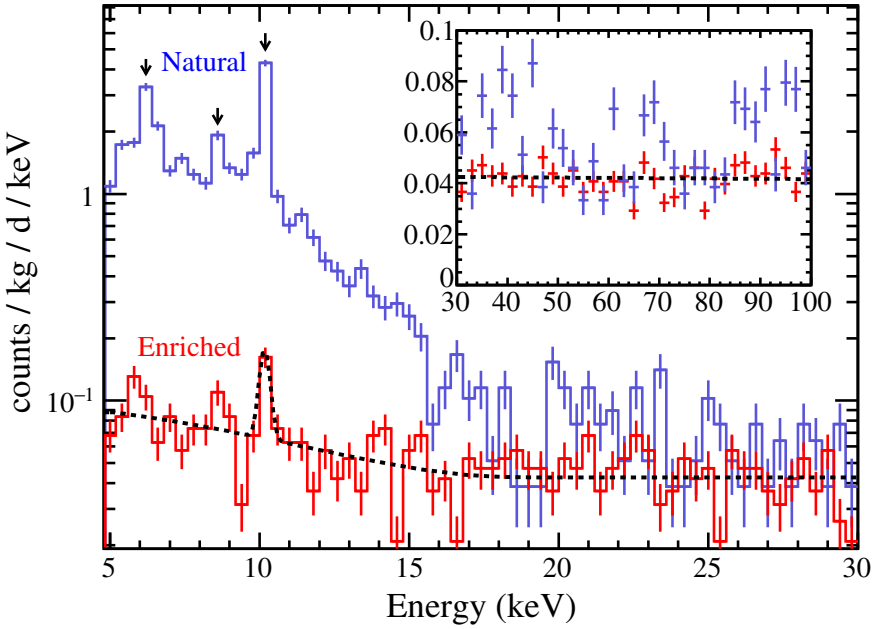

Figure 2.3: Energy spectra from 195 kg d of natural (blue) and 478 kg d of enriched (red) detector data. A fit of the background model (linear + tritium beta spectrum + ^{68}Ge K-shell) to the enriched spectrum is also shown (dotted black). The background rate and slope, along with the tritium and K-shell rate, were floated in the fit. The background fit χ^2/NDF is 75.7/85. Cosmogenic isotopes in the natural detectors produce peaks at 10.36 (^{68}Ge), 8.9 (^{65}Zn), and 6.5 keV (^{55}Fe) on top of a tritium beta decay continuum. The FWHM of the 10.4 keV peak is ~0.4keV. (Figure and caption from [55])

detectors are key in making these analyses feasible. Figure 2.3 is taken from [55] and shows the dramatic difference between the energy spectra of the enriched germanium and natural germanium detectors, which did not receive the same specialized handling processes as the enriched detectors.

2.2 The Comprehensive Assay Campaign for Radiogenic Backgrounds in Components Used to Build the MAJORANA DEMONSTRATOR

The MAJORANA DEMONSTRATOR underwent an extensive material selection and assay campaign prior to its construction [5] that is worth covering in some detail here, as it has a major influence on the construction of the background model of the as-built experiment. All components that were used to build the DEMONSTRATOR were directly assayed by the collaboration, using the methods of gamma-ray counting, Glow Discharge Mass Spectrometry (GDMS), Inductively Coupled Plasma Mass Spectrometry (ICP-MS), or Neutron Activation Analysis (NAA). A brief description of the different assay techniques and their associated uncertainties will follow.

2.2.1 Gamma-ray Counting

Radioactive contaminants in a material can be measured with a gamma-ray detector, in much the same way that the DEMONSTRATOR itself operates. The material to be assayed is placed inside a chamber near a high-resolution germanium detector with a known background spectrum, and the gamma-ray spectrum from the material is then obtained by subtracting the known background from the measured spectrum. This technique is non-destructive of the material assayed, so specific components measured could be used again in the DEMONSTRATOR itself. In the context of ^{238}U and ^{232}Th contamination, which are the two most worrisome potential contaminants, gamma-ray counting is sensitive directly to the parts of the ^{238}U and ^{232}Th chains that actually produce high-energy gammas (primarily ^{214}Bi and ^{208}Tl), so the assumption of secular equilibrium is not required to interpret the results. Unfortunately, gamma-ray counting is generally not as sensitivite as mass-spectrometry techniques like GDMS and ICP-MS, so it cannot be used for components with ultra-low concentrations of contaminants. Because of this limitation, gamma-ray counting was only used for a few of the components with higher expected activities, like the lead bricks or the cables and

Low-Mass Front-End (LMFE) components.

2.2.2 Glow Discharge Mass Spectrometry

In Glow Discharge Mass Spectrometry, the material to be assayed is placed in a low-pressure DC plasma discharge cell as the cathode, and plasma ions are accelerated towards its surface, sputtering atoms that can be analyzed with a mass spectrometer. Although this is a destructive measurement, sample preparation is relatively easy, and GDMS can detect concentrations of trace elements down to tens of parts-per-trillion (see Section 3.2.1 of [5]). Because it only samples atoms sputtered off of the surface of the material, GDMS cannot make measurements of bulk contamination, unless it is known that the surface contamination of a particular material is identical to its bulk contamination.

2.2.3 Inductively Coupled Plasma Mass Spectrometry

The technique of ICP-MS is the most complex of the techniques used by the MAJORANA collaboration, but is also the most sensitive to extremely low levels of trace elements. ICP-MS requires extensive sample preparation, including digestion of any solid samples with acids or bases, followed by aerosolization with (typically argon) gas (see Section 3.2.2 of [5] for more details). The digestion process limits the size of a sample that can be measured, but enables an extremely precise measurement of extremely low-level bulk contamination of the component. Because of its precision and sensitivity, ICP-MS was the most utilized by the MAJORANA collaboration of the measurement techniques presented in this section, and demonstrated sensitivities to U and Th of better than one part-per-trillion [5].

2.2.4 Neutron Activation Analysis

Materials that do not have any long-lived neutron activation products can be irradiated by a neutron beam, and then measured with a gamma detector after the short-lived neutron-

activation products have decayed away. This enables the detection of low levels of ^{238}U and ^{232}Th by looking for decays of the neutron-activation products of ^{239}Np and ^{233}Pa respectively. This technique is most useful for materials containing primarily hydrocarbons (like plastics), which are used as insulators in the DEMONSTRATOR. Plastic components that were assayed for the DEMONSTRATOR were first cleaned to remove any trace contamination of sodium or potassium, both of which can be activated to long-lived radioactive isotopes (^{24}Na and ^{42}K respectively). See Section 3.3 of [5] for more information on how this technique was used for the MAJORANA DEMONSTRATOR.

2.2.5 Results of the MAJORANA Assay Campaign

The full results of the campaign are presented in Table 3 of [5]. Tables 7 and 8 from [5] are included here as Tables 2.1 and 2.2.

Table 2.1 provides an overview of the results of the assay campaign, and Table 2.2 translates those measurements into predictions of background counts in the experiment. These tables include a column projecting the number of counts for the MAJORANA DEMONSTRATOR in units of counts per region-of-interest-ton-year. In these tables, the region of interest (defined in the glossary) was assumed to be 4 keV. The values in Table 2.2 were computed by simulating the detection efficiency for radiogenic backgrounds in all components of the experiment with the `MaGe` software, something that is described in detail in Section 3.1.

Of particular interest are the Low-Mass Front-Ends (LMFEs), which contain small amounts of materials that may contain sources of thorium (strong gamma line at 2614.5 keV) such as gold traces, or uranium (alpha emitter with several gamma lines above 2039 keV) such as silver epoxy and fused silica. The assay and simulation results indicate that these should be the primary contributors to the backgrounds seen by the DEMONSTRATOR, along with thorium- and uranium-chain backgrounds from the lead shield.

Measured levels of thorium and uranium in the underground electroformed copper in-

Material	Typical use	Decay chain	Achieved assay	
			μBq/kg	c/(ROI t yr)
Electroformed Cu	Inner Cu shield, Cryostat,	Th	0.06	0.15
	Coldplate, Thermal shield, Detector mounts	U	0.17	0.08
OFHC	Outer copper shield	Th	1.1	0.26
		U	1.25	0.03
Pb	Lead Shield	Th	5	0.26
		U	36	0.37
PTFE	Detector supports	Th	0.1	0.01
		U	<5	<0.01
Vespel	Coldplate supports,	Th	<12	<0.01
	Connectors	U	<1050	<0.4
Parylene	Cu coating,	Th	2150	0.27
	Cryostat seals	U	3110	0.09
Silica,	Front-end	Th	6530	0.32
Au, Epoxy	Electronics	U	10 570	0.28
Cu Wire,	Cables	Th	2.2	0.01
& FEP		U	145	0.08
Stainless	Service body	Th	13 000	<0.04
Steel		U	<5000	<0.03
Solder	Connectors	Th	210	0.13
Flux		U	335	0.06

Table 2.1: The summary of the contributions to the background based on the assay results given in [5], grouped by detector material. The background values assume that the radioactive chains are in equilibrium. (Table and caption from [5])

dicate that Th- and U-chain backgrounds from UGEFCu components are expected to contribute approximately equally with backgrounds from the commercial copper used to fabricate the outer copper shield. Considering that all of the commercial copper is itself shielded by 2 inches of electroformed copper shielding, and that all of the internal copper components (detector mounts, cryostat vessels, etc.) are fabricated from UGEFCu, this accomplishment was critical to the success of the DEMONSTRATOR and is a testament to the achievements in both materials fabrication and assay by the group that has developed and executed the procedure for producing the electroformed copper.

Background contribution	Rate c/(ROI t yr)
Electroformed Cu	0.23
OFHC Cu shielding	0.29
Pb Shielding	0.63
Cables and internal connectors	<0.38
Front Ends	0.6
U/Th within the Ge	<0.07
Plastics + Other	0.39
^{68}Ge, ^{60}Co within the ^{enr}Ge	0.07
^{60}Co within the Cu	0.09
External γ rays, (alpha,n) reactions	0.1
Rn and surface α emission	0.05
Ge, Cu, Pb (n,n'gamma) reactions	0.21
Ge(n,n') reactions	0.17
Ge(n,γ)	0.13
Direct μ passage	0.03
ν Induced background	<0.01
Total	<3.5

Table 2.2: The summary of all the backgrounds contributing to the DEMONSTRATOR, with radiogenic backgrounds grouped by detector component. The background values assume that the radioactive chains are in equilibrium. (Table and caption from [5])

2.3 Data Sets and Data Acquisition

The MAJORANA DEMONSTRATOR has been running since 2015, and has acquired 7 different named data sets in that time. The data sets are outlined in Table 2.3. Major changes to the detector configuration or data acquisition (DAQ) denote the data set boundaries. Specifically, the inner UGEFCu shield and some UGEFCu shielding in the cross arm tube were installed between DS0 and DS1, and module 2 was installed after DS2. DS3 and DS4 were acquired simultaneously but with completely separate DAQ systems, and the two modules were then joined for DS5. DS2 and DS6 have presumming of the digitized traces, which enables a longer sample of the RC discharge of the electronics to be recorded. This is designed to improve the DCR cut for degraded energy alpha particles (see Section 2.6.2).

The MAJORANA DEMONSTRATOR operates a statistical blinding scheme, with 75% of

data acquired not available for initial analysis. This allows analysts on the experiment to design and implement cuts to the data while mitigating the chance of overfitting. When the blinding scheme is enabled, 31 hours of data are acquired for open analysis, and then the subsequent 93 hours are blind. The blinding scheme was applied for DS2, DS5c, DS6a, and part of DS1. After an analysis has been completed and validated on open data, an application to unblind can be made to the collaboration. This work will only analyze the open data acquired through April 2018, as that is the most well-characterized set of runs.

2.3.1 Detector Signal Readout and Data Acquisition

The signals from the MAJORANA DEMONSTRATOR are read out with electronics designed according to the schematic shown in Figure 2.4. The first stage, the LMFE, contains a feedback resistor made from sputtered amorphous germanium, gold traces, and a JFET mounted to a fused silica board with low-background silver epoxy. The first and second stage amplifiers are located outside of the vacuum chamber to minimize potential sources of background, and the AC-coupled second stage output is digitized at 100 MHz with 14 bit ADC precision using GRETINA digitizers [58]. An onboard trapezoidal trigger ensures that only events crossing a specified threshold are written to disk.

Each detector is instrumented with two channels, a low-gain and a high-gain. The high-gain channel encompasses the energy range of the primary photon peak in the calibration source at 2615 keV, and saturates at a detector-dependent energy several hundred keV above that energy. The low-gain channel extends up to ~12 MeV, enabling sensitivity to most alpha particle interactions. Both channels are acquired and saved to disk (some occasional data acquisition errors notwithstanding), but in the final step of data processing only one channel is saved for each waveform. If the low-gain channel contains a good waveform, it is saved, while if it does not and there is a high-gain waveform available, it is saved instead.

Data Set	Start Date	Data Set Distinction	Enr. Ge Exposure (kg-yr)	Nat. Ge Exposure (kg-yr)
DS0	6/26/15	No Inner Cu Shield	1.13(02)	0.47(01)
DS1	12/31/15	Inner Cu Shield added	1.81(03)	0.173(004)
DS2	5/24/16	Pre-summing	0.291(004)	0.0292(0007)
DS3	8/25/16	M1 and M2 installed	1.01(01)	0.224(005)
DS4	8/25/16	M1 and M2 installed	0.280(004)	0.201(005)
DS5ab	10/13/16	Integrated DAQ	4.57(05)	2.33(04)
DS5c	3/17/17	Blind	0.479(006)	0.236(004)
DS6a	5/11/17	Pre-summing, blind	3.74(04)	1.40(02)
Total			13.31(16)	5.06(09)

Table 2.3: All data analyzed in this work. During data sets DS1, DS2, DS5c, and DS6a a statistical blinding scheme was implemented. The blinded data is not analyzed to produce this background model, but the model will be updated with the blinded data in the future. Some run/detector pairs were removed from this analysis due to intermittent periods of noise that appeared as events with energies below 65 keV. These additional cuts were applied in data sets DS0, DS1, DS3, DS4, and DS5ab. The exposures given in this table were computed by passing the list of run/detector combinations to exclude (identified by the additional cuts outlined in Section 2.3.2) as an argument list to the official MAJORANA exposure calculation code (`ds_livetime`), which accounts for uncertainty in the active mass, as well as all livetime related uncertainties. DS3 is the only data set with no blind data and no runs with high low-energy rates identified by the cuts from Section 2.3.2, and it agrees with the exposure presented in [45] as expected.

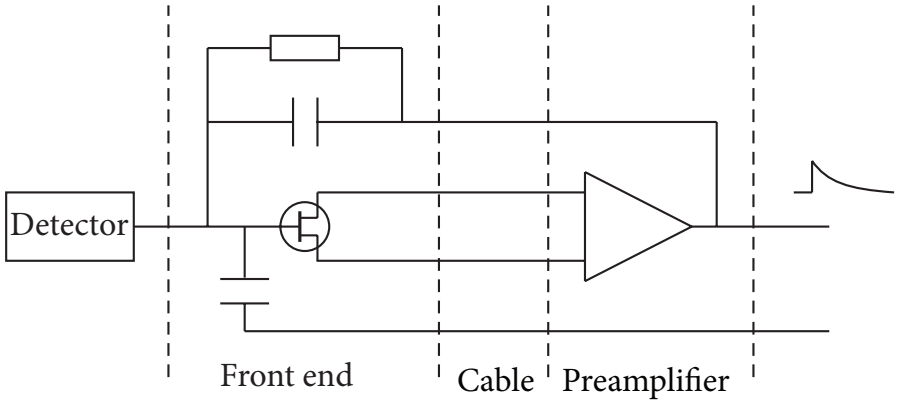

Figure 2.4: Schematic of the readout electronics for a detector in the MAJORANA DEMONSTRATOR. (Figure from [59])

Each detector[1] is instrumented with a pulser capacitively coupled to the readout, which is visible in Figure 2.4 as the bottom line connected to one of the capacitors in the front end. Because the event rate is so low (<1 Hz of physics data for the full array under normal background running), the pulsers are necessary to ensure that each detector's electronics readout is actually operating successfully between each energy detection.

Trapezoidal filters running on the GRETINA card FPGA watch each channel for excursions above the resting baseline level. When a detector crosses its threshold for event detection, its trace is recorded to a memory buffer on the digitizer. Each digitizer's buffer is read to disk once it is full, which means that events recorded by separate digizers are not necessarily recorded in time order in the raw detector output. An algorithm builds the raw output into "events" by time-ordering the waveforms, and placing event boundaries between successive waveforms separated by more than 4 μs. The event building is important because $0\nu\beta\beta$ decay will almost always produce a waveform in a single detector at a time, as is

[1]For four detectors the pulser is not functioning, and these detectors have a higher livetime uncertainty accordingly

described further in Section 2.7.

The muon veto panels mentioned in Section 2.1 have their own readout, but the raw output is saved to disk inline but asynchronously the readout from the germanium detectors. The digitizer cards for the germanium detectors and veto panels all share the same clock, so that they can be synchronized to precisely veto muon events. The data from the veto panels is merged with the germanium data during the event building described in the previous paragraph.

2.3.2 Data Cleaning

Some data cleaning cuts are applied to the data after it is acquired, which are outlined in [60]. These cuts are designed to remove non-physical waveforms and substandard runs from the data set. There are several tags for unphysical waveform shapes, such as when the ADC is saturated, and some timing-based tags to remove pulsers (used to estimate the livetime but not necessary for looking at energy spectra) and noise events associated with fills of the liquid nitrogen dewars for each module. The data cleaning cuts are estimated by the MAJORANA data cleaning group to remove fewer than 0.01% of physical waveforms.

Also, whenever the muon veto panels that surround the detector fire, the subsequent 1 second of data is discarded. Although this is not a data cleaning cut per se, this data is not useable for fitting the background model presented in this work because accurate simulations of cosmic muons and their products have not been produced for the as-built version of the DEMONSTRATOR. Adding this source of background into the model in the future would help improve the result.

In addition to the standard data cleaning cuts, I have implemented an additional algorithm to identify and remove transient periods of excess events which appear in the energy spectrum below 65 keV. Without these additional data cleaning cuts, the spectrum is completely un-analyzable below 65 keV in several of the data sets due to these noise events. An

example of a noise waveform that appears below 65 keV is given in Figure 2.5. The algorithm used to identify periods with these noise waveforms is designed to mimic the process of scanning for high rate runs by eye, but in a reproducable and unbiased way.

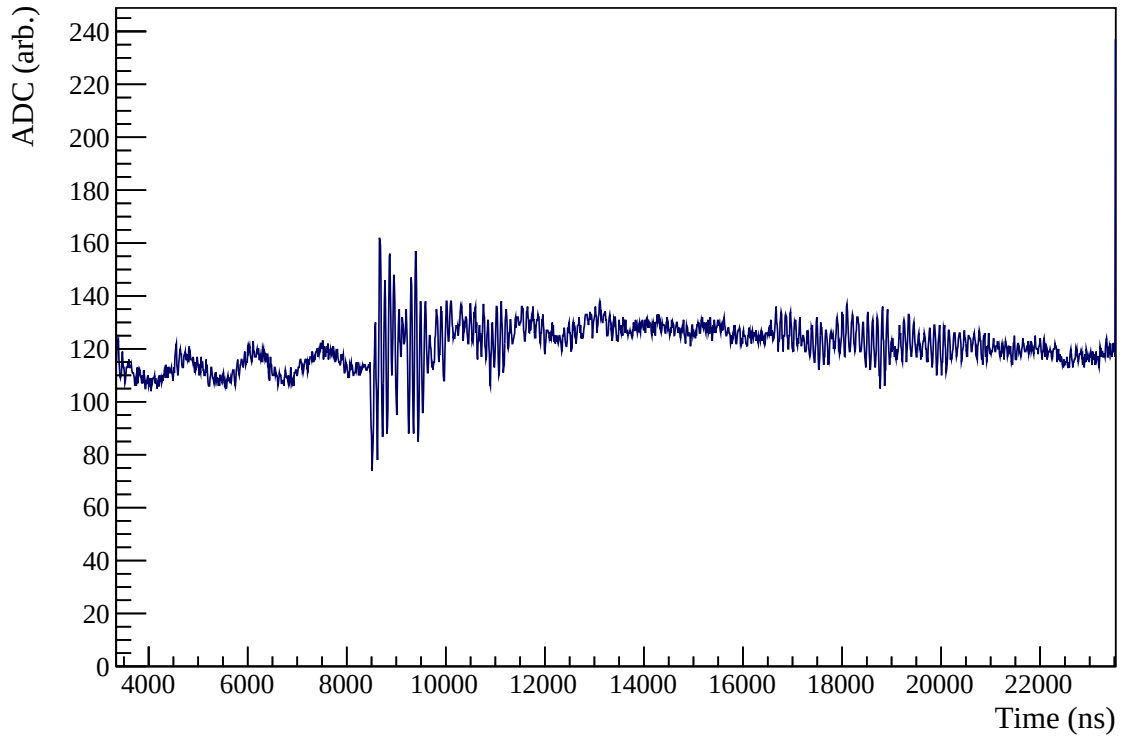

Figure 2.5: Example low-energy noise waveform from data set 5a. This waveform has a reconstructed energy of approximately 6 keV.

Each detector/data set combination is handled individually. Starting with the first run in the data set, the event rate below 65 keV in that detector is calculated. After n runs have been observed with a total number of counts k, a 90% confidence interval on the true rate is

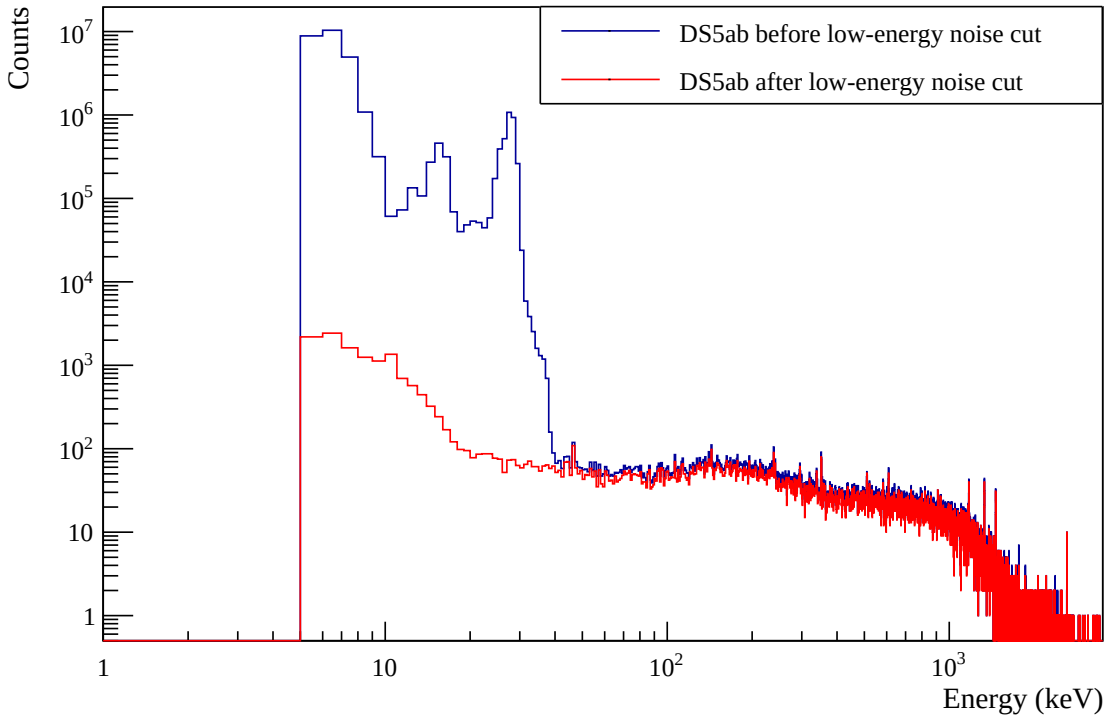

Figure 2.6: Before and after the excision of specific run-and-detector combinations from the DS5 runlist. A similar cut has been applied to all other datasets as well, but the effect is most dramatic for data set 5.

given by:

$$\left(\frac{\chi^2(0.05, 2k)}{2n}, \frac{\chi^2(0.95, 2k+2)}{2n}\right) \tag{2.1}$$

where $\chi^2(x, k)$ is the quantile function for a χ^2 distribution with k degrees of freedom [61]. The relationship between the cumulative distribution function of the Poisson and χ^2 distributions is used to derive this result. Using the upper limit of the 90% confidence interval as a conservative estimate for the true rate, the likelihood of the next run being sampled from the same distribution can be computed. If the next run has a high event rate with a likelihood

(as given by the Poisson CDF) less than 10^{-15}, it is rejected for the corresponding detector. This process is run both forwards and backwards over each detector/data set combination to catch instances where a detector has a high rate at the beginning of the data set. If a run is identified as having a high rate during either the forward or backwards pass, it is rejected for the detector under consideration. The bad runs identified in this manner are then removed from the detector's run list and the total number of counts in each detector is computed.

With the high rate runs removed, each detector should have approximately the same rate, unless one of them was experiencing a high rate in every single run, which would not have been detected by the previous step. If all the detectors have roughly the same rate, the fraction of the total number of counts occuring in each detector should be approximately binomially distributed. Using the Wald method [62] [63] for estimating the confidence interval of a binomial distribution with $z = 10$ (where z is related to the z-score of a standard normal distribution), I obtain a confidence interval on the fractional rate for each detector. If the lower bound of this interval does not include the average detector rate, that detector is completely excluded from the entire data set. The cut is designed to be extremely conservative and only remove runs or detectors where the event rate below 65 keV is clearly elevated above normal. Standard statistical fluctuations will not be removed by these cuts.

Figure 2.6 shows the effect of this cut for data sets 5a and 5b. In data set 5a, an extremely large number of noise events were recorded at low energies during certain periods of time and are responsible for approximately 99.9% of all events. These events were due to the presence of a ground loop, the removal of which signifies the end of data set 5a and beginning of data set 5b. When they are removed from the data set, the X-ray emitted by ^{68}Ge in the detectors becomes visible at 10.35 keV. This is an important line for constraining that contribution to the background model, as it is by far the most prominent feature of the ^{68}Ge+^{68}Ga spectrum (see Figure 2.7). The total enriched exposure removed from data set 5a by this process is 0.73 out of 3.45 kg-y, or about 21%. All other data sets had a much smaller fraction of their

exposure removed, and the total exposure during high-rate periods was 0.86 kg-y out of a total of 14.17 kg-y, or approximately 6%.

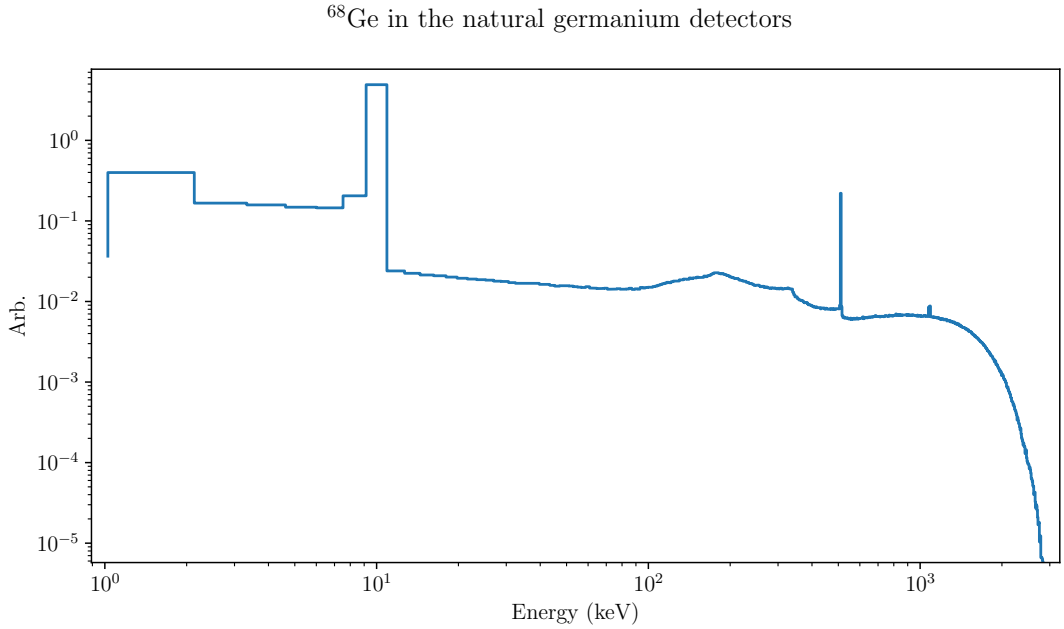

Figure 2.7: An energy spectrum simulated with `MaGe` and `GAT` of ^{68}Ge in the natural germanium detectors. If there are detectable levels of ^{68}Ge in the detectors, the most prominent feature will be the X-ray at 10.35 keV. This is a potentially worrisome background because the daughter of ^{68}Ge, ^{68}Ga, decays via $\beta+$ decay with an 88% branching ratio and an endpoint of 1900 keV. The emitted positron anihillates with a nearby electron and produces two 511 keV photons which can sum with the positron kinetic energy, potentially producing an event with an energy above $Q_{\beta\beta}$, and therefore a background for the $0\nu\beta\beta$-decay signal.

2.4 Sensitive Exposure Calculation

The exposure is a key component of the sensitivity, represented in Equation 1.8 as $TN_{\beta\beta}$ where T is the livetime of the experiment, and $N_{\beta\beta}$ is the number of atoms which can undergo

$0\nu\beta\beta$ decay. The factor following $N_{\beta\beta}$ in Equation 1.8 is ϵ the signal collection efficiency, and there is some variation between experiments on which term they use to account for different sources of loss in exposure. The MAJORANA collaboration typically uses $N_{\beta\beta}$ to refer to the total number of ^{76}Ge atoms in the fully-active regions of the DEMONSTRATOR detectors. Full charge collection is not possible for energy depositions occurring within some small depth of the surface of the detector, so this region is subtracted from the measured mass of the DEMONSTRATOR detectors to obtain the active mass. Other sources of loss of signal are contained in the ϵ term and will be described in subsequent sections.

2.4.1 Active Mass

The electrical contacts on the MAJORANA detectors consist of a point-contact made from implanted boron, and a large outer contact that covers most of the surface of the detector made from lithium drifted into the surface. The thickness of the point-contact is on the order of 1 μm, and the thickness of the outer contact is on the order of 1 mm. In both contacts, the presence of impurities increases the conductivity of the material to the point where it no longer functions as a semiconductor, but rather as a conductor. Charge that is deposited by particles that interact with the detector in the conductive regions is not fully collected.

The thicknesses of both contacts are not necessarily the same for all detectors, and the outer dead-layer is in principle not that difficult to measure. Before delivery of each enriched detector, the manufacturer (ORTEC) measured the thickness of the lithium outer contact. This measurement is typically done with a ^{133}Ba source, which produces two low-energy photons, the detected intensity ratio of which is sensitive to the thickness of the dead-layer. These measurements are used to apply a dead-layer effect specific to each enriched detector. The detectors made from natural germanium do not each have good dead-layer thickness measurements, but instead share a single measurement. The uncertainty on the dead-layer thickness measurement varies from detector to detector, but is typically about 15%. The

measured dead-layer thickensses are used with a geometric model of the detectors to estimate the fraction of the detector volume contained in the dead regions.

Between the point-contacts is a passivated surface that insulates the two contacts from each other. The thickness of the dead layer associated with the passivation is not very well characterized, but is certainly not thicker than the lithium dead layer, and likely much thinner. The Li-contact dead region therefore comprises the large majority of the total dead region for each detector, as it is significantly thicker than the point-contact dead layer and covers most of the surface of each detector. The fraction of the total mass that is active is then approximately 90% $\pm$ 1%. The mass used to calculate the reported exposure is the measured mass of the enriched germanium detectors multiplied by this active fraction. The uncertainty in the active mass dominates the total uncertainty in the reported limit on $0\nu\beta\beta$ decay.

To convert the active mass into a number of ^{76}Ge atoms, the isotopic abundance of ^{76}Ge in the detectors must be computed. The natural detectors contain the natural abundance of ^{76}Ge, which is 7.5%, while the enriched detectors have been found to be composed of 88% ^{76}Ge[64]. This fraction in combination with the known atomic mass of germanium enables a calculation of the total number of ^{76}Ge atoms in the DEMONSTRATOR. Full details for the active mass calculation can be found in [65] [66].

2.4.2 Livetime

To compute the livetime T, the MAJORANA livetime working group has produced a code called `ds_livetime` that calculates the total livetime and uncertainties for each dataset, given a list of runs. A full documentation of the calculation is presented in [67]. The livetime is calculated by summing over all recorded runs and then subtracting for times that are vetoed in the final data set. Specifically, events occurring up to one second after a detection by the muon veto system are vetoed, and events that occur during a fill of the liquid nitrogen

system are also vetoed. The liquid nitrogen fills occur approximately every 36 hours and last for about 30 minutes. Finally, a short deadtime occurs in each channel after a pulse is digitized, which is also accounted for by the livetime code [45]. This short deadtime can also occur after a negative-going signal, even though the digitizers are set to only trigger on positive-going signals [67]. This is due to an error in the digitizer firmware, and is accounted for in `ds_livetime`.

2.5 Energy Estimation and Calibration

A more detailed explanation of the energy estimation and calibration procedures used in the MAJORANA DEMONSTRATOR is provided in [45]. Only a brief overview of the process will be presented here, with a focus on sources of uncertainty most relevant to the background model.

2.5.1 Energy Estimation

The energy of a waveform produced by a MAJORANA DEMONSTRATOR digitizer is estimated using a trapezoidal filter with an extra charge-trapping correction. A charge cloud created by an energy deposition that drifts through the detector will lose some of its charge to trapping sites that release their charge with a long time constant. This process is modeled as an additional exponential term in the tail of the waveform, with the combination of this additional term and the decay from the electronics system having an effective time constant of:

$$\frac{1}{\tau} = \frac{1}{\tau_{\mathrm{RC}}} - \frac{1}{\tau_{\mathrm{CT}}} \tag{2.2}$$

A fast trapezoidal filter (1 μs rise time and 1.5 μs flat-top time) identifies the beginning of the waveform (t_0), and the energy is estimated by selecting a fixed point on the output of a slower trapezoidal filter (4 μs rise time and 2.5 μs flat-top time) 0.5 μs from the end of the flat-top of the slow filter, relative to t_0. The time constant for the charge trapping

correction τ_{CT} is found by minimizing the width of the 2615 keV peak produced by the ^{228}Th calibration source, and is typically approximately 233 μs.

Digitizer Non-linearities

The digitizers used in by the MAJORANA collaboration show significant non-linearities in their response to energy depositions. The primary non-linearity is card- and channel-specific, and resembles a sawtooth when displayed as a function of energy, as can be seen in in Figure 2.8. This non-linearity has been measured for each digitizer channel and corrected for by the collaboration, leading to a reduction in this source of uncertainty from 0.8 keV to 0.1 keV.

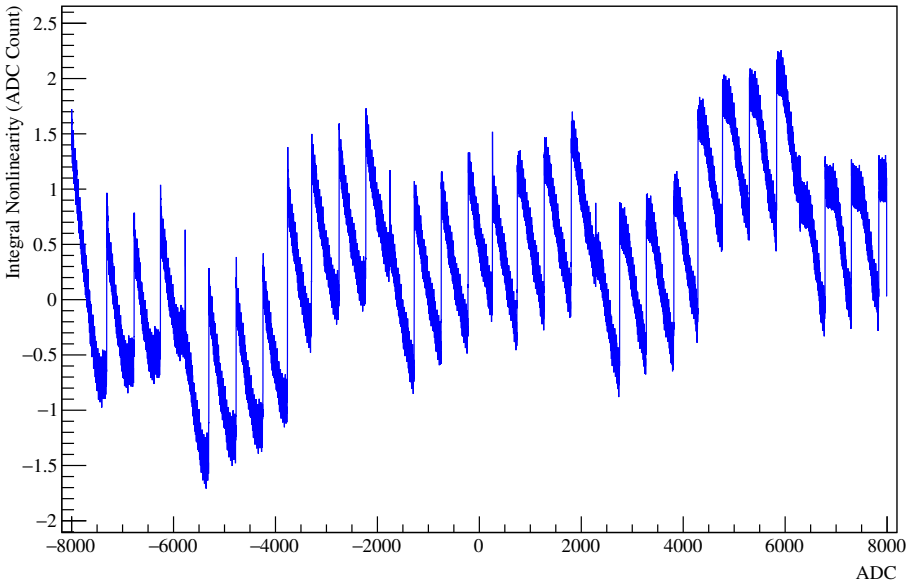

Figure 2.8: An example of the non-linearity of the response for an arbitrary MAJORANA DEMONSTRATOR digitizer channel. Although the maximum error does not exceed 2 ADC units, this can result in an error of 0.8 keV at $Q_{\beta\beta}$ (2039 keV), which is a significant fraction of the achieved FWHM of 2.5 keV at the same energy. (Figure from [45]).

An additional source of global non-linearity affecting all channels equally is present in the MAJORANA data. It was explained by Guinn [68] and can lead to an error in the estimated energy that is as high as 0.5 keV in some detectors below 200 keV. The coarse binning used in this analysis makes the background fits mostly insensitive to this source of bias and so it has been neglected (this will be further motivated in Chapter 5). An update to the primary MAJORANA energy estimator is in progress to remove this bias for future analyses.

2.5.2 Energy Calibration and Detector Resolution

Since each detector is manufactured separately, they all can have different sizes, shapes, and impurity gradients. These parameters all affect the response of a detector to energy depositions, so every detector comprising the DEMONSTRATOR has a distinct set of detector response function parameters. A relatively simple model of the response (or resolution) function that has been used for decades in the germanium detector community is employed by the MAJORANA collaboration. It is characterized as the sum of a Gaussian and an Exponentially Modified Gaussian with a low-energy tail. The functional form is shown below:

$$R(E,\hat{E}) = \frac{1-f(\hat{E})}{\sqrt{2\pi\sigma(\hat{E})}} e^{-\frac{(E-\mu(\hat{E}))^2}{2\sigma(\hat{E})^2}} + \frac{f(\hat{E})}{2\tau(\hat{E})} e^{\frac{1}{2\tau(\hat{E})}\left(2E-\frac{\sigma(\hat{E})^2}{\tau(\hat{E})}-2\mu(\hat{E})\right)} \operatorname{erfc}\left(\frac{E-\frac{\sigma(\hat{E})^2}{\tau(\hat{E})}-\mu(\hat{E})}{\sqrt{2}\sigma(\hat{E})}\right) \tag{2.3}$$

Here, $\hat{E}$ represents the true energy desposited, while E represents the energy estimated from the digitized waveform. f is the fraction of events that are described by the ExGauss part of the resolution function, with $1-f$ being described by the Gaussian part. The Gaussian and ExGaussian distributions are described by μ, representing an offset to the correct energy which is equal to $\hat{E}$ if a detector is calibrated perfectly, σ, representing symmetric contributions to the response function width, and τ, characterizing the width of the low-

energy tail, due mostly to charge trapping in the detectors. A high-energy tail is also often included in a germanium detector response function, but it was not necessary to accurately describe the measured detector response, and was not implemented. The parameters f, μ, σ, and τ are all characterized by hyperparameters that are functions of the true energy $\hat{E}$. They are estimated by performing a simultaneous fit to multiple peaks across the energy calibration spectrum. Their functional forms are:

$$f(\hat{E}) = a_f \qquad \mu(\hat{E}) = a_\mu + b_\mu \hat{E} \qquad \sigma(\hat{E}) = \sqrt{a_\sigma + b_\sigma \hat{E} + c_\sigma \hat{E}^2} \qquad \tau(\hat{E}) = a_\tau + b_\tau \hat{E} \quad (2.4)$$

The fraction of events experiencing significant charge trapping (and ending up in the low-energy tail) is approximately constant in energy, since the probability of charge trapping depends on the location where the energy is deposited in the detector, which does not have a strong dependence on energy for most types of interactions. Therefore, $f(\hat{E})$ is given by a constant. The fraction of energy trapped is also approximately constant in energy, leading to a linear model for the absolute amount of charge trapped as a function of energy which is given by $\tau(\hat{E})$. The energy calibration (given by $\mu(\hat{E})$) is linear since the amount of charge collected is proportional to the energy of the interaction. The expression for the gaussian width $\sigma(\hat{E})$ contains terms to account for electronic noise, Fano noise, and charge trapping respectively.

The Majorana Demonstrator detectors are periodically calibrated with a ^{228}Th source, the process of which is described in detail in [69]. Each detector is separately calibrated by performing a fit of the function from Equation 2.3 to a series of peaks in the calibration data. The process of fitting the peaks is described in Section 2.5.2. The true calibration drifts between calibration measurements, introducing a source of uncertainty into the estimated energy. The effect is not large, but does increase the peak width by approximately 5%, according to [70]. To get an estimate of the peak-shape hyperparameters for an entire data set, all calibration runs from that data set are summed together, enabling a fit to a

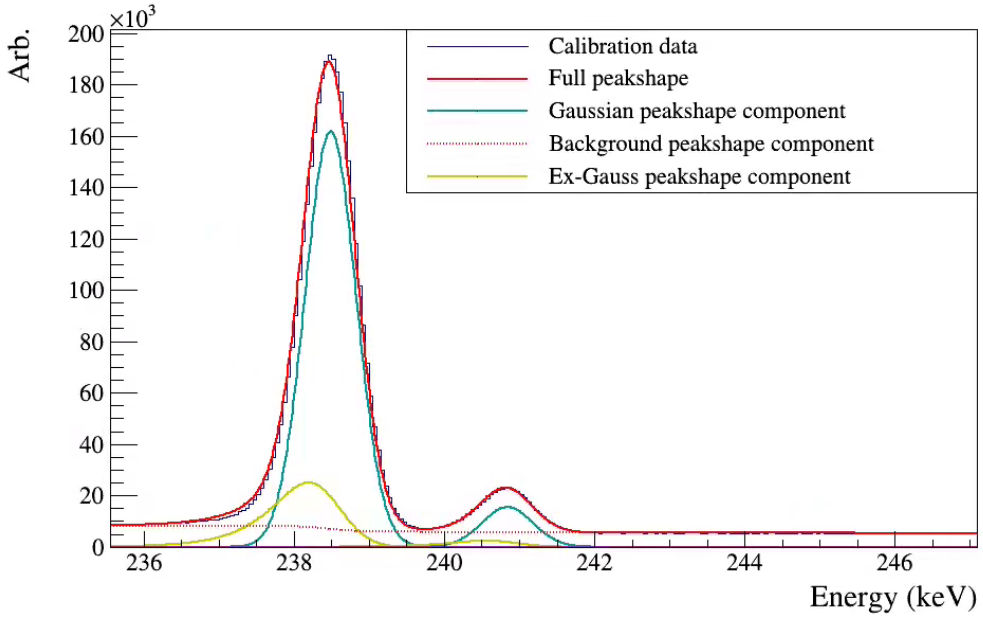

Figure 2.9: The peaks shown are 238 keV and 240 keV photons produced by the ^{228}Th calibration source. The peak-shape function is a Gaussian with a low-energy exponentially-modified Gaussian tail. This peak shape is placed on top of a quadratic background plus a step function which accounts for forward scattering of particles before they reach the detector. The parameters of the various components of the peak shape are described by hyperparameters as a function of detected particle energy.

higher number of peaks which significantly reduces residual nonlinearities and uncertainties in the peak-shape hyperparameters.

Multi-peak Fitting

The sophisticated algorithm used to fit the hyperparameters in Equation 2.4 to many peaks in a single spectrum simultaneously was developed by my collaborator Ian Guinn. This algorithm was used to precisely measure the peak-shape for each detector. This fitter requires

a high-fidelity sampling of the energy spectrum, which necessitates a continuous run with the ^{228}Th calibration source over many hours if a fit to individual detectors is desired. If a fit to just the aggregate array spectrum is desired, sufficient statistics can be obtained in only 1-2 hours. At least once per dataset, data is taken with the ^{228}Th calibration source for a period of time sufficient to characterize the peak-shape functions of all operating detectors, using the fitter developed by Guinn. This enables the precise modeling of the most important spectral features to a high degree of precision. Shorter calibration runs are taken every week to monitor the array for any significant changes in detector response. The peak-shape parameters are generally stable for a given detector in a given dataset, but can change between datasets since often there is some sort of change in the hardware configuration between datasets (see Table 2.3).

To fully model the shape of an arbitrary photon peak in the calibration spectrum, the detector resolution function is added to a heuristic background model that includes a step function to approximate energy lost between emission and detection of the photon, and a quadratic function to approximate background interactions coming from other sources. Shown in Figure 2.9 is a fit using Guinn's fitter to two peaks in the ^{228}Th spectrum.

2.6 Pulse-shape Analysis

After the data cleaning cuts from Section 2.3.2 are applied, several cuts based on the shape of the acquired pulse help remove additional backgrounds. These cuts are critical in enabling MAJORANA to achieve competitive backgrounds, reducing the background rate near the $Q_{\beta\beta}$ region of interest by more than a factor of 10 (see Figure 2.17). The A versus E parameter tags multi-site events in the detectors, and the delayed charge recovery (DCR) parameter tags degraded-energy alpha particles.

2.6.1 A versus E (AvsE)

When a particle interacts with a germanium detector, it typically creates through ionization a number of electron/hole pairs that is proportional to the amount of energy lost in the interaction. The electrons and holes, being oppositely charged, then drift in the electric field to opposite ends of the detector. As they drift, they drive a current through the signal readout circuit, which charges the feedback capacitor, the voltage of which is read out by a digitizer card. The strength of the signal created is proportional to the amount of charge that is drifting and the change in the weighting potential (see Figure 2.10) at the location of the charge. In point-contact detectors the weighting potential is strongly peaked near the point contact, and therefore most of the signal is generated when charges are moving near the point contact.

Because the signal from an energy deposition is mostly generated at the very end of the charge cloud drift, the detectors in the DEMONSTRATOR are able to distinguish multiple energy depositions made by the same particle if they are sufficiently spatially separated. The spatial resolving power varies from detector to detector, but in general energy depositions separated by more than 1 mm are distinguishable. In Figure 2.10 the isochrones of the charge drift paths are shown in white. Points along a given line have identical drift times to collection at the point contact, and consequently energy depositions made along the same isochrone are not resolveable.

This resolving power enables MAJORANA to effectively reject events that deposit charge in multiple locations in a single detector. Because $0\nu\beta\beta$ decay involves only the emission of two electrons which travel ~1 mm, it is a single-site event in the MAJORANA detectors. A small fraction of the time, one of the electrons will produce bremsstrahlung radiation, which either escapes the detector (lowering the detected energy of the event out of the region of interest) or is deposited elsewhere in the detector, giving a multi-site event. Background radiation at that energy is primarily composed of Compton scatters from high-energy photons, which are

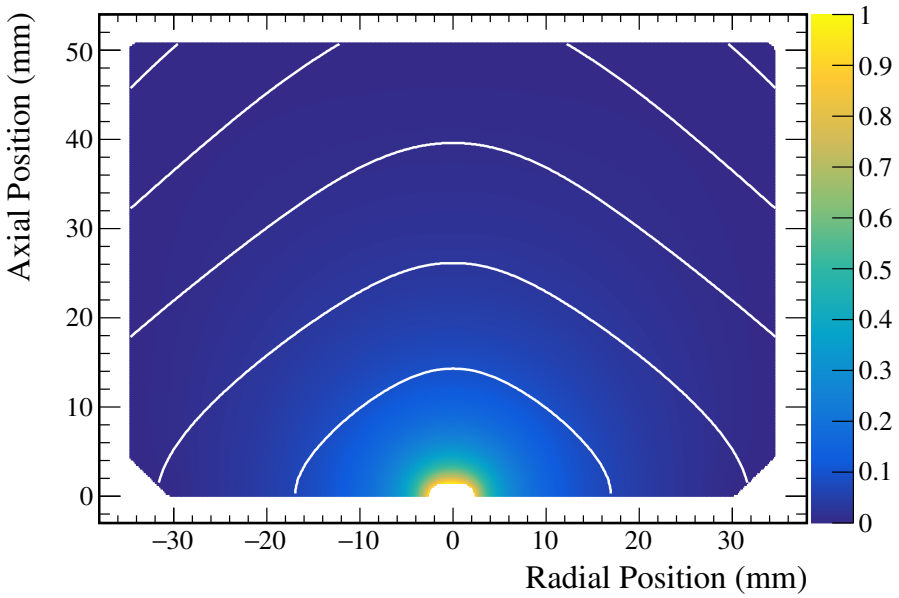

Figure 2.10: The value of the weighting potential for a typical MAJORANA enriched PPC detector is indicated by the color scale. The weighting potential is relatively low in the bulk of the crystal, but quite strong near the point contact at the bottom center. Lines of equal drift time, separated by 200 ns, are indicated by the white curves. (Figure and caption from [45])

much more frequently multi-site. Although the scattering length of photons in germanium at 2615 keV is approximately 5 cm [71], the diameter of a MAJORANA crystal is 5-10 cm, so the chance of multiple scatters is reasonably high. Furthermore, if a 2615 keV photon scatters once in a detector and deposits an energy near $Q_{\beta\beta}$ it will be left with an energy of approximately 600 keV or less. At that energy, the scattering lenth is only 2.5cm, so the chance of multiple scatters in the same detector is higher yet.

A versus E (AvsE) is the name of the technique that is used by MAJORANA to tag these multi-site events, with A standing for the maximum Amplitude of the current pulse, and E

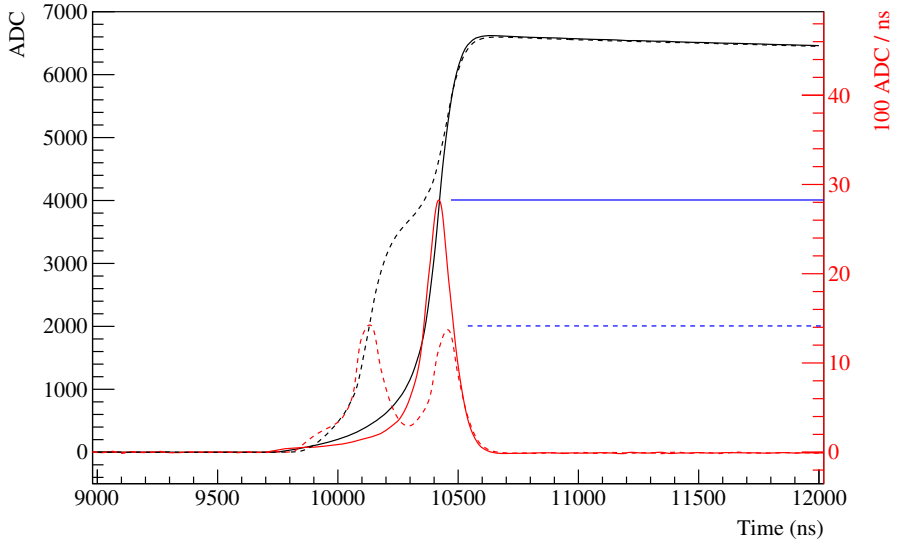

Figure 2.11: Shown in black are example single-site (solid) and multi-site (dashed) events from the 2615 keV ^{208}Tl peak from calibration data for an enriched PPC detector. The current waveforms are shown in red with blue horizontal lines indicating the maximum current. While the amplitudes of the voltage waveforms are the same, the maximum current amplitude is significantly lower for multi-site events. (Figure and caption from [45])

the Energy of the waveform. It is derived from a related technique called A/E developed by the GERDA collaboration which is conceptually very similar. As can be seen in Figure 2.11, two waveforms, one multi-site and one single-site, that share the same energy will have different maximum current amplitudes, unless the energy depositions from the multi-site event lie on the same isochrone. GERDA used a tuned cut on the ratio of A and E to reject multi-site waveforms, which was initially the same method used by MAJORANA. However, MAJORANA has found that A/E does not have good performance at low energies due to the 1/E behavior of the parameter. Instead, we essentially fit a quadratic function to an A versus E relationship, subtract that function from each event's A, and cut events that fail a tuned

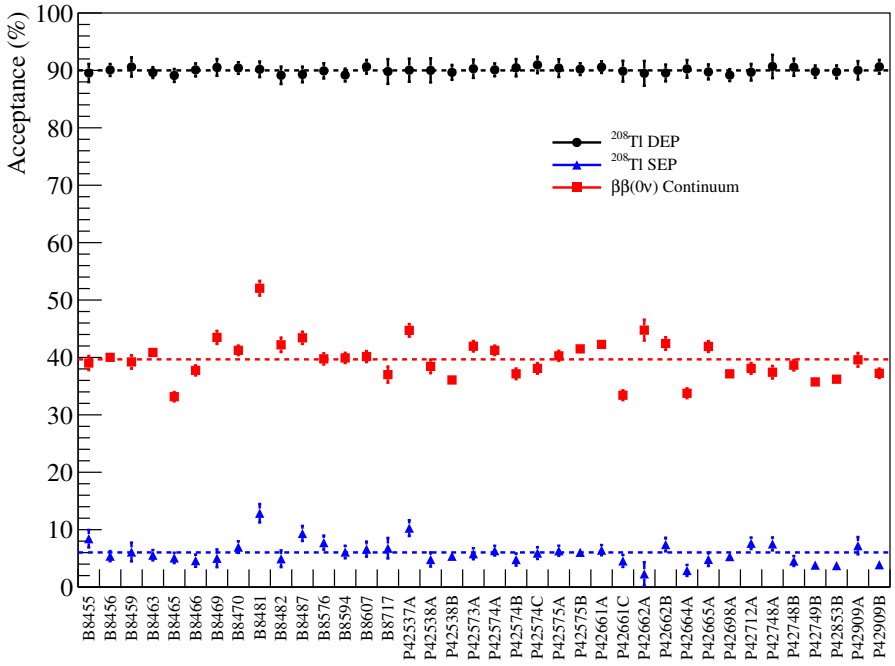

Figure 2.12: The acceptance for each detector in DS6a calibration data for events from the 1593 keV double-escape peak and 2104 keV single-escape peak (see Section 2.6.1 for definition) of the 2615 keV ^{208}Tl decay are shown in black and blue respectively. Shown in red is the acceptance of Compton scattering events from the calibration source with energy in a 100-keV-wide window centered on $Q_{\beta\beta}$ (2039 keV). The errors shown are statistical only, and the horizontal lines indicate the mean value for all calibrated detectors, including natural detectors. The detector serial numbers are shown as the horizontal axis labels with natural detectors grouped on the left and enriched detectors on the right (serial numbers beginning with 'B' and 'P' respectively). Although the detector B8481 has abnormally high acceptance for events outside the double-escape peak, it is a natural detector which is not included in the background spectrum, except for the purposes of rejecting multiple-detector events. (Figure and caption from [45])

threshold. This reduces the chance of Type I error at low energies (i.e. labeling single-site waveforms as multi-site) at the expense of Type II error. We believe this is appropriate because the Type II error is easier to model (as the cut losing efficiency at low energy), and maintains statistics at low energy instead of rejecting most events. The technique used by the MAJORANA collaboration is explained in detail in [72].

The A versus E parameter is tuned using its performance on the double-escape peak of the ^{208}Tl line at 2615 keV from our ^{228}Th calibration source, and the sensitivity of the cut to multi-site events is approximated by computing its effectiveness on the single-escape peak of that same photon line. The single- and double-escape peaks are produced when a photon from the 2615 keV line creates an electron-positron pair and one or two of the resultant pair of 511 keV photons that are produced from the annihilation of the positron escape detection in that detector. Because the double-escape peak necessarily involves just a single interaction with two betas in the detector (similar to $0\nu\beta\beta$ decay), it is dominated by single-site events and is a signal proxy. And because the single-escape peak necessarily involves two interactions, it is dominated by multi-site events which we reject, and thus serves as a sensitive performance measure. Ultimately we care most about the rejection factor for ^{208}Tl Compton continuum events in the vicinity of $Q_{\beta\beta}$, as our background model indicates that this is the dominant background for $0\nu\beta\beta$ decay. Figure 2.12 shows the calibration and performance of the A versus E technique using these two proxys. The cut is placed on the A versus E parameter to retain 90% of the DEP, typically rejects >90% of events in the SEP, and typically rejects about 40% of events in the Compton continuum of the 2615 keV photon peak near $Q_{\beta\beta}$.

The uncertainty on the efficiency of the AvsE cut to retain signal events has been estimated for the region of the energy spectrum near $Q_{\beta\beta}$, and has been found to be approximately 3.5 % (i.e. the efficiency is approximately (90 $\pm$ 3.5) %). The energy dependence of the cut efficiency uncertainty is weak but is still under evaluation. This is one of the reasons

that application of this cut is used only as a cross-check in this analysis.

2.6.2 Delayed Charge Recovery

The lithium contact of the MAJORANA detectors is approximately 1 mm thick, and varies by ~15% from detector to detector. This is thick enough that if an alpha particle impacts the surface of the detector on the lithium contact, it will deposit all of its energy in the dead region and not be detected (see Section 2.4.1 for a detailed description of the lithium dead-layer). The lithium contact covers the entire surface of an enriched germanium detector, except for the side where the point contact is implanted (i.e. ~85% of the detector surface). In the enriched detectors, most of the face with the point contact is covered by a passivation layer to insulate the high-voltage contact from the point contact. The passivation affects the charge collection near that surface in a way that is not very well characterized, but the thickness of the inactive region is much smaller than that of the lithium contact, less than 1 micron instead of approximately 1 millimeter. Alpha particles incident on the passivated surface can penetrate into the active region of the detector and be detected, and can be degraded in energy down into the region of interest around $Q_{\beta\beta}$. In fact, after applying data cleaning and run selection cuts, these degraded alpha particles are the dominant source of background at $Q_{\beta\beta}$ by far, as is visible in Figure 2.13.

The TUBE Detector

To better understand the response of MAJORANA-style germanium detectors to alpha particles, a prototype MAJORANA detector, made from natural germanium but of the same design as the detectors fielded in the DEMONSTRATOR, has been instrumented with a scanning alpha source at the Technical University of Munich. The alpha source is collimated, and can be directed to impact a point on the passivated surface of the detector over a large fraction of the total area. This detector/scanner setup, known as the TUM Upside-down

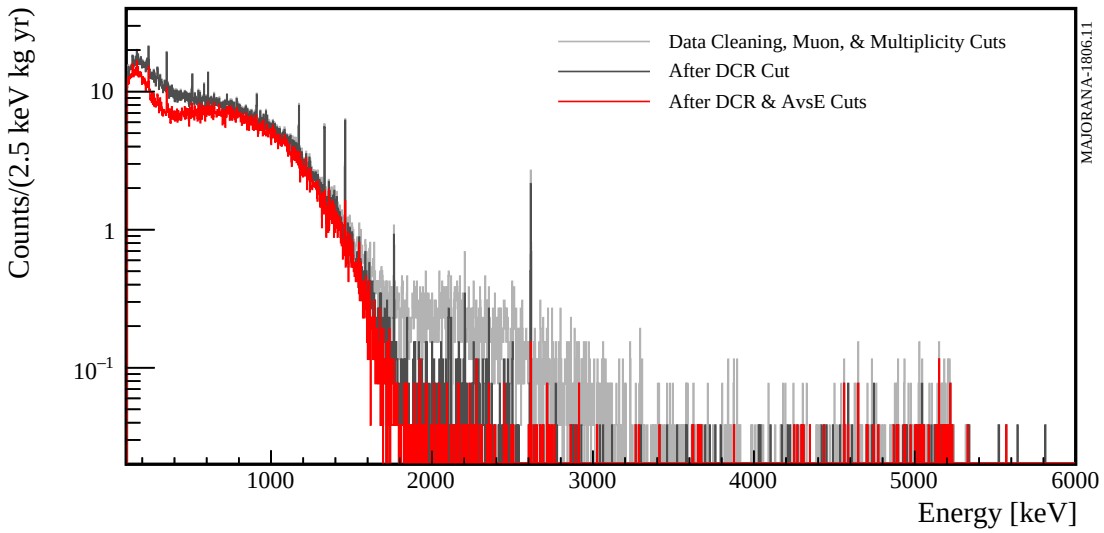

Figure 2.13: Near $Q_{\beta\beta}$, the detected energy spectrum is greatly reduced by the application of the DCR and A vs. E cuts.

BEGe scanner (TUBE), was the focus of the PhD thesis of Julieta Gruszko [73]. Her results illuminated the physical mechanism that drives the degredation of energy for alpha particles incident on the passivated surface of an MAJORANA-style detector.

When an alpha particle penetrates the passivated surface, some fraction of the holes that are created are trapped by trapping centers in that region. The origin of the trapping centers is not yet understood, but they could be arising from crystal defects or impurities created during the passivation process. The re-release time of these holes is on the order of at least a few microseconds, which is short enough to see the collection of additional delayed charge during the RC decay of the primary pulse in the digitized waveforms. The DCR parameter is found by subtracting the average value of the waveform at the very end of the digitization window from the average value of the waveform around the point where it has fallen 97% below its maximum value. Figure 2.14 compares a normal waveform with one tagged by the

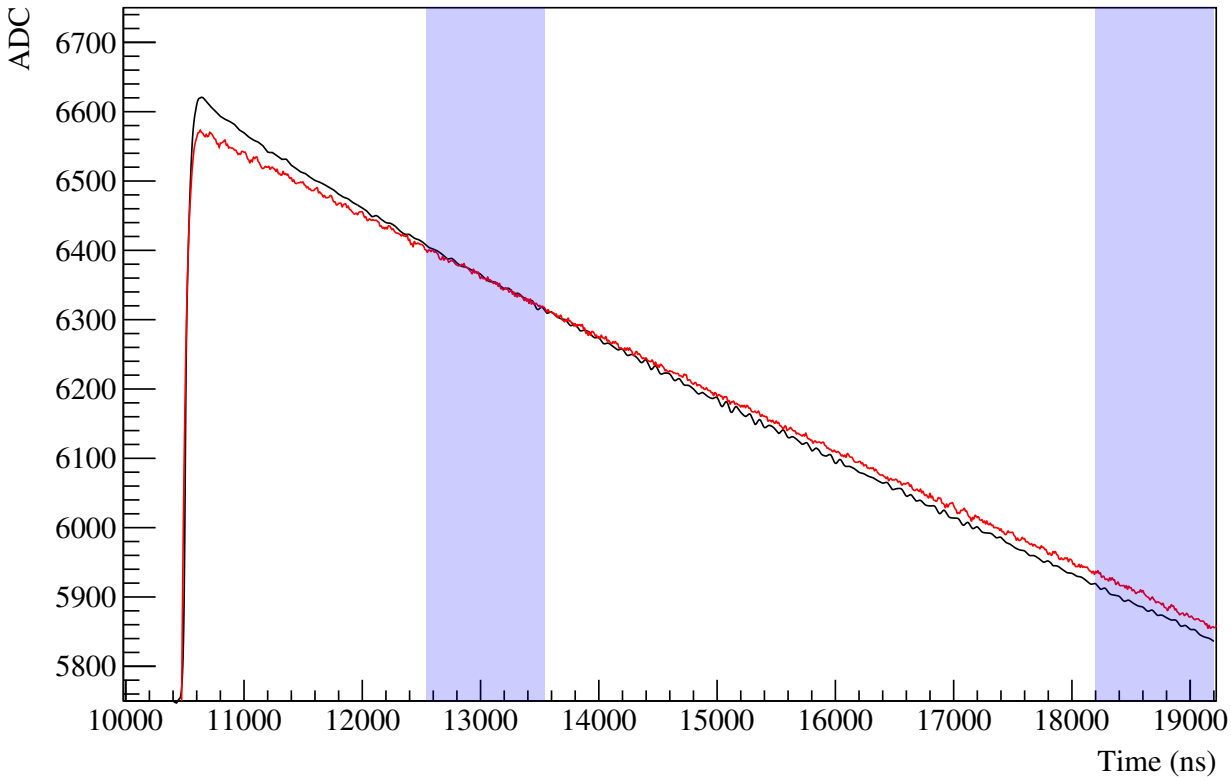

Figure 2.14: The single-site waveform from Figure 2.11 (black) compared to an event in the same detector of the same calibrated energy containing a delayed charge component (red). The waveforms are aligned at 97% of the maximum which is the time reference for the shaded regions that are used in computing the DCR slope parameter. (Figure and caption from [45])

DCR parameter. The DCR waveform (red) has a slower RC decay due to the slow collection of the trapped holes, and it is clear that the DCR parameter would provide a different value for the black and red waveforms. Figure 2.15 shows a comparison of DCR distributions for calibration events and background events, with calibration events (which are dominated by interactions in the bulk of the detector) occuring overwhelmingly with negative values of DCR. Background events, especially those with energies above the ^{208}Tl photon peak at

2615 keV are dominated by alpha interactions and show up with a range of positive DCR values.

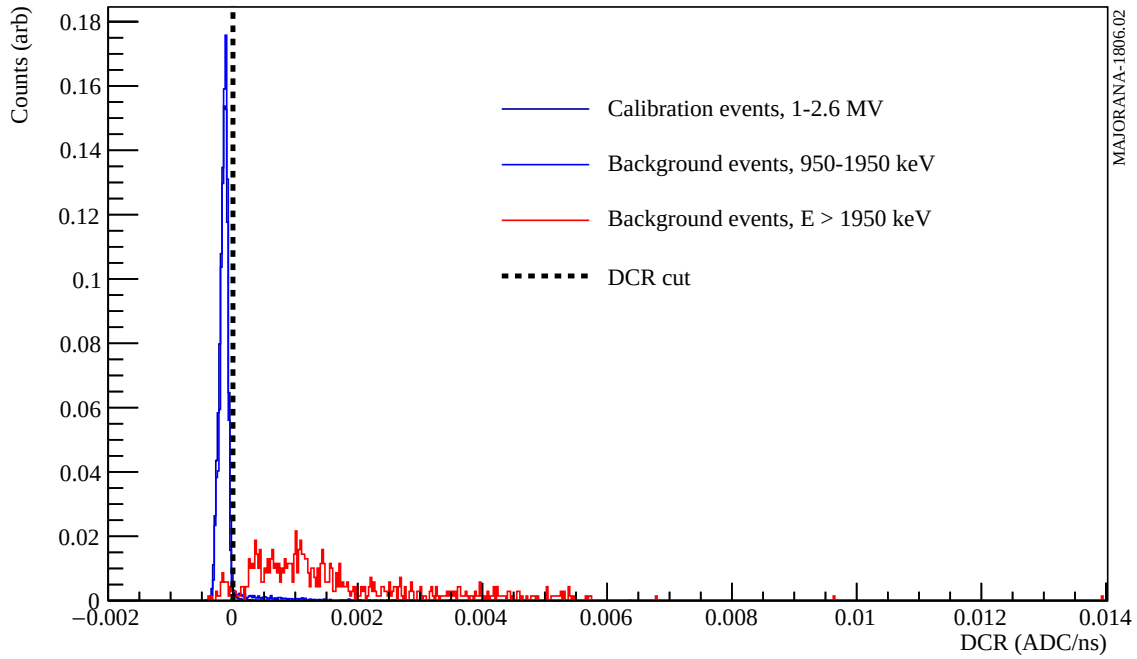

Figure 2.15: The DCR cut is tuned to accept 99% of events from the ^{228}Th spectrum, which is composed virtually entirely of energy depositions occurring in the bulk of the detector. Background events above 2 MeV, however, are primarily composed of degraded alpha interactions and are effectively cut by the DCR cut.

Tuning DCR

The DCR parameter is tuned on ^{228}Th calibration data to retain 99% of bulk events. The true efficiency is calculated by the collaboration, and is typically within 1 percentage point of 99% [45]. Its effectiveness at tagging true alpha interactions was characterized by Gruszko

using TUBE in [73]. Her results indicate that the DCR parameter is extremely effective, cutting virtually 100% of all alpha interactions for all but the part of the passivated surface closest to the point-contact. However, TUBE is only able to test alpha particles that have not experienced any energy degredation, while we expect that some (perhaps sizeable) fraction of the alpha events detected by the DEMONSTRATOR are already energy degraded by the time they reach the detector. As a result, while we expect for MAJORANA, like in TUBE, the DCR cut removes the vast majority of alpha events, we cannot rule out the possibility that a few alpha events remain in the background spectrum after the application of DCR.

The data used to construct the MAJORANA DEMONSTRATOR background model will always have the DCR cut applied, as simulations of the interaction of alpha particles with the passivated surface are not developed enough to be used confidently to generate energy spectral densities for this background component to be used directly in background fitting. We assume that any residual alpha contamination will have a negligible effect on the fitted background model; this assumption is supported by the consistency between the observed continuum background level near $Q_{\beta\beta}$ (where residual alphas would have the most significant impact) and the expected background from Compton scattering based on the observed height of the ^{208}Tl 2615 keV peak, leaving little room for an additional component from alphas. Alpha interactions with the detector passivated surface is a high-priority area of further study under the purvue of the successor experiment to the MAJORANA DEMONSTRATOR, LEGEND (described in Section 2.10).

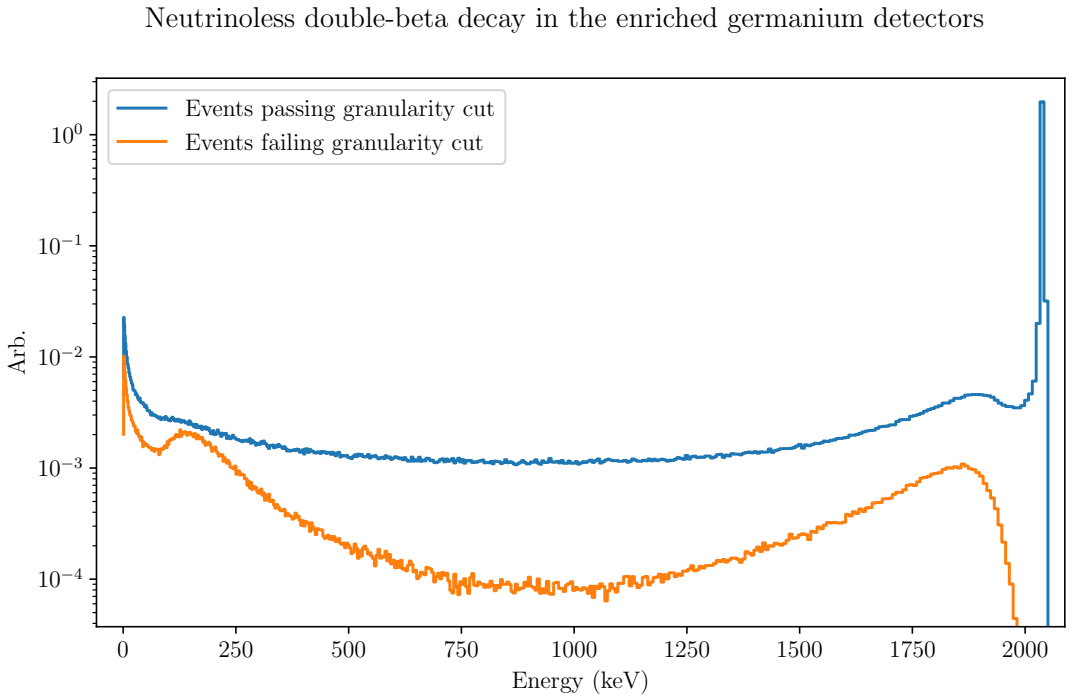

Figure 2.16: An energy spectrum simulated with `MaGe` and `GAT` of $0\nu\beta\beta$ decay in the enriched germanium detectors, showing the effect of the granularity cut on the signal. Approximately 4% of $0\nu\beta\beta$-decay events are tagged by the granularity cut, but all of them are degraded in energy, as can be seen by noticing how the orange histogram vanishes at 2039 keV. Therefore, the efficiency of the granularity cut to retain $0\nu\beta\beta$-decay events with the correct energy is effectively 100%.

2.7 Granularity Cut

Double-beta decay is highly likely to only produce a signal in one detector at a time. This is because the electrons produced during the decay process only travel approximately 1 mm in the germanium, which is too short to exit a detector and penetrate into the fully active region of another without encountering a thick Li dead-layer. Therefore, virtually only via bremsstrahlung radiation is some energy released during a double-beta decay event detected in another detector. For this reason, MAJORANA vetos any event that triggers multiple detectors within the event windowing time, which is set to 4 μs.

Figure 2.16 shows a simulated signal of $0\nu\beta\beta$ decay in the enriched germanium detectors. Approximately 4% of all $0\nu\beta\beta$-decay events are tagged by the granularity cut, but zero events at the correct energy of 2039 keV are tagged by this cut. A lower limit on the efficiency of this cut can be set by taking the 90% upper limit for a Poisson process with 0 counts detected, which is approximately 3 counts, and dividing it by the total number of simulated counts at the correct energy, which is 4022685. This gives a lower limit on the efficiency of the granularity cut to retain signal events of 99.999925%.

2.8 Containment Efficiency and Summary of Efficiencies

The presence of the lithium dead layers prevents full charge collection in some part of each detector. Because of this, not all $0\nu\beta\beta$ decays are detected with the correct energy and therefore are not counted as signal. The fraction of $0\nu\beta\beta$ decays that are lost in this way is $1 - \epsilon_{cont}$ where ϵ_{cont} is referred to as the containmnent efficiency. This efficiency is detector dependent, and is calculated based on simulations of the detectors. The efficiency averaged over the full array is approximately 91%, and values for all data sets are reported in Table 2.4.

The combination of the containment efficiency, AvsE efficiency, and DCR efficiencies for each data set are also presented in Table I of [45], which is reproduced here as Table 2.4.

In general, the total signal detection efficiency is approximately 80%, with the AvsE and containment efficiencies contributing equally, and the DCR efficiency contributing a small amount.

Data Set	Start Date	Data Set Distinction	Active Enr. Mass (kg)	Exposure (kg-yr)	ϵ_{AE}	ϵ_{DCR}	ϵ_{cont}	ϵ_{tot}	$NT\epsilon_{tot}\epsilon_{res}$ (10^{24} atom yr)
DS0	6/26/15	No Inner Cu Shield	10.69(16)	1.26(02)	$0.901^{+0.032}_{-0.035}$	$0.989^{+0.009}_{-0.002}$	0.908(11)	$0.808^{+0.031}_{-0.033}$	$6.34^{+0.25}_{-0.27}$
DS1	12/31/15	Inner Cu Shield added	11.90(17)	2.32(04)	$0.901^{+0.036}_{-0.040}$	$0.991^{+0.010}_{-0.005}$	0.909(11)	$0.811^{+0.035}_{-0.038}$	$11.82^{+0.53}_{-0.58}$
DS2	5/24/16	Pre-summing	11.31(16)	1.22(02)	$0.903^{+0.035}_{-0.037}$	$0.986^{+0.011}_{-0.005}$	0.909(11)	$0.809^{+0.034}_{-0.035}$	$6.24^{+0.28}_{-0.29}$
DS3	8/25/16	M1 and M2 installed	12.63(19)	1.01(01)	$0.900^{+0.030}_{-0.031}$	$0.990^{+0.010}_{-0.003}$	0.909(11)	$0.809^{+0.030}_{-0.030}$	$5.18^{+0.20}_{-0.20}$
DS4	8/25/16	M1 and M2 installed	5.47(08)	0.28(00)	$0.900^{+0.031}_{-0.034}$	$0.992^{+0.011}_{-0.002}$	0.908(10)	$0.809^{+0.030}_{-0.032}$	$1.47^{+0.06}_{-0.06}$
DS5a	10/13/16	Integrated DAQ (noise)	17.48(25)	3.45(05)	$0.900^{+0.034}_{-0.036}$	$0.969^{+0.013}_{-0.013}$	0.909(13)	$0.792^{+0.034}_{-0.035}$	$17.17^{+0.76}_{-0.79}$
DS5b	1/27/17	Optimized Grounding	18.44(26)	1.85(03)	$0.900^{+0.031}_{-0.033}$	$0.985^{+0.014}_{-0.005}$	0.909(13)	$0.805^{+0.032}_{-0.032}$	$9.46^{+0.39}_{-0.39}$
DS5c	3/17/17	Blind	18.44(26)	1.97(03)	$0.900^{+0.031}_{-0.033}$	$0.985^{+0.012}_{-0.003}$	0.908(11)	$0.806^{+0.031}_{-0.031}$	$10.31^{+0.47}_{-0.47}$
DS6a	5/11/17	Pre-summing, blind	18.44(26)	12.67(19)	$0.901^{+0.032}_{-0.032}$	$0.990^{+0.008}_{-0.002}$	0.908(11)	$0.811^{+0.030}_{-0.030}$	$65.10^{+2.92}_{-2.92}$
Total	(DS0-6)			26.02(53)					133.1±6.3
Total	(DS1-4,5b-6)			21.31(41)					110.0±5.1

Table 2.4: A summary of the key parameters of each data set. The exposure calculation is done independently for each detector. Symmetric uncertainties for the last digits are given in parentheses. The value of ϵ_{res} varies slightly for each data set, given the measured peak shape and optimal ROI. The exposure weighted value over all data sets is $\epsilon_{res} = 0.900 \pm 0.007$. (Table from [45])

2.9 Latest Results from the MAJORANA DEMONSTRATOR

The best limit on $0\nu\beta\beta$ decay from MAJORANA is available in [45]. That paper sets a limit of 2.7×10^{25} yrs (90% CL) on the half-life of $0\nu\beta\beta$ in ^{76}Ge, with a median sensitivity of 4.8×10^{25} yrs (90% CL). The analysis in [45] includes all open and blind data through data set 6a, which is 26 kg-yrs of enriched germanium exposure, or slightly less than twice the enriched germanium exposure analyzed in this work. The final spectrum can be seen in Figure 2.17, where the black is with only data cleaning cuts applied and red is with all cuts

applied.

The official background rate is estimated by averaging over an energy region spanning from 1950 to 2350 keV, with four 10 keV-wide regions around three known photon peaks (at 2103 keV due to the ^{208}Tl single-escape peak (^{232}Th-chain), and at 2118 and 2204 keV due to ^{214}Bi (^{238}U-chain) photon peaks) and $Q_{\beta\beta}$ not included, giving a 360-keV-wide background estimation window. The excluded photon peaks were chosen because they were expected to appear prominently above the continuum near $Q_{\beta\beta}$, based on the assay campaign and simulations of the DEMONSTRATOR. The number of counts in this region varies from data set to data set, but dramatic reduction can be seen from data set 0 to the later data sets (see Table 2.5). This is primarily due to the presence of additional shielding that was installed between data sets 0 and 1. The background rate reported in [45] is second only to GERDA's, and is competitive with all other $0\nu\beta\beta$-decay experiments, in part due to the narrow region of interest made possible by the excellent energy resolution achieved by MAJORANA.

Data Set	Window Counts	BI 10^{-3}	ROI (keV)	ROI BG (counts)
DS0	11	$24.3^{+8.4}_{-7.0}$	3.93	0.120
DS1	5	$6.0^{+3.4}_{-2.7}$	4.21	0.058
DS2	2	$4.6^{+5.1}_{-2.9}$	4.34	0.024
DS3	0	<3.6	4.39	0.000
DS4	0	<12.7	4.25	0.000
DS5a	10	$8.0^{+3.1}_{-2.6}$	4.49	0.125
DS5b	0	<1.9	4.33	0.000
DS5c	5	$7.0^{+4.0}_{-3.2}$	4.37	0.061
DS6a	24	$5.3^{+1.2}_{-1.0}$	3.93	0.262
Total	57	6.1 ± 0.8	4.13	0.653
DS1-4,5b-6	36	4.7 ± 0.8	4.14	0.529

Table 2.5: The background (BG) within the 360 keV window defined in the text for each data set. The background index (BI) is given in units of counts/(keV kg yr). The optimum ROI width for each data set is also given, and the final column shows the resulting expected number of background counts within that ROI. The second from last row provides a summary for all data sets, and the final row shows the combined total for the lower-background data sets. (Figure and caption from [45])

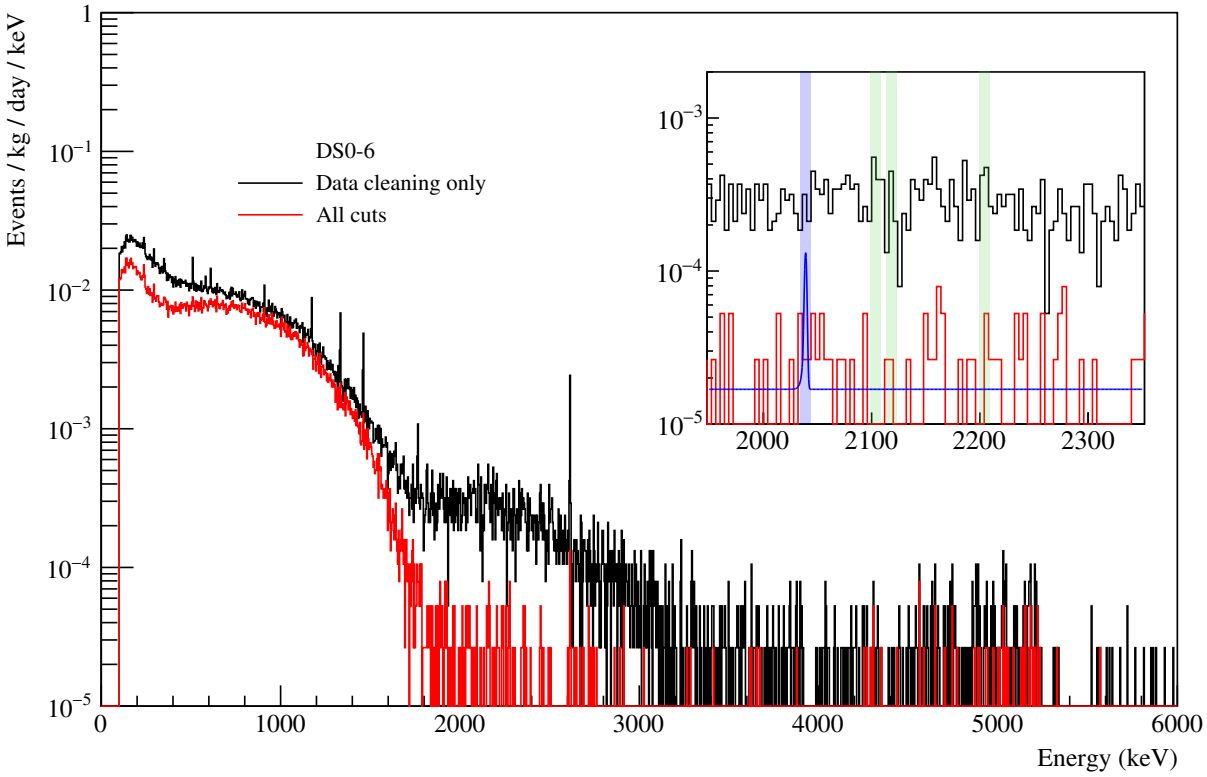

Figure 2.17: Energy spectrum above 100 keV of all seven data sets summed together with only data cleaning and muon veto cuts (black) and after all cuts (red). The inset shows the same spectra in the background estimation window, which spans 1950-2350 keV, with regions excluded due to gamma backgrounds shaded in green and the 10 keV window centered on $Q_{\beta\beta}$ shaded in blue. The solid blue curve shows the flat background estimated from the unshaded regions in the inset plus the 90% CL upper limit on the number of counts in the $Q_{\beta\beta}$ peak for the measured peak shape parameters in each data set weighted by exposure. (Figure and caption from [45]) Notice that the pulse-shape cuts, which bring the black spectrum down to the red spectrum, reduce the background near $Q_{\beta\beta}$ (inset) by more than an order of magnitude.

2.10 Connection to GERDA and LEGEND

From the design phase of the MAJORANA DEMONSTRATOR, there has been a loose collaboration with the GERDA experiment. As both experiments are made from ^{76}Ge, a decision was made early on that the two collaborations would pursue complementary technological approaches, with a formal letter-of-intent specifying the future merging of the two collaborations into one for a later ton-scale experiment. The GERDA experiment pursued the novel approach of immersing their detectors directly in liquid argon, which is then instrumented with wavelength-shifting fibers and silicon photomultipliers, and serves as an active veto for background events external to the detectors. The MAJORANA collaboration would apply the standard approach of operating the detectors in vacuum, but focus more on the production of novel materials — such as the ultra-pure electroformed copper grown underground at the experimental site [59] [74] or the ultra-low-mass front-ends designed and produced by the group at Lawrence Berkeley National Laboratory — and an exacting assay campaign of all components in the experiment [5].

Both experiments were quite successful in achieving their respective goals. The GERDA liquid argon active veto system was initially a risky endeavor, as many novel techniques are. GERDA is the first group to successfully operate detectors long-term in this manner, and the LAr veto system has been instrumental in their achievement of the lowest backgrounds of any operating large-scale $0\nu\beta\beta$-decay experiment. Figures 2.18 and 2.19 are from [44] and show the effect of the LAr active-veto, with the backgrounds in the region-of-interest at 2039 keV being virtually completely suppressed by the combination of the LAr rejection and an additional pulse-shape-based cut to remove degraded alpha particles on the surfaces of their detectors.

The two experiments are nearing the end of their operating lifetimes, and a new supercollaboration called LEGEND (Large Enriched Germanium Experiment for Neutrinoless double-beta Decay) has been formed [75]. LEGEND will combine the best technologies de-

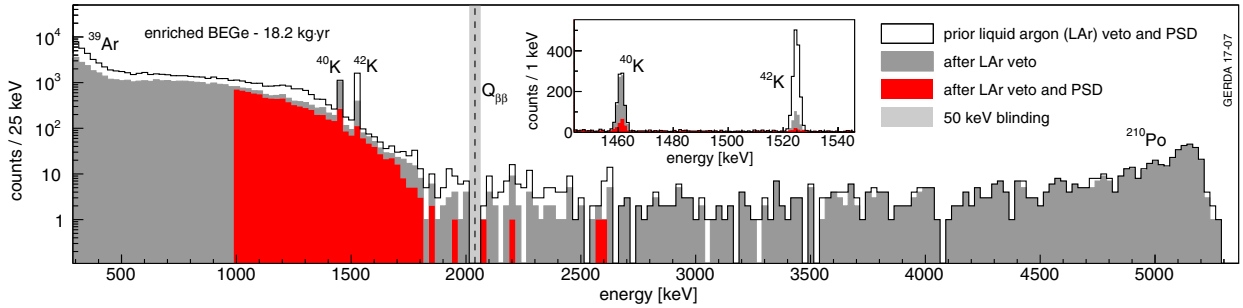

Figure 2.18: Energy spectra of GERDA Phase II low-background BEGe detectors prior to liquid argon veto and PSD cuts (total histogram), after additional LAr veto (dark gray) and after after all cuts (red). The inset shows the spectrum in the energy region of the potassium lines (1460 keV from ^{40}K and 1525 keV from ^{42}K). The gray vertical band indicates the blinded region of ± 25 keV around the $Q_{\beta\beta}$ value. (Caption and figure from [44])

veloped by GERDA and MAJORANA, using many of the ultra-low background materials and components as well as the low-noise electronics of MAJORANA, and the LAr veto system of GERDA. LEGEND is currently in the design phase, but construction is expected to commence soon at LNGS, with initial data taking expected in 2021.

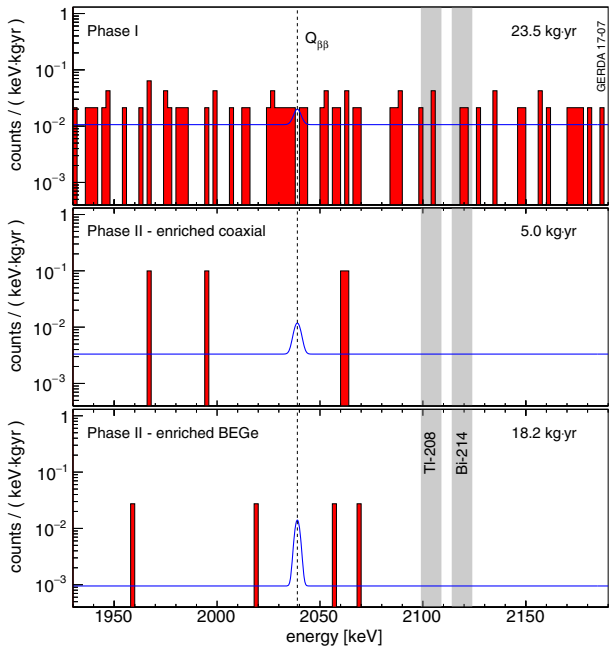

Figure 2.19: Energy spectra in the analysis window for GERDA Phase I and Phase II coaxial detectors and Phase II BEGe detectors, respectively, after all cuts. The binning is 2 keV. The gray vertical bands indicate the intervals excluding known γ lines. The blue lines show the hypothetical $0\nu\beta\beta$ signal for $T_{1/2}^{0\nu} = 8.0 \times 10^{25}$ yr, on top of their respective constant backgrounds. (Caption and figure from [44])

Chapter 3

SIMULATIONS FOR THE MAJORANA DEMONSTRATOR

The first and most important step in modeling the background of the MAJORANA DEMONSTRATOR is the generation of a comprehensive set of simulated energy spectra for possible contaminants in all components of the DEMONSTRATOR. There are 3607 named physical volumes that make up the model of the DEMONSTRATOR, and most of them are candidates for possible contamination of at least 2 isotopes, if not more. Many of the physical volumes can be organized logically into groups (e.g. any contamination of ^{232}Th in underground electroformed copper (UGEFCu) parts is likely to be the same across all UGEFCu parts). A list of all of the component groups and descriptive information about them is given in Appendix A.

Simulations of radiogenic backgrounds are produced through a pipeline of several pieces of software before ending up in their final form for analysis. This chapter will provide an overview of the components of the simulations pipeline.

3.1 `MaGe`

The pipeline begins with `MaGe`[76], a simulation package for the MAJORANA DEMONSTRATOR and GERDA built on top of Geant4 [77] [78]. Geant4, or GEometry ANd Tracking 4, is a well-named standard tool used widely in high-energy and particle physics for simulations of materials and detectors in the presence of energetic particles. While most often used in the context of accelerator and beam experiments, it can also be used to simulate the environment in which the MAJORANA detectors are situated.

Geant4 is highly customizable in the different physical processes it can simulate, and of

course does not specify a particular geometric configuration for a detector *a priori*. Therefore, especially in the context of a complex detector setup like the MAJORANA DEMONSTRATOR, it is useful to create a superstructure around the core of Geant4 that can correctly load and set all of the necessary configuration-specific options consistently and generate the detector geometry. This is what `MaGe` does.

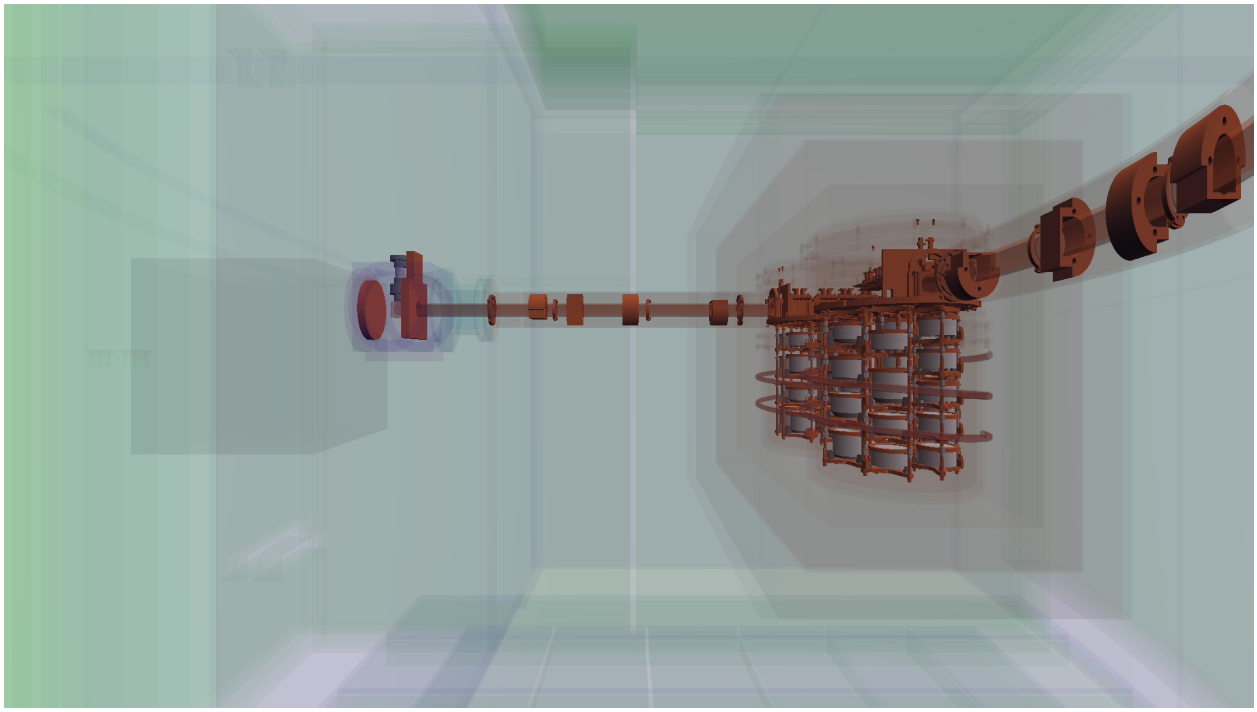

Figure 3.1: A rendering of the internal components of the MAJORANA DEMONSTRATOR made with raytracer in Geant4 with help from T. S. Caldwell. The shielding and copper cryostats are translucent but still visible, and the detectors can be seen in their as-built locations. Module 1 is on the left/behind and module 2 is to the right/in front.

`MaGe` was largely constructed prior to my joining the MAJORANA experiment. I contributed code to correctly model the extra shielding installed inside the cross-arm tube, and fixed several bugs relating to the locations of cryostat components inside the radiation

shield pocket.The geometry for most parts was implemented to match the drawings used to construct the DEMONSTRATOR itself.

The modeled geometry of the MAJORANA DEMONSTRATOR can be seen in Figure 3.1. In this figure the lead and copper plate shielding, copper cryostats, thermosyphons, and infrared shields are translucent, and the detectors are visible in their as-built locations. Copper blocks that were installed between data set 0 and data set 1 are visible inside the crossarm tubes. Module 1 is on the left/behind and module 2 is to the right/in front. The calibration tracks are also visible as translucent helices surrounding the two modules. The calibration sources are deployed into these tracks during calibration, and are retracted and kept outside the lead shield during normal running.

There are small differences in how some of the parts are modeled. For example, none of the screws in the `MaGe` model have threads, even though they of course do have threads in real life. This was done because a threaded screw has a significanly more complex surface than a non-threaded screw which leads directly to an increase in simulation time. Since screw threads don't have a direct line-of-sight to the detectors, and since the total simulated mass of all screws and their mount points is unchanged by neglecting threads, the effect of this approximation should be negligible.

3.1.1 Event Generators In `MaGe`

Most of the simulations produced to create the background model use the default Geant4 isotropic radioactive decay generator. This generator can be handed a list of physical volumes in which to generate decays, and will randomly generate primary decay locations inside them while weighting by density. The component groups listed in Tables A.1, A.3, and A.4 all use this event generator. This work makes use of a number of additional event generators available in `MaGe`, described in this section.

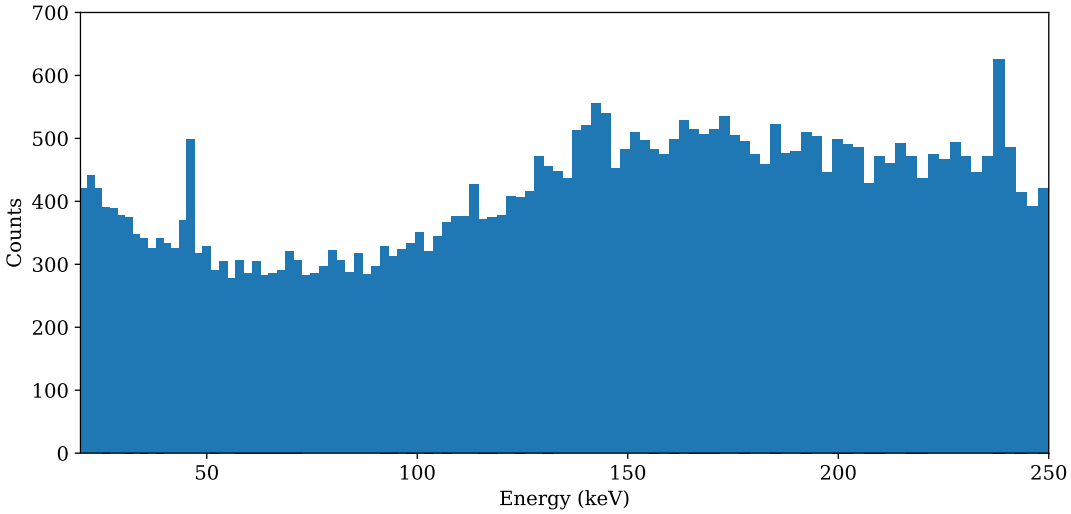

Figure 3.2: The measured energy spectrum for all detectors in data set 5 between 20 and 250 keV in the 2-module configuration. The line at 46 keV from the decay of ^{210}Pb is visible to the left and the line at 238 keV from the decay of ^{212}Pb is visible to the right.

Simulation of Surface Decays in DEMONSTRATOR Components

Some component groups have direct line-of-sight to the detectors, and for those groups surface contamination can be noticeable. Decays that produce betas or low-energy photons can be detected in these parts, but would be attenuated by any intervening non-active components if they did not have a direct line-of-sight. An example of this is the 46 keV photon that is emitted during the decay of ^{210}Pb (see Figure 3.2). This photon is clearly visible in some of the detectors, but must be originating from surface decays on components with direct line-of-sight to the detector, as 46 keV photons have only a 0.3 mm scattering length in copper, or 1.4 cm in PTFE. Furthermore, ^{210}Pb is a decay product of ^{222}Rn, which can plate out onto exposed surfaces, particularly dielectrics prone to static charge buildup. For these reasons, we expect this source of ^{210}Pb to most likely be originating from the plastic

components inside the DEMONSTRATOR modules.

We simulate surface decays of component groups with direct line-of-sight to the detectors using the General Surface Sampler (GSS) developed by Detwiler *et al.* [79] to generate initial locations of primary decays, which can be fed into Geant4. As is shown in [79], the GSS evenly samples any arbitrary surface shape. Because of its generality, it can be slow to sample some pathological types of surfaces (particularly a small number of small parts in a large volume), and so the statistics for the surface simulations are not as good as those of the bulk simulations.

Simulation of ^{210}Pb Decays in the Lead Shield

The lead shield surrounding the DEMONSTRATOR is a potential source of background radiation. In principle, thorium, uranium, potassium, and cosmogenically activated ^{210}Pb can contaminate lead, with thorium and uranium in particlar being capable of producing counts near $Q_{\beta\beta}$. The decay of ^{210}Pb produces a ^{210}Bi daughter, which then beta-decays to ^{210}Po with an endpoint energy of 1,161 keV. This electron can then produce bremsstrahlung radiation as it loses energy in the lead, with energy high enough to be detectable in the DEMONSTRATOR. To mitigate this, we installed in the DEMONSTRATOR a 5 cm liner of high-purity commercial copper inside the lead shield, and inside of that an additional 5 cm liner of UGEFCu. However, during initial data taking in the DS0 configuration, the inner UGEFCu shield had not yet been installed, and the flux of detectable bremsstrahlung gammas from the lead shield was much higher. Although this bremsstrahlung signal is too low in energy to be capable of generating background counts at $Q_{\beta\beta}$, its high contribution at lower energies makes it a key process to include in the full background model as it can strongly influence the overall fit to the data.

Unfortunately, the bremsstrahlung signal from the decaying ^{210}Bi atoms is quite difficult to simulate efficiently. The bremsstrahlung photons are produced with an energy not larger

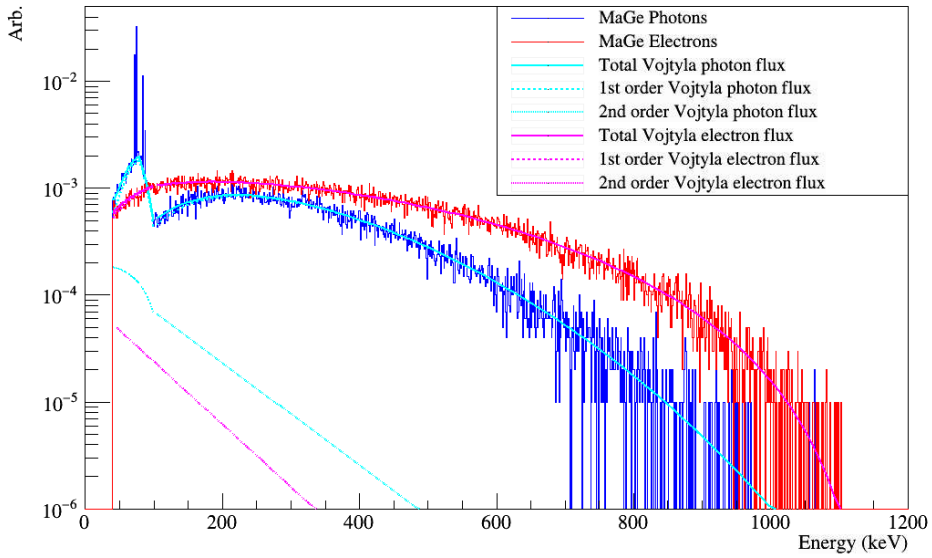

Figure 3.3: A comparison of the the analytical functions outlined in [80] with the flux simulated by their implementation in `MaGe`. The fluxes are normalized so that the sum of their integrals is 1. The X-Rays near 30 keV are treated as separate delta peaks in the Vojtyla model, so are not described by the analytical functions for the bremsstrahlung photons and electrons. The lines for the first-order electrons and photons are virtually coterminous with the lines for the total flux, as the second-order fluxes are so small relative to the first-order fluxes. See the text for a definition of the first- and second-order fluxes.

than the beta-decay endpoint of 1,161 keV, and even with that highest possible energy the attenuation length of photons in lead is approximately 1.4 cm. Therefore, only the innermost few centimeters of the lead shield is even capable of producing detectable radiation and simulating the entire shield is quite inefficient. More importantly, only a fraction of beta decays subsequently produce the bremsstrahlung radiation, adding another significant source of inefficiency to a brute-force first-principles simulation.

To overcome these challenges in simulating the bremsstrahlung signal from the lead shield,

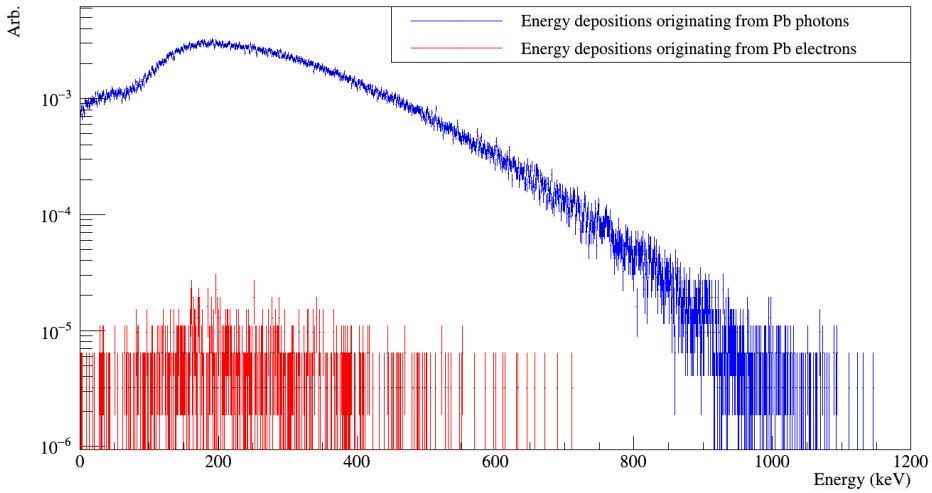

Figure 3.4: Even though they make up approximately 50% of the emitted particle flux, electrons exiting the lead shield contribute negligibly to the spectrum of detected energy depositions originating in the lead shield. The energy depositions originating from these electrons are only produced when they create bremsstrahlung radiation in the copper shield liner just inside the lead shield. This spectrum was produced before any detector effects were applied in post-processing.

`MaGe` implements a specialized event generator based on a heuristic model of the flux of photons and electrons exiting the lead shield developed by Pavol Vojtyla [80]. Instead of simulating all decays directly, just the spectrum of emitted particles is generated, with the energy and angular distributions described by empirical analytical functions (piecewise polynomial approximations of the flux or the logarithm of the flux) that were fit closely to the results of a full simulation in [80]. Figure 3.3 shows the agreement in particle fluxes exiting the DEMONSTRATOR's lead shield between Vojtyla's analytical functions and the spectrum produced by `MaGe` using the Vojtyla generator.

The simulated particles are broken up by Vojtyla into groups by type of decay, which each

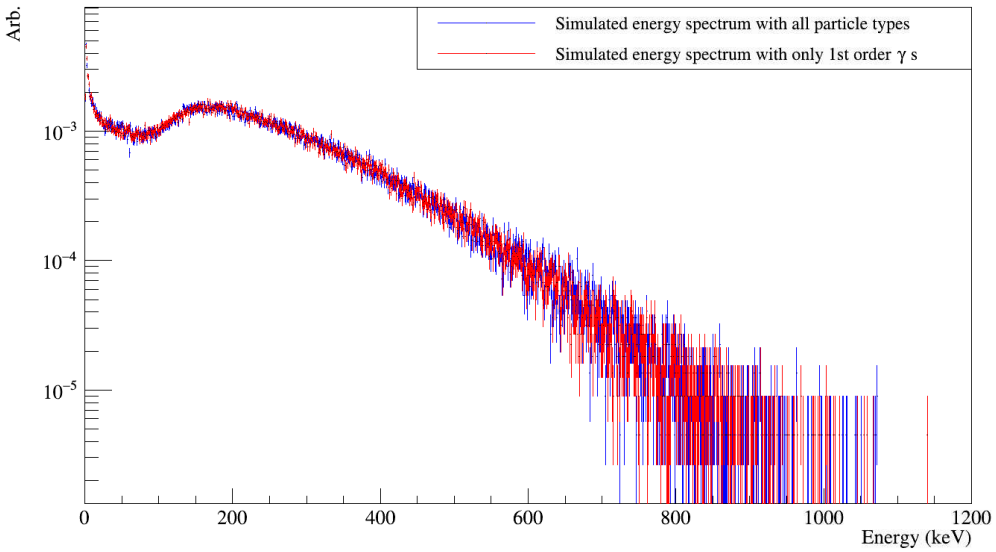

Figure 3.5: Detected radiation originating in the lead shield. The blue spectrum includes only first-order bremsstrahlung photons and the red spectrum additionally includes second-order bremsstrahlung photons, X-rays, and electrons. This simulation includes all detector effects.

group having its own functional form. The groups are first- and second-order photons, first- and second-order electrons, and X-Rays. Although in principle any number of daughter particles can be produced by the decay of ^{210}Bi and its decay products, Vojtyla found in practice that it was highly unlikely that a single ^{210}Bi decay would produce more than 2 particles that would be detected simultaneously. For events where two decay products are detected simultaneously, it is reasonable to approximate the energy and angular distribution of the second particle as independent from the first, for the purposes of generating a simulated detected energy spectrum. The terms first-order and second-order therefore refer to the first and second particles detected from a ^{210}Bi decay. The flux of first-order particles also includes events where just a single decay product is detected, which is the large majority of events

(98% of events according to Vojtyla).

Vojtyla derived the empirical functions used to model the particle fluxes by running a high-statistics simulation of a 15-cm thick lead disc contaminated with ^{210}Pb, and finding approxmate functions to describe the resultant particle fluxes. He then verified them with a full simulation of a detector inside a "lead shield of rectangular shape with inner lead dimensions of $24 \times 24 \times 40$ cm^3 and lead thickness of 15 cm, lined with 1 mm of Cd and 2 mm of Cu", finding excellent agreement up to 900 keV, above which point the statistics in the full simulation were too low to make a comparison. [80]

Due to the excellent agreement Vojtyla found between the empirical and full model, we are confident that this approximation is sufficient to reproduce the full effect of the bremsstrahlung signal from the lead shield in the MAJORANA detectors. Some further simplifications to the model are possible, which are pointed out by Vojtyla. Simulations using only the first-order bremsstrahlung photons emmitted from the shield were indistinguishable from a simulation including the electron flux, second-order bremsstrahlung photons and X-rays. Figure 3.4 shows the simulated energy spectrum of particles detected by the germanium detectors, sorted by the primary particle that was simulated exiting the lead shield. Even though the electron flux makes up approximately 50% of the total flux (see Figure 3.3), very few electrons manage to generate energy depositions in the detectors. This is because they must either penetrate through several cm of copper shielding, or generate bremsstrahlung signals in the copper, both of which are much less likely than the chance of a photon emitted in the same place producing detectable energy in a detector. Figure 3.5 shows a comparison between the detected energy spectrum including all particle fluxes characterized by Vojtyla in the simulation (first- and second-order photons and electrons, and X-Rays, blue histogram), and the energy spectrum produced by just the first-order photons. The two spectra are indistinguishable.

The heuristic generator presented in this section is only used because it is very difficult

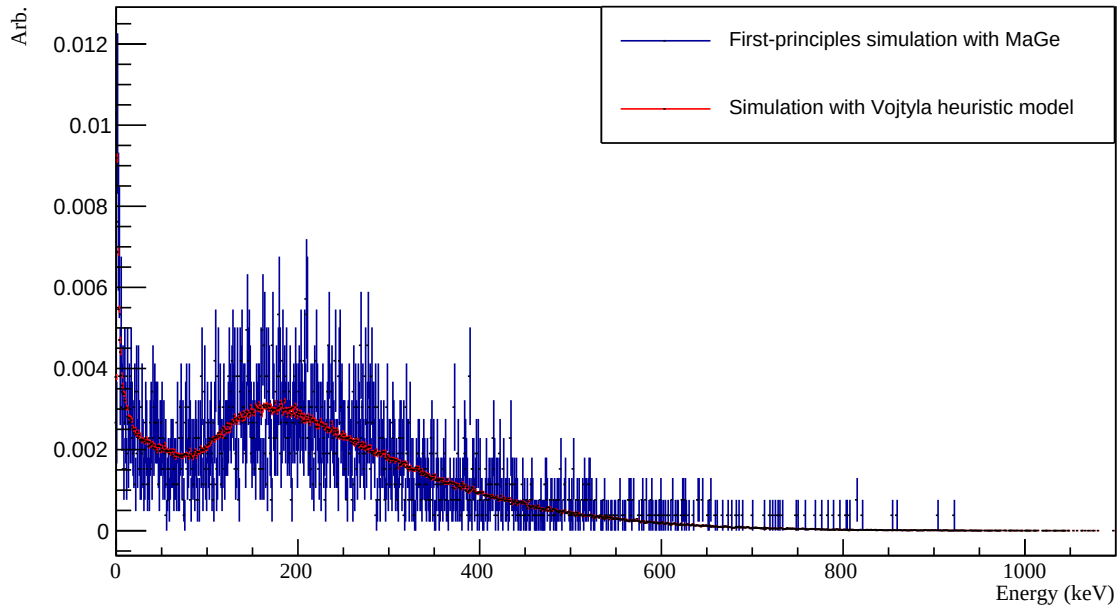

Figure 3.6: Two versions of the simulated detected energy spectrum for the MAJORANA DEMONSTRATOR in the data set 6 configuration. The blue histogram shows the spectrum generated by a first-principles simulation using the default `MaGe` bulk decay generator, and the red histogram shows the spectrum produced by the Vojtyla approximation in this section. A Kolmogorov-Smirnov test of the two spectra returns a p-value of 0.39, indicating that the null hypothesis that the two spectra are generated by the same underlying statistical distribution should not be rejected.

to simulate the lead shield ^{210}Bi bremsstrahlung spectrum from first principles. Therefore, it is difficult to make direct comparisons of the efficacy of the Vojtyla approximation by comparing to `MaGe`. That said, a low-stats histogram for decays of ^{210}Bi in the lead shield was produced with the default bulk-decay generator in `MaGe`, and can be compared to the spectrum produced by the Vojtyla generator. That comparison is presented in Figure 3.6.

The blue histogram shows the spectrum generated by a first-principles simulation using the default `MaGe` bulk decay generator, and the red histogram shows the spectrum produced by the Vojtyla approximation in this section. A Kolmogorov-Smirnov test of the two spectra returns a p-value of 0.39, indicating that the null hypothesis that the two spectra are generated by the same underlying statistical distribution should not be rejected.

Other Event Generators

Generators for $2\nu\beta\beta$ and $0\nu\beta\beta$ decay based on [81], are included in `MaGe`. They generate decays uniformly in a specified volume, typically the enriched or natural germanium detectors. A generator for a helical line source around each module represents the calibration system. There are also generators for energetic neutrons and cosmic muons. We do not include either of those sources in this background model, since after application of the muon veto they are subdominant to radioactive backgrounds.

The signal and high-voltage cables have specific event generators, and are broken up into groups based on their locations in the experiment. The signal and HV cables below the cold plate are modeled separately as line sources, in the physical location of the installed cables. In the DEMONSTRATOR, slack in the signal and HV cables is stored above the cold plate, where the cables are wound around cable takeups. This means that the distribution of cables above the cold plate is not uniform. In `MaGe`, the cold plate cables are modeled as a flat disk above the cold plate. The cables then are routed down the cross arm, in the space between the thermosyphon and the cross arm vacuum vessel itself. `MaGe` models these cables as a tube just inside the cross arm vacuum vessel, which is similar to how they are actually distributed. The cold plate cables are the only cable component/generator where the `MaGe` model differs significantly from the true distribution.

3.1.2 Physics Lists Used in This Analysis

The Geant4 physics lists used in this analysis include the "shielding" standard Geant4 physics list, as well as the Livermore low-energy EM option enabled. Angular correlations between successive photons emitted in a cascade are enabled (although see comments on this in Section 5.2.2), and we use the AllParticleHP package with the TENDL libraries.

The MAJORANA collaboration also has produced a validation suite that checks a variety of physics processes and compares them to literature values. This validation suite automatically produces a report and has been run on previous versions of Geant4, including Geant4.9.3 [82] and Geant4.10.3 [83]. As of this writing, the first chapter of the report gives a brief overview of the results of the rest of the report. Chapter 2 reports on the radioactive decay of 10 different isotopes (^{46}Sc, ^{59}Fe, ^{56}Co, ^{57}Co, ^{60}Co, ^{73}As, ^{74}As, ^{133}Ba, ^{208}Tl, and ^{214}Bi). Branching ratios and energies of prominent photons, beta particles, and secondary electrons, as well as the decay constant of the isotope, are computed for each isotope and compared to values in the literature. Chapters 3, 4, and 5 compare measured penetration depth and attenuation functions of photons, electrons, and alpha particles respectively in lead, copper, and natural germanium. The version of Geant4 used in this work — Geant4.10.4 — has not yet been validated by this suite, but efforts within the collaboration are currently underway to update the validation code to run successfully on this version of Geant4. This will be briefly discussed again in Chapter 5.

3.1.3 Description of `MaGe` *Output Files*

In the configuration used for the simulations analyzed in this document, a single run of `MaGe` produces a file containing a single ROOT [84] [85] TTree. Other output styles are available but are not used here.

By default, Geant4 will propagate a radioactive decay until the primary nucleus has reached a stable isotope, or has exited preset boundaries on the number of protons and/or

neutrons in the nucleus. For decay chains containing intermediate states with long half-lives, this can be inefficient and produce events containing energy depositions separated by extremely long periods of time. To prevent this, MaGe windows Geant4 events by an adjustable period of time, with a windowing time of 1 day used for the simulations presented in this document. Therefore, each entry in the output TTree is a record of all the interactions a single radioactive decay produced in the sensitive volumes of the DEMONSTRATOR (i.e. the germanium detectors and optionally also the muon veto panels), until the primary nucleus reaches a state with a half-life of 1 day or longer. The stepping information of the primary and daughter particles through the detector system can be processed later by GAT into a format that is more similar to the actual data from the DEMONSTRATOR.

Name of Branch	Description
fMCRun	Number of primaries, settings for run, MaGe version tag, etc.
eventHeader	Event ID, total energy
eventSteps	List of stepping information for non-zero energy depositions in sensitive volumes. Items in the list include particle type, location, energy, momentum, and track ID.
eventPrimaries	List of initial particles with same structure as eventSteps

Table 3.1: Each MaGe output file contains this information.

3.2 GAT and Detector Response

Once the raw simulations are produced with MaGe, the stepping information in the MaGe output is processed with the Germanium Analysis Toolkit, or GAT. It is at this stage that detector effects, including the energy resolution and effects from partial charge collection in the dead layer are applied. GAT is a software package that performs several functions for

the MAJORANA collaboration, the primary two of which are processing the data from the experiment, and processing the output from `MaGe`. Only the parts of `GAT` relevant to the processing of `MaGe` output will be covered in this chapter.

3.2.1 Overview of Steps in `GAT` *Simulations Post-Processing*

`GAT` uses the modular processing framework of `TAM`, which itself uses the TSelector framework built into ROOT. In this framework, one develops modules that operate on sequential data, in this case the events in the `MaGe` output (see Section 3.1.3). The framework is designed for the modules to operate sequentially on each element in the data stream, with each module able to access the output of all previous modules. A description of the different modules and their functions is given as Table 3.2. Two processors in particular, the energy-adjuster and the dead-layer processor, are rather complex and of critical importance for accurate modeling of the background spectrum. They will be covered in detail in the next two sections.

Table 3.2: When a file containing output from `MaGe` is processed with `GAT`, these processors operate to convert it to a format more similar to the output of the actual DEMONSTRATOR.

Name of Processor	Description
MC steps windower	As described in Seciton 3.1.3, the `MaGe` output groups tracks within 1 day of each other into `MaGe` events, so we reorganize the recorded energy depositions into timing windows for each detector. For each `MaGe` event, the energy depositions are ordered in time. A window boundary is inserted between any two energy depositions that are separated by more than the specified windowing time, which is 200 μs for the simulations presented here. The timing window is set to emulate the event timing window used in the data, so the steps are effectively reorganized into waveforms.
Dead layer processor	The deadness is calculated for the position of each energy deposition according to the dead-layer configuration parameters (see sec. 3.2.3)
Energy adjuster	The detector energy resolution is applied here, according to the measured peak-shape function (see sec. 3.2.2)
Clusterer	Energy depositions are clustered based on the spatial and temporal resolution of the detectors to facilitate more efficient waveform simulation and PSA emulation, using a method identical to that of the windower. The clustering distances used here are 0.1 mm and 5 ns, so any energy depositions separated by less than both of these values are merged.

Name of Processor	Description
PSA emulator	Here the dT heuristic (which emulates the effect of the A vs. E cut) is calculated according to the method described in [86], using the configuration parameters in [87]. A description of the method and a reference to specific values used is presented in Section 3.3.2.
Veto only tagger	Some detectors have poor energy resolution or other behavior and are not included in the analysis, except to serve as veto-only detectors for the granularity cut. Detectors are designated as veto-only by the Run Selection and Data Cleaning Working Group and are documented in [60].

3.2.2 Detector Resolution

Since `MaGe` does not simulate any detector effects, the resolution function of each detector – described in Section 2.5.2 – must be applied with `GAT`. Only the effects represented in Equation 2.3 are applied at this stage; the quadratic background and step function are produced by physical effects simulated from first-principles by `MaGe`. The hyperparameters given in Equation 2.4 are evaluated for each detector in each data set with fits to measured calibration data, and are used by the energy adjuster to calculate the detector response for each energy deposition simulated by `MaGe`. The simulated energy depositions are then randomly adjusted according to the measured peak-shape. The specific parameters used for modeling the response of each detector are saved on the NERSC global filesystem in the same directory as the output from `GAT`. For the results presented in this document, they are located in `/global/projecta/projectdirs/majorana/sim/MJDG41004GAT/det_config_floatingDB_value_AllDS013456.json`, as well as on Github at `https://github.com/buuck/GAT/tree/bkg_model/MJBackgroundModel/bkgModel2018/det_config_floatingDB_`

`value_AllDS013456.json`.

3.2.3 Detector Dead-Layer Characterization

The dead-layers of the MAJORANA detectors were described in Section 2.4.1. There are two primary models we have explored to model them. The standard approach is to assume zero charge is collected for any energy depositions that occur within the thickness of the dead-layer from the surface of the detector. I will refer to this model as the "flat" dead layer. This approach is sufficient for many purposes, but it is not the most accurate model as is shown in Graham Giovanetti's PhD thesis [88]. Using the code `siggen` — developed by David Radford at Oak Ridge National Laboratory to simulate charge collection as a function of time in germanium detectors — and data taken with a ^{241}Am source, Giovanetti and Radford showed that some charge is actually collected in nearly every energy deposition. Since the energy resolution of germanium detectors is so good, even just a small amount of charge loss (on the order of 1%) degrades an event enough to remove it from a peak. But instead of removing that event entirely from the energy spectrum, it instead appears in the spectrum with a smaller energy.

In [88], Giovanetti simulated the drifted lithium contact as a cloud of precipitates that penetrate some depth into the germanium. Each precipitate functions as a charge recombination site, so energy depositions that occur in the region containing the precipitates will not have their full charge collected as some of the resultant charge cloud will be lost at these precipitate sites. The amount of charge collected changes as a function of the distance from the surface of the detector in which the charge was deposited. It is also affected by the characteristics of the lithium precipitate cloud, including the diameter of the precipitate sites, the overall density of the precipitates, and the depth that the precipitate cloud penetrates into the detector. The effect that each of these parameters has on the fraction of charge collected for a given energy deposition is shown in Figure 3.7.

Giovanetti did not give a functional form for the dead-layer profile in [88], so I developed one based on the results shown in chapter 4 of [88]. The amount of charge collected depends on the previously-mentioned characteristics of the detector, but all of the charge collection profiles shown in the figures in that section can be quite accurately approximated by a piecewise exponential and linear function. The fraction of the deposited charge collected, or the activeness, increases in an exponential fashion until the effective lithium drift depth in the detector. At that point, the collected charge increases linearly until all the charge is collected at which point the detector is fully active. This approximation is shown in 3.7 which is from [88] with the approximating function overlaid.

The functional form of this approximation is the following:

$$F(x) = \begin{cases} 0 & x \leq 0 \\ Ae^{Bx} + C & 0 \leq x \leq x_t \\ Mx + D & x_t \leq x \leq t \\ 1 & x \geq t \end{cases} \tag{3.1}$$

where x is the depth from the surface of the detector, t is the dead-layer thickness, and x_t the point where the function transitions from an exponential form to a linear form. In this case, the dead-layer thickness refers to the depth where the crystal fully collects the deposited charge. Additional constraints are applied to ensure that the function is continuous and differentiable at x_t, equal to 0 at $x = 0$, and equal to 1 at $x = t$. This set of constraints leads to 3 free parameters, which can be simulated and fit to data to obtain the correct parameterization for a particular detector. Typically, x_t (the depth at which the exponential-to-linear transition occurs)[1], $F(x_t) = f$ (the activeness at that point), and t (the thickness of the dead layer) are allowed to float and fit to data. For the simulations presented in this document, the overall thickness of the dead-layer was floated between 50% and 500% of the

[1]Technically the fit parameters is implemented as x_t/t and constrained to lie between 0 and 1.

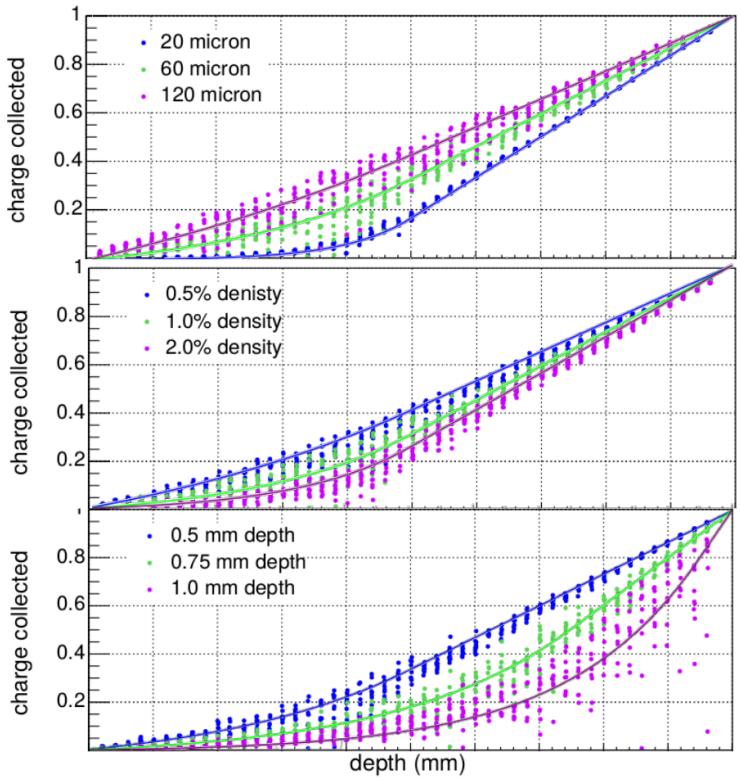

Figure 3.7: The three panels in this figure and the associated data points are from [88]. Each data point shows the amount of charge collected for a simulated energy deposition given the specified parameters for the lithium dead layer. The trend lines drawn are piecewise exponential and linear functions following the form described in Section 3.2.3

measured thickness specified by the detectector manufacturer, ORTEC.

How the Dead-Layer Parameters were Determined

The parameters needed to characterize the transition-layer profile for each detector were found using a grid search over the 3D parameter space of x_t the transition point, f the transition level, and t the dead layer thickness. For each combination of dataset, detector, and

transition layer parameters, the simulated ^{228}Th calibration spectrum and measured calibration spectrum were both normalized to 1. The sum-of-squared-errors was then computed and for each dataset and detector pair, the set of dead layer parameters that minimized the sum-of-squared-errors (SSE) was chosen. Because certain regions of the energy spectrum are much more sensitive to the effect of the transition layer parameters than others, the SSE used as a figure-of-merit was only computed over those regions of the energy spectrum. The three most prominent photon peaks in the energy spectrum were used to compute the SSE, because they are particularly sensitive to the transition layer parameters. The energy ranges for the peaks were 237-240, 580.5-585, and 2605-2618 keV.

The grid search was performed detector-by-detector and the resulting best fit parameters can be found in the same JSON file containing the detector resolution parameters (see Section 3.2.2). An example plot showing the shape of the parameter space for a single detector is shown in Figure 3.8. If the thickness of the transition layer is allowed to float, in many cases a better fit can be obtained. This represents an effectively thicker dead layer than what was measured by the manufacturer. It is not clear that this implies that the dead layer is actually thicker than what the manufacturer specified, or if there is a different effect that is effectively aliased by this model.

Comparison of Simulations with Dead-Layers to Calibration Data

Both of these approaches are compared to ^{228}Th calibration data in Figures 3.9 and 3.10. Figure 3.11 includes both approaches and the calibration data in the same plots. The differences between the two methods are most apparent at energies below ~100 keV, in the peak-to-compton ratios throughout the spectrum, and in the region between the 2615 keV photon peak and its associated Compton edge at 2380 keV. Without accounting for the dead layer, this region is only populated by photons with <9% energy loss due to forward scattering, and events with multiple high-energy Compton scatters in the same detector. If

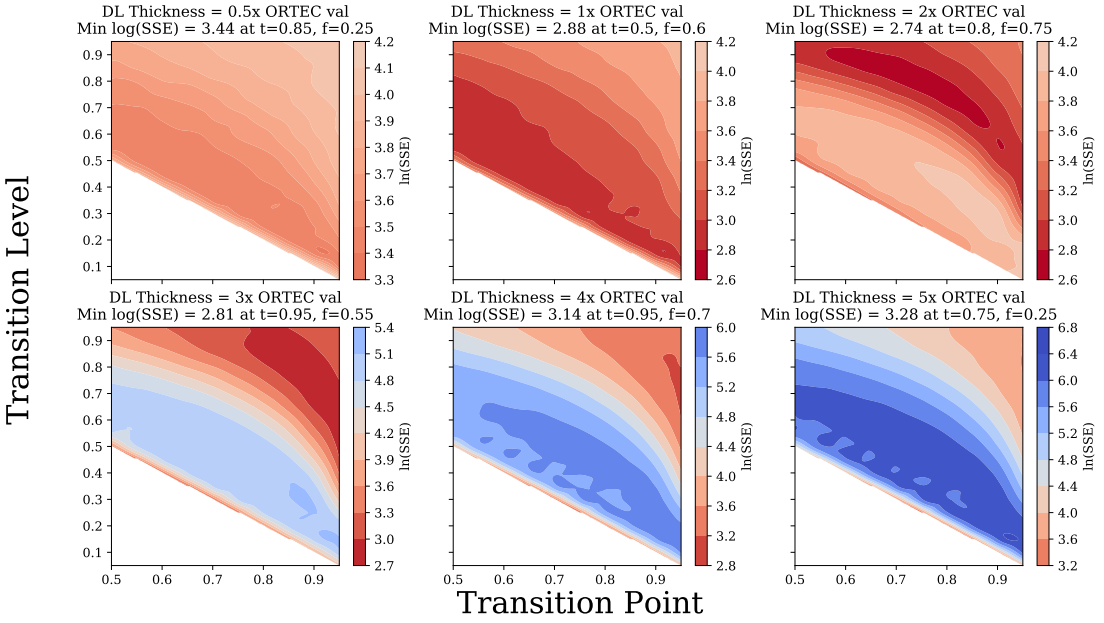

Figure 3.8: This figure shows the natural logarithm of the sum of squared errors between various sets of transition layer models. The transition layer parameters of x_t/t and f are shown here on the Y and X axes respectively, and the overall dead layer thickness is different in the different panels. The model is actually implemented as the deadness instead of the activeness, or $1 - F(x)$, and f is constrained to be greater than or equal to x_t/t. The global minimum can be seen on the upper-right panel, where the overall dead layer thickness is simulated as twice the measured value in the detector database.

the standard flat dead layer model is used, only these two effects are meaningful, and are not sufficient to recreate what is seen in the data. When the new transition-layer model is instead used for the dead layer, the simulation matches the data quite well. At low energies, the transition-layer model creates a population of events that rises with decreasing energy. It should be noted that the agreement with calibration data achieved below 200 keV was not

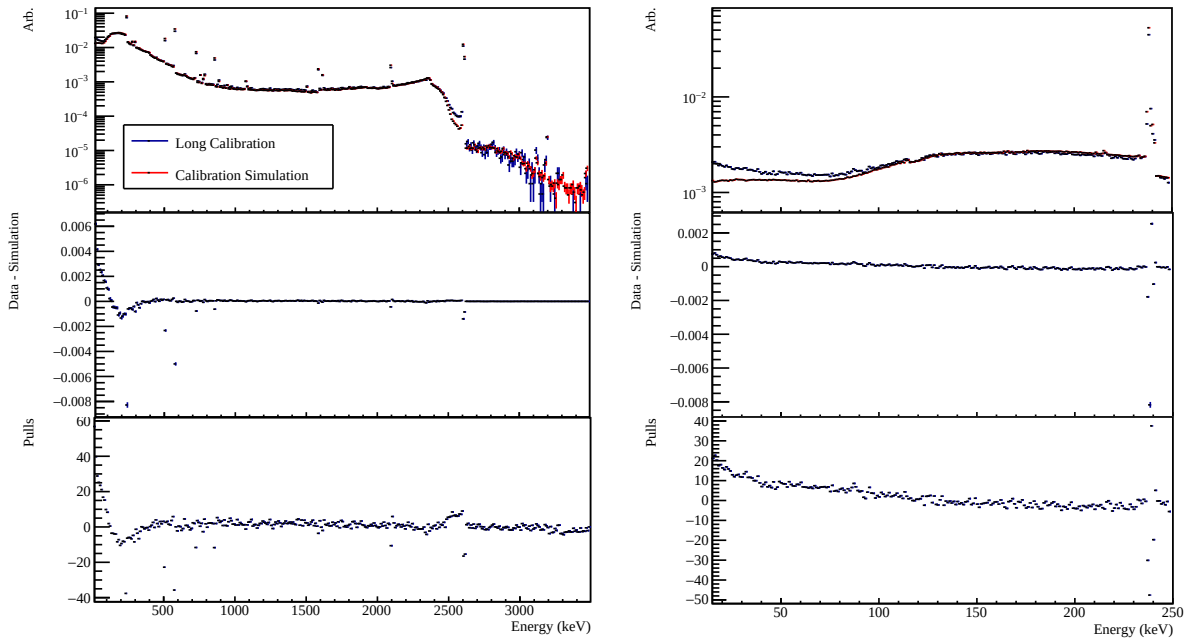

Figure 3.9: Full-spectrum comparison of simulated calibration data using the flat dead-layer model to data taken with the module 1 calibration source. Each spectrum is normalized such that the sum of its bin contents is 1. The error bars on the residuals include the statisical uncertainty for both simulation and data.

explicitly fit out, since the lowest energy window that was fit did not extend below 237 keV. Rather, the rise at low energy appears to be a natural behavior of this parameterization of the dead layer, and robust over a wide range of the dead-layer parameter values. This effect is not reproduced at all with the standard dead-layer model but can be seen quite clearly by comparing Figure 3.9 (flat dead layer) with Figure 3.10 (transition dead layer). At energies below 200 keV, the flat dead layer model does not match the data as well as the transition layer model, and has much higher residuals.

Figure 3.12 shows a comparison of the simulated spectrum for decays of ^{222}Rn in the volume between the inner shield pocket and the cryostats, which is continuously purged

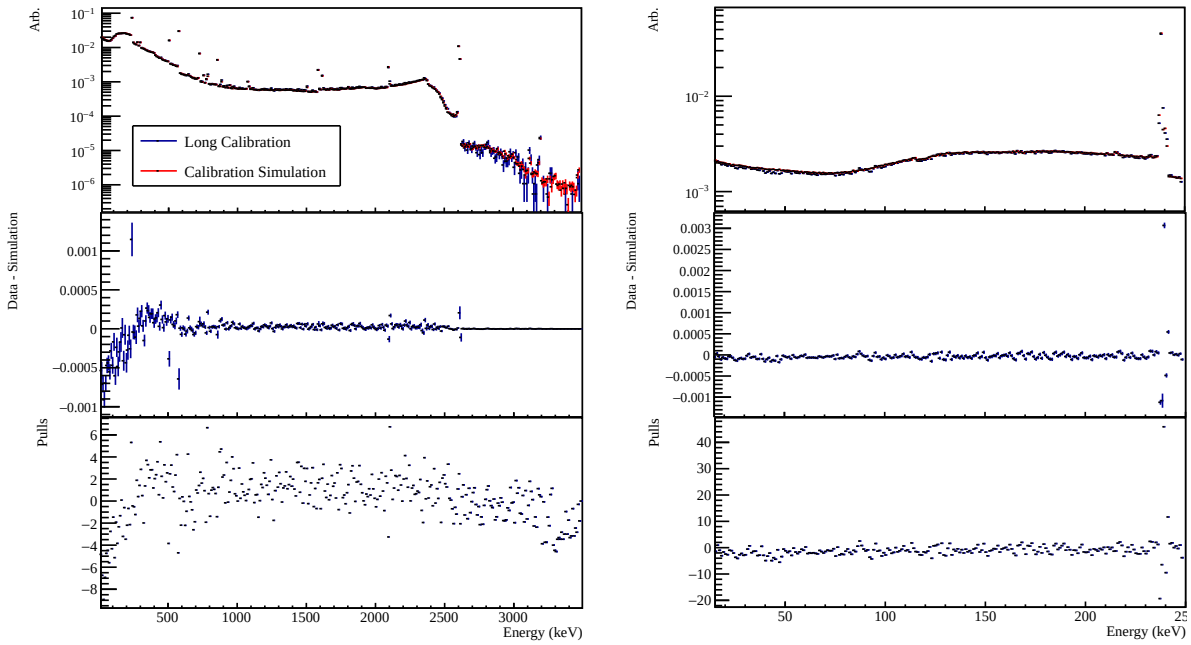

Figure 3.10: Full-spectrum comparison of simulated calibration data using the transition dead-layer model to data taken with the module 1 calibration source. Each spectrum is normalized such that the sum of its bin contents is 1. The error bars on the residuals include the statisical uncertainty for both simulation and data.

with with boil-off from liquid nitrogen. In data set 0, the purge was disabled for a period of time to enable radon from the lab air to penetrate this volume, enabling the acquisition of a ^{222}Rn energy spectrum. Only decays along the surface of the N2 volume are simulated for the plots on the left side of Figure 3.12, while the right side is a simulation of decays of ^{222}Rn in the bulk of the N2 volume. Even though the detector resolution and dead-layer parameters were characterized using data from the ^{228}Th calibration system, the simulated ^{222}Rn spectrum matches the true ^{222}Rn spectrum quite well. It should be stressed that no fitting was performed, other than setting the integrals of both spectra equal to 1. In particular, the simulation is good enough to be able to distinguish between the bulk and

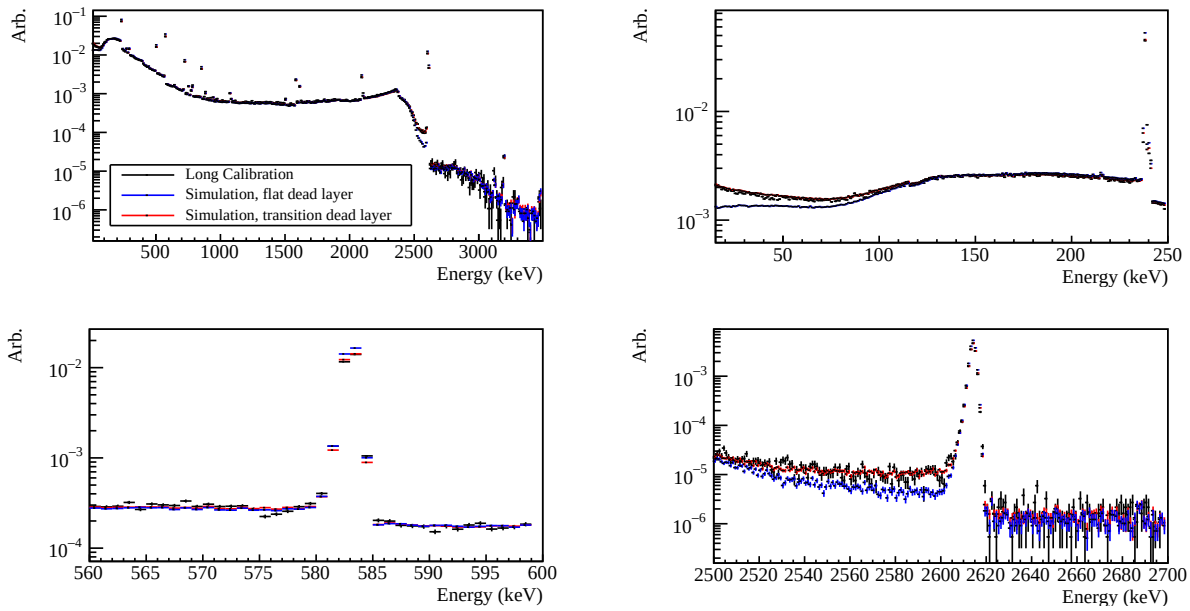

Figure 3.11: Full-spectrum comparison of both the flat and transition dead-layer models to data taken with the module 1 calibration source. Each spectrum is normalized such that the sum of its bin contents is 1.

surface simulations of ^{222}Rn in the N2 volume, as can be seen in in Figure 3.12. This gives us confidence that the parameters extracted from the calibration data can accurately model energy spectra from other components and isotopes.

In Figures 3.9-3.12, the spectra are all simply normalized to 1, giving a good comparison of the shapes of the spectra, but not the overall rates. In Appendix C of his PhD thesis, MAJORANA collaborator Tom Gilliss compared the simulated calibration spectra for each detector individually while normalizing absolutely to the measured activity of the ^{228}Th source used by MAJORANA. He found mostly good agreement between the simulated spectra and the calibration spectra for all but one detector [89] in module 2, which had an overall simulated rate ~30% higher than what was observed in the calibration data.

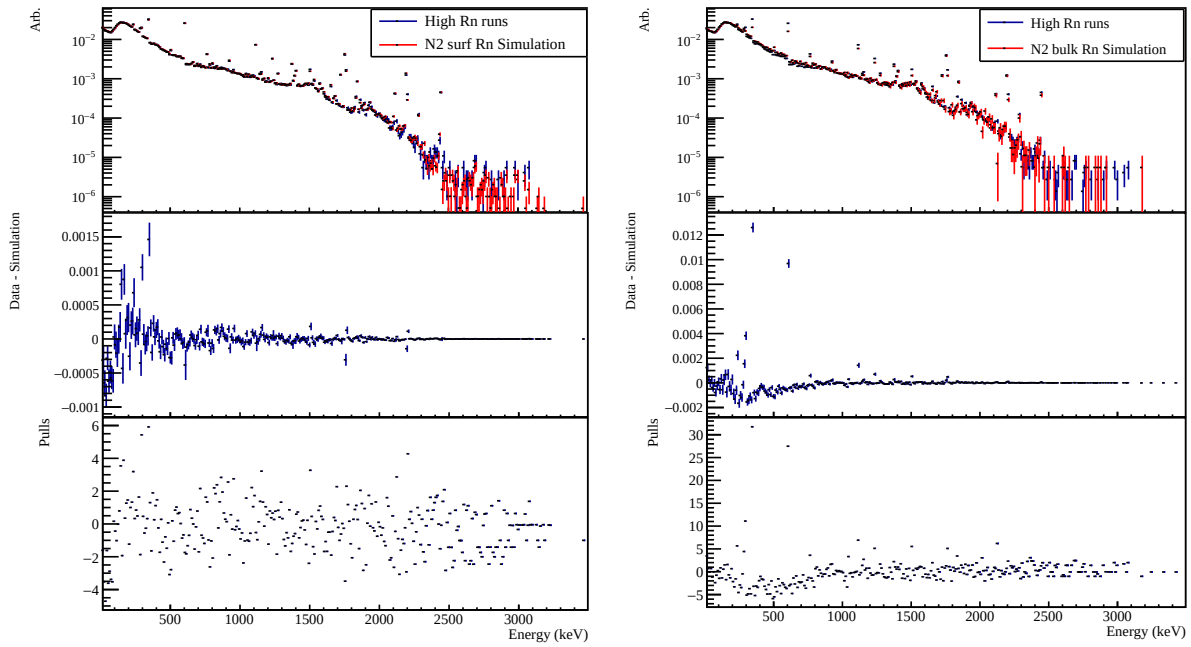

Figure 3.12: Full-spectrum comparison of simulated radon data to data taken with lab air (radon) in the shield cavity. The left side shows a simulation of decays of ^{222}Rn on the surface of the N2 cavity, while the right side shows a simulation of decays of ^{222}Rn in the bulk of the N2 cavity. The simulation is sensitive enough to distinguish between the two, and indicates that ^{222}Rn is much more accurately described by the surface simulation rather than the bulk simulation. Each spectrum is normalized such that the sum of its bin contents is 1. The error bars on the residuals include the statisical uncertainty for both simulation and data.

There is a fairly significant disagreement between the simulated and the true calibration spectra in some detectors if the overall thickness of the dead layer is not allowed to float and instead fixed to the value measured by the detector manufacutrer (ORTEC for the enriched detectors, Canberra for the natural detectors). Figures 3.13 and 3.14 illustrate this effect, with the detector exhibiting this effect most strongly shown. The best fitting thickness for

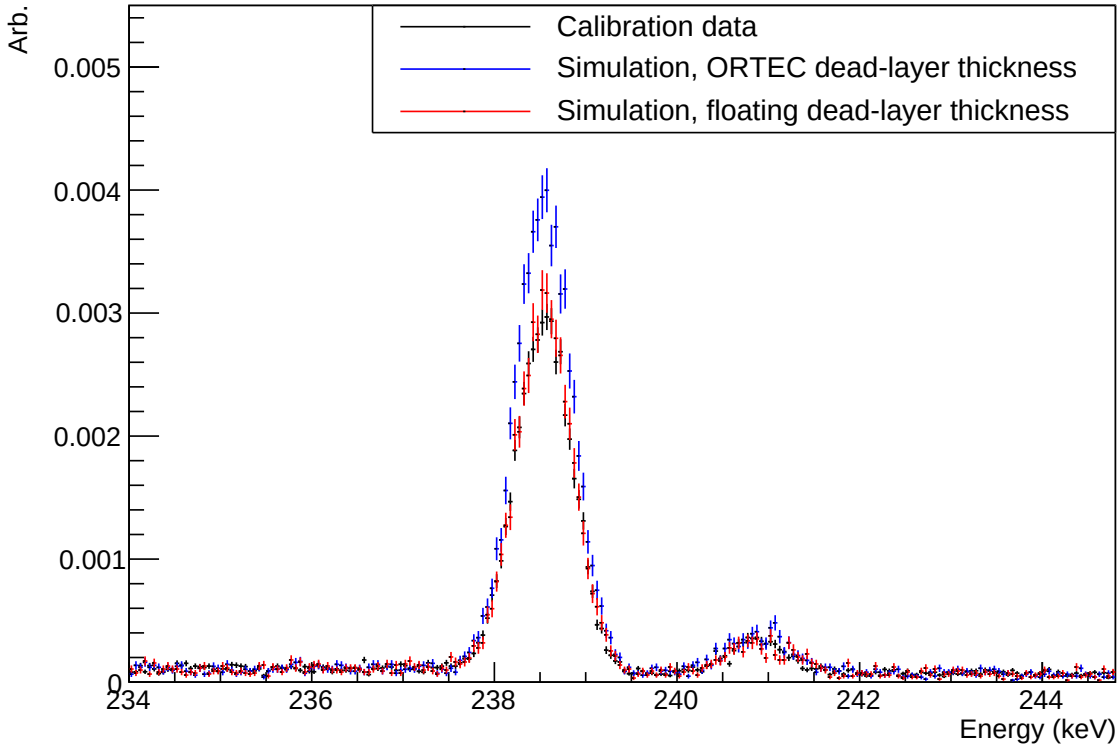

Figure 3.13: Shown is a comparison for a single detector of a simulation with the overall dead-layer thickness fixed to the value measured by the detector manufacturer (blue) and with the thickness allowed to float (red) compared to data (black), at the 238 keV photon peak in the decay of ^{212}Pb. The detector chosen is C1P7D3, which exhibits the largest deviation from the measured thickness. The calibration data shown is from data set 5, and each spectrum is normalized such that the sum of its bin contents is 1.

this detector was 4 times as thick as that measured by the manufacturer. Because this effect can be so strong for some detectors, I have allowed the overall thickness to float when measuring the dead-layer model parameters on the calibration data. Some discussion of what

could be causing this effect and how it might affect the results of the background modeling process is presented in Section 5.2.4.

Recently, the CDEX experiment published a paper with a different, but similar, mathematical representation of the transition dead layer [90]. Like the representation presented here, it includes a section that is concave up followed by a section that is approximately linear, but also includes a fully dead region near the surface of the crystal. This is in conflict with the precipitate model (simulations of it and comparison to data) from [88], which indicates that some charge can be collected all the way out to the surface. CDEX was able to separate both their simulated and calibration data into bulk and surface events (based on the waveform 10%-90% risetime for the calibration data), which gave them an extra piece of information to constrain the parameters of their model. Clint Wiseman developed a surface-event tagger [91] that could be used to do the same thing with MAJORANA data, likely improving the accuracy of the simulated dead-layer parameters. It would also be interesting to compare the performance of the two models, to see if one is noticeably more accurate than the other.

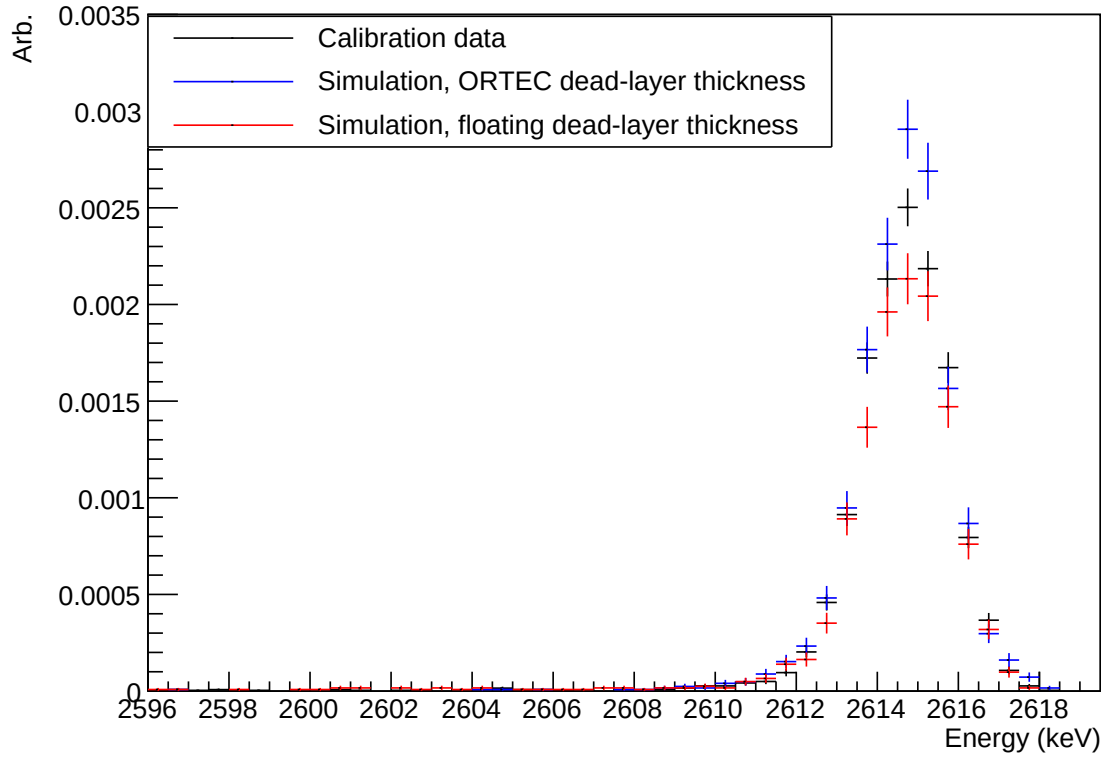

Figure 3.14: Shown is a comparison for a single detector of a simulation with the overall dead-layer thickness fixed to the value measured by the detector manufacturer (blue) and with the thickness allowed to float (red) compared to data (black), at the 2615 keV photon peak in the decay of ^{208}Tl. The detector chosen is C1P7D3, which exhibits the largest deviation from the measured thickness. The calibration data shown is from data set 5, and each spectrum is normalized such that the sum of its bin contents is 1.

3.3 Simulation of Analysis Cuts and Comparison to Data

This section will assess the accuracy of the modeling of the major cuts applied to the data during the analysis stage: Granularity, and A versus E. The DCR effect (see Section 2.6.2) is currently not simulated as the model of the exact mechanism is not sophisticated enough yet to be included here. Therefore, we always apply the DCR cut when fitting to data from the DEMONSTRATOR, and assume the residual contribution of alphas to the spectrum is negligible compared to the other backgrounds within the energy ranges of the fits discussed in the following chapters. The best-fit background models are consistent with this assumption.

3.3.1 Granularity Cut Modeling

The granularity cut is modeled well in the simulations. Because this cut does not rely on any waveform analysis or tunable parameters, it is straightforward to emulate and implement with `MaGe` and `GAT`. Figure 3.15 shows a data-to-simulation comparison of the ^{228}Th calibration source energy spectrum after application of the granularity cut. The two pulls (normalized residuals) with the largest magnitude are located around the 511 keV peak, primarily composed of annihilation photons, which experience some physical effects causing extra broadening that are not well-modeled by Geant4. Otherwise the pulls are mostly well-behaved.

3.3.2 A versus E Cut Modeling

The A versus E cut is more difficult to model well in the simulations because it is a waveform-shape-based cut. Emulation of waveforms in the DEMONSTRATOR has been an ongoing project within the collaboration [92] [93], but was not fully implemented in time to be used for this analysis. Because the DEMONSTRATOR consists of 58 individually instrumented detectors, each must be characterized individually if accurate waveform emulation is to be achieved. Instead of waveform emulation, an heuristic was developed to approximate the A

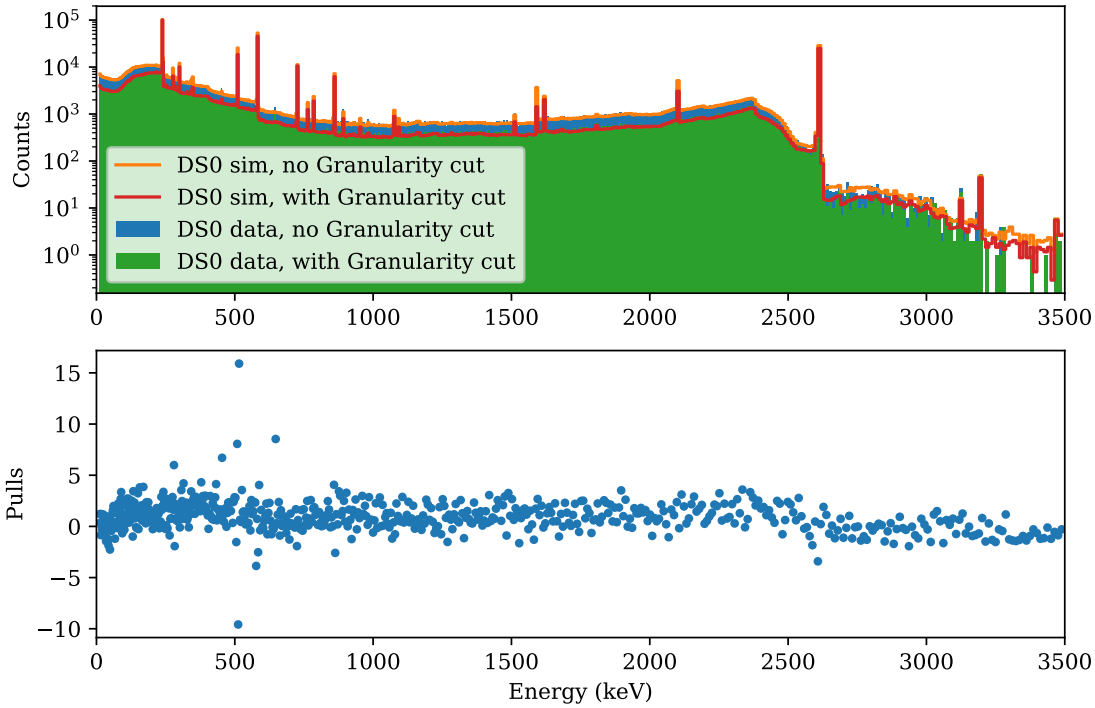

Figure 3.15: A comparison of simulation and data for the granularity cut on the ^{228}Th calibration source energy spectrum. Each spectrum without the granularity cut (blue and orange) is normalized such that it sums to 1. The spectra with the granularity cut included are normalized by the same factor. The pulls (normalized residuals) include errors from both the simulated and acquired data.

versus E cut [87].

The heuristic is the maximum of an energy-weighted timing difference calculated for all pairwise combinations of simultaneous energy depositions in a detector. Conceptually, the easiest type of multi-site event to detect is one where two large and equally-sized energy depositions happen in regions of the detector with significantly different drift times. As the

energies of the pulses get smaller or more asymmetric, or the drift times get more similar, the multi-site event becomes harder to distinguish from a single-site event. Each detector is somewhat different from all the others, and so a detector-by-detector tuning of the dT heuristic cutoff used in the simulation was done by Ethan Blalock [87]. With the tuning, the agreement between data and simulation of the ^{228}Th calibration source energy spectrum is still not as good as that of the granularity cut, particularly below 500 keV. For this reason, the dT heuristic/A versus E cut is not used in fitting the background model. However it is accurate enough at high energies that it can be used as a crosscheck of the background spectrum near $Q_{\beta\beta}$ after a fitted model is found.

Figures 3.16 and 3.17 show the comparison of the simulated dT heuristic cutoff to the calibration data with the A vs. E cut applied. Note the agreement between simulation and data is much worse than for the granularity cut. Since background fits based on the dT heuristic were not used in the final background model fits, any inaccuracies will not have any effect on the results presented here. However, if the accuracy could be improved, including it in future background models could improve the overall precision and/or accuracy of the best-fit background model.

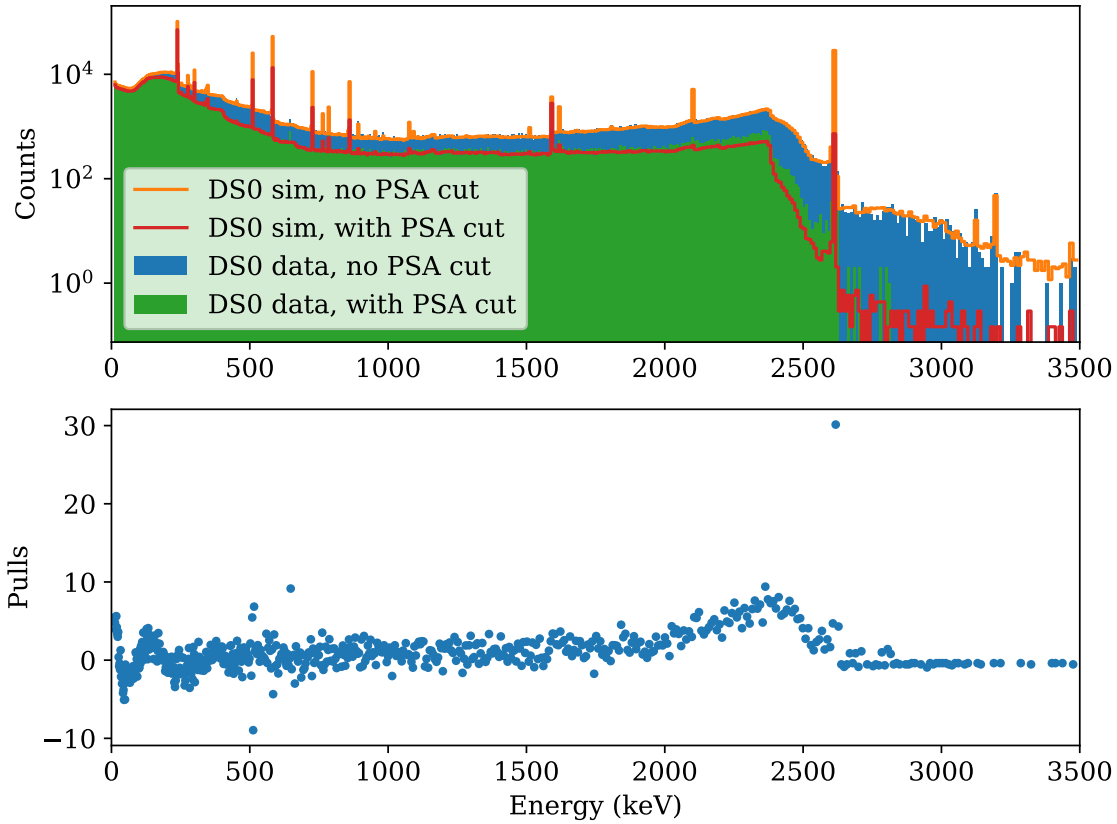

Figure 3.16: A comparison of simulation and data for the A vs. E cut on the ^{228}Th calibration source energy spectrum. Each spectrum without the PSA cut (blue and orange) is normalized such that it sums to 1. The spectra with the PSA cut included are normalized by the same factor. The pulls (normalized residuals) include errors from both the simulated and acquired data.

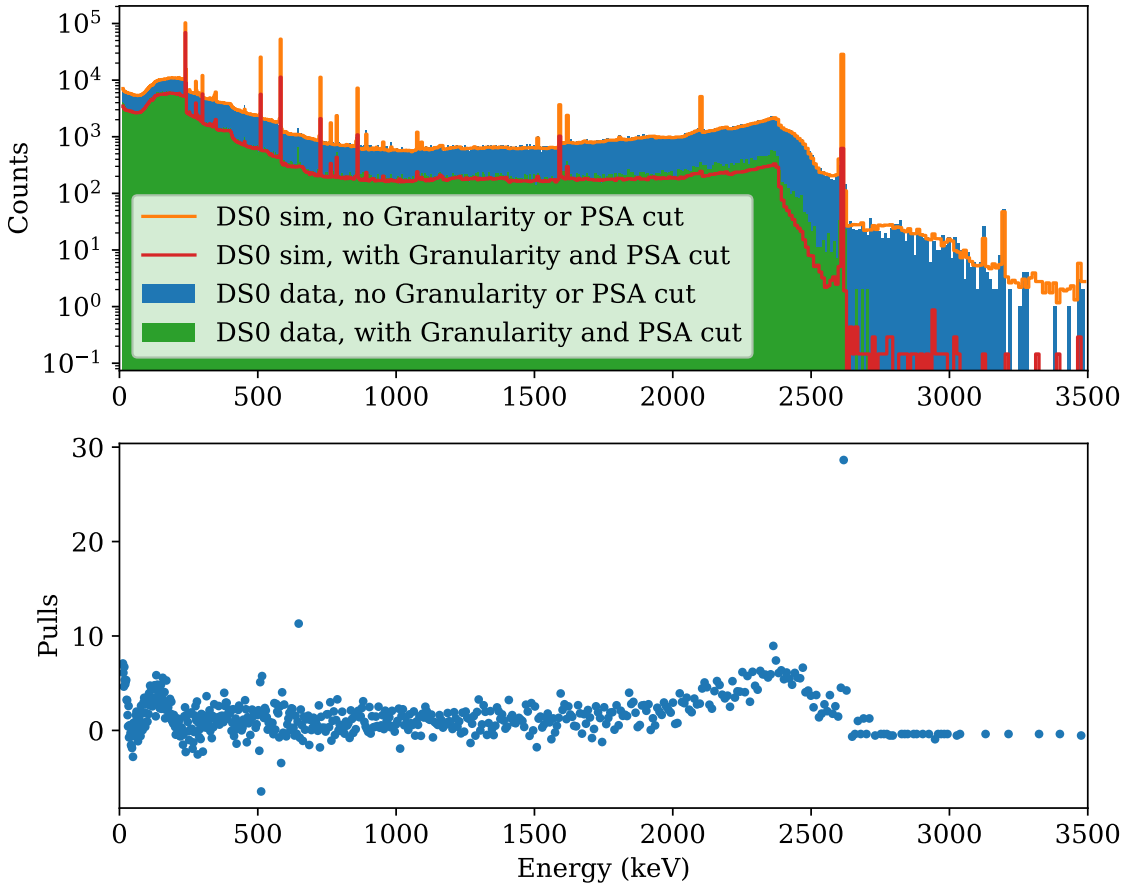

Figure 3.17: A comparison of simulation and data for the granularity and A vs. E cuts on the ^{228}Th calibration source energy spectrum. Each spectrum without either the granularity cut or the PSA cut (blue and orange) is normalized such that it sums to 1. The spectra with the cuts included are normalized by the same factor. The pulls (normalized residuals) include errors from both the simulated and acquired data.

3.4 Overview of the statistics of simulations done for this work

Fitting 1 dimensional spectral data to a simulated spectrum as is done in this work can be sensitive to statistical fluctuations in the simulations, as well as in the data. Two things were done to mitigate this source of uncertainty in this result. First of all, we endeavored to simulate enough primary decays for each PDF in the model so that the number of detected energy depositions in the PDF would be 10x the size of the entire fitted data set. This does not eliminate this source of uncertainty, especially for PDFs where part of the energy spectrum has low efficiency but is nonetheless very important to the overall fit (e.g. high energy events from decays of ^{232}Th or ^{238}U in the lead shield). But it should suppress it to the point where it becomes a subdominant source of uncertainty.

In the end, the construction of the likelihood function naturally accounts for the statistics of the simulations (see Sections 4.2 and the beginning of Chapter 5). Therefore, although high-statistics simulations can improve the precision of the result, the statistical uncertainty does not need to be handled separately. See Appendix A for a comprehensive listing of the simulations produced for this analysis.

Chapter 4

MODELING THE BACKGROUNDS OF THE MAJORANA DEMONSTRATOR

The goal of the MAJORANA DEMONSTRATOR background model is to identify with maximum possible confidence the sources of the background radiation we detect. There are several possible approaches one could take to achieve this, ranging in sophistication from the most basic strategy of looking at histograms of the energy spectra produced by the array and comparing heights of gamma peaks by hand, to a much more sophisticated approach taken in this work of simultaneously fitting multiple detector spectra across multiple data sets with shared parameters. I will present the results of the simultaneous fitting approach in this chapter.

4.1 Simultaneous Fitting of Detectors and Data Sets

The array nature of the DEMONSTRATOR gives it some additional sensitivity to the location of radiogenic backgrounds that a similarly sized giant crystal of ^{76}Ge would not have, were such a crystal possible to fabricate. Since each detector is independently instrumented, the energy spectrum for the full array can be broken down all the way into the spectra observed by each individual detector. It is then possible in principle to simulate the energy spectrum for each potential background source for each detector and fit them all simultaneously, floating the activity densities of contamination in each component. Since the number of counts detected in each bin of the energy spectrum of a detector is independent of the number of counts in all the other bins, a simultaneous fit to all 58 detectors is equivalent to a fit to an energy spectrum that is 58 times as long as that of a single detector.

In addition to the inherent granularity of the array, the two major analysis cuts we simulate — the granularity (multi-detector) cut and the A vs. E cut — can in principle be utilized in the fit. From these two cuts, four independent spectra can be constructed out of the original energy spectrum: hits passing both cuts, hits failing both cuts, and hits that pass one cut and fail the other. This can also be thought of as a fourfold increase in the number of bins in the energy spectrum, bringing the total number of independent observations up to 232 times higher than a fit to the full array spectrum with no cuts applied.

Finally, MAJORANA has acquired data with the DEMONSTRATOR over more than 7 different data sets (see Table 2.3). Some of these data sets are demarcated by changes to the data acquisition system or data-taking parameters that should not affect the measured energy spectra used in these fits, but there were two big changes to the detector and shielding configurations during this time. The first change happened during the transition from data set 0 to data set 1, when the inner UGEFCu shield was installed inside of the outer OFHCCu shield and additional shielding blocks made from UGEFCu were placed inside the module 1 cross arm. The second major change was between data sets 2 and 3/4, when module 2 was installed. The transition from data sets 3/4 to 5 is also potentially significant, since data set 5 is the first data set with both modules and therefore has a more effective granularity cut.

Besides the geometric considerations outlined in the previous paragraphs, the relatively short half-life of some of our potential contaminants gives us an additional reason to fit data sets independently. ^{60}Co, ^{57}Co, ^{68}Ge, ^{54}Mn, ^{210}Pb, and ^{3}H all have half-lives that are short enough to be detectable in the DEMONSTRATOR given that it now has several years worth of data. To account for these decays, the activity that is floated in the fit is the activity at the beginning of data set 0. The effective activity for each contaminant is then computed for each data set by assuming an exponential decay and computing the expected value of the activity, given the official start and end points of the data set. This is still an approximation since it does not correctly account for down time within a data set, but

the down time since data set 0 has been minimal enough that this approximation should be sufficient. For example, data sets 5a and 5b were acquired over the course of 156 days, but the DEMONSTRATOR was only taking good background data for 121 days (the remainder mostly being periods of calibration). If we assume that all of the non-background data periods came at the beginning of the data set (an extremely conservative assumption as they are actually spaced quite evenly throughout), then the true data-set-averaged activity for ^{60}Co would be 81.45% of what it was at the beginning of data set 0. But we would compute a data-set-averaged activity of 81.98% of the beginning-of-data-set-0 activity. Other isotopes would see a similar extremely small maximum possible bias.

In practice, all of these increases in the effective size of the spectrum are only useful if the simulation of them is accurate. In Section 3.3 I gave an overview of the apparent accuracy of those simulations. Because the simulated A versus E cut is distorted significantly from that measured in calibration data, I have not included it in my fits of the background model, but I have included the granularity cut. Furthermore, increasing the effective size of the spectrum can lead to an increase in computation time for a binned fit, which does become a problem for the particular form of the likelihood function defined in the next section.

4.2 Constructing the Likelihood Function

Roger Barlow and Christine Beeston outlined in [94] a method to perform a fit of a linear combination of simulated PDFs that may contain bins with high statistical uncertainty, to a data set like that obtained by the MAJORANA DEMONSTRATOR.

The simplest way one might want to perform a fit like this would be to minimize the sum of Neyman χ^2 statistics for each bin of data. In that case, the function one needs to minimize to fit the model to the data is given by equation 4 in [94]:

$$\chi^2 = \sum_i \frac{(d_i - f_i)^2}{d_i} \tag{4.1}$$

where d_i is the number of counts in the data in bin i and f_i is the number of counts in bin i

according to the fitted model. This however does not account for two facts that can have a sizeable effect on the final result: (1) the bin errors are assumed to be normally distributed, but in fact they are only asymptotically normally distributed in the limit of high bin counts, and (2) the simulated PDFs are assumed to be exact when in fact they themselves are simulated with Poisson errors similar to that of the binned data. Both of these facts can be handled correctly with a modification to the likelihood function and are given by equation 9 in [94]:

$$\ln \mathcal{L} = \sum_{i=1}^{n} d_i \ln(f_i) - f_i + \sum_{i=1}^{n}\sum_{j=1}^{m} a_{ji} \ln(A_{ji}) - A_{ji} \tag{4.2}$$

where d_i is the number of counts in the data in bin i, $f_i = \sum_{j=1}^{m} p_j A_{ji}$ is the number of counts fitted to the data in bin i, a_{ji} is the number of counts from simulated source j in bin i, A_{ji} is the "true" number of counts from source j in bin i (i.e. what the a_{ji} converge to as the number of simulated particles increases without bound), and the p_j are the free weighting parameters that fit the model to the data. In the implementation used for this result, the parameters that are floated are P_j in the equation

$$p_j = P_j \epsilon_j m_j t \tag{4.3}$$

where the P_j are activity densities with units of Bq/kg, the ϵ_j are the simulated total efficiencies for each source j (the total number of counts in the simulated spectrum divided by the number of decays simulated, with units of counts/decay), m_j is the mass of component j, and t is the livetime of the detector. So the likelihood function becomes:

$$\ln \mathcal{L} = \sum_{i=1}^{n} d_i \ln\left(\sum_{j=1}^{m} P_j \epsilon_j m_j A_{ji} t\right) - \sum_{j=1}^{m} P_j \epsilon_j m_j A_{ji} t + \sum_{i=1}^{n}\sum_{j=1}^{m} a_{ji} \ln(A_{ji}) - A_{ji} \tag{4.4}$$

This formulation now correctly incorporates all sources of statistical uncertainty, but the A_{ji} are not known and are treated as free parameters. This in principle explodes the dimensionality of the space of free parameters, bringing it from just m free paramaters associated with the p_j to $m \cdot (n+1)$ parameters for all the p_j and A_{ji}. However, Barlow and

Beeston show that the optimal values for the A_{ji} are completely determined by the values for the p_j so the fit still only has m independent degrees of freedom. They define the useful equation 4.5.

$$A_{ji} = \frac{a_{ji}}{1 + p_j t_i} \tag{4.5}$$

When the likelihood function is evaluated for a specific value of the parameters p_j, one only needs to solve the transcendental equation 4.6 for each bin i in the binned data.

$$\frac{d_i}{1 - t_i} = \sum_j \frac{p_j a_{ji}}{1 + p_j t_i} \tag{4.6}$$

Now the number of free parameters is back down to m, but the transcendental equation 4.6 does create some additional overhead, since it must be solved for each bin every time the likelihood function is evaluated for a new set of p_j. This is the primary disadvantage of the approach from [94]: its slow computation. Because it correctly handles the problems of low simulated statistics, it is the approach we use to fit the MAJORANA DEMONSTRATOR background model. But because of its slowness, I have had to make some concessions to get a version of this likelihood function implemented that computes in a reasonable amount of time.

Instead of fitting all detectors, data sets, and cut spectra simultaneously, I only fit a reduced set of these partitions of the data. The detectors in the two modules are fitted separately, as are the enriched and natural germanium detectors for a total of four effective "detector" energy spectra. Because of the aforementioned concerns about the accuracy of the simulated A vs. E cut over the entirety of the energy spectrum, I only fit to the two spectra generated by applying the granularity cut. And instead of fitting all data sets from DS0 to DS6a individually, I fit only the three groups of data sets demarcated by changes to the physical configuration of the DEMONSTRATOR: DS0, DS1+DS2, and DS3/4 and beyond

[1]. This gives an effective spectrum that is only 24x as big as the full-array spectrum from all data sets with no cuts, and can be fitted to the full set of simulated background PDFs in a few days. The likelihood function itself is implemented in Cython [95], a Python package that facilitates translating Python code into C for often significant improvements in speed. Implementing the likelihood function in Cython (which also allows it to be parallelized with OpenMP) led to a tenfold decrease in the computation time for evaluation over a previous implementation in NumPy [6].

4.3 Binning the Data and Simulations

Due to the world-class energy resolution of the MAJORANA DEMONSTRATOR, many features are visible in the detected energy spectrum. There are peaks visible from photons emitted in the decays of ^{40}K, ^{60}Co, ^{57}Co, ^{210}Pb, ^{232}Th, ^{238}U, ^{54}Mn, ^{68}Ge, and ^{65}Zn. There is even a hint of a peak from ^{137}Cs in some of the natural germanium detectors, but it is too weak to include in the background model. Because the peaks all are clearly identifiable and exist at specific energies, the data were binned to a histogram with variable width bins that are designed to ensure that nearly all events from a given photon peak are in the same bin. This was done by identifying a list of peaks to which to pin the binning scheme (given in Table 4.1), aligning the bin edges so that according to the computed peak-shape at that energy, 99% of all decays would be placed in that bin, and then linearly increasing the width of bins between the specified peaks. This has the effect of producing a bin width of ~2 keV at the lowest energy (~7 keV) and ~13 keV at the highest energy (~3500 keV)[2] A plot of the bin

[1]The two modules took data with separate data acquisition systems during data sets 3 and 4, so the granularity cut is slightly less effective. But nothing about the background environment of the modules changed between DS3/4 and DS5. Simulations of the configuration from DS3/4 are available, and suggestions are made in Section 6.2.2 about what it would take to utilize them.

[2]The data used in the fit is produced by the standard MAJORANA skim file generator, which utilizes both gain channels (as described in Section 2.3.1). This means that any concerns about possible extra dead-time incurred from using only the high-gain channels to construct the data do not apply, since the low-gain channels were used correctly to avoid this source of deadtime.

width used as a function of energy is given in Figure 4.1. Due to minor variations in the energy resolution function over time, the specific bin edges used are custom to each data set, a choice that could be revised in future work.

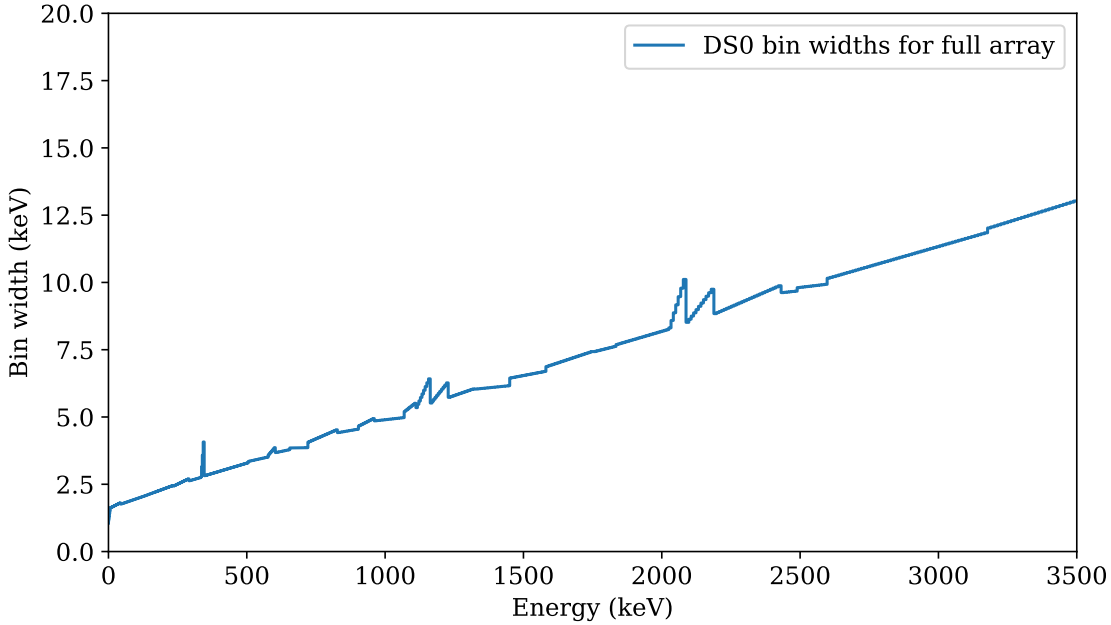

Figure 4.1: Bin widths used for data set 0 full array spectrum. Apparent discontinuities appear between peaks that are relatively close together, due to the necessity of keeping both peaks optimally located in the binning scheme while also having an integer number of bins between peaks.

The peaks included in the binning scheme were chosen based on simulations of the DEMONSTRATOR. For several contaminants (^{40}K, ^{60}Co, ^{57}Co, ^{210}Pb, ^{54}Mn, and ^{68}Ge), only a few (< 5) peaks are possibly visible in the DEMONSTRATOR, so they were all included. ^{65}Zn has a potentially prominent X-Ray at 8 keV, but that peak is close enough to the ^{68}Ge X-Ray at 10.35 keV that it is not possible to fit a bin in between them. Since ^{68}Ge is expected

to be more of a concern than ^{65}Zn, it was prioritized. ^{232}Th and ^{238}U both produce a rich spectrum with many possible photon peaks, too many to include all of them in the binning scheme. A visual inspection of the simulated spectrum for decays of ^{232}Th and ^{238}U in the LMFEs was performed, and the most prominent peaks were included in the binning scheme. Because the number of bins in between each peak included in the binning scheme must be an integer, peaks that are very close together in energy can produce significant discontinuities in the bin widths, as is visible in Figure 4.1. Preventing these discontinuities from becoming too severe or numerous is what determined the point at which a peak in the simulated ^{232}Th or ^{238}U spectrum was determined to be insufficiently prominent to include in the binning scheme.

An example of a peak fitted to calibration data is shown in Figure 2.9. The bin associated with this peak is computed by integrating equation 2.3 such that 0.5% of the peak shape extends outside the bin edges on either side. In this case, the bin extends from 236.8 keV to 239.5 keV, and because the peak shape is assymetric, the peak mode is not centered in the bin. Bins associated with other peaks in the binning scheme are computed in a similar fashion.

Peak energy (keV)	Parent nuclide (parent in chain)	Bin width in data set 6 (keV)
10.35	^{68}Ge	1.8
46.539	^{210}Pb	2.0
136.47356+6.404	^{57}Co	2.4
238.632	^{212}Pb (^{232}Th)	2.7
295.2228	^{214}Pb (^{238}U)	2.9
338.320	^{228}Ac (^{232}Th)	3.1
351.9321	^{214}Pb (^{238}U)	3.1
510.9989	electron annihilation/^{208}Tl (^{232}Th)	3.7
583.187	^{208}Tl (^{232}Th)	3.9
609.320	^{214}Bi (^{238}U)	4.0
661.657	^{137}Cs	4.2
727.330	^{212}Bi (^{232}Th)	4.4
834.848	^{54}Mn	4.7
911.204	^{228}Ac (^{232}Th)	5.0
968.971	^{228}Ac (^{232}Th)	5.1
1077.34	^{68}Ga (^{68}Ge)	5.5
1120.294	^{214}Bi (^{238}U)	5.6
1173.228	^{60}Co	5.8
1238.122	^{214}Bi (^{238}U)	6.0
1332.492	^{60}Co	6.3
1460.820	^{40}K	6.6
2614.511-2*510.9989	^{208}Tl DEP (^{232}Th)	7.0
1764.491	^{214}Bi (^{238}U)	7.5
1847.429	^{214}Bi (^{238}U)	7.8
2039.061	$Q_{\beta\beta}$	8.3
2614.511-510.9989	^{208}Tl SEP (^{232}Th)	8.5
2204.059	^{214}Bi (^{238}U)	8.8
2447.70	^{214}Bi (^{238}U)	9.5
1173.228+1332.492	^{60}Co	9.7
2614.511	^{208}Tl (^{232}Th)	10.0
2614.511+583.187	^{208}Tl (^{232}Th)	11.7

Table 4.1: Peaks used to pin the binning scheme. The bins are designed so that 99% of events in each peak will end up in the same bin.

4.4 Method for fitting simulated PDFs to background data

As described in the previous chapter, the MAJORANA DEMONSTRATOR contains a large number of parts, nearly all of which have been simulated using the detailed geometrical model constructed with `MaGe`. There are approximately 20 component groups and several radioactive isotopes that have been simulated in the different component groups. A full documentation of all simulations performed comprises the entirety of Appendix A, and plots showing the location of each component group comprise the entirety of Appendix B. The specific simulated energy spectra included in the fits presented in this chapter are available with the full results in Appendix C. Furthermore, the component groups that have a direct line-of-sight to the detectors have both bulk and surface contamination simulated separately. In total, 123 PDFs are simulated and fit to the data which is segmented by data set, module, detector type (enriched or natural), and multiplicity (granularity), leading to 24 histograms fit to each PDF. They are fit to an energy range from 7 to 3500 keV. The lower bound is set to be sensitive to the ^{65}Zn X-Ray at 8 keV, and the upper bound is high enough to detect the sum-peak of the 583 and 2614 keV photons from the decay of the ^{232}Th-chain isotope of ^{208}Tl.

Producing a model from these 123 PDFs is not a trivial task, and one cannot necessarily expect a naive approach of fitting all of them simultaneously to produce a good result. Many of them are nearly degenerate with each other (especially PDFs of the same isotopic contaminant from components with similar locations), and so any attempt to find a minimum in the likelihood function could easily find a local minimum instead of the global minimum. Furthermore, as the number of PDFs in the model increases, the time for any particular minimization algorithm to converge increases, perhaps past the point of what is computationally tractable.

The problem of a simple minimization of the likelihood function finding a local but not global minimum can in principle be mitigated by performing many fits of the full model to

the data with different starting values of the parameters. If the space of all possible starting values is sampled densely enough, one of the many iterations of the minimization algorithm will find the global minimum of the likelihood function. In practice, it is not possible to know if one has found the global minimum of the likelihood function just by looking at the results of many fits to the data with randomized starting values. However, with a moderately sized sampling of the space of starting values, we can see the relationship between the best-fit amplitude of each PDF in the model with the found minimum of that iteration of the minimization algorithm.

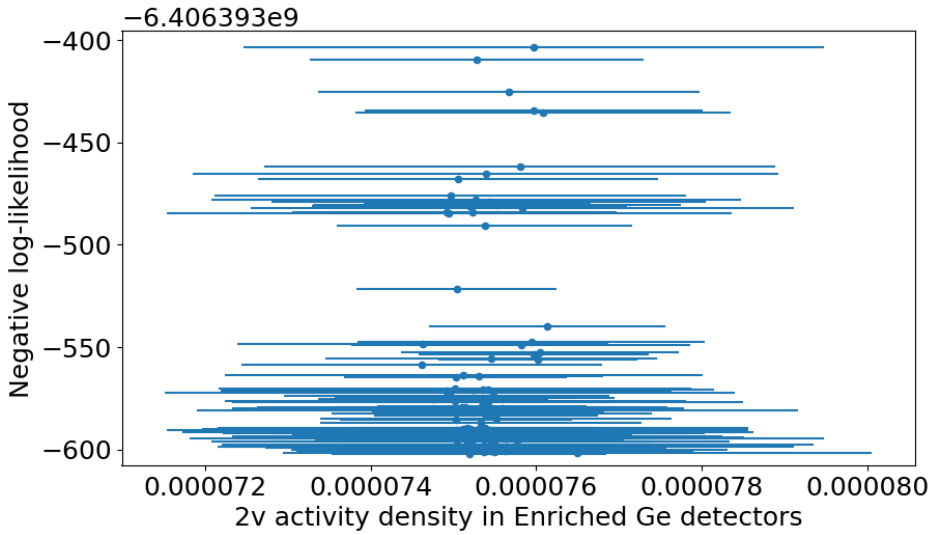

Figure 4.2: Each point on this plot shows the best-fit value found by the Nelder-Mead minimizer for the activity density of $0\nu\beta\beta$ decay in the enriched germanium detectors. Only the starting values for the activity densities are changed to produce the different points on this plot. The error bars are found by applying Wilks' theorem to the neighborhood of the found minimum, using an MCMC technique to explore that neighborhood. For this PDF, the estimated uncertainty from any given run of the minimizer is significantly greater than the variability induced by a different choice of starting values.

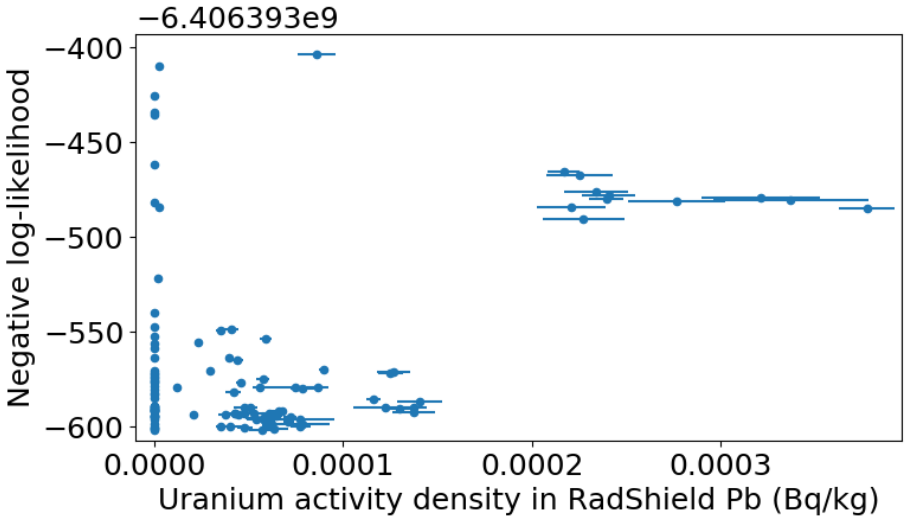

Figure 4.3: Each point on this plot shows the best-fit value found by the Nelder-Mead minimizer for the activity density of decays of ^{238}U and its daughters in the lead shield. Only the starting values for the activity densities are changed to produce the different points on this plot. The error bars are found by applying Wilks' theorem to the neighborhood of the found minimum, using an MCMC technique to explore that neighborhood. For this PDF, the estimated uncertainty from any given run of the minimizer is significantly smaller than the variability induced by a different choice of starting values. Points that appear to be located at an activity density of 0 are in fact located with a very small value with correspondingly small error bars. This comes from the fact that the Nelder-Mead algorithm, being unable to handle constraints on the domain of the parameters, requires that they be log-transformed before minimization so that negative activity densities are forbidden.

Figures 4.2 and 4.3 show this relationship. For some PDFs in the model, such as $0\nu\beta\beta$ decay in the enriched germanium detectors, the best-fit activity density is consistent regardless of the choice of starting values. For others, such as decays of ^{238}U and its daughters in the lead shield, the choice of starting values has a large effect, and the estimated uncertainty

from a single fit and choice of starting values does not accurately return the true uncertainty in that parameter. Including this dependence on starting values in the final estimated uncertainty is necessary to get an accurate result.

The algorithm proposed and employed in this work to fit the simulated PDFs to the background data is then:

1. Fit a model with all possible candidate PDFs to the data set in question while seeding the starting values randomly. In this work, the PDF amplitudes have units of Bq/kg, which represents the activity density of the contamination of a particular radioactive isotope in a particular component or component group. Because equal activity densities in two PDFs do not necessarily generate an equal number of counts detected, the amplitudes were scaled such that all PDFs included in the model started with an activity density generating an equal number of counts. The amplitudes were then each scaled by a random floating-point number between 0 and 2, and then the activity densities of all component groups for each isotope were scaled to better match the most promenent photon peak from that isotope. [3]

2. Perform step 1 many times. In this work, approximately 100 random models were generated in this fashion. The number of random models was chosen to maximize the available computing resources (this would fully utilize the computing cluster I had access to at CENPA). Further work could be done to determine how many random models are sufficient to accurately estimate the best-fit uncertainties, for example by forming a figure of merit. One suggested figure of merit would be to require enough

[3] I chose to randomly linearly scale the randomized activity densities because I wanted to ensure that for each PDF, there was a good chance that it would be seeded with a high total number of counts over the course of all iterations of the method. I suspect that, for PDFs with degenerate shapes, the one that starts with a high value will be more likely to end up with a high best-fit value. If I had scaled logarithmically, the number of times a PDF would start high would have been reduced since the total number of counts must remain constant. I scaled between 0 and 2 because that would, on average, not change the total starting number of counts.

statistics that one finds $\mathrm{Var}_\Delta(\mu_i) << \mathrm{Mean}_\Delta(\sigma_i^2)$ and $\mathrm{RMS}_\Delta(\sigma_i^2) << \mathrm{Mean}_\Delta(\sigma_i^2)$, where $\mathrm{stat}_\Delta(\mathrm{set})$ refers to the statistical value "stat" evaluated over those N members in "set" for which the log-likelihood is less than "Δ", where $N >> 1$. Fit parameters found to be "precise" (to be defined later) were observed to qualitatively meet this criterion (see for example Figure 4.2).

3. Use the results of steps 1 and 2 to calculate a mean and standard error for the fitted activity densities of each component in the model. Calculate the precision of each PDF, which is given by the mean divided by the estimated uncertainty given by the MCMC method.

A single fit in step 1 above is implemented in Python using the `minimize` method of the SciPy.Optimize package [7]. The `minimize` method is a generic method for numerical minimization of scalar functions, and offers several methods. Which method is optimal depends on the problem at hand, and can be affected by the presence or absence of constraints and/or bounds on the floating parameters.

For the background model, we have the constraint that the best-fit activities cannot be negative. This can be enforced in one of two ways: choose a minimization algorithm that allows for parameter bounds, or fit to a transformed version of the parameters, such as the logarithm of the parameters. I explored both of these options, and found that the Nelder-Mead algorithm [96], which requires a log-transformation of the parameters, was consistently the method most robust against failures to converge, and consistently found the lowest value of the likelihood. [4] The Nelder-Mead algorithm does not allow for parameter bounds and thus minimizes the likelihood function in the space of the logarithm of the parameters. A modification to the algorithm was published in 2012 [97] that improves its efficiency with

[4]The results of the studies showing that Nelder-Mead was the best-performing minimization method can be found in Section 4.6.

problems of high dimensionality such as this one. It can be enabled in SciPy.Optimize with an optional argument while still specifying Nelder-Mead as the minimization method, and is used in this analysis.

After the minimum of the likelihood function is found with the Nelder-Mead algorithm, I use a Markov-Chain Monte-Carlo sampling of the likelihood function to estimate the uncertainty on the location of the minimum with the python package `lmfit` [98], which in turn uses the package `emcee` [99]. `lmfit` returns standard error estimates for each parameter given the likelihood function, but the estimates from each fit to the background model need to be combined into a single estimate of the uncertainty, as described in the following subsection.

4.4.1 Calculating the standard error

The fits in step 2 outlined above are not independent, since they consist of the same model fitted to the same data, with only the starting parameters varying. If the minization were capable of finding the exact global minimum of the likelihood function with 100% accuracy independent from the starting parameters, then the standard error estimated with `lmfit` would be comprehensive. Because the found minimum of the likelihood function seems to have some dependence on the starting parameters, however, we must combine the estimates and uncertainties for each parameter into a single estimate. The approach taken here is to treat each estimate and uncertainty as symmetric with Gaussian errors, and to combine them into a multi-Gaussian with the associated mean and standard deviation.

The functional form for a multi-Gaussian is

$$\mathrm{PDF}(x) = \frac{1}{N}\sum_{i=1}^{N} \frac{1}{\sqrt{2\pi\sigma_i^2}} e^{\frac{(x-\mu_i)^2}{2\sigma_i^2}} \tag{4.7}$$

for N summed Gaussian functions with equal amplitude. The mean and standard deviation can quickly be inferred from the expected values for X and X^2 for $X \sim \mathcal{N}(\mu, \sigma)$ where

$\mathcal{N}(\mu, \sigma)$ is a normal distribution with mean μ and standard deviation σ. They are:

$$\mathrm{E}[X] = \frac{1}{N}\sum_{i=1}^{N}\mu_i,\ \mathrm{E}[X^2] = \frac{1}{N}\sum_{i=1}^{N}\mu_i^2 + \sigma_i^2 \tag{4.8}$$

The mean and standard deviation for the multi-Gaussian are then

$$\mu = \mathrm{E}[X] = \frac{1}{N}\sum_{i=1}^{N}\mu_i,\ \sigma = \sqrt{\mathrm{E}[X^2] - (\mathrm{E}[X])^2} = \frac{1}{N}\sqrt{N\left(\sum_{i=1}^{N}\mu_i^2 + \sigma_i^2\right) - \left(\sum_{i=1}^{N}\mu_i\right)^2} \tag{4.9}$$

Once μ and σ have been calculated, they are used as the estimate and estimated uncertainty for the parameter. In the limit that $\mu_i << \sigma_i$ for all i, these expressions reduce to $\mu = \frac{1}{N}\sum_{i=1}^{N}\mu_i$ and $\sigma = \frac{1}{N}\sum_{i=1}^{N}\sigma_i$. In the limit that $\sigma_i << \mu_i$ for all i, these expressions reduce to $\mu = \frac{1}{N}\sum_{i=1}^{N}\mu_i$ and $\sigma = \frac{1}{N}\sqrt{N\left(\sum_{i=1}^{N}\mu_i^2\right) - \left(\sum_{i=1}^{N}\mu_i\right)^2}$, or the standard deviation of the μ_i.

4.4.2 Strategy for validation

Two approaches will be taken to validate the simulations and the method proposed in Section 4.4, and will comprise the next two sections. Section 4.5 will use toy-Monte-Carlo generated data to assess the accuracy of the uncertainties estimated by the model, and Section 4.6 will use calibration data acquired using the DEMONSTRATOR's ^{228}Th source, and ^{222}Rn data collected during a short period during data set 0. This section is designed to test the accuracy of the simulated PDFs.

The tests in Section 4.6 use a slightly modified version of the method from Section 4.4, which is outlined at the beginning of Section 4.6. Because only two sources of calibration data were readily available, the complexity of the data set that could be constructed from them was limited. Therefore, I decided to run a shorter method that enabled testing of different potential configuration choices, such as the choice of minimizer in SciPy.Optimize.Minimize, and the whether to use in the fit the granularity cut (see Sections 2.7 and 3.3.1), the PSA cut (see Sections 2.6 and 3.3.2), both, or neither.

Finally, the method from Section 4.4 will be applied to the background data in Section 4.7. The background data combines the large number of possible sources of the toy MC tests with the realistic data of the calibration tests. However, we are not able to test a large number of realistic sources, since that would be tantamount to knowing our backgrounds *a priori*, making the construction of a background model unnecessary. The combination of these two effects could have non-linear effects on the resulting background model, which are difficult to quantify. Some suggestions for estimating the potential effects of incorrectly modeled background sources on the final result are presented in Chapter 6.

4.5 Tests of the Background Fitting Method on Monte Carlo Data Generated from the Simulated PDFs

In order to test the statistical validity of the background model selection algorithm presented above, I have generated a toy Monte Carlo data set from the simulated PDFs. The data set is produced by specifying specific activity densities for each PDF, and generating an energy spectrum using a specified livetime for the detector. To facilitate a test as similar to the acquired data as possible, the livetimes for each acquired data set were also used to generate the toy MC data. Since the assay information should be close to correct, it was used to specify the activity densities for all components for which we had assay data. For the few remaining components, such as cosmogenic ^{68}Ge and ^{3}H in the enriched and natural germanium, arbitrary values reasonably close to what is seen in the DEMONSTRATOR were specified. The toy MC energy spectrum is shown in Figure 4.4, and contains ~140,000 simulated counts. The binned toy MC data agree with the energy spectrum from which they were drawn to within Poisson errors, as they should.

Figures 4.4 through 4.7 contain a lot of information, and similar plots also appear in Section 4.7 and Appendix D, so a brief tutorial on their contents will now be provided. The top panel shows the data being fit in black, with colored lines representing the different PDFs. Each colored line is actually the sum of of a class of PDFs, which are grouped either

by isotope or physical location in the DEMONSTRATOR, depending on the plot. The labels in the legend are in descending order of number of best-fit counts in the spectrum. The blue line on top of the black histogram is the best-fit model, and also the sum of all the other colored lines (for Figs 4.4 and 4.5 the colored lines are the true distribution from which the black histogram was drawn). The second panel is identical to the top panel, but with a linear y-scale instead of log. The lower-left panel shows the residuals between the black histogram and the blue spectrum, with error bars including the Poisson errors for the data and the best-fit model, as well as errors for each parameter computed from the likelihood minimum. The lower-center panel shows the pulls of the residual plot, or the value of each residual divided by the error opposite its sign (so the upper error for a negative residual and a lower error for a positive residual). The lower-right panel shows a histogram of the pulls overlaid with a standard normal distribution. If the residual uncertainties are estimated correctly and the best-fit model matches the data, the pulls will be distributed according to a standard-normal distribution.

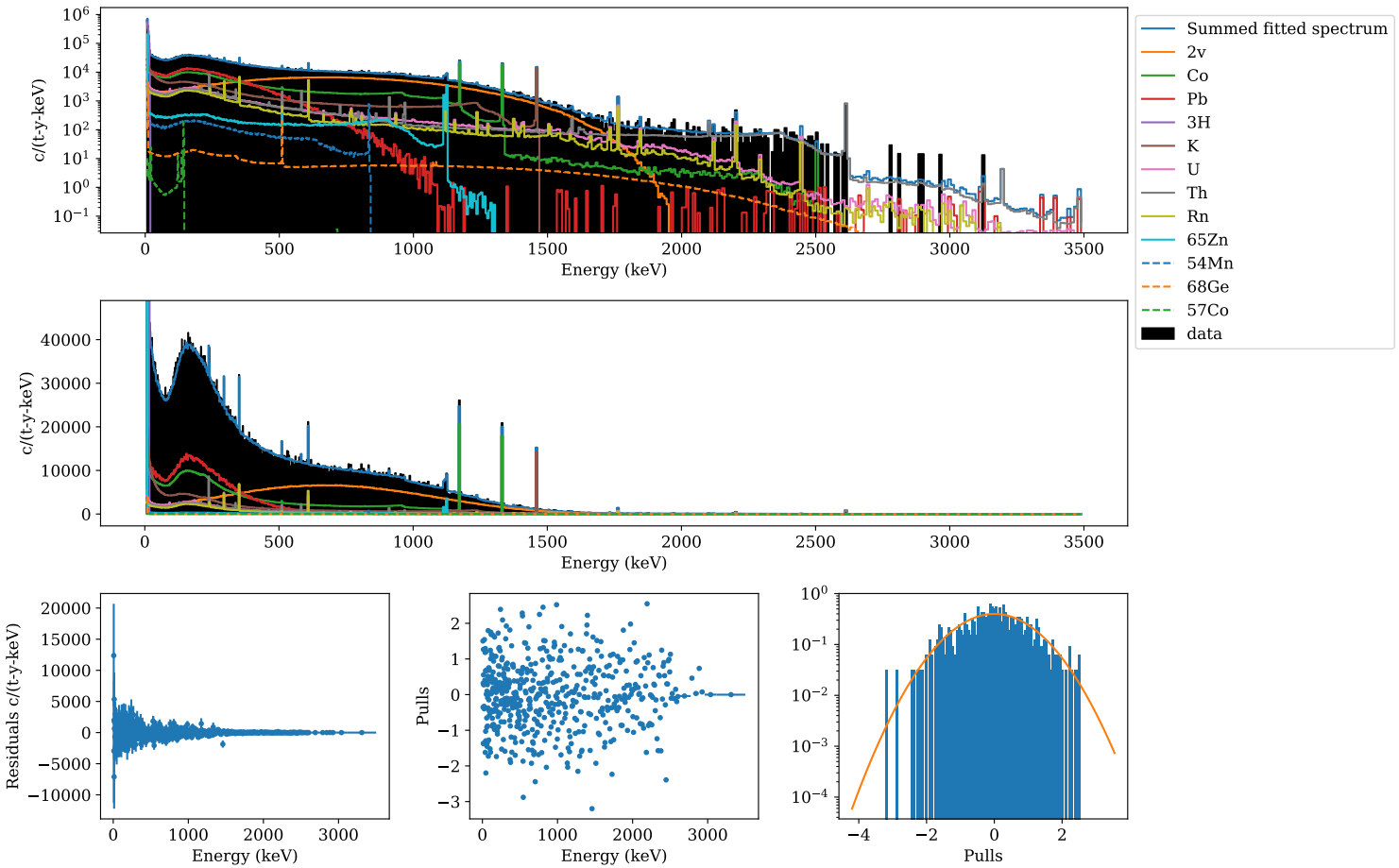

Figure 4.4: The energy spectrum used to generate the toy MC data set used to validate the model selection algorithm is shown in blue. The data generated from the solid blue spectrum are given by the black histogram. In this figure the various isotopic contaminants are broken out, all data sets and detectors are included, and no analysis cuts have been applied. The orange line in the histogram of pulls is a standard normal distribution.

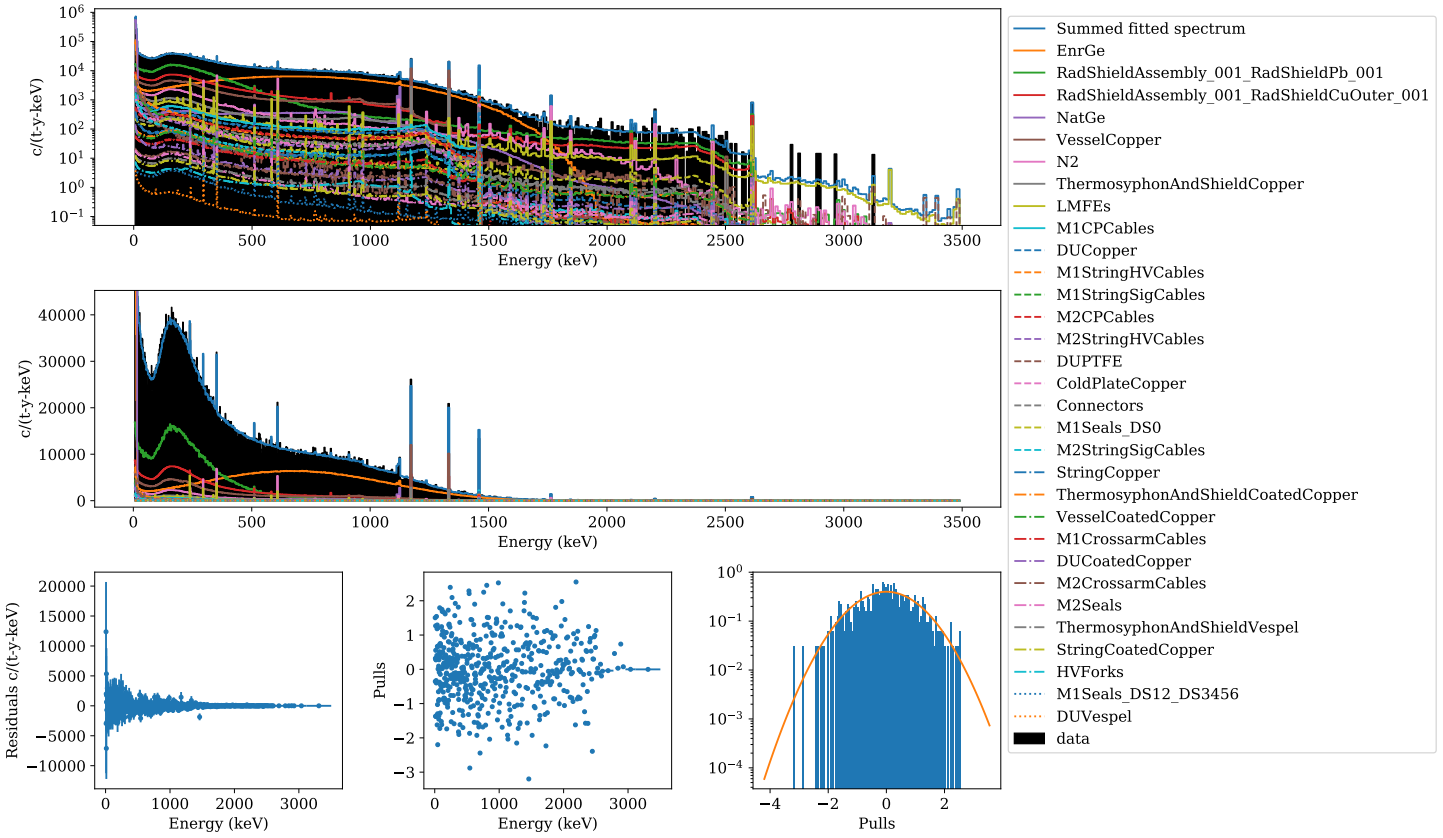

Figure 4.5: Same as Figure 4.4, except that in this figure, contributions from the various component groups are broken out.

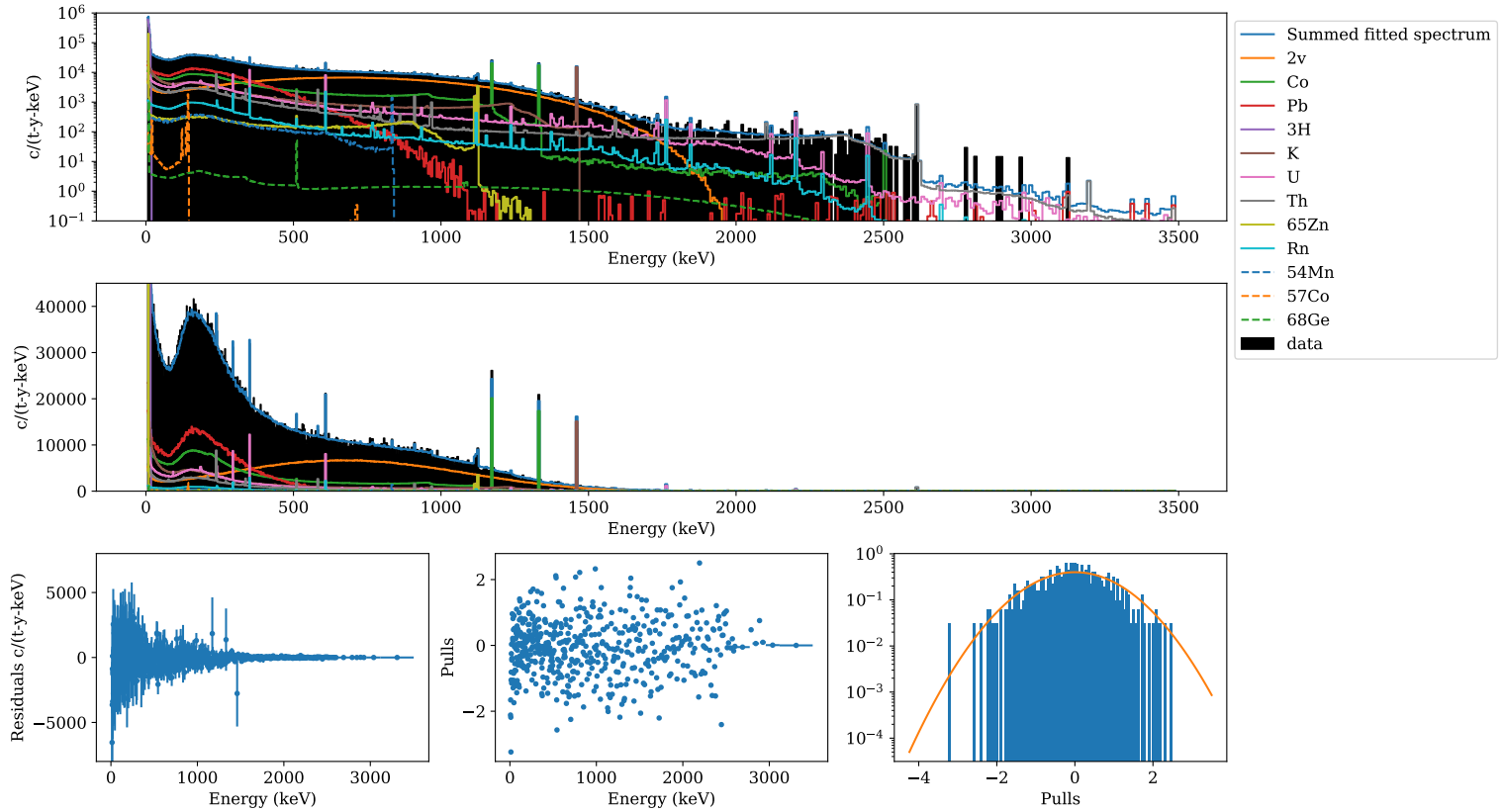

Figure 4.6: The best-fit results presented in Table C.1 are plotted here. The residual errors include both purely statistical Poisson uncertainty as well as the uncertainties from Table C.1. In this figure the various isotopic contaminants are broken out, all data sets and detectors are included, and no analysis cuts have been applied. The orange line in the histogram of pulls is a standard normal distribution.

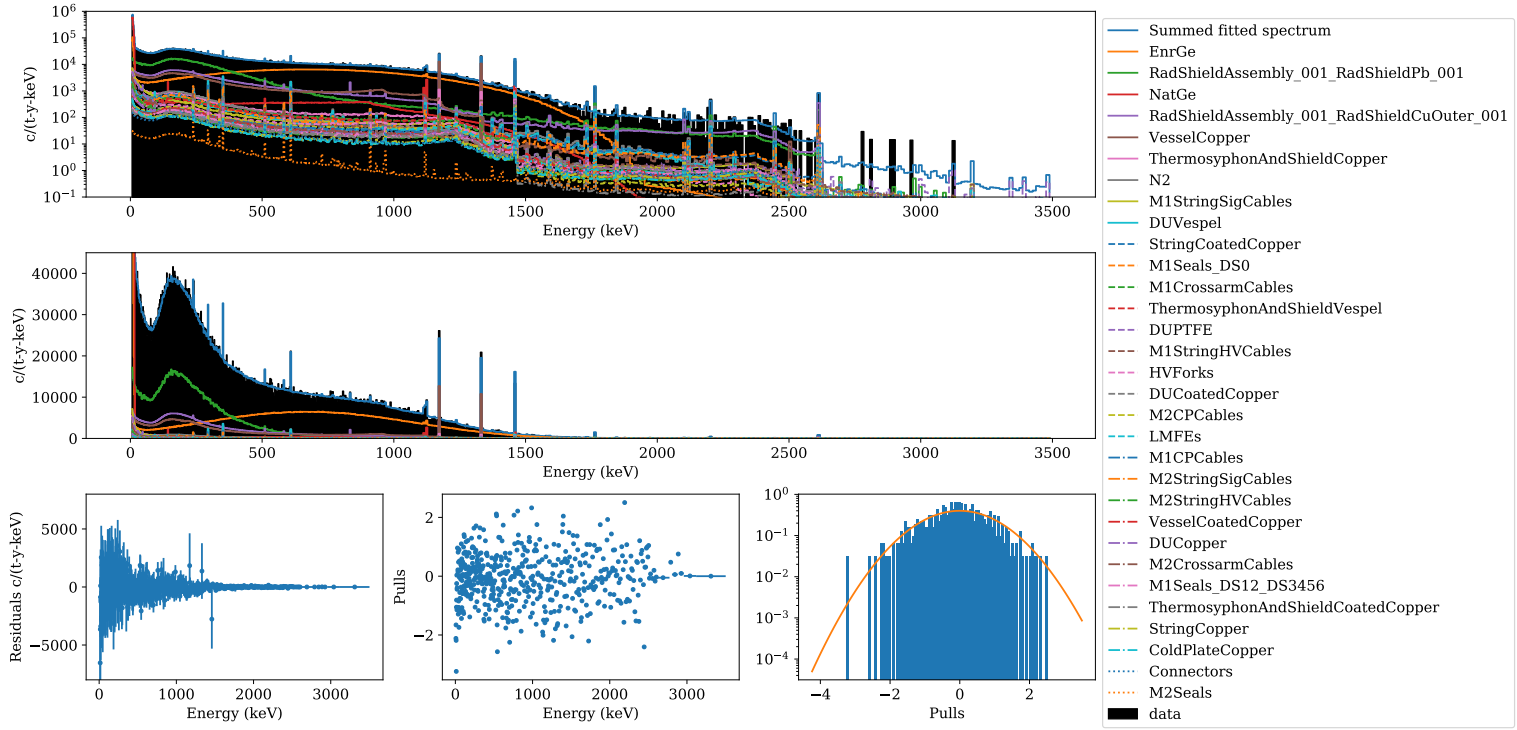

Figure 4.7: Same as Figure 4.6, except that in this figure, contributions from the various component groups are broken out.

The results of the application of the background model selection algorithm described in Section 4.4 are presented in Table C.1. Because the true values of the activity densities P_j are known, we are able to compute exactly how many units of standard error the best-fit values are from the true values. This variable will be called the normalized error and is formally defined as

$$\mathrm{NE}_j = \frac{\hat{P}_j - P_j}{s_j} \tag{4.10}$$

where $\hat{P}_j$ is the true activity density of source j, P_j is the best-fit activity density of source j, and s_j is the standard error for P_j, equivalent to σ as defined in Section 4.4.1.

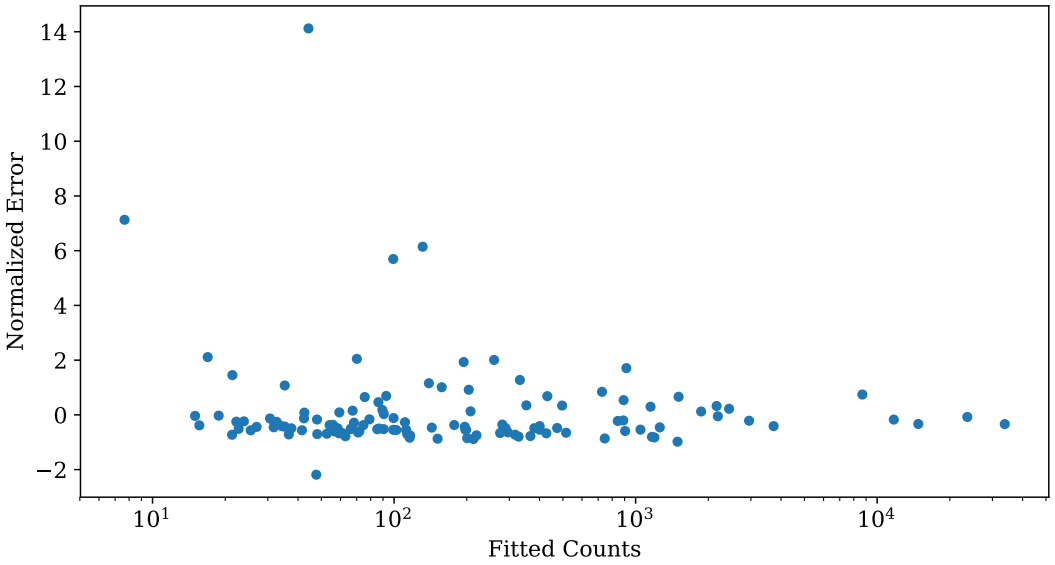

Figure 4.8: The normalized error (eq. 4.10) is plotted against the best-fit number of counts for all estimated activity densities. Estimates for parameters that fit to 1,000 counts or more are more accurate.

It is helpful to look at the normalized errors of the best-fit parameters of the model against a couple of other variables. Figure 4.8 shows the normalized errors vs. the number

of best-fit counts. Parameters with a best-fit value of 1,000 counts or fewer are not estimated as accurately as parameters with a large best-fit number of counts.

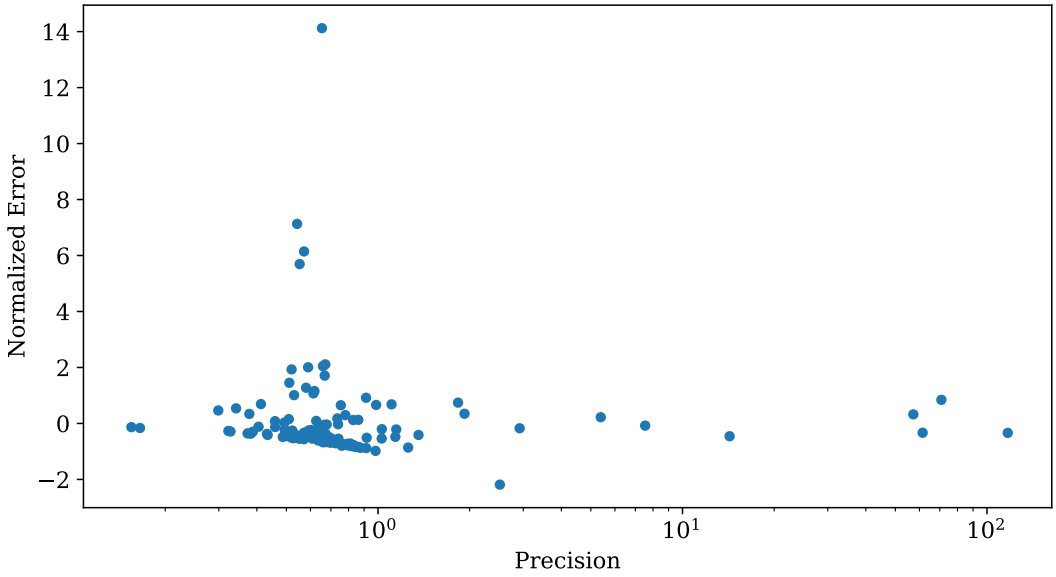

Figure 4.9: The normalized error (eq. 4.10) is plotted against the precision (eq. 4.11) for all estimated activity densities. The overdensity of points with a precision just below 1 is not very well understood, but it appears to be comprised mostly of parameters with true values that are expected to generate very few counts.

Another useful variable is the precision, which is defined in this work as the ratio of the best-fit value of a parameter to its standard error:

$$\text{Precision}_j = \frac{P_j}{s_j} \tag{4.11}$$

Figure 4.9 illustrates that, much like with the best-fit number of counts, there appears to be a precision below which the normalized errors are not well-behaved. This plot indicates that cutoff to be located at precision ≈ 1.

The normalized errors for all best-fit parameters are presented as a histogram in Figure 4.11. Ideally, the errors should be symmetric about 0 with a standard deviation of 1. Clearly, the blue histogram (which includes one count for each best-fit parameter) is not distributed as such. A Kolmogorov-Smirnov test of the blue histogram to a normal distribution returns a p-value of 3.6×10^{-6}, indicating with very high confidence that the true distribution is not normal. The orange histogram includes only best-fit parameters for which the precision (defined in Equation 4.11) is greater than 1. A KS test of this histogram to a normal distribution returns a p-value of 0.41, indicating that the null hypothesis of a normal distribution should not be rejected. Similarly, the green histogram, which includes only parameters for which the best-fit number of counts was greater than 1,000, returns a p-value of 0.14 for a KS test to a standard normal distribution, also indicating that the null hypothesis of a normal distribution should not be rejected.

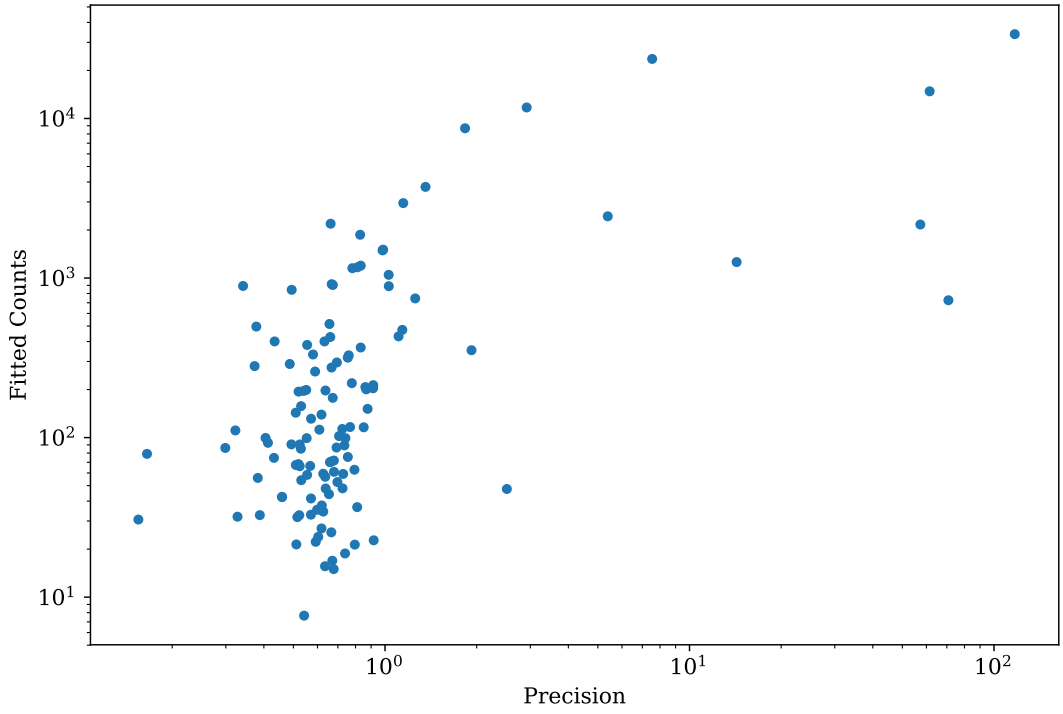

Figure 4.10: The best-fit number of counts is plotted against the precision (eq. 4.11) for all estimated activity densities. There is a clear positive relationship between the two, but there are also parameters where the precision can be quite high while the number of best-fit counts is low. This is the case for PDFs that have prominent features that are not mimicked by any other PDF, such as ^{65}Zn in the natural or enriched detectors.

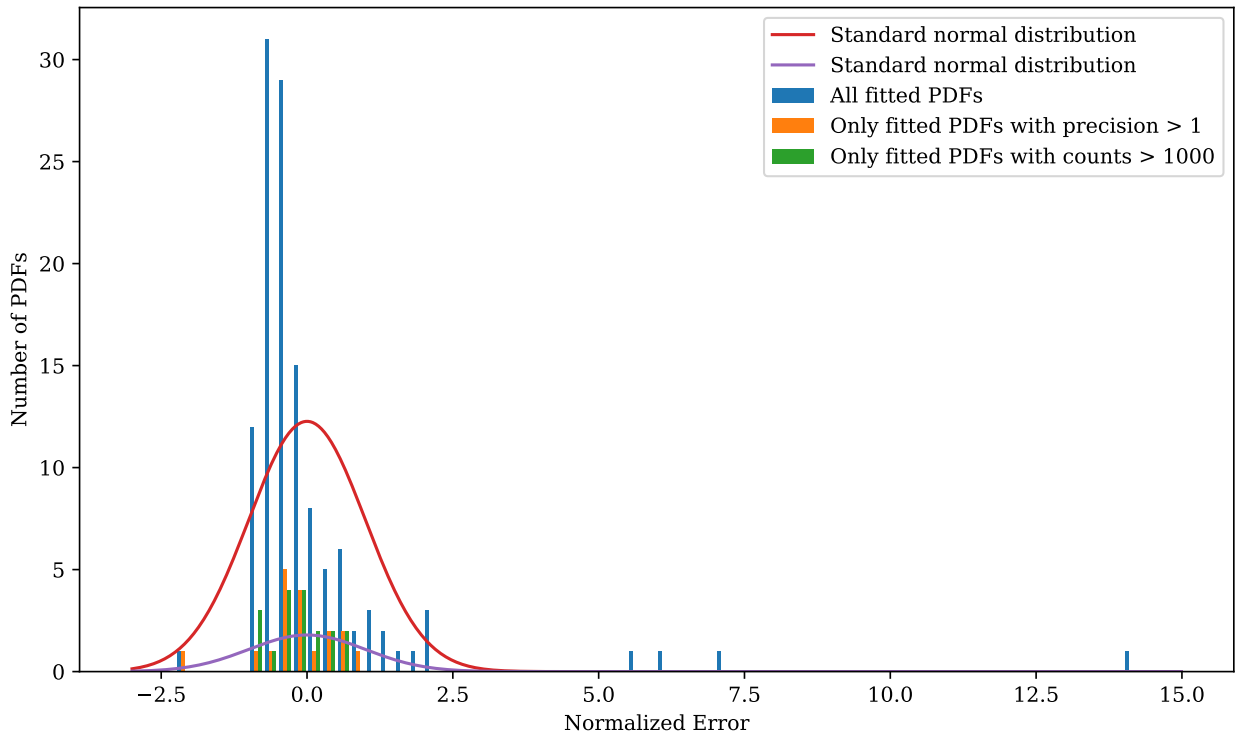

Figure 4.11: The blue histogram shows the normalized errors (eq. 4.10) for all PDFs in the model. The orange histogram shows the normalized errors for only PDFs with a best-fit precision greater than 1. The green histogram shows the normalized errors for only PDFs with a best-fit number of counts greater than 1,000. Standard normal distributions with amplitudes matching the histogram sizes are overlaid, and it is clear that the blue histogram fits poorly to the normal distribution. A KS test to a standard normal gives a p-value of 0.41 for the orange distribution, a p-value of 0.14 for the green histogram, and a p-value of 3.6×10^{-6} for the blue histogram.

4.6 Tests of the Background Fitting Method on Calibration Data

I performed tests of a slightly different version of the background fitting method on calibration data. This has the benefit of testing the behavior of the fitting and model selection processes against real data that does not necessarily exactly match the spectral shape of the simulated PDFs (unlike in the previous section), while still allowing for a comparison to a true answer.

The data used in these fits come from the long ^{228}Th calibration from data set 0, and a period of runs where the nitrogen purge to the inside of the shield was reduced, allowing for the acquisition of a ^{222}Rn spectrum since ^{222}Rn occurs naturally in the lab air underground. The two calibration data sets can be mixed together with an arbitrary ratio, and then fitted to a selection of PDFs.

A different model selection algorithm is used in this section than was outlined in Section 4.4 (which is the method used in Section 4.5 and for the results in Section 4.7). The algorithm used here is an earlier version of the algorithm from Section 4.4. I performed these tests with calibration data during the development of the model, but believe they contain useful information even though they were not obtained using the main method from Section 4.4.

The method used for this section follows below:

1. Generate a randomly selected data set of ^{228}Th and ^{222}Rn data, with the number of events from each source chosen randomly between 0 and ~370,000 [5]

2. Generate a random integer between 0 and the size of the set of PDFs available to be fit. Then randomly sample without replacement that number of PDFs from the full set of PDFs available. Add the module 1 ^{228}Th line source, and the surface and bulk sources for ^{222}Rn in the volume inside the shield if they are not already in the set of PDFs to fit.

[5]The number of events was set by the data available. The total number of high ^{222}Rn runs taken in data set 0 contain only about 370,000 events.

3. Fit this selection of PDFs to the generated data set, and rank the best-fit PDFs by number of counts assigned to each one

4. Fit a series of models, adding in one PDF at a time in order of number of counts assigned in step 3, and compute the AIC [100] at each step

5. After step 4 is complete, the model with the smallest AIC is the best model

This method is computationally simpler than the one outlined in Section 4.4 (and used for the main analysis), because it only requires fitting the full selection of PDFs once for each trial. This enables testing of some extra variables, such as which minimization method in SciPy.Optimize.Minimize works best, and what combination of analysis cut spectra works best. If we wanted to apply the full method from Section 4.4, we would have to reduce the number of independent tests we do by a factor of 100 or so. A test of the full method on the calibration data would be useful to perform in the future, but is not included in this result (due to the good performance observed for the toy MC fits in Section 4.5).

I ran this simplified fit method 1,000 times, during which I randomly assigned the SciPy.Optimize.Minimize minimization algorithm used (L-BFGS-B [101], TNC [102], Nelder-Mead [96], Powell [103], CG [104], or BFGS [105], [106], [107], [108]) and the analysis cuts used (no cuts, granularity cut only, A vs. E only, or both granularity and A vs. E). Each run performed the above algorithm twice: once with all detectors summed into a single energy histogram, and once with the enriched and natural germanium detectors split and fit simultaneously. Because the data are from data set 0 before module 2 was installed, it was not possible to fit to spectra separated by module.

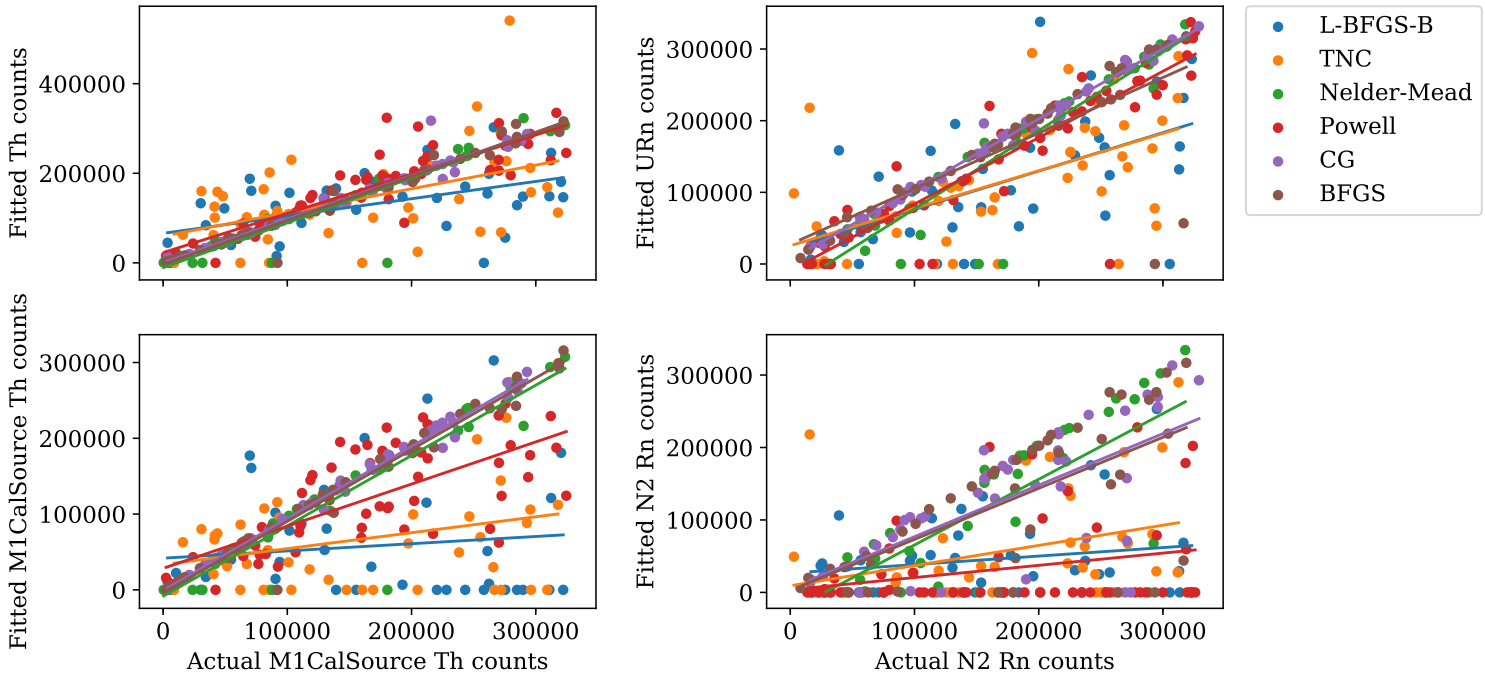

Figure 4.12: Each panel in this plot shows the best-fit number of counts vs. the true number of counts in the calibration data. Each dot is an independent run of the method outlined in this section, and the colored lines are linear regressions to the corresponding points. The upper-left panel shows the best-fit number of counts assigned to all thorium PDFs included in the model, the upper-right panel shows the best-fit number of counts assigned to all ^{238}U and ^{222}Rn PDFs included in the model, the lower-left panel shows the best-fit number of counts assigned to just the module 1 calibration ^{228}Th source, which is the true source of all the thorium events, and the lower-right panel shows the best-fit number of counts assigned to the N2 volume, including both decays on the surface and decays in the bulk, which is the true source of all the ^{222}Rn events.

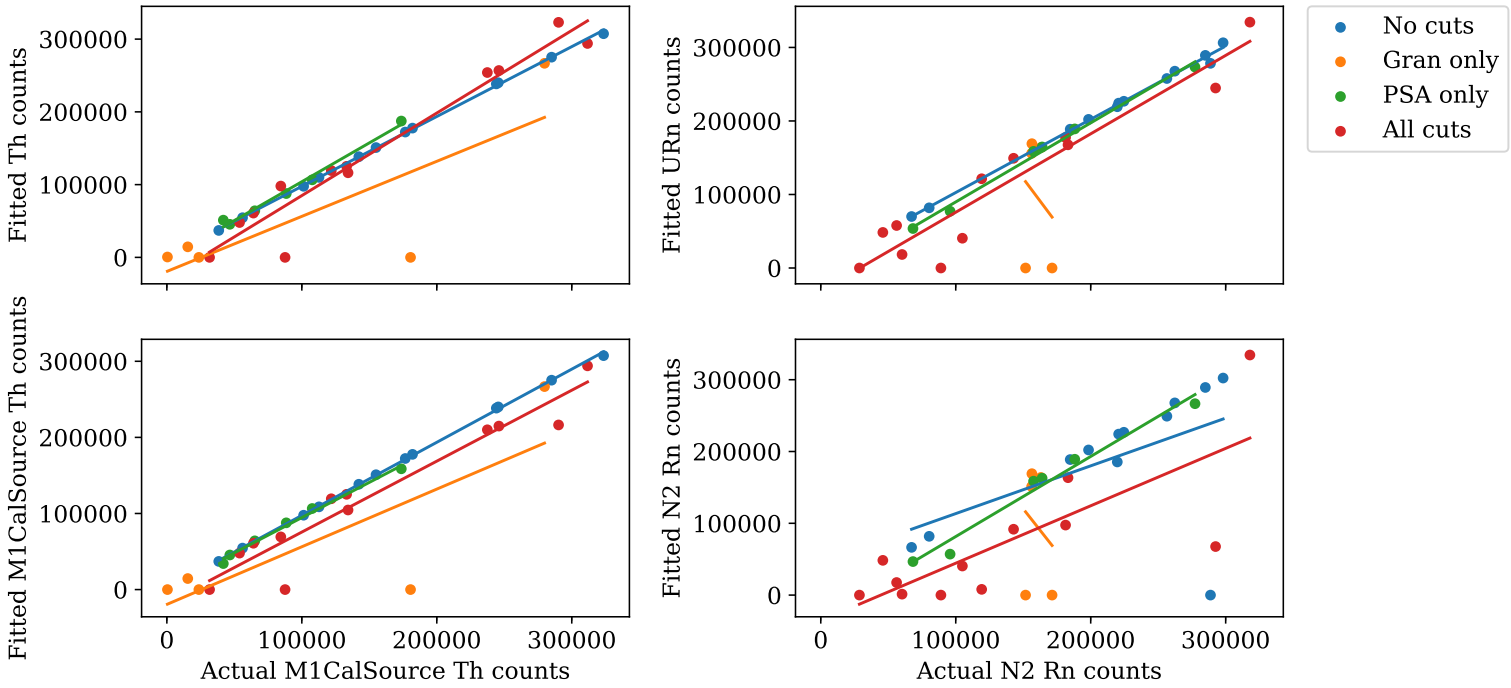

Figure 4.13: Same as Figure 4.12, but including only runs that used the Nelder-Mead minimization algorithm and broken out by choice of analysis cuts.

We can learn a few things from these results. First of all, this simpler method does not always do a perfect job of identifying the correct number of counts from the calibration sources, but the results are generally close to correct for some minimization methods. Each of the plots in this section has trendlines for each of the tested methods or analysis cut options, depending on the plot. It is clear from Figure 4.12 that the Nelder-Mead, CG, and BFGS methods perform the best in correctly identifying the source of the ^{222}Rn as the nitrogen volume. All methods are better at identifying the correct source of the thorium spectrum (bottom-left panel of Figure 4.12), which is perhaps not surprising as the simulations for the thorium calibration sources have very high statistics. By contrast, it is more difficult in general for the minimizer to find the correct number of events for the surface and bulk N2 ^{222}Rn sources (lower-left panel of Figure 4.12). If all sources of ^{222}Rn and ^{238}U are looked at (upper-right panel of Figure 4.12, the ^{222}Rn and ^{238}U spectra being nearly identical), all of the methods do better.

These results motivate the choice of the Nelder-Mead algorithm for all fits done with the main model-selection algorithm in Sections 4.5 and 4.7. Nelder-Mead was chosen over CG and BFGS because it exhibited superior convergence behavior in general, as well as nearly always outperforming the other two methods in finding the minimum of the likelihood function.

Now looking at just the runs of the method that used the Nelder-Mead algorithm as the minimizer, Figure 4.13 shows how the different choice of analysis cuts affects the accuracy of the result. Since we can simulate the granularity and the A vs. E cuts (see Section 3.3), we can test whether breaking the data into separate spectra by these cuts and fitting with shared parameters improves the result. We see in Figure 4.13 that the choice of cut spectra does not have a strong effect on the accuracy of the best-fit number of counts for the correct PDFs. This can be seen by noticing that the regression lines in all the panels in Figure 4.13 are roughly parallel (except for the orange line for the granularity cut, which is fit to just 4 points and therefore has a large uncertainty). This result, combined with previously

expressed reservations about the accuracy of the simulated A vs. E cut (the dT heuristic, sec. 3.3.2), motivate the decision to only use the granularity cut in fits of both the toy MC data and the data from the DEMONSTRATOR.

Finally, whether or not the natural and enriched germanium detectors are split into separate energy spectra does not seem to have a large effect in these tests, based on calibration source and high-^{222}Rn data. However, this is not particularly surprising as there is no reason to expect that these particular sources would differentially affect the natural and enriched detectors. The natural germanium detectors are mostly located near the top of the cryostat, but both the shield-internal nitrogen volume and the calibration source track are arranged symmectrically around the cryostat. Also, since both sources are external to the detectors, they will be observed by the detectors identically. This is not the case with many of the sources we expect to see in the DEMONSTRATOR background data. For example, MAJORANA has already published a low energy spectrum showing that the natural germanium detectors have a clearly observable cosmogenic tritium spectrum (as well as ^{68}Ge), while that the enriched germanium detectors contain a much smaller amount of both tritium and ^{68}Ge [55]. Also, the enriched detectors will see a much higher rate of $2\nu\beta\beta$ decays.

It is also reasonable to assume that there could be some sources of external radiation that are not symmetric about the two installed cryostats, since the cables and connectors for module 1 were disassembled and rebuilt (and therefore were handled multiple times), while the cables and connectors for module 2 were not. Therefore, for example, the signal and HV cables and connectors that sit above the cold plate could have uneven levels of radioactivity between the two modules, which might be more detectable if the spectra from the two modules are split (giving sensitivity in the horizontal dimension). The natural detectors also tend to be located near the top of each cryostat, so fitting those spectra separately can give some sensitivity in the vertical dimension. For these reasons, we separate the detectors into four groups for the fits in Sections 4.5 and 4.7: module 1 enriched germanium detectors,

module 1 natural germanium detectors, module 2 enriched germanium detectors, and module 2 natural germanium detectors.

4.7 Results of Fitting the Background Model to Data

After applying the run and detector selection criteria described in Section 2.3.2, and applying data cleaning, muon veto, and LN fill cuts (see Section 2.3.2), 133,458 events are found for all data sets, which have an exposure of 18.37 kg-d (enriched + natural), as listed in Table 2.3. [6] The number of events cut are consistent with efficiency estimates, as is shown in [45] since the cuts (except for the low-energy noise cut) used here are identical to the cuts used there. The data are binned according to the method described in Section 4.3 and the resulting spectra are shown in the plots contained in Appendix D.

Now it is time to apply the full model-selection algorithm (presented in Section 4.4) to the actual data collected with the MAJORANA DEMONSTRATOR. [7] Plots of the results are shown in Figures 4.14 through 4.24, and Tables 4.2 and 4.3. The comprehensive results are presented in Section C.2, and an exhaustive set of plots comprises the entirety of Appendix D. We find mostly good agreement with the results of the assay campaign from Section 2.2.

4.7.1 Plots of results and analysis of the plots

Selected plots of the result of the application of the model-selection algorithm presented in Section 4.4 are shown here. Figure 4.14 shows the best-fit spectrum overlaid onto the data from the enriched germanium detectors (excluding data set 0), and with no analysis cuts (i.e. granularity or PSA cuts), except for DCR. The subsequent figures are all included to illustrate a particular feature of or provide a constrast to Figure 4.14. See Section 4.5 for a detailed explanation of each panel of these types of plots.

---

[6] The exposure calculation is described in Section 2.4.

[7] Constraints based on the assay campaign were not applied to the likelihood function.

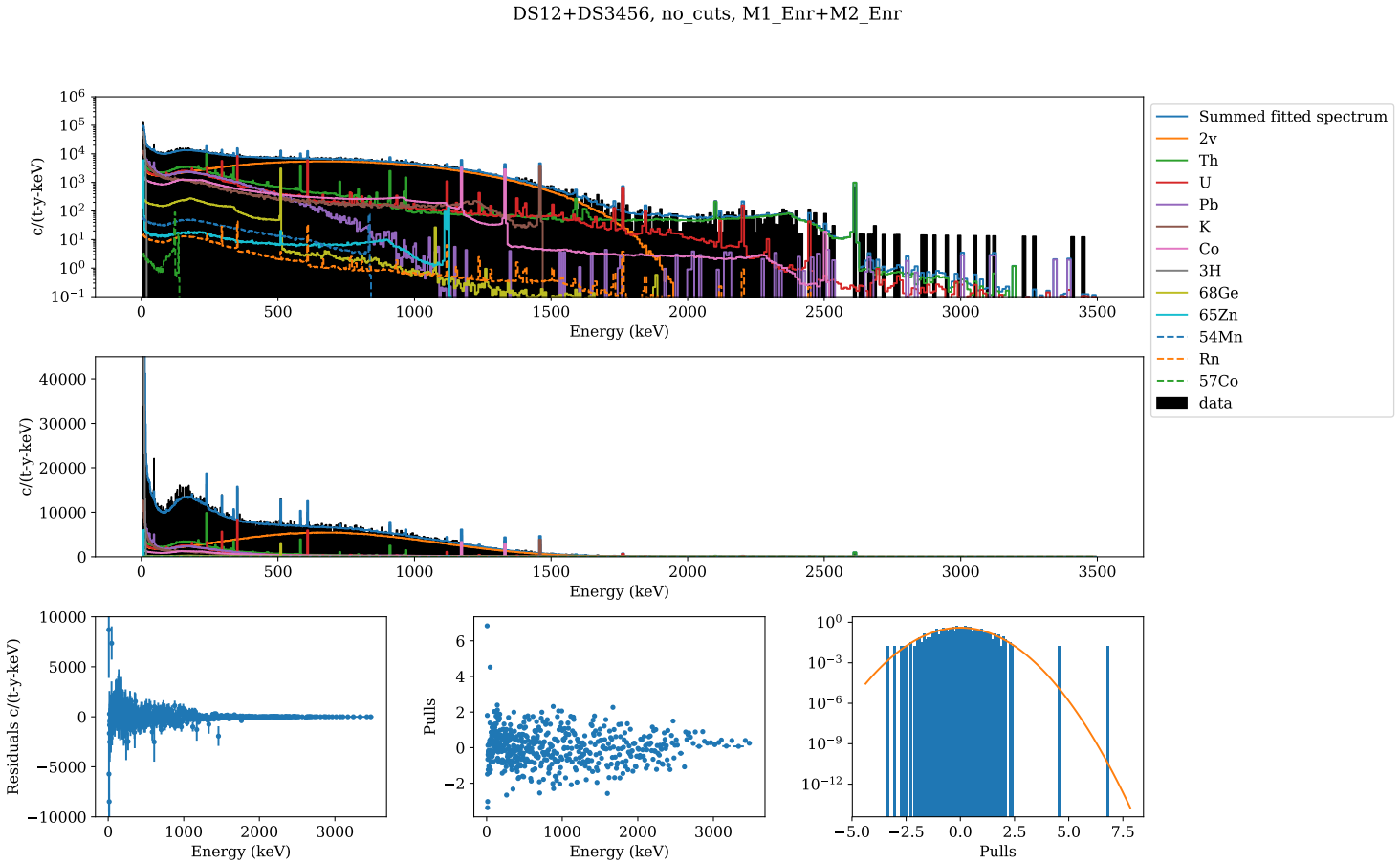

Figure 4.14: Best-fit model to data sets 1 and beyond with no analysis cuts, enriched Ge detectors only, broken down by contaminant.

Several things should be highlighted from Figure 4.14. First of all, the residuals and associated uncertainties of the best-fit model mostly follow a standard normal distribution, as desired. Significant disagreement occurs only at very low energy, which can be seen more clearly in Figure 4.15. The two lowest energy bins disagree significantly, and the 46 keV photon from decays of ^{210}Pb is also an outlier.

The two most likely explanations for the disagreement in the two lowest-energy bins are that the data cleaning at low energy described in Section 2.3.2 left events in the data set that should have been removed, or else that the transition dead-layer parameters – which are very sensitive to the low-energy part of the energy spectrum – do not sufficiently match the data.

The disagreement at 46 keV can likely be improved by including more sophisticated sources for that peak in the set of simulated PDFs. Since the mean-free-path of photons in solid materials at that energy is so small (approximately 300 μm in copper), only decays of ^{210}Pb with virtually no intervening material can penetrate into the sensitive region of the MAJORANA detectors. The only PDF in the model capable of producing this peak was decays of ^{210}Pb on the surface of the detector unit PTFE components. If the distribution of this source is non-uniform within the cryostats, this PDF would not fit very well to the data.

Figures 4.16 and 4.17 show zoom-ins on the high-energy region, including the photon peak at 2615 keV from decays of ^{208}Tl, and $Q_{\beta\beta}$ at 2039 keV. In Figure 4.16, ^{232}Th is clearly the dominant contributor to the spectrum, especially above the $2\nu\beta\beta$-decay spectrum, which is negligible above 1900 keV. Figure 4.17 illustrates that this ^{232}Th spectrum is not overwhelmingly dominated by any single component, but the module 1 cold plate cables (M1CPCables) do rise above all other components at nearly every energy above 1900 keV.

Figures 4.18 and 4.19 show the $Q_{\beta\beta}$ region of the spectrum for the module 1 and module 2 detectors respectively. They illustrate why components specific to module 1 fit higher than

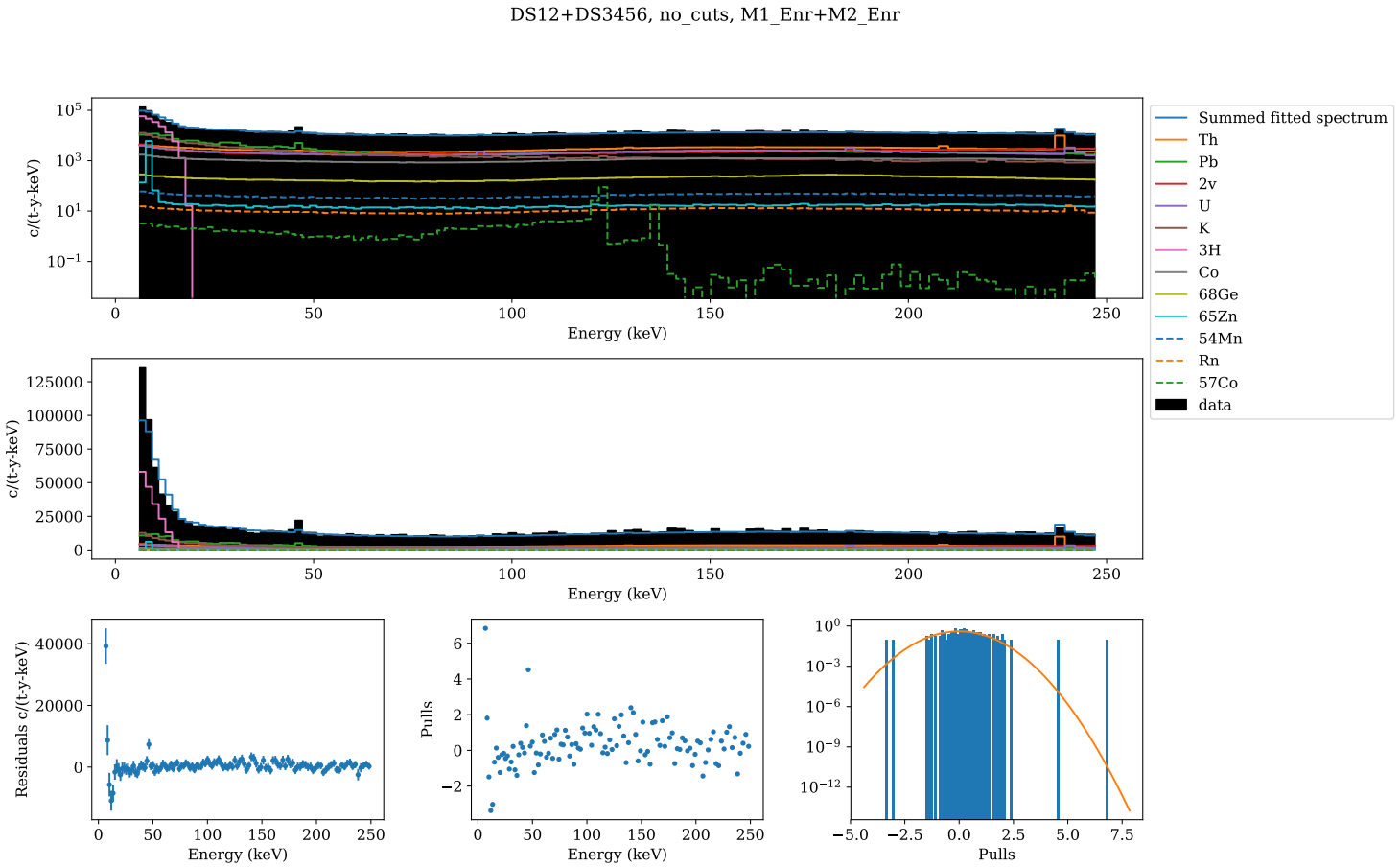

Figure 4.15: Best-fit model to data sets 1 and beyond with no analysis cuts, enriched Ge detectors only, broken down by contaminant, focusing on the low-energy part of the spectrum.

components specific to module 2. Notice that the peak at 2614 keV for ^{208}Tl is significantly higher in the module 1 spectrum, even when weighted by exposure as these plots are.

Figure 4.20 shows the energy spectrum for the natural germanium detectors with no analysis cuts, from data sets 1 and beyond. The ^{68}Ge and ^{3}H spectra are much more prominent, while the $2\nu\beta\beta$ spectrum is less prominent. Interestingly, the agreement in the lowest energy bins is better in the natural detectors than the enriched detectors, although that may just be due to a higher estimated uncertainty in those bins.

Figure 4.21 shows the results of the best-fit model to the data set 0 spectrum. Because the UGEFCu inner copper shield was not installed until after data set 0, the difference between this spectrum and the spectrum in Figure 4.22 sets strong constraints on the activity of components outside the inner copper shield. In particular, this includes the outer copper shield and the lead shield. The ^{210}Pb spectrum from the lead shield (orange in Figure 4.21) is suppressed by more than an order of magnitude when the inner copper shield is installed, and the photon peaks at 1173 and 1332 keV from decays of ^{60}Co in the outer copper shield are greatly suppressed as well. The same effect acts on the spectra for decays of ^{232}Th- and ^{238}U-chain isotopes in the outer copper and lead shields, but is less apparent because there are many other sources of ^{232}Th and ^{238}U in the spectrum.

Finally, Figures 4.22, 4.23, and 4.24 compare the best-fit model after applying the granularity and dT heuristic/AvsE cuts to the simulations and data. The 2614 keV peak is now underpredicted, where it was slightly overpredicted before (in Figure 4.17). This is not surprising, as the dT heuristic does not well-reproduce the rejection efficiency of the A vs. E cut over this part of the energy spectrum (see Section 3.3.2).

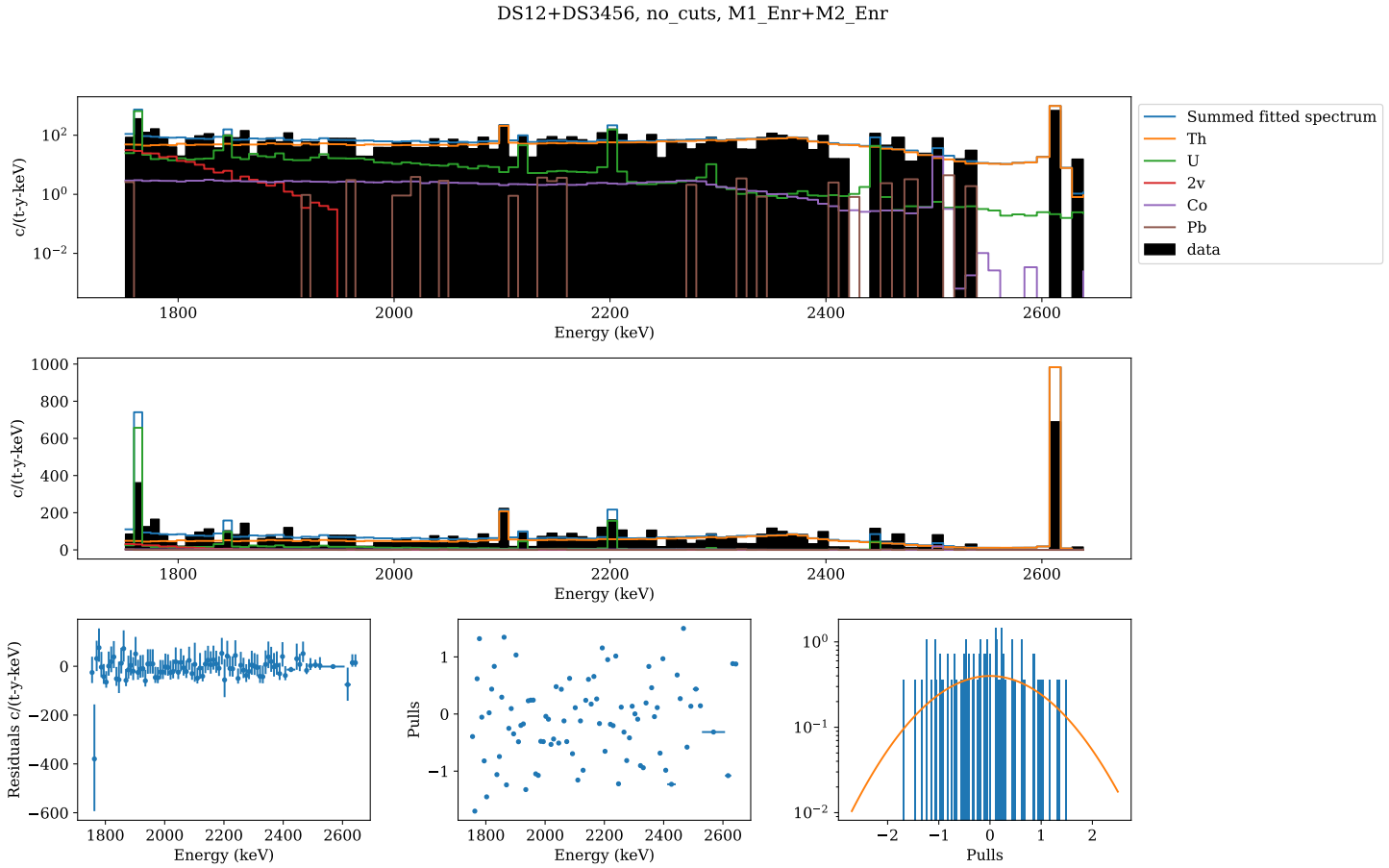

Figure 4.16: Best-fit model to data sets 1 and beyond with no analysis cuts, enriched Ge detectors only, broken down by contaminant, focusing on the part of the spectrum near $Q_{\beta\beta}$.

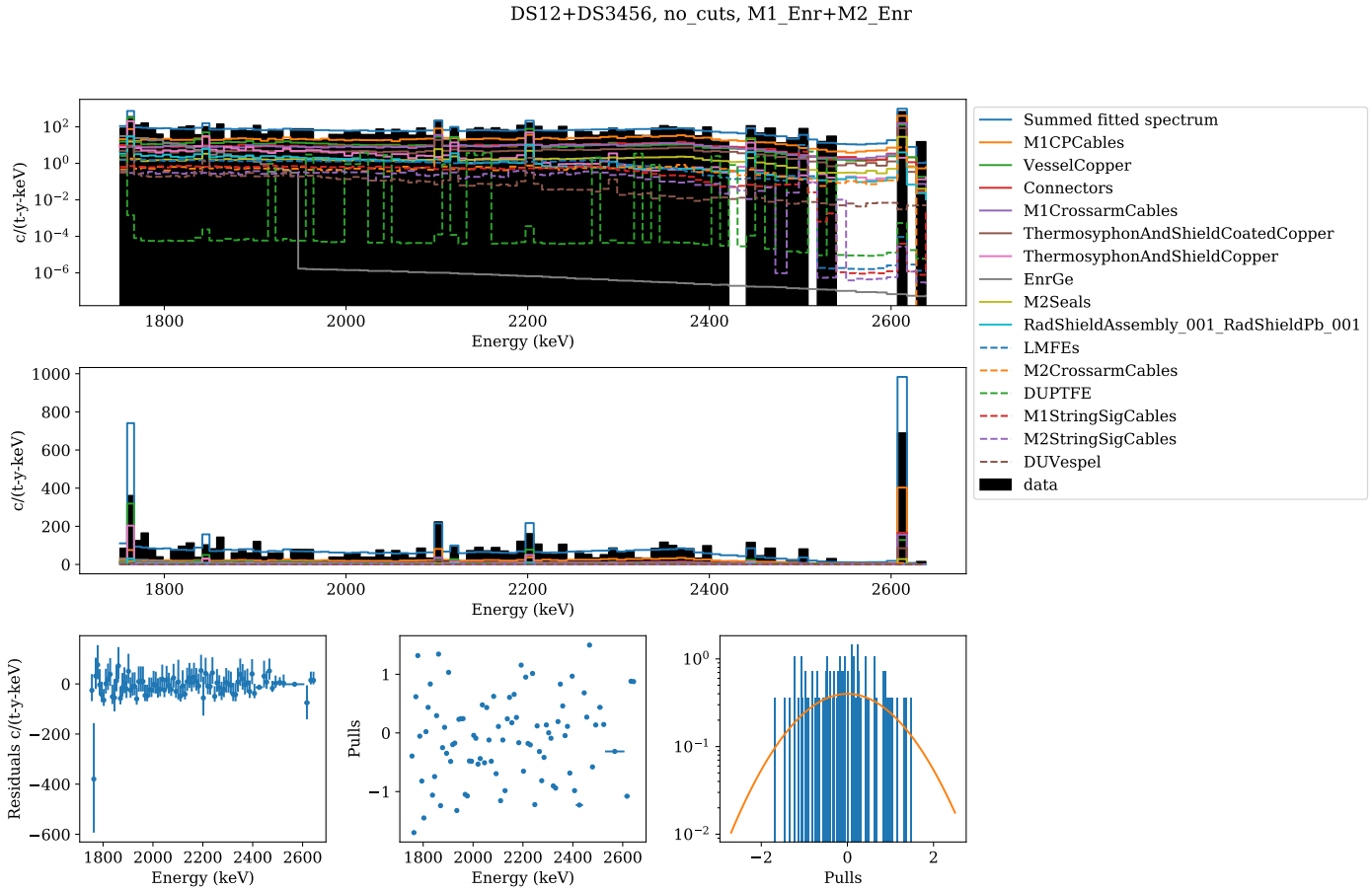

Figure 4.17: Best-fit model to data sets 1 and beyond with no analysis cuts, enriched Ge detectors only, broken down by component, focusing on the part of the spectrum near $Q_{\beta\beta}$.

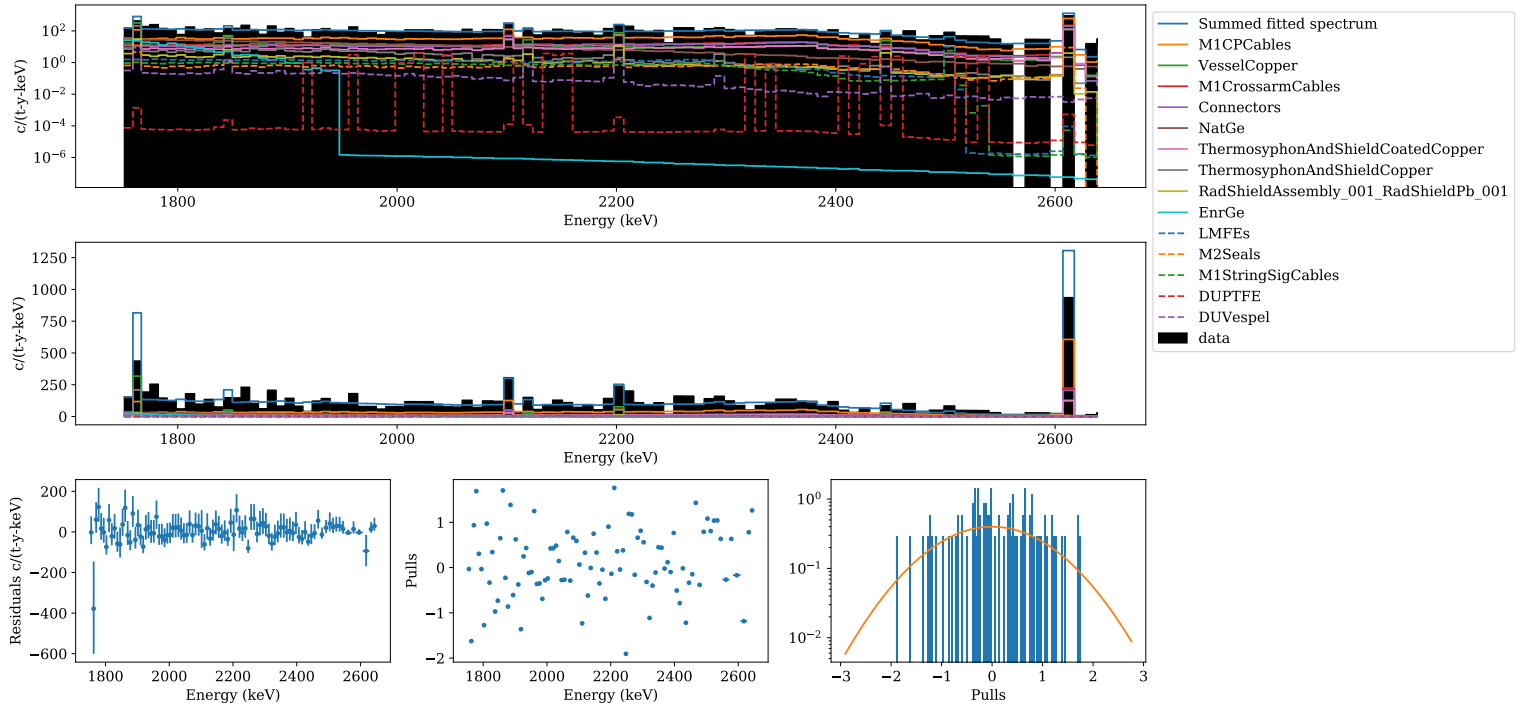

Figure 4.18: Best-fit model to data sets 1 and beyond with no analysis cuts, module 1 only, broken down by components, focusing on the part of the spectrum near $Q_{\beta\beta}$.

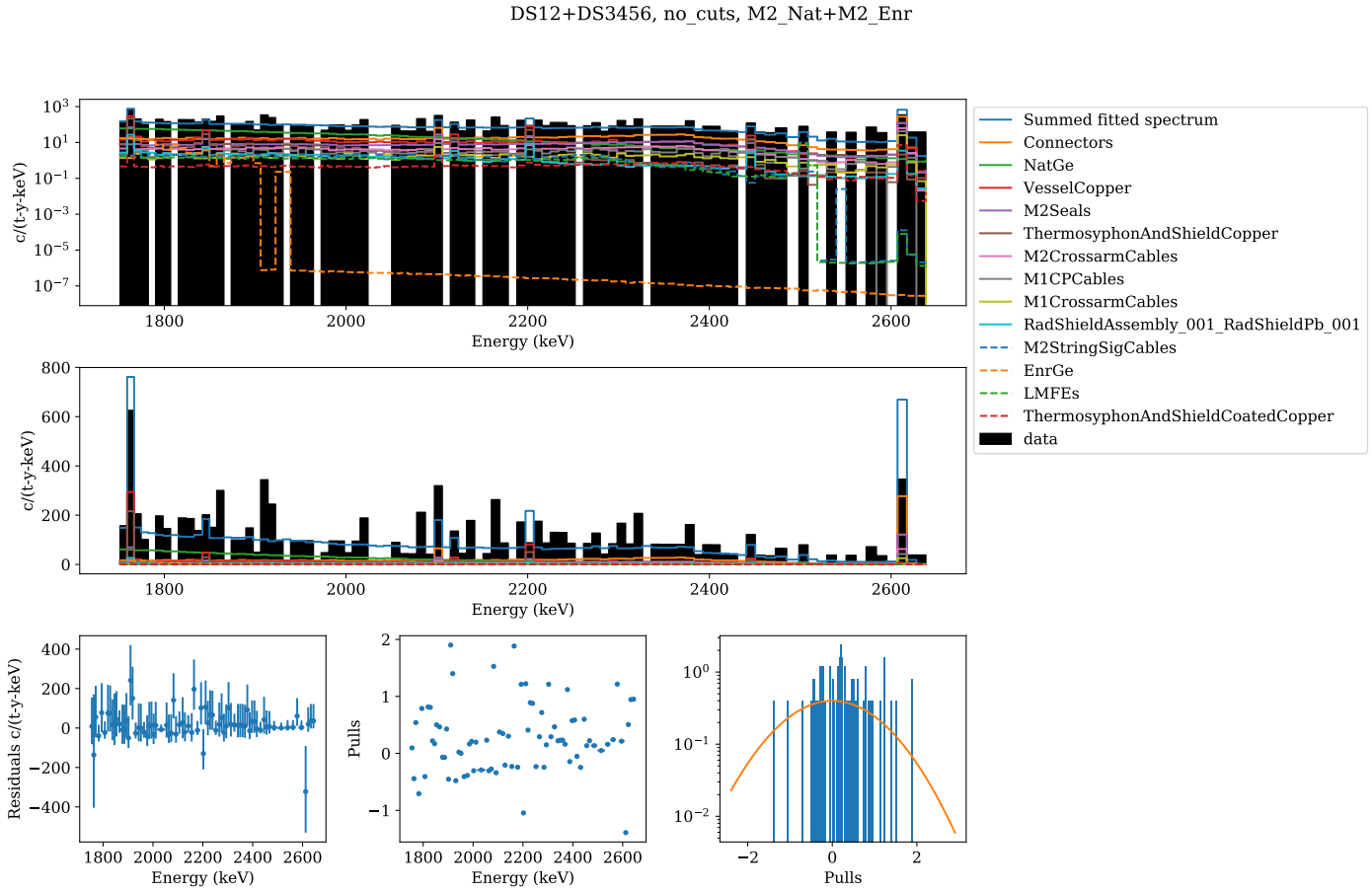

Figure 4.19: Best-fit model to data sets 1 and beyond with no analysis cuts, module 2 only, broken down by component, focusing on the part of the spectrum near $Q_{\beta\beta}$.

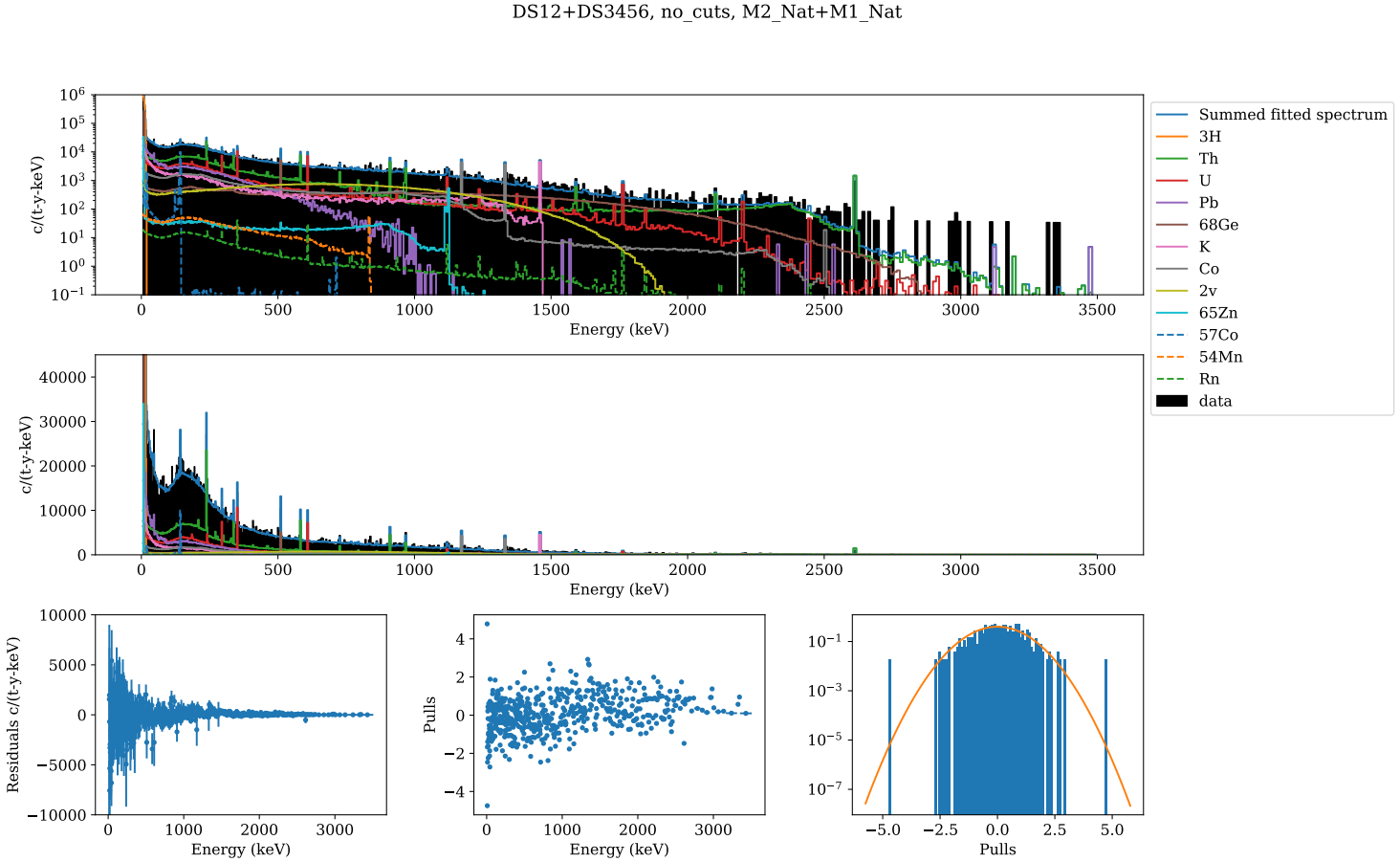

Figure 4.20: Best-fit model to data sets 1 and beyond with no analysis cuts, natural Ge detectors only, broken down by contaminant.

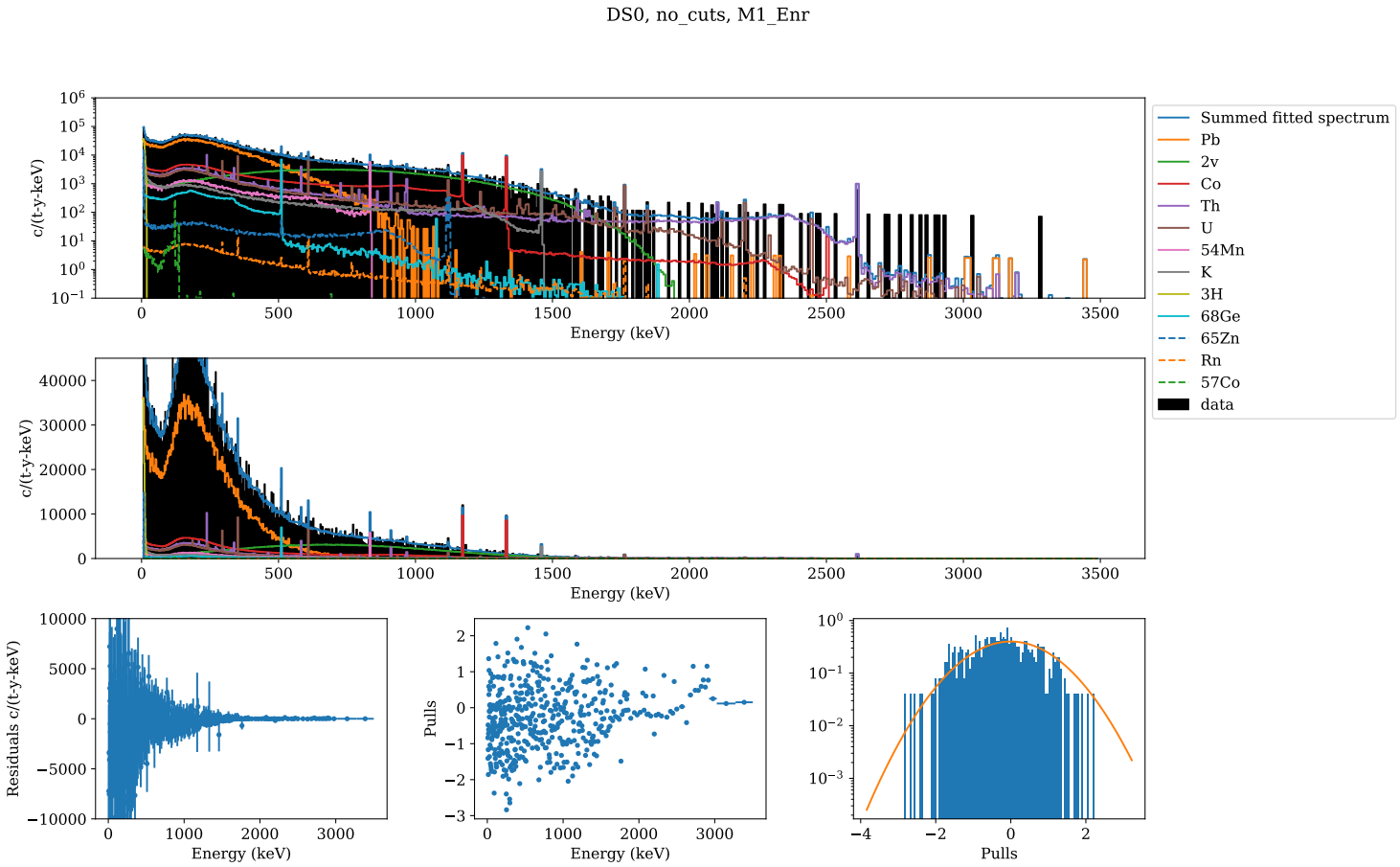

Figure 4.21: Best-fit model to data set 0 with no analysis cuts, enriched Ge detectors only, broken down by contaminant.

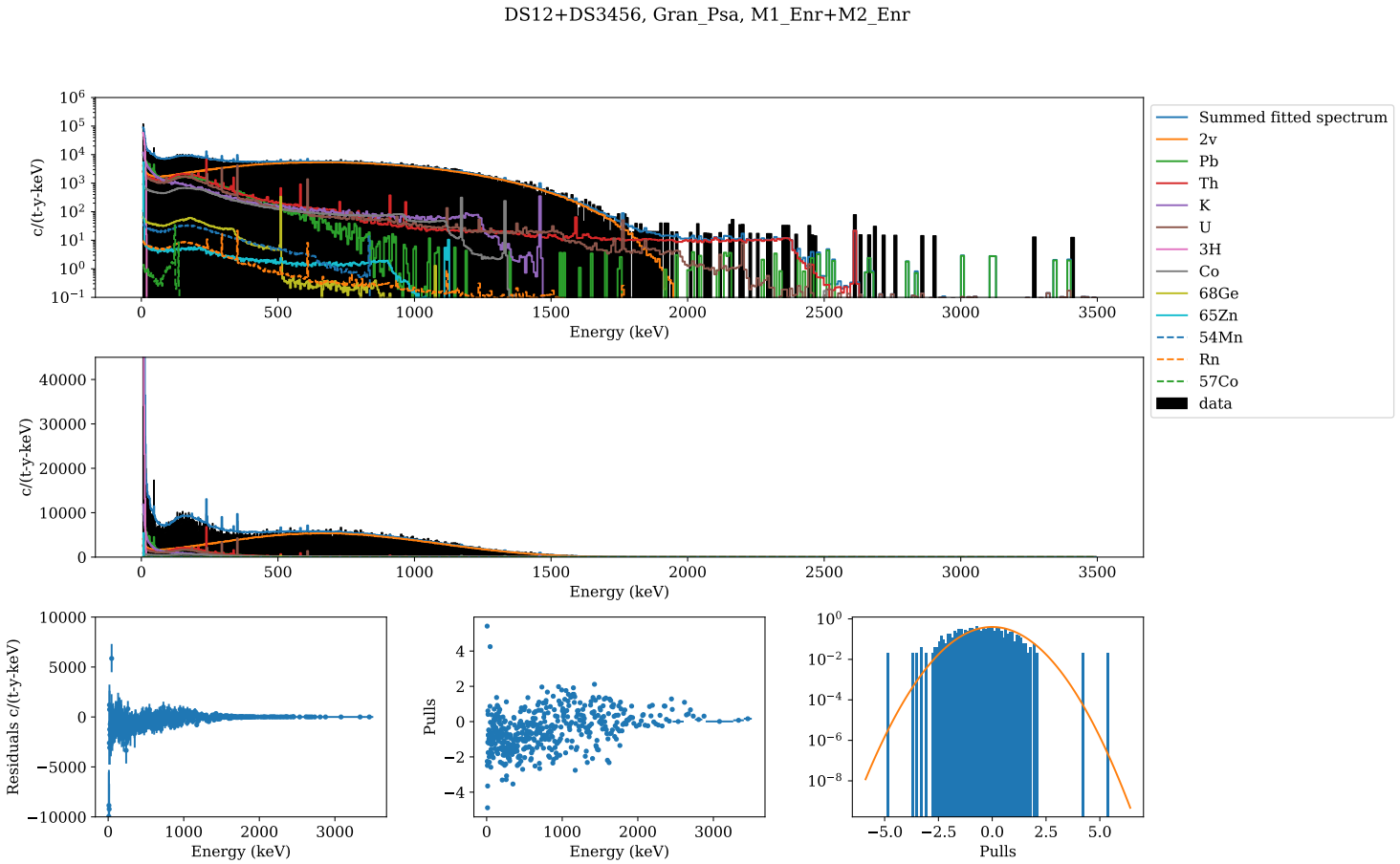

Figure 4.22: Best-fit model to data sets 1 and beyond with both the granularity and A vs. E/dT heuristic cuts applied, enriched Ge detectors only, broken down by contaminant.

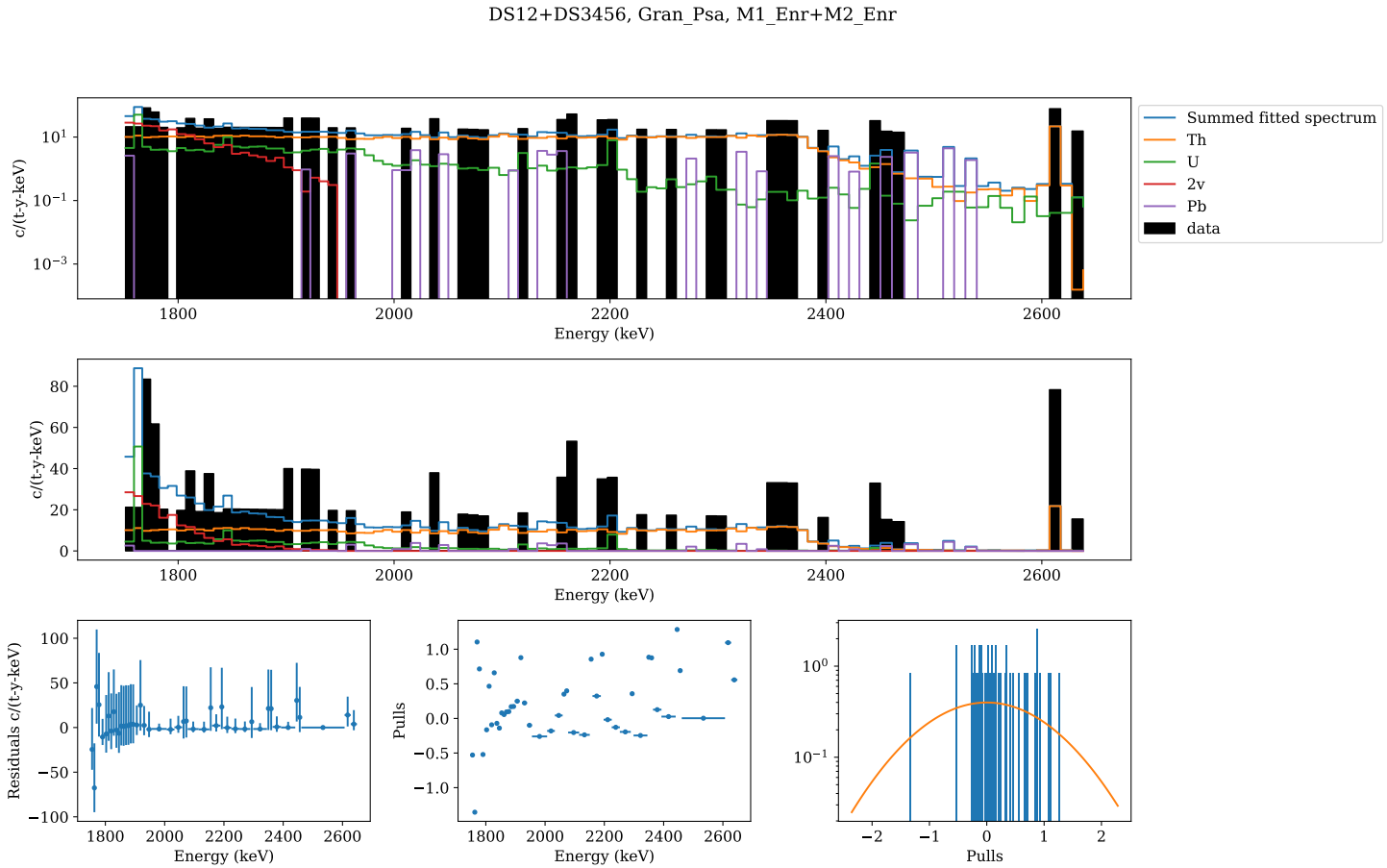

Figure 4.23: Best-fit model to data sets 1 and beyond with both the granularity and A vs. E/dT heuristic cuts applied, enriched Ge detectors only, broken down by contaminant, and focusing on the region of the energy spectrum near $Q_{\beta\beta}$.

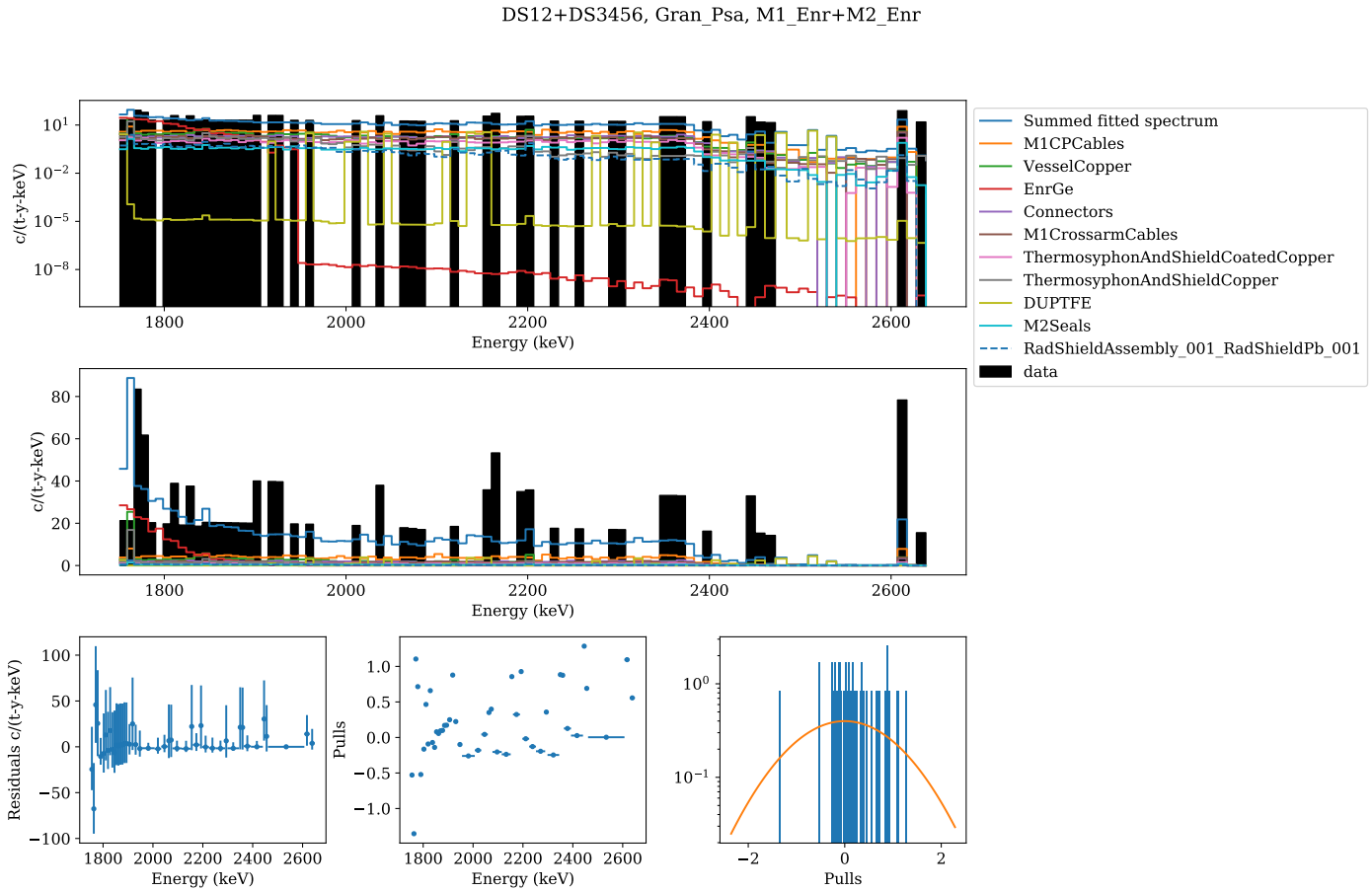

Figure 4.24: Best-fit model to data sets 1 and beyond with both the granularity and A vs. E/dT heuristic cuts applied, enriched Ge detectors only, broken down by component, broken down by contaminant, and focusing on the region of the energy spectrum near $Q_{\beta\beta}$.

4.7.2 Tables of results and analysis of the tables

Table 4.2 contains results for all backgrounds with precision > 1. As demonstrated in Section 4.5, these are the most robust results for which the statistical and model-fitting-related systematic uncertainties are best controlled and characterized. With 123 PDFs being fit, we would expect approximately one of them to have a deviation greater than 2.6 standard errors from the predicted assay values arising purely from statistical fluctuations. In fact, we find 4 PDFs with deviations exceeding 2.6 standard errors:

- RadShieldPb ^{210}Pb pbbrem: best-fit value is 49.5 standard errors too low
- M1CPCables ^{232}Th bulk: best-fit value is 3.29 standard errors too high
- ThermosyphonAndShieldCopper ^{40}K surface: best-fit value is 2.74 standard errors too high
- ThermosyphonAndShieldCoatedCopper ^{232}Th bulk: best-fit value is 3.05 standard errors too high

The estimate for the ^{210}Pb bremsstrahlung events from the lead shield is somewhat suspect due to the custom generator used. While we have high confidence that the shape of the spectrum is accurate due to testing and comparisions with full simulations, the total amplitude could be incorrect. Because the generator seeds the primary decays on the surface of the lead, there is an effectively higher efficiency for detection of these primaries by the detectors than there is for a standard bulk simulation. I attempted to compensate for this effect by comparing to the full simulation, but the statistics were not very good in the full simulation and it is possible this compensation was incorrect.

Table 4.2: Aggregated results of fits with 123 PDFs to data acquired with the MAJORANA DEMONSTRATOR. The data sets included are described in Table 2.3. Only PDFs that fitted with a precision > 1 are included here. For a full list of results, please see Table C.2.

Component group	**Contaminant**	**Source type**	**Best-fit counts**	**Best-fit activity density (Bq/kg)**	**Precision**	**Assayed activity density (Bq/kg)**
EnrGe	$2\nu\beta\beta$	bulk	34485 ± 1081	7.53e-05 ± 2.36e-06	193	7.99e-05 ± 3.90e-06
RadShieldPb	^{210}Pb	pbbrem	22620 ± 1079	4.96e-01 ± 2.37e-02	43.1	3.02e+01 ± 6.0e-01
NatGe	^{3}H	bulk	13648 ± 635	2.14e-04 ± 9.94e-06	35.9	N/A
M1CPCables	^{232}Th	bulk	6536 ± 1984	1.19e-02 ± 3.60e-03	3.42	1.63e-05 ± 1.63e-06
ThermosyphonAndShieldCopper	^{40}K	surface	5753 ± 1929	4.73e-04 ± 1.59e-04	3.06	0.00e+00 ± 6.80e-05
RadShieldCuOuter	^{60}Co	bulk	5716 ± 2624	3.00e-05 ± 1.38e-05	2.22	0.00e+00 ± 1.50e-04
NatGe	^{68}Ge	bulk	4522 ± 1108	3.88e-05 ± 9.52e-06	4.26	0.00e+00 ± 3.47e-04
VesselCopper	^{238}U	bulk	4396 ± 2842	1.19e-05 ± 7.71e-06	1.57	2.16e-07 ± 5.15e-08
Connectors	^{232}Th	bulk	3302 ± 1814	8.49e-03 ± 4.67e-03	1.84	2.11e-04 ± 1.85e-04
DUPTFE	^{210}Pb	surface	3171 ± 292	1.25e-02 ± 1.15e-03	21.3	N/A
ThermosyphonAndShieldCopper	^{238}U	bulk	3099 ± 2767	3.68e-05 ± 3.29e-05	1.13	2.16e-07 ± 5.15e-08
M1CrossarmCables	^{232}Th	bulk	2297 ± 1604	6.09e-02 ± 4.25e-02	1.45	1.63e-05 ± 1.63e-06
ThermosyphonAndShieldCoatedCopper	^{232}Th	bulk	2078 ± 657	6.27e-02 ± 1.98e-02	3.30	2.16e-03 ± 1.20e-04
EnrGe	^{3}H	bulk	2033 ± 143	1.29e-05 ± 9.10e-07	74.2	N/A

Component group	**Contaminant**	**Source type**	**Best-fit counts**	**Best-fit activity density (Bq/kg)**	**Precision**	**Assayed activity density (Bq/kg)**
VesselCopper	^{232}Th	bulk	1817 ± 1153	3.93e-06 ± 2.50e-06	1.60	4.40e-08 ± 1.00e-09
NatGe	$2\nu\beta\beta$	bulk	1803 ± 166	9.55e-06 ± 8.80e-07	19.6	7.33e-06 ± 3.58e-07
RadShieldCuOuter	^{54}Mn	bulk	926 ± 209	2.11e-05 ± 4.74e-06	4.80	N/A
M1StringSigCables	^{60}Co	bulk	882 ± 804	8.81e-03 ± 8.03e-03	1.10	0.00e+00 ± 6.67e-05
M2StringSigCables	^{60}Co	bulk	683 ± 435	1.57e-02 ± 1.00e-02	1.59	0.00e+00 ± 6.67e-05
LMFEs	^{60}Co	bulk	674 ± 561	8.02e-03 ± 6.67e-03	1.22	0.00e+00 ± 2.31e-03
M1Seals DS0	^{238}U	bulk	640 ± 318	2.47e-02 ± 1.23e-02	2.05	8.82e-03 ± 2.81e-05
M2Seals	^{232}Th	bulk	634 ± 570	2.74e-03 ± 2.46e-03	1.12	6.53e-05 ± 1.05e-05
NatGe	^{65}Zn	bulk	335 ± 149	7.23e-06 ± 3.23e-06	2.30	N/A
NatGe	^{57}Co	bulk	164 ± 24	3.26e-06 ± 4.81e-07	9.43	N/A
EnrGe	^{65}Zn	bulk	153 ± 40	1.16e-06 ± 3.04e-07	4.11	N/A

There is also some similarity between the shape of the lead shield ^{210}Pb spectrum and the low-energy Compton hump in other spectra with high-energy photons (like ^{232}Th, ^{238}U, ^{40}K, and ^{60}Co). However, the difference in shielding between data set 0 and later data sets significantly reduces the possibility of any confusion between these spectra. Specifically, only component groups outside the inner copper shield that was installed after data set 0 could be confused with the lead shield ^{210}Pb spectrum. Furthermore, the rolloff of the bremsstrahlung spectrum as the energy increases is less steep than the rolloff for the Compton continuum spectra, giving yet another distinction between the shape of the lead shield ^{210}Pb spectrum and the other isotope spectra.

The estimates for the other three PDFs in disagreement with the assay data are harder to explain. They are likely candidates for elevated sources of activity seen by the DEMONSTRATOR. Given the inherent ambiguities in the confidence of a model-building process like this one, it is hard to assess exactly how accurate these results are. Clearly there is elevated ^{232}Th, which appears to be more apparent in module 1 than in module 2. Because the eight different cable PDFs (cross arm, cold plate, string HV, and string signal for each module) are the only components fit separately between the two modules in this model, they are the only PDFs capable of explaining this difference between the two modules. Therefore, it is probably premature to assume that excess ^{232}Th is coming from the module 1 cold plate cables. It is safer to instead infer that there is an unexpected source of ^{232}Th that is on the module 1 side and is not internal to the cryostat and below the cold plate (or else the string HV and/or string signal cables, which are below the cold plate, would have fit higher). The only PDFs included in the model that are capable of explaining this are the module 1 cross arm cables (M1CrossarmCables) and the module 1 cold plate cables (M1CPCables). The M1CrossarmCables actually fit to an activity density approximately 6 times higher than that of the M1CPCables, but due to their distance from the detectors they have a much lower efficiency for detection.

If the module-1 and module-2-specific components were all split into separate PDFs and allowed to float independently, it is quite possible that these results would be affected. For example, it is possible that the signal connectors used in module 1 have a higher activity than those used in module 2. Module 1 took longer to assemble, and the cables and connectors had to be reinstalled between data sets 0 and 1. This additional handling could possibly have imparted extra activity onto those components. It is important to remember that we are trying to identify the physical location of a very weak source of ^{232}Th, so it is plausible that it could happen to be confined to a single signal connector or a single stretch of cable.

A further caveat to make is that late in the analysis, it was discovered that the simulations used for data set 0 had erroneously included the copper shielding blocks in the cross arm that were installed between data sets 0 and 1. This could potentially affect the simulated detection efficiency in data set 0 for components that are located along or behind the cross arm, which include the cold plate cables, thermosyphon and shield copper, thermosyphon and shield vespel, and the stainless steel cube that sits at the far end of the cross arm. If the effect is large enough, this could possibly impact the best-fit parameter estimates. The cube was not included in the model because the simulated efficiency was too low to produce a simulated PDF, but with the correct shielding in place for data set 0 it is possible that the efficiency could be high enough to simulate it. The high fits to the cold plate cables and thermosyphon components could be compensating for these geometry imperfections. The data set 0 simulations will be corrected in the future.

Table 4.3 shows how counts in the 360 keV background counting region (defined in Section 2.9) are distributed according to the best-fit background model. Before applying any analysis cuts, there are 161 counts remaining in the best-fit model of the background counting region in the enriched detectors, in all data sets except data set 0. All but 7 of these counts are in components with a precision > 1, which are listed in Table 4.3. After applying the granularity and dT heuristic cuts (which appears to *over*-reject Compton continuum

backgrounds near 2039 keV, see Figure 3.17), there are 24 counts remaining in the best-fit model. This compares to 17 counts seen in the DEMONSTRATOR, which is a difference of 1.1 standard errors, assuming square-root Poisson errors on the number of counts [8]. ^{232}Th in the module 1 cold plate cables account for 8 of the 24 counts. The signal connectors, thermosyphon and shield parylene-coated copper parts, module 1 cross arm cables, and copper cryostat vessel account for a further 12 counts, but given the estimated uncertainties in the best-fit activity densities, none of these were individually statistically significantly elevated above expectations. The expected number of counts based on the assay data is 4 [9], which is statistically consistent with the expected number of counts in the background model for the remainder of the PDFs.

[8]Note that the recent results from [45], which are presented in Table 2.5, include blinded data that was not analyzed in this work.

[9]The 4 counts comes from taking the ratio of the assay-projected background rate of 3 c/(ROI-t-y) and the measured rate of 12 c/(ROI-t-y), and multiplying it by the number of background counts detected.

Table 4.3: Comparison of effect of analysis cuts for best-fit model, including only PDFs with a precision > 1. Only enriched detectors are included in this table, and only data sets 1-6a are included. This roughly matches the data set analyzed in [109]. The PDFs are listed in precision order, with the most precise estimates appearing first. In this table the ROI refers to the 360 keV window extending from 1950 to 2350 keV (with 4 10 keV excisions) that is used to estimate the background rate in [109] and [45].

Component group	**Contaminant**	**Source type**	**Best-fit counts**	**Best-fit counts in ROI**	**After granularity cut**	**After granularity and A vs. E cuts**
EnrGe	$2\nu\beta\beta$	bulk	31227 ± 979	0 ± 0	0 ± 0	0 ± 0
NatGe	^{3}H	bulk	0 ± 0	0 ± 0	0 ± 0	0 ± 0
RadShieldPb	^{210}Pb	pbbrem	4186 ± 200	0 ± 0	0 ± 0	0 ± 0
EnrGe	^{3}H	bulk	1825 ± 128	0 ± 0	0 ± 0	0 ± 0
DUPTFE	^{210}Pb	surface	1574 ± 145	1 ± 0	1 ± 0	1 ± 0
NatGe	$2\nu\beta\beta$	bulk	4 ± 0	0 ± 0	0 ± 0	0 ± 0
NatGe	^{57}Co	bulk	3 ± 0	0 ± 0	0 ± 0	0 ± 0
RadShieldCuOuter	^{54}Mn	bulk	114 ± 26	0 ± 0	0 ± 0	0 ± 0
NatGe	^{68}Ge	bulk	529 ± 130	0 ± 0	0 ± 0	0 ± 0
EnrGe	^{65}Zn	bulk	101 ± 26	0 ± 0	0 ± 0	0 ± 0

Component group	**Contaminant**	**Source type**	**Best-fit counts**	**Best-fit counts in ROI**	**Best-fit counts in ROI after granularity cut**	**Best-fit counts in ROI after granularity and A vs. E cuts**
M1CPCables	^{232}Th	bulk	3459 ± 1050	53 ± 16	32 ± 10	8 ± 2
ThermosyphonAndShieldCoatedCopper	^{232}Th	bulk	747 ± 236	12 ± 4	8 ± 3	2 ± 1
ThermosyphonAndShieldCopper	^{40}K	surface	3769 ± 1264	0 ± 0	0 ± 0	0 ± 0
NatGe	^{65}Zn	bulk	29 ± 13	0 ± 0	0 ± 0	0 ± 0
RadShieldCuOuter	^{60}Co	bulk	1902 ± 873	0 ± 0	0 ± 0	0 ± 0
M1Seals DS0	^{238}U	bulk	0 ± 0	0 ± 0	0 ± 0	0 ± 0
Connectors	^{232}Th	bulk	1368 ± 751	23 ± 13	15 ± 8	4 ± 2
VesselCopper	^{232}Th	bulk	1125 ± 714	17 ± 11	10 ± 6	3 ± 2
M2StringSigCables	^{60}Co	bulk	303 ± 193	1 ± 1	0 ± 0	0 ± 0
VesselCopper	^{238}U	bulk	2723 ± 1761	10 ± 6	9 ± 6	1 ± 1
M1CrossarmCables	^{232}Th	bulk	1314 ± 918	22 ± 15	14 ± 10	3 ± 2
LMFEs	^{60}Co	bulk	425 ± 353	3 ± 2	2 ± 2	0 ± 0
ThermosyphonAndShieldCopper	^{238}U	bulk	1779 ± 1589	7 ± 6	6 ± 5	1 ± 1
M2Seals	^{232}Th	bulk	244 ± 219	4 ± 4	2 ± 2	1 ± 1
M1StringSigCables	^{60}Co	bulk	550 ± 502	1 ± 1	1 ± 1	0 ± 0

Chapter 5

UNCERTAINTY ANALYSIS FOR THE BEST-FIT BACKGROUND MODEL

Possible sources of uncertainty that may affect the results presented in Section 4.7 can be identified by analyzing the log-likelihood function that was minimized to produce the results. It is given as Equation 4.4, and is reproduced here for convenience.

$$\ln \mathcal{L} = \sum_{i=1}^{n} d_i \ln \left(\sum_{j=1}^{m} P_j \epsilon_j m_j A_{ji} t \right) - \sum_{j=1}^{m} P_j \epsilon_j m_j A_{ji} t + \sum_{i=1}^{n} \sum_{j=1}^{m} a_{ji} \ln(A_{ji}) - A_{ji} \qquad (5.1)$$

This formulation is for a single detector or single effective detector, with the full array log-likelihood being a sum of the individual detector or effective detector log-likelihoods [1]. The uncertainties reported in Tables 4.2 and C.2 are calculated uncertainties on the P_j in equation 5.1. The d_i and a_{ji} are the data and simulated histograms respectively, and contain sources of statistical uncertainty, which are correctly incorporated by the construction of the log-likelihood function.

Every parameter in Equation 5.1 also can contribute systematic uncertainty to the final result (except for the P_j and the A_{ji} which are free parameters). For the purposes of this uncertainty analysis, the data (d_i) will be treated as free from systematic uncertainty, and potential sources of systematic uncertainty from the d_i will be attributed to the a_{ji} and discussed in Section 5.1. Sources of systematic uncertainty in the simulations (ϵ_j, m_j, and

[1] In the analysis presented in this document, recall that the actual detectors are grouped by module and enrichment, resulting in 4 groups of effective detectors. Furthermore, the spectra are separated by the granularity cut, and by data set, resulting in 24 effective detector spectra each treated as a single histogram, with likelihoods given by Equation 5.1, that are summed together to obtain the full likelihood. The ϵ_j and a_{ji} are summed together appropriately as well.

a_{ji}) will be analyzed in Section 5.2. Finally, the process of constructing the model itself (choice of PDFs, minimization of the likelihood function) can introduce additional systematic uncertainties. These will be analyzed in Section 5.3.

It should be mentioned that, although the calculation of the active mass in the DEMONSTRATOR is the dominant source of uncertainty in the limit on $0\nu\beta\beta$ decay presented in [45] and in Section 2.4.1, that particular calculation does not enter into the analysis of uncertainty in this chapter. Uncertainty in the active mass only enters indirectly through the sensitivity of the best-fit activity densities to the dead-layer parameters used in the simulation, which will be discussed in Section 5.2.4. This fact can be seen by noticing that the active mass, unlike the other major component of the exposure (the livetime t), does not directly appear in Equation 5.1. If one wants to convert the best-fit activity densities to a modeled background index, then the active mass calculation would be relevant. Except when scaling the y-axes of plots like those contained in Section 4.7.1, that type of comparison is not done in this document; only the raw number of measured counts are compared, which does not require an explicit calculation of the active mass.

5.1 Data Selection and Estimate of Related Sources of Uncertainty

The degree to which known biases and uncertainties, related to how the data were acquired, are accounted for in the simulations will be addressed in this section. Since the data are organized in histograms of the detected energy, any uncertainties can be thought of as relating to the x-axis or the y-axis. The following is a list of possible sources of uncertainty that is as comprehensive as possible.

- X-axis related uncertainties
  - Energy estimation
- Y-axis related uncertainties

– Efficiency of various data selection and analysis cuts

– Detector thresholds

Finally, the uncertainty in the livetime (t) will be addressed in its own subsection.

5.1.1 Uncertainties in the Estimated Energy

The energy estimation working group of the MAJORANA collaboration has made an effort to quantify all of the uncertainties related to the estimation of the energy of detected waveforms. Those sources of uncertainty are detailed in the internal document [70], where Appendix J specifies that the bias in the estimated energy of a particular energy deposition is less than 0.2 keV at $Q_{\beta\beta}$ (2039 keV). At energies below 200 keV, an effect previously identified [70] and recently explained by Guinn [68] that has not yet been corrected for in the data can lead to an error in the estimated energy that is as high as 0.5 keV in some detectors.

In both cases, the binning scheme used to fit the background model (described in Section 4.3) makes these deviations from perfect energy calibration negligible. As can be seen in Table 4.1, the bin width at $Q_{\beta\beta}$ is 8.3 keV. A 0.2 keV deviation in the peak location changes the expected fraction of the peak captured in that bin from 99% to 98.6%, a negligible change given other much more dominant sources of uncertainty to be discussed shortly.

At the lowest energy peak of 10.35 keV the bin width is 1.8 keV. Assuming the worst-case scenario where every detector experienced the maximum possible deviation from the expected peak location of 0.5 keV, a much more significant change to the expected fraction of the peak captured would occur: from 99% to 50%. Fortunately, the situation is not that dire. Figure 5.1 shows the histogram of all hits in all natural germanium detectors from DS1 to DS6 with bins of width 0.1 keV. Only the natural germanium detectors are shown because the 10.35 keV ^{68}Ge X-Ray is much more prominent in their spectra than in the enriched detectors'. A gaussian fit to this peak gives a value for the mean of 10.51 ± 0.01 keV, a 0.15 keV offset from where it should be. The bin for this peak extends from 9.85 keV to

10.84 keV and still should capture 96% of the hits in the peak instead of the nominal 99%. Since this peak is expected to have the worst uncertainty in its location as a fraction of the bin width at that energy, the uncertainty in the number of counts in a bin from this effect is taken to be negligible relative to other sources of uncertainty.

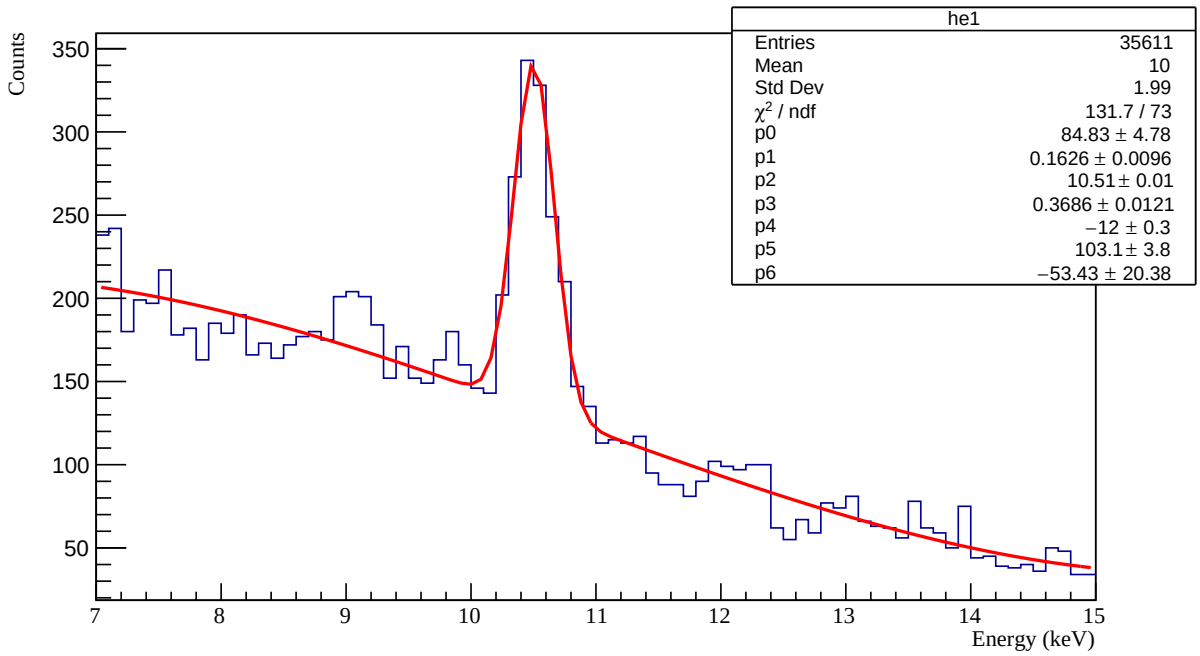

Figure 5.1: This X-Ray has a nominal energy of 10.35 keV but is located at 10.5 keV in the MAJORANA data due to residual nonlinearities in the energy calibration. This is not expected to have a significant effect on the best-fit background model. The fit function is a sum of a gaussian and a cubic: $f(x) = p_0/\sqrt{2\pi p_1^2}\exp\left(-(x-p_2)^2/(2p_1^2)\right) + p_3x^3 + p_4x^2 + p_5x + p_6$

Wide bins also help reduce sensitivity to steplike features in the energy spectrum. An example of this is the Compton edge of the 2614 keV peak, which occurs at 2380 keV. If we conservatively approximate the Compton edge as a step function, and place a bin edge at

exactly 2380 keV, and assume a miscalibration of δ keV, then the number of counts in the bin just below 2380 keV changes from nw to nw (where n is the density of counts and w is the bin width in keV), and the number of counts in the bin just above 2380 keV changes from 0 to $n\delta$. What matters most is the change in the ratio of the two bins, which goes from 0 to $\frac{\delta}{w}$. As long as $\delta << w$, which is the case in this example as δ is less than 0.2 keV and w is ~8 keV, then this change should also be negligible. As the 2380 keV Compton edge of ^{208}Tl is the sharpest non-peaking feature in the DEMONSTRATOR energy spectrum, neglecting this possible source of error should not impact the best-fit result.

5.1.2 Data selection and analysis cuts

The MAJORANA collaboration makes every effort to keep the DEMONSTRATOR operational as much as possible. Because the limit that is set on $0\nu\beta\beta$ decay increases in direct relation to the total exposure of the experiment, the collaboration tries to use as much of the acquired data as possible. To this end, the run selection and data cleaning working group has produced a vetted set of open data available for use to the rest of the collaboration. An overview of the open data was included in [109] as Table I. Since the publication of that paper, two additional sets of open data have been acquired — DS5c and DS6a — and are included in this analysis. DS5c and DS6a are also included in [45] which has been accepted for publication in Physical Review C.

The only new cut that has been added specifically for this analysis is the cut to remove periods with high low-energy noise outlined in Section 2.3.2. Because entire runs are removed, the effect of this cut on good data does not depend on the energy of the event. Therefore, as long as the livetime and its uncertainty is calculated correctly, this selection will not contribute to the uncertainty of the best-fit background model.

There are also pulse-shape- and timing-based data cleaning cuts used for the analysis in [109] and [45]. These cuts are also used in this work and are effectively 100% efficient, as

was shown in Section 2.3.2. That is, they remove a negligible number of good waveforms (estimated by the data cleaning working group to be less than 0.01% [60]). During the process of constructing the MAJORANA background model, I identified a small number of events that were not tagged by the standard data cleaning cuts from [109] but were easily rejected by existing calculated parameters. These cuts removed only about 300 waveforms from the total dataset, so a hand scan through those was sufficient to determine that none were good waveforms. The uncertainty on the data cleaning efficiency is thus negligible compared to other sources of uncertainty (such as the estimated uncertainty from the model-building algorithm (see Section 5.3), and is ignored in this analysis.

DCR and passivated surface model uncertainties

Our model and understanding of the exact configuration of the electric field near the passivated surface and how particles interact with it is still under development. We know that there is some charge trapping that leads to a slow release of charge over time, which makes the DCR cut effective (see Section 2.6.2 and [73]). We also know that there is a loss of the electron signal that results in position-dependent energy degradation. However, simulations of this effect are still in development and are not included in the model presented in this work. If the DCR cut on the data leaves some significant population of degraded alpha particles between 1800 and 2600 keV, it could have an impact on the result of the best-fit model. Specifically, it would artificially depress the peak-to-Compton ratio of the ^{232}Th-chain 2615 keV photon peak seen in the background data, as degraded alpha particles would almost certainly not be peaked at 2615 keV.

Julieta Gruszko presented evidence in [73] that a combination of the DCR and A versus E parameters was virtually 100% effective in identifying full-energy ^{210}Po alpha particle interactions with the detector surface. The effectiveness of the DCR cut drops as the interactions get closer to the point contact of the detector, but applying a high cut on the A

versus E parameter is able to compensate for this fact. Adding in a high A versus E cut to the data would give more confidence that degraded alpha interactions have been completely eliminated from the data sets and might be more straightforward than trying to simulate alpha particle interactions. Of course in the long run, simulations of alpha interactions will be critical to idenfity any excess alpha sources.

5.1.3 Threshold-related Uncertainties

The MAJORANA digitizers utilize a trigger system so that only periods of time when a waveform is actually being detected are saved to disk. Because this system must be implemented with a trigger threshold, events that deposit energy near the trigger threshold will not always cause the trigger to fire, leading to an efficiency to detect events that starts to drop noticeably from 100% below a certain energy. The digitizer trigger efficiency as a function of energy was calculated by Clint Wiseman and Brian Zhu of the MAJORANA low-energy working group and was found to be effectively 100% above 7 keV for most detectors. Some periods of time with low-energy noise may have effective thresholds above 7 keV, but those periods were removed from the analysis with the cuts described in Section 2.3.2. Since events below 7 keV are not analyzed in this work, the trigger efficiency is treated as 100%. Any deviation from this assumption would be much less than 1%, which is subdominant to sources of statisical uncertainty, and is therefore ignored in this analysis.

5.1.4 Uncertainties in the Estimated Livetime

In order to convert the best-fit parameters of the background model which have units of activity density (Bq/kg) into a number of counts expected, the total amount of time the DEMONSTRATOR was live must be incorporated into the calculation. The process of calculating the live time was described in Section 2.4.2.

Any effects from uncertainties or errors in calculating the livetime that affect all detectors

identically would have the effect of biasing the resultant activities of the best-fit background model. However, as long as the sources of uncertainty are highly correlated across the detectors, the relative activities produced by the model would not be affected. Furthermore, the estimated uncertainty in the livetime produced by `ds_livetime` is extremely small, on the order of 1 part in 10^6. This is subdominant to statistical uncertainties, and is neglected in this analysis.

5.2 Uncertainties Associated with `MaGe` *Simulations*

The terms in Equation 5.1 that are related to the simuations are the simulated efficiency for a decay from source j to deposit energy in a detector (ϵ_j), the simulated mass of source j (m_j), and the simulated spectrum (a_{ji}). By design, sources of statistical uncertainty in the actual simulated spectra (a_{ji}) are incorporated into the A_{ji} terms, and do not need to be independently assessed. Uncertainties in ϵ_j are also incorporated into the discussion of uncertainties in the a_{ji} and do not need to be discussed independently.

The analysis of possible sources of uncertainty in the simulations will be broken down by the mechanisms by which possible sources could arise, rather than by how they might affect the result of the minimum likelihood. This is because possible uncertainties in the simulations have in general a very non-linear effect on the final uncertainties in the best-fit parameters, and cannot be incorporated analytically. Therefore, it is easier to think about where they are coming from, and how that might affect the result. An important future project would be to assess through simulation the effect that simulation-related systematic uncertainties might have on the final result.

The types of systematic uncertainty that will be addressed in this section are:

- Uncertainties in the simulated DEMONSTRATOR geometry

- Uncertainties in the simulation of physics processes and other internal processes in

Geant4 and `MaGe`

- Uncertainties in the primary particle generators
- Uncertainties in the post-processing with `GAT`
  - Uncertainties from the dead-layer model
- Violation of certain assumptions in the simulations

5.2.1 Geometric uncertainties

The MAJORANA DEMONSTRATOR is a complex system with thousands of parts, and the encoding of its geometry into `MaGe` is correspondingly also complex. `MaGe` has been in development since 2004 by the MAJORANA and GERDA collaborations, and has received contributions from 33 different people, according to the statistics on Github where it is remotely hosted. The geometry of the DEMONSTRATOR was encoded into `MaGe` based on the engineering drawings that were used to fabricate the parts. Although care has been taken to ensure that the simulated version of the DEMONSTRATOR matches the true version of the experiment, of course there can always be inconsistencies that have been overlooked.

For example, it was discovered after the simulations presented in this work had been produced that the copper shielding in the cross-arm tube for module 1 was included in the simulations for DS0, even though it was not installed until after DS0 was complete. This inconsistency will be rectified in the near future by running simulations with the correct cross-arm shielding for DS0 in place, but it was not feasible to do this before the creation of this document. It is possible that fixing the cross-arm shielding inconsistencies could meaningfully change the best-fit background model, as the differences in shielding between DS0 and the later data sets provide useful information as to which components in the DEMONSTRATOR are producing counts in the detectors (e.g. the dramatic drop in the ^{60}Co peaks at 1173 keV

and 1332 keV suggests a major ^{60}Co source must be outside the inner copper shield that was installed after DS0).

There are a few other known discrepancies between the simulated and as-built versions of the DEMONSTRATOR. The calibration track, which consists of approximately 2 cm diameter plastic tubing wrapped 3 times around each module, is not included in the simulated geometry, nor are the calibration track mounts which were fabricated from electroformed copper. The calibration source is simulated as a series of connected arcs which are arranged to mimic the position of the calibration track. These parts do not have a line-of-sight to the detectors, and are made from the same material as many components that do. They are also not big enough to provide a significant level of shielding to any of the detectors, except possibly for internal point-sources in pathological locations. Therefore, their exclusion from the simulated as-built geometry is not expected to significantly alter the best-fit background model.

A collection of plots showing the location of simulated decays in various components is included in this document as Appendix B, and a rendering of the simulated geometry can be seen in Chapter 3.

The masses used in the likelihood function (m_j) are computed by `MaGe`, based on the implemented geometry. Each component's volume is calculated, and is multiplied by the density of its material. Therefore, assuming that uncertainties in the component densities are negligible compared to uncertainties in the volumes, the uncertainty in each component's mass is proportional to its volume uncertainty. These masses were systematically compared to the masses expected based on the CAD drawings, and in some cases with actual measurements of components, and found to be consistent. Geant4 contains tools to look for overlaps of simulated parts, which were used on the as-built geometry. Furthermore, since all components were implemented based on the engineering drawings for the DEMONSTRATOR, any deviations from the true volumes should be small; almost certainly subdominant

to statistical uncertainties. Therefore, uncertainties in the simulated component masses are ignored in this analysis.

The only exception to the above paragraph relates to the signal and high-voltage cables. The cables are not actually implemented as physical volumes in the DEMONSTRATOR `MaGe` model, but are rather just generated as empty line or volume sources at specific locations in the simulated geometry. Therefore, their masses were not calculated by Geant4, but rather were estimated based on the design of the `MaGe` cable generator and the measured linear mass density of the cables installed in the DEMONSTRATOR. Any uncertainties related to this calculation are also ignored in this analysis, but should be carefully checked in the future, given the evidence in Section 4.7 that cables are a significantly elevated source of background events.

The comparison of the shape of the simulated ^{228}Th and ^{222}Rn spectra to the measured spectra given in Section 3.2.3 give confidence that there are no large errors in the simulated components inside the shield pocket, as well as the comparisons performed by Tom Gilliss referenced in Section 3.2.3. The single detector where he found poor agreement was an enriched germanium detector in module 2, and comprised ~11% of the total exposure for module 2 enriched germanium detectors. The module 2 enriched germanium detectors in turn comprise only ~22% of the enriched exposure for data sets where both modules were operating. The discrepancy between the simulated and measured calibration spectra for this detector deserves investigation, but its inclusion in this analysis is unlikely to have a significant impact on the results, given its contribution to the total exposure.

5.2.2 Errors in Geant4 Physics Processes

`MaGe` uses Geant4 to simulate the physical processes that produce energy depositions in the MAJORANA detectors. Geant4 has a large user base and a fairly long history of development, having existed since 1998 [77], which gives confidence that few large-scale unnoticed bugs

persist in the code. Extensive validation of Geant4 has been performed in the last two decades, and can be found in the literature (e.g. [110]).

As was discussed in Section 3.1.2, the MAJORANA collaboration also has produced a validation suite that checks a variety of physics processes and compares them to literature values, but the version of Geant4 used in this work — Geant4.10.4 — has not yet been validated by this suite. Efforts are underway within the collaboration to update the validation code to run successfully on this version of Geant4. Once this is in place, any significant deviations of physical processes from the literature values should be investigated for their possible effect on the background model result.

That said, there are a couple of known issues with Geant4 that may not have been fully accounted for in this analysis. Jason Detwiler contributed code to Geant4 that would correctly handle angular correlations between photons emitted as part of a gamma cascade, according to Appendix F of [111]. This correction to the handling of angular correlations was not correctly enabled in `MaGe` until late in the simulations campaign and may not have been correctly applied in all simulations. However, measurements of the angular correlation of photons emitted in a cascade indicate that the angular correlations were in fact enabled, even though the associated configuration flag was not enabled. Whether they were enabled or not, it is reasonable to think that for most components, any ill effects from neglecting these correlations are minimal, as the agreement between the simulated granularity cut and that measured during detector calibration with the ^{228}Th source is quite good (see Figure 3.15). It may be prudent to check (and redo if necessary) simulations of components inside the calibration track, since they would expect to see the biggest change from neglecting this effect.

Another error was discovered by MAJORANA collaborator Brian Zhu in 2018 regarding the incorrect handling by `MaGe`/Geant4 of certain types of decays with a high branching ratio from internal conversion processes. This particularly affected the spectrum of the decay of

^{210}Pb, which produces several X-Rays and electrons at low energies. This was corrected for the only surface simulation of ^{210}Pb that was included in the model: that of ^{210}Pb on the surface of the detector unit PTFE (DUPTFE).[2] Bulk decays of ^{210}Pb would likely not be changed by this error as the X-Rays and electrons are too low in energy to escape from all but the thinnest components.

5.2.3 Uncertainties in the primary particle generators

There are 5 different primary particle generators used to produce this result, each of which could contribute to the systematic uncertainty of the result:

- Bulk decays in components
- Surface decays on components
- The calibration line source
- The lead shield ^{210}Pb generator
- The cable generator

Bulk decay generator

The bulk decay generator is part of Geant4 [77] [110] and seeds decays uniformly within a specified physical volume, weighting by mass. Any deviation from a non-uniform seeding of primary locations would be minor and is neglected in this result. Of course, if the

[2]Other surface sources of ^{210}Pb were not included because of the relative importance of the high-energy part of the spectrum vs. the low-energy part. Since the ^{210}Pb X-Ray is very likely coming from decays on a surface with line-of-sight to the detectors, and since the hypothesis that it was the DUPTFE seemed reasonable due to its ability to electrostatically attract ionized ^{222}Rn daughters, I did not focus on exploring alternative surface sources of ^{210}Pb.

DEMONSTRATOR contains significant sources that are non-uniformly distributed within single physical volumes, the simulated histograms will not be able to correctly model this. At the moment there is no indication that this is a particular area of concern.

Surface decays generator

The surface decay generator uses the Generic Surface Sampler (GSS) [79] to seed its decay locations. The reference [79] shows that the GSS will evenly sample any arbitrary surface, so deviations from a uniform sampling are also neglected in this analysis.

The calibration line source

The calibration source is modeled in `MaGe` as a series of connected toroidal segments, which approximate the true helical shape of the calibration source quite well. Deviations from the nominal source location (e.g. the source is not being inserted correctly, or the source track has shifted from its nominal location) could lead to some disagreements between the simulated calibration source and the calibration data. However, the calibration source is not part of the background model, so any disagreements between simulation and data would only be included indirectly through other sources (e.g. the modeling of the transition dead-layer profile is incorrect), and do not need to be explicitly included in the analysis of uncertainty for the result from Section 4.7.

The cable source generator

The signal and HV cables of the DEMONSTRATOR (described in Section 3.1.1) are not implemented as physical volumes, due to the difficulty of accurately representing their exact locations. With 58 detectors in 2 modules, each instrumented with a 4-braid signal cable and an HV cable (so 116 cables in total), the effort to record and simulate the locations of all cables accurately would be significant, and other activities were prioritized over it.

Uncertainties arising from the approximations here are potentially significant, but were not included in this analysis. Since the cables appear to be important in correctly modeling the DEMONSTRATOR's backgrounds, improving their primary event generator could improve our confidence in the best-fit background model.

5.2.4 Uncertainties in post-processing with `GAT`

Some of the modules from Table 3.2 can potentially inject systematic uncertainty into the best-fit model. In particular, the Energy Adjuster and the Dead Layer Processor must be accounted for. The degree to which the Energy Adjuster accurately reproduces the resolution function of the acquired data was already discussed in Section 5.1.1, but the Dead Layer Processor requires more attention.

Uncertainties Related to Detector Dead-layer Model

The ad-hoc model for the transition layer of the detector dead layers is a possible source of uncertainty for the final result. While the model is fairly well motivated from tests and simulations of the MALBEK detector [88], it is only a heuristic model and a full simulation of charge collection in each MAJORANA detector with `siggen` (following [88]) would likely be more accurate.

Furthermore, allowing the thickness of the dead layer to float in the fit for each detector could be a source of error. The decision to do this was made for two reasons. First of all, it generally improved the fit of the simulated calibration energy spectrum to the measured calibration energy spectrum, largely because it reduces the peak-to-Compton ratio, for low energy peaks in particular. Second of all, it appears that there is some evidence that the ratio of the 238 keV photon peak to the Compton continuum in the ^{228}Th calibration spectrum has not remained stable over time for all detectors (e.g. Figures 5.2 and 5.3). It is not clear to me what could be causing this effect. Several possible explanations include:

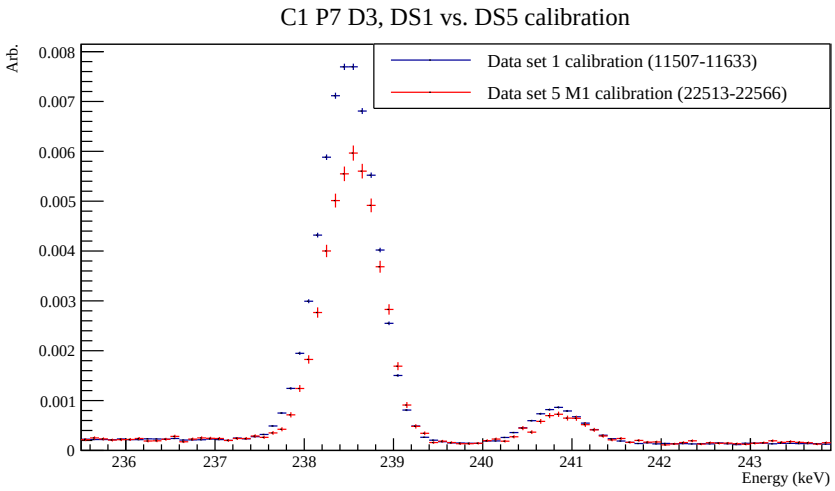

Figure 5.2: The detector with the worst observed degredation in its peak-to-Compton ratio for the 238 keV ^{212}Pb peak in calibration data is shown here: C1P7D3. Only a segment of the full energy spectrum, which extends from 0 to 3500 keV, is shown. The spectra were normalized so that their integrals above 5 keV would be 1. Clearly the red spectrum from data set 5 has a smaller integral under the peak at 238 keV than the spectrum from data set 1. In between these data sets, the electronics chain for this detector was changed, as it is on channel 594 in data set 1 but on channel 674 in data set 5.

- **Detectors are losing depletion** This is unlikely to be the case, and is certainly not correct in at least some cases. Detector C1P7D4 has a measured depletion of 600V, and was operated at 4500V until November 2017 when its bias was reduced to 2000V. Over time its peak-to-Compton ratio slowly decreased, but there was no corresponding large jump when the bias was reduced, which one would expect if it was already starting to lose depletion at 4500V. It is possible that certain regions of the detector are losing depletion (such as the corners far from the point-contact), but that most of the detector is still well above depletion. This effect could have an impact on the active mass and

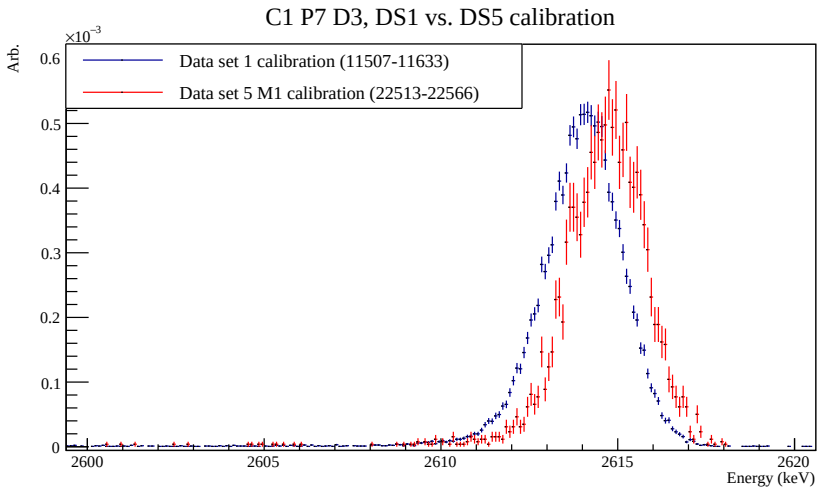

Figure 5.3: The 2615 keV ^{208}Tl peak for C1P7D3 does not show a similar degredation in its peak-to-Compton ratio. The two peaks are slightly miscalibrated, but the areas are clearly much more similar than in the previous figure. The spectra were normalized so that their integrals above 5 keV would be 1. In between these data sets, the electronics chain for this detector was changed, as it is on channel 594 in data set 1 but on channel 674 in data set 5.

is important to rule out.

- **Dead-layer is getting thicker as lithium drifts** This is unlikely to be the case as the detectors are all held near 77K, at which temperature the possible drift of Li atoms in the Ge bulk is negligible over the time periods concerned. Reference [112] contains a plot of lithium diffusion coefficient in germanium vs. temperature. The penetration depth of lithium in germanium is related to $\sqrt{Dt}$, where D is the diffusion coefficient and t is the length of time of diffusion (see Equation 1 in [113]). The measured diffusion coefficient at 77K is well off-scale of the plot from [112], but should be many orders of magnitude lower than the lower limit of the plot, which is at $D = 2 \times 10^{-8}\text{cm}^2/\text{s}$. At that rate, the drift depth of lithium into a germanium detector would be less than 1 cm,

so a diffusion constant many orders of magnitude below that would be inconsequential.

- **Th source is reaching a new equilibrium** This cannot be the case, because ^{228}Th has a longer half-life than all of its daughters until ^{208}Pb, which is stable. The Borexino experiment found that their ^{228}Th source contained significant amounts of ^{229}Th and ^{230}Th [114], but they decay with much longer half-lives than ^{228}Th and have correspondingly much lower intensities. Furthermore, since this effect is seen non-uniformly across the detectors, source contamination would also have to be significantly non-uniform. This explanation seems less likely than depletion loss, but could be investigated with simulations.

Even though we have no physically motivated reason to explain this effect, it is well-modeled by allowing the effective thickness of the transition layers to increase. Therefore, we have created and used simulations with a floating transition layer thickness matched to the calibration data for each detector.

5.2.5 Violation of Certain Assumptions in the Simulations

Assumption of Secular Equilibrium in Decay Chains

We assume secular equilibrium for all decay chains fitted in the model. Specifically, this applies to the ^{232}Th, ^{238}U, ^{222}Rn, and ^{210}Pb decay chains. This is a good assumption to the extent that we employ it. The half-lives of all components of the ^{232}Th decay chain are much shorter than that of ^{232}Th, and are also short on the time scale of the experiment. ^{238}U also has a much longer half-life than any of the daughters in its decay chain, so any ^{238}U that is ultimately coming from natural sources should be in secular equilibrium. In the places where these assumptions might be violated (in the detectors, the lab air, ^{210}Pb on surfaces), we break out the ^{210}Pb and or ^{222}Rn components of the ^{238}U decay chain and fit them separately. Furthermore, the detected ^{238}U and ^{222}Rn energy spectra are extremely

similar, since only a single gamma line with sufficient intensity to be detected is emitted at 186 keV (from ^{226}Ra) in the ^{238}U chain before ^{222}Rn. [3]

Potential Non-uniformity of Source Distributions

Potential non-uniformity of sources within specific physical volumes was already discussed in Section 5.2.3. This section will focus on a slightly different consideration: the effect that non-uniformity of sources within a component group might have on the best-fit model.

The model of the DEMONSTRATOR contains 3607 named physical volumes, too many to fit each one separately. For this reason, we group many of them into groups of components that are made from identical materials and have been handled with identical procedures. Because these groupings each share the same best-fit activity density, the model is not sensitive to possible deviations from uniform contamination in a given component group. There is some evidence in the data that there may be non-uniformity of contamination within some of the component groups in the model. Specifically, the elevated activity of ^{232}Th fit to the module 1 cross arm and cold plate cables is somewhat suspect, as was discussed in Section 4.7. Because the cables and vacuum seals are the only components in the model that are fit separately between the two modules, a source of ^{232}Th that sits on top of the cold plate would likely fit well to the cables, even if it is actually coming from the signal connectors, for example. Also, analysis of counts in characteristic photon peaks (e.g. 2014 keV from ^{208}Tl) by detector weakly indicates the possible presence of hotspots.

Efforts to fit a model with all component groups that are specfic to one module or the other split between the two modules have not yet been successful. Splitting the PDFs between modules adds approximately 80 new PDFs to the full model, increasing the number of fitted PDFs from about 120 to about 200. This increase in dimensionality increased the

[3] This statment is based on the simulated energy histograms of decays ^{238}U-chain and ^{222}Rn-chain nuclei in the N2 volume.

convergence time of the likelihood minimization faster than linearly, because it caused both an increase in the dimensionality of the problem as well as an increase in the amount of time it took to evaluate the likelihood function itself. I had some success with a feature bagging approach which could be a fruitful avenue to explore in the future, and will be briefly discussed in Chapter 6.

5.3 Uncertainties Related to the Model Selection Method

I have made significant progress in quantifying uncertainties arising from the model selection method. The toy MC studies from Section 4.5 were instrumental in proving that the uncertainties estimated by the model fitting algorithm are distributed as expected. The calibration studies from 4.6 give further confidence that the Nelder-Mead method used to minimize the likelihood function is the optimal choice from among the methods available in SciPy.Optimize. I believe that the systematic uncertainties associated with the numerical minimization of the likelihood function have been successfully assessed, and incorporated into the reported estimated activity densities in Table 4.2.

This of course only applies to parameters that have been estimated with precision $>$ 1. For parameters with precision $<$ 1, the uncertainty estimate produced by the modeling process is not well-behaved. Some suggestions of how to improve the estimated uncertainty for parameters with low-precision estimates, and ideas for alternatives to precision as a discriminator between parameters with well- and poorly characterized estimates are presented in Chapter 6.

The calibration data tests from Section 4.6 give an idea of how possible mismatches between the simulations and the data could impact the estimated uncertainty of the results in Table 4.2. Figure 5.4 shows the fractional error as a function of the true number of counts in the data, for both of the available calibration sources. Because the simplified method used to produce these results did not estimate the uncertainty for each trial, only the absolute

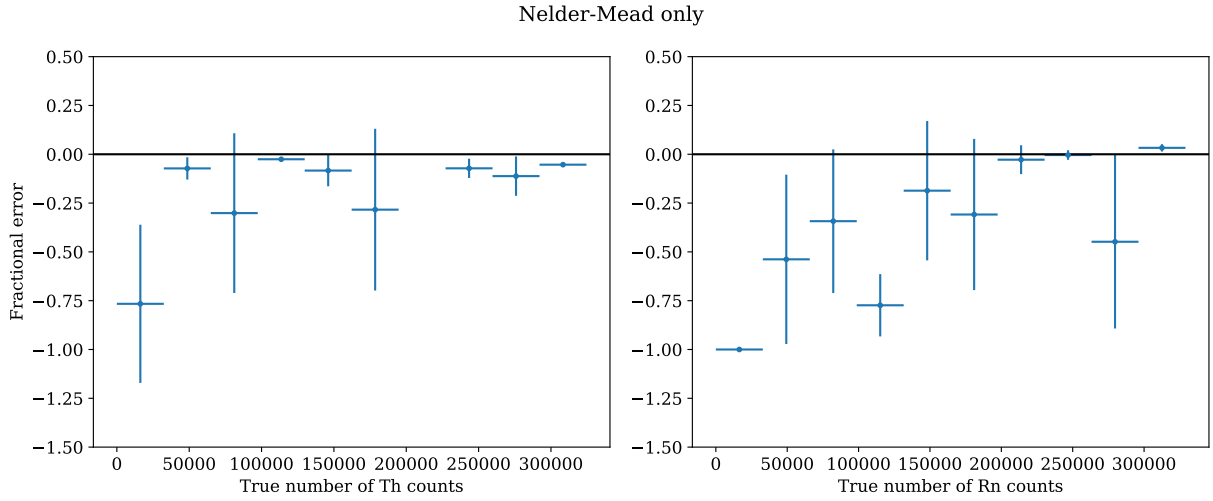

Figure 5.4: Shown is the fractional error for the calibration tests presented in Section 4.6. The error in each panel is the difference between the number of counts fitted to ^{228}Th from the module 1 calibration source or ^{222}Rn from the nitrogen-purged shield pocket (both surface and volume PDFs) and the number of counts in the data, divided by the number of counts in the data. Only trials using the Nelder-Mead algorithm are included. The error on each bin is just the standard deviation of all the trials in that bin.

error can be computed. By binning the trials by the starting number of counts, we can estimate the error to some degree, and we find that as the true number of counts increases, the fractional error decreases as expected. This plot shows that when statistics are high enough to constrain a component, it is resolved well, and mostly unbiased at the less than 10% level. At lower count levels the components are not as well resolved, but still typically fit to the right order of magnitude. The fitted number of counts is usually below the correct number, which makes sense since usually there are other ^{232}Th or ^{238}U (similar to ^{222}Rn) PDFs in the model that could account for the missing counts (this effect can be seen in Figure 4.12).

There are two primary remaining sources of model-selection-related uncertainty. The first is in the choice of PDFs to include in the model, given the assumption that the way the simulated data has been grouped into PDFs is immutable (e.g. not considering the possibility of generating new PDFs by splitting up component groups that are spread across the two modules). This source of uncertainty was tested in Section 4.6. The tests in that section showed that a simplified version of the model building routine will typically fit out the components of ^{232}Th and ^{222}Rn with reasonably good accuracy, even with all of the imperfections in the simulated PDFs described in the previous sections, and even when there are extraneous PDFs in the fit. Further suggestions to quantify this kind of uncertainty will be presented in Chapter 6.

The second type of model-selection-related uncertainty arises from the alternative possible groupings of the physical volumes of the `MaGe` model. As was stated at the beginning of Chapter 3, there are 3607 physical volumes in the simulated `MaGe` model, which gives a significantly larger set of possible partitionings. The component groups that were used in this result were selected based on the best *a priori* knowledge of our expected backgrounds available, but now that data has been collected we can see that other groupings could possibly be superior to the groupings used here. An example of the kind of effect this can have on the result was discussed in Section 5.2.5. Given the size of the space of possible alternative PDF groupings, a full quantification of this source of uncertainty is not pracitical to quantitatively estimate. Changes to the best-fit parameters under alternative groupings can and should be investigated in the future (see Chapter 6), but this will still not provide a comprehensive quantification of this type of uncertainty. Additional tests can be done to estimate the effect that things like spectral distortion might have on the best-fit results, which will also be discussed in Chapter 6.

Chapter 6
DISCUSSION AND CONCLUSION

6.1 How should we interpret these results in the context of the experiment?

We should have reasonably high confidence that the activity density estimates presented in table 4.2 are accurate, under the assumption that the choice of PDFs included in the model is immutable. Of course, this is not necessarily a good assumption, but even if it is violated to some extent it's unlikely that elevated sources of ^{232}Th exist below the cold plate inside the cryostat. This is because none of the components below the cold plate showed elevated levels of ^{232}Th in the results presented in Section 4.7, while several components above the cold plate (e.g. the module 1 cold plate and cross arm cables and the signal connectors) had best-fit activity densities suggesting they were contributing strongly to the ^{232}Th in the background spectrum (with the module 1 cold plate cables elevated above their assay-predicted values by a statistically significant amount). This is a significant result, as one of the primary goals of the Majorana Demonstrator was to demonstrate backgrounds significantly low to scale up the experiment. It is precisely backgrounds from components below the Demonstrator cold plate that are relevant for the first stage of LEGEND, because much of the Majorana contribution to the LEGEND design is centered around those components.

I believe we can state with even higher confidence that there is a source of elevated ^{232}Th present near module 1 that is not present near module 2, given that the module 1 cold plate and cross arm cables fit to an activity density about 1000 times higher that their counterparts in module 2. That said, the exposure for module 1 is significantly higher because it was installed well before module 2, and is the only operating module before data set 3.

Based on the assay model, the component with the highest expected contribution to the background budget was the collection of low-mass front-ends (LMFEs). Assay results for ^{232}Th and ^{238}U presented in [5] suggested that approximately 1000 counts from ^{232}Th and 1500 from ^{238}U should be visible in the DEMONSTRATOR data analyzed here. The best-fit activity densities for the LMFEs (presented in C.2) are too imprecise to be accurate, but it is likely that their activity in ^{232}Th and ^{238}U is at most as high as was measured in [5]. According to Figure 4.10, all PDFs that fit with counts above ~3,000 have precisions high enough to result in an accurate estimate (precision > 1). That means that if the LMFEs were twice as active as they were predicted to be, that should have been detectable. Following this argument, we can set a rough upper limit on the activity of ^{232}Th in the LMFEs of 150 mBq/kg, compared to the assay prediction of 76 ± 12 mBq/kg. The LMFEs are one of the components from the DEMONSTRATOR that will be used in the next generation experiment LEGEND (see Section 2.10). The fact that the LMFEs used in construction of the DEMONSTRATOR do not appear to obviously be a large source of ^{232}Th decays is reassuring.

All other components except the 4 identified in Section 4.7 as being in disagreement with the assay campaign values are either in agreement with their expected activity densities, or are not hot enough to detect. This is an enviable position to be in, that the DEMONSTRATOR does not see enough activity to detect any elevations above what was predicted except a couple of potentially elevated sources. If the MAJORANA collaboration had done a worse job constructing the DEMONSTRATOR, resulting in higher backgrounds, the job of identifying the locations of elevated background sources would certainly be easier.

6.1.1 Comparision to Results from Dissertation of Tom Gilliss

MAJORANA collaborator Tom Gilliss recently completed his PhD dissertation, which also focused on constructing a background model for the MAJORANA DEMONSTRATOR from simulated PDFs [89]. He employed a Bayesian technique, using MCMC to explore the

posterior distribution of the space of possible contaminants given the assay measurements as priors and the measured spectrum as the likelihood. In his conclusion, he states

> "In general, the MCMC procedure found that simulated components increased in activity, counteracting the assay-based underestimates of activity in order to better match the observed data. Particularly, components farther from the detectors showed the greatest increase. These include distant EFCu parts, Pb shields, and coldplate cables. Small parts close to detectors, integral to the low-background experiment, did not account for the assay-based underestimates of background index. Such small parts saw more modest increases in their estimated activities or remained the same."

This is broadly in agreement with the results presented in this document. The cold plate cables show an elevated level of activity, and components below the cold plate seem to be in agreement with their pre-experiment measurements. Although Gilliss and I used the same set of simulations to arrive at this result, the model-building and analysis were done completely independently with different techniques. This gives additional confidence in the conclusions drawn in the previous section.

Gilliss's results showed higher activity from ^{232}Th and ^{238}U in the lead shield than the results I have obtained. Two likely explanations for this disagreement are that the priors used by Gilliss are responsible for producing this effect, and that the shapes of the PDFs for distant parts are similar enough that they can be highly correlated. This disagreement is something that should be investigated.

6.2 What items can be improved in future backgound modeling efforts?

More studies to understand how systematic uncertainties in the simulations interact non-linearly with the estimated uncertainties on the best-fit parameters should be performed.

There are also a number of avenues for improvement on this result which should be incorporated into future versions of the MAJORANA DEMONSTRATOR background model. Some of them are fairly straightfoward and should have only small effects on the fitted model. Others have the potential to make a bigger impact, but will be more difficult to implement.

6.2.1 Studies to improve understanding of systematic uncertainties

As was mentioned at the end of Chapter 5, the degee that uncertainties inherent to the model-selection process or the simulations affect the final result is non-linear and can only be assessed through simulations. I am most concerned about the degree to which uncertainty or imperfect modeling of the transition dead-layer model could translate into a different result. Studies of the sensitivity of the best-fit model to different parameterizations of the dead-layer would be useful, although computationally intensive. Such a campaign would likely involve re-processing the `MaGe` output with different dead-layer parameters in `GAT`, and attempting to determine the degree to which changing those parameters affected the best-fit model. Good candidate alternative dead-layer models to compare would be:

1. The best-fit dead layers from this analysis

2. The dead-layer model from Section 3.2.3 but with the dead-layer thicknesses constrained to the ORTEC measurements

3. The dead-layer model from [90]

4. The flat dead layer model

The variability of the best-fit high-precision (or spectrally-preferred) activity densities under those models can be checked, and the top contributors should be the same in all cases.

Some concern in the collaboration has been expressed about the degree that distortions of the simulated energy spectra could have on the best-fit results. Assessing this would

also require new simulations, along with some kind of hypothesized physical mechanism for generating them. Simple distortions of the energy spectra not connected to any specific mechanism could be tested by simply reweighting the bins of the histograms used in the fits in Chapter 4 and re-running the model-selection algorithm. The successes so far of testing the simplified method on calibration data (see Sections 4.6 and 5.3) can assuage these concerns to some degree. Whatever spectral distortions are currently present in the calibration data, the model is still able to mostly reproduce the correct result, as long as the statistics are high enough.

A fuller analysis of the effect that the choice of PDFs used in the model has on the result should also be performed, expanding on the results from Section 4.6. This analysis would use more of the full model-selection routine from Section 4.4, and would add in contributions from other available calibration source data (currently MAJORANA has data taken with a line source of ^{56}Co and ^{60}Co using the ^{228}Th source calibration track). One should also test what happens when a PDF known to be present in the data is missing – for example shield pocket surface ^{222}Rn PDF were not included, we would expect the ^{222}Rn to fit out to the bulk shield pocket ^{222}Rn simulations, or perhaps simulations of ^{238}U or ^{222}Rn in the cryostats or inner copper shield. Finally, the background data could be "salted" with additional known contributions from one or more of the calibration sources. Then a fit with the additional counts could be compared to the true background spectrum to see if the modeling process is able to extract the correct activity-densities.

Finally, an information criterion, such as the AIC [100] or simply $\Delta\chi^2$, might perform better than precision as a discriminator between best-fit activity densities with well-behaved estimated uncertainties and those with poorly behaved estimated uncertainties. Using an information criterion significantly increases the computational load, as now instead of doing the model-selection algorithm from Section 4.4 once, it must be performed $n+1$ times where n is the number of PDFs in the model. However, if the compute time for the minimization

of the likelihood function can be reduced as is suggested in Section 6.2.2, then this kind of approach could be feasible.

6.2.2 Improvements to the model and fitting routines

The first item is to fix some bugs and check for a few potential others in the simulations. It should be verified that angular correlations between photons emitted in a cascade (see Section 5.2.2) were actually enabled during the simulations, and the simulations of components inside the calibration track redone if they were not. The cable source generator could benefit from an update, and the masses of the cables should be double-checked. Also, the simulations for data set 0 should be updated with the correct shielding in the cross arm. This is merely a matter of obtaining the necessary computing time and running the jobs through the system.

Next, the list of component groups in the background model should probably be expanded. At the very least, components above the cold plate but inside the cryostat should be separated between the two modules. This includes the connectors, the cold plate itself, and the parylene coated components. It would be more systematic to separate all component groups which contain copies for both modules into separately handled PDFs. I have already produced these PDFs, and they increase the size of the full set from ~120 to ~200. As mentioned in Section 5.2.5, my attempts to fit a model with this expanded set of PDFs have not yet yielded success. It appears that the model fitting process used in this work becomes intractable on a reasonable time scale ($<$ 1 week to convergence) somewhere between 120 and 200 PDFs. It may also be possible to eliminate some PDFs from the model entirely, keeping the total number close to or under 100 which would decrease complexity and increase tractability.

I attempted a feature-bagging approach when fitting with an increased number of PDFs (mentioned in 5.2.5). This approach involves randomly selecting a subset of PDFs for each fit to the data, and possibly subtracting off the assay-predicted activity density values for

the rest of the PDFs from the data. This can greatly reduce computation time at the cost of resulting in a worse fit to the data. It also is less clear what the correct approach for aggregating the random models would be, since the fitted result for each run depends on the subset of PDFs used in that run, rather than just the randomized starting values for the fit. Probably the same approach used here of simply averaging over the fitted results for each run would be the first thing to try.

A variation on the feature-bagging approach would be to start with a best-fit model, then reduce all best-fit activity-densities that are in excess of the assay results from Section 2.2 to their assay upper limits, then fix that as the "assay floor". Then instead of doing one fit to the full set of PDFs, fit to the "assay floor" once for each PDF in the model by releasing them one at a time. If a good fit is still not obtained, then iterate, fitting to combinations of additional contributions in a similar manner until you achieve a "minimal background model" in this way (i.e. assay floor plus the minimal number of additional components required to fit the spectrum).

A better understanding of the low-precision activity density estimates is desirable. For example, the bimodal behavior of the estimated activity density for ^{238}U in the lead shield shown in Figure 4.3 is somewhat concerning. It would be prudent to determine and implement a good figure-of-merit to measure convergence of the full method from Section 4.4.

Currently, the model-fitting code is implemented in Cython [95], which converts raw Python into C for significant speed increases. Cython allows for some parallelization with OpenMP, but it is likely that further performance improvements are possible if the code is reimplemented into a language with better performance, such as C++. Rewriting the code into C++ with parallelism in mind from the start (rather than shoehorning it in with Cython at the end), using libraries like MPI, and better utilizing the massively parallel machines available at NERSC (Cori) could make the existing method fast enough to allow for faster turnaround in the analysis, and maybe even make the feature-bagging approach suggested

in the previous paragraph unnecessary.

If better performance can be obtained with the suggestions in the previous paragraph, some additional improvements to the fitting process could be investigated. Separating data sets 3 and 4 to account for changes to the DAQ between those data sets and data set 5 will increase the computational load, but this will not be a problem if the code is made faster. Furthermore, a true simultaneous fit of all detectors might be possible if a speedup of 10x or so can be achieved.

A "catch-and-release" scheme has also been suggested to improve the best-fit result, where for some of the iterations from step 2 of the method from Section 4.4, parameters that have good stability are fixed in place to remove them as free parameters. Then the number of free parameters can be reduced until a better minimum is found when all parameters could be released for a final minimization.

Other members of the collaboration are currently assessing whether a linearized likelihood function which does not correctly handle statistical uncertainty or Poisson statistics might still be useful to obtain better starting parameters for this method. It has the advantage of converging to a result much quicker than the method from Section 4.4 (~minutes instead of ~days).

Finally, once a sufficient understanding of systematic uncertainties has been established, data that was acquired as blind can be added and fit to the background model. The size of the blinded data set is between 2 and 3 times as large as the open data, and the total enriched germanium exposure in [45] is 26.02 kg-yrs, compared to the 13.31 kg-yrs analyzed here. Doubling the total size of the fitted data could improve the accuracy and precision of estimates of activity densities in the components of the model, especially for parts like the LMFEs that are expected to give a non-negligible contribution but are probably currently just on the edge of detectability. To add blind data from data sets 1, 2, 5c, and 6a, only the burst cut script described in Section 2.3.2 needs to be run on the new data. To add open

and blind data acquired since the end of data set 6a, it would also be prudent to compute new energy resolution and dead layer functions for all detectors, because they can shift over time.

Once these improvements to the model and studies of sources of uncertainty are made, the next set of improvements will likely become apparent. Such is the nature of science! In the immortal words of George Box, "All models are wrong, but some are useful." I believe that in this work I have presented a useful model, and I think there is still more to learn from it and its future iterations about the MAJORANA DEMONSTRATOR.

BIBLIOGRAPHY

[1] E. Palma, "La Procura: Ettore Majorana vivo in Venezuela fra il 1955 e il 1959," *Corriere della Sera*, Feb 2015.

[2] S. Nadj-Perge, I. K. Drozdov, J. Li, H. Chen, S. Jeon, J. Seo, A. H. MacDonald, B. A. Bernevig, and A. Yazdani, "Observation of Majorana Fermions in Ferromagnetic Atomic Chains on a Superconductor," *Science*, vol. 346, pp. 602–607, 2014.

[3] C. E. Aalseth *et al.*, "The Majorana neutrinoless double beta decay experiment," *Phys. Atom. Nucl.*, vol. 67, pp. 2002–2010, 2004. [Yad. Fiz.67,2025(2004)].

[4] N. Abgrall *et al.*, "The Processing of Enriched Germanium for the MAJORANA DEMONSTRATOR and R&D for a Possible Future Ton-Scale ^{76}Ge Double-Beta Decay Experiment," *Nucl. Instrum. Meth.*, vol. A877, pp. 314–322, 2018.

[5] N. Abgrall *et al.*, "The MAJORANA DEMONSTRATOR radioassay program," *Nucl. Instrum. Meth.*, vol. A828, pp. 22–36, 2016.

[6] S. van der Walt, S. C. Colbert, and G. Varoquaux, "The NumPy Array: A Structure for Efficient Numerical Computation," *Comput. Sci. Eng.*, vol. 13, no. 2, pp. 22–30, 2011.

[7] E. Jones, T. Oliphant, P. Peterson, *et al.*, "SciPy: Open source scientific tools for Python," 2001–. [Online; accessed August 13, 2019].

[8] J. D. Hunter, "Matplotlib: A 2D graphics environment," *Computing in Science & Engineering*, vol. 9, no. 3, pp. 90–95, 2007.

[9] IPCC Core Writing Team, *Climate Change 2014: Synthesis Report. Contribution of Working Groups I, II and III to the Fifth Assessment Report of the Intergovernmental Panel on Climate Change*. Geneva, Switzerland: IPCC, 2014.

[10] IPBES, *Global assessment report on biodiversity and ecosystem services of the Intergovernmental Science- Policy Platform on Biodiversity and Ecosystem Services*. Bonn, Germany: IPBES Secretariat, 2019.

[11] L. M. Brown, "The idea of the neutrino," *Phys. Today*, vol. 31N9, pp. 23–28, 1978.

[12] J. Chadwick, "The Existence of a Neutron," *Proc. Roy. Soc. Lond.*, vol. A136, no. 830, pp. 692–708, 1932.

[13] E. Fermi, "An attempt of a theory of beta radiation. 1.," *Z. Phys.*, vol. 88, pp. 161–177, 1934.

[14] C. L. Cowan, F. Reines, F. B. Harrison, H. W. Kruse, and A. D. McGuire, "Detection of the free neutrino: A Confirmation," *Science*, vol. 124, pp. 103–104, 1956.

[15] F. P. An *et al.*, "Measurement of electron antineutrino oscillation based on 1230 days of operation of the Daya Bay experiment," *Phys. Rev.*, vol. D95, no. 7, p. 072006, 2017.

[16] Y. Abe *et al.*, "Improved measurements of the neutrino mixing angle θ_{13} with the Double Chooz detector," *JHEP*, vol. 10, p. 086, 2014. [Erratum: JHEP02,074(2015)].

[17] J. K. Ahn *et al.*, "Observation of Reactor Electron Antineutrino Disappearance in the RENO Experiment," *Phys. Rev. Lett.*, vol. 108, p. 191802, 2012.

[18] T. Araki *et al.*, "Measurement of neutrino oscillation with KamLAND: Evidence of spectral distortion," *Phys. Rev. Lett.*, vol. 94, p. 081801, 2005.

[19] C. Kraus *et al.*, "Final results from phase II of the Mainz neutrino mass search in tritium beta decay," *Eur. Phys. J.*, vol. C40, pp. 447–468, 2005.

[20] V. N. Aseev *et al.*, "An upper limit on electron antineutrino mass from Troitsk experiment," *Phys. Rev.*, vol. D84, p. 112003, 2011.

[21] L. Bornschein, B. Bornschein, S. Ebenhöch, M. Hackenjos, F. Priester, M. Röllig, M. Sturm, T. Thümmler, and K. Collaboration, "Status of the Karlsruhe Tritium Neutrino Mass Experiment KATRIN," *Fusion Science and Technology*, vol. 71, no. 4, pp. 485–490, 2017.

[22] B. T. Cleveland, T. Daily, R. Davis, Jr., J. R. Distel, K. Lande, C. K. Lee, P. S. Wildenhain, and J. Ullman, "Measurement of the solar electron neutrino flux with the Homestake chlorine detector," *Astrophys. J.*, vol. 496, pp. 505–526, 1998.

[23] B. Pontecorvo, "Inverse beta processes and nonconservation of lepton charge," *Sov. Phys. JETP*, vol. 7, pp. 172–173, 1958. [Zh. Eksp. Teor. Fiz.34,247(1957)].

[24] S. N. Ahmed *et al.*, "Measurement of the total active B-8 solar neutrino flux at the Sudbury Neutrino Observatory with enhanced neutral current sensitivity," *Phys. Rev. Lett.*, vol. 92, p. 181301, 2004.

[25] Y. Fukuda *et al.*, "Evidence for oscillation of atmospheric neutrinos," *Phys. Rev. Lett.*, vol. 81, pp. 1562–1567, 1998.

[26] Z. Maki, M. Nakagawa, and S. Sakata, "Remarks on the Unified Model of Elementary Particles," *Progress of Theoretical Physics*, vol. 28, pp. 870–880, 11 1962.

[27] V. N. Gribov and B. Pontecorvo, "Neutrino astronomy and lepton charge," *Phys. Lett.*, vol. 28B, p. 493, 1969.

[28] A. K. Mann and H. Primakoff, "Neutrino oscillations and the number of neutrino types," *Phys. Rev. D*, vol. 15, pp. 655–665, Feb 1977.

[29] P. A. M. Dirac, "The quantum theory of the electron," *Proc. Roy. Soc. Lond.*, vol. A117, pp. 610–624, 1928.

[30] P. A. M. Dirac, "The Quantum theory of the electron. 2.," *Proc. Roy. Soc. Lond.*, vol. A118, p. 351, 1928.

[31] C. D. Anderson, "The Positive Electron," *Phys. Rev.*, vol. 43, pp. 491–494, 1933.

[32] E. Majorana, "Teoria simmetrica dell'elettrone e del positrone," *Nuovo Cim.*, vol. 14, pp. 171–184, 1937.

[33] A. D. Sakharov, "Violation of CP Invariance, C asymmetry, and baryon asymmetry of the universe," *Pisma Zh. Eksp. Teor. Fiz.*, vol. 5, pp. 32–35, 1967. [Usp. Fiz. Nauk161,no.5,61(1991)].

[34] S. Davidson, E. Nardi, and Y. Nir, "Leptogenesis," *Phys. Rept.*, vol. 466, pp. 105–177, 2008.

[35] S. R. Elliott, A. A. Hahn, and M. K. Moe, "Direct Evidence for Two Neutrino Double Beta Decay in ^{82}Se," *Phys. Rev. Lett.*, vol. 59, pp. 2020–2023, 1987. [,989(1987)].

[36] M. Kobayashi and T. Maskawa, "CP Violation in the Renormalizable Theory of Weak Interaction," *Prog. Theor. Phys.*, vol. 49, pp. 652–657, 1973.

[37] S. Stone, "New physics from flavour," *PoS*, vol. ICHEP2012, p. 033, 2013.

[38] S. Dell'Oro, S. Marcocci, M. Viel, and F. Vissani, "Neutrinoless double beta decay: 2015 review," *Adv. High Energy Phys.*, vol. 2016, p. 2162659, 2016.

[39] J. Engel and J. Menéndez, "Status and Future of Nuclear Matrix Elements for Neutrinoless Double-Beta Decay: A Review," *Rept. Prog. Phys.*, vol. 80, no. 4, p. 046301, 2017.

[40] L.-J. Wang, J. Engel, and J. M. Yao, "Quenching of nuclear matrix elements for $0\nu\beta\beta$ decay by chiral two-body currents," *Phys. Rev.*, vol. C98, no. 3, p. 031301, 2018.

[41] M. Agostini, G. Benato, and J. Detwiler, "Discovery probability of next-generation neutrinoless double-β decay experiments," *Phys. Rev.*, vol. D96, no. 5, p. 053001, 2017.

[42] R. Arnold *et al.*, "Probing New Physics Models of Neutrinoless Double Beta Decay with SuperNEMO," *Eur. Phys. J.*, vol. C70, pp. 927–943, 2010.

[43] C. Macolino, "Search for neutrinoless double-beta decay with the SuperNEMO demonstrator," *PoS*, vol. EPS-HEP2017, p. 121, 2017.

[44] M. Agostini *et al.*, "Improved Limit on Neutrinoless Double-β Decay of ^{76}Ge from GERDA Phase II," *Phys. Rev. Lett.*, vol. 120, no. 13, p. 132503, 2018.

[45] S. I. Alvis *et al.*, "A Search for Neutrinoless Double-Beta Decay in ^{76}Ge with 26 kg-yr of Exposure from the Majorana Demonstrator," 2019. preprint.

[46] J. B. Albert *et al.*, "Search for Neutrinoless Double-Beta Decay with the Upgraded EXO-200 Detector," *Phys. Rev. Lett.*, vol. 120, no. 7, p. 072701, 2018.

[47] J. Martín-Albo *et al.*, "Sensitivity of NEXT-100 to Neutrinoless Double Beta Decay," *JHEP*, vol. 05, p. 159, 2016.

[48] A. Gando *et al.*, "Search for Majorana Neutrinos near the Inverted Mass Hierarchy Region with KamLAND-Zen," *Phys. Rev. Lett.*, vol. 117, no. 8, p. 082503, 2016. [Addendum: Phys. Rev. Lett.117,no.10,109903(2016)].

[49] J. B. Albert *et al.*, "Sensitivity and Discovery Potential of nEXO to Neutrinoless Double Beta Decay," *Phys. Rev.*, vol. C97, no. 6, p. 065503, 2018.

[50] C. Alduino *et al.*, "First Results from CUORE: A Search for Lepton Number Violation via $0\nu\beta\beta$ Decay of ^{130}Te," *Phys. Rev. Lett.*, vol. 120, no. 13, p. 132501, 2018.

[51] S. Andringa *et al.*, "Current Status and Future Prospects of the SNO+ Experiment," *Adv. High Energy Phys.*, vol. 2016, p. 6194250, 2016.

[52] H. V. Klapdor-Kleingrothaus, A. Dietz, H. L. Harney, and I. V. Krivosheina, "Evidence for neutrinoless double beta decay," *Mod. Phys. Lett.*, vol. A16, pp. 2409–2420, 2001.

[53] S. I. Alvis *et al.*, "Search for trinucleon decay in the Majorana Demonstrator," *Phys. Rev.*, vol. D99, no. 7, p. 072004, 2019.

[54] S. I. Alvis *et al.*, "First Limit on the Direct Detection of Lightly Ionizing Particles for Electric Charge as Low as e/1000 with the Majorana Demonstrator," *Phys. Rev. Lett.*, vol. 120, no. 21, p. 211804, 2018.

[55] N. Abgrall *et al.*, "New limits on Bosonic Dark Matter, Solar Axions, Pauli Exclusion Principle Violation, and Electron Decay from the Majorana Demonstrator," *Phys. Rev. Lett.*, vol. 118, no. 16, p. 161801, 2017.

[56] J. Heise, "The Sanford Underground Research Facility at Homestake," *AIP Conf. Proc.*, vol. 1604, no. 1, pp. 331–344, 2015.

[57] N. Abgrall *et al.*, "Muon Flux Measurements at the Davis Campus of the Sanford Underground Research Facility with the Majorana Demonstrator Veto System," *Astropart. Phys.*, vol. 93, pp. 70–75, 2017.

[58] S. Paschalis, I. Lee, A. Macchiavelli, C. Campbell, M. Cromaz, S. Gros, J. Pavan, J. Qian, R. Clark, H. Crawford, D. Doering, P. Fallon, C. Lionberger, T. Loew, M. Petri, T. Stezelberger, S. Zimmermann, D. Radford, K. Lagergren, D. Weisshaar, R. Winkler, T. Glasmacher, J. Anderson, and C. Beausang, "The performance of the Gamma-Ray Energy Tracking In-beam Nuclear Array GRETINA," *Nucl. Instrum. Meth.*, vol. A709, pp. 44–55, 2013.

[59] N. Abgrall *et al.*, "The Majorana Demonstrator Neutrinoless Double-Beta Decay Experiment," *Adv. High Energy Phys.*, vol. 2014, p. 365432, 2014.

[60] A. Reine, T. Caldwell, C. Cuesta, I. Guinn, and J. Myslik, "Run selection and data cleaning of DS5 (M1 and M2) (Internal)," Tech. Rep. 2017-020, University of North Carolina at Chapel Hill, May 2018.

[61] H. Sahai and A. Khurshid, "Confidence intervals for the mean of a poisson distribution: A review," *Biometrical Journal*, vol. 35, no. 7, pp. 857–867, 1993.

[62] P. S. Laplace, *Théorie analytique des probabilités*. 1812.

[63] A. Agresti and B. A. Coull, "Approximate is better than "exact" for interval estimation of binomial proportions," *The American Statistician*, vol. 52, no. 2, pp. 119–126, 1998.

[64] N. Abgrall *et al.*, "The Processing of Enriched Germanium for the MAJORANA DEMONSTRATOR and R&D for a Possible Future Ton-Scale ^{76}Ge Double-Beta Decay Experiment," *Nucl. Instrum. Meth.*, vol. A877, pp. 314–322, 2018.

[65] M. Buuck, "Calculating the Active Mass of the MJ Detectors (Internal)," tech. rep., University of Washington, September 2016.

[66] M. Buuck, "Updated Active Mass Calculation (Internal)," tech. rep., University of Washington, January 2019.

[67] D. Edwins, V. Guiseppe, D. Tedeschi, C. Wiseman, S. Meijer, A. Reine, T. Caldwell, T. Gilliss, C. Haufe, and D. Radford, "Livetime and Exposure for the Majorana Demonstrator Data Sets 0-6 (Internal)," Tech. Rep. 2018-32, University of South Carolina, May 2018.

[68] I. S. Guinn, "Fixing the charge trapping nonlinearity (Internal)," tech. rep., University of Washington, June 2018.

[69] N. Abgrall *et al.*, "The Majorana Demonstrator calibration system," *Nucl. Instrum. Meth.*, vol. A872, pp. 16–22, 2017.

[70] P. H. Chu, J. A. Detwiler, I. S. Guinn, and W. Xu, "Energy Systematic of Majorana Demonstrator (Internal)," Tech. Rep. 2017-21, Los Alamos National Laboratory, May 2018.

[71] "NIST XCOM: Photon Cross Sections Database." `https://physics.nist.gov/PhysRefData/Xcom/html/xcom1.html`. Accessed: 2019-06-14.

[72] S. I. Alvis *et al.*, "Multi-site event discrimination for the Majorana Demonstrator," *Phys. Rev.*, vol. C99, no. 6, p. 065501, 2019.

[73] J. Gruszko, *Surface alpha interactions in P-Type point-contact HPGe detectors: maximizing sensitivity of ^{76}Ge neutrinoless double-beta decay searches*. PhD thesis, The University of Washington, 2017.

[74] C. D. Christofferson *et al.*, "Contamination Control and Assay Results for the MAJORANA DEMONSTRATOR Ultra Clean Components," *AIP Conf. Proc.*, vol. 1921, no. 1, p. 060005, 2018.

[75] N. Abgrall *et al.*, "The Large Enriched Germanium Experiment for Neutrinoless Double Beta Decay (LEGEND)," *AIP Conf. Proc.*, vol. 1894, no. 1, p. 020027, 2017.

[76] M. Boswell *et al.*, "MaGe-a Geant4-based Monte Carlo Application Framework for Low-background Germanium Experiments," *IEEE Trans. Nucl. Sci.*, vol. 58, pp. 1212–1220, 2011.

[77] S. Agostinelli *et al.*, "GEANT4: A Simulation toolkit," *Nucl. Instrum. Meth.*, vol. A506, pp. 250–303, 2003.

[78] J. Allison *et al.*, "Recent developments in Geant4," *Nucl. Instrum. Meth.*, vol. A835, pp. 186–225, 2016.

[79] J. A. Detwiler, R. Henning, R. A. Johnson, and M. G. Marino, "A Generic Surface Sampler for Monte Carlo Simulations," *IEEE Trans. Nucl. Sci.*, vol. 55, pp. 2329–2333, 2008.

[80] P. Vojtyla, "Fast computer simulations of background of low-level Ge γ-spectrometers induced by ^{210}Pb^{210}Bi in shielding lead," *Nuclear Instruments and Methods in Physics Research Section B: Beam Interactions with Materials and Atoms*, vol. 117, no. 1, pp. 189 – 198, 1996.

[81] J. Kotila and F. Iachello, "Phase space factors for double-β decay," *Phys. Rev.*, vol. C85, p. 034316, 2012.

[82] A. G. Schubert and F. Fraenkle, "`MaGe` Validation Report (Internal)," Tech. Rep. 2012-063, University of Washington, July 2012.

[83] T. Gilliss and F. Fraenkle, "`MaGe` Validation Report (Internal)," Tech. Rep. 2018-085, University of North Carolina at Chapel Hill, October 2017.

[84] R. Brun and F. Rademakers, "ROOT: An object oriented data analysis framework," *Nucl. Instrum. Meth.*, vol. A389, pp. 81–86, 1997.

[85] I. Antcheva *et al.*, "ROOT: A C++ framework for petabyte data storage, statistical analysis and visualization," *Comput. Phys. Commun.*, vol. 180, pp. 2499–2512, 2009.

[86] R. Cooper and D. Radford, "Pulse Shape Analysis Heuristic Code (Internal)," Tech. Rep. 2009-010, Oak Ridge National Laboratory, January 2009.

[87] E. Blalock and M. Green, "Calculation of DtHeuristic Cutoffs for PSA Cut on MAJORANA Simulations (Internal)," Tech. Rep. 2018-039, North Carolina State University, December 2018.

[88] G. K. Giovanetti, *P-type point contact germanium detectors and their application in rare-event searches*. PhD thesis, The University of North Carolina at Chapel Hill, 2015.

[89] T. F. Gilliss, *Statistical Modeling and Markov Chain Monte Carlo Inference of* MAJORANA DEMONSTRATOR *Background Data*. PhD thesis, The University of North Carolina at Chapel Hill, 2019.

[90] J. Ma, Q. Yue, Q. Wang, J. Li, H. Wong, S. Lin, S. Liu, L. Wang, H. Jiang, L. Yang, L. Jia, J. Chen, and W. Zhao, "Study of inactive layer uniformity and charge collection efficiency of a p-type point-contact germanium detector," *Applied Radiation and Isotopes*, vol. 127, pp. 130 – 136, 2017.

[91] C. Wiseman, *An Axion Search with the* MAJORANA DEMONSTRATOR. PhD thesis, The University of South Carolina, 2018.

[92] B. Shanks, *High Precision Modeling of Germanium Detector Waveforms Using Bayesian Machine Learning*. PhD thesis, The University of North Carolina at Chapel Hill, 2017.

[93] S. J. Meijer, *Precision Modeling of Germanium Detector Waveforms For Rare Event Searches*. PhD thesis, The University of North Carolina at Chapel Hill, 2019.

[94] R. J. Barlow and C. Beeston, "Fitting using finite Monte Carlo samples," *Comput. Phys. Commun.*, vol. 77, pp. 219–228, 1993.

[95] S. Behnel, R. Bradshaw, C. Citro, L. Dalcin, D. S. Seljebotn, and K. Smith, "Cython: The Best of Both Worlds," *Comput. Sci. Eng.*, vol. 13, pp. 31–39, 2011.

[96] J. A. Nelder and R. Mead, "A Simplex Method for Function Minimization," *Comput. J.*, vol. 7, pp. 308–313, 1965.

[97] F. Gao and L. Han, "Implementing the Nelder-Mead simplex algorithm with adaptive parameters," *Comput. Optim. Appl.*, vol. 51, pp. 259–277, 2012.

[98] M. Newville, T. Stensitzki, D. B. Allen, and A. Ingargiola, "LMFIT: Non-Linear Least-Square Minimization and Curve-Fitting for Python," Sept. 2014.

[99] D. Foreman-Mackey, D. W. Hogg, D. Lang, and J. Goodman, "emcee: The MCMC hammer," *Publications of the Astronomical Society of the Pacific*, vol. 125, pp. 306–312, mar 2013.

[100] H. Akaike, "A new look at the statistical model identification," *IEEE Transactions on Automatic Control*, vol. 19, pp. 716–723, December 1974.

[101] C. Zhu, R. H. Byrd, P. Lu, and J. Nocedal, "Algorithm 778: L-BFGS-B: Fortran Subroutines for Large-scale Bound-constrained Optimization," *ACM Trans. Math. Softw.*, vol. 23, pp. 550–560, Dec. 1997.

[102] S. Nash, "Newton-Type Minimization via the Lanczos Method," *SIAM Journal on Numerical Analysis*, vol. 21, no. 4, pp. 770–788, 1984.

[103] M. J. D. Powell, "An efficient method for finding the minimum of a function of several variables without calculating derivatives," *The Computer Journal*, vol. 7, pp. 155–162, 01 1964.

[104] M. R. Hestenes and E. Stiefel, "Methods of conjugate gradients for solving linear systems," *J. Research Nat. Bur. Standards*, vol. 49, p. 409–436, 1952.

[105] C. G. Broyden, "The Convergence of a Class of Double-rank Minimization Algorithms 1. General Considerations," *IMA Journal of Applied Mathematics*, vol. 6, pp. 76–90, 03 1970.

[106] R. Fletcher, "A new approach to variable metric algorithms," *The Computer Journal*, vol. 13, pp. 317–322, 01 1970.

[107] D. Goldfarb, "A Family of Variable Metric Updates Derived by Variational Means," *Mathematics of Computation*, vol. 24, no. 109, p. 23–26, 1970.

[108] D. F. Shanno, "Conditioning of quasi-Newton methods for function minimization," *Mathematics of Computation*, vol. 24, p. 647–656, 7 1970.

[109] C. E. Aalseth *et al.*, "Search for Neutrinoless Double-β Decay in ^{76}Ge with the Majorana Demonstrator," *Phys. Rev. Lett.*, vol. 120, no. 13, p. 132502, 2018.

[110] K. Amako *et al.*, "Geant4 and its validation," *Nucl. Phys. Proc. Suppl.*, vol. 150, pp. 44–49, 2006. [,44(2006)].

[111] K. Alder and A. Winther, *Electromagnetic excitation: Theory of Coulomb excitation with heavy ions*. Amsterdam, New York: North-Holland Pub. Co. Sole distributors for the U.S.A., American Elsevier Pub. Co, 1975.

[112] C. S. Fuller and J. A. Ditzenberger, "Diffusion of Lithium into Germanium and Silicon," *Phys. Rev.*, vol. 91, pp. 193–193, Jul 1953.

[113] B. Pratt and F. Friedman, "Diffusion of Lithium into Ge and Si," *Journal of Applied Physics*, vol. 37, no. 4, pp. 1893–1896, 1966.

[114] W. Maneschg *et al.*, "Production and characterization of a custom-made ^{228}Th source with reduced neutron source strength for the Borexino experiment," *Nucl. Instrum. Meth.*, vol. A680, pp. 161–167, 2012.

Appendix A

COMPILED STATISTICS ON MaGe SIMULATIONS FOR THIS BACKGROUND MODEL

Three configurations of the DEMONSTRATOR have been simulated:

- DS0, with only module 1, no inner UGEFCu shield, and no cross arm shielding
- DS1, with only module 1 and full shielding
- 2-module, with both modules and full shielding

Furthermore, there are three types of background simulations and an additional type of calibration simulation that are handled distinctly:

- Background simulations
  - Bulk decays, using the default Geant4 bulk decay primary event generator
  - Surface decays, using the MaGe General Surface Sampler (GSS) [79] to get a list of primary locations. Because the GSS imposes a significant computational cost, surface simulations were only run for component groups with direct line-of-sight to the detectors.
  - Pb brem decays, using the custom lead bremsstrahlung event generator described in section 3.1.1.
- Calibration simulations

- Line source decays, using a custom line source generator for the calibration source which is more computationally efficient than the standard Geant4 bulk decay generator

Some component groups can be separated between the two modules (e.g. EnrGe and NatGe), simply by requiring the location of the primary particle to be on the correct side of the simulation. These PDFs are listed in table A.5, but are not listed in any of the tables with simulation statistics due to this redundant nature. Additionally, some component groups were grouped together into supergroups due to the possibility that they could have common activity densities. These PDFs are listed in table A.6 but are not listed in any of the tables with simulation statistics due to their reduncancy.

The names of the component groups are mostly self-explanatory, but a few may not be obvious. DU refers to Detector Unit, component groups with Coated in the name include only the parts that were coated with Parylene™, and CPCables refers to cables spooled above the Cold Plate.

A.1 Production of Simulations on NERSC High-Performance Computing Systems

The MAJORANA collaboration uses the National Energy Research Scientific Computing (NERSC) facility at the Lawrence Berkeley National Laboratory (LBNL) for all of its major computing needs, including simulations and data processing. The systems available at NERSC during the course of operation of the DEMONSTRATOR include Cori, Edison, and PDSF, of which PDSF was by far the system most heavily used by MAJORANA.

A package of submission scripts and control codes was written to facilitate the production of the DEMONSTRATOR simulations and is hosted on Github. Each simulation has a unique ID number which is contained in the filename. There are separate scripts for the different source types (bulk decays, surface decays, and linesource decays), and each requires the

specification of a starting isotope, the component group (selected from the list in section A.2), and the desired number of primary decays.

A.2 Compiled Statistics on Simulations

Table A.1: All bulk simulations in the 2-module configuration of component groups used in the background model

Component group	**Contaminants simulated**	**Primary decays**	**Counts per decay/kg**
ColdPlateCopper	^{40}K	4.50e+07	2.92e-01
	^{238}U	5.00e+06	4.41e+00
	^{232}Th	5.50e+06	5.50e+00
Connectors	^{40}K	9.00e+07	1.22e-03
	^{238}U	5.50e+06	1.71e-02
	^{232}Th	1.00e+07	2.14e-02
DUCoatedCopper	^{40}K	1.25e+07	4.94e-05
	^{238}U	1.25e+07	5.53e-04
	^{232}Th	1.25e+07	6.31e-04
DUCopper	^{40}K	2.50e+07	5.61e-01
	^{238}U	2.50e+07	8.26e+00
	^{232}Th	2.50e+07	1.01e+01
DUPTFE	^{40}K	2.55e+07	1.33e-02
	^{238}U	2.55e+07	1.76e-01
	^{232}Th	2.55e+07	2.07e-01
DUVespel	^{40}K	2.45e+07	1.07e-05
	^{238}U	5.00e+06	1.34e-04
	^{232}Th	5.00e+06	1.58e-04
EnrGe	$2\nu\beta\beta$ decay	7.00e+06	2.18e+01
	$0\nu\beta\beta$ decay	7.00e+06	2.26e+01
	^{68}Ge	4.00e+06	5.48e+01

Component group	**Contaminants simulated**	**Primary decays**	**Counts per decay/kg**
HVForks	^{60}Co	5.00e+06	1.74e-02
	^{40}K	2.50e+07	1.28e-03
	^{238}U	5.00e+06	1.90e-02
	^{232}Th	5.00e+06	2.32e-02
LMFEs	^{60}Co	5.00e+06	5.29e-03
	^{40}K	1.70e+07	3.66e-04
	^{238}U	5.00e+06	6.02e-03
	^{232}Th	5.00e+06	7.49e-03
M1CPCables	^{60}Co	2.64e+06	2.50e-02
	^{40}K	3.30e+07	1.49e-03
	^{238}U	2.20e+06	1.95e-02
	^{232}Th	3.96e+06	2.46e-02
M1CrossarmCables	^{60}Co	2.84e+07	1.69e-03
	^{40}K	2.54e+08	9.91e-05
	^{238}U	2.57e+07	1.22e-03
	^{232}Th	4.60e+07	1.56e-03
M1Seals	^{40}K	6.15e+07	2.83e-04
	^{238}U	1.00e+07	4.49e-03
	^{232}Th	1.05e+07	5.69e-03
M1StringHVCables	^{60}Co	2.20e+06	8.71e-03
	^{40}K	1.01e+07	1.70e-03
	^{238}U	2.20e+06	2.34e-02
	^{232}Th	2.42e+06	2.24e-02
M1StringSigCables	^{60}Co	9.02e+06	5.31e-03
	^{40}K	2.20e+06	1.08e-03
	^{238}U	2.20e+06	1.50e-02
	^{232}Th	2.42e+06	1.41e-02
M2CPCables	^{60}Co	4.84e+06	2.28e-02
	^{40}K	3.22e+07	1.35e-03
	^{238}U	2.20e+06	1.81e-02
	^{232}Th	3.74e+06	2.29e-02

Component group	**Contaminants simulated**	**Primary decays**	**Counts per decay/kg**
M2CrossarmCables	^{60}Co	3.52e+07	1.13e-03
	^{40}K	2.74e+08	6.65e-05
	^{238}U	3.12e+07	8.09e-04
	^{232}Th	5.32e+07	1.03e-03
M2Seals	^{40}K	2.50e+07	8.35e-04
	^{238}U	1.00e+07	1.38e-02
	^{232}Th	1.00e+07	1.76e-02
M2StringHVCables	^{60}Co	2.20e+06	7.39e-03
	^{40}K	1.19e+07	1.18e-03
	^{238}U	2.20e+06	1.68e-02
	^{232}Th	2.86e+06	1.67e-02
M2StringSigCables	^{60}Co	2.20e+06	4.32e-03
	^{40}K	1.12e+07	6.93e-04
	^{238}U	2.20e+06	9.87e-03
	^{232}Th	2.64e+06	9.75e-03
N2	^{222}Rn	2.00e+07	9.70e-03
NatGe	$2\nu\beta\beta$ decay	7.00e+06	1.06e+01
	$0\nu\beta\beta$ decay	7.00e+06	1.10e+01
	^{68}Ge	4.00e+06	2.59e+01
	^{57}Co	1.05e+06	1.10e+01
RadShieldCuInner	^{60}Co	9.00e+08	5.15e+01
	^{40}K	9.00e+08	3.05e+00
	^{238}U	9.00e+08	3.57e+01
	^{232}Th	9.00e+08	4.50e+01
RadShieldCuOuter	^{60}Co	1.78e+09	6.23e+00
	^{40}K	3.04e+09	4.20e-01
	^{238}U	1.78e+09	3.59e+00
	^{232}Th	1.78e+09	4.94e+00
RadShieldPb	^{40}K	3.98e+10	5.49e-02
	^{238}U	1.53e+10	4.46e-01
	^{232}Th	1.75e+10	7.23e-01

Component group	**Contaminants simulated**	**Primary decays**	**Counts per decay/kg**
StringCoatedCopper	^{40}K	1.25e+07	9.38e-06
	^{238}U	1.25e+07	1.44e-04
	^{232}Th	1.25e+07	1.80e-04
StringCopper	^{40}K	2.75e+07	1.14e-01
	^{238}U	5.00e+06	1.84e+00
	^{232}Th	5.00e+06	2.30e+00
ThermosyphonAndShieldCoatedCopper	^{40}K	1.25e+07	5.06e-06
	^{238}U	1.25e+07	6.83e-05
	^{232}Th	1.25e+07	8.52e-05
ThermosyphonAndShieldCopper	^{60}Co	8.50e+06	4.59e+00
	^{40}K	9.00e+07	3.19e-01
	^{238}U	6.00e+06	4.40e+00
	^{232}Th	1.05e+07	5.38e+00
ThermosyphonAndShieldVespel	^{40}K	5.50e+08	1.23e-04
	^{238}U	3.51e+07	1.57e-03
	^{232}Th	7.00e+07	1.97e-03
VesselCoatedCopper	^{40}K	1.25e+07	2.06e-06
	^{238}U	1.25e+07	2.91e-05
	^{232}Th	1.25e+07	3.63e-05
VesselCopper	^{60}Co	7.00e+06	2.17e+01
	^{40}K	8.00e+07	1.27e+00
	^{238}U	5.00e+06	1.92e+01
	^{232}Th	9.00e+06	2.40e+01

Table A.2: All surface and ^{210}Pb bremsstrahlung simulations of component groups used in the background model

Component group	**Type**	**Configuration**	**Contaminants simulated**	**Primary decays**	**Counts per decay/kg**
ColdPlateCopper	Surface	2-module	^{40}K	5.98e+05	5.01e-01
			^{238}U	3.48e+06	7.32e+00
			^{232}Th	6.09e+06	7.88e+00
DUCopper	Surface	2-module	^{40}K	1.86e+06	1.25e+00
			^{238}U	4.64e+06	1.86e+01
			^{232}Th	6.27e+06	1.86e+01
DUVespel	Surface	2-module	^{40}K	1.08e+03	1.18e-05
			^{238}U	1.09e+03	1.54e-04
			^{232}Th	1.05e+03	1.73e-04
N2	Surface	2-module	^{222}Rn	7.58e+06	9.19e-03
N2	Surface	DS0	^{222}Rn	3.02e+07	1.39e-02
N2	Surface	DS1	^{222}Rn	1.61e+07	9.61e-03
RadShieldPb	Lead brem	2-module	^{210}Pb	2.22e+10	6.53e-04
RadShieldPb	Lead brem	DS0	^{210}Pb	2.53e+08	1.01e-02
RadShieldPb	Lead brem	DS1	^{210}Pb	2.94e+09	5.45e-04
StringCopper	Surface	2-module	^{40}K	5.30e+05	1.70e-01
			^{238}U	2.38e+06	2.68e+00
			^{232}Th	3.93e+06	3.04e+00
ThermosyphonAndShieldCopper	Surface	2-module	^{40}K	4.58e+06	8.59e-01
			^{238}U	6.49e+06	1.19e+01
			^{232}Th	1.06e+07	1.27e+01
ThermosyphonAndShieldVespel	Surface	2-module	^{40}K	4.64e+04	2.52e-04
			^{238}U	4.69e+04	3.27e-03
			^{232}Th	4.65e+04	4.23e-03

Table A.3: All bulk simulations in the DS0 configuration of component groups used in the background model are included in this table.

Component group	**Contaminants simulated**	**Primary decays**	**Counts per decay/kg**
M1CrossarmCables	^{60}Co	1.55e+06	1.30e-03
	^{40}K	1.55e+06	7.59e-05
	^{238}U	1.55e+06	9.33e-04
	^{232}Th	1.55e+06	1.20e-03
N2	^{222}Rn	1.55e+06	5.19e-03
RadShieldCuOuter	^{60}Co	1.03e+09	3.09e+01
	^{40}K	1.03e+09	1.82e+00
	^{238}U	1.03e+09	2.15e+01
	^{232}Th	1.03e+09	2.71e+01
RadShieldPb	^{40}K	9.09e+09	2.44e-01
	^{238}U	2.59e+09	1.95e+00
	^{232}Th	2.59e+09	2.67e+00
ThermosyphonAndShieldCopper	^{60}Co	7.65e+06	2.21e+00
	^{40}K	2.26e+07	1.58e-01
	^{238}U	6.95e+06	2.24e+00
	^{232}Th	6.95e+06	2.76e+00
ThermosyphonAndShieldVespel	^{40}K	1.26e+08	6.41e-05
	^{238}U	9.11e+06	8.69e-04
	^{232}Th	1.67e+07	1.09e-03
VesselCopper	^{60}Co	2.20e+06	1.00e+01
	^{40}K	2.02e+07	5.88e-01
	^{238}U	2.20e+06	9.16e+00
	^{232}Th	2.20e+06	1.15e+01

Table A.4: All bulk simulations in the DS1 configuration of component groups used in the background model are included in this table.

Component group	**Contaminants simulated**	**Primary decays**	**Counts per decay/kg**
N2	^{222}Rn	2.20e+06	6.64e-03
RadShieldCuInner	^{60}Co	5.28e+06	2.27e+01
	^{40}K	9.84e+07	1.34e+00
	^{238}U	5.81e+06	1.57e+01
	^{232}Th	1.21e+07	1.98e+01
RadShieldCuOuter	^{60}Co	5.94e+07	2.98e+00
	^{40}K	9.07e+08	1.99e-01
	^{238}U	7.83e+07	1.71e+00
	^{232}Th	1.51e+08	2.35e+00
RadShieldPb	^{40}K	4.90e+10	2.71e-02
	^{238}U	4.46e+09	2.19e-01
	^{232}Th	1.71e+10	3.52e-01
ThermosyphonAndShieldCopper	^{60}Co	2.20e+06	1.82e+00
	^{40}K	1.54e+07	1.26e-01
	^{238}U	2.20e+06	1.81e+00
	^{232}Th	2.20e+06	2.25e+00
ThermosyphonAndShieldVespel	^{40}K	9.14e+07	5.83e-05
	^{238}U	5.08e+06	7.66e-04
	^{232}Th	9.68e+06	9.63e-04
VesselCopper	^{60}Co	2.20e+06	8.12e+00
	^{40}K	1.76e+07	4.75e-01
	^{238}U	2.20e+06	7.38e+00
	^{232}Th	2.20e+06	9.25e+00

Table A.5: All PDFs that can be split between modules that are extracted from PDFs that are not simulated as split between modules.

Component group
ColdPlateCopper
Connectors
DUCoatedCopper
DUCopper
DUPTFE
DUVespel
EnrGe
HVForks
LMFEs
NatGe
SSCFVacHW
StringCoatedCopper
StringCopper
ThermosyphonAndShieldCoatedCopper
ThermosyphonAndShieldCopper
ThermosyphonAndShieldVespel
VesselCoatedCopper
VesselCopper

Table A.6: All component groups that are constructed from linear combinations of other component groups.

Supergroup	**Constituent component groups**
VesselAndTSSCopper	VesselCopper
	ThermosyphonAndShieldCopper
EFCopper	RadShieldCuInner
	VesselCopper
	ColdPlateCopper
	DUCopper
	StringCopper
	ThermosyphonAndShieldCopper
	HVForks
InteriorEFCopper	DUCopper
	StringCopper
	ColdPlateCopper
Vespel	DUVespel
	ThermosyphonAndShieldVespel
M1Cables	M1CrossarmCables
	M1StringSigCables
	M1StringHVCables
M2Cables	M2CrossarmCables
	M2StringSigCables
	M2StringHVCables
Cables	M1CrossarmCables
	M1StringSigCables
	M1StringHVCables
	M2CrossarmCables
	M2StringSigCables
	M2StringHVCables

Appendix B

PRIMARY DECAY LOCATIONS IN MaGe SIMULATIONS

Each figure shows the location of ^{238}U atoms that decayed in a MaGe simulation and were eventually detected by the MAJORANA DEMONSTRATOR. All plots were made in the 2-module configuration, and show the basic location of all the named components in the model. The point of view in these plots is slightly above the DEMONSTRATOR, looking in a northeasterly direction with module 1 on the left side and module 2 on the right.

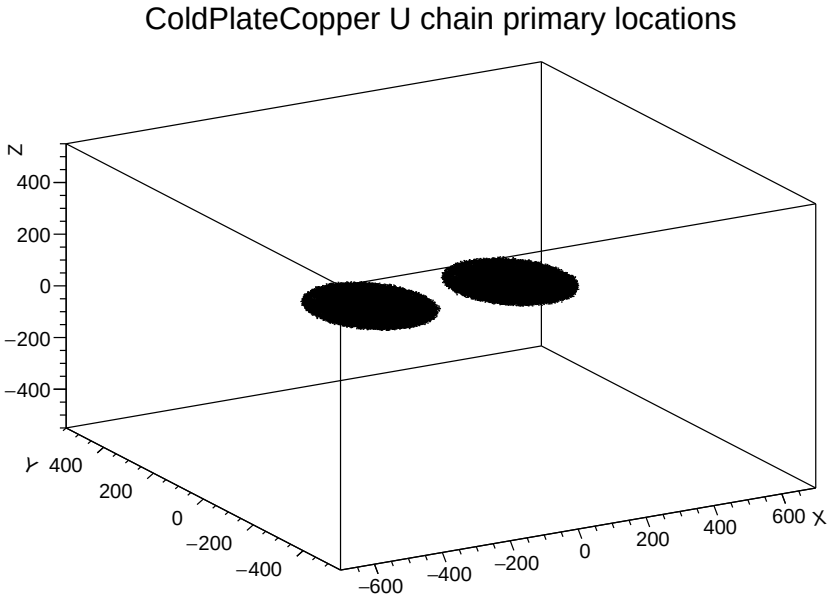

Connectors U chain primary locations

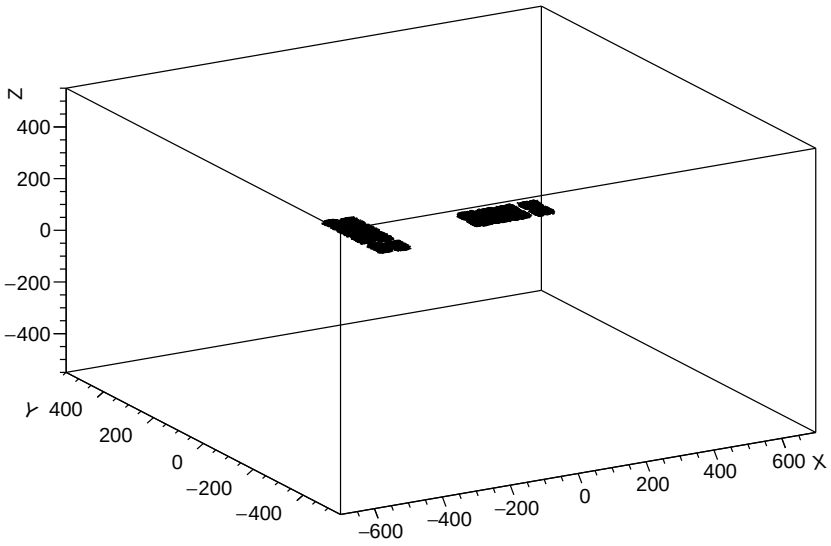

DUCoatedCopper U chain primary locations

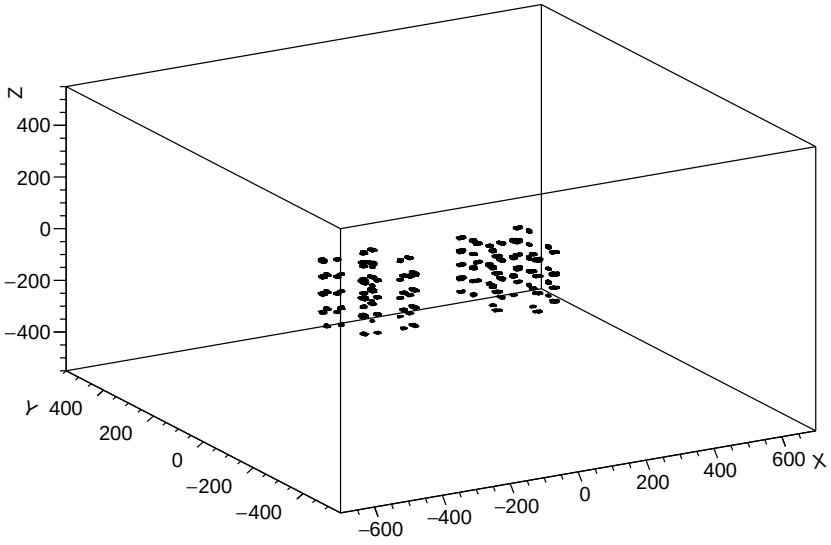

DUCopper U chain primary locations

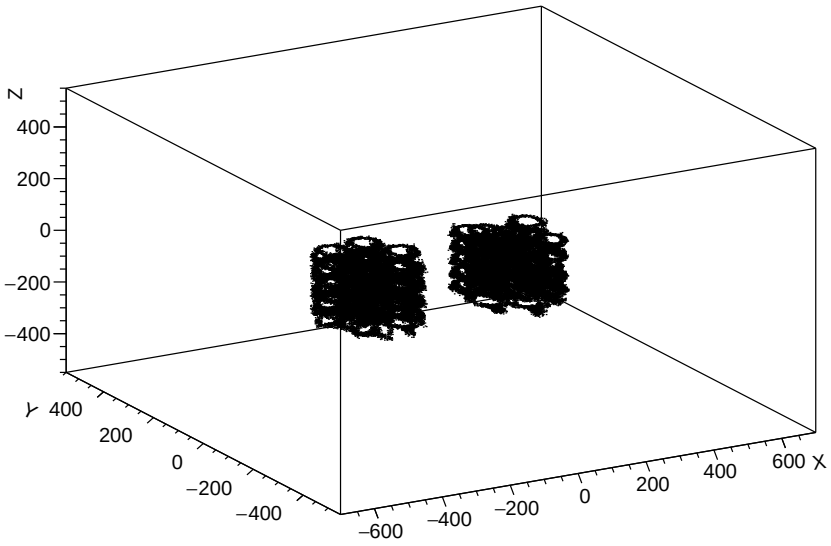

DUPTFE U chain primary locations

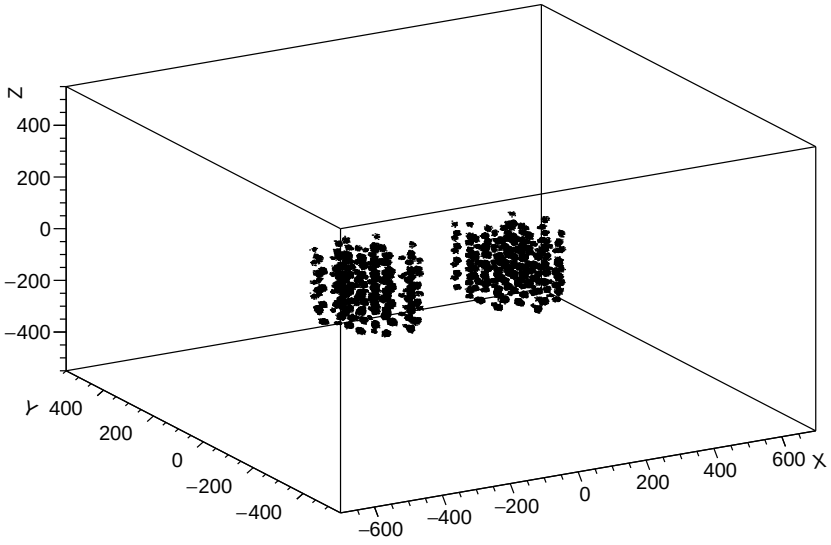

DUVespel U chain primary locations

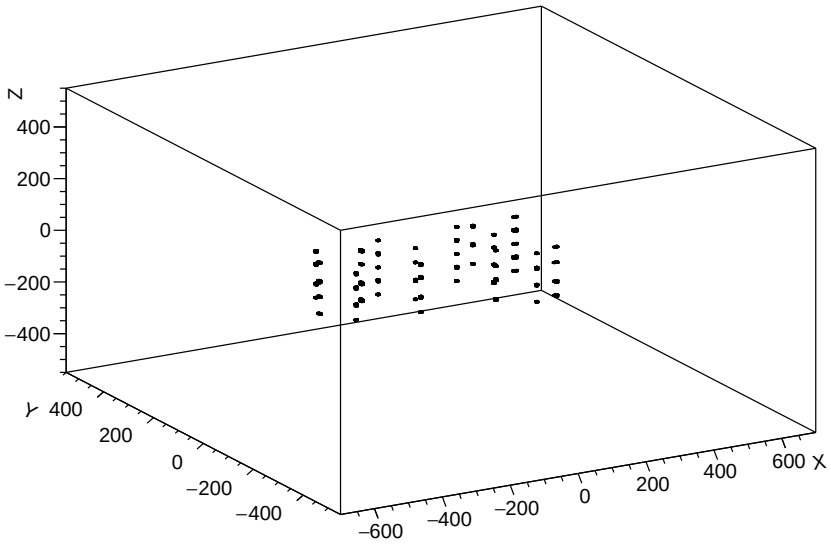

EnrGe U chain primary locations

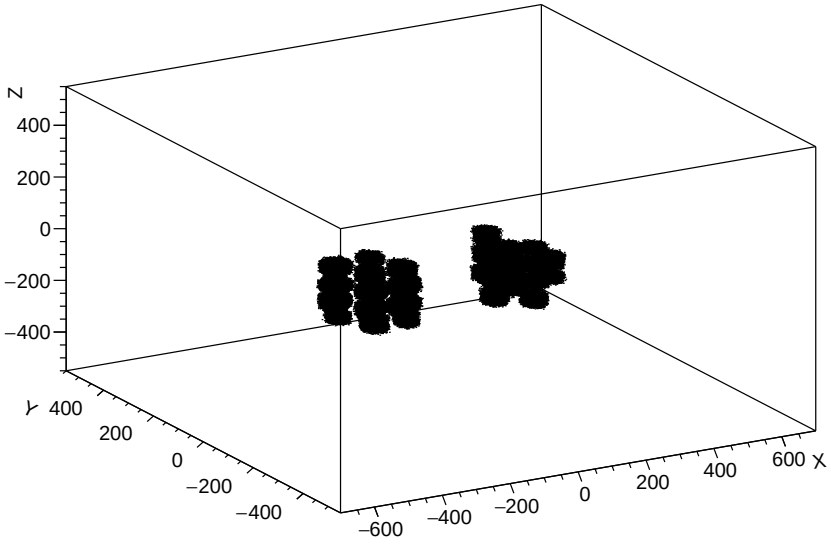

HVForks U chain primary locations

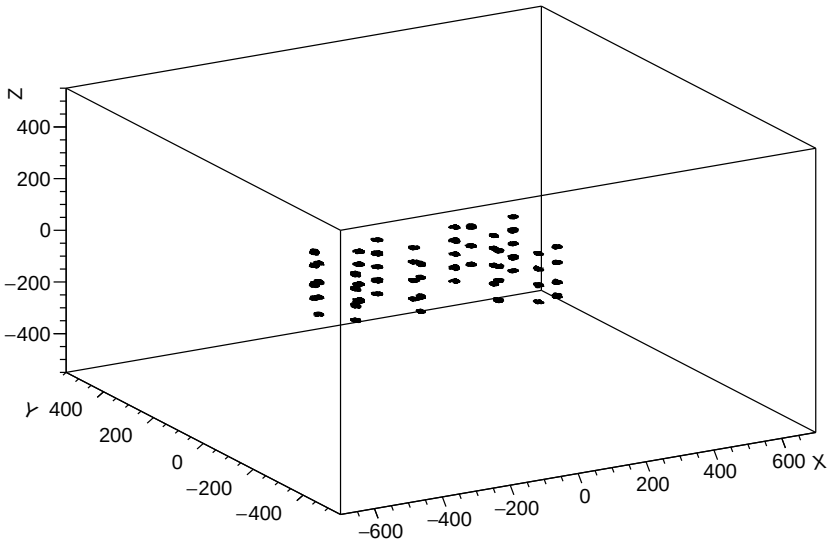

LMFEs U chain primary locations

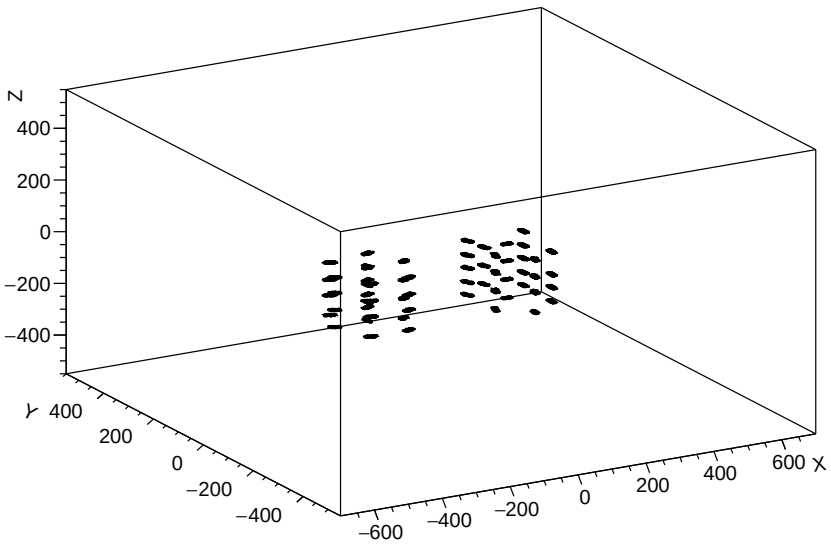

M1BottomSeal U chain primary locations

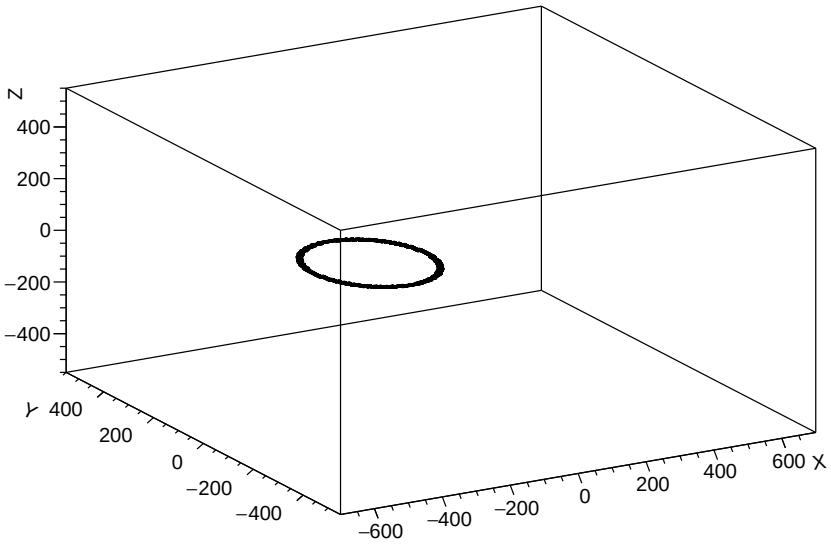

M1CPCables U chain primary locations

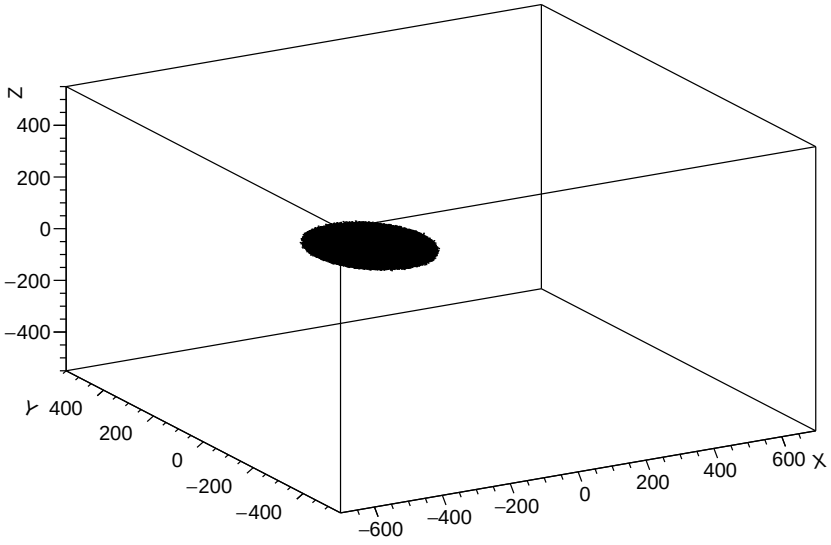

M1CrossarmCables U chain primary locations

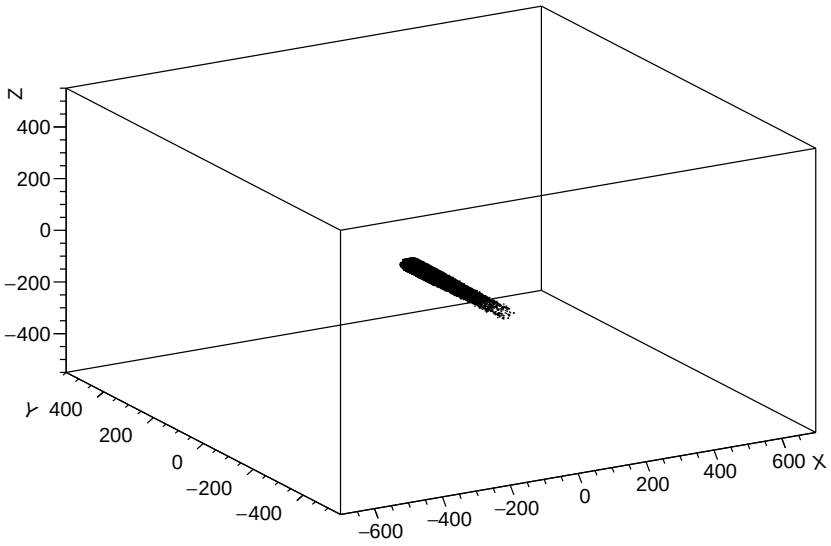

M1StringHVCables U chain primary locations

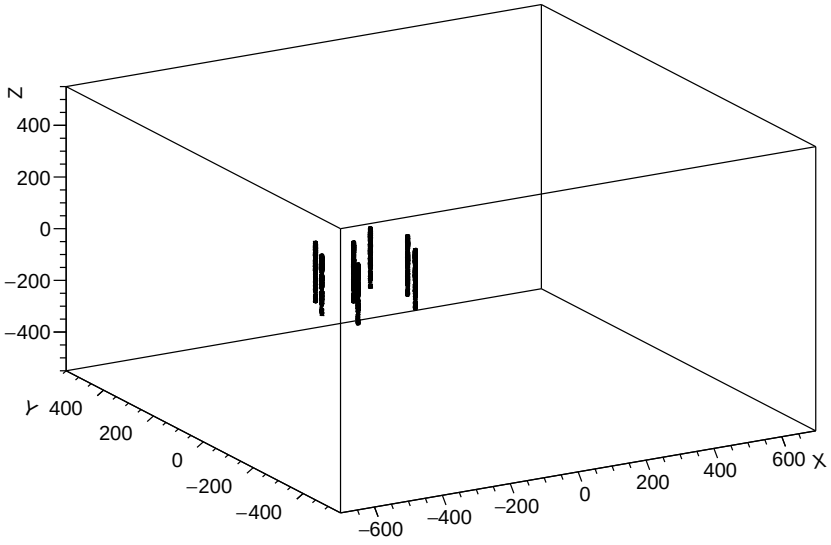

M1StringSigCables U chain primary locations

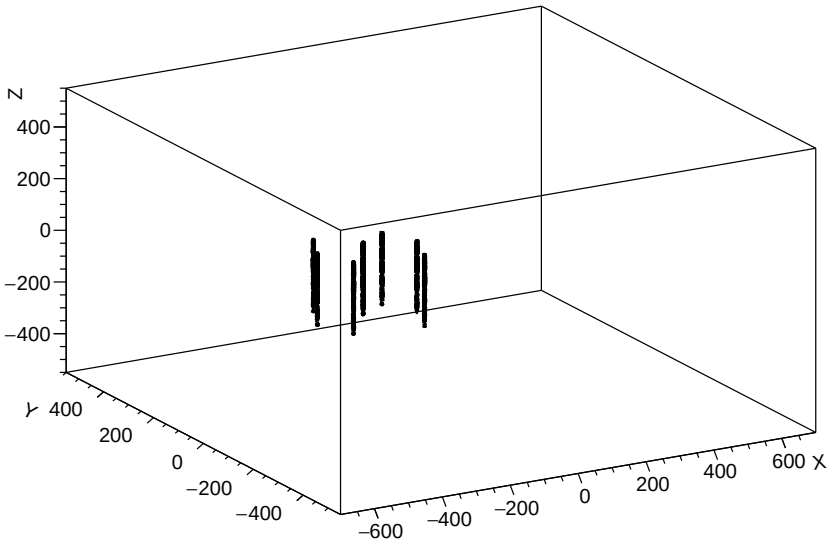

M1TopSeal U chain primary locations

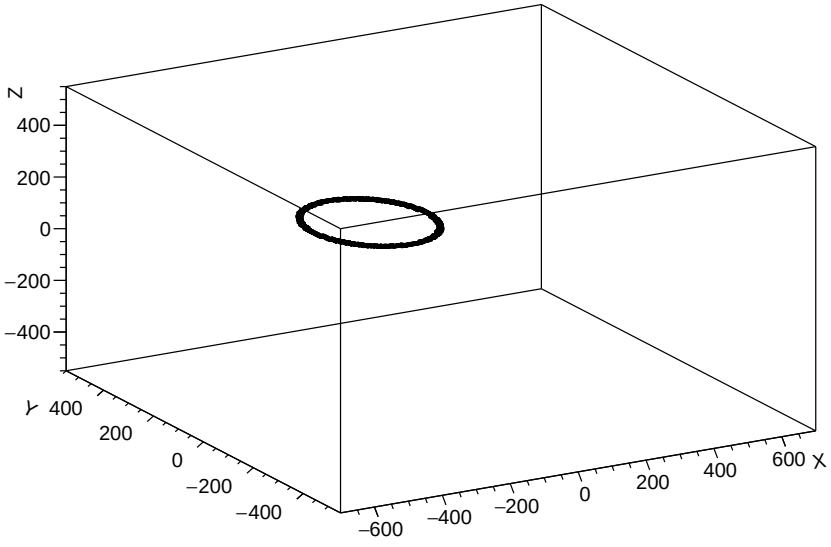

M2BottomSeal U chain primary locations

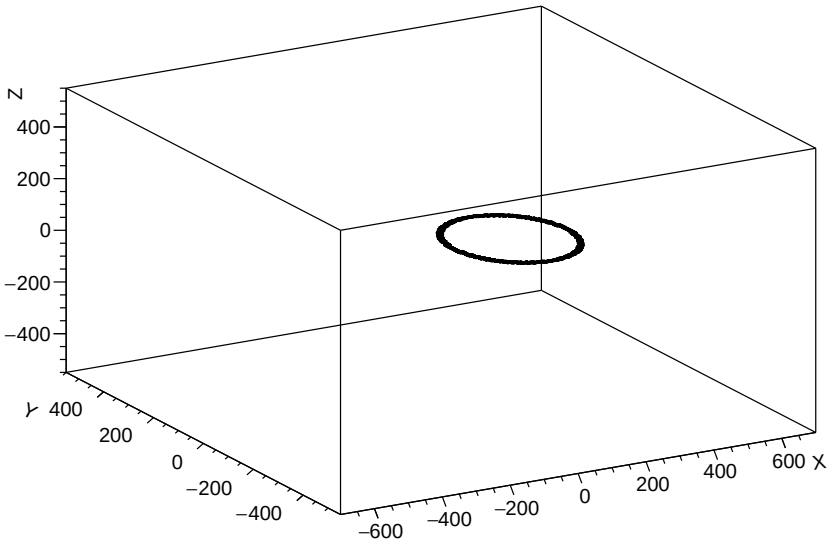

M2CPCables U chain primary locations

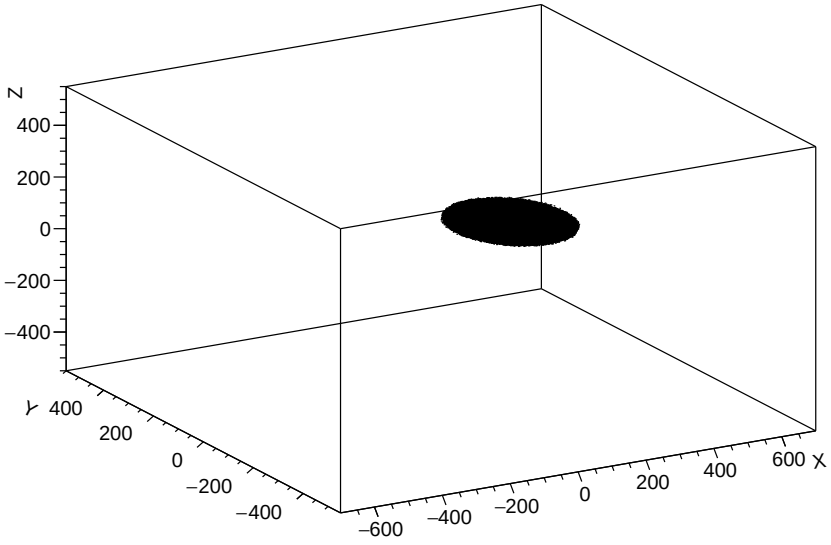

M2CrossarmCables U chain primary locations

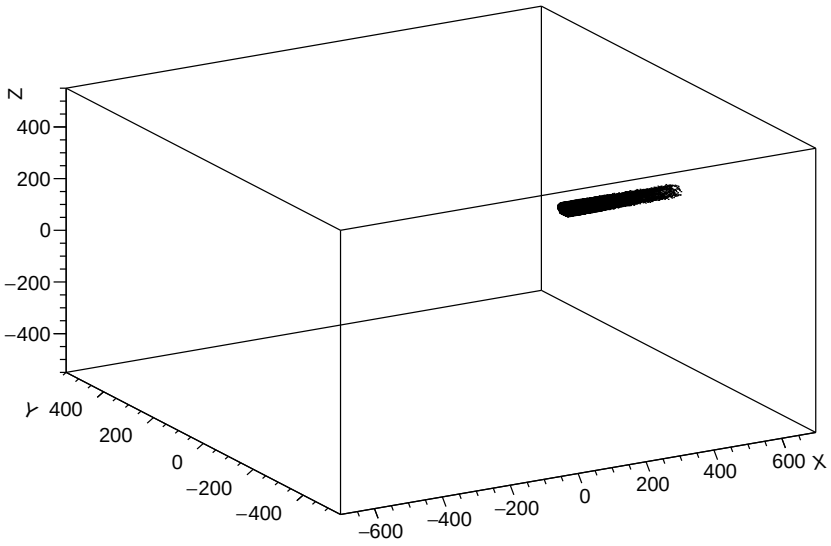

M2StringHVCables U chain primary locations

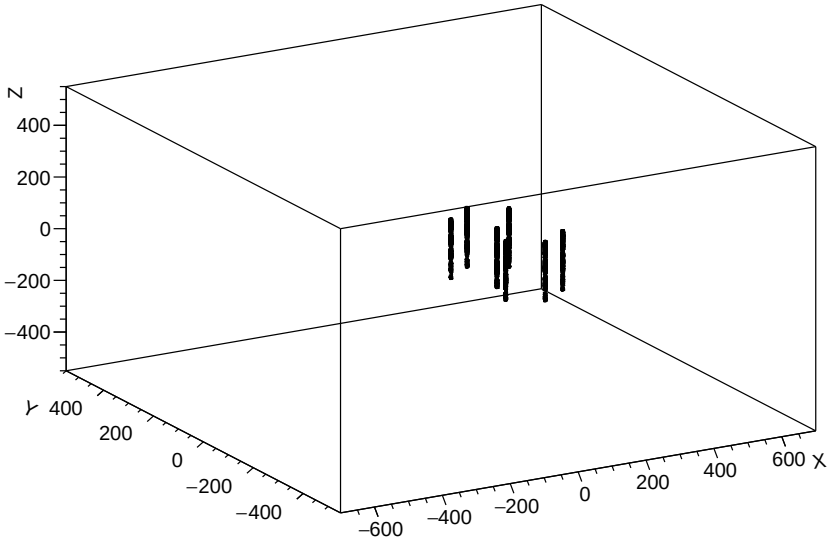

M2StringSigCables U chain primary locations

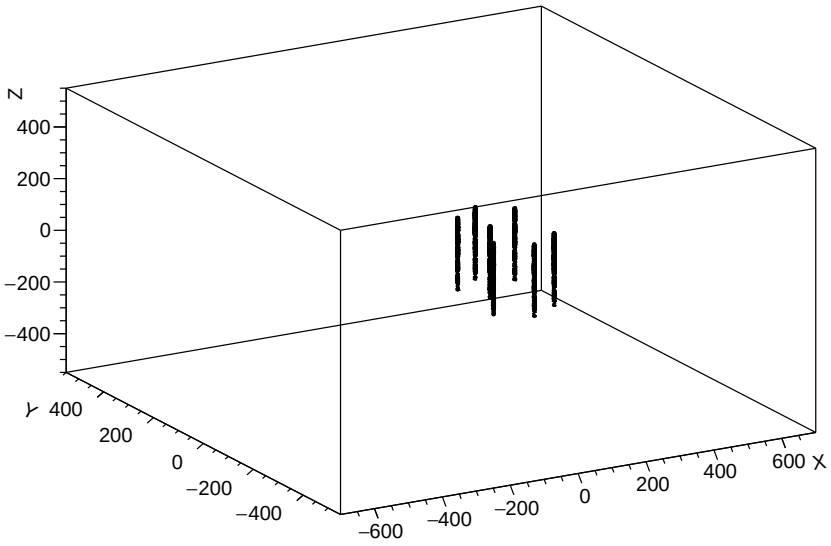

M2TopSeal U chain primary locations

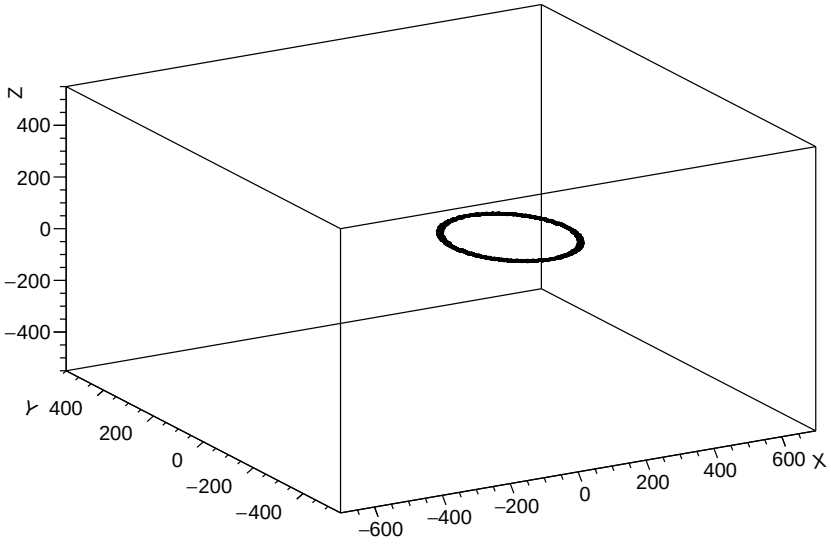

N2 U chain primary locations

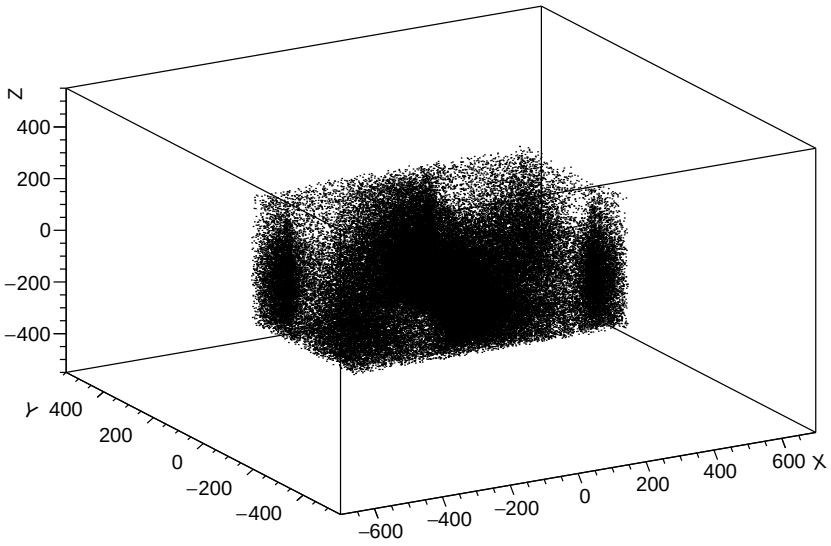

NatGe U chain primary locations

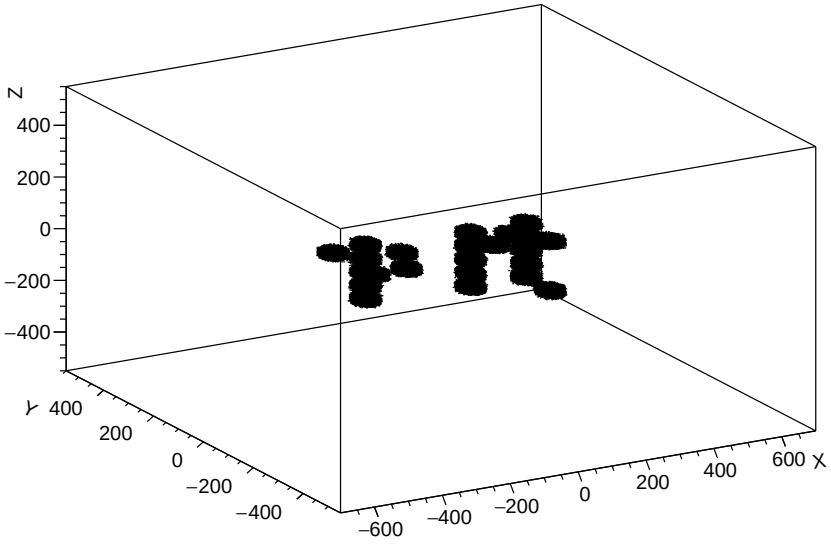

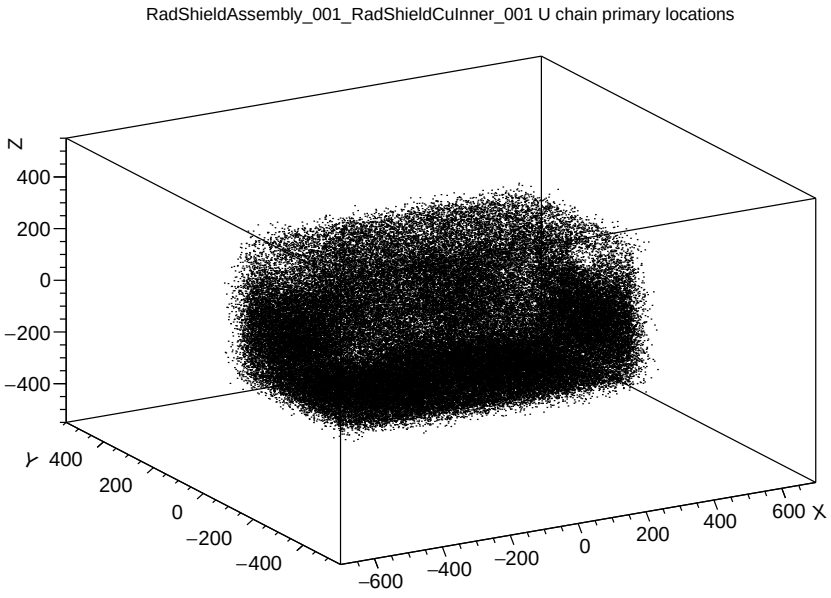
RadShieldAssembly_001_RadShieldCuInner_001 U chain primary locations
Z
400
200
0
−200
−400
Y 400
200
0
−200
−400
−600
−400
−200
0
200
400
600 X

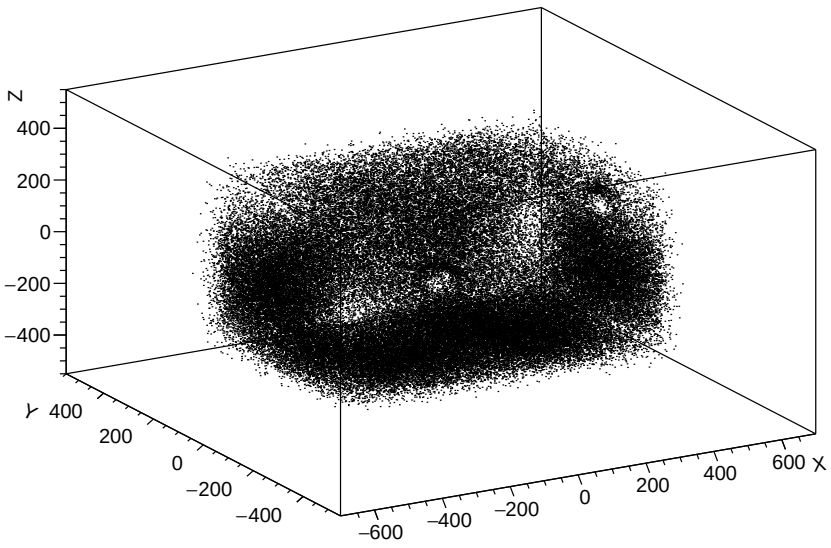
RadShieldAssembly_001_RadShieldCuOuter_001 U chain primary locations
Z
400
200
0
−200
−400
Y 400
200
0
−200
−400
−600
−400
−200
0
200
400
600 X

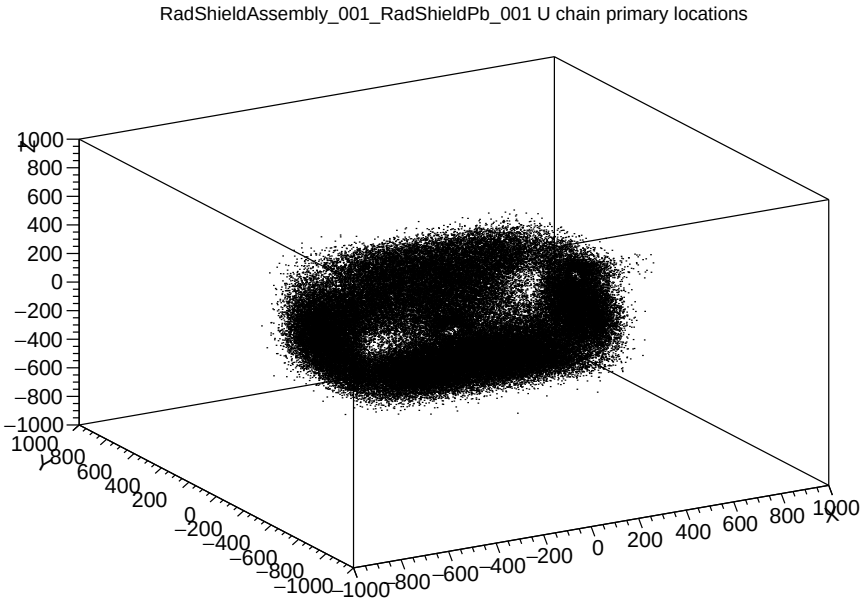
RadShieldAssembly_001_RadShieldPb_001 U chain primary locations
Z
1000
800
600
400
200
0
−200
−400
−600
−800
−1000
Y
1000
800
600
400
200
0
−200
−400
−600
−800
−1000
X
−1000
−800
−600
−400
−200
0
200
400
600
800
1000

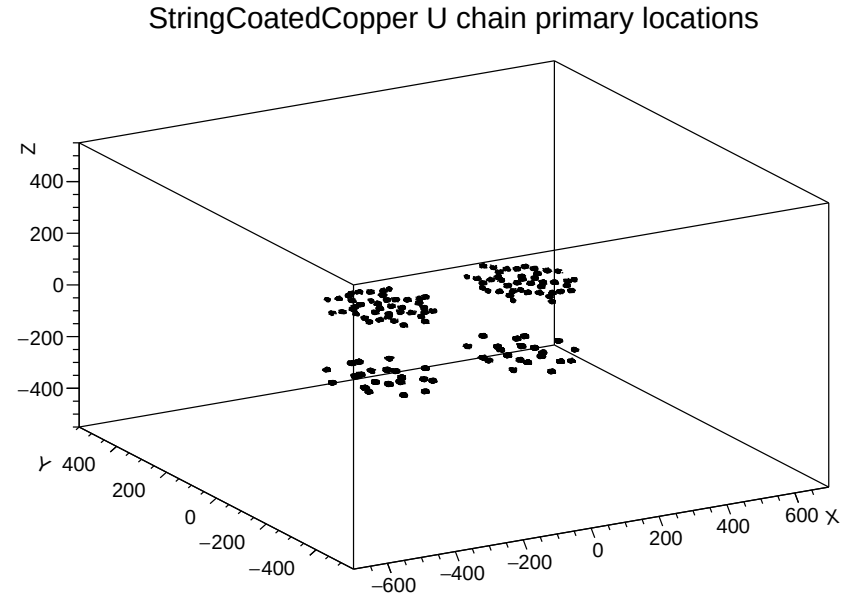
StringCoatedCopper U chain primary locations
Z
400
200
0
−200
−400
Y
400
200
0
−200
−400
X
−600
−400
−200
0
200
400
600

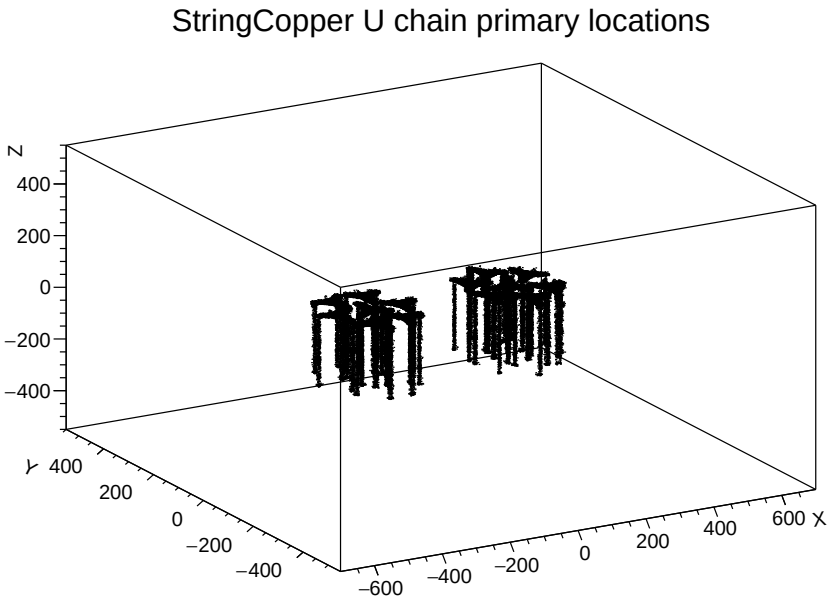
StringCopper U chain primary locations
Z
400
200
0
−200
−400
Y 400
200
0
−200
−400
−600
−400
−200
0
200
400
600 X

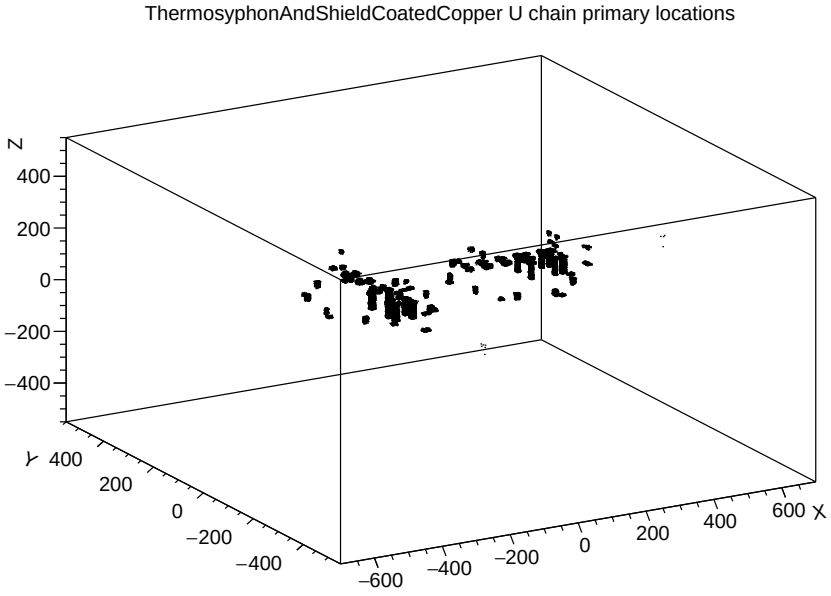
ThermosyphonAndShieldCoatedCopper U chain primary locations
Z
400
200
0
−200
−400
Y 400
200
0
−200
−400
−600
−400
−200
0
200
400
600 X

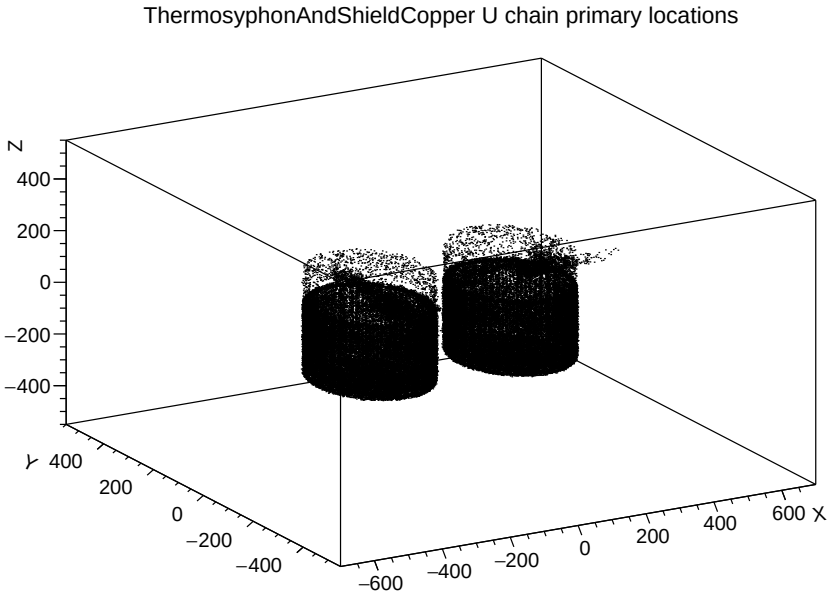
ThermosyphonAndShieldCopper U chain primary locations
Z
400
200
0
−200
−400
Y 400
200
0
−200
−400
−600
−400
−200
0
200
400
600 X

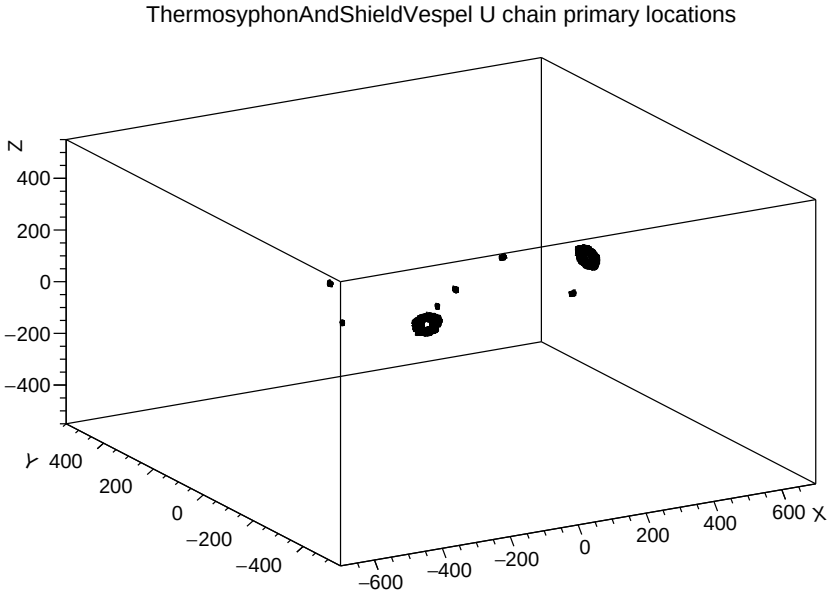
ThermosyphonAndShieldVespel U chain primary locations
Z
400
200
0
−200
−400
Y 400
200
0
−200
−400
−600
−400
−200
0
200
400
600 X

VesselCoatedCopper U chain primary locations

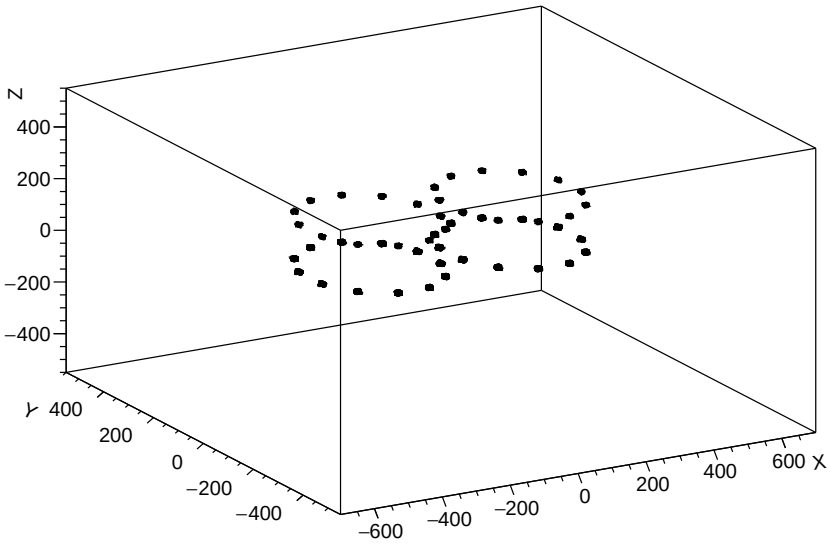

VesselCopper U chain primary locations

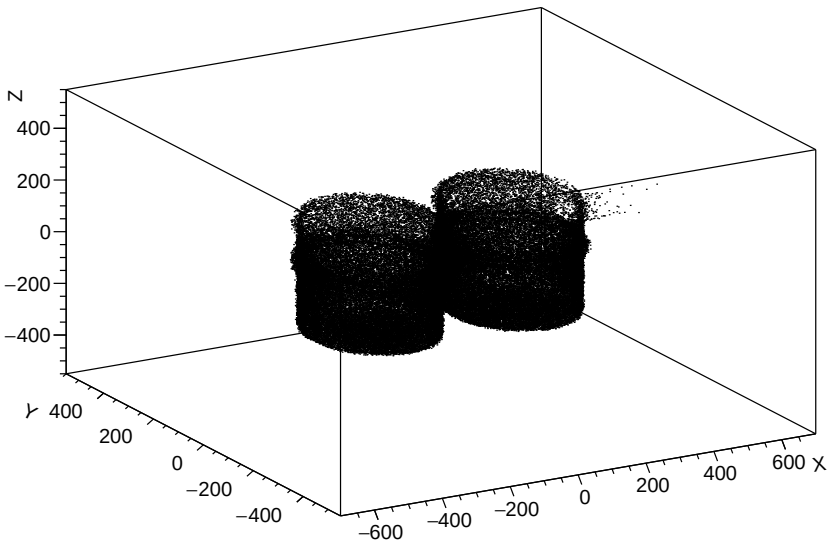

Appendix C

TABLES OF RESULTS OF FITS TO TOY MC AND EXPERIMENTAL DATA

C.1 Toy MC Fits

Table C.1: Aggregated results of fits with 123 PDFs to toy MC-generated data from section 4.5.

Component group	**Contaminant**	**Source type**	**Fitted counts**	**Fitted activity density (Bq/kg)**	**Precision**	**Correct activity density**	**Normalized error**
EnrGe	$2\nu\beta\beta$	bulk	33758 ± 1079	8.08e-05 ± 2.58e-06	1.17e+02	7.99e-05	-3.37e-01
RadShieldPb	^{210}Pb	pbbrem	23615 ± 3305	5.34e-01 ± 7.47e-02	7.54e+00	5.28e-01	-7.71e-02
NatGe	^{3}H	bulk	14800 ± 614	2.63e-04 ± 1.09e-05	6.15e+01	2.60e-04	-3.32e-01
VesselCopper	^{60}Co	bulk	11721 ± 4082	3.96e-05 ± 1.38e-05	2.92e+00	3.72e-05	-1.72e-01
RadShieldCuOuter	^{60}Co	bulk	8684 ± 4799	4.82e-05 ± 2.66e-05	1.83e+00	6.80e-05	7.44e-01
RadShieldPb	^{238}U	bulk	3727 ± 2775	2.72e-04 ± 2.02e-04	1.36e+00	1.89e-04	-4.11e-01
RadShieldCuOuter	^{232}Th	bulk	2949 ± 2604	1.74e-05 ± 1.53e-05	1.15e+00	1.41e-05	-2.14e-01
NatGe	^{65}Zn	bulk	2437 ± 496	5.83e-05 ± 1.19e-05	5.39e+00	6.09e-05	2.23e-01
RadShieldPb	^{40}K	bulk	2190 ± 3315	1.36e-03 ± 2.05e-03	6.63e-01	1.25e-03	-5.08e-02
EnrGe	^{3}H	bulk	2165 ± 161	1.45e-05 ± 1.08e-06	5.73e+01	1.48e-05	3.24e-01
RadShieldCuOuter	^{238}U	bulk	1867 ± 2284	1.44e-05 ± 1.76e-05	8.28e-01	1.66e-05	1.23e-01
RadShieldPb	^{232}Th	bulk	1506 ± 1540	7.32e-05 ± 7.48e-05	9.86e-01	1.23e-04	6.62e-01

Component group	Contaminant	Source type	Fitted counts	Fitted activity density (Bq/kg)	Precision	Correct activity density	Normalized error
DUVespel	^{238}U	bulk	1491 ± 1520	6.83e-01 ± 6.96e-01	9.81e-01	4.47e-04	-9.80e-01
NatGe	$2\nu\beta\beta$	bulk	1259 ± 141	7.72e-06 ± 8.67e-07	1.43e+01	7.33e-06	-4.57e-01
StringCoatedCopper	^{238}U	bulk	1196 ± 1439	4.92e-01 ± 5.92e-01	8.32e-01	3.10e-03	-8.26e-01
ThermosyphonAndShieldVespel	^{40}K	bulk	1169 ± 1439	6.14e-01 ± 7.56e-01	8.12e-01	6.00e-03	-8.04e-01
N2	^{222}Rn	surface	1153 ± 1485	5.18e-03 ± 6.68e-03	7.81e-01	7.17e-03	2.98e-01
ThermosyphonAndShieldCopper	^{40}K	surface	1047 ± 1027	1.15e-04 ± 1.13e-04	1.03e+00	5.43e-05	-5.39e-01
N2	^{222}Rn	bulk	915 ± 1376	5.03e-03 ± 7.55e-03	6.68e-01	1.79e-02	1.71e+00
M1CrossarmCables	^{40}K	bulk	905 ± 1348	4.78e-01 ± 7.12e-01	6.74e-01	5.82e-02	-5.89e-01
ThermosyphonAndShieldCopper	^{60}Co	bulk	892 ± 2620	1.44e-05 ± 4.23e-05	3.42e-01	3.72e-05	5.39e-01
M1StringSigCables	^{40}K	bulk	889 ± 870	7.28e-02 ± 7.13e-02	1.03e+00	5.82e-02	-2.04e-01
RadShieldCuOuter	^{54}Mn	bulk	844 ± 1718	1.95e-05 ± 3.97e-05	4.94e-01	1.07e-05	-2.22e-01
M1Seals DS0	^{238}U	bulk	745 ± 599	2.86e-02 ± 2.30e-02	1.26e+00	8.82e-03	-8.61e-01
EnrGe	^{65}Zn	bulk	726 ± 71	5.80e-06 ± 5.64e-07	7.08e+01	6.28e-06	8.43e-01
HVForks	^{40}K	bulk	515 ± 788	2.78e-02 ± 4.24e-02	6.57e-01	5.43e-05	-6.53e-01
RadShieldCuOuter	^{40}K	bulk	496 ± 1319	4.08e-05 ± 1.08e-04	3.78e-01	7.78e-05	3.41e-01
M1Seals DS0	^{232}Th	bulk	473 ± 425	1.44e-02 ± 1.30e-02	1.14e+00	8.21e-03	-4.80e-01
M2CPCables	^{40}K	bulk	431 ± 394	3.59e-02 ± 3.28e-02	1.11e+00	5.82e-02	6.83e-01
M1Seals DS0	^{40}K	bulk	427 ± 634	2.55e-01 ± 3.79e-01	6.61e-01	0.00e+00	-6.74e-01
DUCoatedCopper	^{40}K	bulk	401 ± 932	6.40e-01 ± 1.49e+00	4.34e-01	2.86e-02	-4.11e-01

Component group	Contaminant	Source type	Fitted counts	Fitted activity density (Bq/kg)	Precision	Correct activity density	Normalized error
ThermosyphonAndShieldCoatedCopper	^{40}K	bulk	401 ± 632	1.99e-01 ± 3.15e-01	6.33e-01	2.86e-02	-5.43e-01
VesselCoatedCopper	^{40}K	bulk	381 ± 668	1.98e-01 ± 3.48e-01	5.55e-01	2.86e-02	-4.88e-01
LMFEs	^{40}K	bulk	367 ± 446	6.38e-02 ± 7.75e-02	8.32e-01	3.76e-03	-7.74e-01
DUPTFE	^{210}Pb	surface	353 ± 187	2.41e-03 ± 1.27e-03	1.92e+00	2.85e-03	3.48e-01
VesselCopper	^{40}K	bulk	332 ± 573	1.69e-05 ± 2.93e-05	5.80e-01	5.43e-05	1.28e+00
StringCoatedCopper	^{232}Th	bulk	328 ± 403	1.05e-01 ± 1.30e-01	7.60e-01	2.16e-03	-7.96e-01
M1StringHVCables	^{60}Co	bulk	317 ± 426	2.12e-03 ± 2.85e-03	7.55e-01	5.32e-05	-7.25e-01
M1CPCables	^{60}Co	bulk	296 ± 429	7.21e-04 ± 1.05e-03	6.95e-01	5.32e-05	-6.39e-01
M1CrossarmCables	^{60}Co	bulk	289 ± 596	1.02e-02 ± 2.11e-02	4.86e-01	5.32e-05	-4.83e-01
HVForks	^{60}Co	bulk	281 ± 754	1.15e-03 ± 3.09e-03	3.73e-01	5.32e-05	-3.55e-01
M1Seals DS12DS3456	^{40}K	bulk	275 ± 414	6.01e-02 ± 9.06e-02	6.67e-01	0.00e+00	-6.63e-01
M1StringHVCables	^{40}K	bulk	259 ± 443	1.32e-02 ± 2.25e-02	5.89e-01	5.82e-02	2.01e+00
M1StringSigCables	^{60}Co	bulk	219 ± 287	2.40e-03 ± 3.14e-03	7.78e-01	5.32e-05	-7.47e-01
M1StringHVCables	^{232}Th	bulk	213 ± 235	6.33e-04 ± 6.99e-04	9.15e-01	1.65e-05	-8.82e-01
M2StringSigCables	^{40}K	bulk	207 ± 243	5.06e-02 ± 5.92e-02	8.62e-01	5.82e-02	1.29e-01
M2StringHVCables	^{40}K	bulk	204 ± 225	2.89e-02 ± 3.19e-02	9.14e-01	5.82e-02	9.18e-01
M1StringSigCables	^{232}Th	bulk	201 ± 232	9.59e-04 ± 1.11e-03	8.67e-01	1.60e-05	-8.49e-01
DUPTFE	^{40}K	bulk	199 ± 363	1.10e-03 ± 2.00e-03	5.51e-01	4.65e-06	-5.46e-01
DUCoatedCopper	^{238}U	bulk	197 ± 312	2.15e-02 ± 3.39e-02	6.37e-01	3.10e-03	-5.41e-01
M2CrossarmCables	^{40}K	bulk	196 ± 365	3.08e-01 ± 5.74e-01	5.41e-01	5.82e-02	-4.36e-01
DUCopper	^{40}K	surface	194 ± 377	1.14e-05 ± 2.22e-05	5.20e-01	5.43e-05	1.93e+00
VesselCoatedCopper	^{238}U	bulk	177 ± 266	7.00e-03 ± 1.05e-02	6.73e-01	3.10e-03	-3.72e-01

Component group	Contaminant	Source type	Fitted counts	Fitted activity density (Bq/kg)	Precision	Correct activity density	Normalized error
DUCopper	^{40}K	bulk	157 ± 299	1.86e-05 ± 3.53e-05	5.30e-01	5.43e-05	1.01e+00
M2CrossarmCables	^{60}Co	bulk	151 ± 173	1.63e-02 ± 1.87e-02	8.76e-01	5.32e-05	-8.70e-01
DUPTFE	^{238}U	bulk	143 ± 282	4.91e-05 ± 9.67e-05	5.09e-01	3.99e-06	-4.66e-01
Connectors	^{40}K	bulk	139 ± 228	8.01e-03 ± 1.31e-02	6.18e-01	2.31e-02	1.16e+00
M1CPCables	^{40}K	bulk	131 ± 232	4.92e-03 ± 8.68e-03	5.72e-01	5.82e-02	6.15e+00
M1Seals DS12 DS3456	^{232}Th	bulk	116 ± 153	1.16e-03 ± 1.52e-03	7.68e-01	1.66e-05	-7.50e-01
DUPTFE	^{40}K	surface	116 ± 138	5.34e-04 ± 6.34e-04	8.51e-01	4.65e-06	-8.36e-01
M1CrossarmCables	^{238}U	bulk	113 ± 159	4.61e-03 ± 6.45e-03	7.24e-01	9.26e-05	-6.99e-01
ThermosyphonAndShieldVespel	^{238}U	bulk	112 ± 185	4.28e-03 ± 7.06e-03	6.09e-01	4.47e-04	-5.43e-01
VesselCopper	^{232}Th	bulk	111 ± 345	2.70e-07 ± 8.41e-07	3.22e-01	4.40e-08	-2.69e-01
M1StringSigCables	^{238}U	bulk	102 ± 146	5.25e-04 ± 7.49e-04	7.06e-01	1.11e-04	-5.54e-01
VesselCopper	^{238}U	bulk	100 ± 248	3.04e-07 ± 7.57e-07	4.05e-01	2.16e-07	-1.17e-01
M1StringHVCables	^{238}U	bulk	99 ± 135	3.20e-04 ± 4.35e-04	7.41e-01	8.30e-05	-5.46e-01
LMFEs	^{238}U	bulk	99 ± 180	9.31e-04 ± 1.69e-03	5.53e-01	1.06e-02	5.69e+00
ThermosyphonAndShieldCopper	^{40}K	bulk	93 ± 225	2.03e-05 ± 4.91e-05	4.13e-01	5.43e-05	6.92e-01
Connectors	^{232}Th	bulk	91 ± 185	2.78e-04 ± 5.67e-04	4.93e-01	2.95e-04	3.02e-02
HVForks	^{238}U	bulk	91 ± 174	2.84e-04 ± 5.44e-04	5.25e-01	2.16e-07	-5.21e-01
StringCopper	^{40}K	surface	89 ± 123	4.35e-05 ± 5.98e-05	7.35e-01	5.43e-05	1.79e-01
DUCoatedCopper	^{232}Th	bulk	87 ± 127	7.97e-03 ± 1.17e-02	6.93e-01	2.16e-03	-4.99e-01
ColdPlateCopper	^{40}K	bulk	86 ± 289	2.12e-05 ± 7.12e-05	2.99e-01	5.43e-05	4.64e-01

Component group	Contaminant	Source type	Fitted counts	Fitted activity density (Bq/kg)	Precision	Correct activity density	Normalized error
M1CrossarmCables	^{232}Th	bulk	85 ± 162	2.72e-03 ± 5.16e-03	5.29e-01	1.63e-05	-5.24e-01
DUVespel	^{40}K	bulk	79 ± 480	5.74e-01 ± 3.49e+00	1.65e-01	6.00e-03	-1.63e-01
LMFEs	^{60}Co	bulk	76 ± 102	9.85e-04 ± 1.32e-03	7.55e-01	1.85e-03	6.51e-01
M2CPCables	^{60}Co	bulk	75 ± 174	4.17e-04 ± 9.73e-04	4.32e-01	5.32e-05	-3.74e-01
M1CPCables	^{232}Th	bulk	72 ± 106	1.51e-04 ± 2.23e-04	6.79e-01	1.63e-05	-6.03e-01
M2StringSigCables	^{60}Co	bulk	71 ± 107	2.03e-03 ± 3.07e-03	6.68e-01	5.32e-05	-6.43e-01
ColdPlateCopper	^{40}K	surface	70 ± 107	1.31e-05 ± 2.01e-05	6.59e-01	5.43e-05	2.05e+00
ThermosyphonAndShieldCopper	^{238}U	surface	68 ± 133	4.86e-07 ± 9.45e-07	5.20e-01	2.16e-07	-2.86e-01
StringCopper	^{40}K	bulk	67 ± 133	4.16e-05 ± 8.22e-05	5.09e-01	5.43e-05	1.54e-01
ThermosyphonAndShieldCopper	^{232}Th	surface	66 ± 118	4.14e-07 ± 7.33e-07	5.68e-01	4.40e-08	-5.05e-01
DUPTFE	^{232}Th	surface	66 ± 127	1.69e-05 ± 3.25e-05	5.24e-01	1.02e-07	-5.18e-01
ThermosyphonAndShieldVespel	^{232}Th	bulk	63 ± 80	1.91e-03 ± 2.43e-03	7.93e-01	9.42e-06	-7.80e-01
M2CrossarmCables	^{238}U	bulk	61 ± 91	7.11e-03 ± 1.06e-02	6.80e-01	9.26e-05	-6.65e-01
VesselCoatedCopper	^{232}Th	bulk	59 ± 95	1.88e-03 ± 3.02e-03	6.27e-01	2.16e-03	9.12e-02
M2StringHVCables	^{60}Co	bulk	59 ± 83	1.02e-03 ± 1.44e-03	7.28e-01	5.32e-05	-6.73e-01
M1Seals DS12DS3456	^{238}U	bulk	58 ± 108	7.44e-04 ± 1.37e-03	5.55e-01	7.54e-05	-4.88e-01
M2StringHVCables	^{232}Th	bulk	57 ± 90	4.26e-04 ± 6.74e-04	6.36e-01	1.65e-05	-6.08e-01
StringCopper	^{232}Th	surface	56 ± 148	1.31e-06 ± 3.48e-06	3.82e-01	4.40e-08	-3.65e-01

Component group	Contaminant	Source type	Fitted counts	Fitted activity density (Bq/kg)	Precision	Correct activity density	Normalized error
ThermosyphonAndShieldCopper	^{238}U	bulk	54 ± 103	7.41e-07 ± 1.41e-06	5.31e-01	2.16e-07	-3.72e-01
M2CrossarmCables	^{232}Th	bulk	53 ± 76	4.83e-03 ± 6.98e-03	6.98e-01	1.63e-05	-6.89e-01
M2StringSigCables	^{232}Th	bulk	48 ± 67	6.17e-04 ± 8.56e-04	7.25e-01	1.60e-05	-7.02e-01
M1CPCables	^{238}U	bulk	48 ± 77	1.27e-04 ± 2.05e-04	6.38e-01	9.26e-05	-1.70e-01
NatGe	^{57}Co	bulk	48 ± 20	1.05e-06 ± 4.32e-07	2.51e+00	1.07e-07	2.19e+00
LMFEs	^{232}Th	bulk	44 ± 68	3.33e-04 ± 5.14e-04	6.54e-01	7.60e-03	1.41e+01
DUCopper	^{238}U	surface	43 ± 93	1.83e-07 ± 3.99e-07	4.59e-01	2.16e-07	8.21e-02
DUCopper	^{238}U	bulk	42 ± 92	2.99e-07 ± 6.53e-07	4.59e-01	2.16e-07	-1.28e-01
DUPTFE	^{232}Th	bulk	42 ± 73	1.17e-05 ± 2.07e-05	5.71e-01	1.02e-07	-5.62e-01
M2StringSigCables	^{238}U	bulk	38 ± 61	5.50e-04 ± 8.94e-04	6.20e-01	1.11e-04	-4.92e-01
ThermosyphonAndShieldCopper	^{232}Th	bulk	37 ± 46	4.05e-07 ± 5.05e-07	8.10e-01	4.40e-08	-7.15e-01
M2StringHVCables	^{238}U	bulk	35 ± 59	2.97e-04 ± 5.00e-04	5.98e-01	8.30e-05	-4.29e-01
Connectors	^{238}U	bulk	35 ± 58	1.35e-04 ± 2.21e-04	6.13e-01	3.73e-04	1.07e+00
DUCopper	^{232}Th	surface	34 ± 56	1.35e-07 ± 2.18e-07	6.27e-01	4.40e-08	-4.18e-01
DUPTFE	^{238}U	surface	33 ± 58	9.69e-06 ± 1.72e-05	5.71e-01	3.99e-06	-3.32e-01
StringCopper	^{238}U	surface	33 ± 85	9.26e-07 ± 2.40e-06	3.88e-01	2.16e-07	-2.96e-01
M2CPCables	^{238}U	bulk	33 ± 63	1.81e-04 ± 3.47e-04	5.23e-01	9.26e-05	-2.54e-01
ColdPlateCopper	^{232}Th	surface	32 ± 98	3.71e-07 ± 1.14e-06	3.28e-01	4.40e-08	-2.88e-01
ColdPlateCopper	^{232}Th	bulk	32 ± 62	3.81e-07 ± 7.44e-07	5.15e-01	4.40e-08	-4.53e-01
StringCoatedCopper	^{40}K	bulk	31 ± 201	2.15e-01 ± 1.41e+00	1.55e-01	2.86e-02	-1.32e-01

Component group	Contaminant	Source type	Fitted counts	Fitted activity density (Bq/kg)	Precision	Correct activity density	Normalized error
DUCopper	^{232}Th	bulk	27 ± 44	1.54e-07 ± 2.51e-07	6.18e-01	4.40e-08	-4.39e-01
M2CPCables	^{232}Th	bulk	25 ± 39	1.11e-04 ± 1.68e-04	6.66e-01	1.63e-05	-5.65e-01
M2Seals	^{238}U	bulk	24 ± 40	1.54e-04 ± 2.57e-04	6.03e-01	9.34e-05	-2.37e-01
EnrGe	^{68}Ge	bulk	23 ± 25	7.32e-08 ± 8.06e-08	9.18e-01	3.20e-08	-5.12e-01
M2Seals	^{232}Th	bulk	22 ± 38	1.14e-04 ± 1.94e-04	5.92e-01	6.53e-05	-2.50e-01
ThermosyphonAndShieldCoatedCopper	^{238}U	bulk	21 ± 43	7.97e-04 ± 1.59e-03	5.11e-01	3.10e-03	1.45e+00
StringCopper	^{232}Th	bulk	21 ± 27	6.03e-07 ± 7.68e-07	7.96e-01	4.40e-08	-7.27e-01
ColdPlateCopper	^{238}U	surface	19 ± 26	2.25e-07 ± 3.15e-07	7.39e-01	2.16e-07	-2.87e-02
ThermosyphonAndShieldCoatedCopper	^{232}Th	bulk	17 ± 26	5.13e-04 ± 7.80e-04	6.71e-01	2.16e-03	2.11e+00
StringCopper	^{238}U	bulk	16 ± 25	5.50e-07 ± 8.74e-07	6.35e-01	2.16e-07	-3.82e-01
ColdPlateCopper	^{238}U	bulk	15 ± 23	2.28e-07 ± 3.44e-07	6.78e-01	2.16e-07	-3.72e-02
NatGe	^{68}Ge	bulk	8 ± 14	7.17e-08 ± 1.33e-07	5.42e-01	1.02e-06	7.13e+00

Table C.2: Aggregated results of fits with 123 PDFs to data acquired with the Majorana Demonstrator. The data sets included are described in table 2.3.

Component group	**Contaminant**	**Source type**	**Fitted counts**	**Fitted activity density (Bq/kg)**	**Precision**	**Assayed activity density (Bq/kg)**
EnrGe	$2\nu\beta\beta$	bulk	34485 ± 1081	7.53e-05 ± 2.36e-06	1.93e+02	7.99e-05 ± 3.90e-06
RadShieldPb	^{210}Pb	pbbrem	22620 ± 1079	4.96e-01 ± 2.37e-02	4.31e+01	3.02e+01 ± 6.00e-01
NatGe	^{3}H	bulk	13648 ± 635	2.14e-04 ± 9.94e-06	3.59e+01	N/A
M1CPCables	^{232}Th	bulk	6536 ± 1984	1.19e-02 ± 3.60e-03	3.42e+00	1.63e-05 ± 1.63e-06
ThermosyphonAndShieldCopper	^{40}K	surface	5753 ± 1929	4.73e-04 ± 1.59e-04	3.06e+00	0.00e+00 ± 6.80e-05
RadShieldCuOuter	^{60}Co	bulk	5716 ± 2624	3.00e-05 ± 1.38e-05	2.22e+00	0.00e+00 ± 1.50e-04
NatGe	^{68}Ge	bulk	4522 ± 1108	3.88e-05 ± 9.52e-06	4.26e+00	0.00e+00 ± 3.47e-04
VesselCopper	^{238}U	bulk	4396 ± 2842	1.19e-05 ± 7.71e-06	1.57e+00	2.16e-07 ± 5.15e-08
Connectors	^{232}Th	bulk	3302 ± 1814	8.49e-03 ± 4.67e-03	1.84e+00	2.11e-04 ± 1.85e-04
DUPTFE	^{210}Pb	surface	3171 ± 292	1.25e-02 ± 1.15e-03	2.13e+01	N/A
ThermosyphonAndShieldCopper	^{238}U	bulk	3099 ± 2767	3.68e-05 ± 3.29e-05	1.13e+00	2.16e-07 ± 5.15e-08
M1CrossarmCables	^{232}Th	bulk	2297 ± 1604	6.09e-02 ± 4.25e-02	1.45e+00	1.63e-05 ± 1.63e-06
ThermosyphonAndShieldCoatedCopper	^{232}Th	bulk	2078 ± 657	6.27e-02 ± 1.98e-02	3.30e+00	2.16e-03 ± 1.20e-04
EnrGe	^{3}H	bulk	2033 ± 143	1.29e-05 ± 9.10e-07	7.42e+01	N/A
VesselCopper	^{232}Th	bulk	1817 ± 1153	3.93e-06 ± 2.50e-06	1.60e+00	4.40e-08 ± 1.00e-09

Component group	Contaminant	Source type	Fitted counts	Fitted activity density (Bq/kg)	Precision	Assayed activity density (Bq/kg)
NatGe	$2\nu\beta\beta$	bulk	1803 ± 166	9.55e-06 ± 8.80e-07	1.96e+01	7.33e-06 ± 3.58e-07
RadShieldPb	^{238}U	bulk	1092 ± 1638	7.46e-05 ± 1.12e-04	6.77e-01	3.60e-05 ± 2.50e-05
M1CPCables	^{238}U	bulk	954 ± 977	2.19e-03 ± 2.24e-03	9.89e-01	9.26e-05 ± 9.26e-06
RadShieldCuOuter	^{54}Mn	bulk	926 ± 209	2.11e-05 ± 4.74e-06	4.80e+00	N/A
M1StringSigCables	^{60}Co	bulk	882 ± 804	8.81e-03 ± 8.03e-03	1.10e+00	0.00e+00 ± 6.67e-05
M1CPCables	^{60}Co	bulk	734 ± 955	1.58e-03 ± 2.05e-03	7.75e-01	0.00e+00 ± 6.67e-05
M2StringSigCables	^{60}Co	bulk	683 ± 435	1.57e-02 ± 1.00e-02	1.59e+00	0.00e+00 ± 6.67e-05
LMFEs	^{60}Co	bulk	674 ± 561	8.02e-03 ± 6.67e-03	1.22e+00	0.00e+00 ± 2.31e-03
M1Seals DS0	^{238}U	bulk	640 ± 318	2.47e-02 ± 1.23e-02	2.05e+00	8.82e-03 ± 2.81e-05
M2Seals	^{232}Th	bulk	634 ± 570	2.74e-03 ± 2.46e-03	1.12e+00	6.53e-05 ± 1.05e-05
RadShieldPb	^{40}K	bulk	435 ± 1237	2.54e-04 ± 7.21e-04	3.53e-01	4.19e-04 ± 4.67e-04
ThermosyphonAndShieldCoatedCopper	^{238}U	bulk	369 ± 447	1.39e-02 ± 1.68e-02	8.31e-01	3.10e-03 ± 7.50e-04
NatGe	^{65}Zn	bulk	335 ± 149	7.23e-06 ± 3.23e-06	2.30e+00	N/A
M2Seals	^{238}U	bulk	315 ± 349	1.72e-03 ± 1.91e-03	9.08e-01	0.00e+00 ± 1.17e-04
DUCopper	^{40}K	surface	309 ± 1023	1.53e-05 ± 5.07e-05	3.03e-01	0.00e+00 ± 6.80e-05
M1StringHVCables	^{60}Co	bulk	289 ± 641	1.77e-03 ± 3.93e-03	4.52e-01	0.00e+00 ± 6.67e-05
ThermosyphonAndShieldCoatedCopper	^{40}K	bulk	265 ± 339	1.39e-01 ± 1.77e-01	7.89e-01	2.86e-02 ± 2.67e-03
M2CrossarmCables	^{232}Th	bulk	263 ± 524	1.97e-02 ± 3.93e-02	5.03e-01	1.63e-05 ± 1.63e-06
ThermosyphonAndShieldCopper	^{238}U	surface	220 ± 698	1.14e-06 ± 3.63e-06	3.16e-01	2.16e-07 ± 5.15e-08
M2StringHVCables	^{60}Co	bulk	179 ± 346	2.43e-03 ± 4.70e-03	5.20e-01	0.00e+00 ± 6.67e-05
NatGe	^{57}Co	bulk	164 ± 24	3.26e-06 ± 4.81e-07	9.43e+00	N/A
ColdPlateCopper	^{40}K	bulk	153 ± 385	3.19e-05 ± 8.02e-05	4.00e-01	0.00e+00 ± 6.80e-05

Component group	Contaminant	Source type	Fitted counts	Fitted activity density (Bq/kg)	Precision	Assayed activity density (Bq/kg)
EnrGe	^{65}Zn	bulk	153 ± 40	1.16e-06 ± 3.04e-07	4.11e+00	N/A
DUVespel	^{238}U	bulk	113 ± 546	4.54e-02 ± 2.20e-01	2.07e-01	0.00e+00 ± 5.60e-04
M1Seals DS0	^{232}Th	bulk	109 ± 194	3.31e-03 ± 5.89e-03	5.64e-01	8.21e-03 ± 3.68e-04
M1StringHVCables	^{40}K	bulk	87 ± 242	3.01e-03 ± 8.37e-03	3.61e-01	0.00e+00 ± 7.30e-02
RadShieldPb	^{232}Th	bulk	82 ± 334	3.71e-06 ± 1.51e-05	2.45e-01	5.30e-06 ± 5.30e-06
HVForks	^{60}Co	bulk	80 ± 422	2.94e-04 ± 1.55e-03	1.90e-01	0.00e+00 ± 6.67e-05
M2CrossarmCables	^{40}K	bulk	75 ± 142	9.72e-02 ± 1.84e-01	5.30e-01	0.00e+00 ± 7.30e-02
HVForks	^{238}U	bulk	70 ± 503	1.95e-04 ± 1.39e-03	1.40e-01	2.16e-07 ± 5.15e-08
DUCoatedCopper	^{40}K	bulk	63 ± 358	8.19e-02 ± 4.64e-01	1.77e-01	2.86e-02 ± 2.67e-03
M2CPCables	^{40}K	bulk	63 ± 104	3.98e-03 ± 6.56e-03	6.10e-01	0.00e+00 ± 7.30e-02
RadShieldCuOuter	^{238}U	bulk	60 ± 308	4.41e-07 ± 2.25e-06	1.96e-01	3.08e-07 ± 2.83e-07
M1Seals DS0	^{40}K	bulk	58 ± 129	3.64e-02 ± 8.07e-02	4.54e-01	N/A
M2CrossarmCables	^{238}U	bulk	57 ± 187	5.46e-03 ± 1.78e-02	3.07e-01	9.26e-05 ± 9.26e-06
N2	^{222}Rn	bulk	48 ± 335	2.35e-04 ± 1.63e-03	1.45e-01	0.00e+00 ± 2.25e-02
Connectors	^{40}K	bulk	46 ± 234	2.27e-03 ± 1.16e-02	1.97e-01	0.00e+00 ± 2.90e-02
DUPTFE	^{40}K	surface	38 ± 230	1.46e-04 ± 8.73e-04	1.68e-01	4.65e-06 ± 6.20e-07
RadShieldCuOuter	^{40}K	bulk	37 ± 287	2.89e-06 ± 2.21e-05	1.31e-01	0.00e+00 ± 1.52e-03
M1Seals DS12 DS3456	^{238}U	bulk	34 ± 256	3.80e-04 ± 2.86e-03	1.33e-01	0.00e+00 ± 9.45e-05
ThermosyphonAndShieldCopper	^{232}Th	bulk	31 ± 182	2.95e-07 ± 1.76e-06	1.68e-01	4.40e-08 ± 1.00e-09
RadShieldCuOuter	^{232}Th	bulk	27 ± 267	1.51e-07 ± 1.48e-06	1.03e-01	1.98e-07 ± 3.90e-08
DUCoatedCopper	^{238}U	bulk	24 ± 155	2.27e-03 ± 1.49e-02	1.53e-01	3.10e-03 ± 7.50e-04
VesselCoatedCopper	^{232}Th	bulk	21 ± 129	6.65e-04 ± 4.07e-03	1.63e-01	2.16e-03 ± 1.20e-04
ColdPlateCopper	^{238}U	bulk	20 ± 119	2.57e-07 ± 1.51e-06	1.70e-01	2.16e-07 ± 5.15e-08

Component group	Contaminant	Source type	Fitted counts	Fitted activity density (Bq/kg)	Precision	Assayed activity density (Bq/kg)
M2CPCables	^{232}Th	bulk	19 ± 107	6.28e-05 ± 3.54e-04	1.78e-01	1.63e-05 ± 1.63e-06
Connectors	^{238}U	bulk	19 ± 88	6.08e-05 ± 2.84e-04	2.15e-01	3.36e-04 ± 2.12e-04
ColdPlateCopper	^{40}K	surface	18 ± 82	2.52e-06 ± 1.14e-05	2.22e-01	0.00e+00 ± 6.80e-05
M1CrossarmCables	^{60}Co	bulk	16 ± 159	4.90e-04 ± 4.77e-03	1.03e-01	0.00e+00 ± 6.67e-05
StringCoatedCopper	^{238}U	bulk	16 ± 155	5.74e-03 ± 5.59e-02	1.03e-01	3.10e-03 ± 7.50e-04
M1CPCables	^{40}K	bulk	15 ± 98	4.87e-04 ± 3.23e-03	1.51e-01	0.00e+00 ± 7.30e-02
VesselCoatedCopper	^{40}K	bulk	14 ± 52	8.06e-03 ± 2.94e-02	2.77e-01	2.86e-02 ± 2.67e-03
M2CPCables	^{238}U	bulk	14 ± 88	5.94e-05 ± 3.70e-04	1.61e-01	9.26e-05 ± 9.26e-06
ThermosyphonAndShieldVespel	^{232}Th	bulk	4 ± 39	1.05e-04 ± 1.01e-03	1.04e-01	0.00e+00 ± 1.18e-05
M2CPCables	^{60}Co	bulk	4 ± 38	1.67e-05 ± 1.63e-04	1.03e-01	0.00e+00 ± 6.67e-05
M2CrossarmCables	^{60}Co	bulk	2 ± 24	2.13e-04 ± 2.13e-03	1.03e-01	0.00e+00 ± 6.67e-05
ThermosyphonAndShieldVespel	^{40}K	bulk	2 ± 19	9.23e-04 ± 8.80e-03	1.05e-01	6.00e-03 ± 9.60e-04
M1CrossarmCables	^{40}K	bulk	0 ± 0	4.45e-05 ± 1.88e-04	2.36e-01	0.00e+00 ± 7.30e-02
M1CrossarmCables	^{238}U	bulk	0 ± 0	1.95e-06 ± 7.99e-06	2.46e-01	9.26e-05 ± 9.26e-06
ThermosyphonAndShieldVespel	^{238}U	bulk	0 ± 0	7.87e-07 ± 4.41e-06	1.79e-01	0.00e+00 ± 5.60e-04
DUPTFE	^{238}U	bulk	0 ± 0	4.61e-09 ± 2.80e-08	1.65e-01	0.00e+00 ± 5.00e-06
M1StringSigCables	^{40}K	bulk	0 ± 0	7.13e-07 ± 4.97e-06	1.44e-01	0.00e+00 ± 7.30e-02
M1Seals DS12 DS3456	^{232}Th	bulk	0 ± 0	1.05e-07 ± 5.45e-07	1.94e-01	0.00e+00 ± 2.08e-05
ThermosyphonAndShieldCopper	^{232}Th	surface	0 ± 0	5.47e-11 ± 2.49e-10	2.19e-01	4.40e-08 ± 1.00e-09

Component group	Contaminant	Source type	Fitted counts	Fitted activity density (Bq/kg)	Precision	Assayed activity density (Bq/kg)
ThermosyphonAndShieldCopper	^{60}Co	bulk	0 ± 0	1.54e-10 ± 7.23e-10	2.13e-01	0.00e+00 ± 4.67e-05
StringCoatedCopper	^{232}Th	bulk	0 ± 0	2.91e-06 ± 1.51e-05	1.95e-01	2.16e-03 ± 1.20e-04
DUCopper	^{238}U	bulk	0 ± 0	5.90e-11 ± 4.91e-10	1.17e-01	2.16e-07 ± 5.15e-08
ThermosyphonAndShieldCopper	^{40}K	bulk	0 ± 0	1.48e-09 ± 5.71e-09	2.61e-01	0.00e+00 ± 6.80e-05
N2	^{222}Rn	surface	0 ± 0	3.15e-08 ± 1.29e-07	2.45e-01	0.00e+00 ± 2.25e-02
VesselCopper	^{60}Co	bulk	0 ± 0	1.91e-11 ± 1.09e-10	2.38e-01	0.00e+00 ± 4.67e-05
StringCopper	^{238}U	bulk	0 ± 0	1.84e-10 ± 8.20e-10	2.25e-01	2.16e-07 ± 5.15e-08
DUPTFE	^{40}K	bulk	0 ± 0	2.73e-08 ± 1.85e-07	1.48e-01	4.65e-06 ± 6.20e-07
StringCopper	^{40}K	surface	0 ± 0	2.17e-09 ± 1.09e-08	1.99e-01	0.00e+00 ± 6.80e-05
M1Seals DS12DS3456	^{40}K	bulk	0 ± 0	1.03e-06 ± 5.02e-06	2.05e-01	4.65e-06 ± 6.20e-07
ColdPlateCopper	^{232}Th	bulk	0 ± 0	5.33e-11 ± 2.30e-10	2.33e-01	4.40e-08 ± 1.00e-09
DUPTFE	^{232}Th	bulk	0 ± 0	1.29e-09 ± 1.07e-08	1.21e-01	1.02e-07 ± 8.00e-09
DUCopper	^{238}U	surface	0 ± 0	1.70e-11 ± 8.93e-11	2.14e-01	2.16e-07 ± 5.15e-08
M1StringSigCables	^{238}U	bulk	0 ± 0	1.55e-08 ± 1.27e-07	1.22e-01	1.11e-04 ± 1.11e-05
DUVespel	^{40}K	bulk	0 ± 0	2.57e-05 ± 2.51e-04	1.03e-01	6.00e-03 ± 9.60e-04
HVForks	^{40}K	bulk	0 ± 0	1.57e-07 ± 1.13e-06	1.40e-01	0.00e+00 ± 6.80e-05
LMFEs	^{238}U	bulk	0 ± 0	2.65e-08 ± 1.63e-07	1.63e-01	1.06e-02 ± 2.62e-04
DUCopper	^{232}Th	bulk	0 ± 0	1.97e-11 ± 8.64e-11	2.02e-01	4.40e-08 ± 1.00e-09
VesselCoatedCopper	^{238}U	bulk	0 ± 0	1.12e-07 ± 5.38e-07	2.10e-01	3.10e-03 ± 7.50e-04
DUPTFE	^{232}Th	surface	0 ± 0	5.30e-10 ± 2.56e-09	2.07e-01	1.02e-07 ± 8.00e-09
StringCopper	^{40}K	bulk	0 ± 0	1.37e-09 ± 6.54e-09	2.11e-01	0.00e+00 ± 6.80e-05
M2StringHVCables	^{238}U	bulk	0 ± 0	1.01e-08 ± 6.61e-08	1.53e-01	8.30e-05 ± 8.30e-06

Component group	**Contaminant**	**Source type**	**Fitted counts**	**Fitted activity density (Bq/kg)**	**Precision**	**Assayed activity density (Bq/kg)**
M1StringHVCables	^{232}Th	bulk	0 ± 0	4.70e-09 ± 2.05e-08	2.29e-01	1.65e-05 ± 1.65e-06
DUCopper	^{40}K	bulk	0 ± 0	2.18e-10 ± 9.07e-10	2.41e-01	0.00e+00 ± 6.80e-05
DUPTFE	^{238}U	surface	0 ± 0	3.72e-10 ± 1.83e-09	2.04e-01	0.00e+00 ± 5.00e-06
M2StringSigCables	^{238}U	bulk	0 ± 0	1.07e-08 ± 5.05e-08	2.14e-01	1.11e-04 ± 1.11e-05
StringCopper	^{232}Th	surface	0 ± 0	2.48e-11 ± 1.47e-10	1.73e-01	4.40e-08 ± 1.00e-09
M1StringHVCables	^{238}U	bulk	0 ± 0	2.62e-09 ± 1.48e-08	1.78e-01	8.30e-05 ± 8.30e-06
LMFEs	^{232}Th	bulk	0 ± 0	8.13e-09 ± 7.91e-08	1.04e-01	7.60e-03 ± 1.17e-03
VesselCopper	^{40}K	bulk	0 ± 0	5.20e-11 ± 2.53e-10	2.06e-01	0.00e+00 ± 6.80e-05
ColdPlateCopper	^{238}U	surface	0 ± 0	9.03e-12 ± 7.23e-11	1.25e-01	2.16e-07 ± 5.15e-08
StringCopper	^{238}U	surface	0 ± 0	1.99e-11 ± 7.64e-11	2.61e-01	2.16e-07 ± 5.15e-08
M1StringSigCables	^{232}Th	bulk	0 ± 0	3.18e-09 ± 1.80e-08	1.77e-01	1.60e-05 ± 1.60e-06
M2StringSigCables	^{232}Th	bulk	0 ± 0	7.05e-09 ± 3.94e-08	1.79e-01	1.60e-05 ± 1.60e-06
DUCoatedCopper	^{232}Th	bulk	0 ± 0	6.50e-08 ± 3.28e-07	1.98e-01	2.16e-03 ± 1.20e-04
StringCopper	^{232}Th	bulk	0 ± 0	1.43e-11 ± 1.14e-10	1.90e-01	4.40e-08 ± 1.00e-09
LMFEs	^{40}K	bulk	0 ± 0	7.87e-08 ± 7.31e-07	1.08e-01	0.00e+00 ± 4.72e-03
M2StringHVCables	^{232}Th	bulk	0 ± 0	2.33e-09 ± 9.71e-09	2.40e-01	1.65e-05 ± 1.65e-06
DUCopper	^{232}Th	surface	0 ± 0	1.01e-12 ± 1.60e-11	2.26e-01	4.40e-08 ± 1.00e-09
M2StringHVCables	^{40}K	bulk	0 ± 0	1.67e-08 ± 1.36e-07	1.22e-01	0.00e+00 ± 7.30e-02
M2StringSigCables	^{40}K	bulk	0 ± 0	2.60e-08 ± 1.68e-07	1.56e-01	0.00e+00 ± 7.30e-02
EnrGe	^{68}Ge	bulk	0 ± 0	6.00e-13 ± 3.85e-11	1.82e-01	N/A
ColdPlateCopper	^{232}Th	surface	0 ± 0	1.24e-12 ± 7.12e-12	1.75e-01	4.40e-08 ± 1.00e-09
StringCoatedCopper	^{40}K	bulk	0 ± 0	2.33e-08 ± 1.86e-07	1.29e-01	2.86e-02 ± 2.67e-03

Table C.3: Comparison of effect of analysis cuts for fitted model. Only enriched detectors are included in this table, and only data sets 1-6a are included. This roughly matches the data set analyzed in [109]. The PDFs are listed in precision order, with the most precise estimates appearing first. In this table the ROI refers to the 360 keV window extending from 1950 to 2350 keV (with 4 10 keV excisions) that is used to estimate the background rate in [109] and [45].

Component group	**Contaminant**	**Source type**	**Fitted counts**	**Fitted counts in ROI**	**After granularity cut**	**After granularity and PSA cuts**
EnrGe	$2\nu\beta\beta$	bulk	31227 ± 979	0 ± 0	0 ± 0	0 ± 0
NatGe	^{3}H	bulk	0 ± 0	0 ± 0	0 ± 0	0 ± 0
RadShieldPb	^{210}Pb	pbbrem	4186 ± 200	0 ± 0	0 ± 0	0 ± 0
EnrGe	^{3}H	bulk	1825 ± 128	0 ± 0	0 ± 0	0 ± 0
DUPTFE	^{210}Pb	surface	1574 ± 145	1 ± 0	1 ± 0	1 ± 0
NatGe	$2\nu\beta\beta$	bulk	4 ± 0	0 ± 0	0 ± 0	0 ± 0
NatGe	^{57}Co	bulk	3 ± 0	0 ± 0	0 ± 0	0 ± 0
RadShieldCuOuter	^{54}Mn	bulk	114 ± 26	0 ± 0	0 ± 0	0 ± 0
NatGe	^{68}Ge	bulk	529 ± 130	0 ± 0	0 ± 0	0 ± 0
EnrGe	^{65}Zn	bulk	101 ± 26	0 ± 0	0 ± 0	0 ± 0
M1CPCables	^{232}Th	bulk	3459 ± 1050	53 ± 16	32 ± 10	8 ± 2

Component group	**Contaminant**	**Source type**	**Fitted counts**	**Fitted counts in ROI**	**Fitted counts in ROI after granularity cut**	**Fitted counts in ROI after granularity and PSA cuts**
ThermosyphonAndShieldCoatedCopper	^{232}Th	bulk	747 ± 236	12 ± 4	8 ± 3	2 ± 1
ThermosyphonAndShieldCopper	^{40}K	surface	3769 ± 1264	0 ± 0	0 ± 0	0 ± 0
NatGe	^{65}Zn	bulk	29 ± 13	0 ± 0	0 ± 0	0 ± 0
RadShieldCuOuter	^{60}Co	bulk	1902 ± 873	0 ± 0	0 ± 0	0 ± 0
M1Seals DS0	^{238}U	bulk	0 ± 0	0 ± 0	0 ± 0	0 ± 0
Connectors	^{232}Th	bulk	1368 ± 751	23 ± 13	15 ± 8	4 ± 2
VesselCopper	^{232}Th	bulk	1125 ± 714	17 ± 11	10 ± 6	3 ± 2
M2StringSigCables	^{60}Co	bulk	303 ± 193	1 ± 1	0 ± 0	0 ± 0
VesselCopper	^{238}U	bulk	2723 ± 1761	10 ± 6	9 ± 6	1 ± 1
M1CrossarmCables	^{232}Th	bulk	1314 ± 918	22 ± 15	14 ± 10	3 ± 2
LMFEs	^{60}Co	bulk	425 ± 353	3 ± 2	2 ± 2	0 ± 0
ThermosyphonAndShieldCopper	^{238}U	bulk	1779 ± 1589	7 ± 6	6 ± 5	1 ± 1
M2Seals	^{232}Th	bulk	244 ± 219	4 ± 4	2 ± 2	1 ± 1
M1StringSigCables	^{60}Co	bulk	550 ± 502	1 ± 1	1 ± 1	0 ± 0
M1CPCables	^{238}U	bulk	506 ± 518	2 ± 2	2 ± 2	0 ± 0
M2Seals	^{238}U	bulk	122 ± 135	0 ± 0	0 ± 0	0 ± 0
ThermosyphonAndShieldCoatedCopper	^{238}U	bulk	132 ± 160	0 ± 0	0 ± 0	0 ± 0

Component group	**Contaminant**	**Source type**	**Fitted counts**	**Fitted counts in ROI**	**Fitted counts in ROI after granularity cut**	**Fitted counts in ROI after granularity and PSA cuts**
ThermosyphonAndShieldCoatedCopper	^{40}K	bulk	98 ± 125	0 ± 0	0 ± 0	0 ± 0
M1CPCables	^{60}Co	bulk	392 ± 510	0 ± 0	0 ± 0	0 ± 0
RadShieldPb	^{238}U	bulk	423 ± 635	2 ± 3	2 ± 3	0 ± 0
M2CPCables	^{40}K	bulk	18 ± 30	0 ± 0	0 ± 0	0 ± 0
M1Seals DS0	^{232}Th	bulk	0 ± 0	0 ± 0	0 ± 0	0 ± 0
M2CrossarmCables	^{40}K	bulk	22 ± 42	0 ± 0	0 ± 0	0 ± 0
M2StringHVCables	^{60}Co	bulk	75 ± 145	0 ± 0	0 ± 0	0 ± 0
M2CrossarmCables	^{232}Th	bulk	67 ± 133	1 ± 2	1 ± 2	0 ± 0
M1Seals DS0	^{40}K	bulk	0 ± 0	0 ± 0	0 ± 0	0 ± 0
M1StringHVCables	^{60}Co	bulk	178 ± 395	0 ± 0	0 ± 0	0 ± 0
ColdPlateCopper	^{40}K	bulk	67 ± 168	0 ± 0	0 ± 0	0 ± 0
M1StringHVCables	^{40}K	bulk	56 ± 156	0 ± 0	0 ± 0	0 ± 0
RadShieldPb	^{40}K	bulk	161 ± 458	0 ± 0	0 ± 0	0 ± 0
ThermosyphonAndShieldCopper	^{238}U	surface	142 ± 450	0 ± 0	0 ± 0	0 ± 0
M2CrossarmCables	^{238}U	bulk	14 ± 46	0 ± 0	0 ± 0	0 ± 0
DUCopper	^{40}K	surface	205 ± 678	0 ± 0	0 ± 0	0 ± 0
VesselCoatedCopper	^{40}K	bulk	7 ± 26	0 ± 0	0 ± 0	0 ± 0
StringCopper	^{238}U	surface	0 ± 0	0 ± 0	0 ± 0	0 ± 0
ThermosyphonAndShieldCopper	^{40}K	bulk	0 ± 0	0 ± 0	0 ± 0	0 ± 0

Component group	**Contaminant**	**Source type**	**Fitted counts**	**Fitted counts in ROI**	**Fitted counts in ROI after granularity cut**	**Fitted counts in ROI after granularity and PSA cuts**
RadShieldPb	^{232}Th	bulk	34 ± 139	1 ± 4	1 ± 4	0 ± 0
M1CrossarmCables	^{238}U	bulk	0 ± 0	0 ± 0	0 ± 0	0 ± 0
N2	^{222}Rn	surface	0 ± 0	0 ± 0	0 ± 0	0 ± 0
DUCopper	^{40}K	bulk	0 ± 0	0 ± 0	0 ± 0	0 ± 0
M2StringHVCables	^{232}Th	bulk	0 ± 0	0 ± 0	0 ± 0	0 ± 0
M1CrossarmCables	^{40}K	bulk	0 ± 0	0 ± 0	0 ± 0	0 ± 0
ColdPlateCopper	^{232}Th	bulk	0 ± 0	0 ± 0	0 ± 0	0 ± 0
M1StringHVCables	^{232}Th	bulk	0 ± 0	0 ± 0	0 ± 0	0 ± 0
DUCopper	^{232}Th	bulk	0 ± 0	0 ± 0	0 ± 0	0 ± 0
StringCopper	^{238}U	bulk	0 ± 0	0 ± 0	0 ± 0	0 ± 0
ColdPlateCopper	^{40}K	surface	7 ± 32	0 ± 0	0 ± 0	0 ± 0
ThermosyphonAndShieldCopper	^{232}Th	surface	0 ± 0	0 ± 0	0 ± 0	0 ± 0
Connectors	^{238}U	bulk	8 ± 37	0 ± 0	0 ± 0	0 ± 0
ThermosyphonAndShieldCopper	^{60}Co	bulk	0 ± 0	0 ± 0	0 ± 0	0 ± 0
M2StringSigCables	^{238}U	bulk	0 ± 0	0 ± 0	0 ± 0	0 ± 0
StringCopper	^{40}K	bulk	0 ± 0	0 ± 0	0 ± 0	0 ± 0
VesselCoatedCopper	^{238}U	bulk	0 ± 0	0 ± 0	0 ± 0	0 ± 0
DUPTFE	^{232}Th	surface	0 ± 0	0 ± 0	0 ± 0	0 ± 0
DUVespel	^{238}U	bulk	68 ± 329	0 ± 0	0 ± 0	0 ± 0
VesselCopper	^{40}K	bulk	0 ± 0	0 ± 0	0 ± 0	0 ± 0

Component group	**Contaminant**	**Source type**	**Fitted counts**	**Fitted counts in ROI**	**Fitted counts in ROI after granularity cut**	**Fitted counts in ROI after granularity and PSA cuts**
M1Seals DS12 DS3456	^{40}K	bulk	0 ± 0	0 ± 0	0 ± 0	0 ± 0
DUPTFE	^{238}U	surface	0 ± 0	0 ± 0	0 ± 0	0 ± 0
StringCopper	^{40}K	surface	0 ± 0	0 ± 0	0 ± 0	0 ± 0
DUCoatedCopper	^{232}Th	bulk	0 ± 0	0 ± 0	0 ± 0	0 ± 0
Connectors	^{40}K	bulk	20 ± 102	0 ± 0	0 ± 0	0 ± 0
RadShieldCuOuter	^{238}U	bulk	20 ± 102	0 ± 0	0 ± 0	0 ± 0
StringCoatedCopper	^{232}Th	bulk	0 ± 0	0 ± 0	0 ± 0	0 ± 0
M1Seals DS12 DS3456	^{232}Th	bulk	0 ± 0	0 ± 0	0 ± 0	0 ± 0
DUCopper	^{238}U	surface	0 ± 0	0 ± 0	0 ± 0	0 ± 0
HVForks	^{60}Co	bulk	48 ± 254	0 ± 0	0 ± 0	0 ± 0
M2StringSigCables	^{232}Th	bulk	0 ± 0	0 ± 0	0 ± 0	0 ± 0
ThermosyphonAnd-ShieldVespel	^{238}U	bulk	0 ± 0	0 ± 0	0 ± 0	0 ± 0
M1StringHVCables	^{238}U	bulk	0 ± 0	0 ± 0	0 ± 0	0 ± 0
M2CPCables	^{232}Th	bulk	5 ± 28	0 ± 0	0 ± 0	0 ± 0
M1StringSigCables	^{232}Th	bulk	0 ± 0	0 ± 0	0 ± 0	0 ± 0
DUCoatedCopper	^{40}K	bulk	41 ± 232	0 ± 0	0 ± 0	0 ± 0
VesselCopper	^{60}Co	bulk	0 ± 0	0 ± 0	0 ± 0	0 ± 0
ColdPlateCopper	^{232}Th	surface	0 ± 0	0 ± 0	0 ± 0	0 ± 0
ColdPlateCopper	^{238}U	bulk	8 ± 47	0 ± 0	0 ± 0	0 ± 0

Component group	**Contaminant**	**Source type**	**Fitted counts**	**Fitted counts in ROI**	**Fitted counts in ROI after granularity cut**	**Fitted counts in ROI after granularity and PSA cuts**
StringCopper	^{232}Th	surface	0 ± 0	0 ± 0	0 ± 0	0 ± 0
ThermosyphonAndShieldCopper	^{232}Th	bulk	18 ± 107	0 ± 0	0 ± 0	0 ± 0
DUPTFE	^{40}K	surface	21 ± 126	0 ± 0	0 ± 0	0 ± 0
DUPTFE	^{238}U	bulk	0 ± 0	0 ± 0	0 ± 0	0 ± 0
VesselCoatedCopper	^{232}Th	bulk	10 ± 61	0 ± 0	0 ± 0	0 ± 0
LMFEs	^{238}U	bulk	0 ± 0	0 ± 0	0 ± 0	0 ± 0
M2CPCables	^{238}U	bulk	4 ± 25	0 ± 0	0 ± 0	0 ± 0
M2StringSigCables	^{40}K	bulk	0 ± 0	0 ± 0	0 ± 0	0 ± 0
M2StringHVCables	^{238}U	bulk	0 ± 0	0 ± 0	0 ± 0	0 ± 0
DUCoatedCopper	^{238}U	bulk	15 ± 99	0 ± 0	0 ± 0	0 ± 0
M1CPCables	^{40}K	bulk	8 ± 53	0 ± 0	0 ± 0	0 ± 0
DUPTFE	^{40}K	bulk	0 ± 0	0 ± 0	0 ± 0	0 ± 0
N2	^{222}Rn	bulk	31 ± 215	0 ± 0	0 ± 0	0 ± 0
M1StringSigCables	^{40}K	bulk	0 ± 0	0 ± 0	0 ± 0	0 ± 0
HVForks	^{238}U	bulk	43 ± 307	0 ± 0	0 ± 0	0 ± 0
HVForks	^{40}K	bulk	0 ± 0	0 ± 0	0 ± 0	0 ± 0
M1Seals DS12 DS3456	^{238}U	bulk	23 ± 173	0 ± 0	0 ± 0	0 ± 0
RadShieldCuOuter	^{40}K	bulk	14 ± 107	0 ± 0	0 ± 0	0 ± 0
StringCopper	^{232}Th	bulk	0 ± 0	0 ± 0	0 ± 0	0 ± 0
StringCoatedCopper	^{40}K	bulk	0 ± 0	0 ± 0	0 ± 0	0 ± 0

Component group	**Contaminant**	**Source type**	**Fitted counts**	**Fitted counts in ROI**	**Fitted counts in ROI after granularity cut**	**Fitted counts in ROI after granularity and PSA cuts**
ColdPlateCopper	^{238}U	surface	0 ± 0	0 ± 0	0 ± 0	0 ± 0
M2StringHVCables	^{40}K	bulk	0 ± 0	0 ± 0	0 ± 0	0 ± 0
M1StringSigCables	^{238}U	bulk	0 ± 0	0 ± 0	0 ± 0	0 ± 0
DUPTFE	^{232}Th	bulk	0 ± 0	0 ± 0	0 ± 0	0 ± 0
DUCopper	^{238}U	bulk	0 ± 0	0 ± 0	0 ± 0	0 ± 0
LMFEs	^{40}K	bulk	0 ± 0	0 ± 0	0 ± 0	0 ± 0
ThermosyphonAndShieldVespel	^{40}K	bulk	1 ± 10	0 ± 0	0 ± 0	0 ± 0
ThermosyphonAndShieldVespel	^{232}Th	bulk	2 ± 19	0 ± 0	0 ± 0	0 ± 0
LMFEs	^{232}Th	bulk	0 ± 0	0 ± 0	0 ± 0	0 ± 0
StringCoatedCopper	^{238}U	bulk	9 ± 88	0 ± 0	0 ± 0	0 ± 0
M1CrossarmCables	^{60}Co	bulk	9 ± 88	0 ± 0	0 ± 0	0 ± 0
M2CPCables	^{60}Co	bulk	1 ± 10	0 ± 0	0 ± 0	0 ± 0
RadShieldCuOuter	^{232}Th	bulk	10 ± 98	0 ± 0	0 ± 0	0 ± 0
DUVespel	^{40}K	bulk	0 ± 0	0 ± 0	0 ± 0	0 ± 0
M2CrossarmCables	^{60}Co	bulk	1 ± 10	0 ± 0	0 ± 0	0 ± 0
DUCopper	^{232}Th	surface	0 ± 0	0 ± 0	0 ± 0	0 ± 0
EnrGe	^{68}Ge	bulk	0 ± 0	0 ± 0	0 ± 0	0 ± 0

Appendix D

PLOTS OF RESULTS OF FITS TO TOY MC AND EXPERIMENTAL DATA

The figures included here represent a hopefully comprehensive look at the model fitted to the energy spectrum. They are grouped in a few different ways:

- **Data set** Data set 0, and data sets 1-6a
- **Module** Module 1 vs module 2
- **Type of crystal** Enriched germanium vs. natural germanium
- **Analysis cut** No analysis cuts applied (no_cuts), granularity cut only applied (Gran), and both granularity and multi-site PSA (A vs. E/dT heuristic) applied (Gran_Psa)
- **Energy range** Full spectrum (0-3500 keV), region of interest (1750-2650 keV), and low energy (0-250 keV)

The top panel of each figure shows the energy spectrum as a black histogram on a log scale with the fitted model overlaid in colored lines. The middle panel is the same as the top panel but on a linear y-scale. The bottom 3 panels show the residuals for each bin with errors, the normalized residuals (or pulls), and a histogram of the pulls with a standard normal distribution overlaid, going left to right respectively. A fitted model with correctly estimated errors will have a pull distribution that is distributed according to a standard normal distribution.

Captions are omitted to keep entries for these plots from appearing on the list of figures, since they would be too long. The figure titles indicate what is in each one.

DS0, no_cuts, M1_Nat+M1_Enr

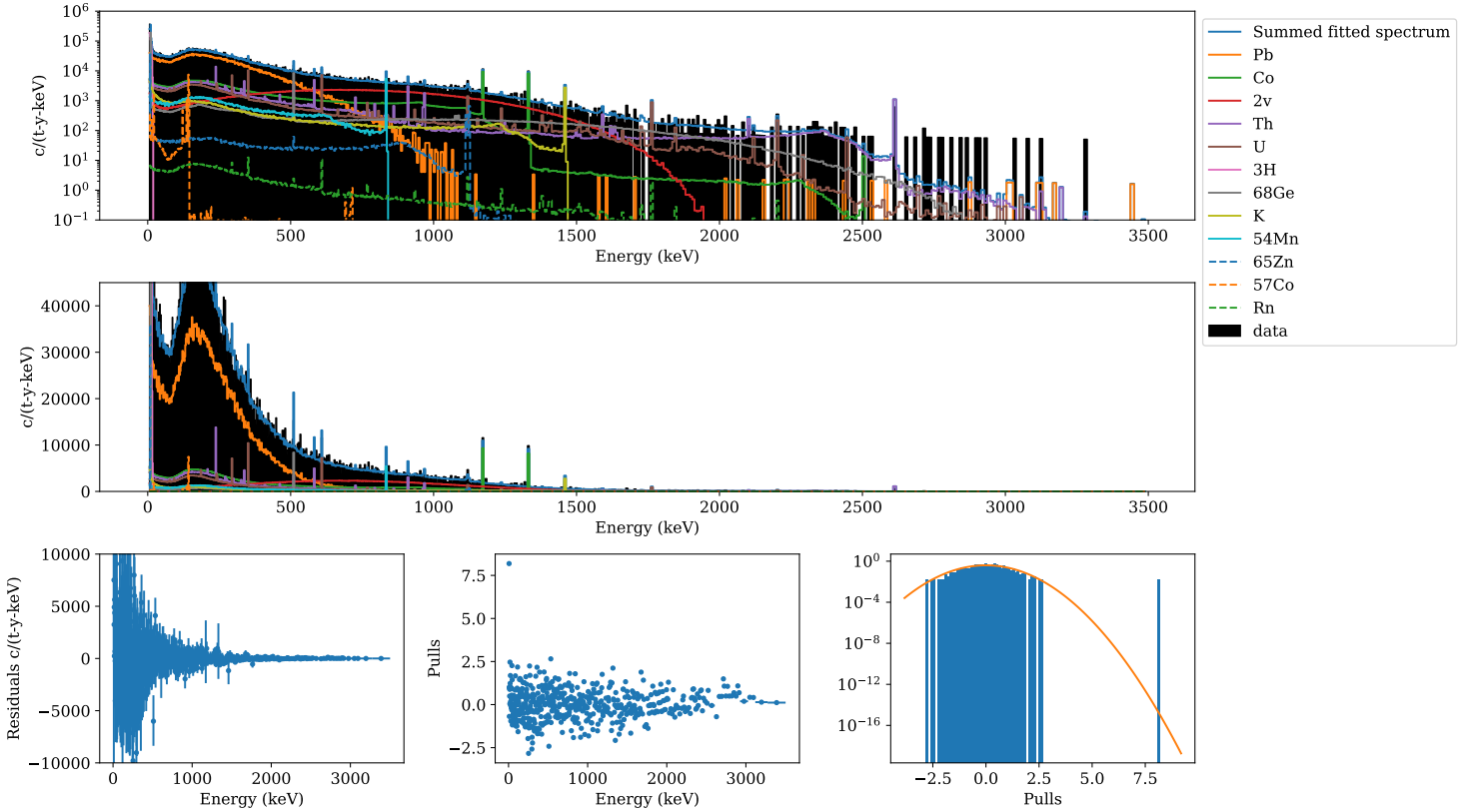

DS0, no_cuts, M1_Nat+M1_Enr

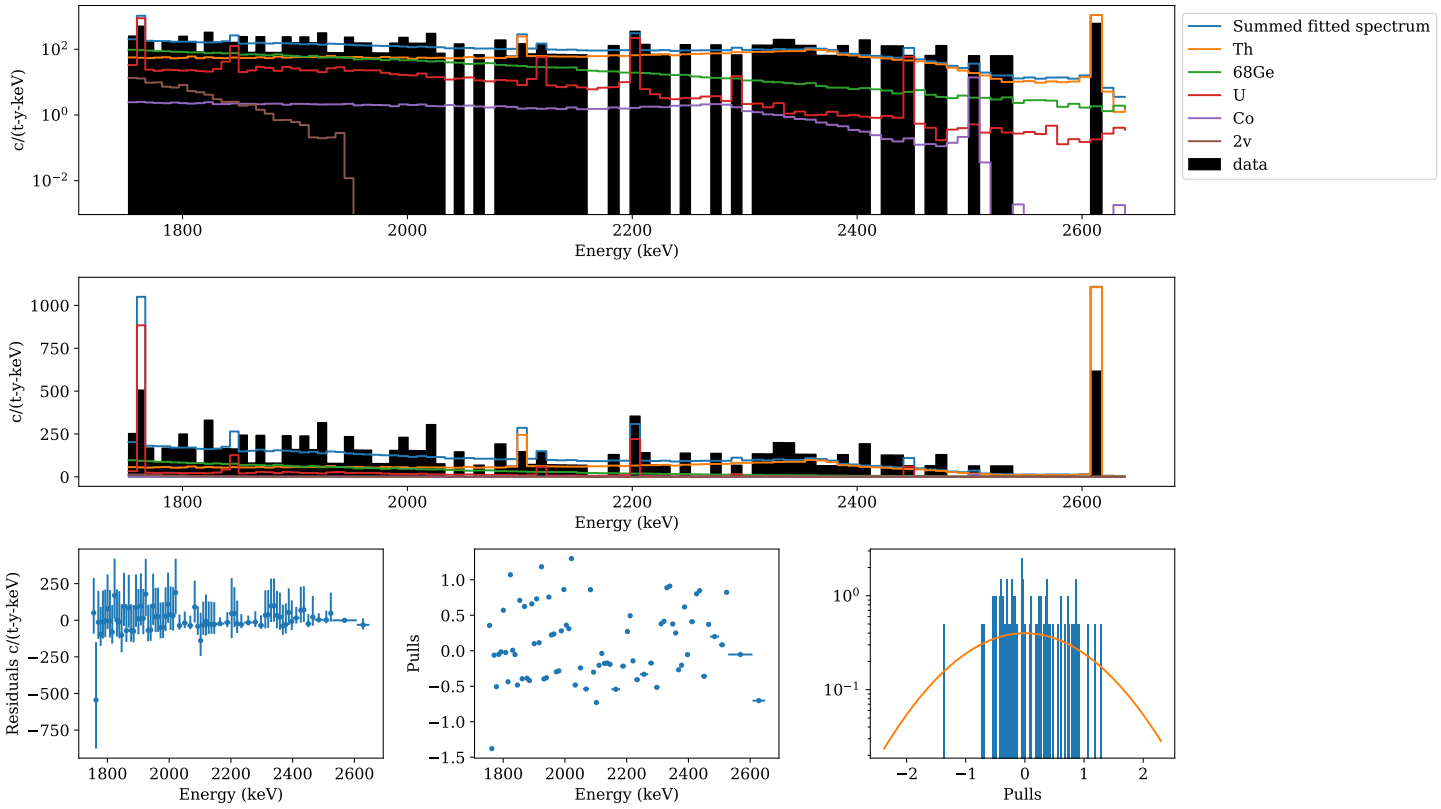

DS0, no_cuts, M1_Nat+M1_Enr

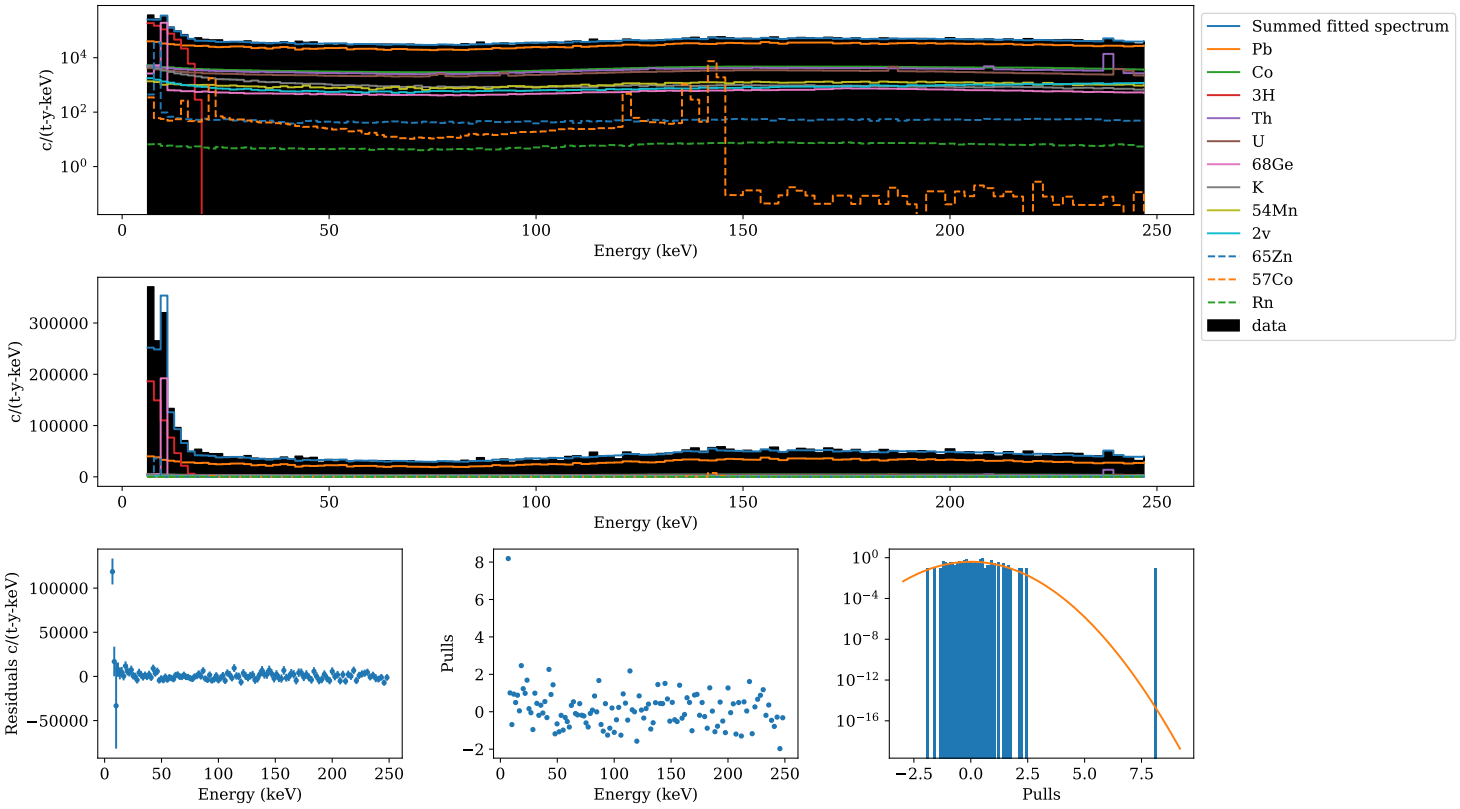

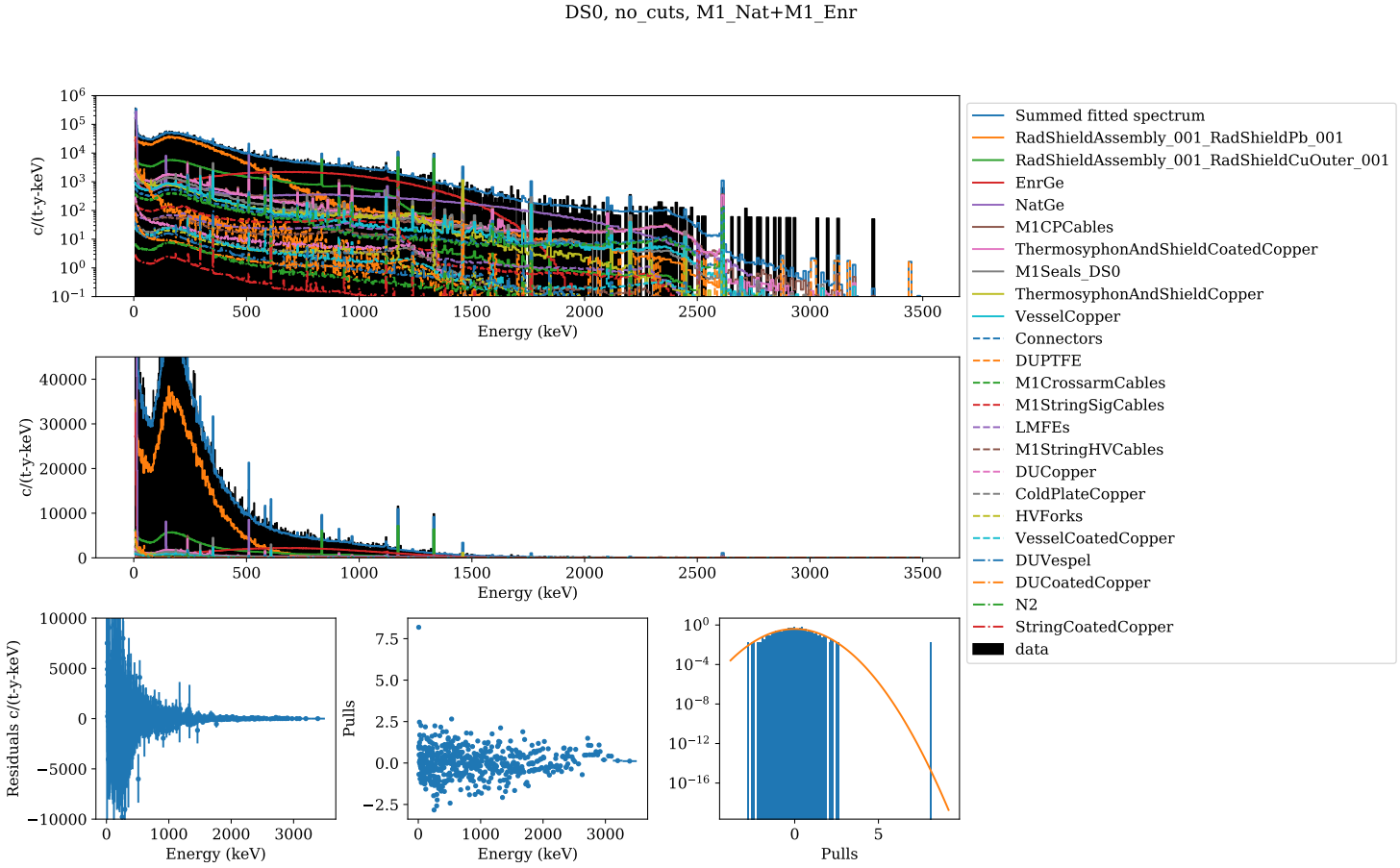
DS0, no_cuts, M1_Nat+M1_Enr
c/(t-y-keV)
Energy (keV)
Residuals c/(t-y-keV)
Pulls
Summed fitted spectrum
RadShieldAssembly_001_RadShieldPb_001
RadShieldAssembly_001_RadShieldCuOuter_001
EnrGe
NatGe
M1CPCables
ThermosyphonAndShieldCoatedCopper
M1Seals_DS0
ThermosyphonAndShieldCopper
VesselCopper
Connectors
DUPTFE
M1CrossarmCables
M1StringSigCables
LMFEs
M1StringHVCables
DUCopper
ColdPlateCopper
HVForks
VesselCoatedCopper
DUVespel
DUCoatedCopper
N2
StringCoatedCopper
data

DS0, no_cuts, M1_Nat+M1_Enr

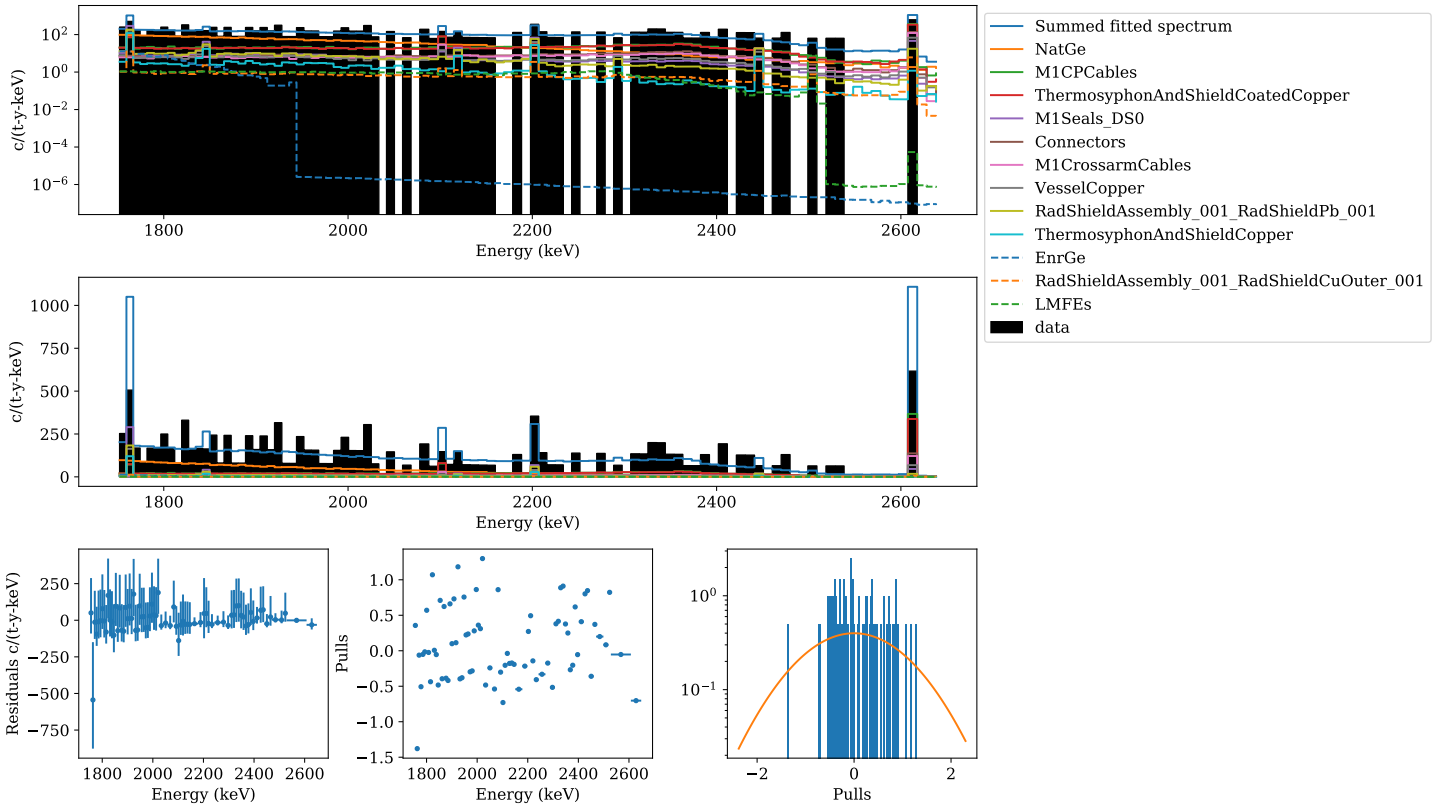

DS0, no_cuts, M1_Nat+M1_Enr

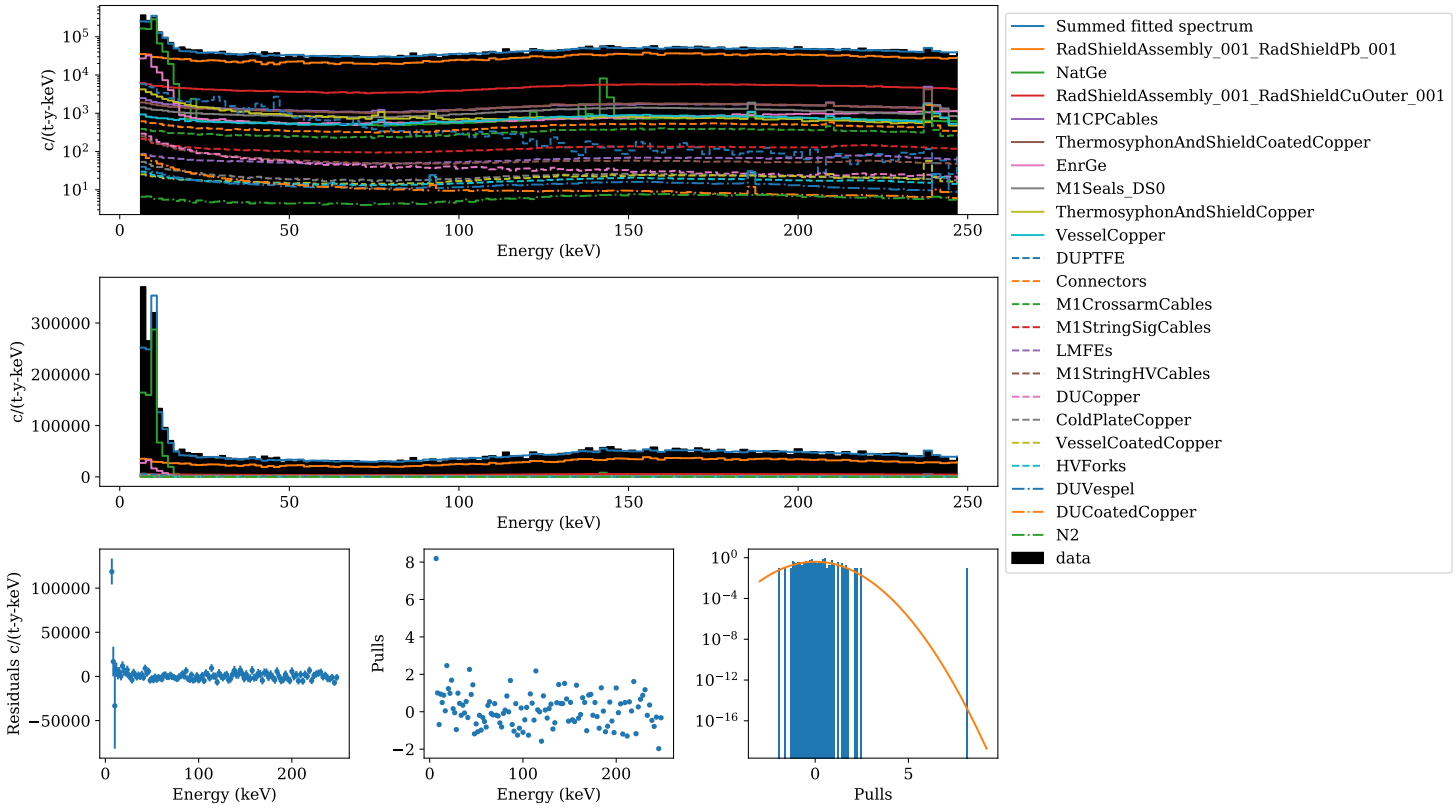

DS12+DS3456, no_cuts, M1_Nat+M1_Enr

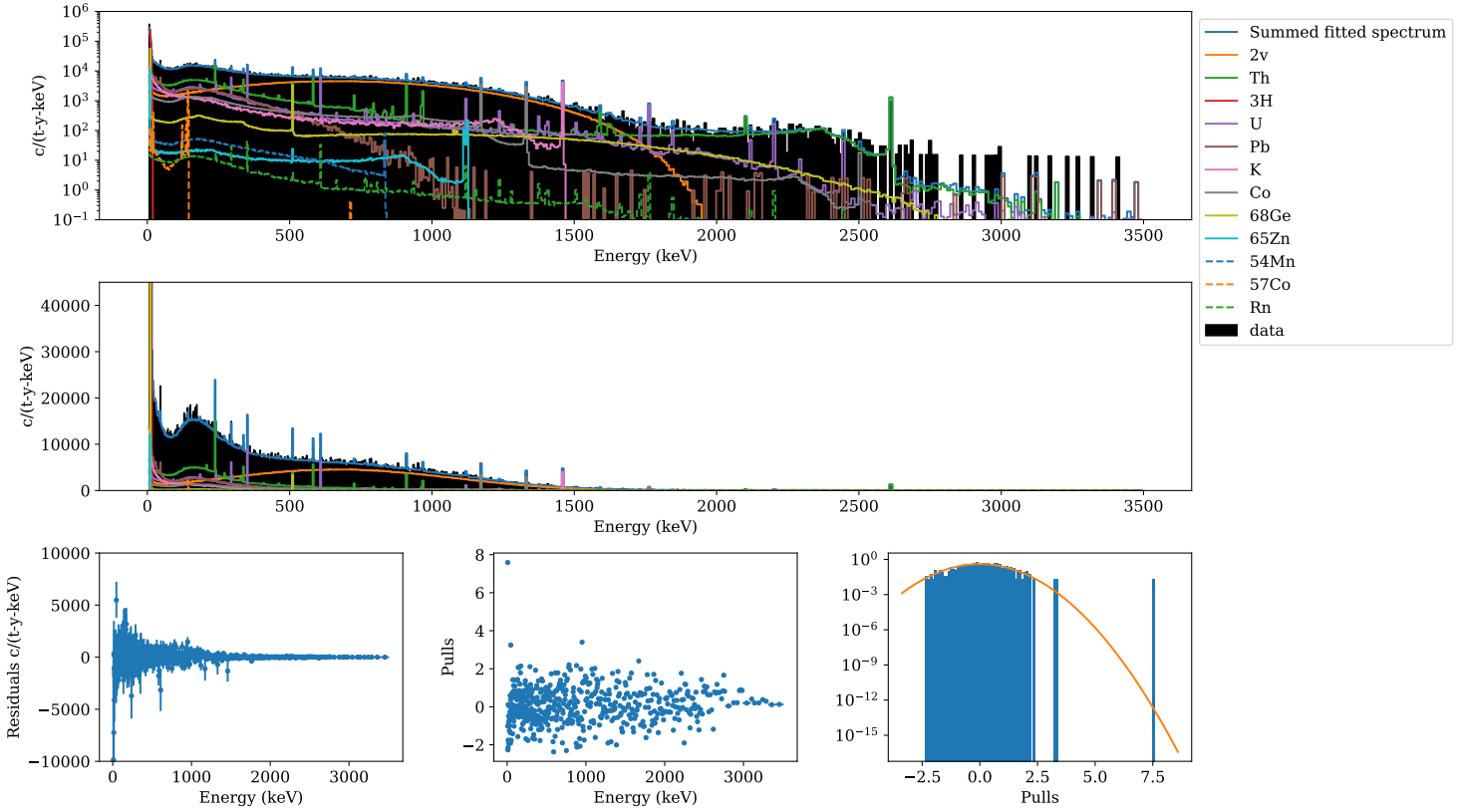

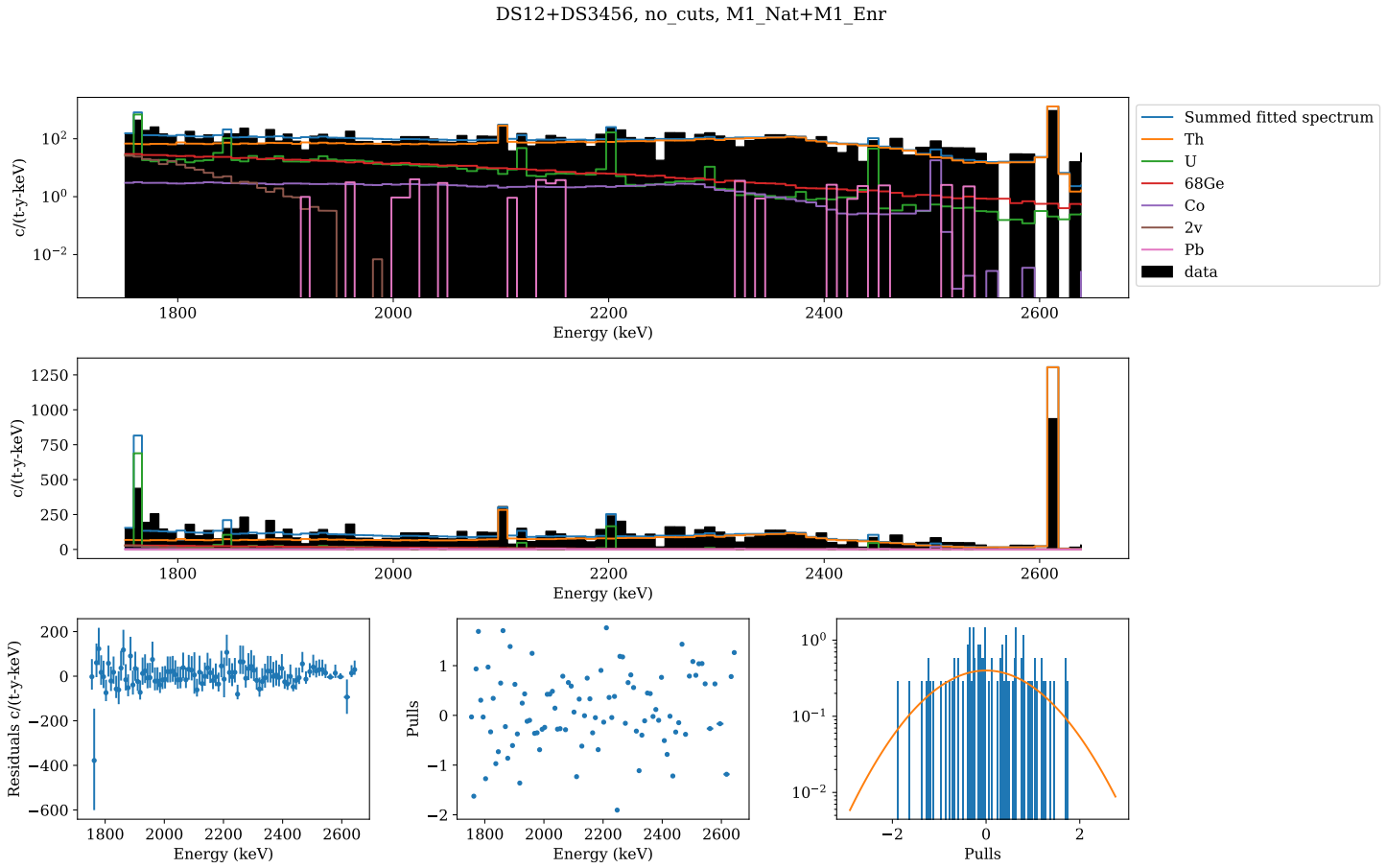
DS12+DS3456, no_cuts, M1_Nat+M1_Enr
Summed fitted spectrum
Th
U
68Ge
Co
2v
Pb
data
c/(t-y-keV)
Energy (keV)
Residuals c/(t-y-keV)
Pulls

DS12+DS3456, no_cuts, M1_Nat+M1_Enr

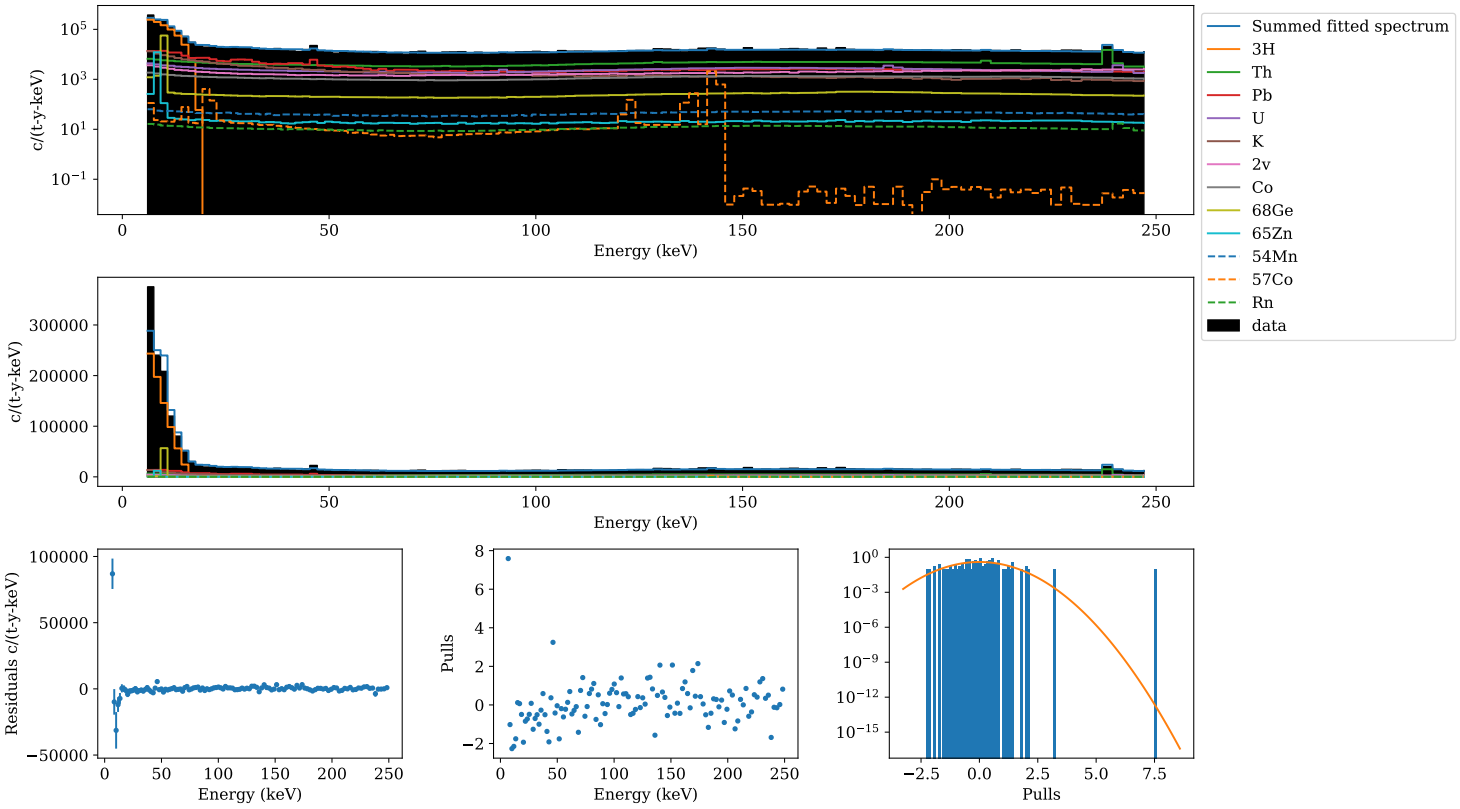

DS12+DS3456, no_cuts, M1_Nat+M1_Enr

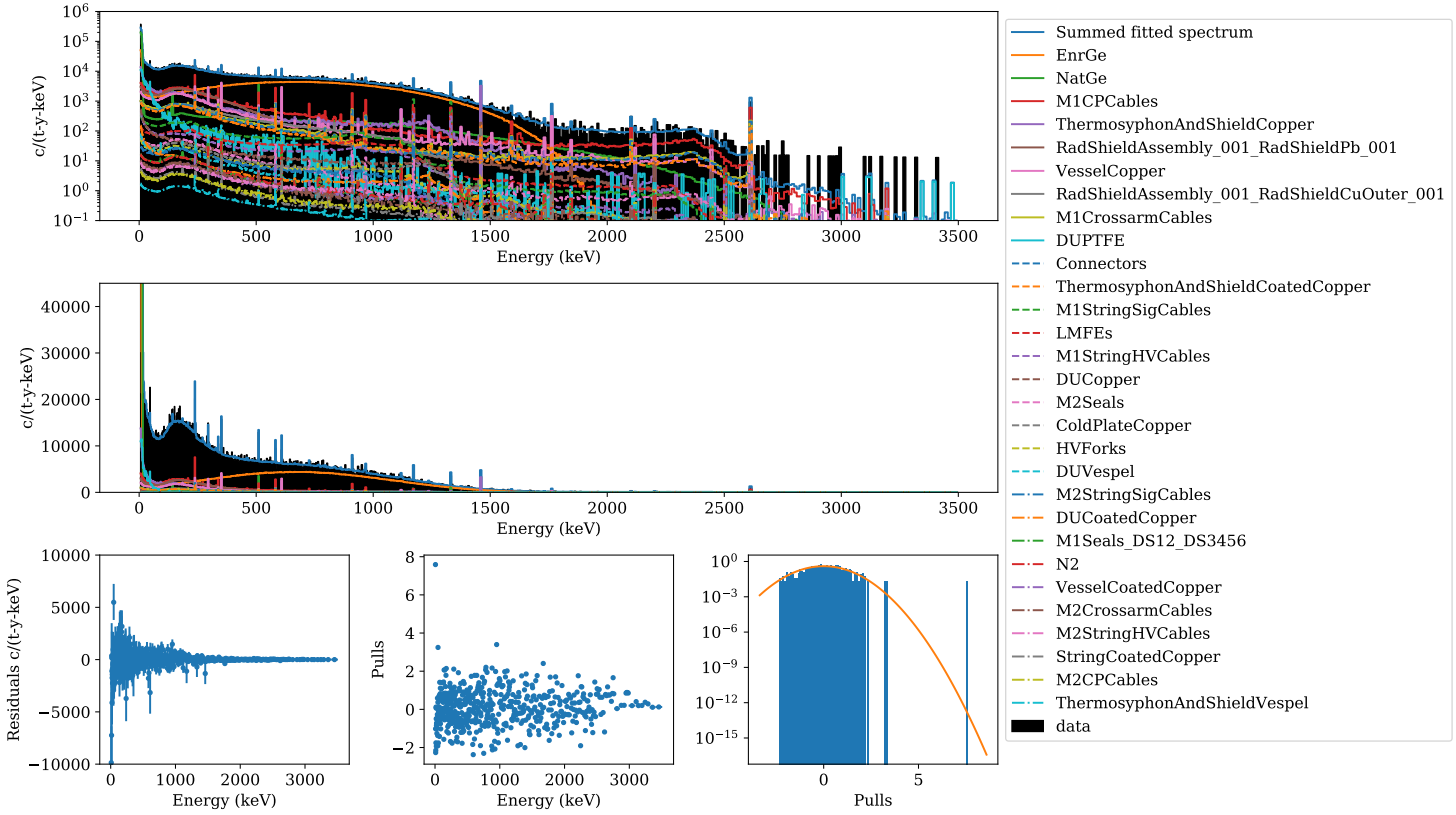

DS12+DS3456, no_cuts, M1_Nat+M1_Enr

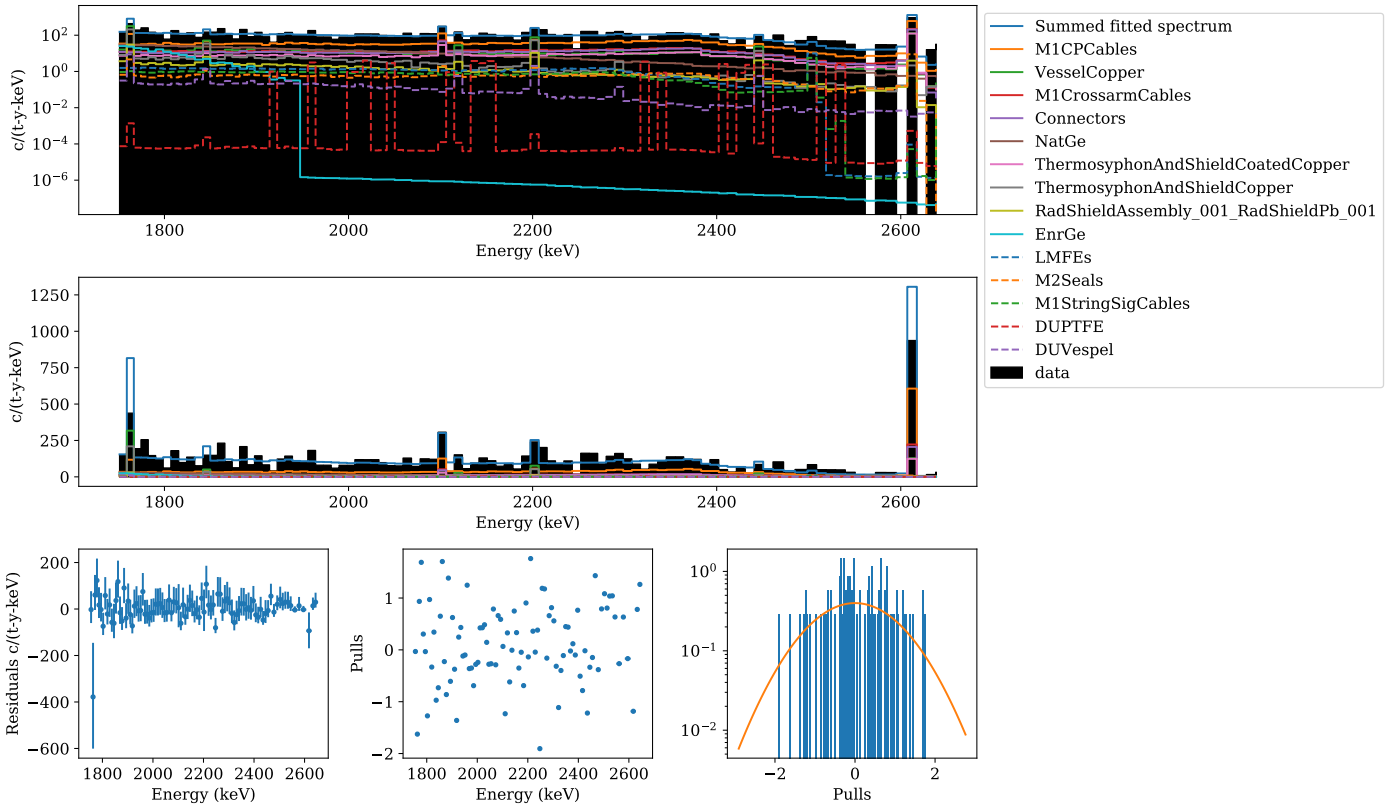

DS12+DS3456, no_cuts, M1_Nat+M1_Enr

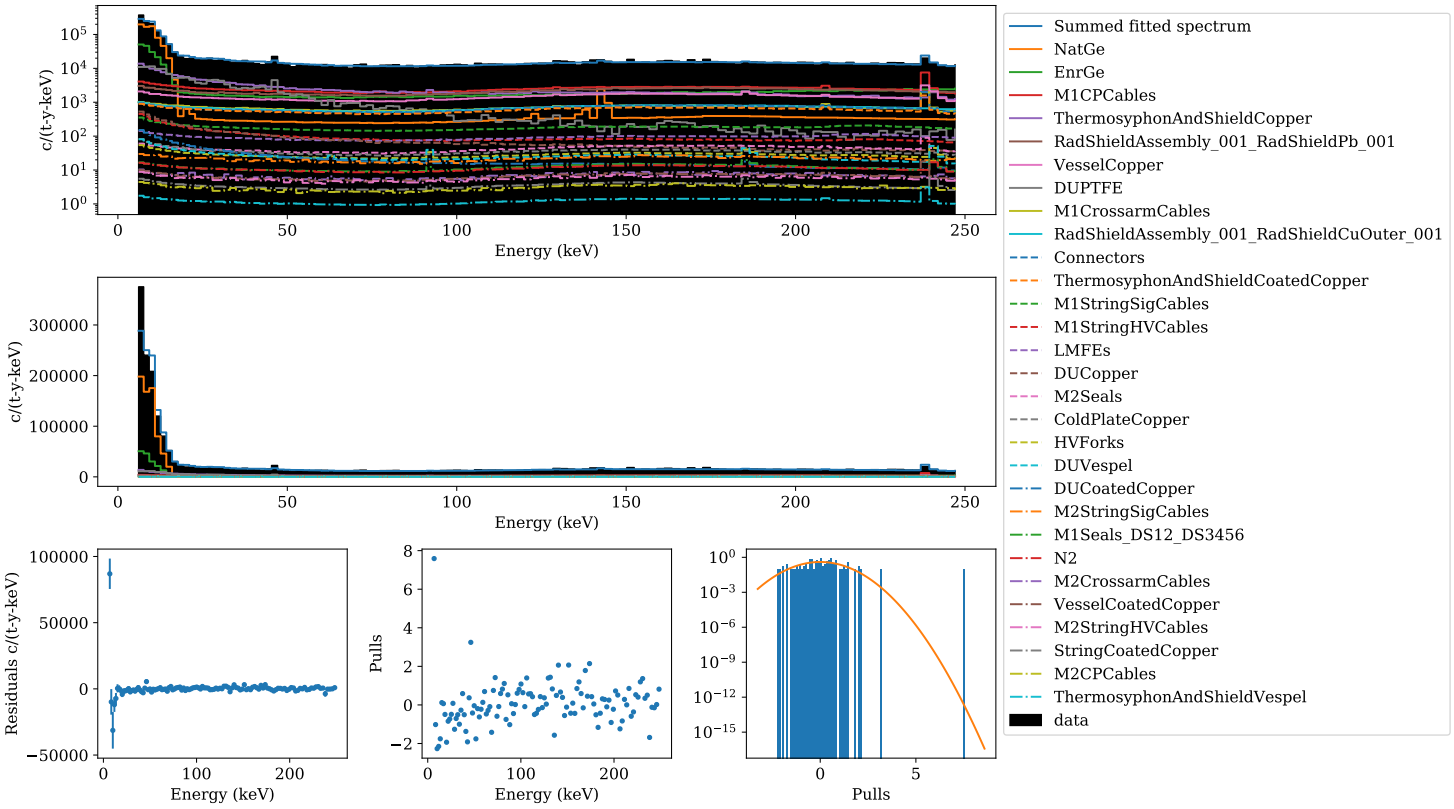

DS12+DS3456, no_cuts, M2_Nat+M2_Enr

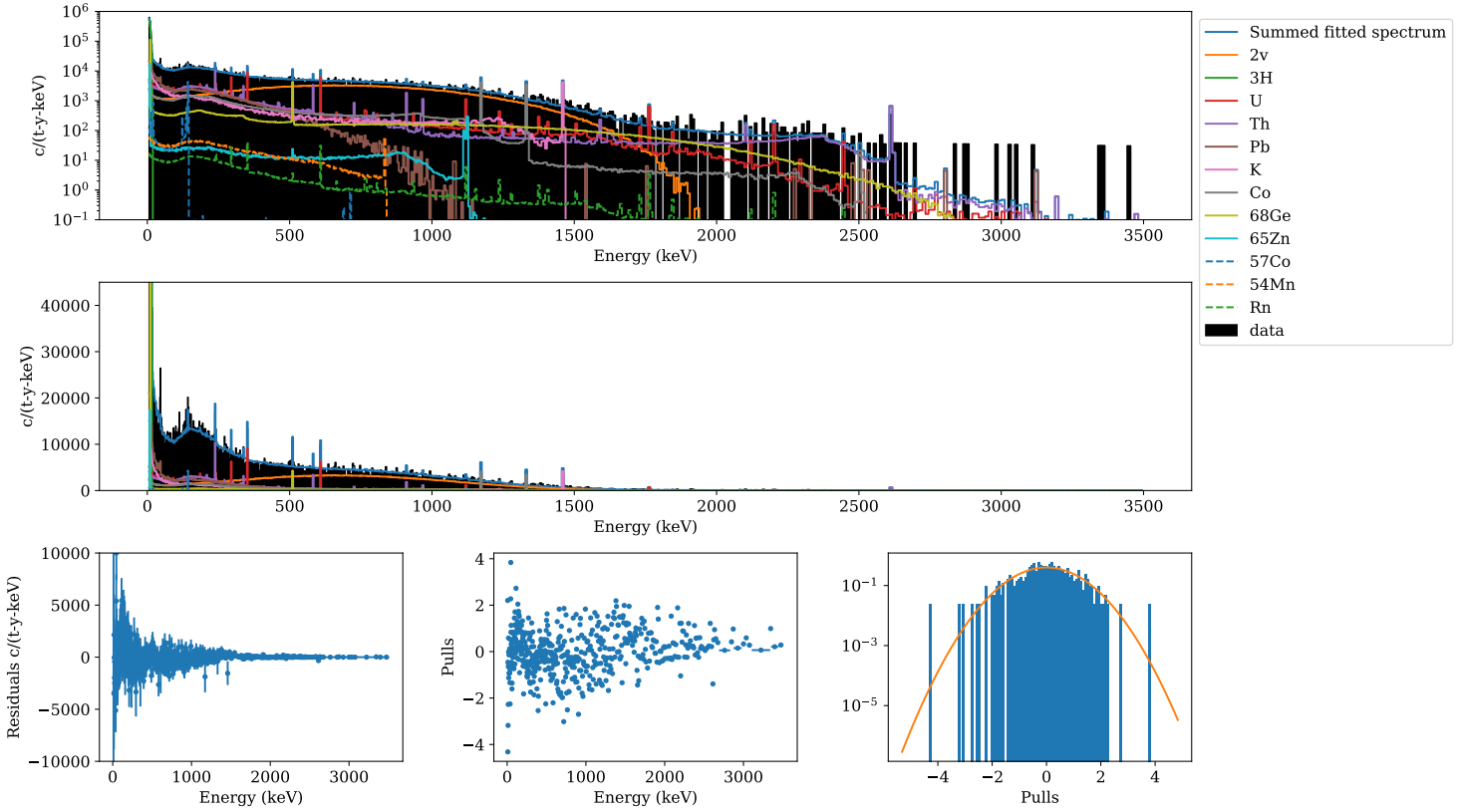

DS12+DS3456, no_cuts, M2_Nat+M2_Enr

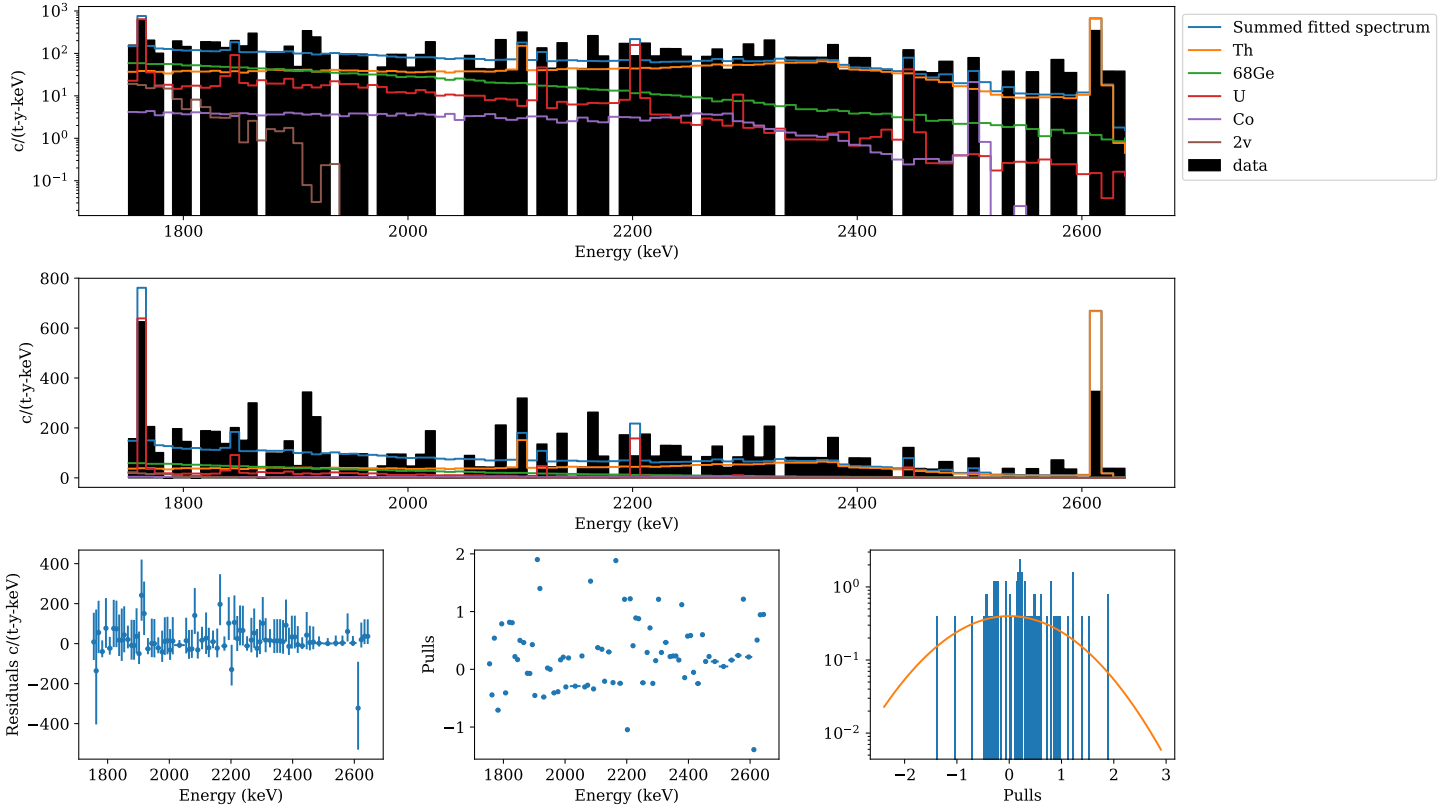

DS12+DS3456, no_cuts, M2_Nat+M2_Enr

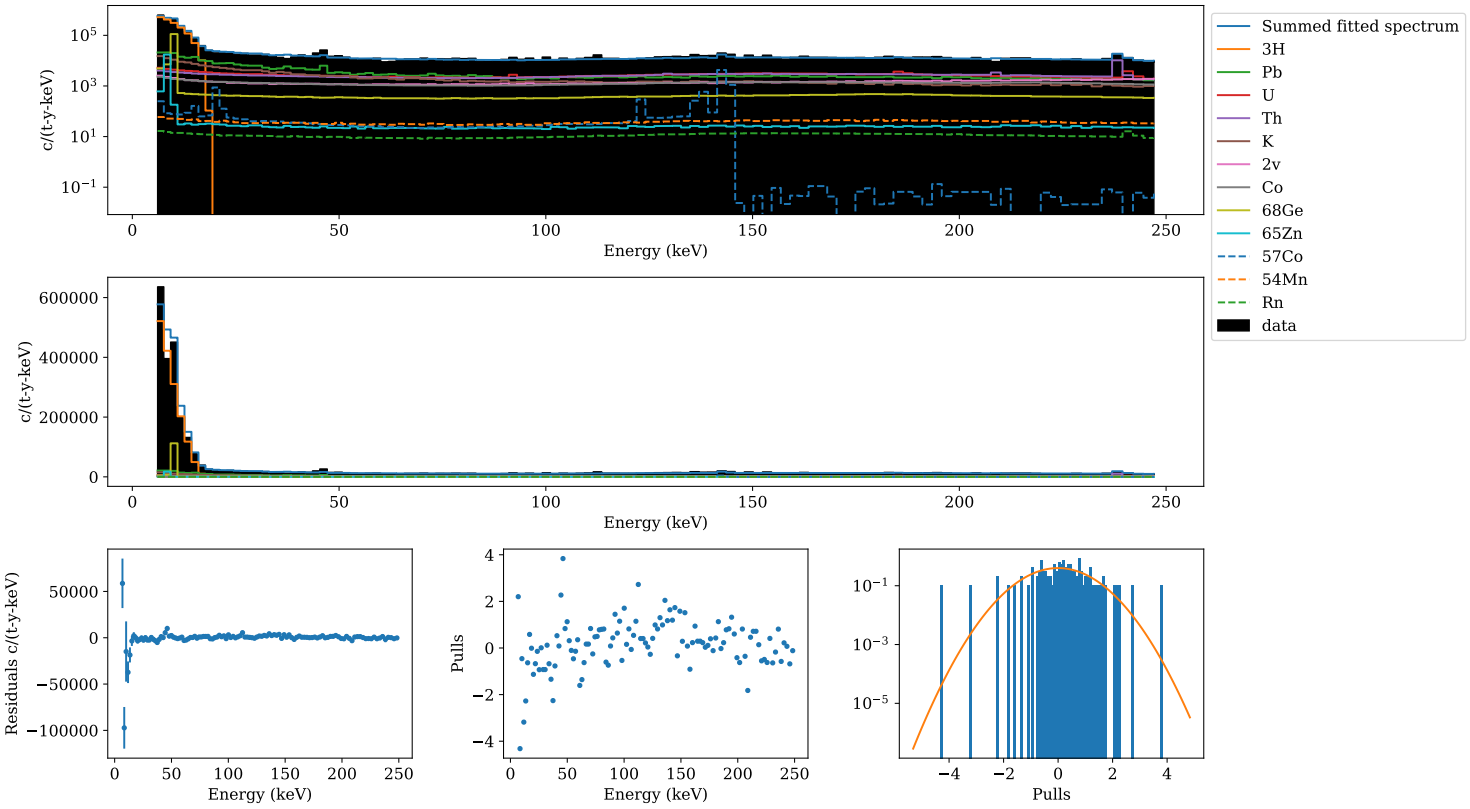

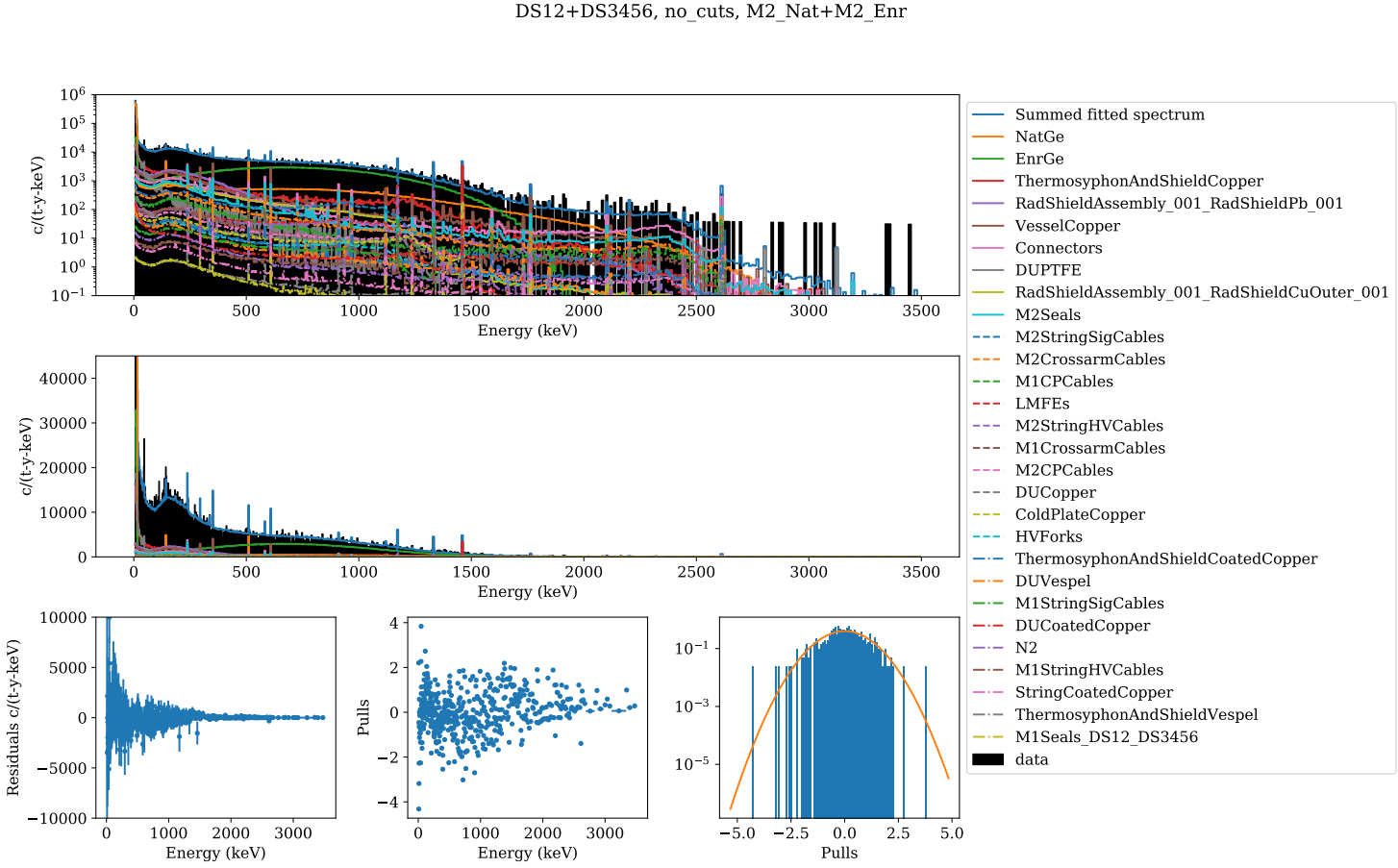
DS12+DS3456, no_cuts, M2_Nat+M2_Enr
c/(t-y-keV)
Energy (keV)
Residuals c/(t-y-keV)
Pulls
Summed fitted spectrum
NatGe
EnrGe
ThermosyphonAndShieldCopper
RadShieldAssembly_001_RadShieldPb_001
VesselCopper
Connectors
DUPTFE
RadShieldAssembly_001_RadShieldCuOuter_001
M2Seals
M2StringSigCables
M2CrossarmCables
M1CPCables
LMFEs
M2StringHVCables
M1CrossarmCables
M2CPCables
DUCopper
ColdPlateCopper
HVForks
ThermosyphonAndShieldCoatedCopper
DUVespel
M1StringSigCables
DUCoatedCopper
N2
M1StringHVCables
StringCoatedCopper
ThermosyphonAndShieldVespel
M1Seals_DS12_DS3456
data

DS12+DS3456, no_cuts, M2_Nat+M2_Enr

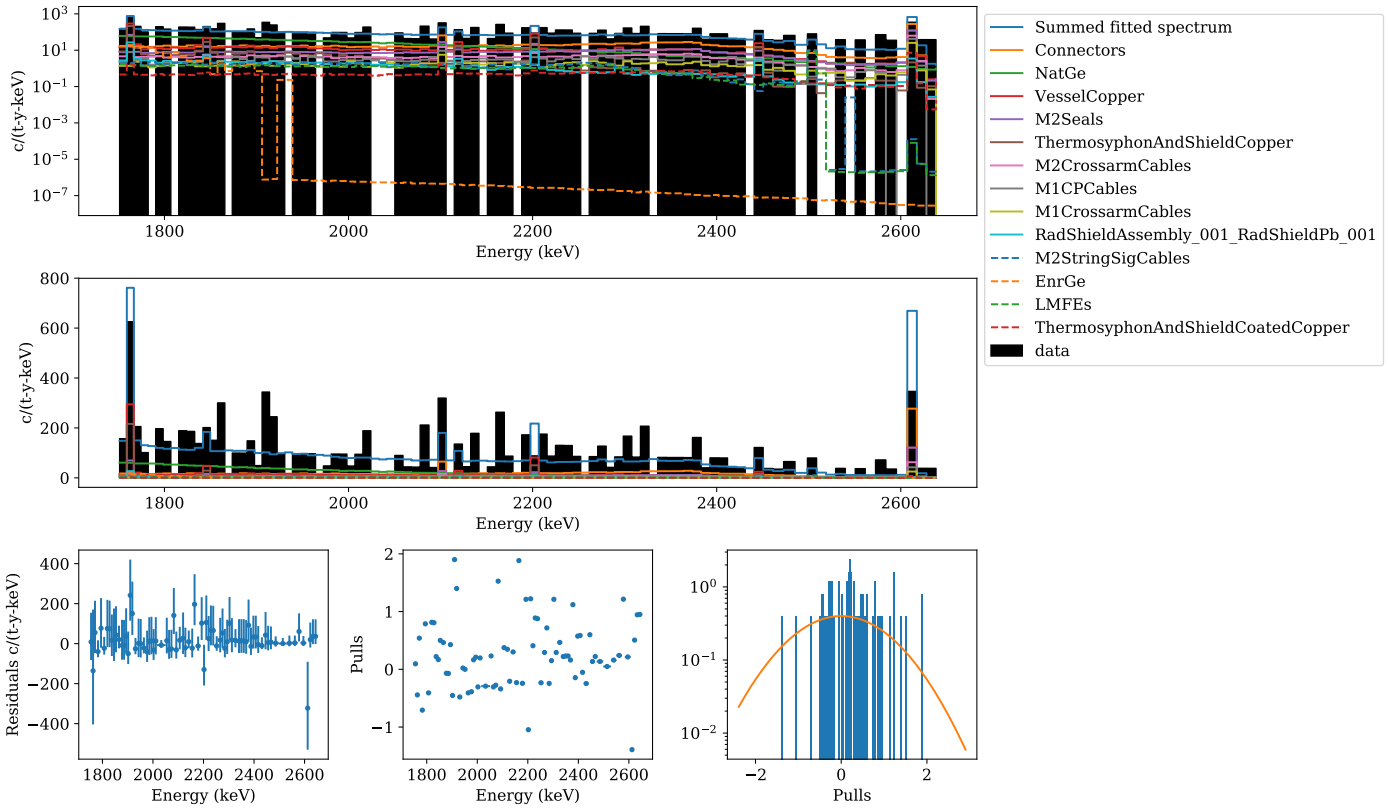

DS12+DS3456, no_cuts, M2_Nat+M2_Enr

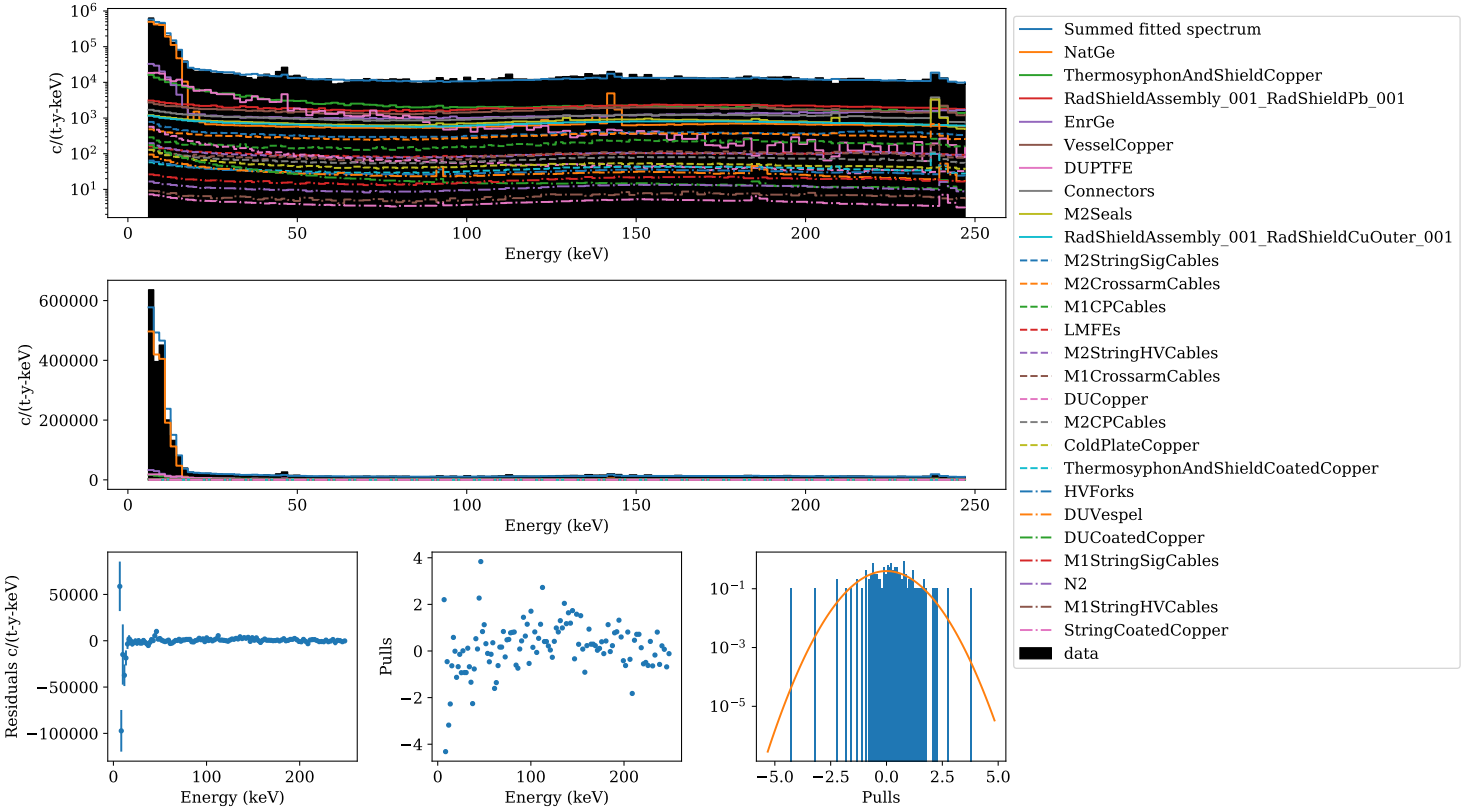

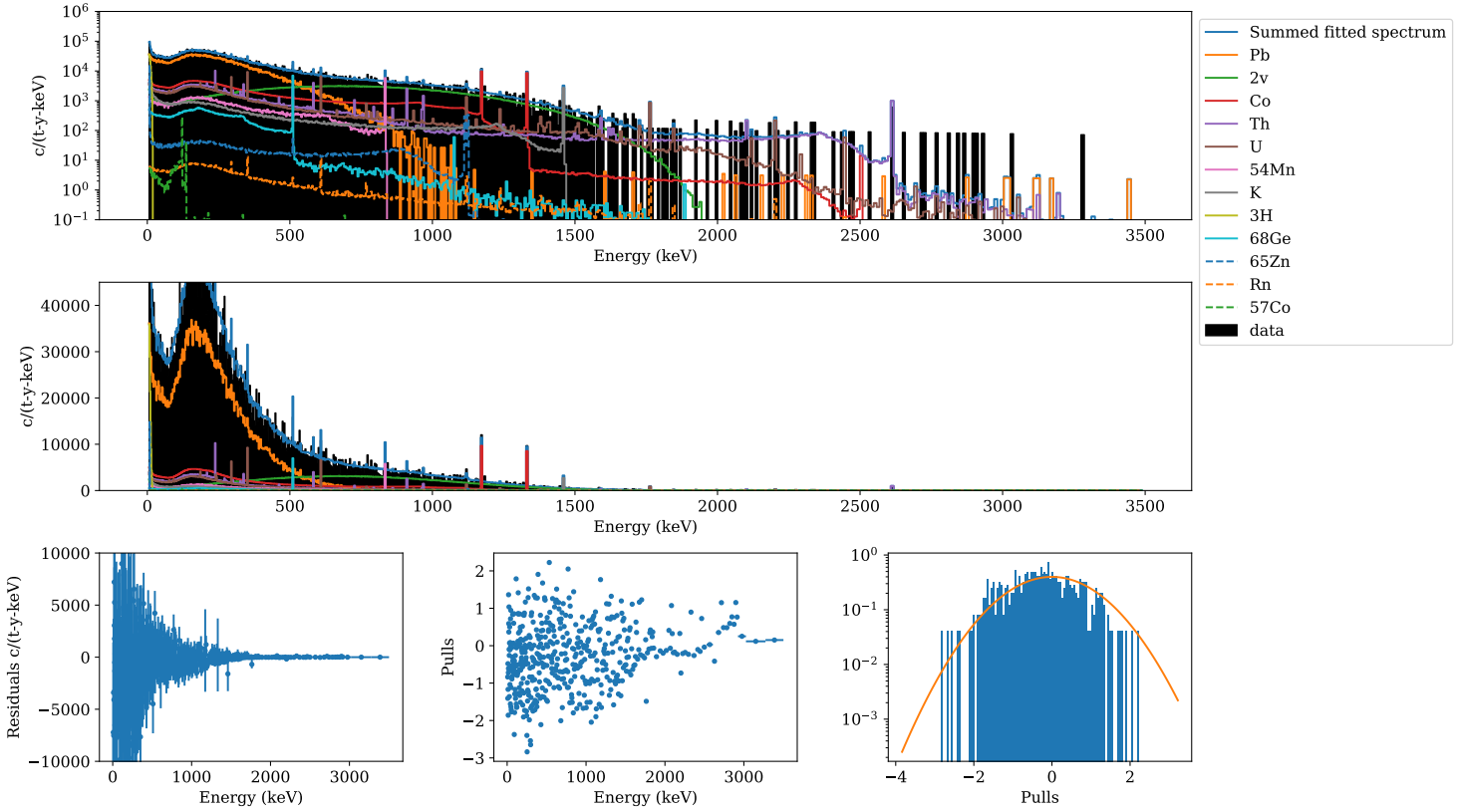
DS0, no_cuts, M1_Enr
c/(t-y-keV)
Energy (keV)
Summed fitted spectrum
Pb
2v
Co
Th
U
54Mn
K
3H
68Ge
65Zn
Rn
57Co
data
Residuals c/(t-y-keV)
Pulls

DS0, no_cuts, M1_Enr

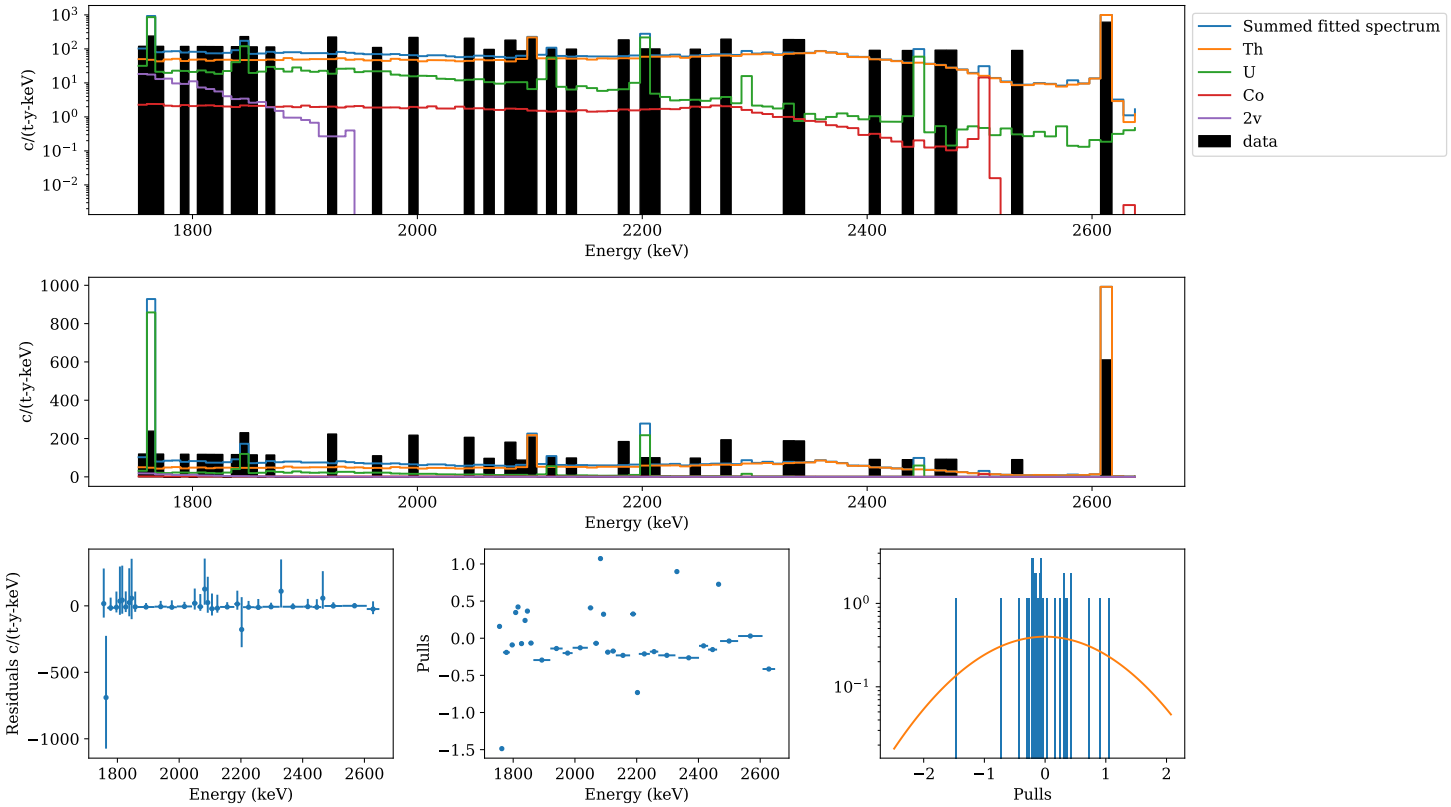

DS0, no_cuts, M1_Enr

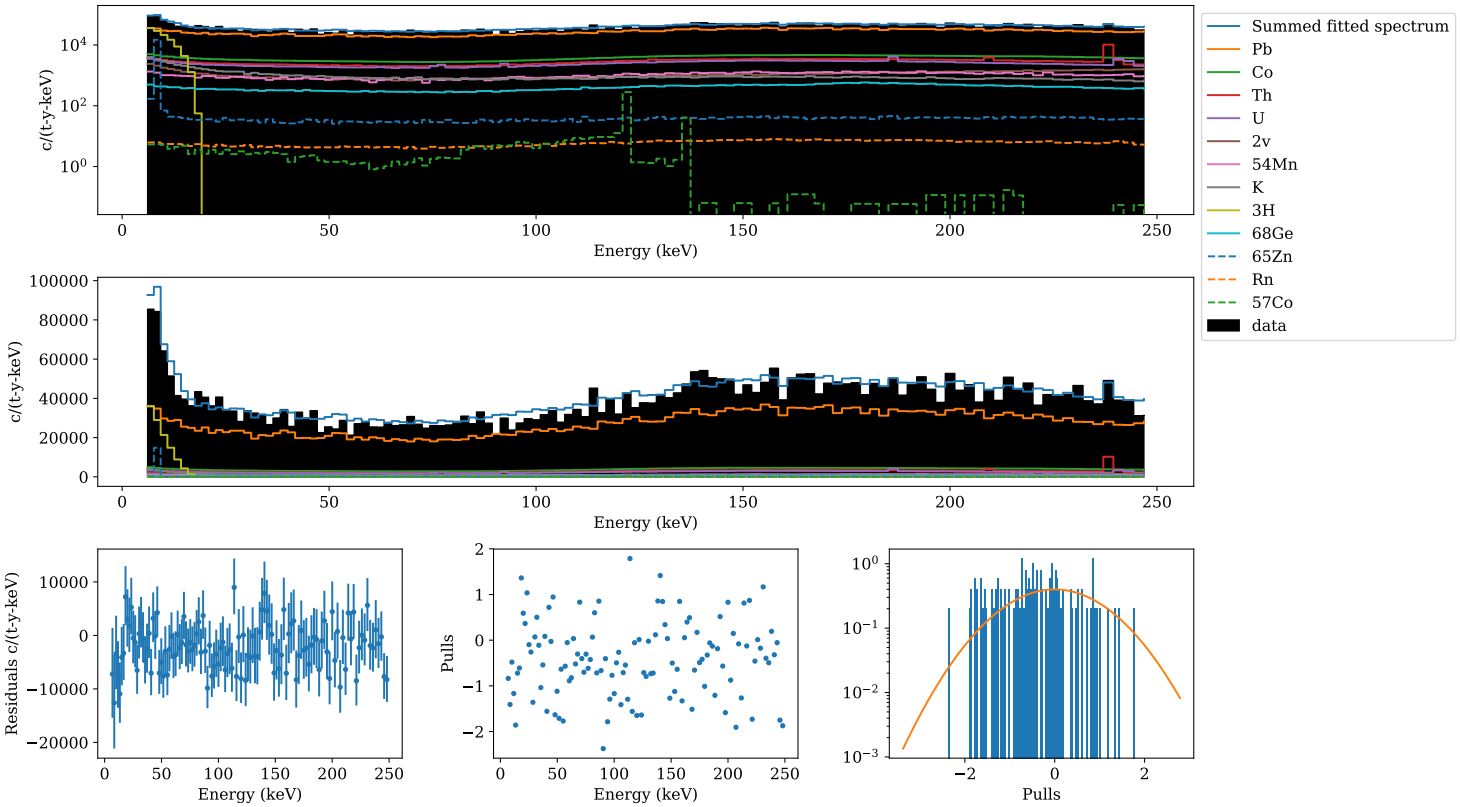

DS0, no_cuts, M1_Enr

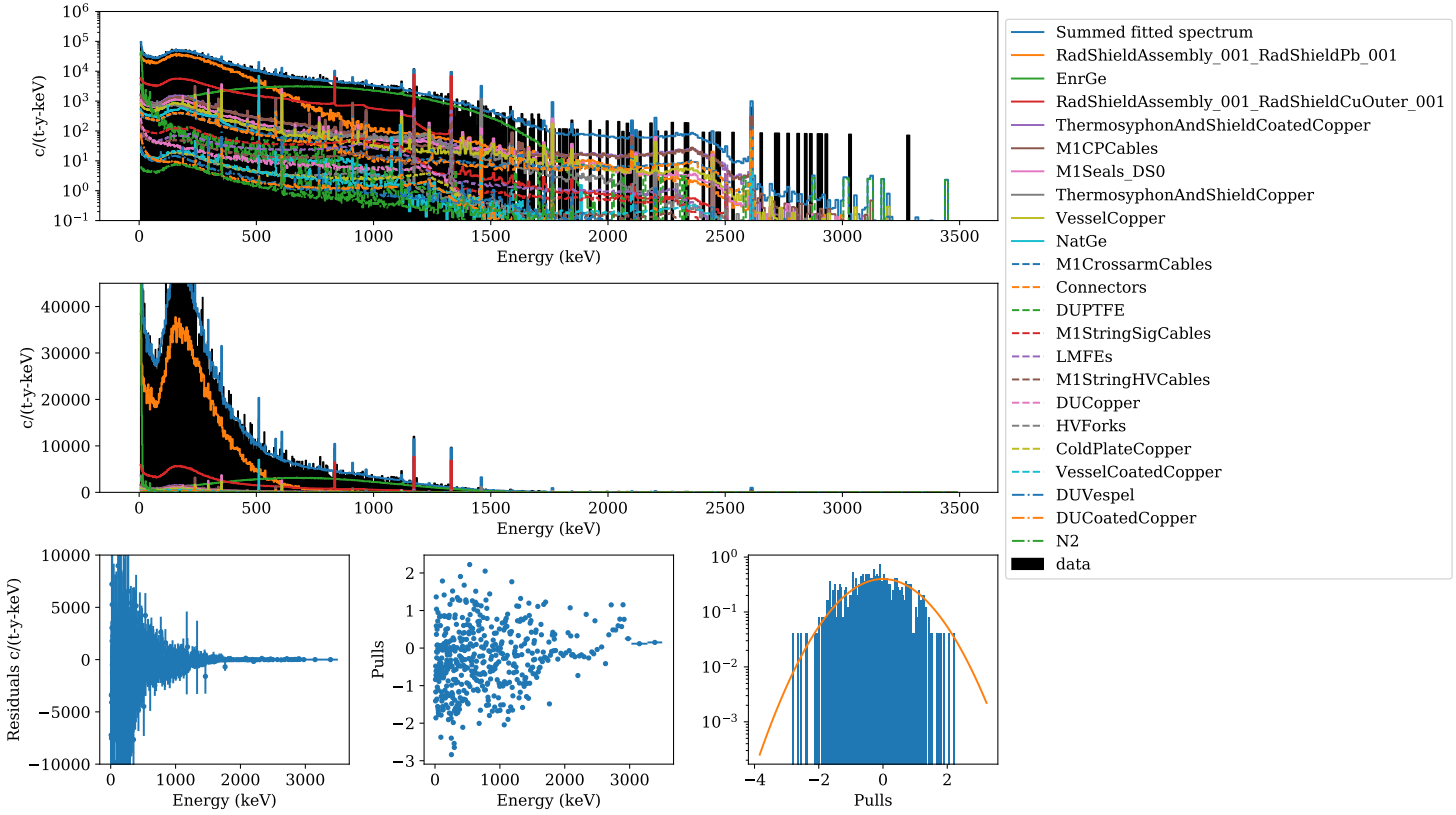

DS0, no_cuts, M1_Enr

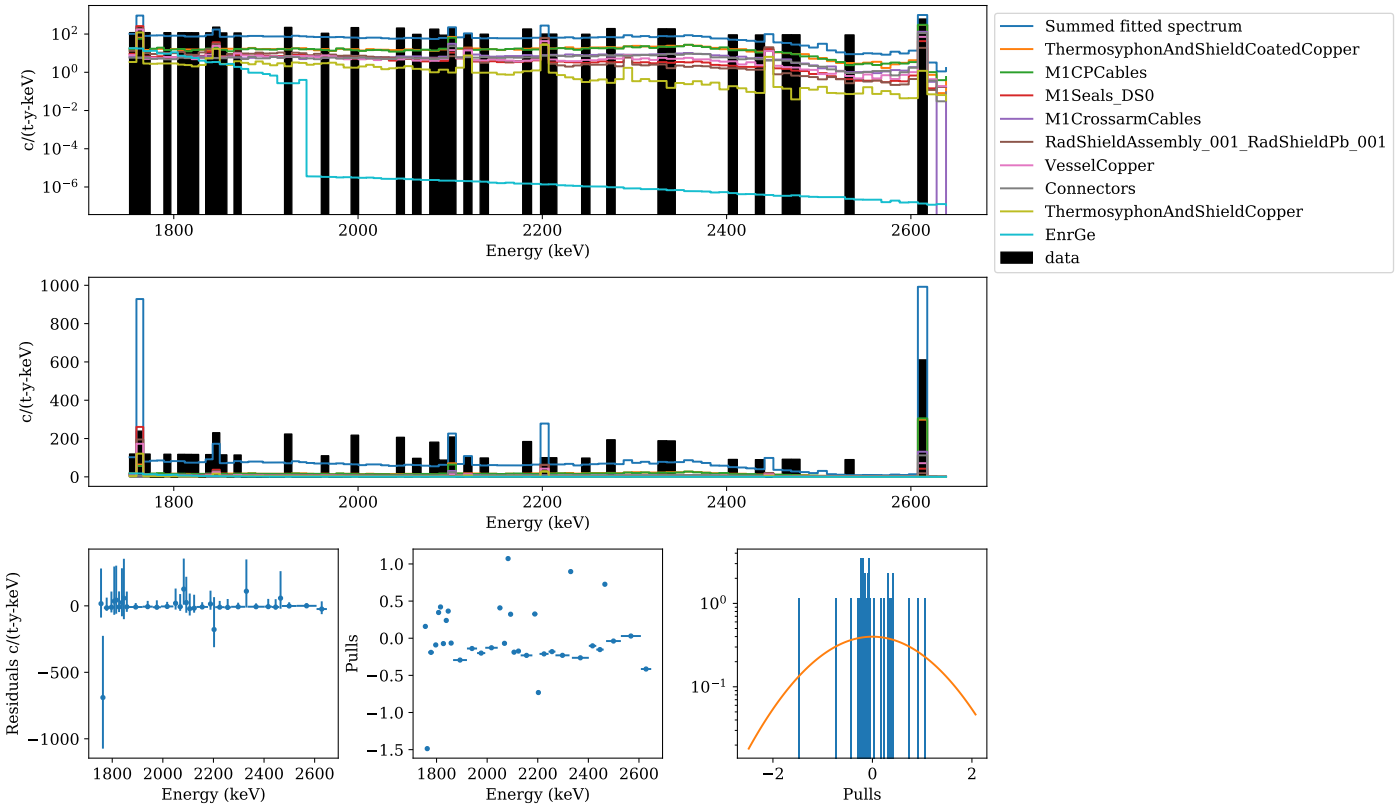

DS0, no_cuts, M1_Enr

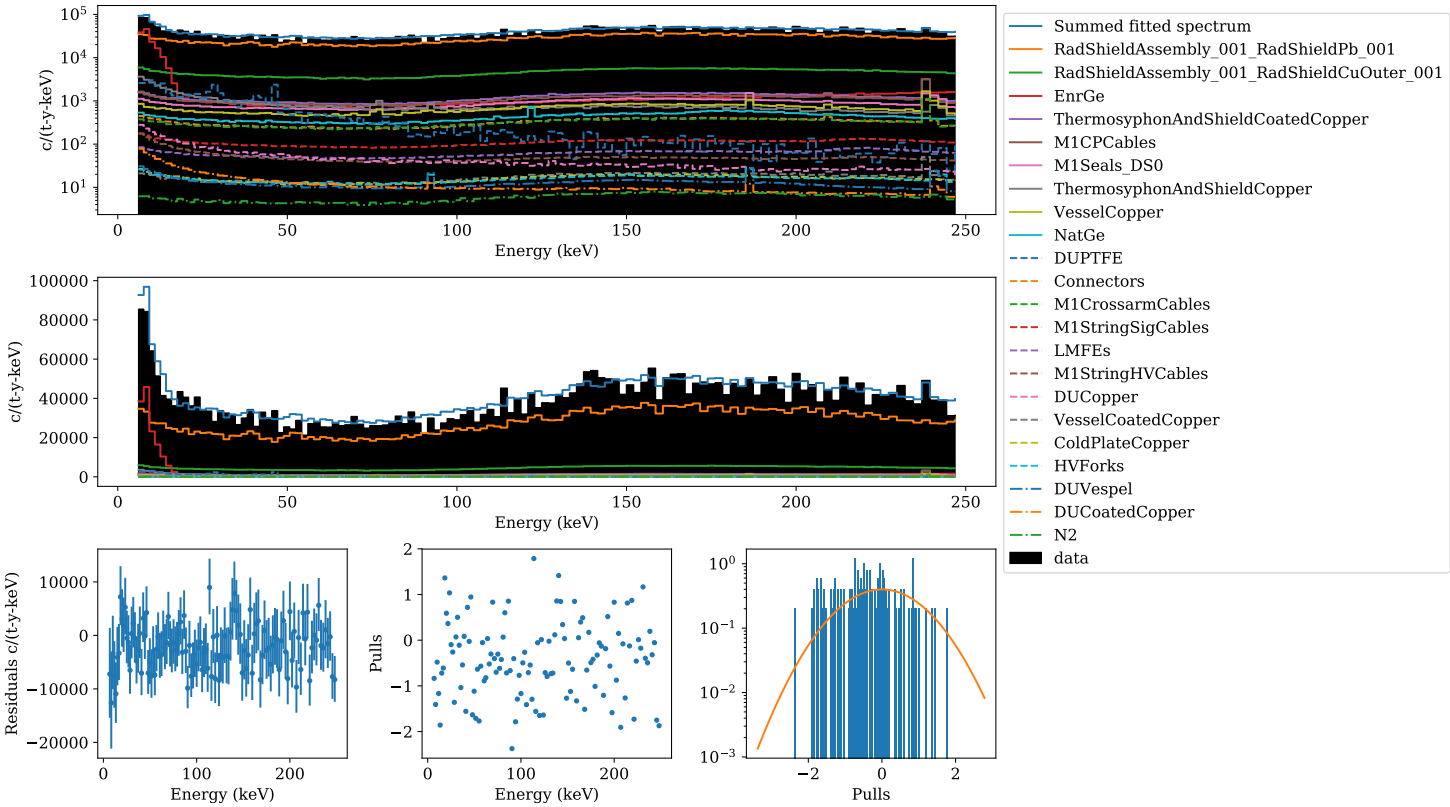

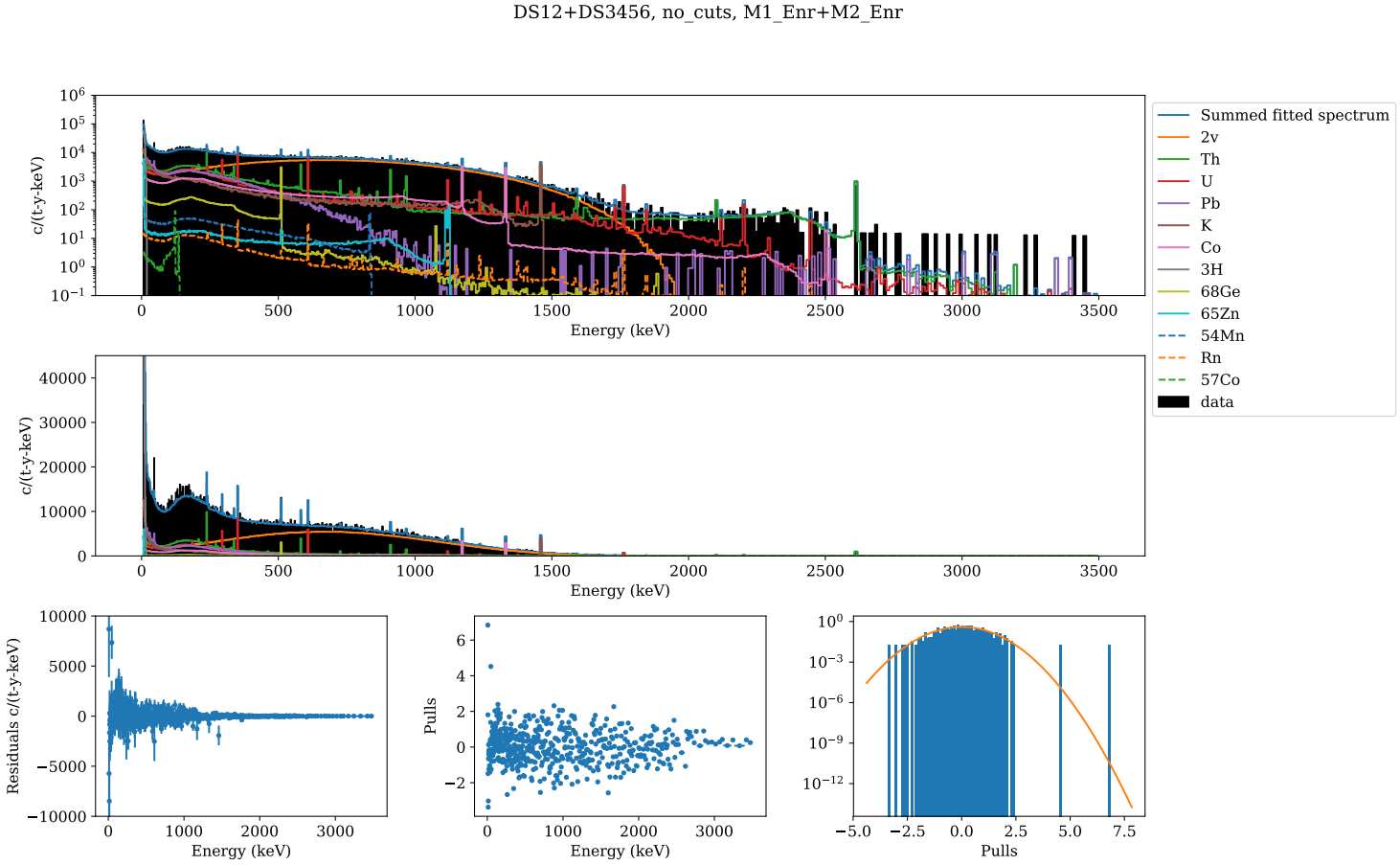
DS12+DS3456, no_cuts, M1_Enr+M2_Enr
c/(t-y-keV)
Energy (keV)
Summed fitted spectrum
2v
Th
U
Pb
K
Co
3H
68Ge
65Zn
54Mn
Rn
57Co
data
Residuals c/(t-y-keV)
Pulls
Pulls

DS12+DS3456, no_cuts, M1_Enr+M2_Enr

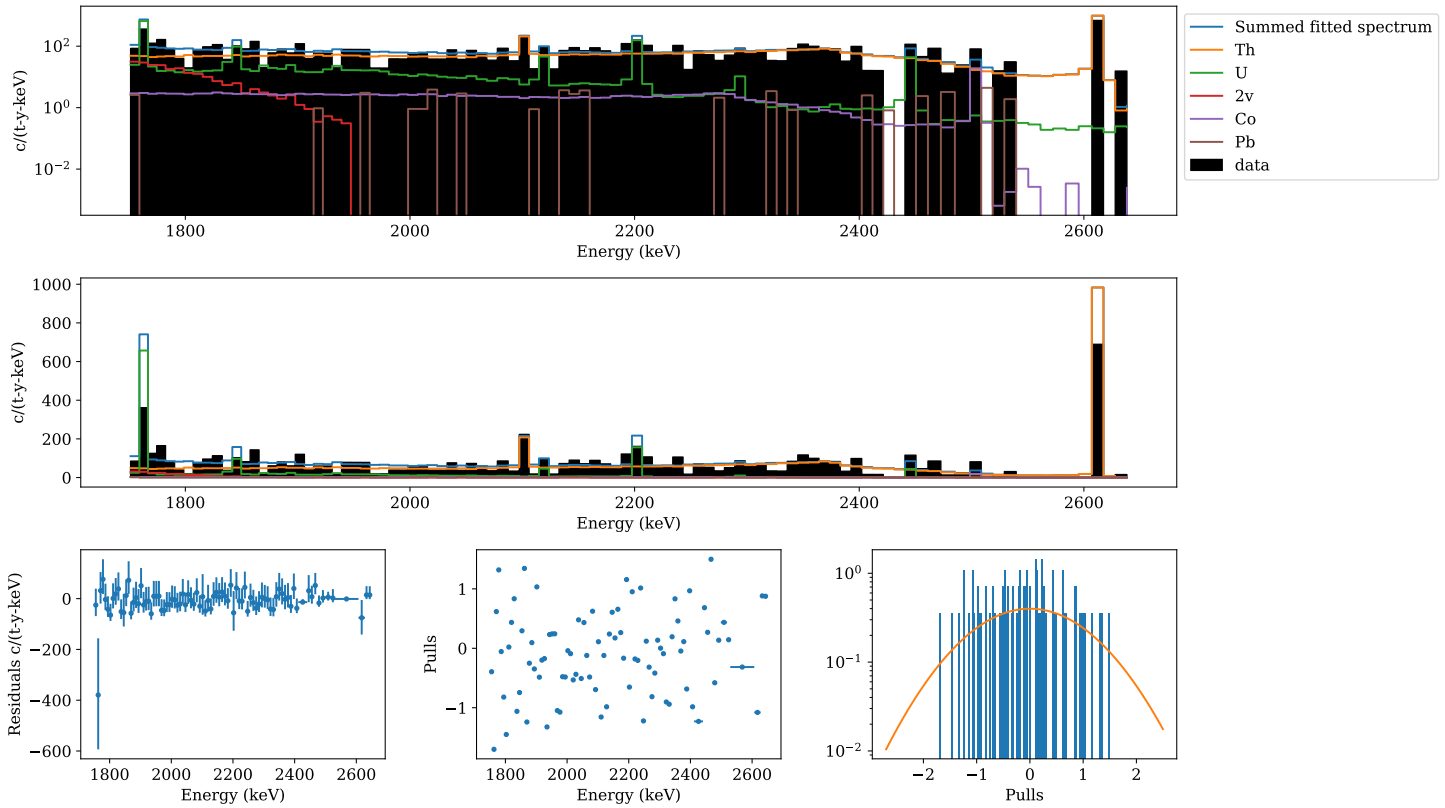

DS12+DS3456, no_cuts, M1_Enr+M2_Enr

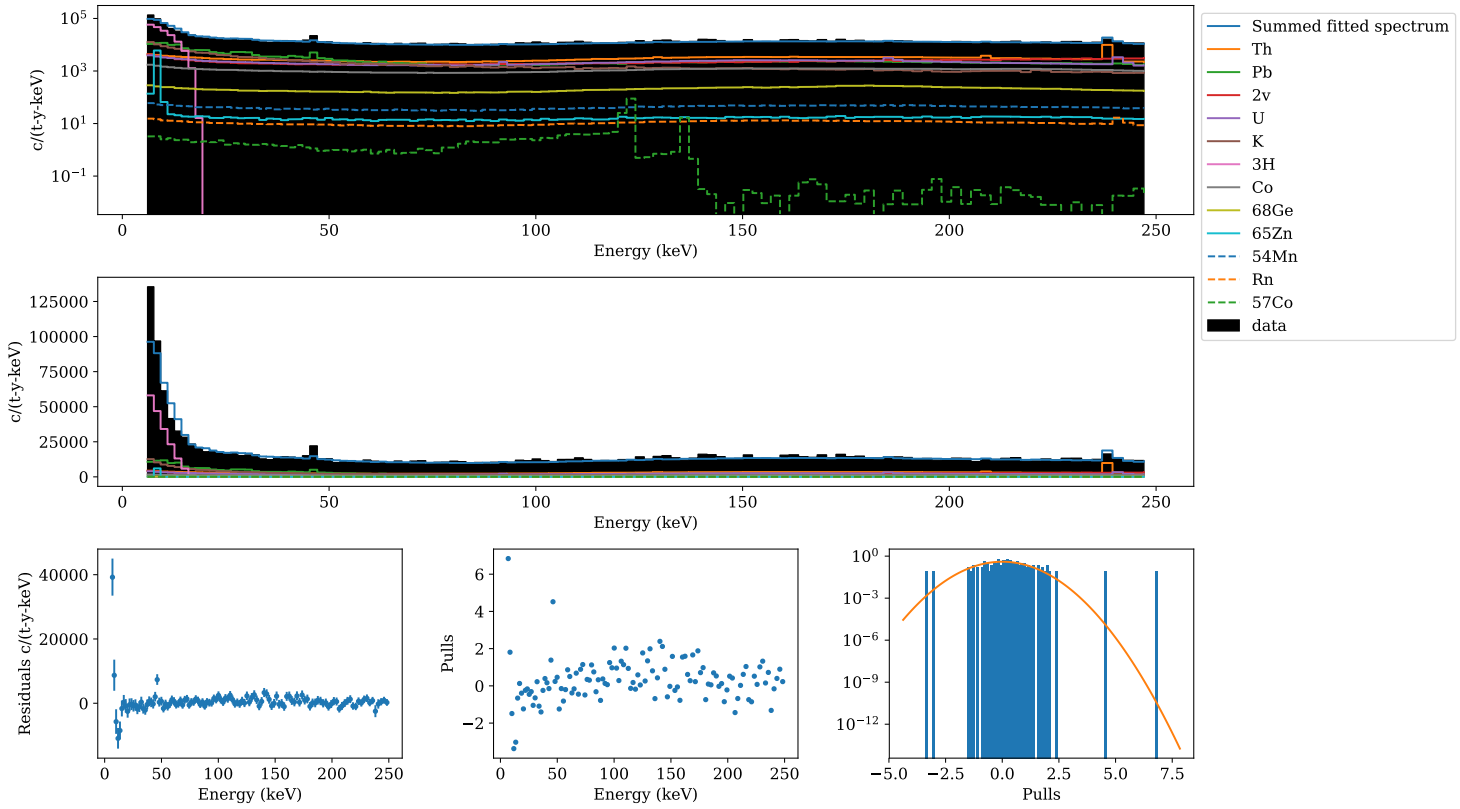

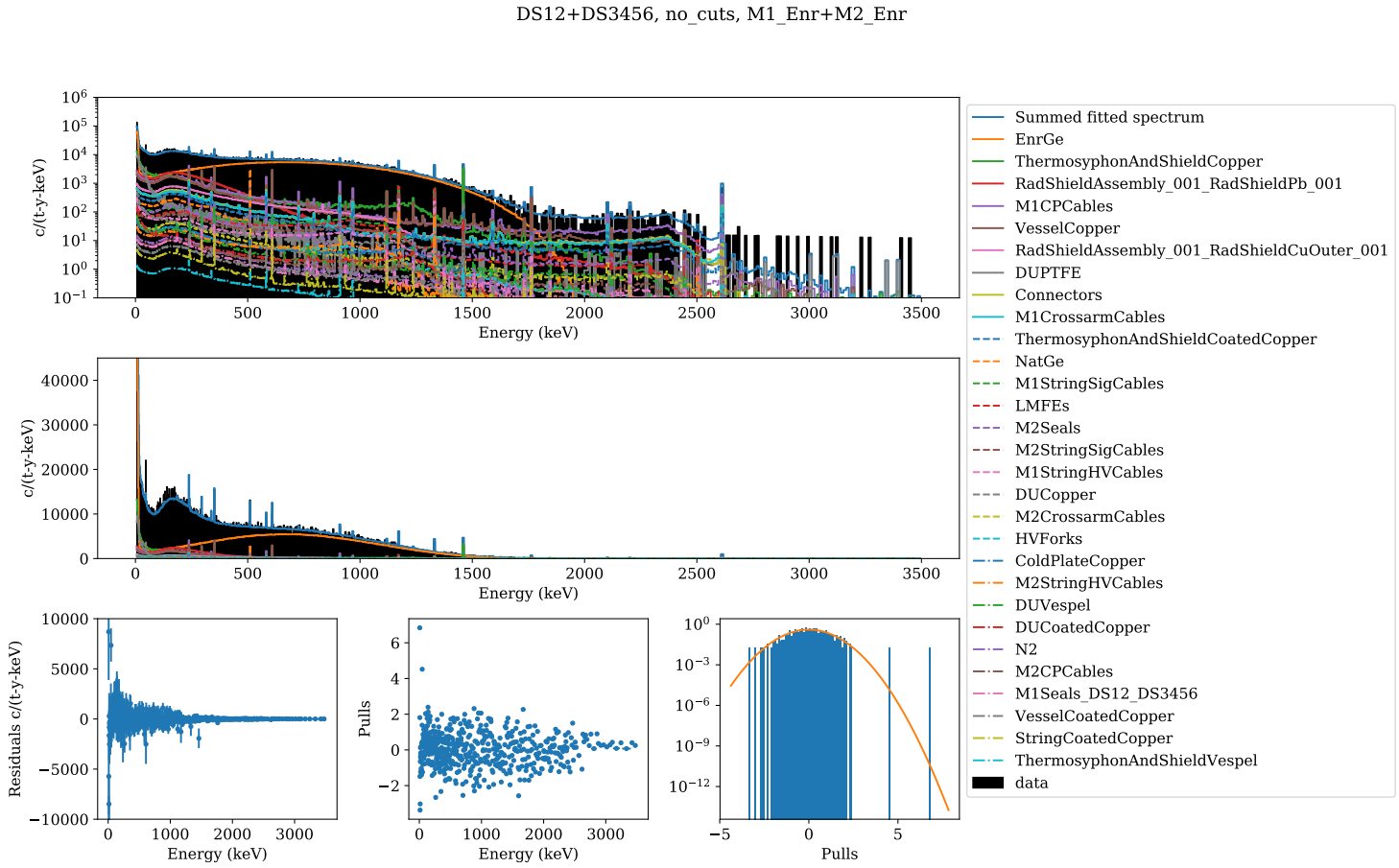
DS12+DS3456, no_cuts, M1_Enr+M2_Enr
c/(t-y-keV)
Energy (keV)
Residuals c/(t-y-keV)
Pulls
Summed fitted spectrum
EnrGe
ThermosyphonAndShieldCopper
RadShieldAssembly_001_RadShieldPb_001
M1CPCables
VesselCopper
RadShieldAssembly_001_RadShieldCuOuter_001
DUPTFE
Connectors
M1CrossarmCables
ThermosyphonAndShieldCoatedCopper
NatGe
M1StringSigCables
LMFEs
M2Seals
M2StringSigCables
M1StringHVCables
DUCopper
M2CrossarmCables
HVForks
ColdPlateCopper
M2StringHVCables
DUVespel
DUCoatedCopper
N2
M2CPCables
M1Seals_DS12_DS3456
VesselCoatedCopper
StringCoatedCopper
ThermosyphonAndShieldVespel
data

DS12+DS3456, no_cuts, M1_Enr+M2_Enr

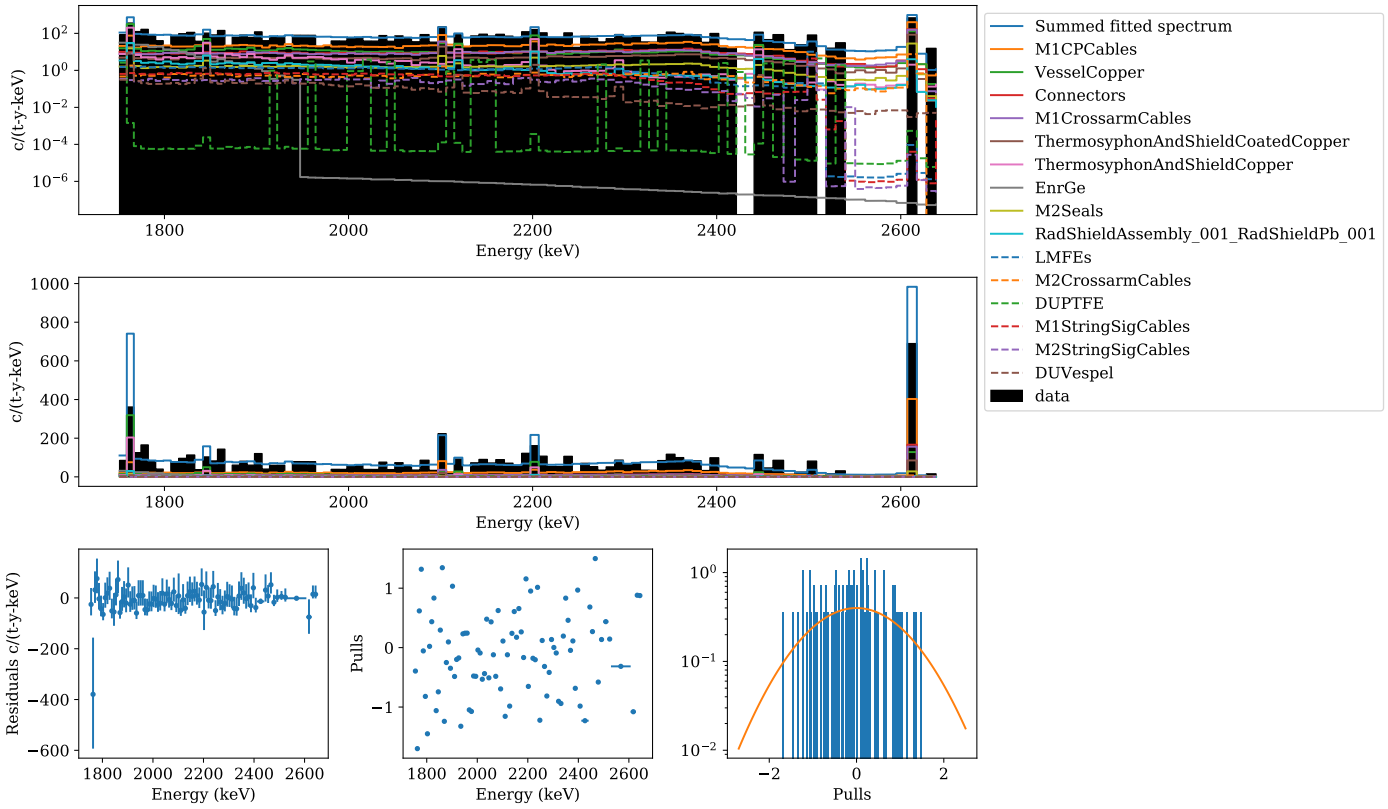

DS12+DS3456, no_cuts, M1_Enr+M2_Enr

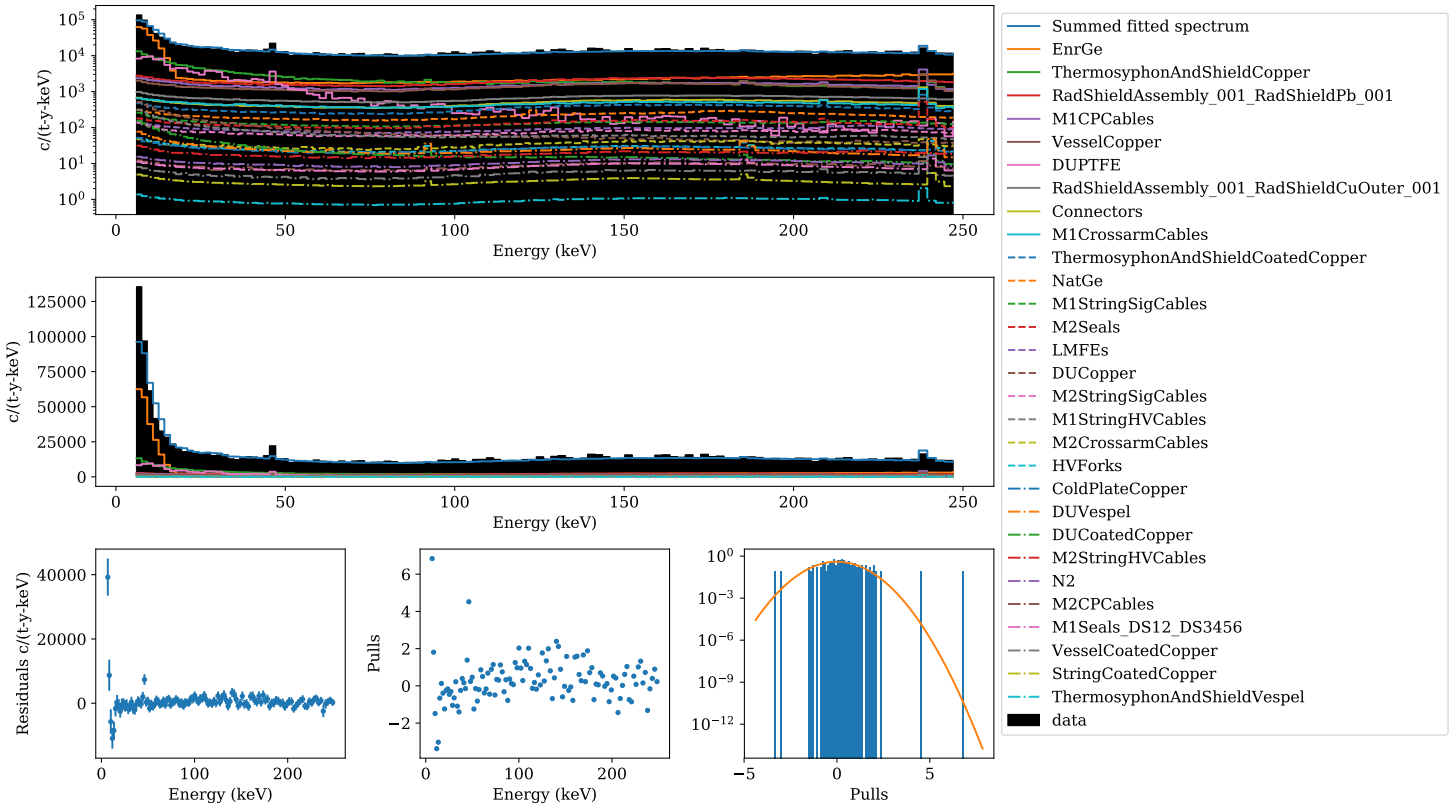

DS0, no_cuts, M1_Nat

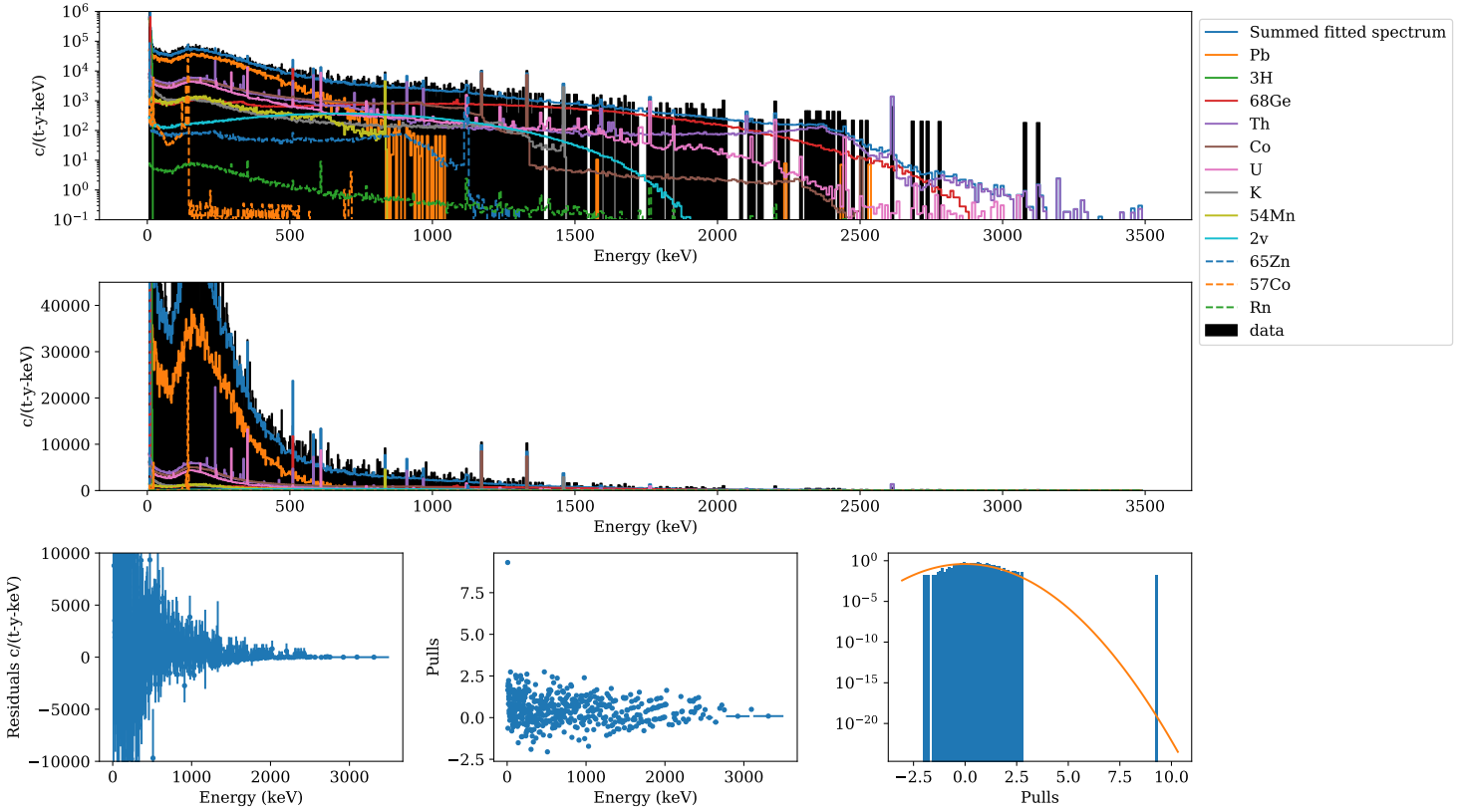

DS0, no_cuts, M1_Nat

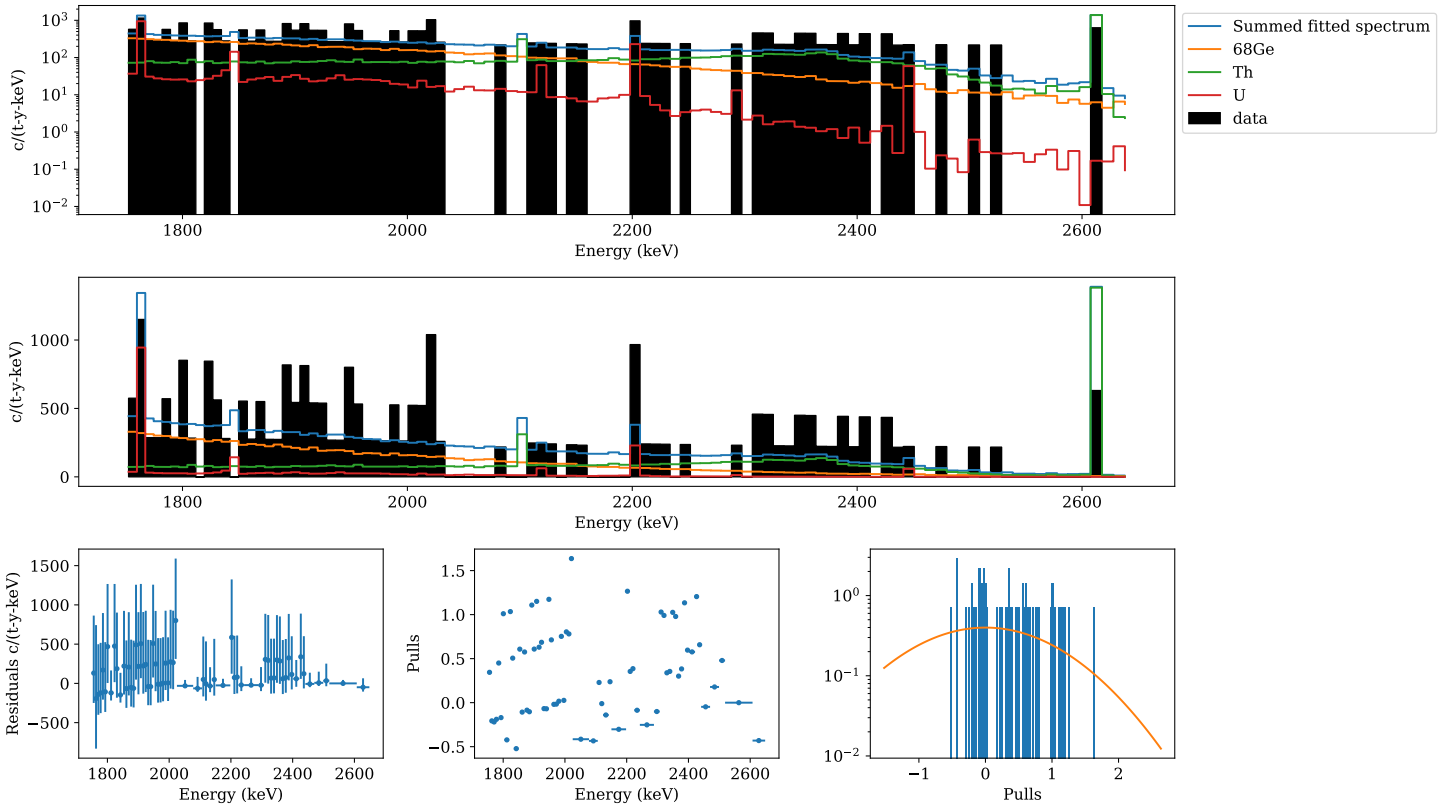

DS0, no_cuts, M1_Nat

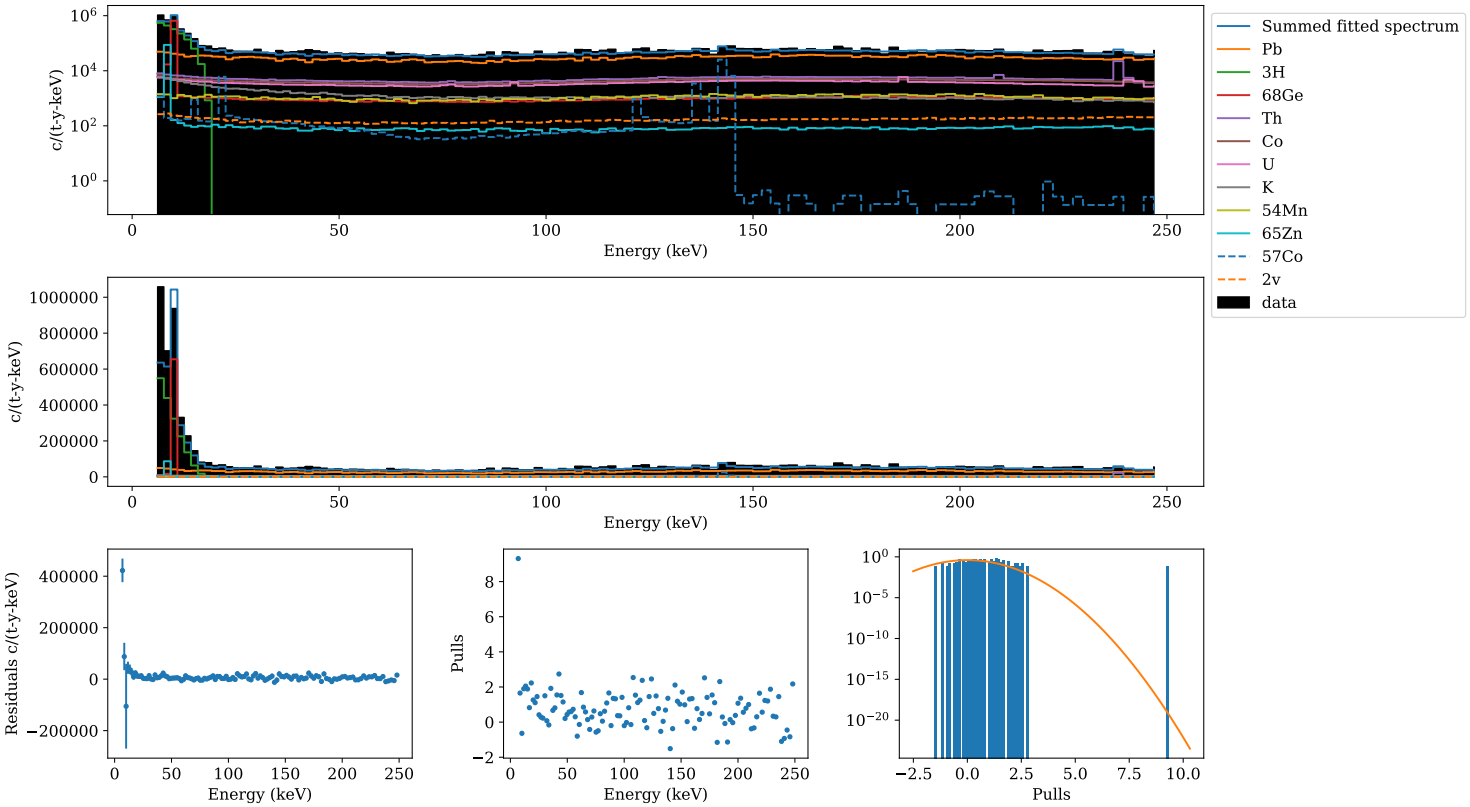

DS0, no_cuts, M1_Nat

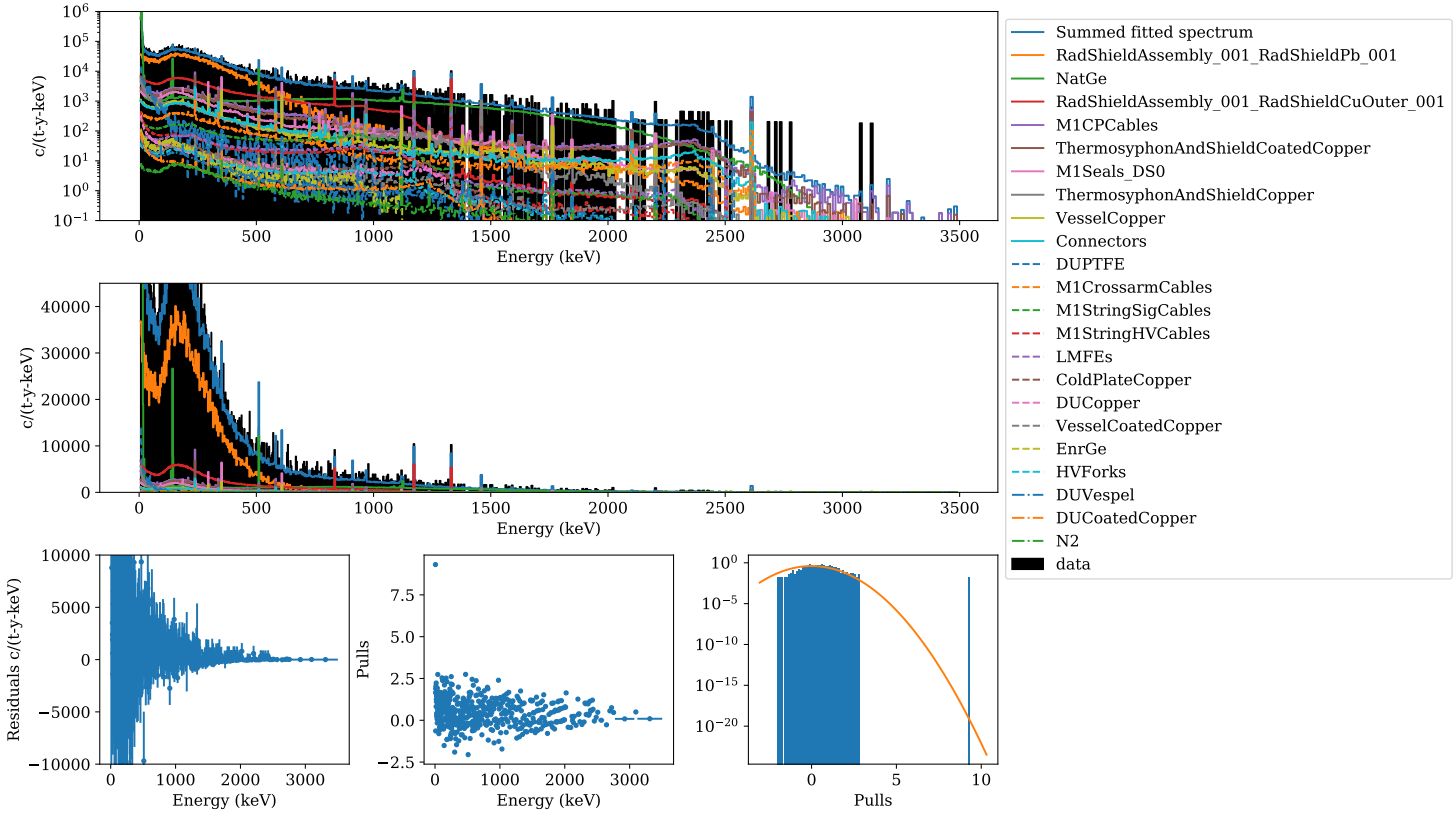

DS0, no_cuts, M1_Nat

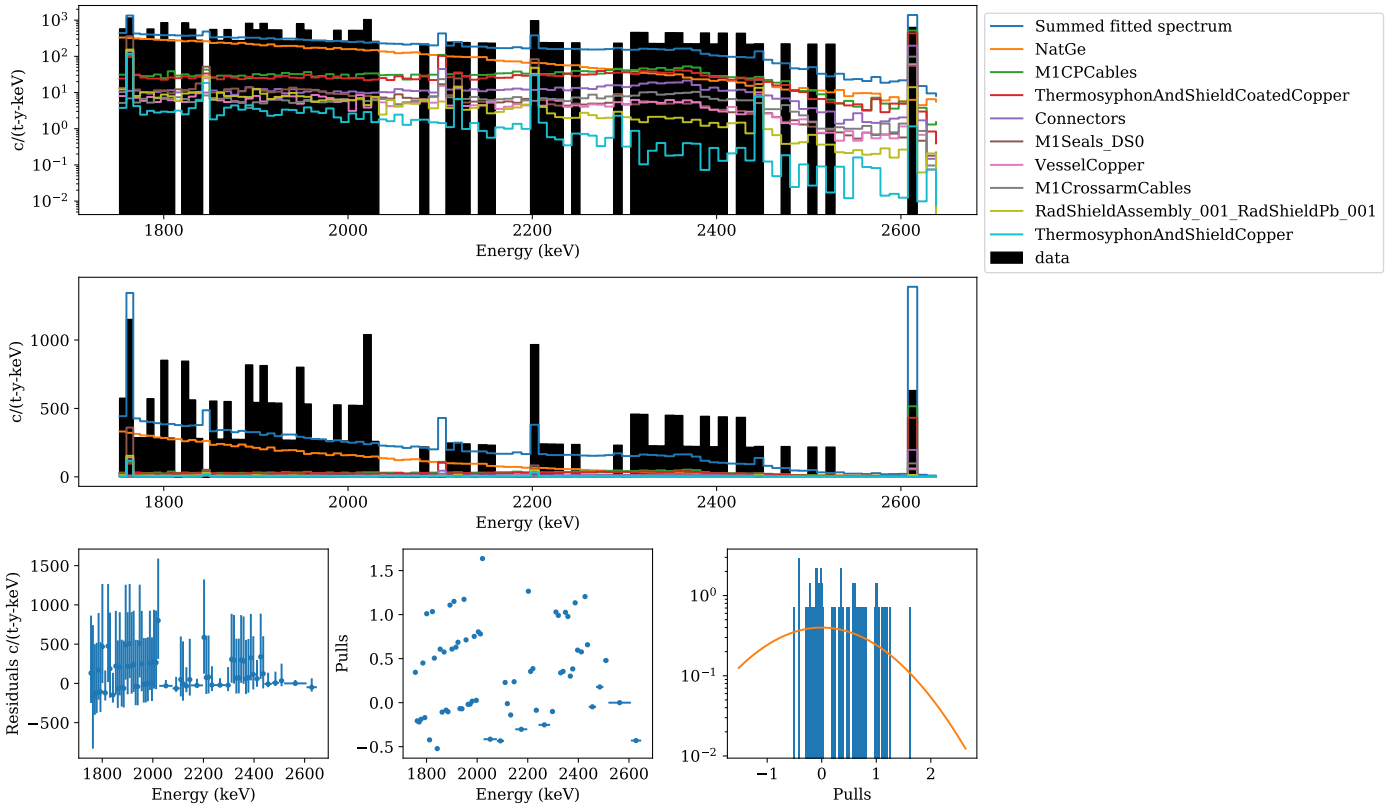

DS0, no_cuts, M1_Nat

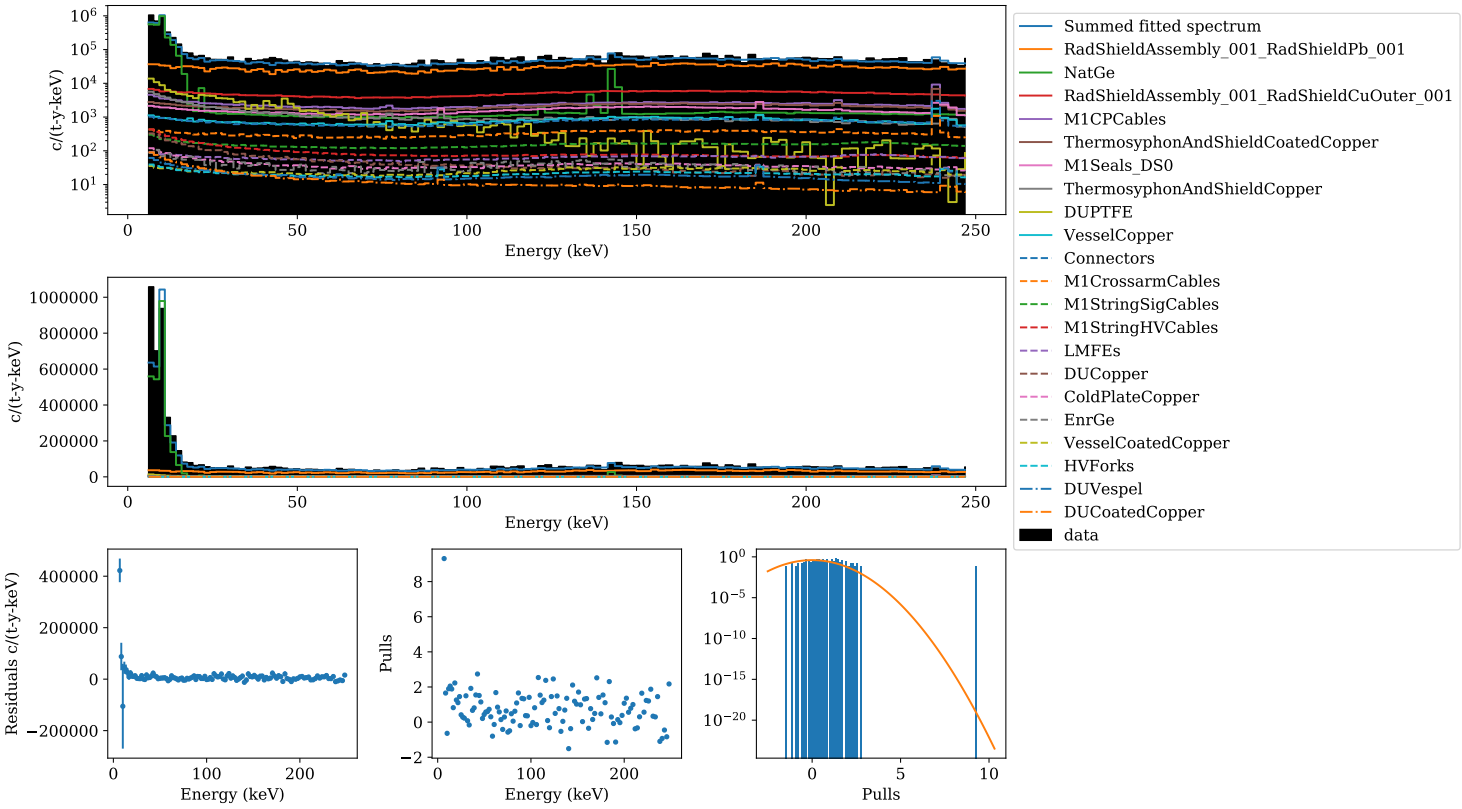

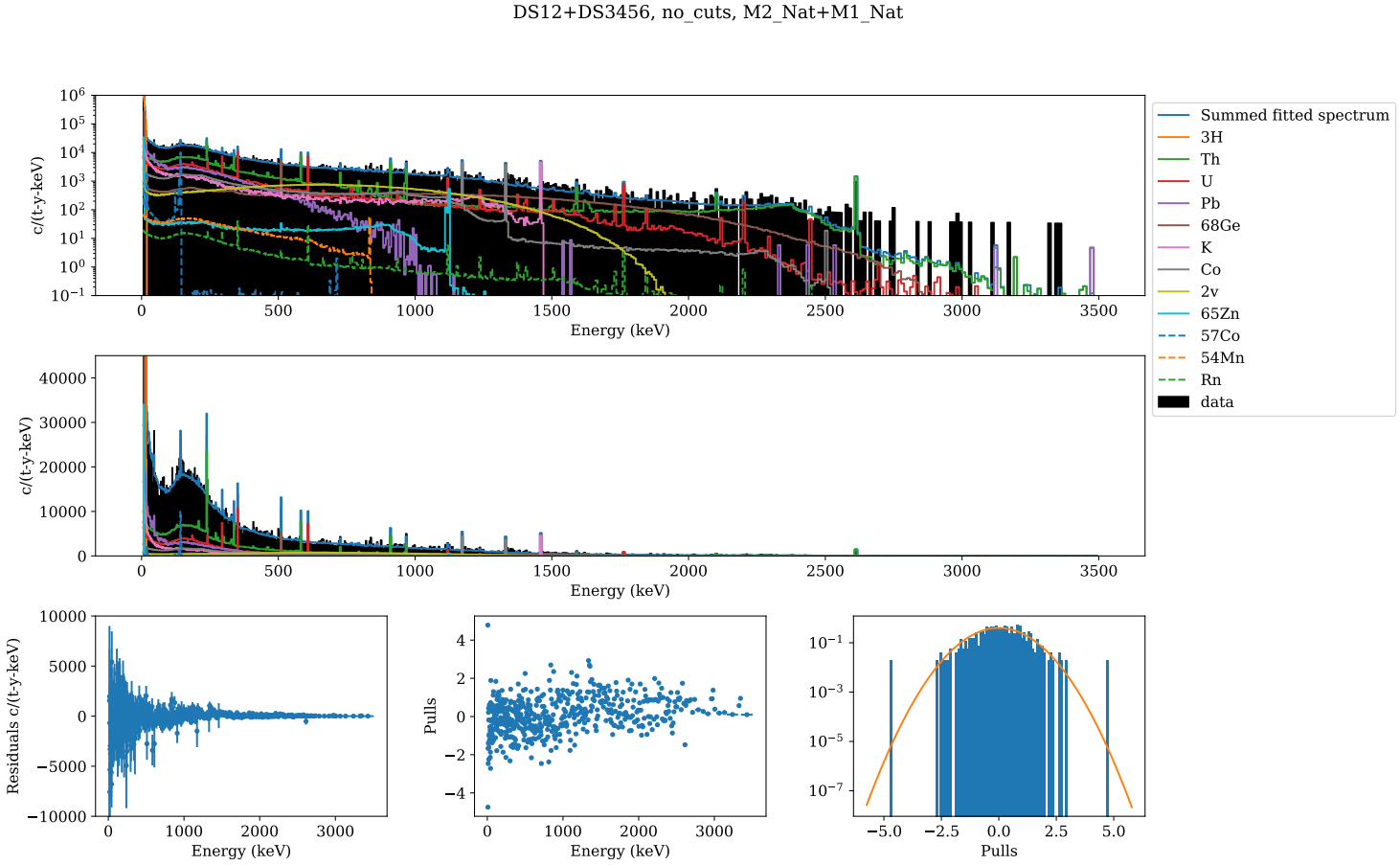
DS12+DS3456, no_cuts, M2_Nat+M1_Nat
c/(t-y-keV)
Energy (keV)
Residuals c/(t-y-keV)
Pulls
Summed fitted spectrum
3H
Th
U
Pb
68Ge
K
Co
2v
65Zn
57Co
54Mn
Rn
data

DS12+DS3456, no_cuts, M2_Nat+M1_Nat

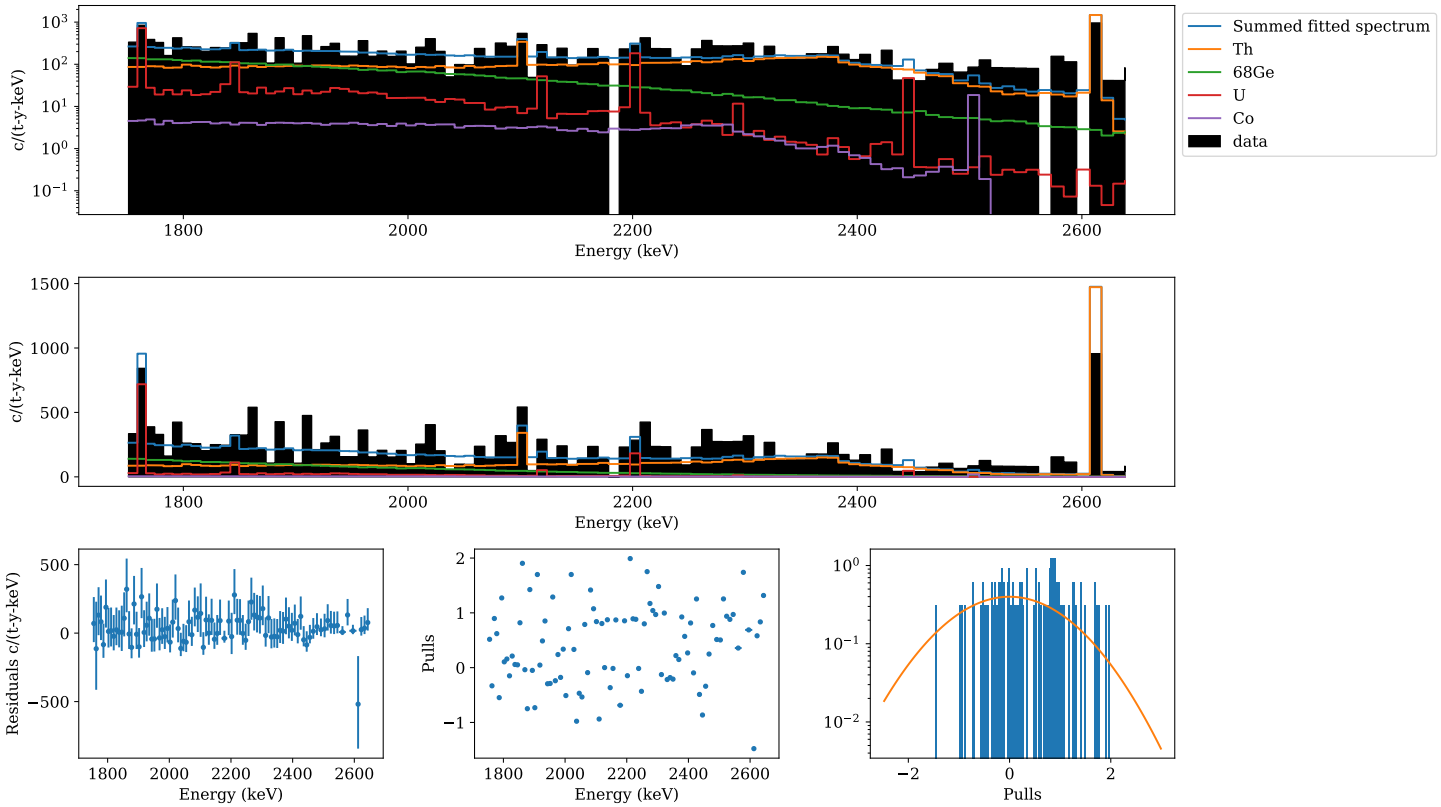

DS12+DS3456, no_cuts, M2_Nat+M1_Nat

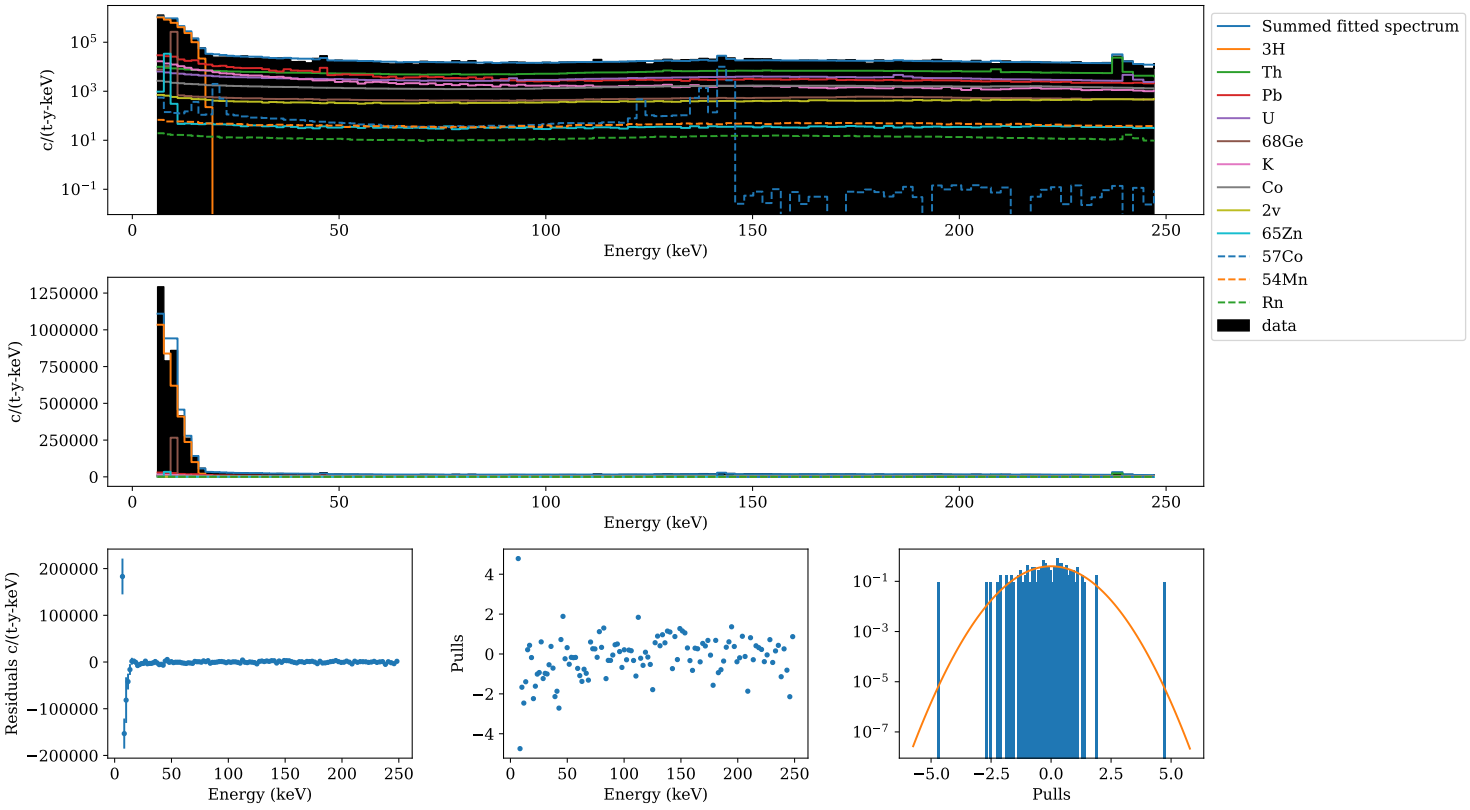

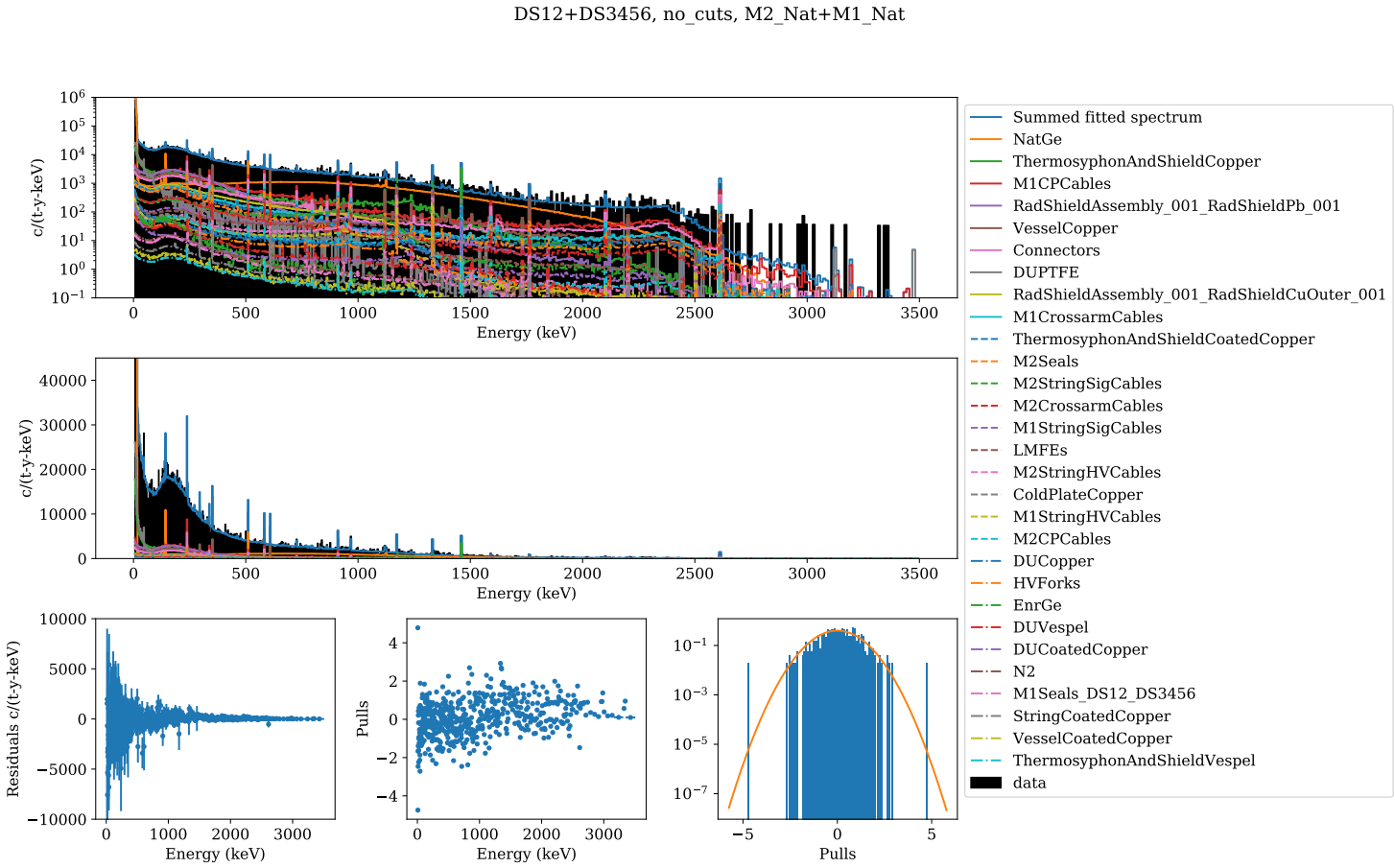
DS12+DS3456, no_cuts, M2_Nat+M1_Nat
c/(t-y-keV)
Energy (keV)
Residuals c/(t-y-keV)
Pulls
Summed fitted spectrum
NatGe
ThermosyphonAndShieldCopper
M1CPCables
RadShieldAssembly_001_RadShieldPb_001
VesselCopper
Connectors
DUPTFE
RadShieldAssembly_001_RadShieldCuOuter_001
M1CrossarmCables
ThermosyphonAndShieldCoatedCopper
M2Seals
M2StringSigCables
M2CrossarmCables
M1StringSigCables
LMFEs
M2StringHVCables
ColdPlateCopper
M1StringHVCables
M2CPCables
DUCopper
HVForks
EnrGe
DUVespel
DUCoatedCopper
N2
M1Seals_DS12_DS3456
StringCoatedCopper
VesselCoatedCopper
ThermosyphonAndShieldVespel
data

DS12+DS3456, no_cuts, M2_Nat+M1_Nat

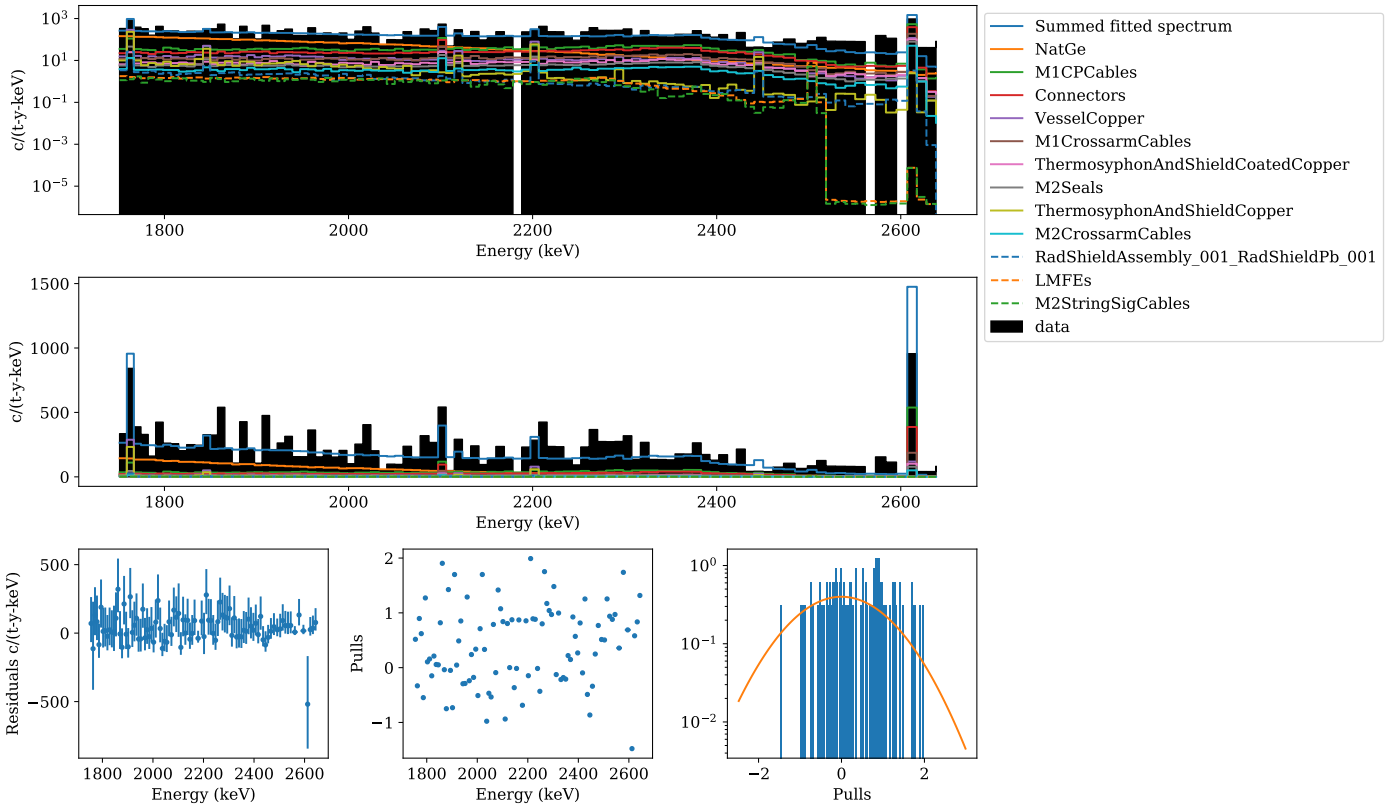

DS12+DS3456, no_cuts, M2_Nat+M1_Nat

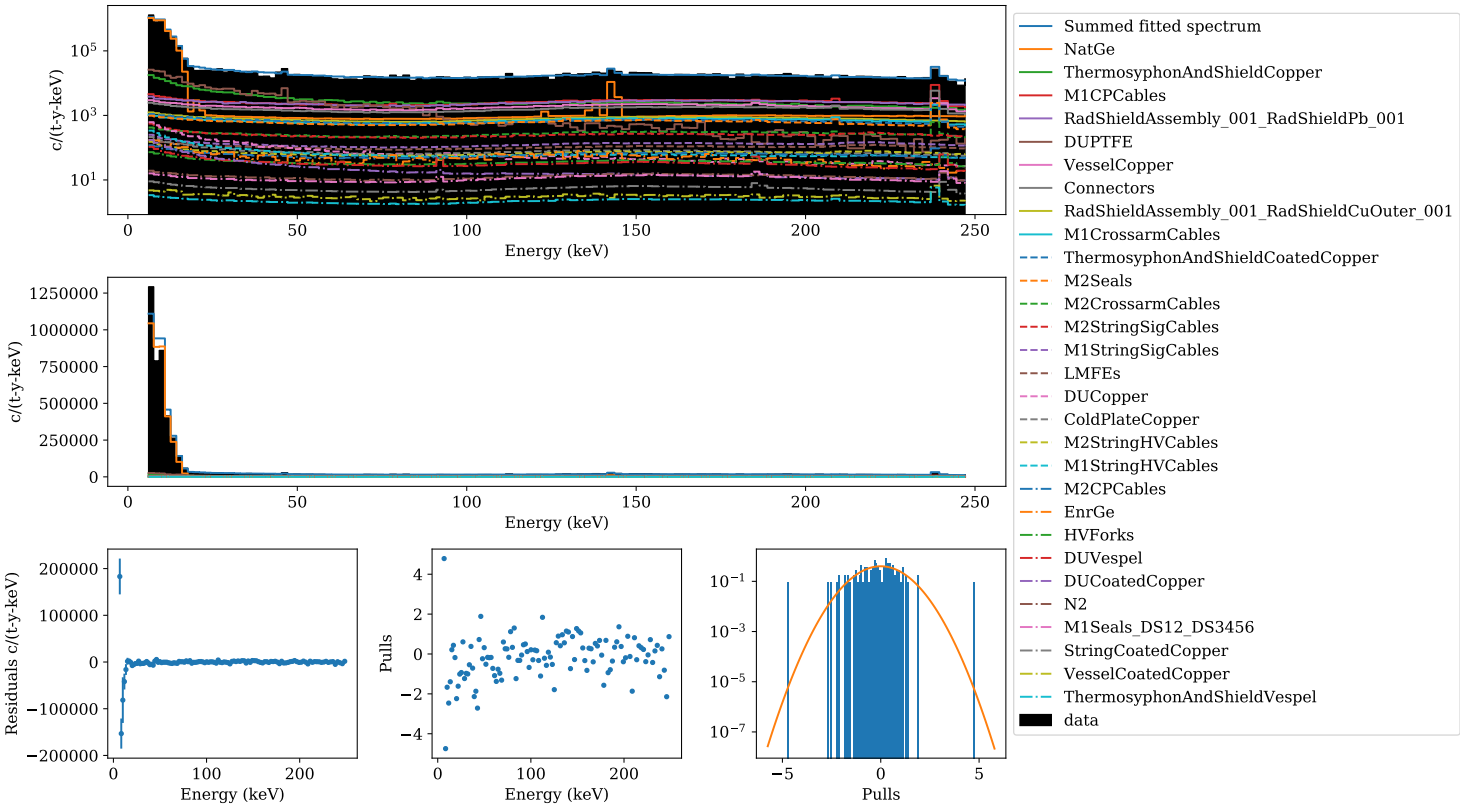

DS0, Gran, M1_Nat+M1_Enr

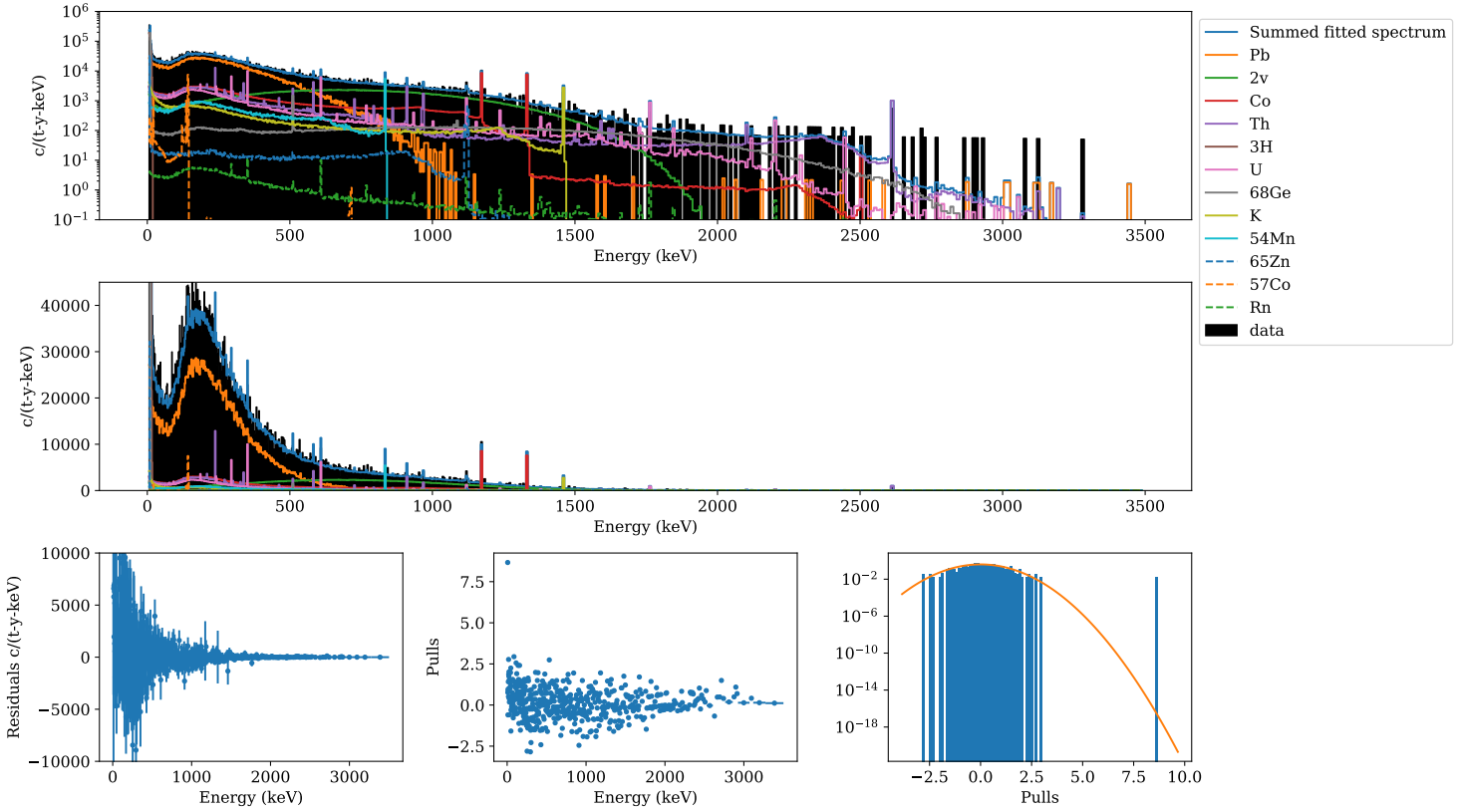

DS0, Gran, M1_Nat+M1_Enr

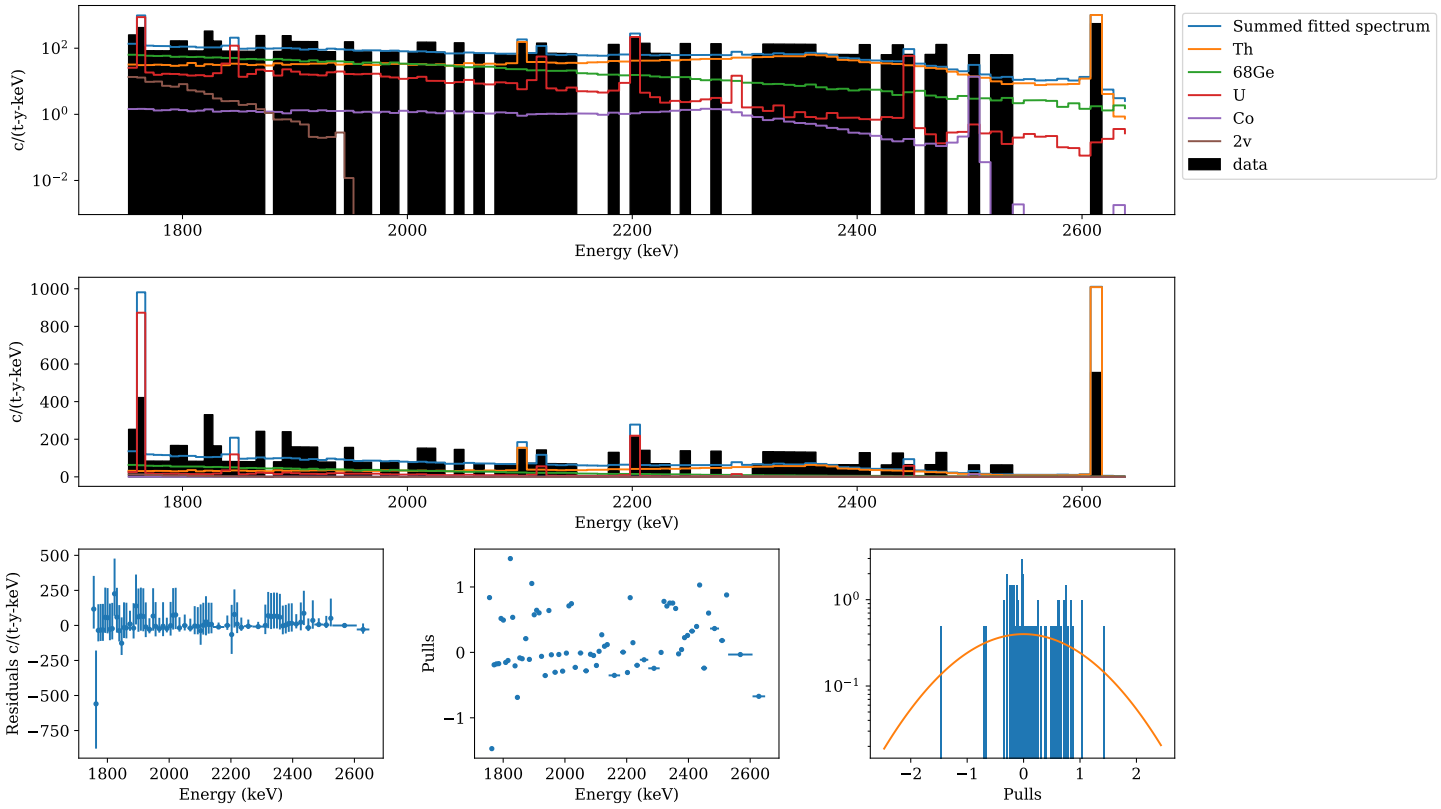

DS0, Gran, M1_Nat+M1_Enr

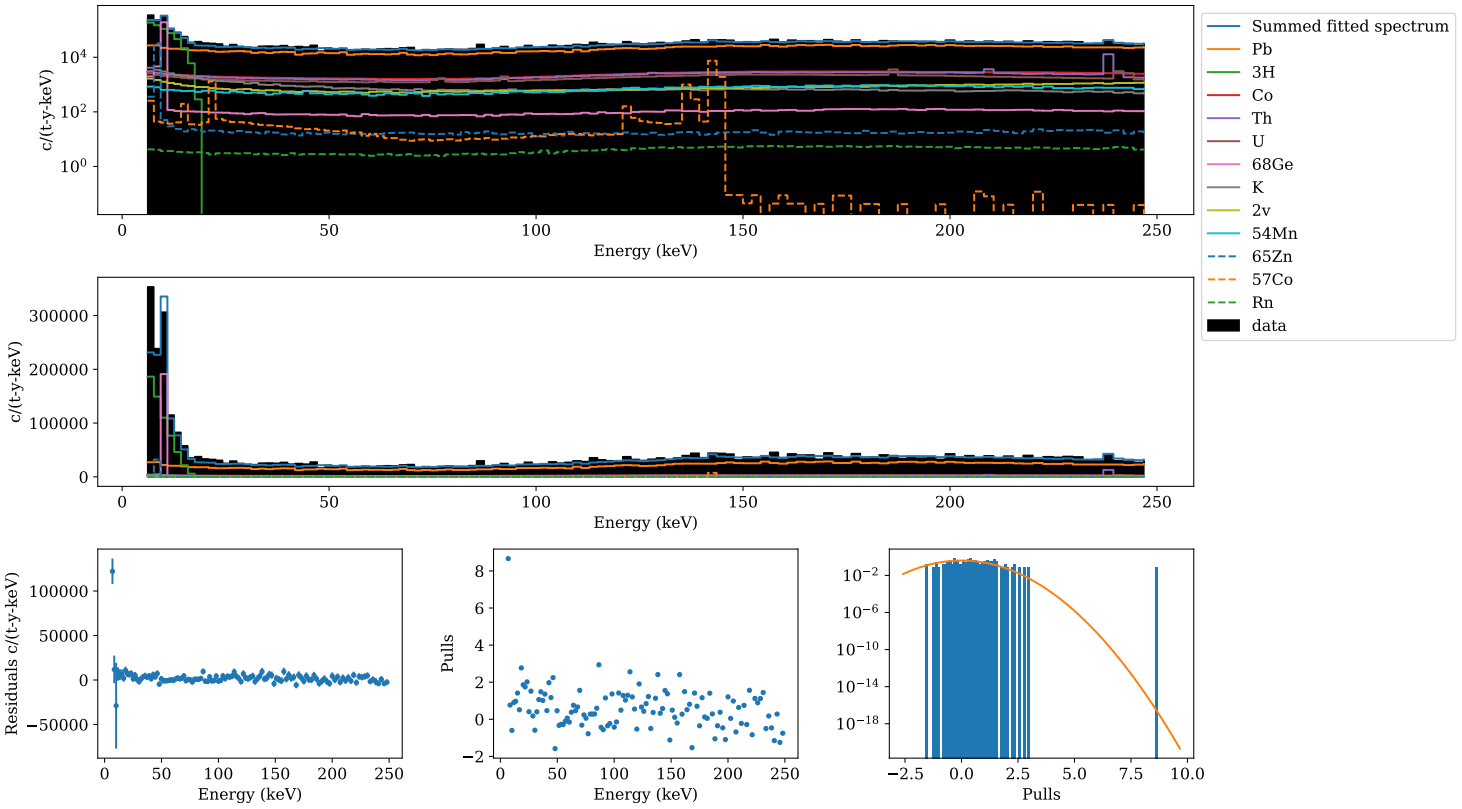

DS0, Gran, M1_Nat+M1_Enr

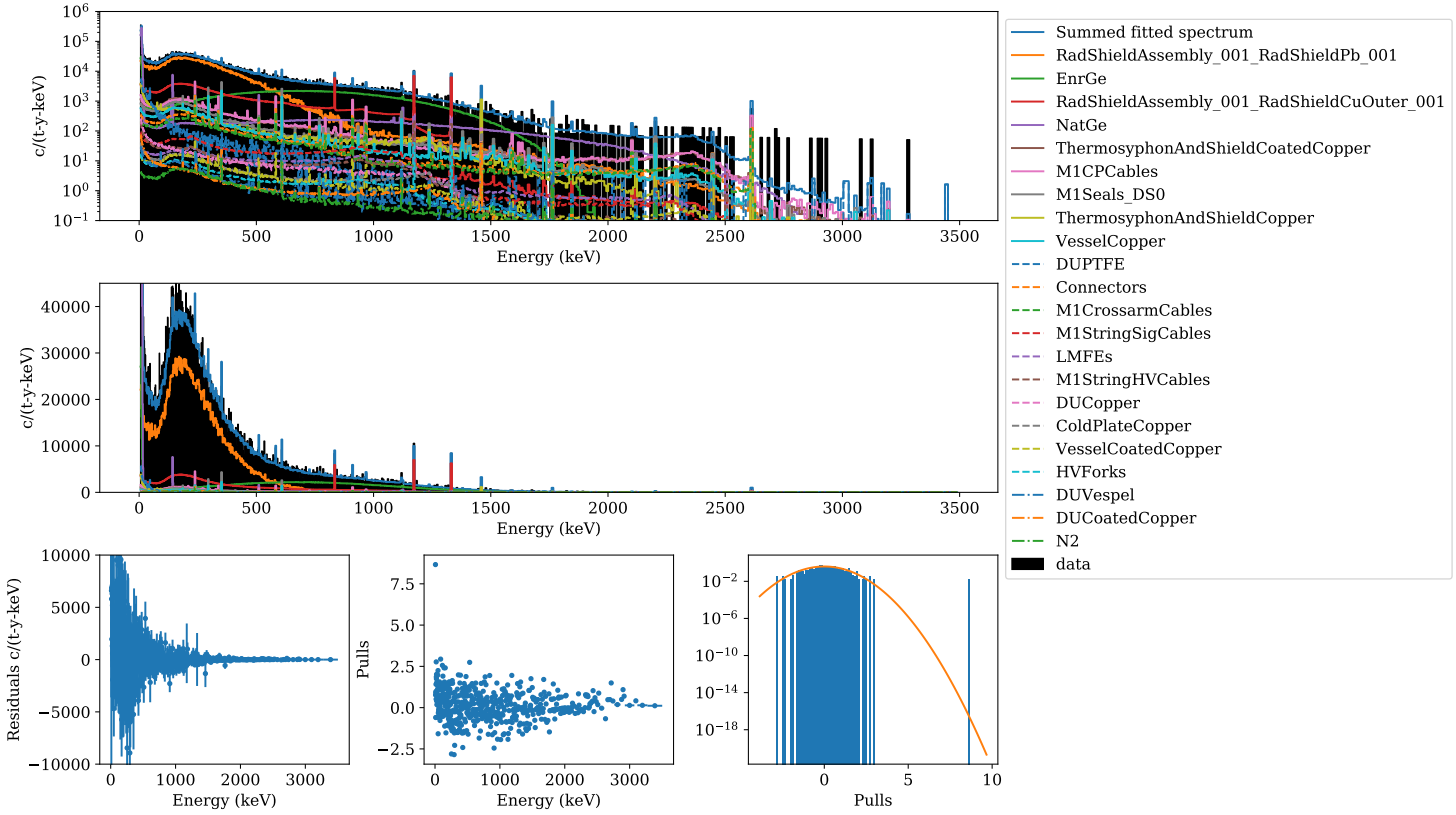

DS0, Gran, M1_Nat+M1_Enr

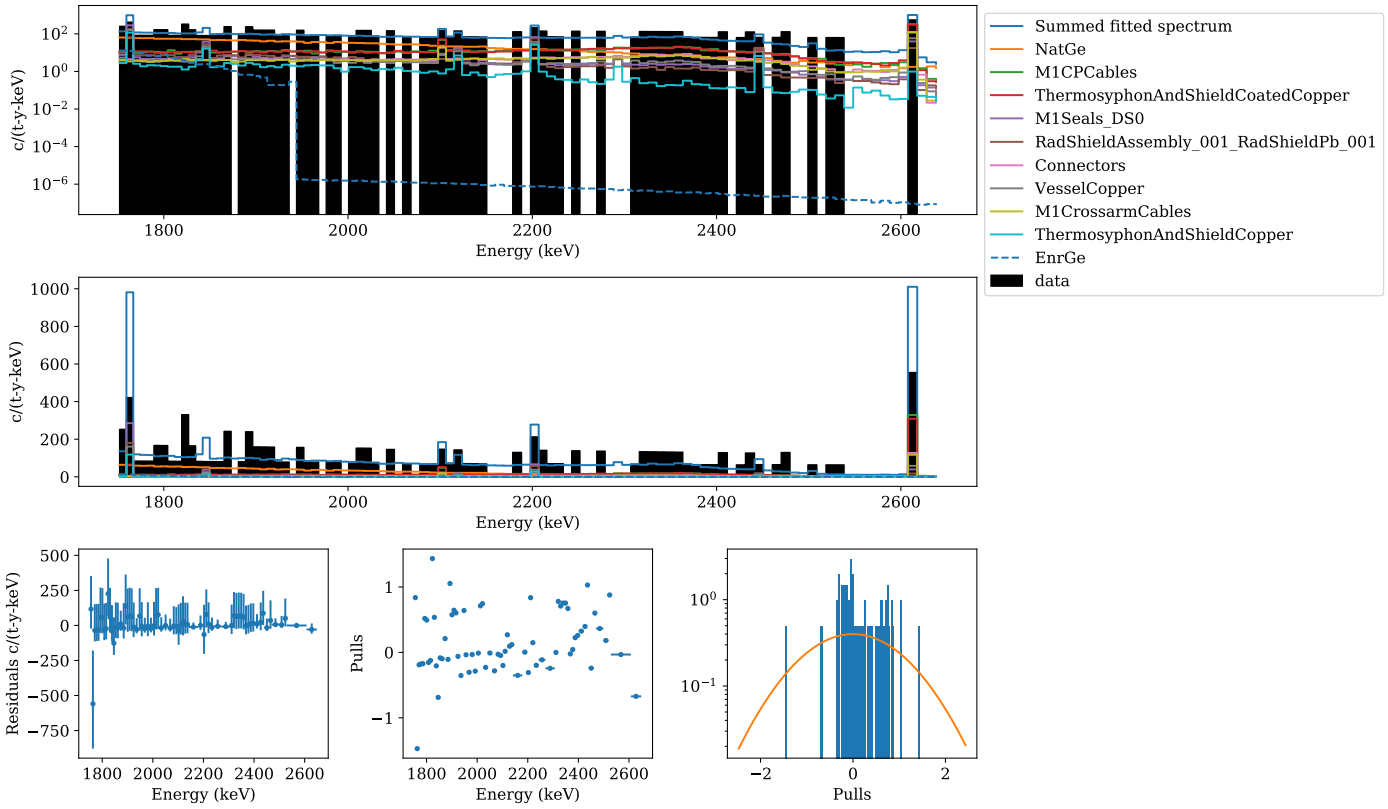

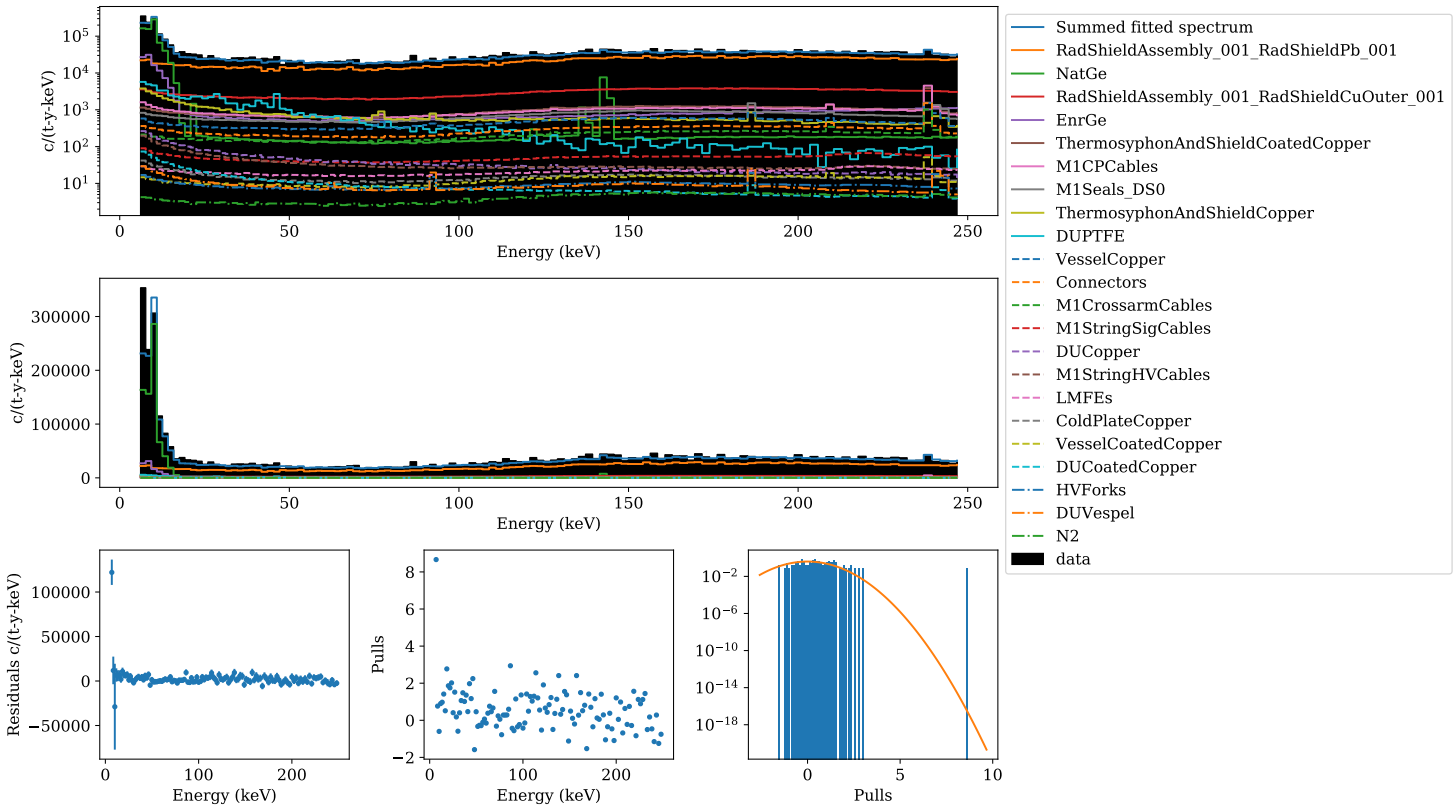
DS0, Gran, M1_Nat+M1_Enr
c/(t-y-keV)
Energy (keV)
Residuals c/(t-y-keV)
Pulls
Summed fitted spectrum
RadShieldAssembly_001_RadShieldPb_001
NatGe
RadShieldAssembly_001_RadShieldCuOuter_001
EnrGe
ThermosyphonAndShieldCoatedCopper
M1CPCables
M1Seals_DS0
ThermosyphonAndShieldCopper
DUPTFE
VesselCopper
Connectors
M1CrossarmCables
M1StringSigCables
DUCopper
M1StringHVCables
LMFEs
ColdPlateCopper
VesselCoatedCopper
DUCoatedCopper
HVForks
DUVespel
N2
data

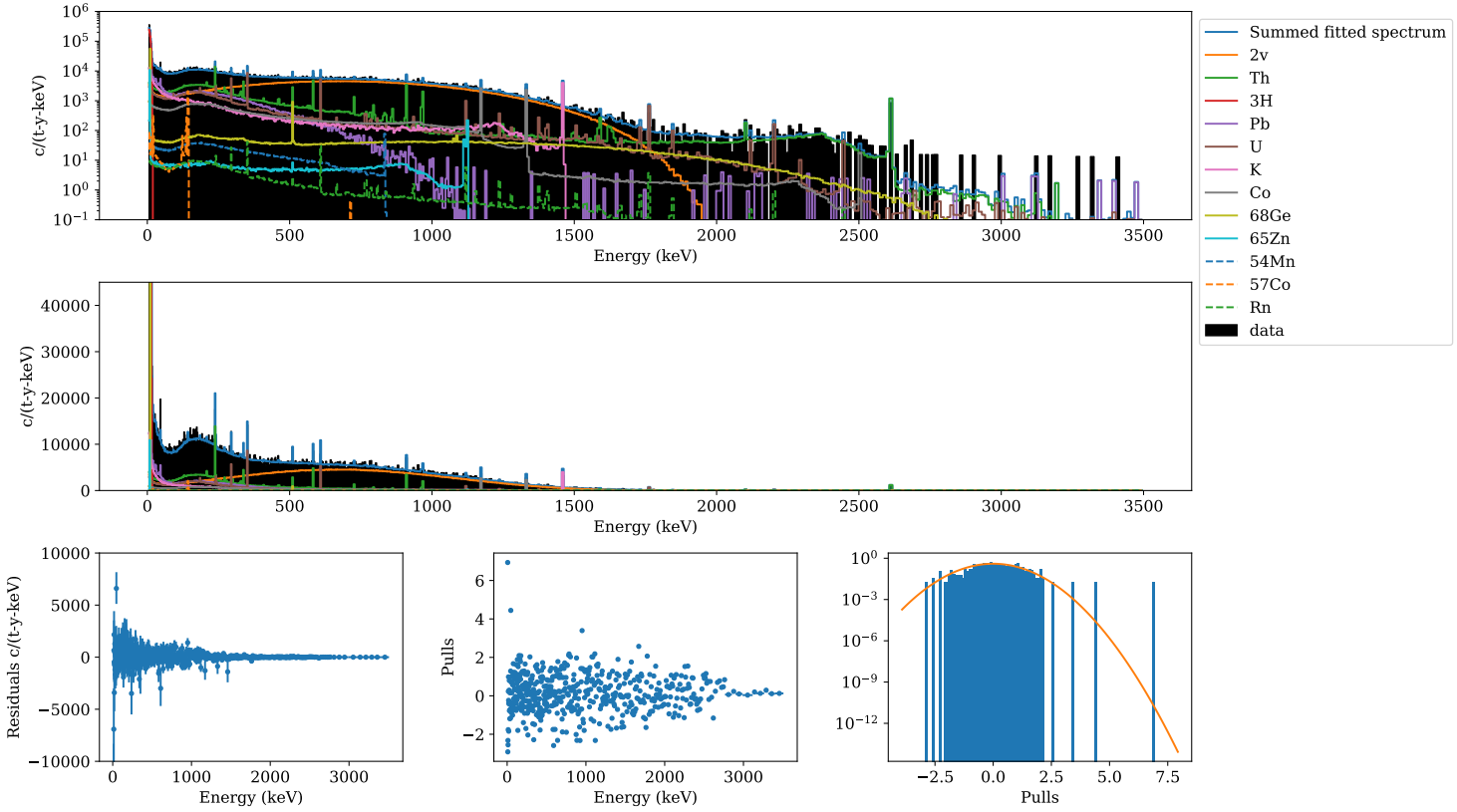
DS12+DS3456, Gran, M1_Nat+M1_Enr
c/(t-y-keV)
Energy (keV)
Summed fitted spectrum
2v
Th
3H
Pb
U
K
Co
68Ge
65Zn
54Mn
57Co
Rn
data
Residuals c/(t-y-keV)
Pulls
Energy (keV)
Pulls

DS12+DS3456, Gran, M1_Nat+M1_Enr

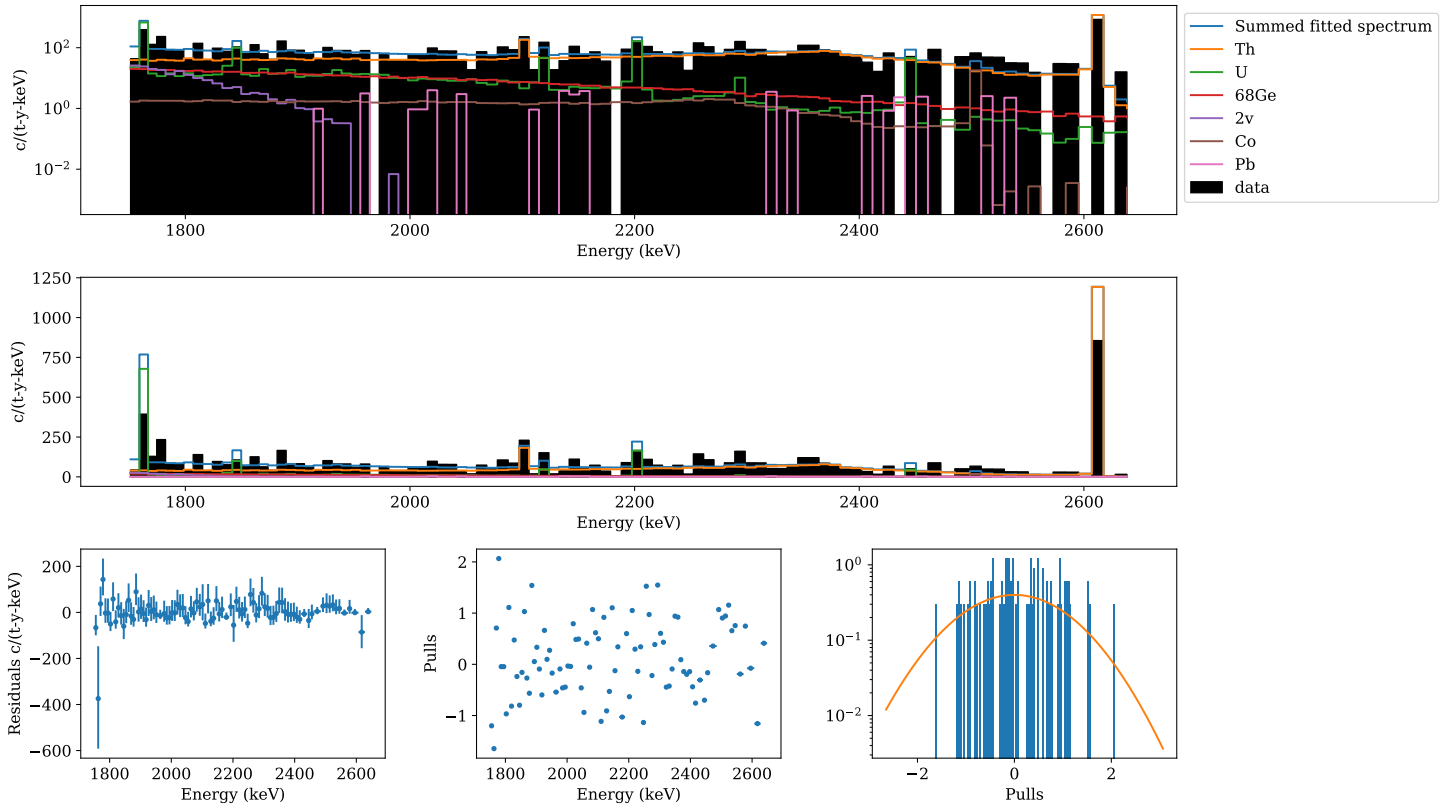

DS12+DS3456, Gran, M1_Nat+M1_Enr

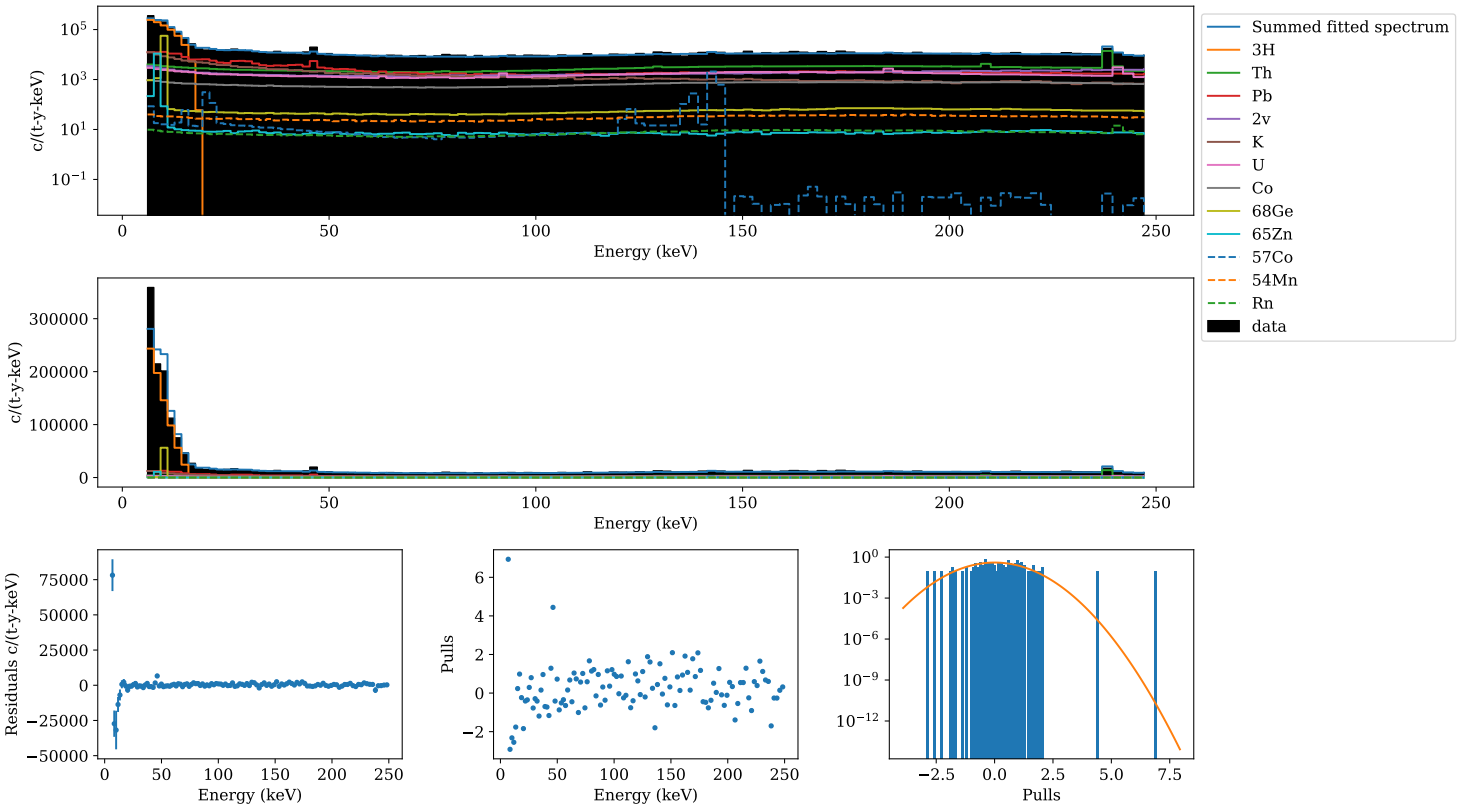

DS12+DS3456, Gran, M1_Nat+M1_Enr

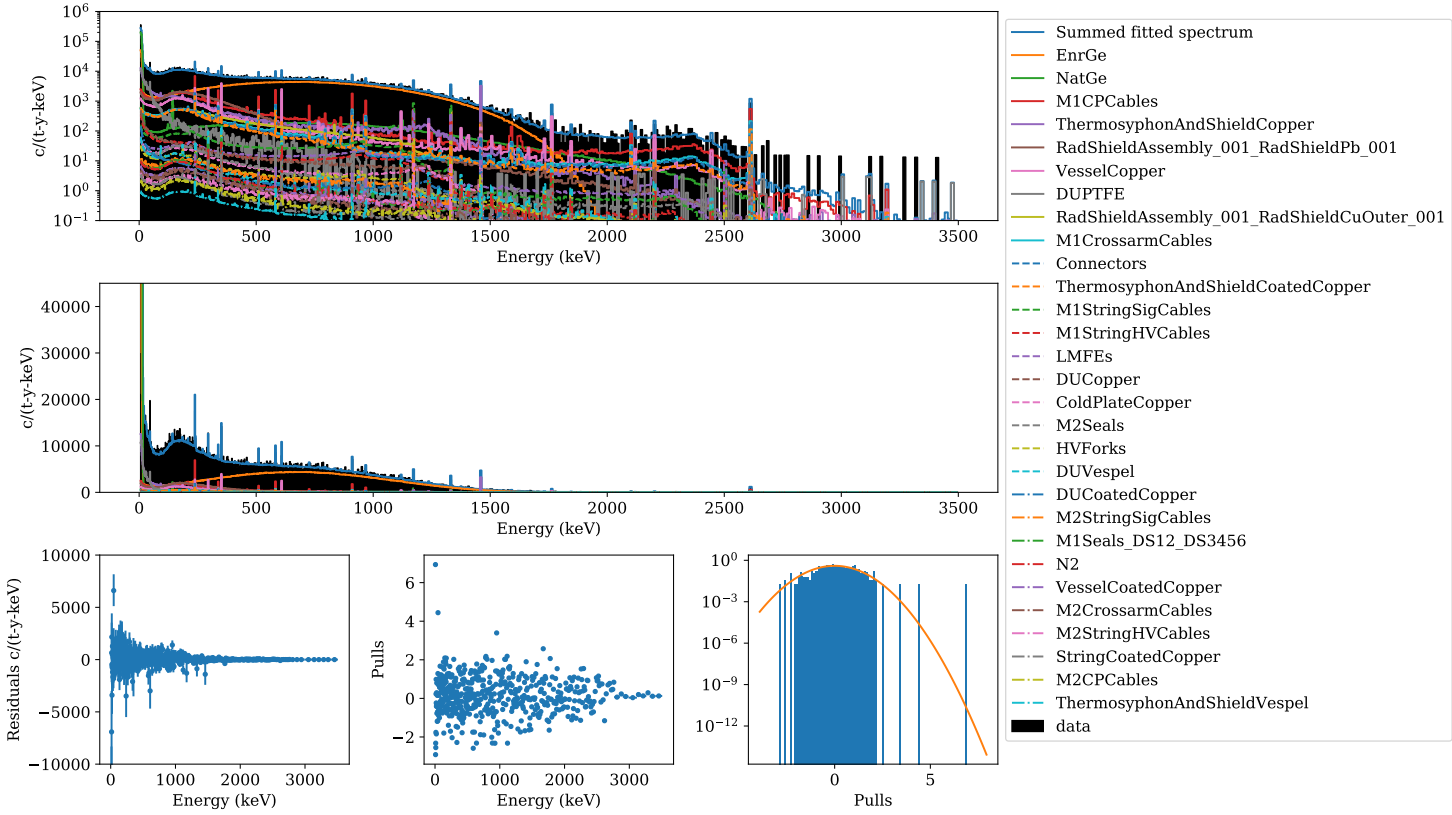

DS12+DS3456, Gran, M1_Nat+M1_Enr

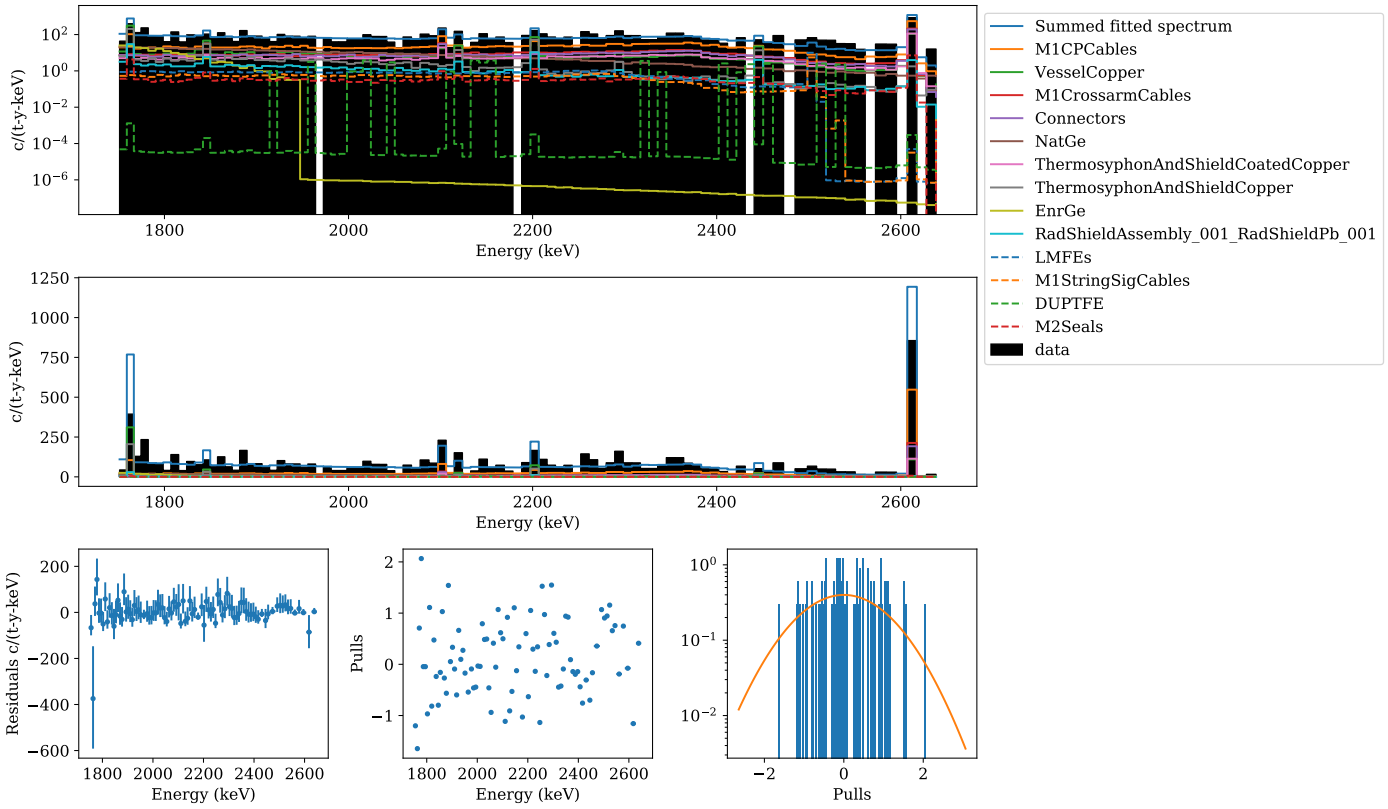

DS12+DS3456, Gran, M1_Nat+M1_Enr

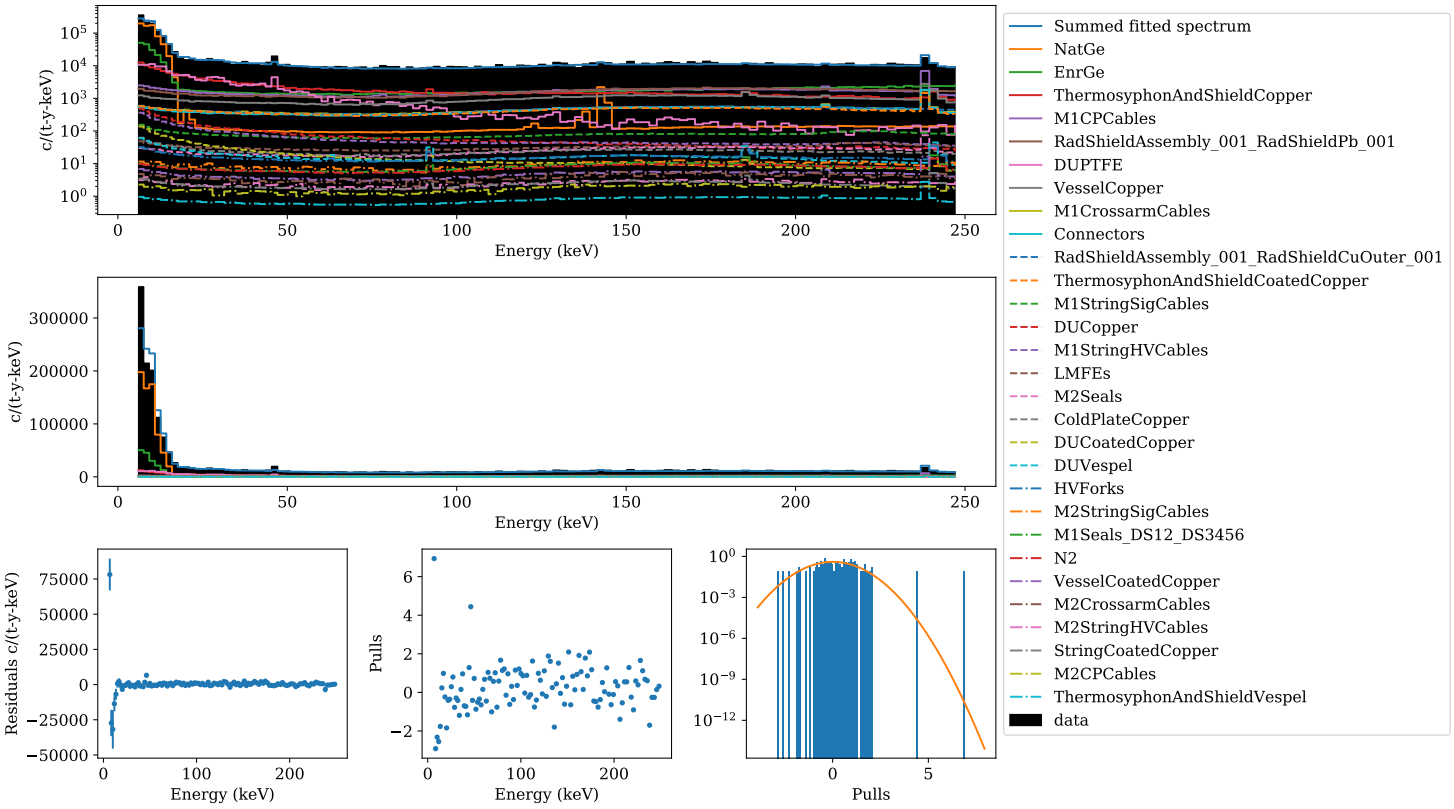

DS12+DS3456, Gran, M2_Nat+M2_Enr

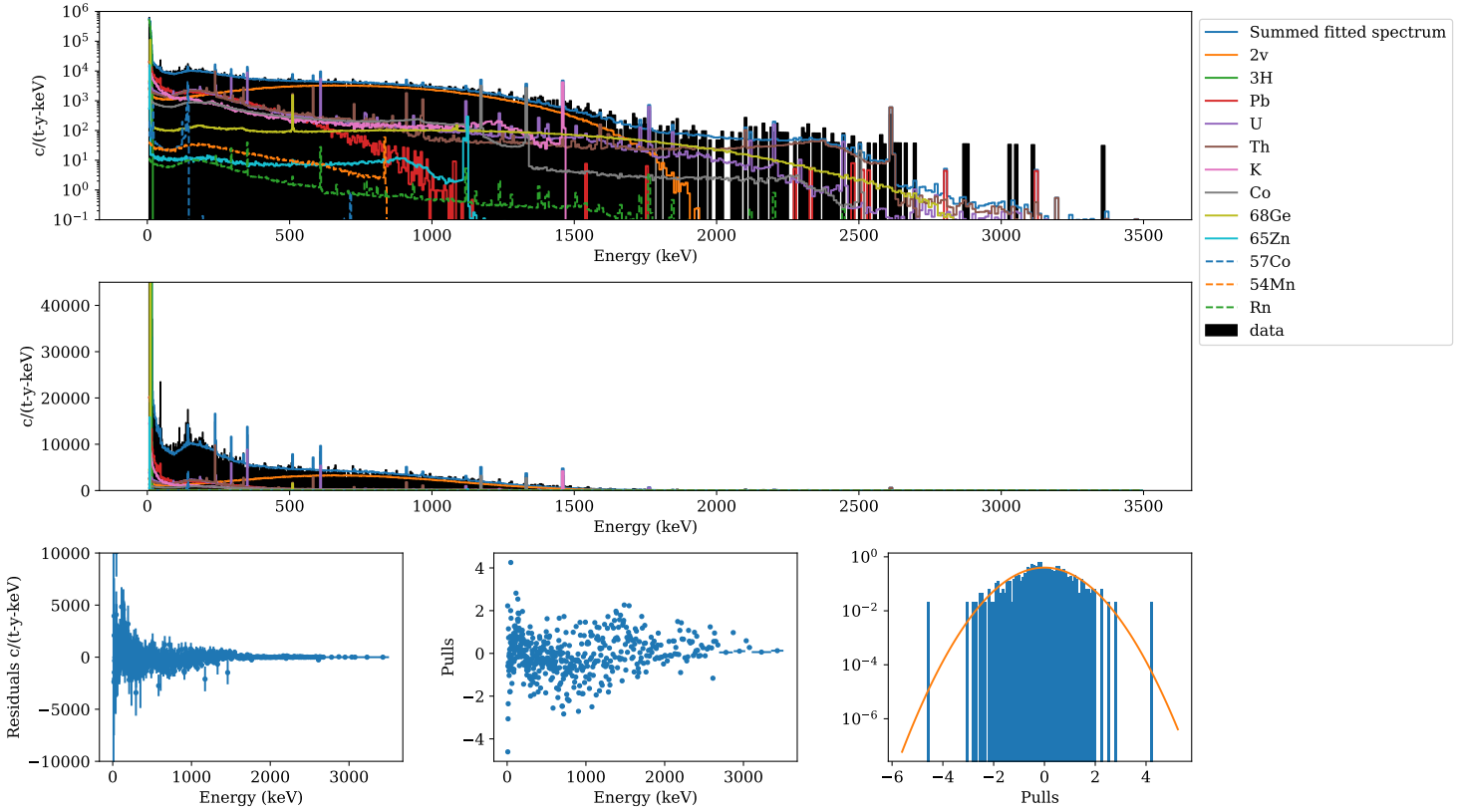

DS12+DS3456, Gran, M2_Nat+M2_Enr

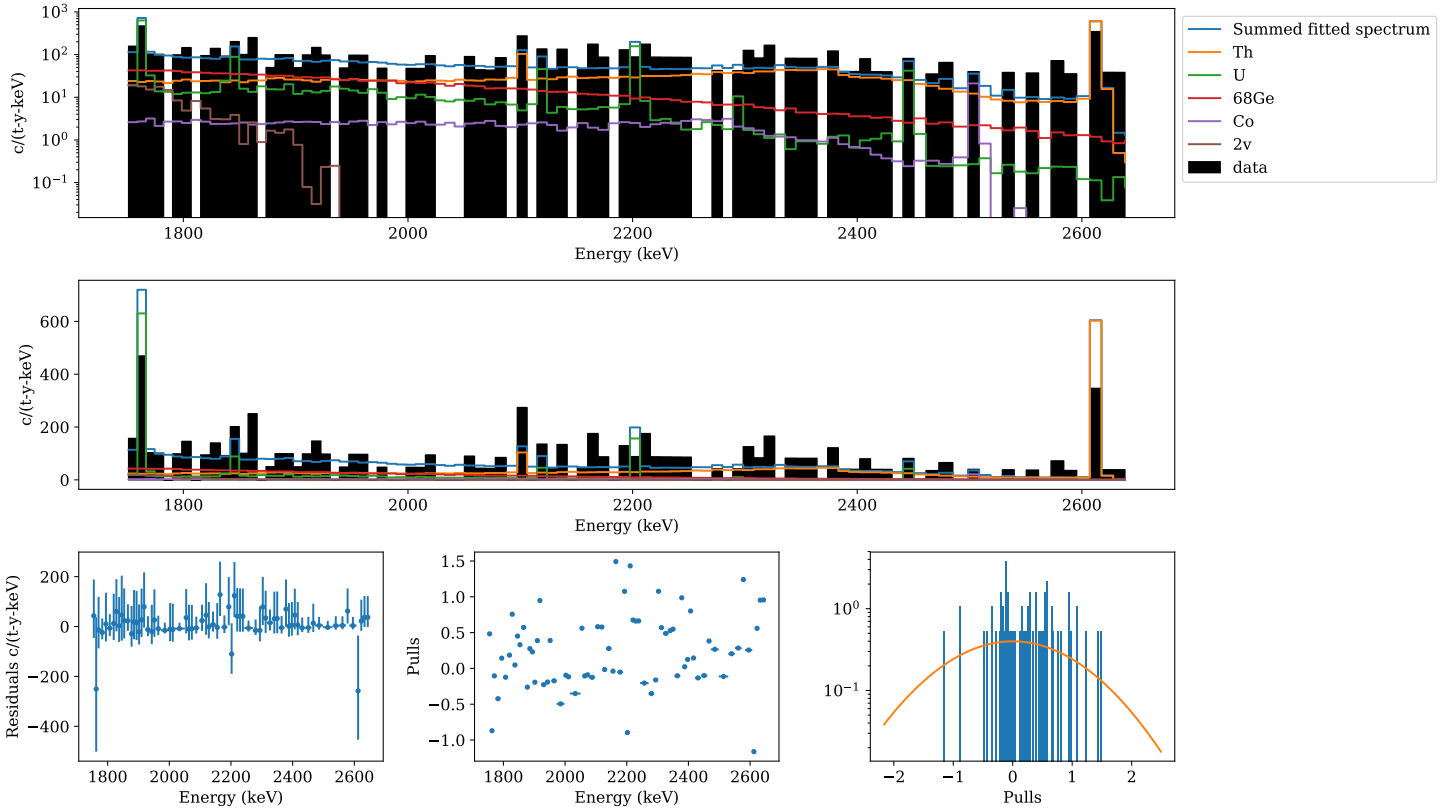

DS12+DS3456, Gran, M2_Nat+M2_Enr

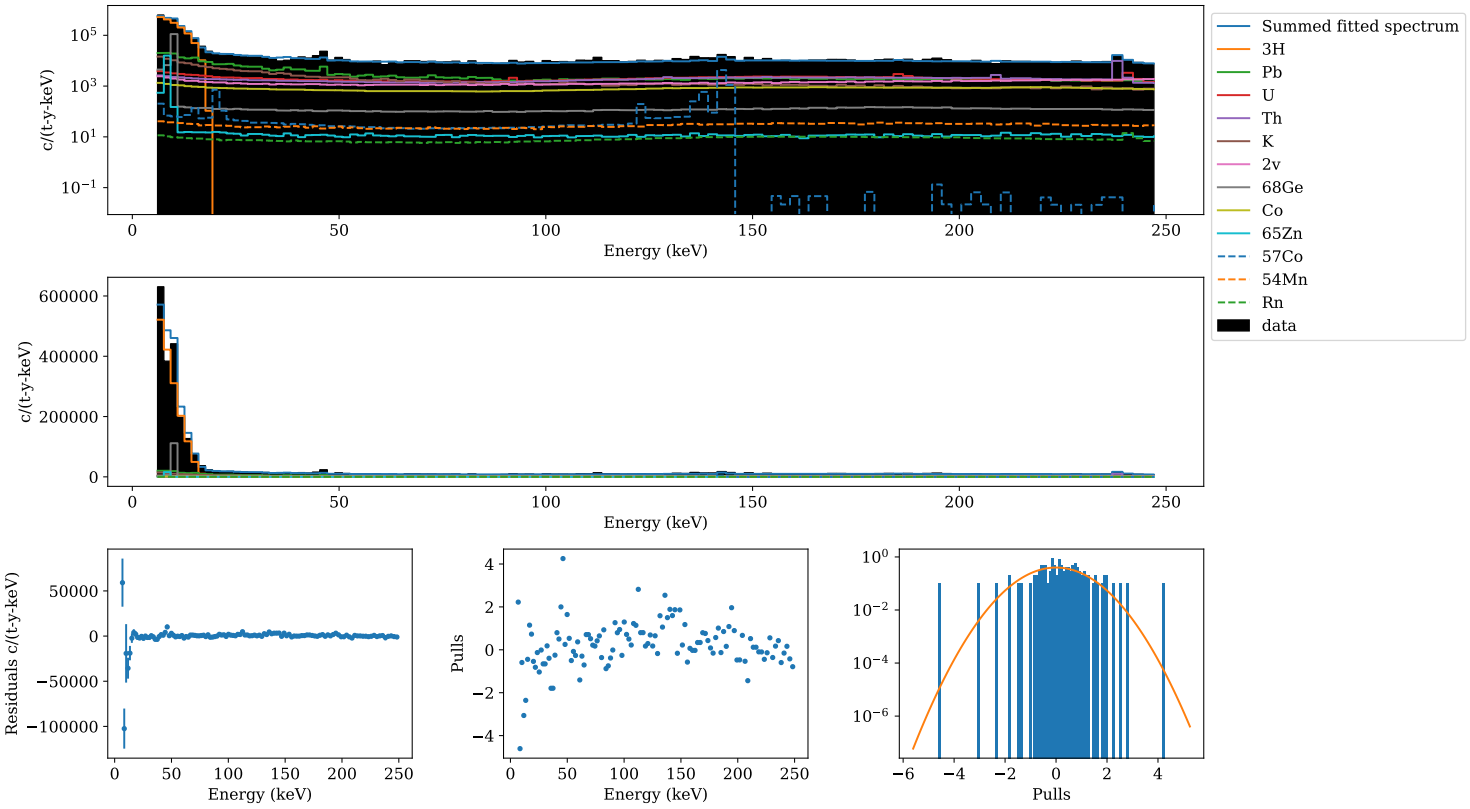

DS12+DS3456, Gran, M2_Nat+M2_Enr

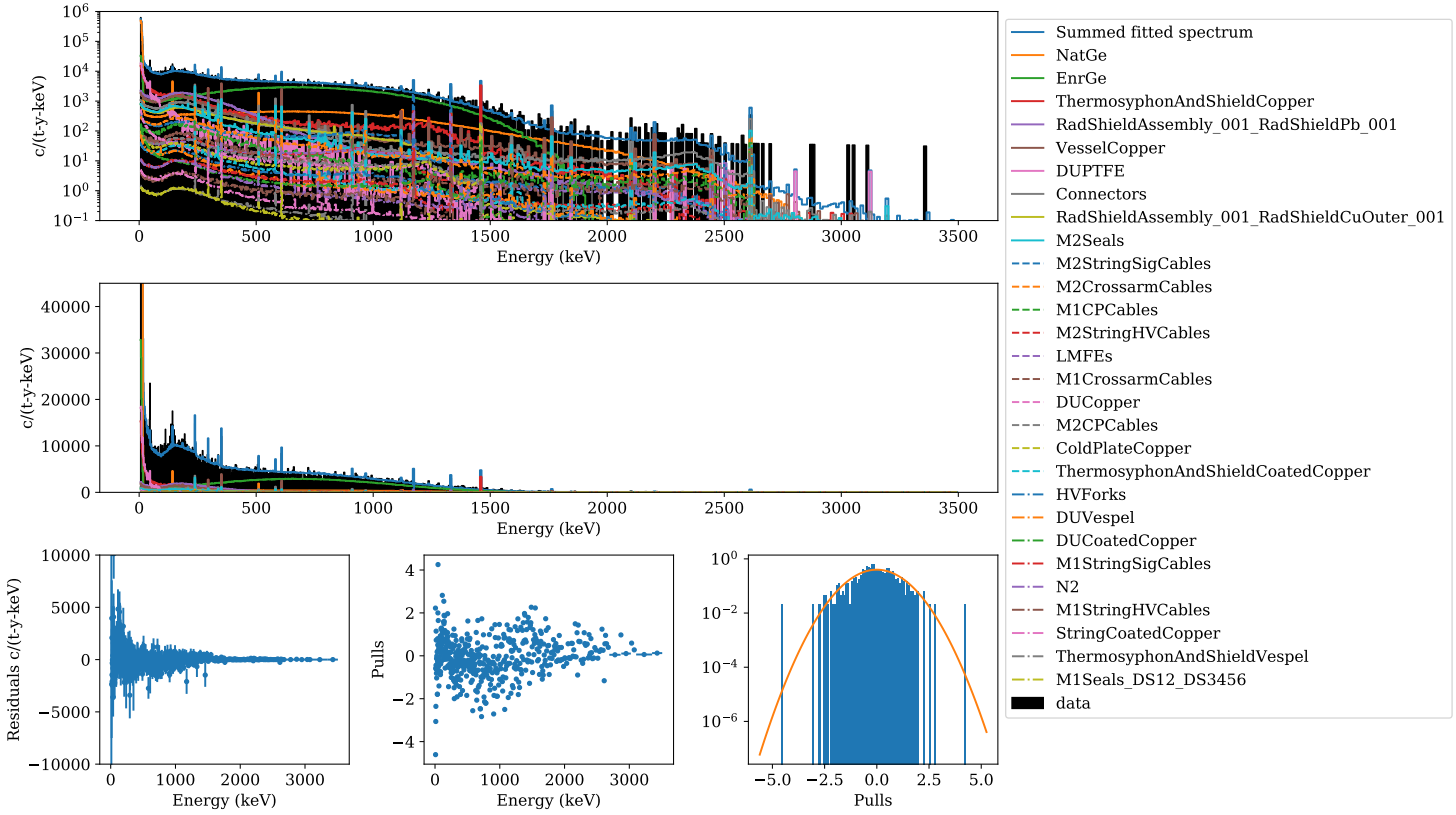

DS12+DS3456, Gran, M2_Nat+M2_Enr

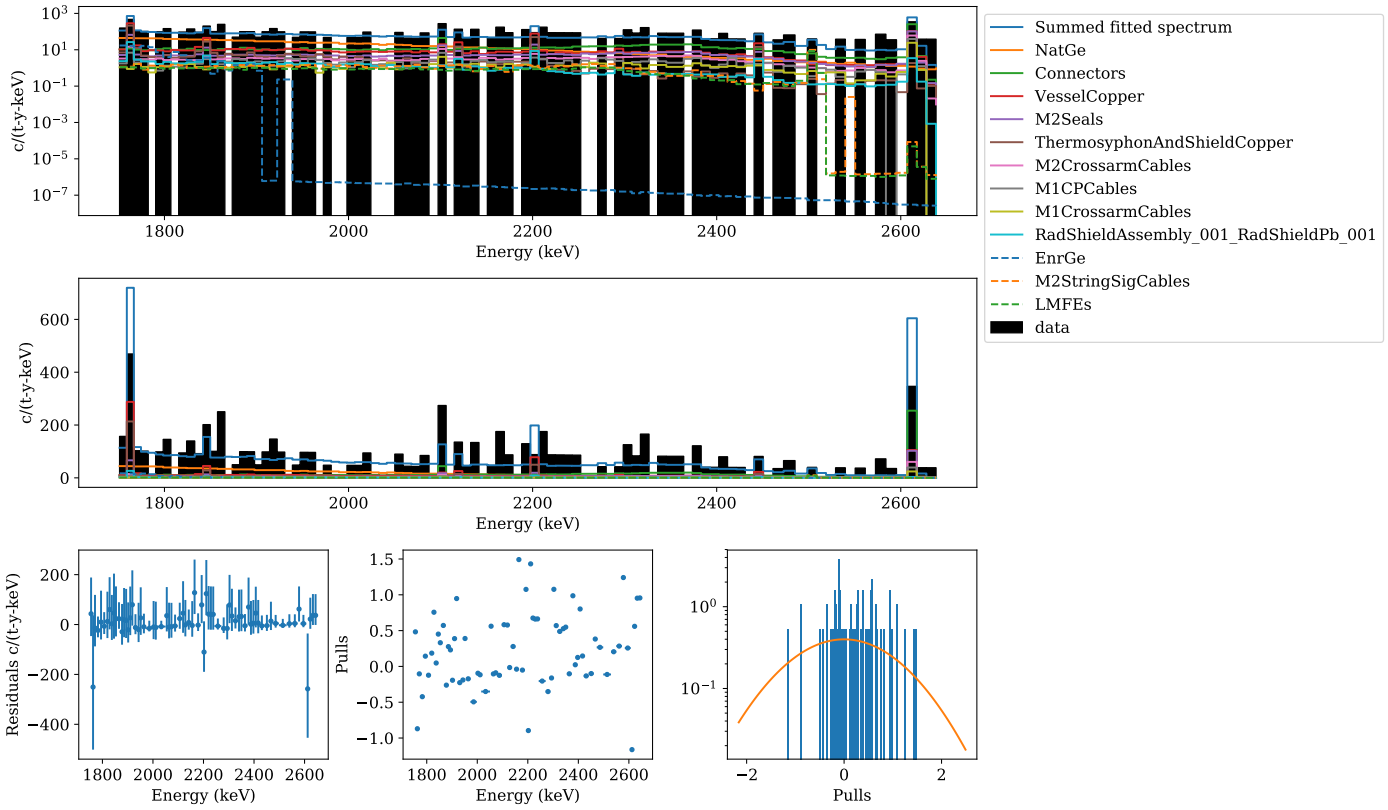

DS12+DS3456, Gran, M2_Nat+M2_Enr

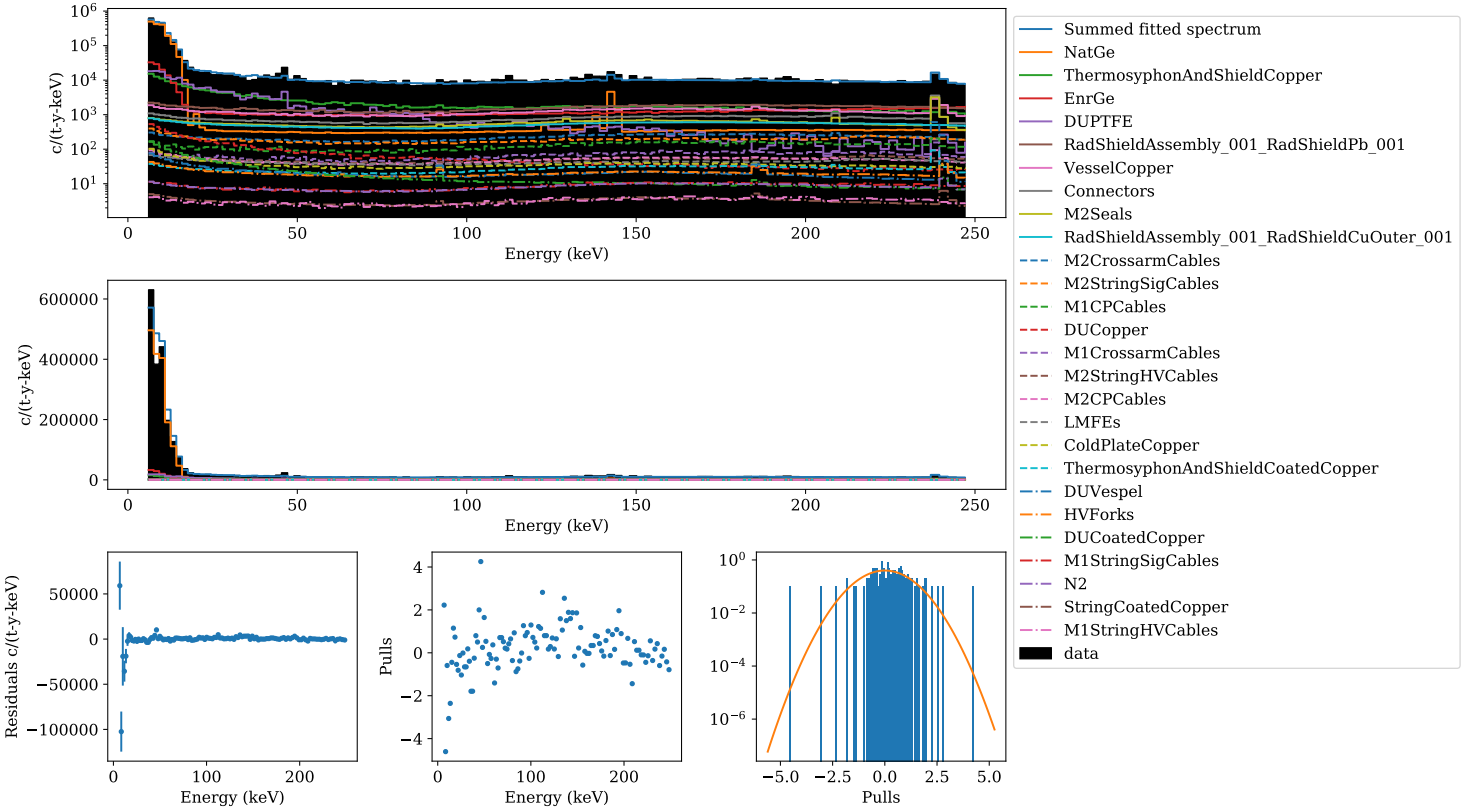

DS0, Gran, M1_Enr

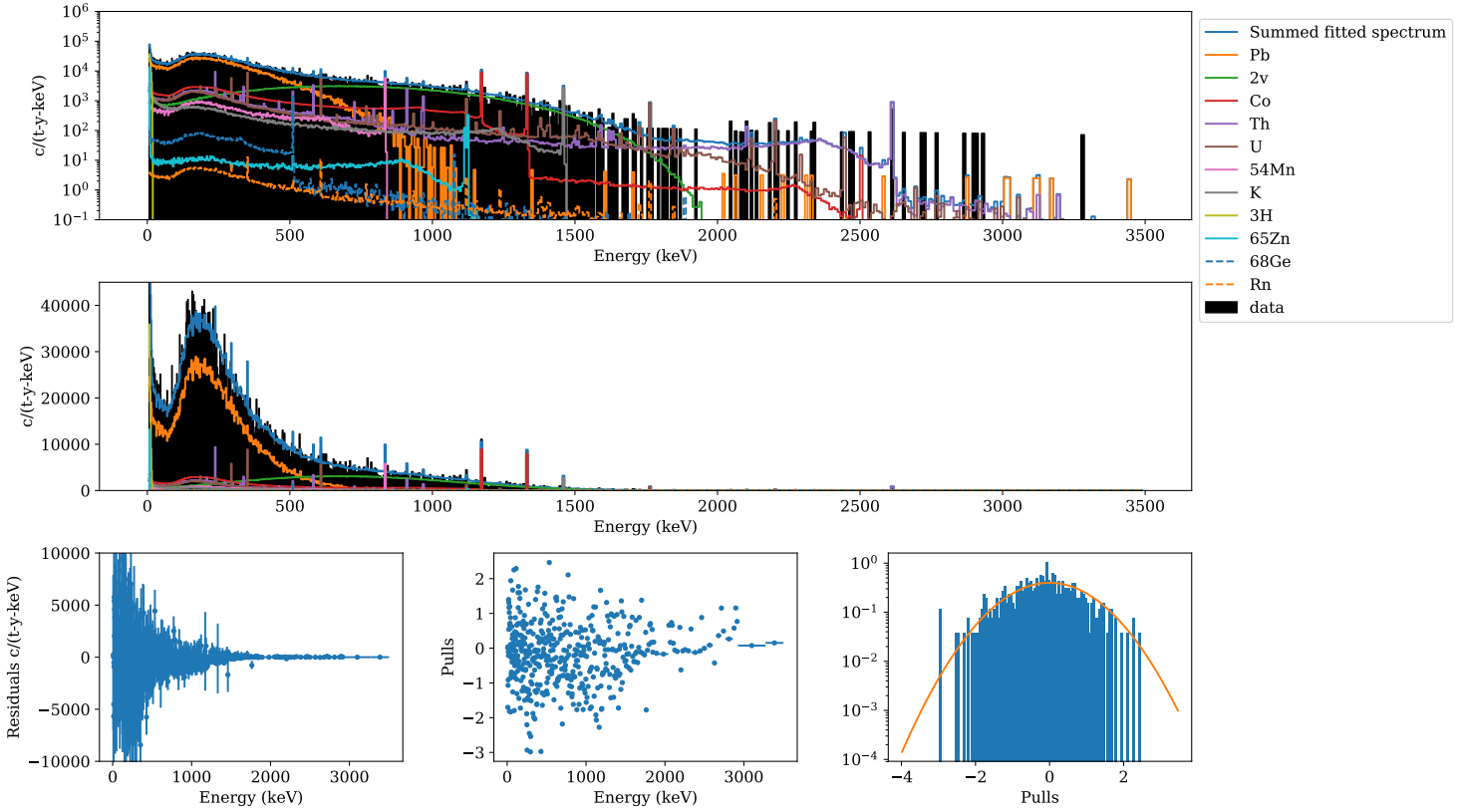

DS0, Gran, M1_Enr

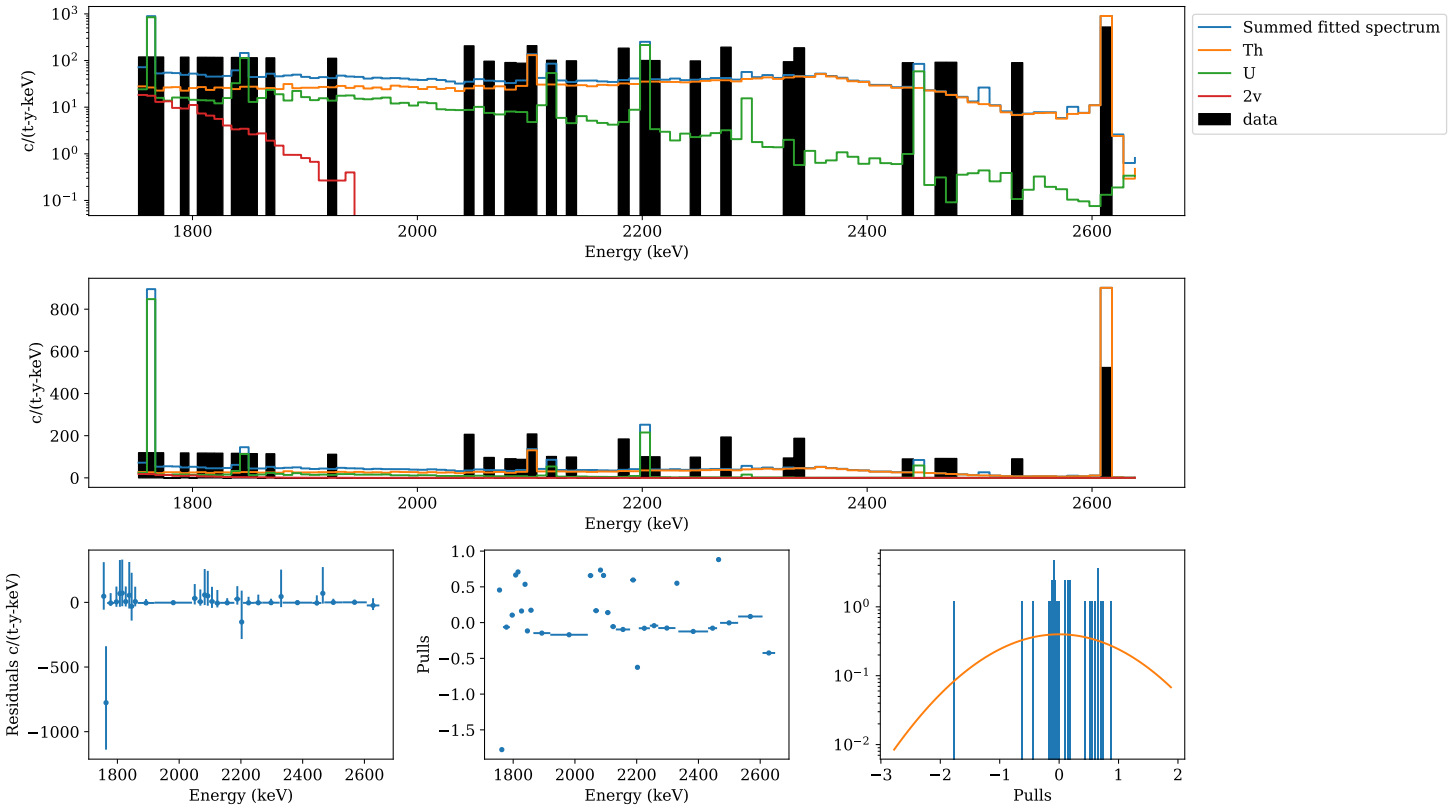

DS0, Gran, M1_Enr

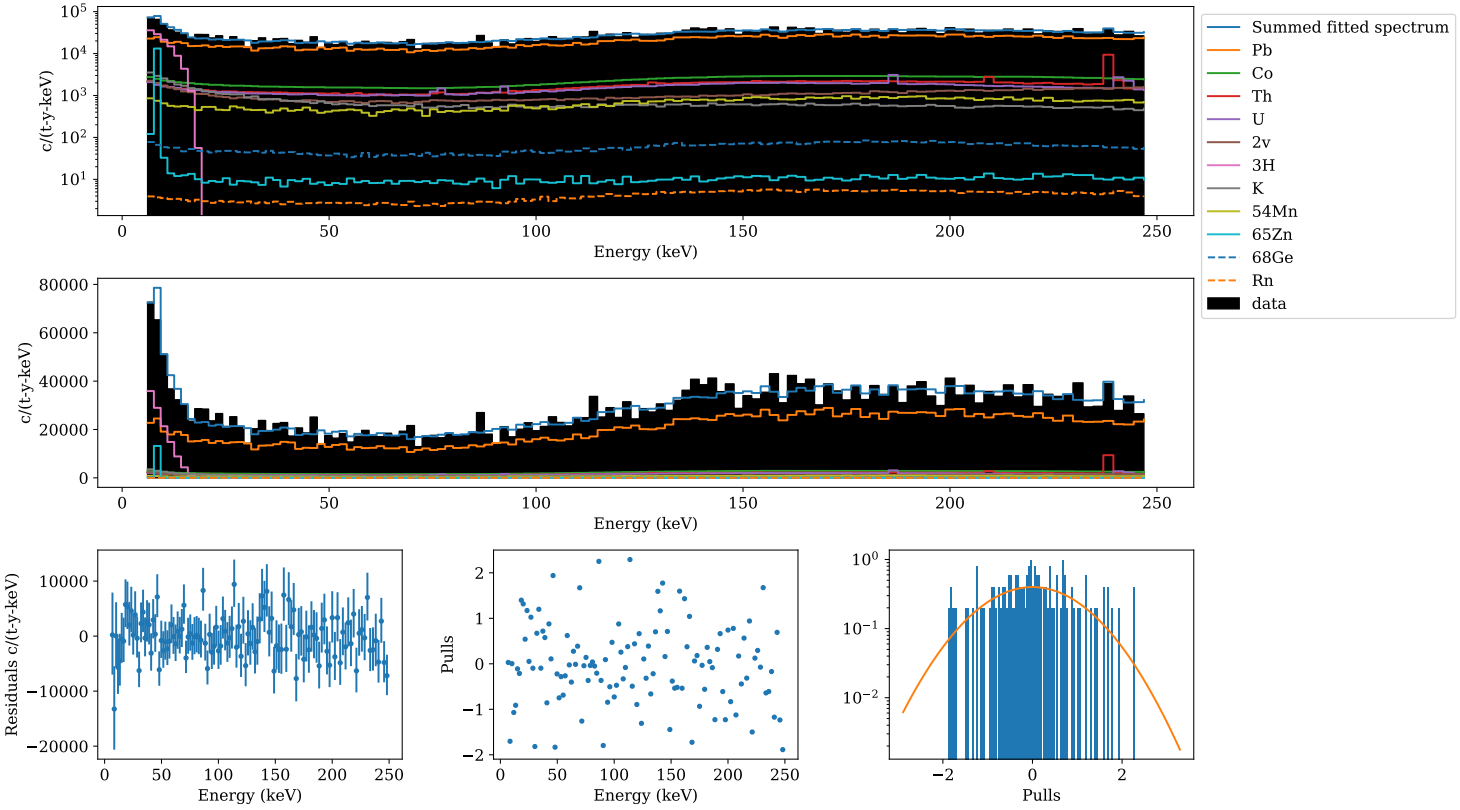

DS0, Gran, M1_Enr

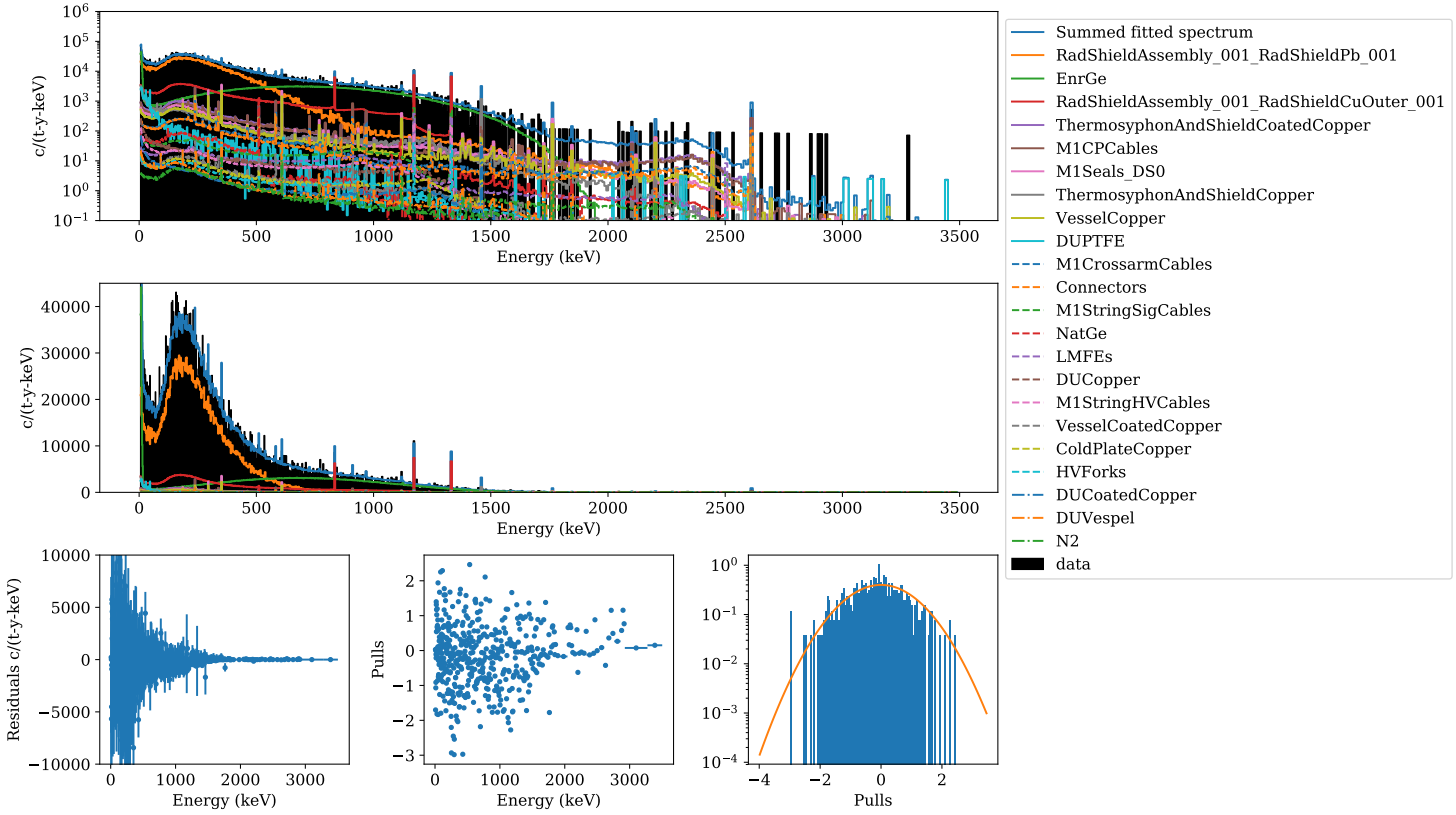

DS0, Gran, M1_Enr

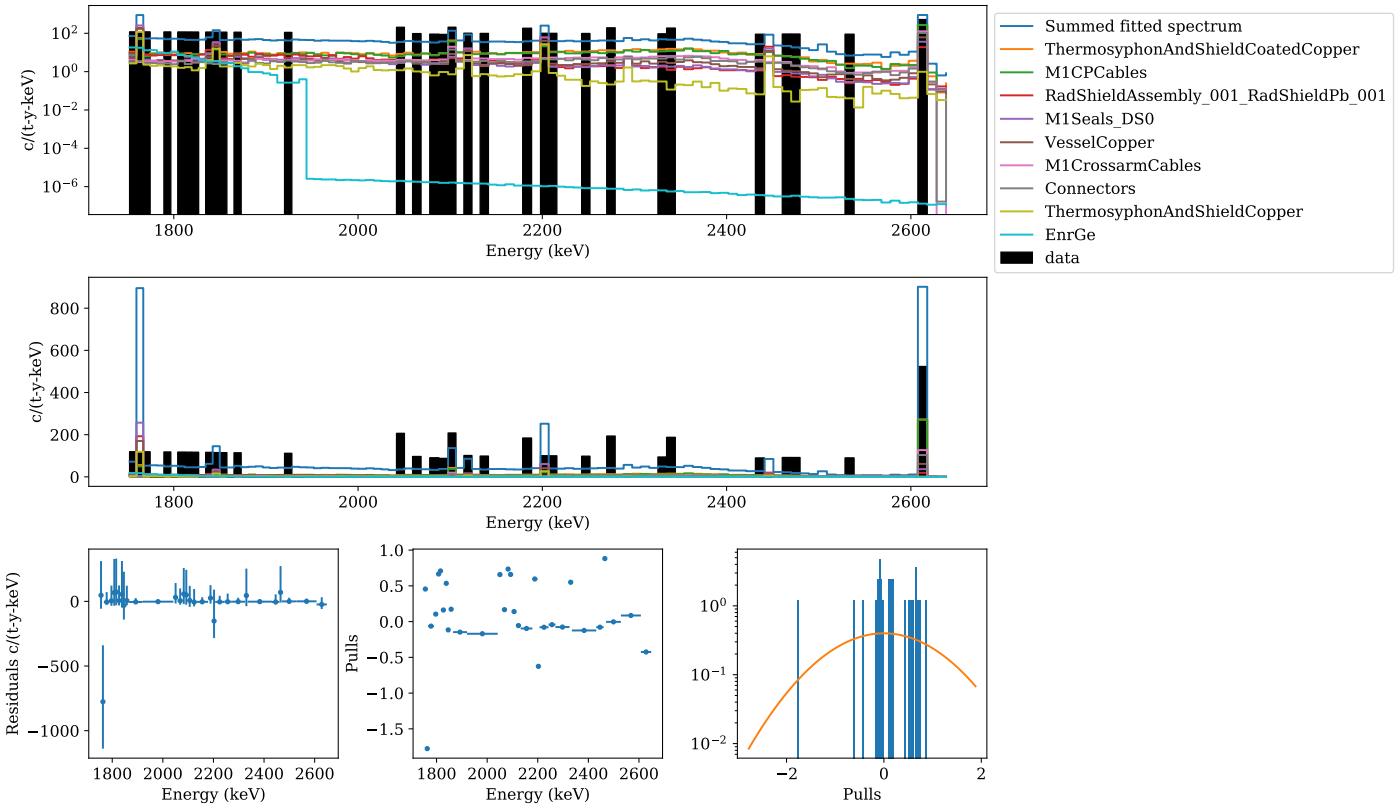

DS0, Gran, M1_Enr

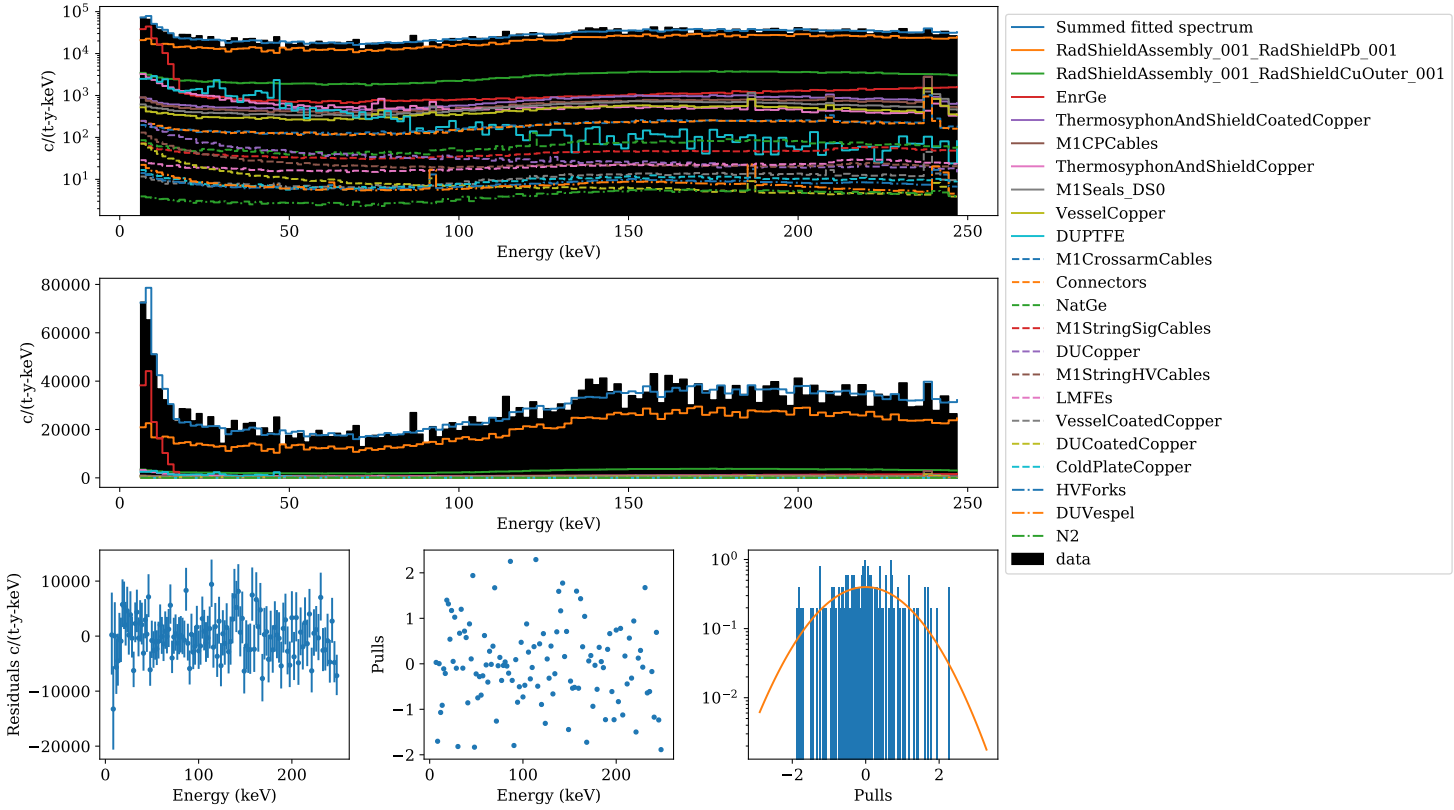

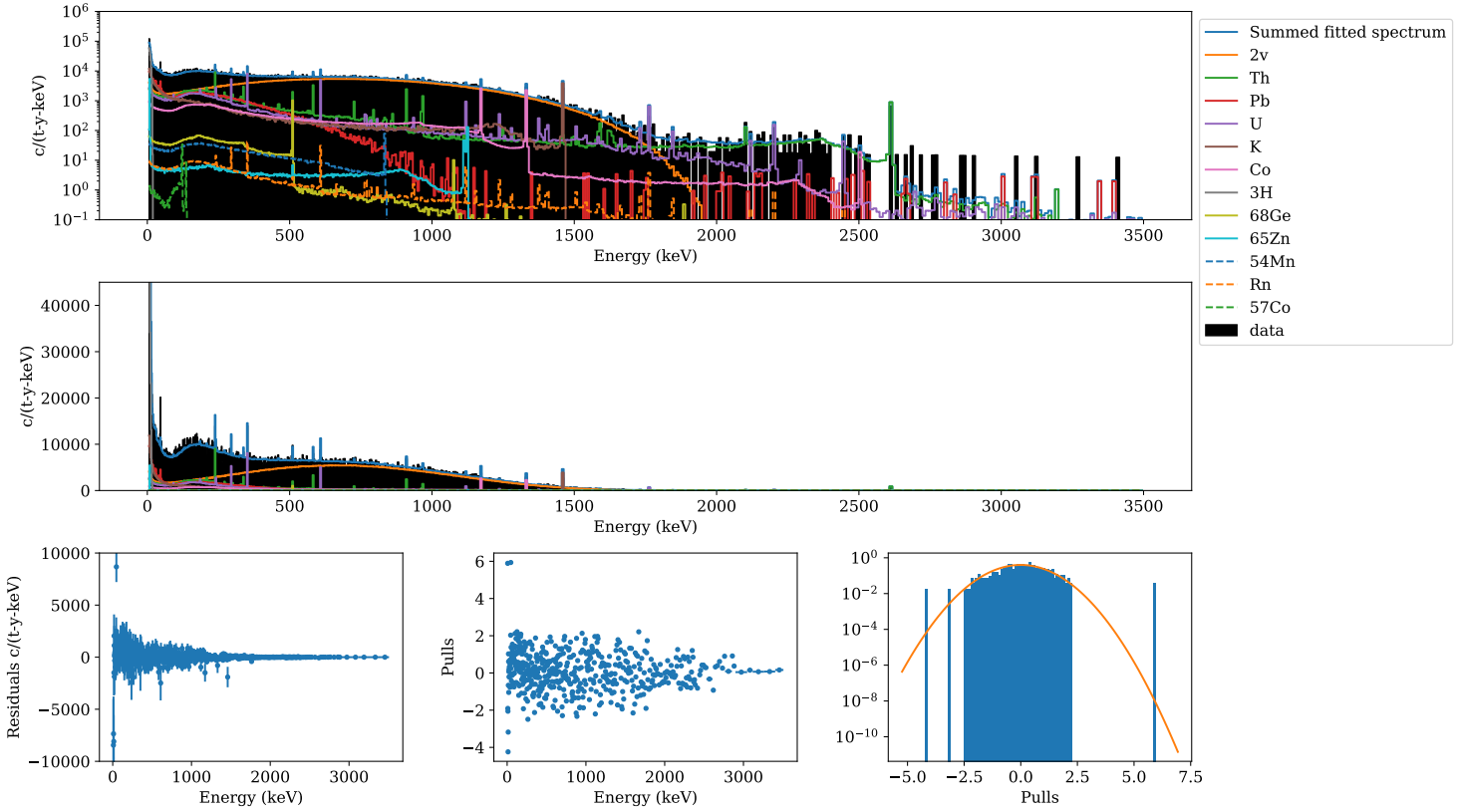
DS12+DS3456, Gran, M1_Enr+M2_Enr
c/(t-y-keV)
Energy (keV)
Summed fitted spectrum
2v
Th
Pb
U
K
Co
3H
68Ge
65Zn
54Mn
Rn
57Co
data
Residuals c/(t-y-keV)
Pulls

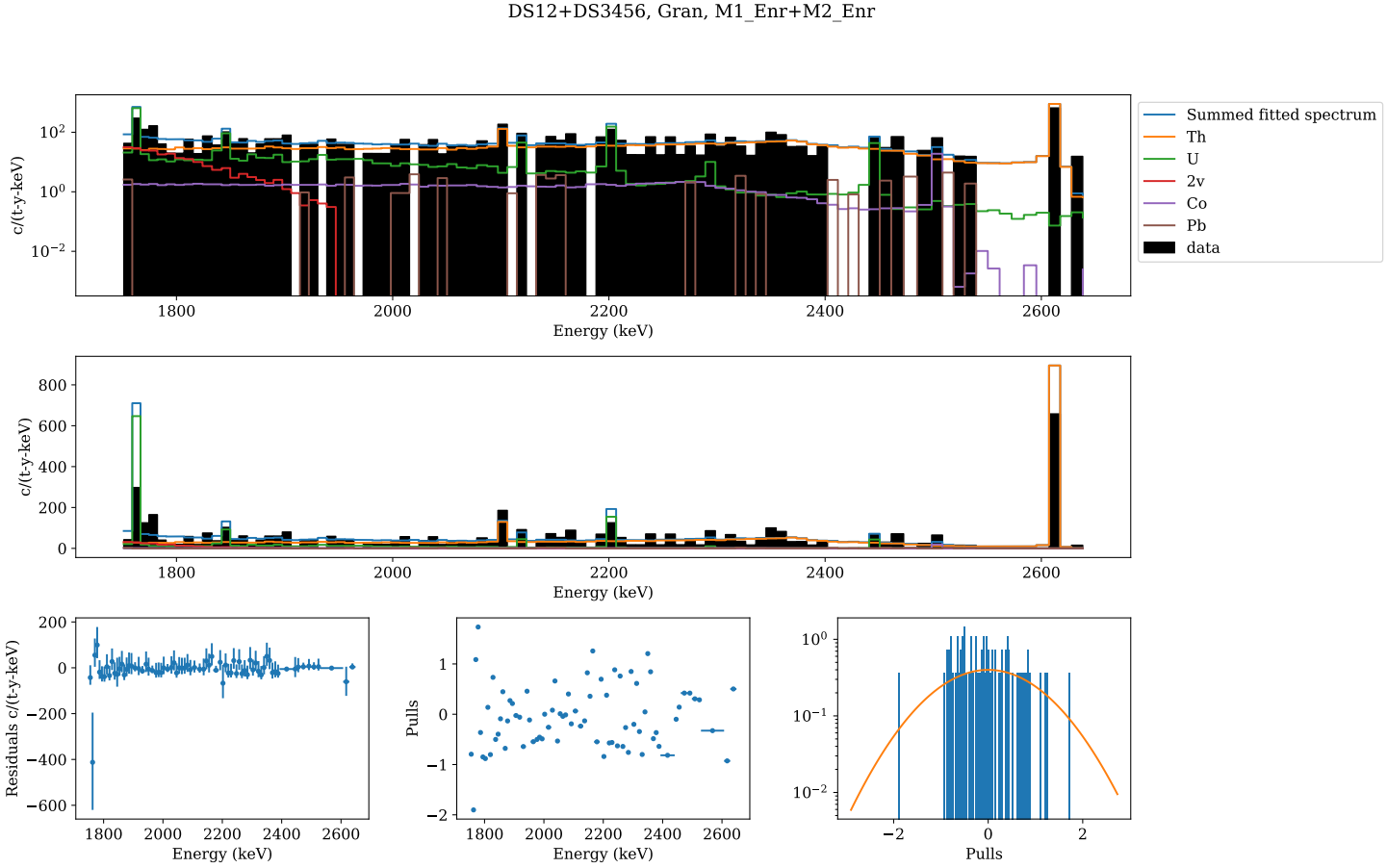
DS12+DS3456, Gran, M1_Enr+M2_Enr
Summed fitted spectrum
Th
U
2v
Co
Pb
data
c/(t-y-keV)
Energy (keV)
Residuals c/(t-y-keV)
Pulls

DS12+DS3456, Gran, M1_Enr+M2_Enr

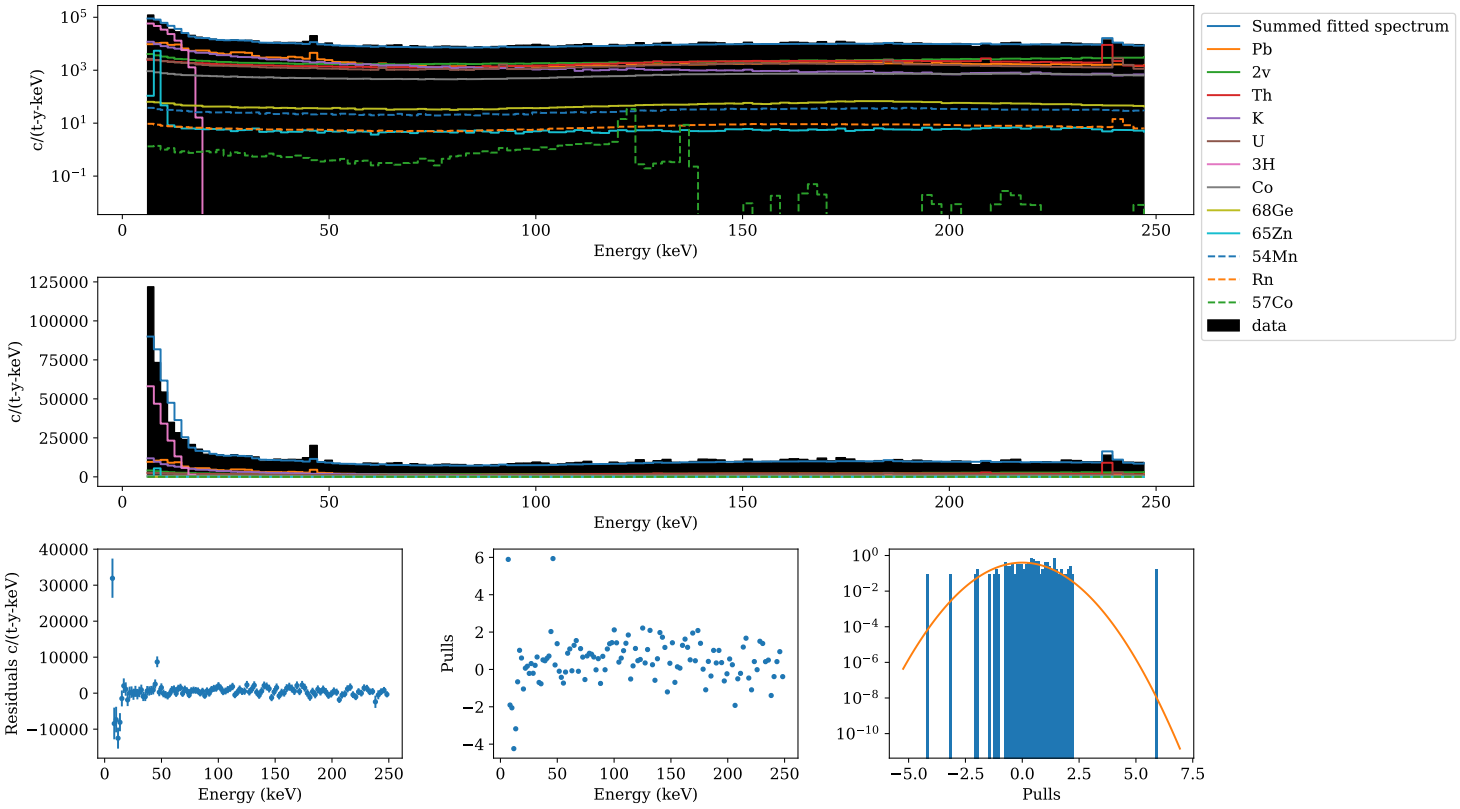

DS12+DS3456, Gran, M1_Enr+M2_Enr

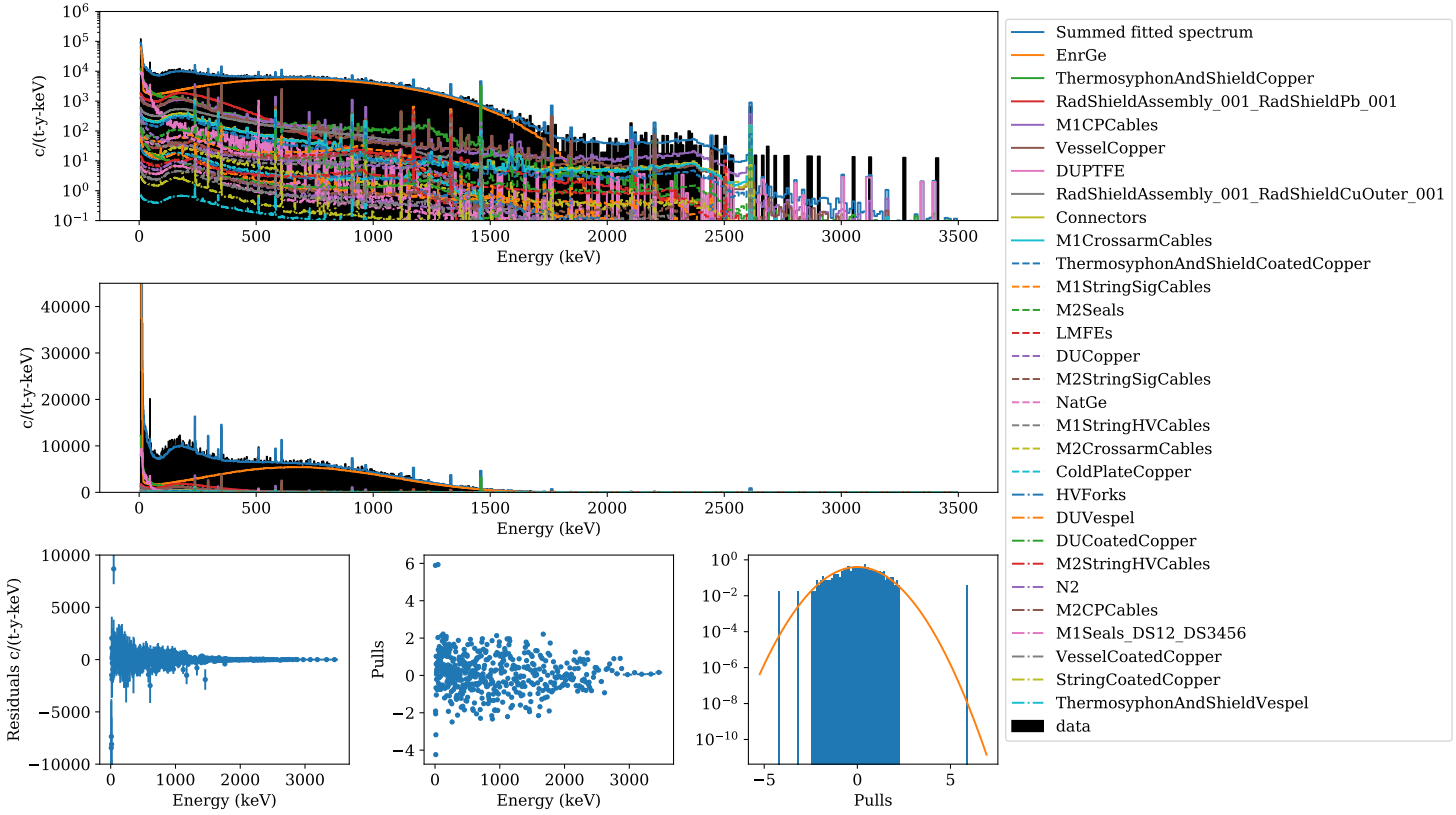

DS12+DS3456, Gran, M1_Enr+M2_Enr

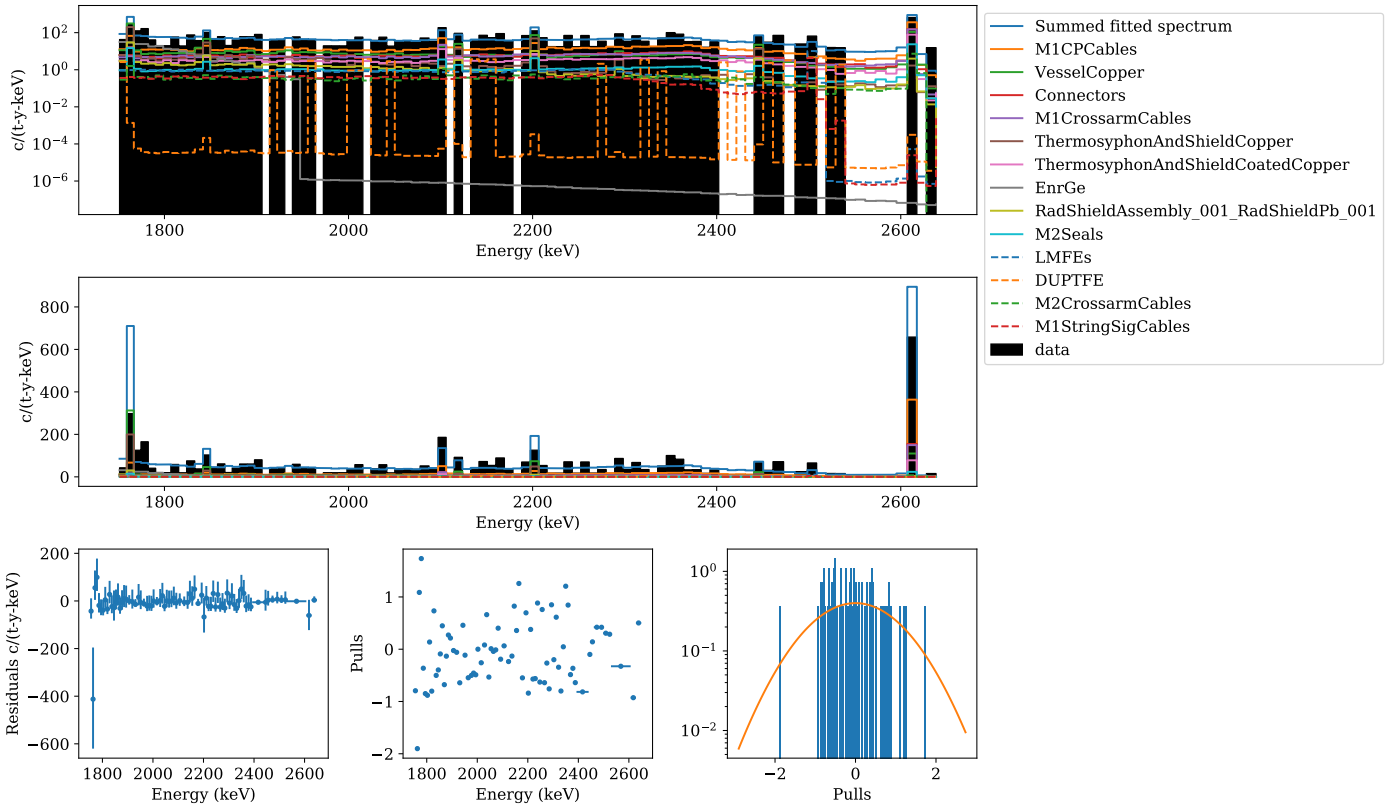

DS12+DS3456, Gran, M1_Enr+M2_Enr

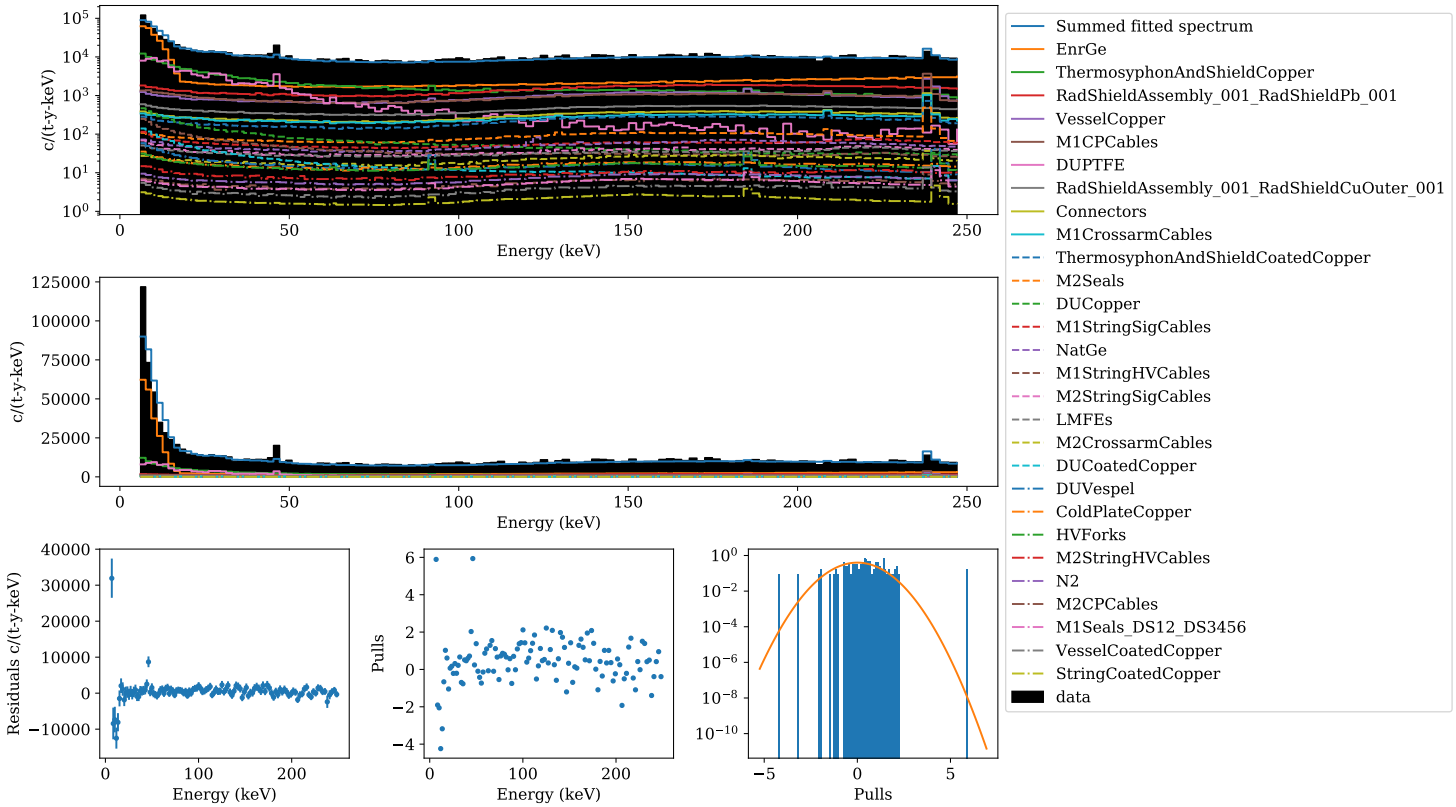

DS0, Gran, M1_Nat

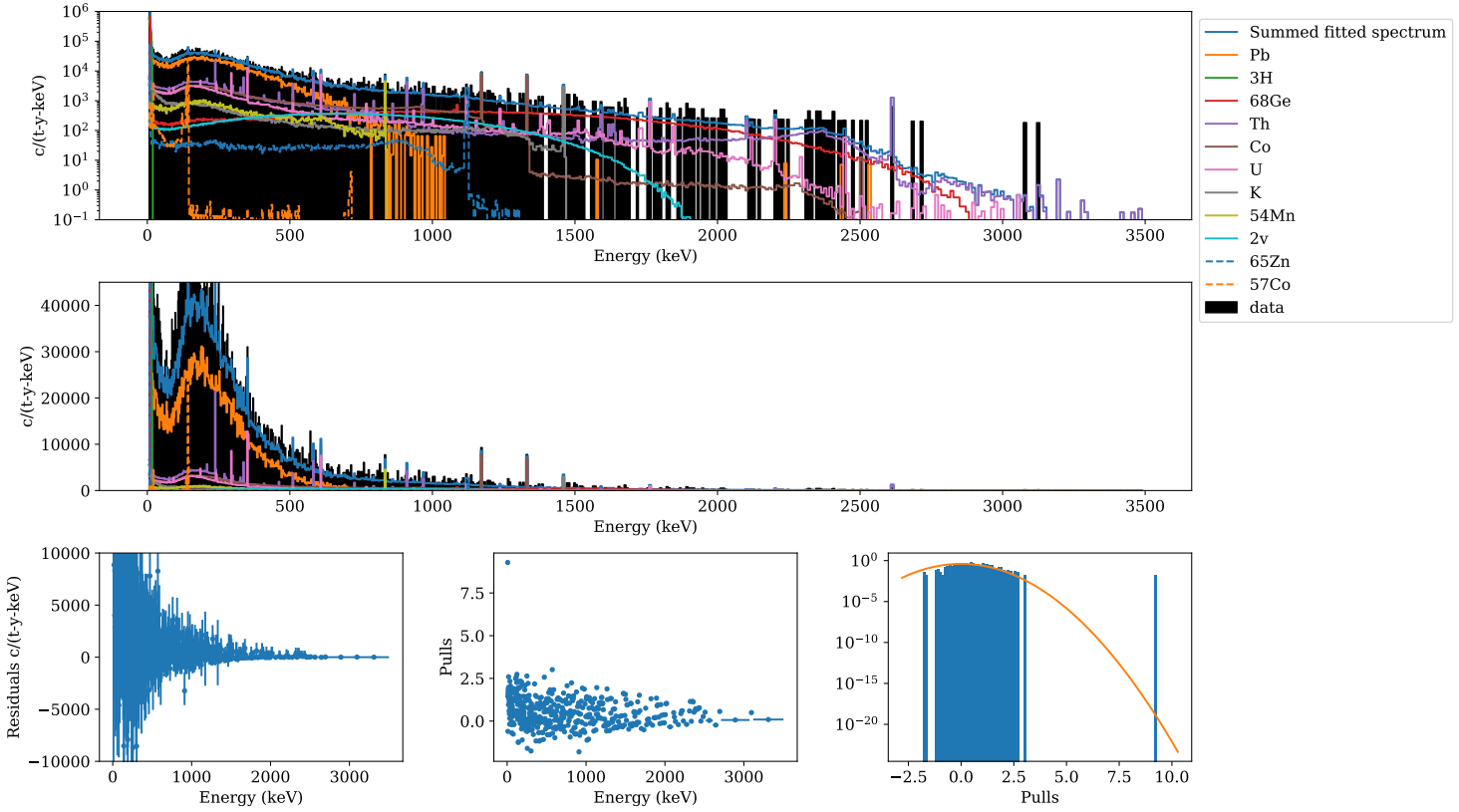

DS0, Gran, M1_Nat

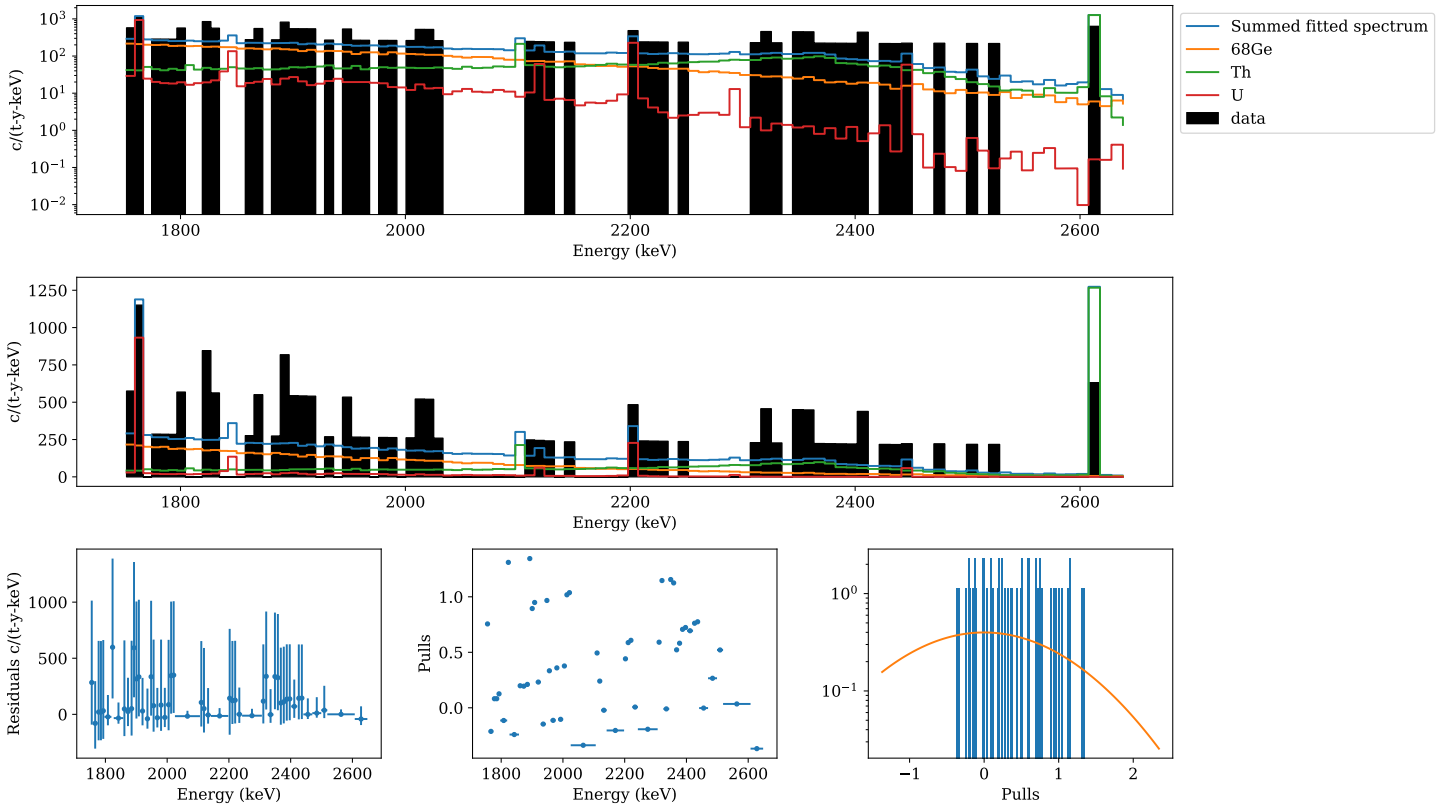

DS0, Gran, M1_Nat

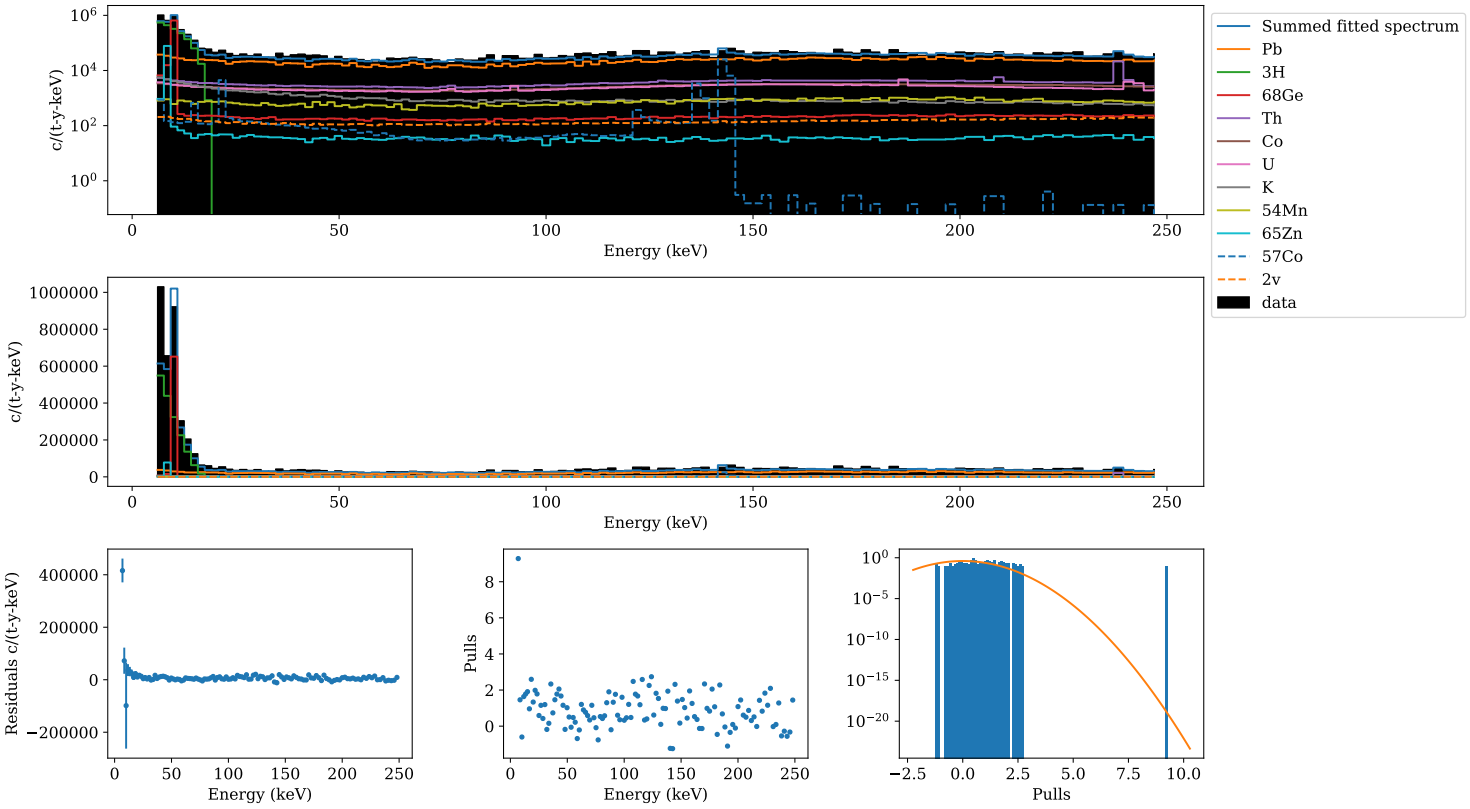

DS0, Gran, M1_Nat

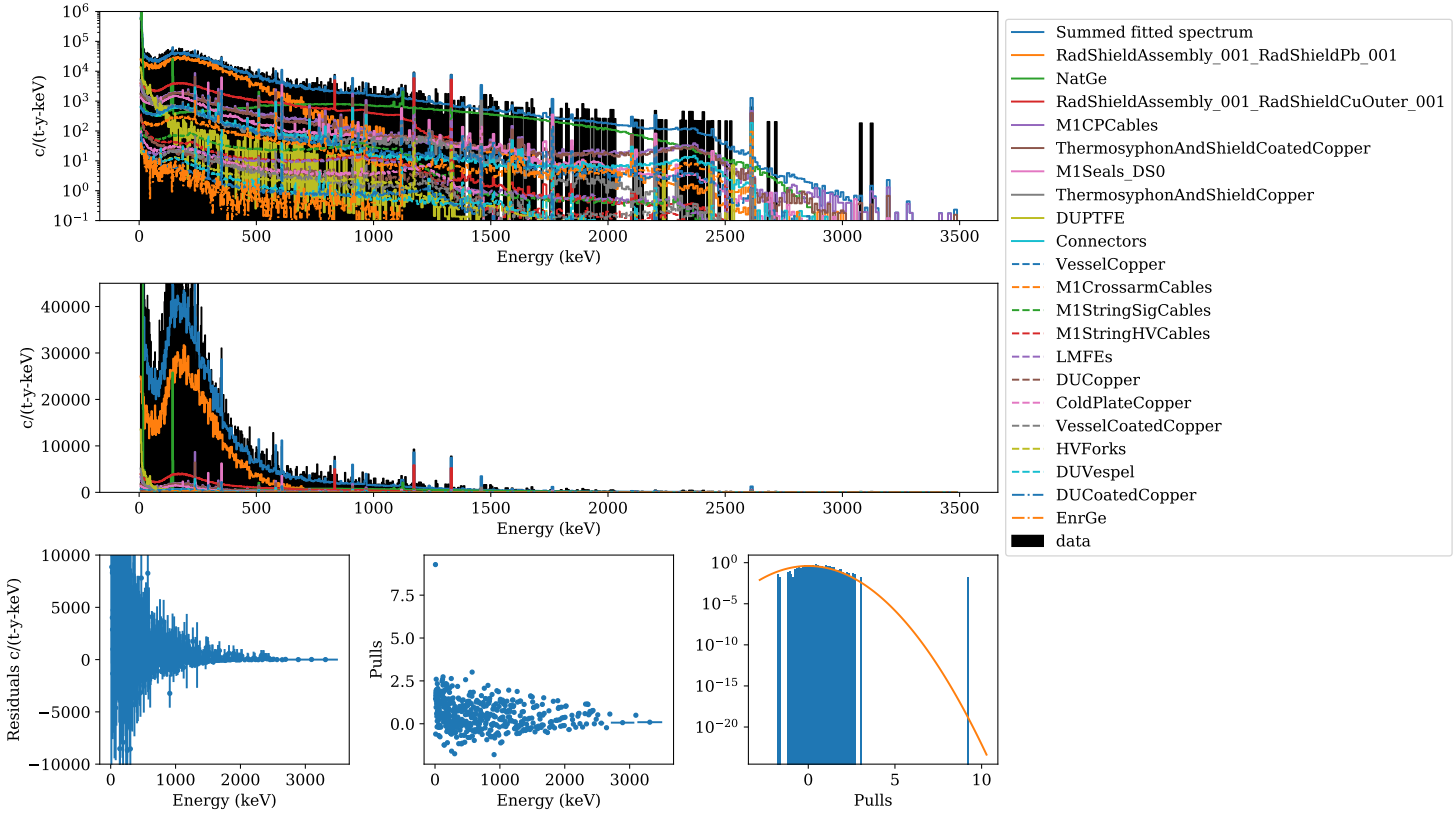

DS0, Gran, M1_Nat

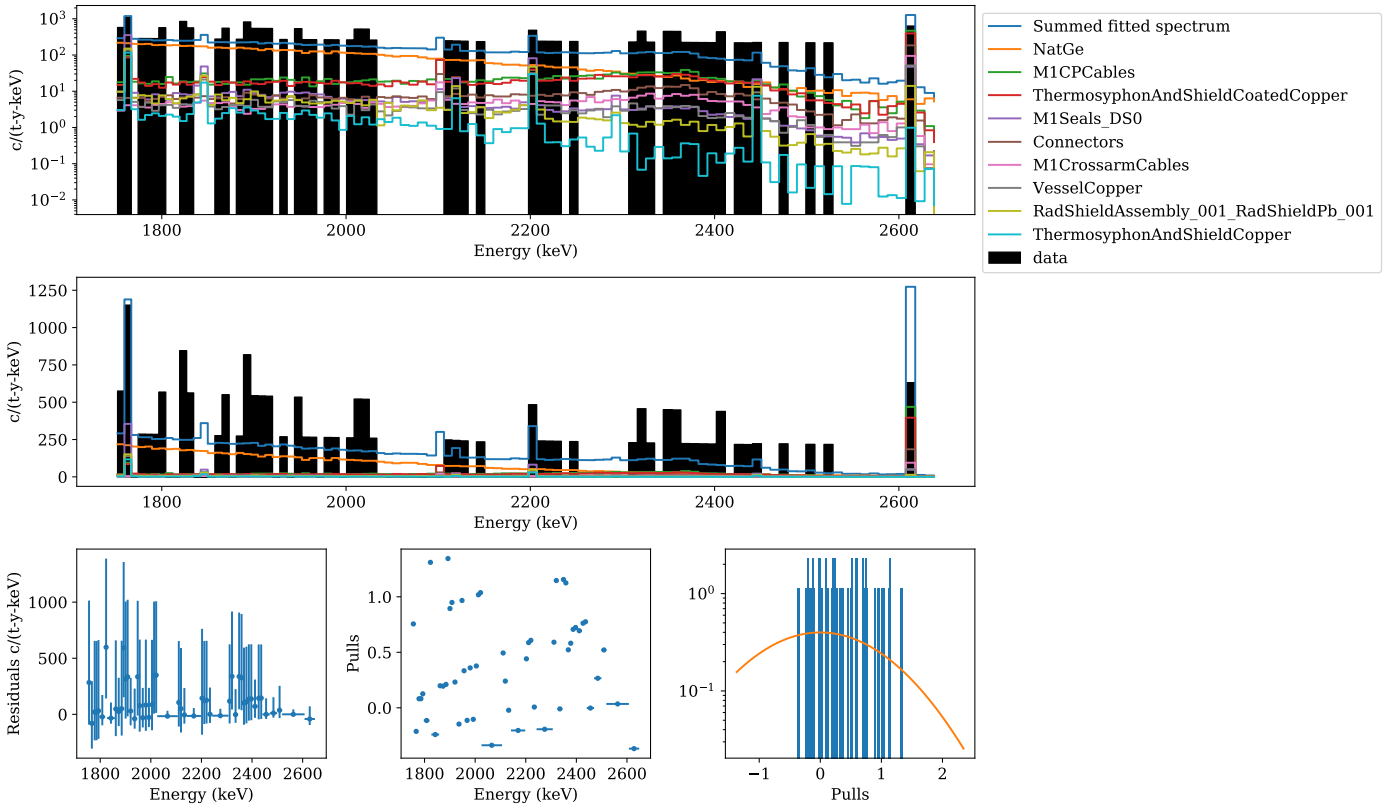

DS0, Gran, M1_Nat

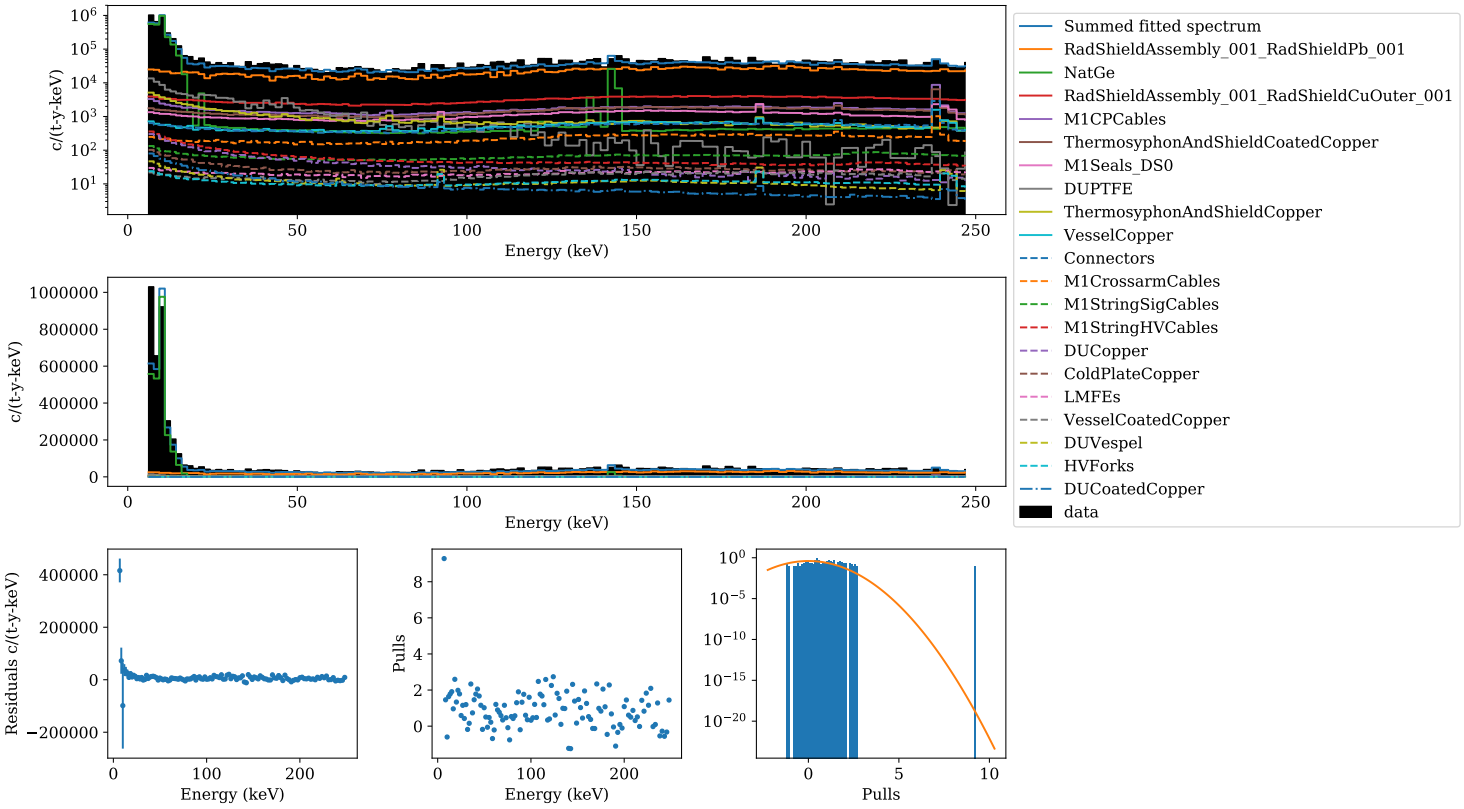

DS12+DS3456, Gran, M2_Nat+M1_Nat

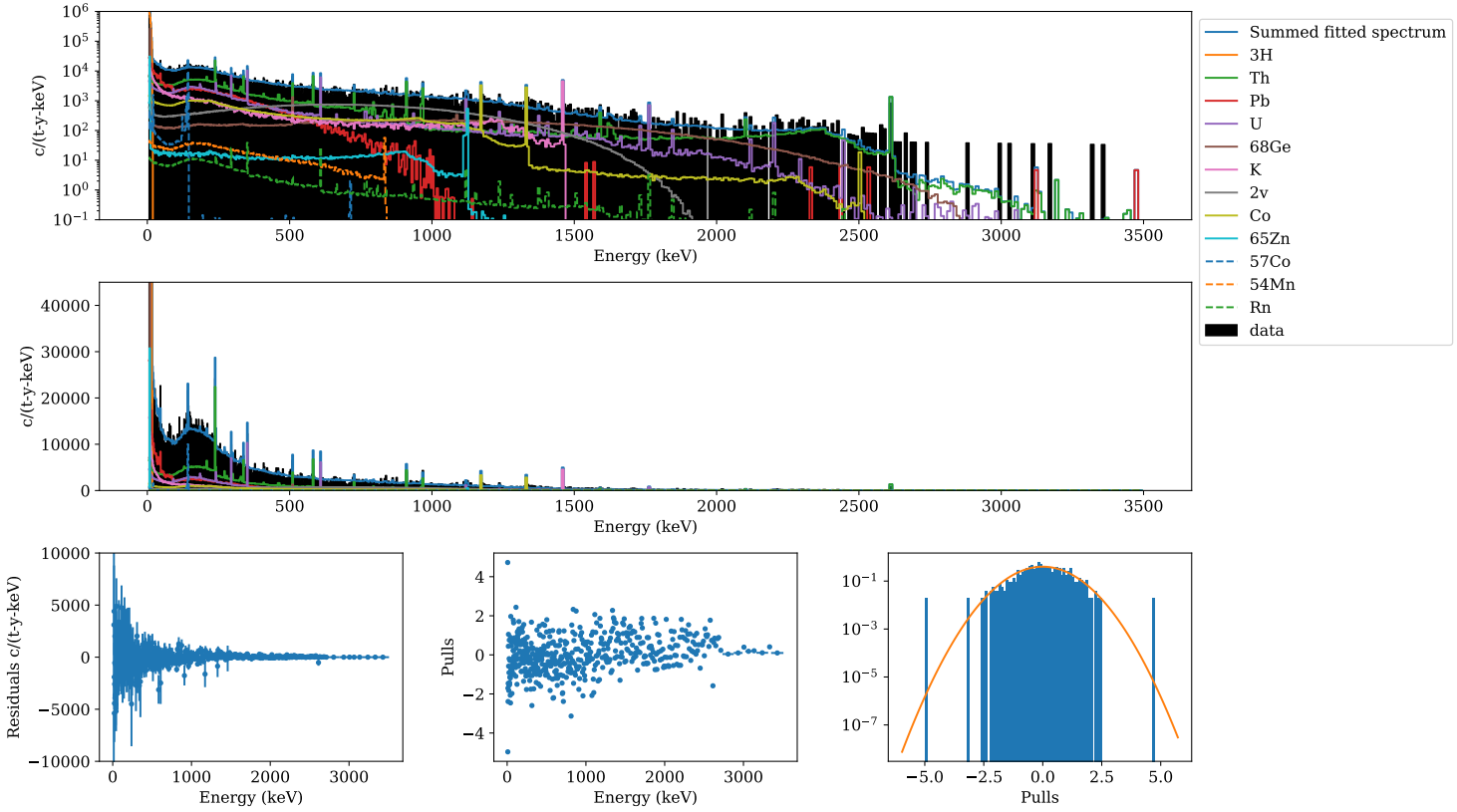

DS12+DS3456, Gran, M2_Nat+M1_Nat

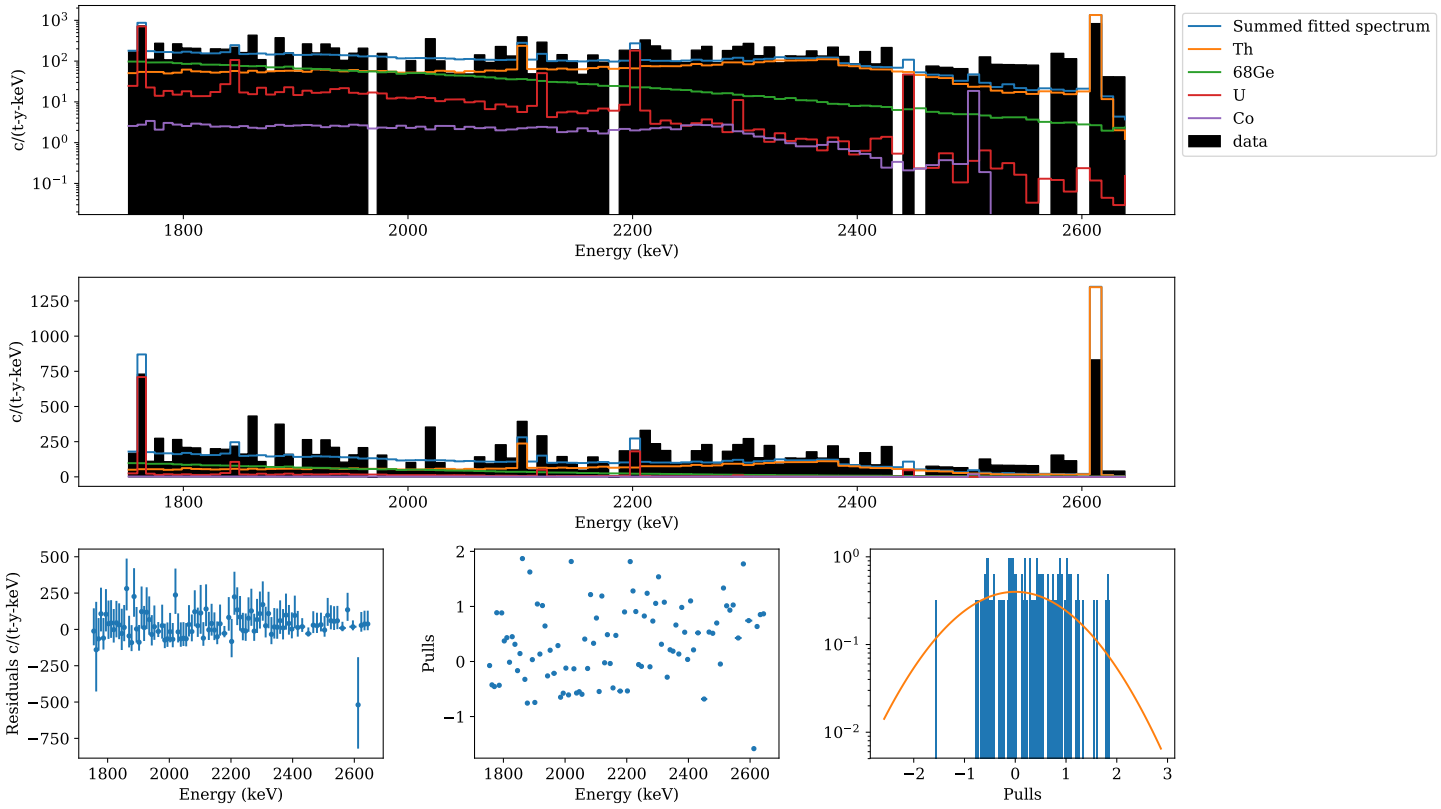

DS12+DS3456, Gran, M2_Nat+M1_Nat

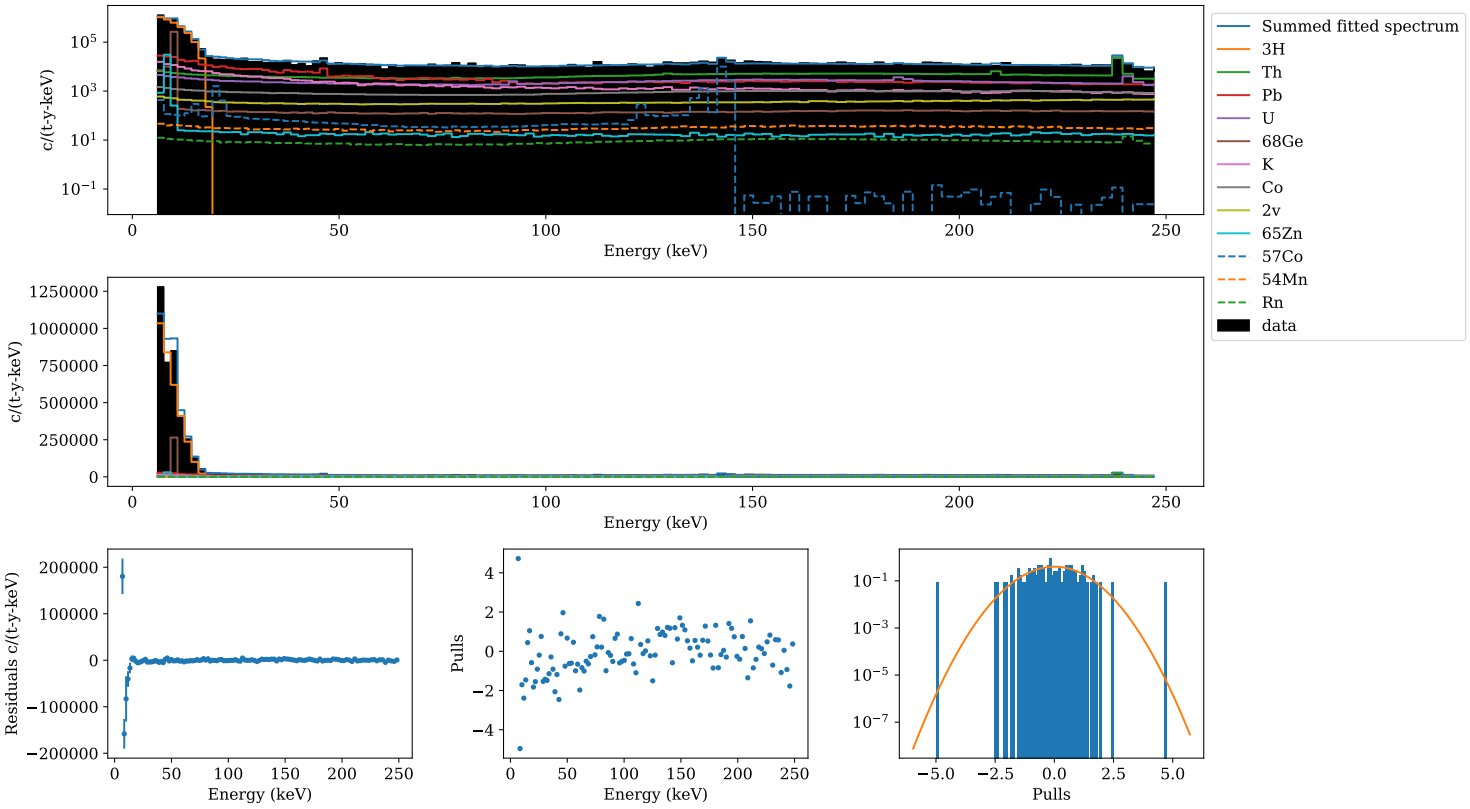

DS12+DS3456, Gran, M2_Nat+M1_Nat

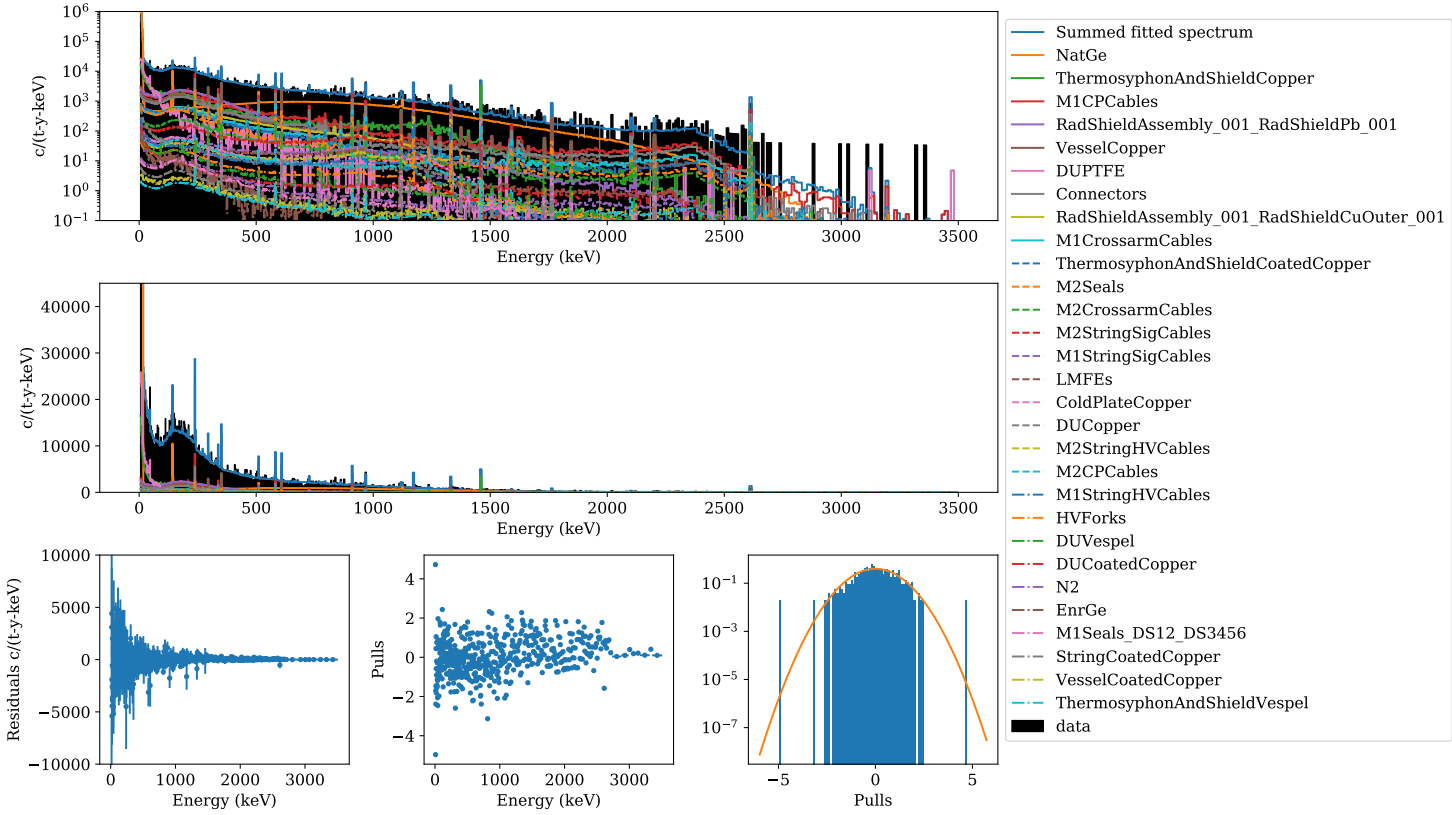

DS12+DS3456, Gran, M2_Nat+M1_Nat

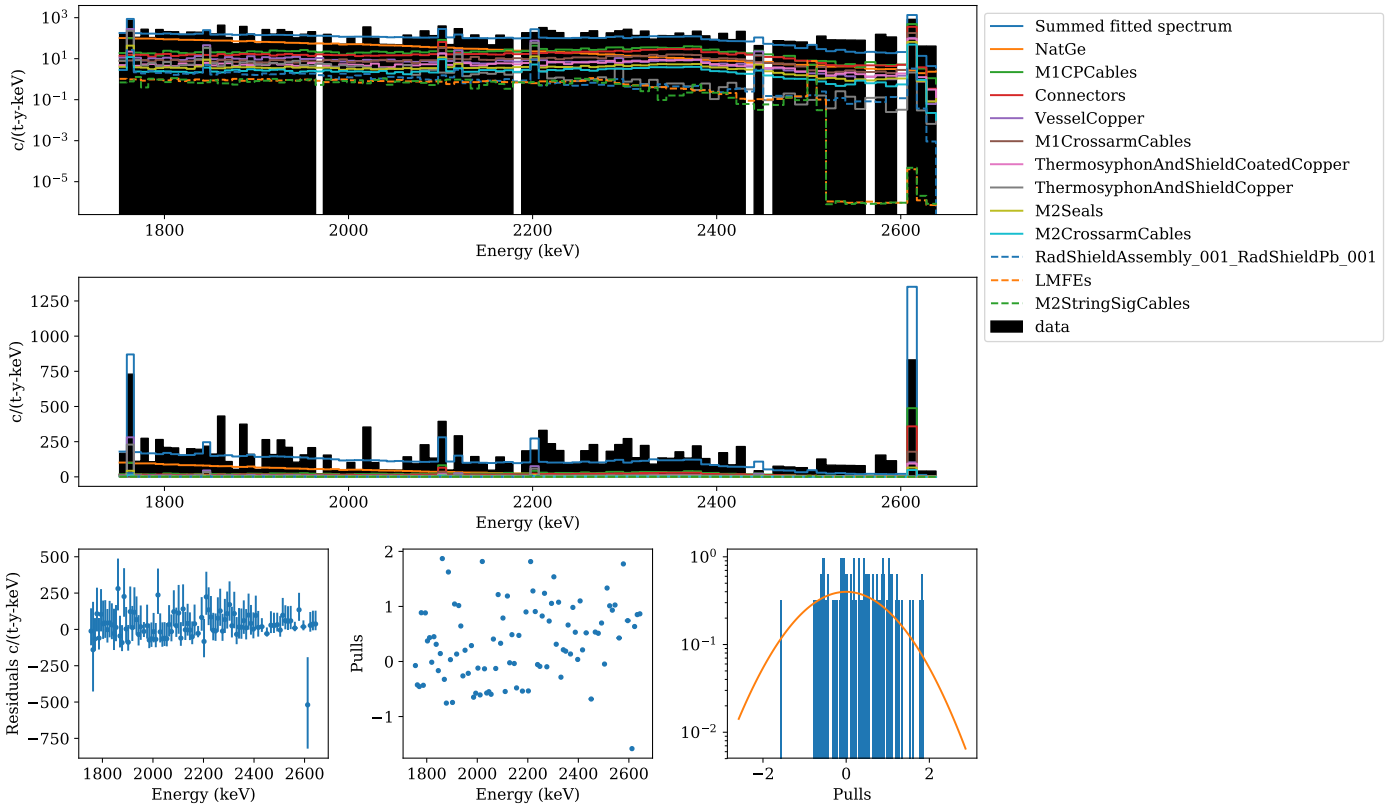

DS12+DS3456, Gran, M2_Nat+M1_Nat

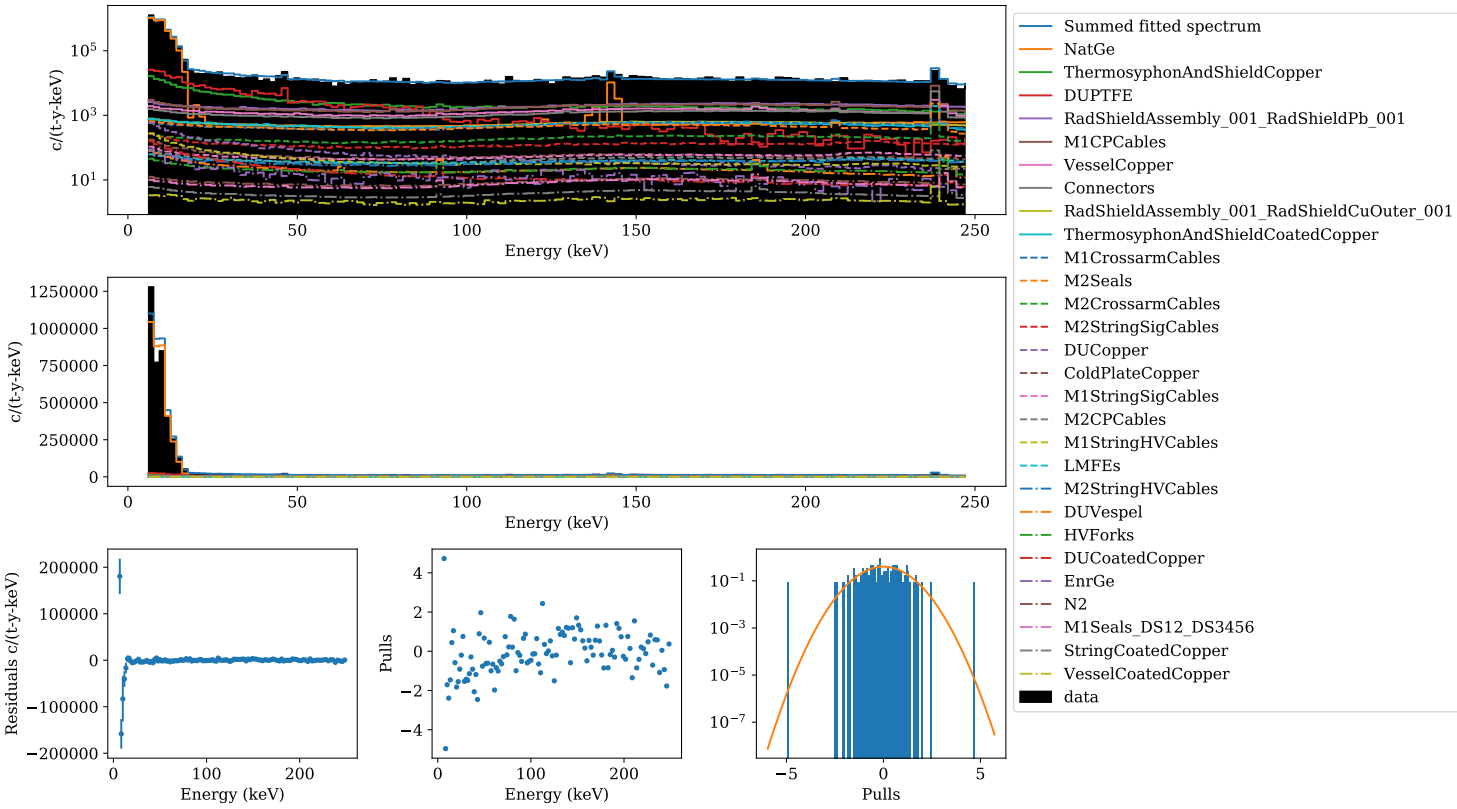

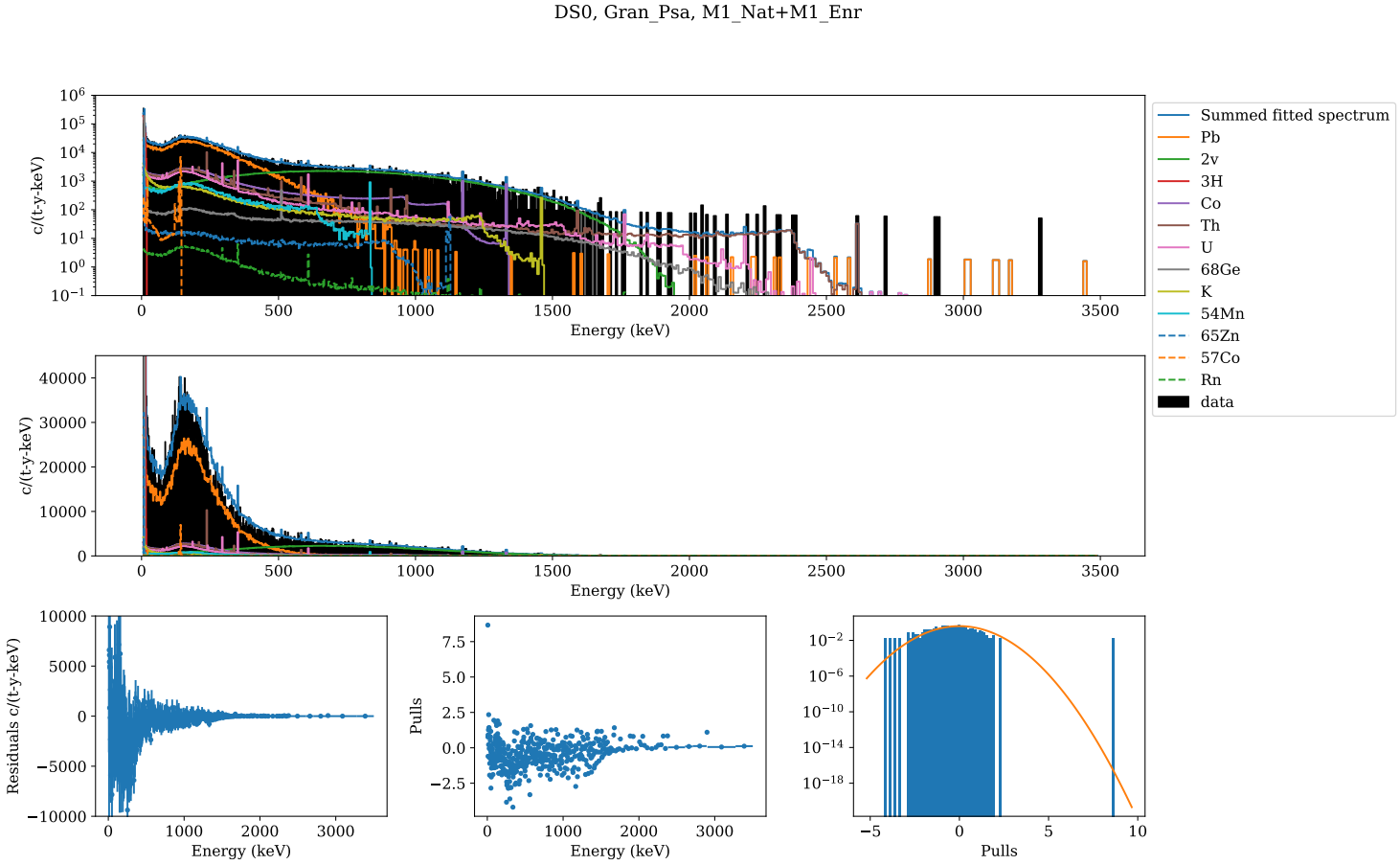
DS0, Gran_Psa, M1_Nat+M1_Enr
c/(t-y-keV)
Energy (keV)
Summed fitted spectrum
Pb
2v
3H
Co
Th
U
68Ge
K
54Mn
65Zn
57Co
Rn
data
Residuals c/(t-y-keV)
Pulls
Energy (keV)
Pulls

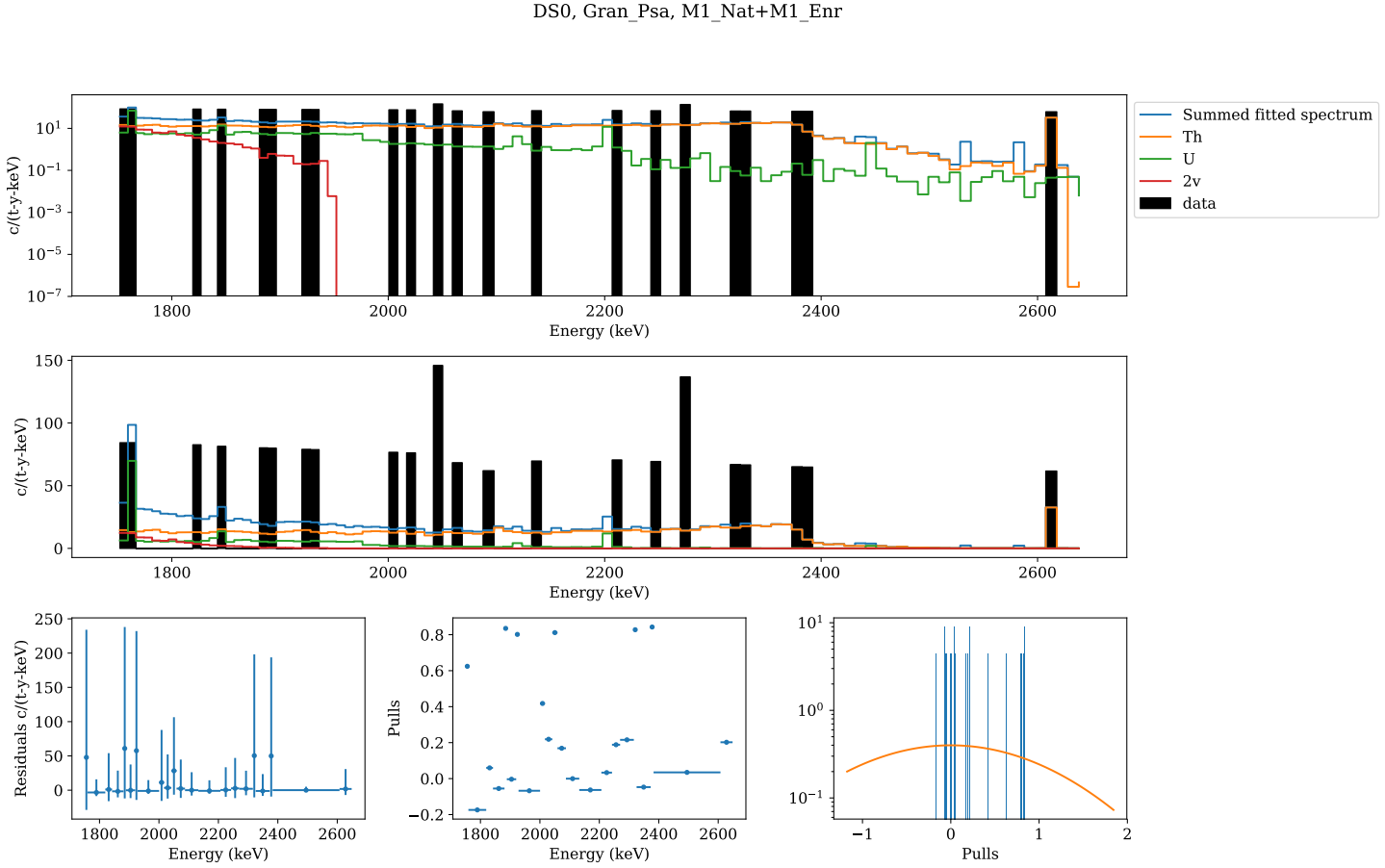
DS0, Gran_Psa, M1_Nat+M1_Enr
Summed fitted spectrum
Th
U
2v
data
c/(t-y-keV)
Energy (keV)
Residuals c/(t-y-keV)
Pulls

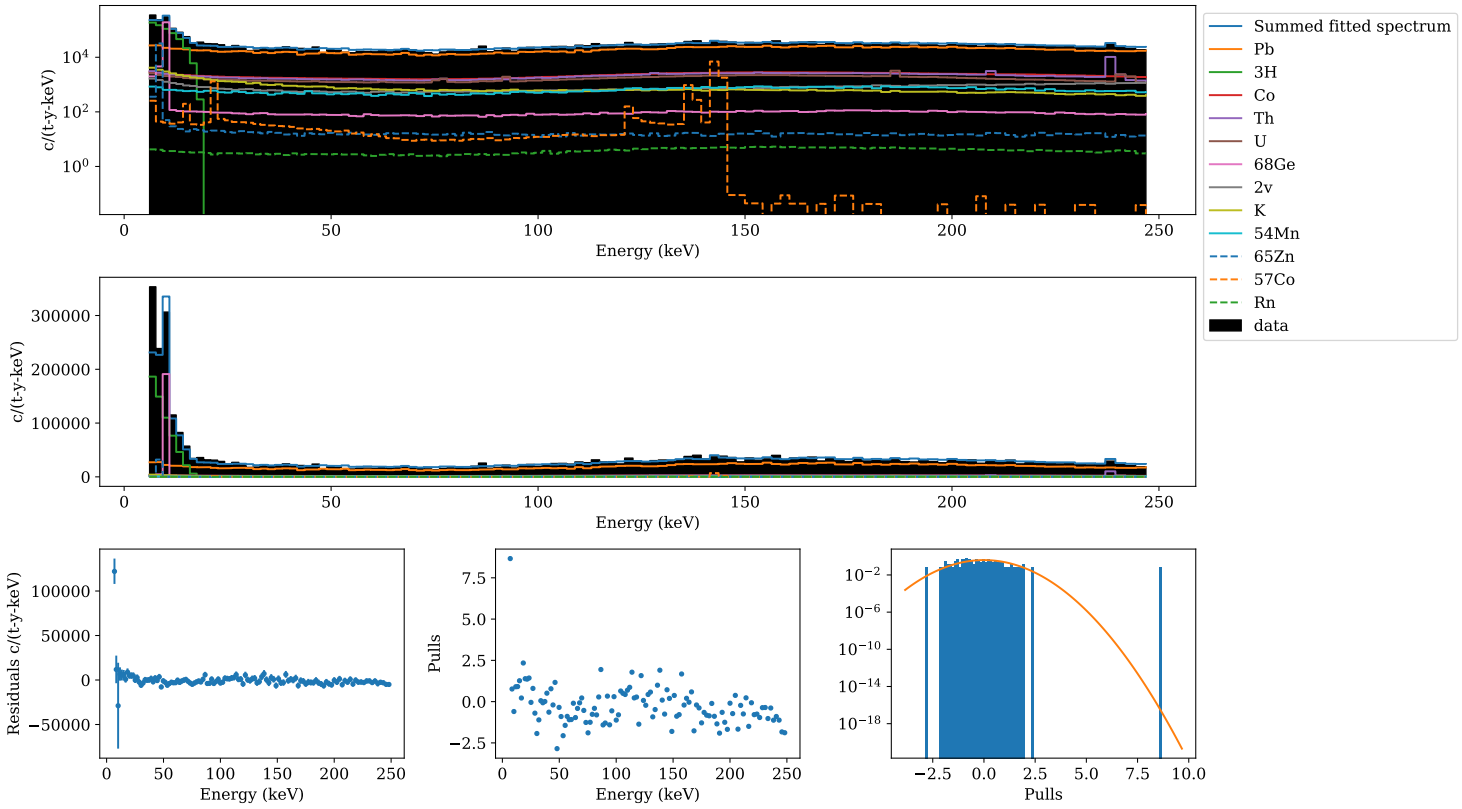
DS0, Gran_Psa, M1_Nat+M1_Enr
c/(t-y-keV)
Energy (keV)
Summed fitted spectrum
Pb
3H
Co
Th
U
68Ge
2v
K
54Mn
65Zn
57Co
Rn
data
Residuals c/(t-y-keV)
Pulls

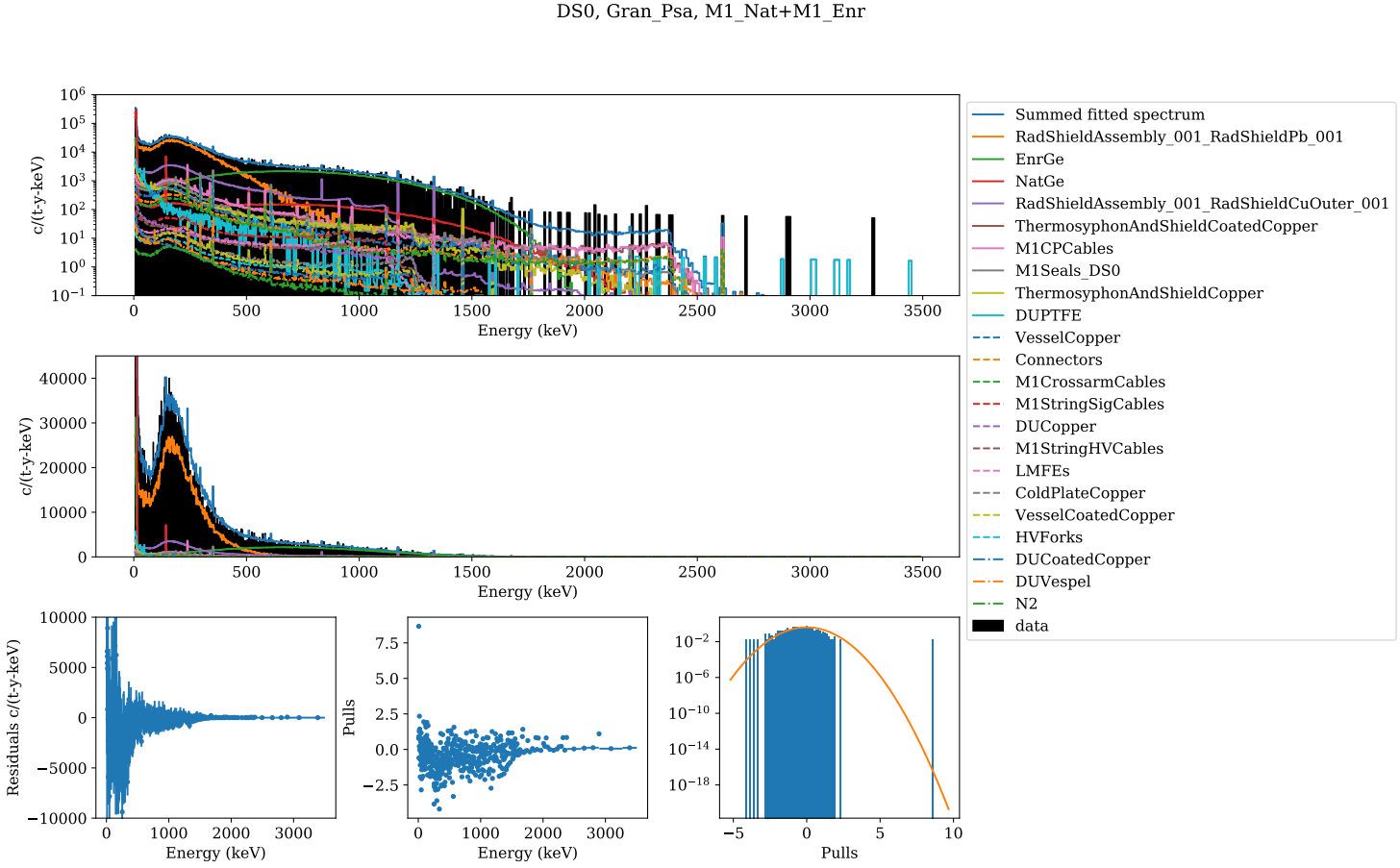
DS0, Gran_Psa, M1_Nat+M1_Enr
c/(t-y-keV)
Energy (keV)
Residuals c/(t-y-keV)
Pulls
Summed fitted spectrum
RadShieldAssembly_001_RadShieldPb_001
EnrGe
NatGe
RadShieldAssembly_001_RadShieldCuOuter_001
ThermosyphonAndShieldCoatedCopper
M1CPCables
M1Seals_DS0
ThermosyphonAndShieldCopper
DUPTFE
VesselCopper
Connectors
M1CrossarmCables
M1StringSigCables
DUCopper
M1StringHVCables
LMFEs
ColdPlateCopper
VesselCoatedCopper
HVForks
DUCoatedCopper
DUVespel
N2
data

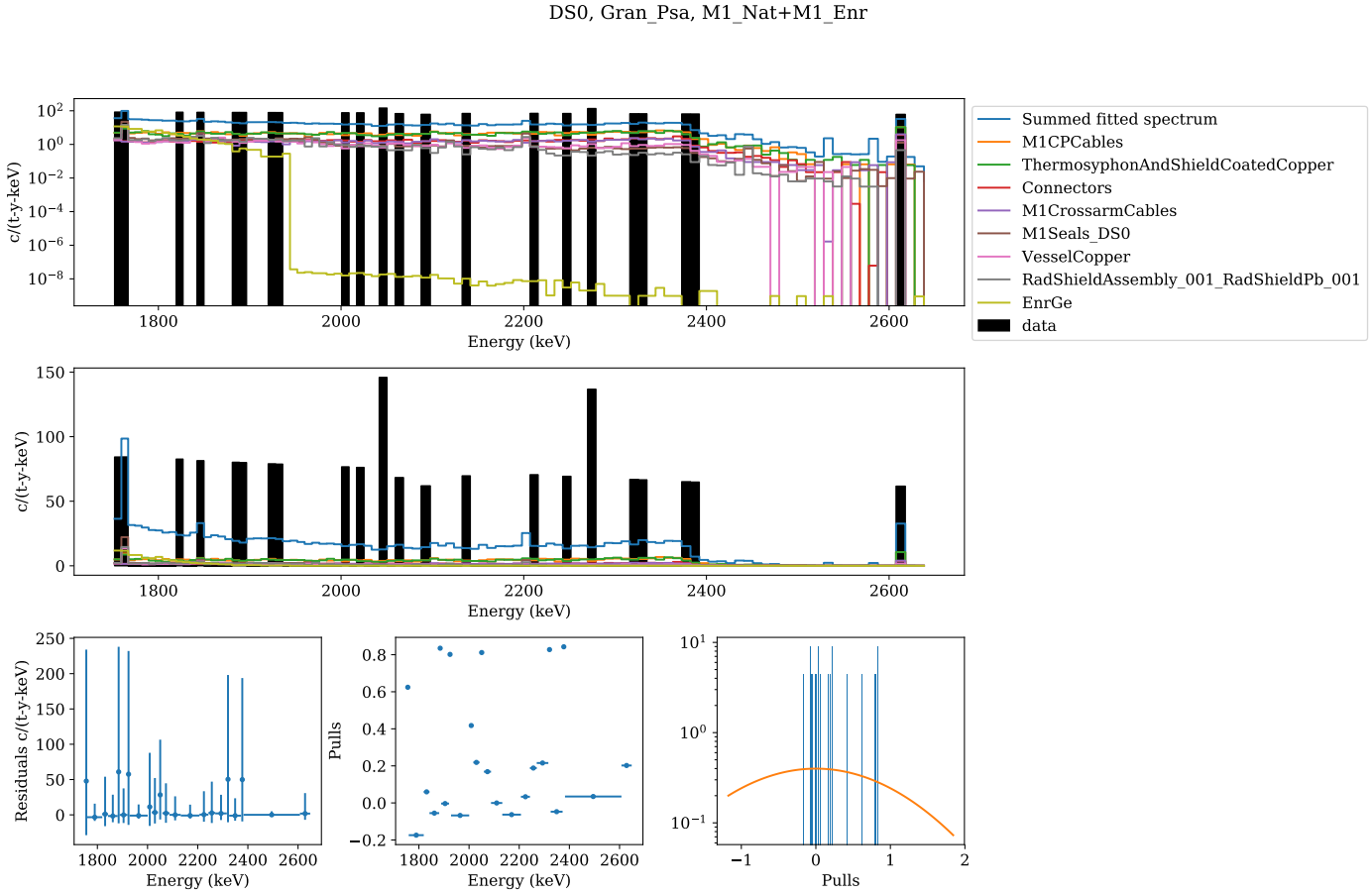
DS0, Gran_Psa, M1_Nat+M1_Enr
c/(t-y-keV)
Energy (keV)
Summed fitted spectrum
M1CPCables
ThermosyphonAndShieldCoatedCopper
Connectors
M1CrossarmCables
M1Seals_DS0
VesselCopper
RadShieldAssembly_001_RadShieldPb_001
EnrGe
data
Residuals c/(t-y-keV)
Pulls

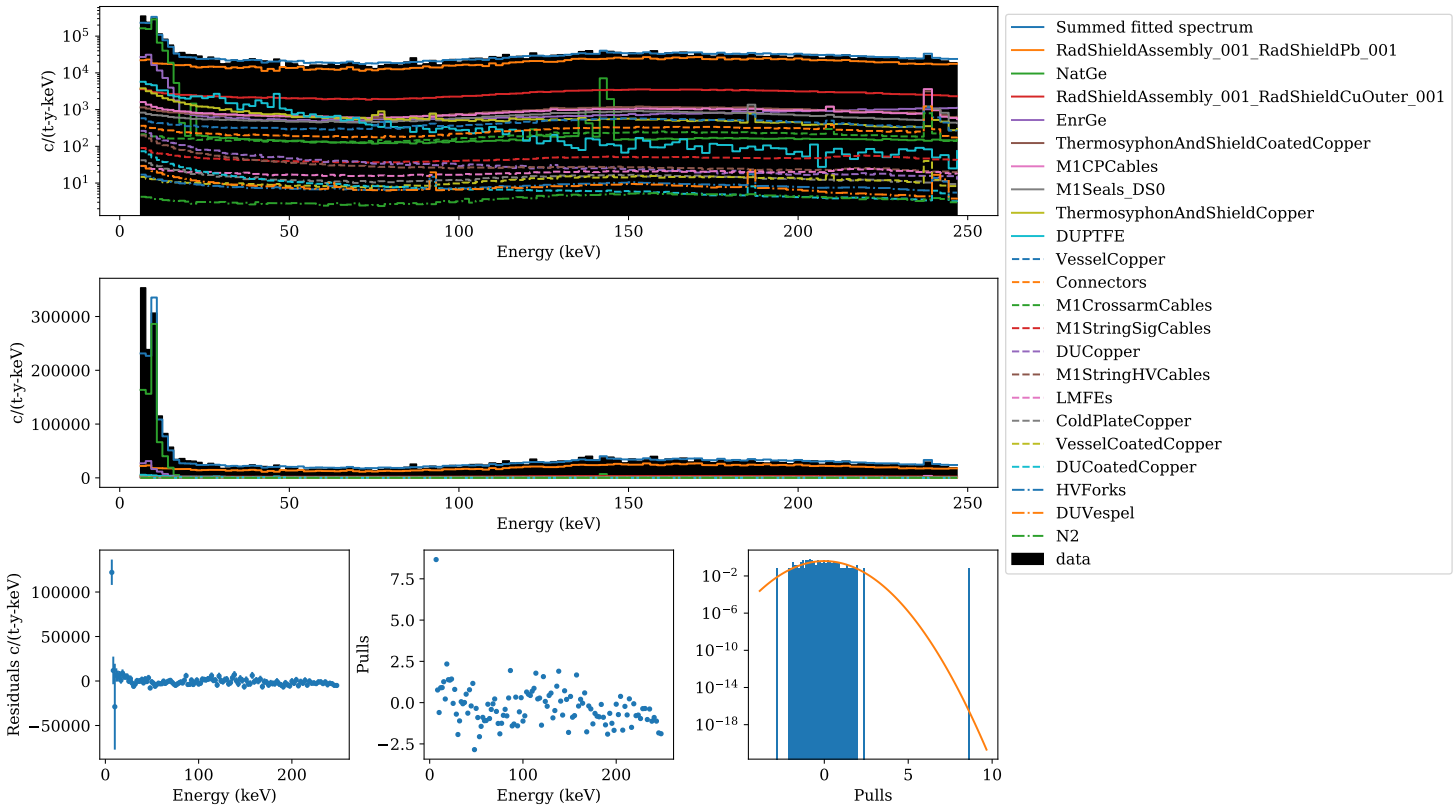
DS0, Gran_Psa, M1_Nat+M1_Enr
c/(t-y-keV)
Energy (keV)
Residuals c/(t-y-keV)
Pulls
Summed fitted spectrum
RadShieldAssembly_001_RadShieldPb_001
NatGe
RadShieldAssembly_001_RadShieldCuOuter_001
EnrGe
ThermosyphonAndShieldCoatedCopper
M1CPCables
M1Seals_DS0
ThermosyphonAndShieldCopper
DUPTFE
VesselCopper
Connectors
M1CrossarmCables
M1StringSigCables
DUCopper
M1StringHVCables
LMFEs
ColdPlateCopper
VesselCoatedCopper
DUCoatedCopper
HVForks
DUVespel
N2
data

DS12+DS3456, Gran_Psa, M1_Nat+M1_Enr

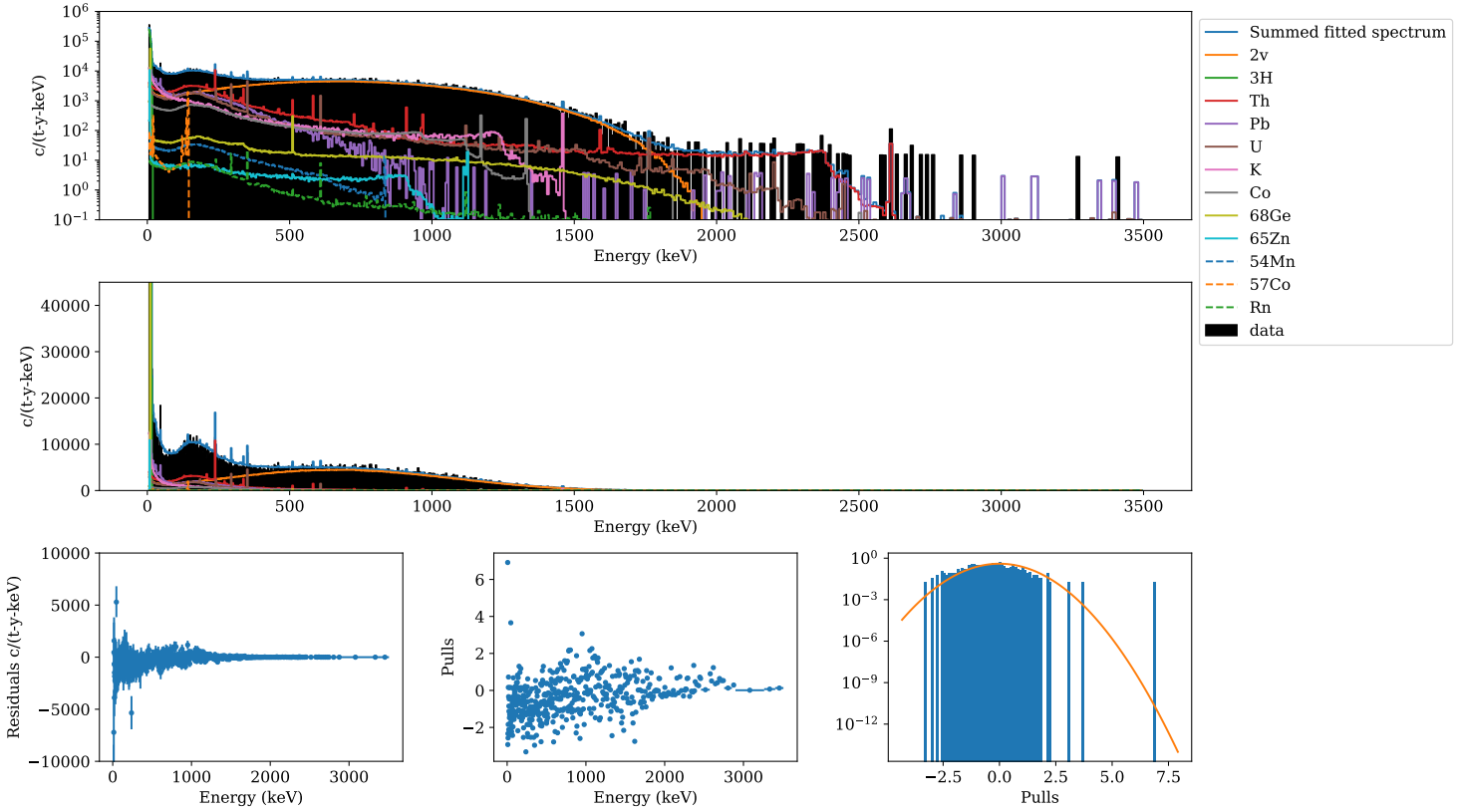

DS12+DS3456, Gran_Psa, M1_Nat+M1_Enr

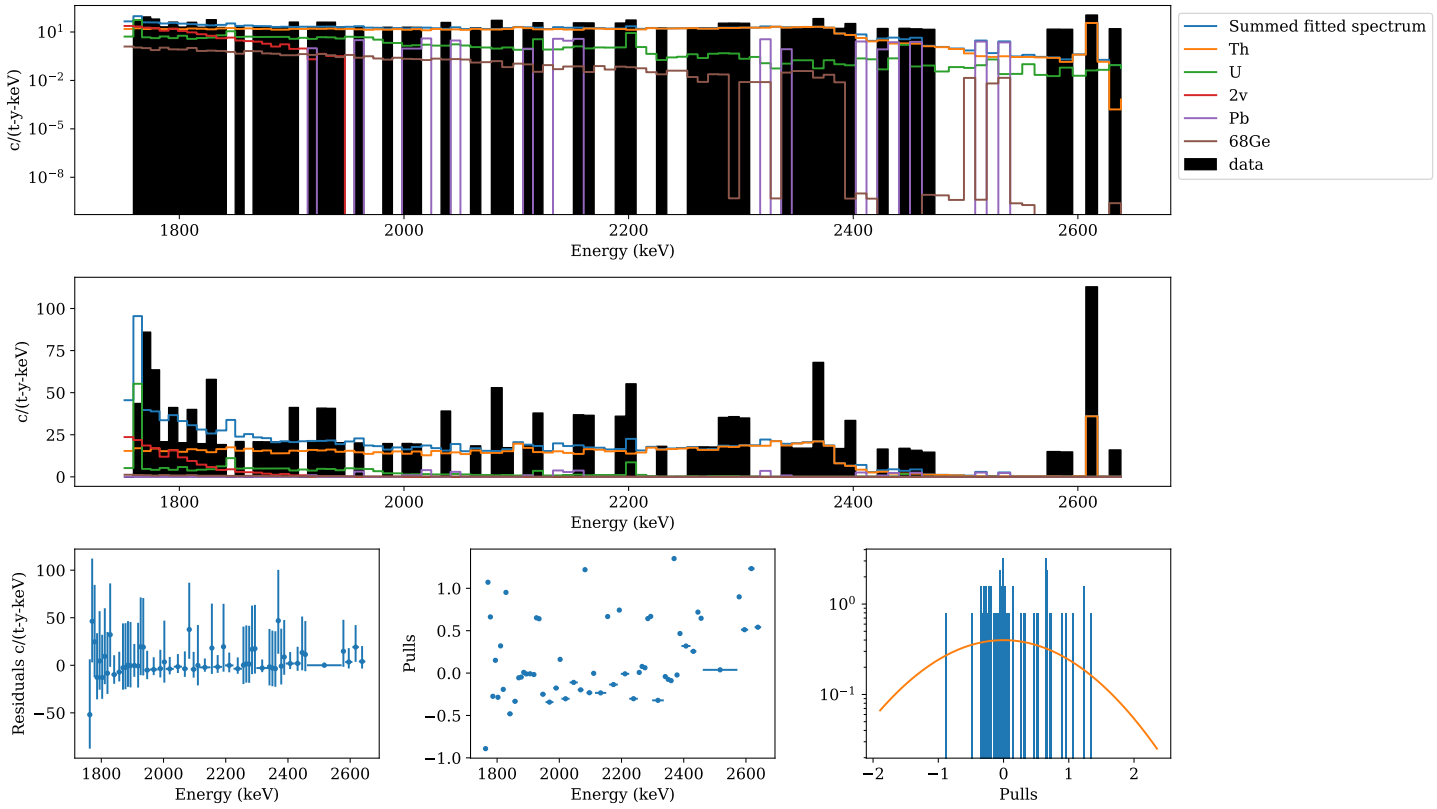

DS12+DS3456, Gran_Psa, M1_Nat+M1_Enr

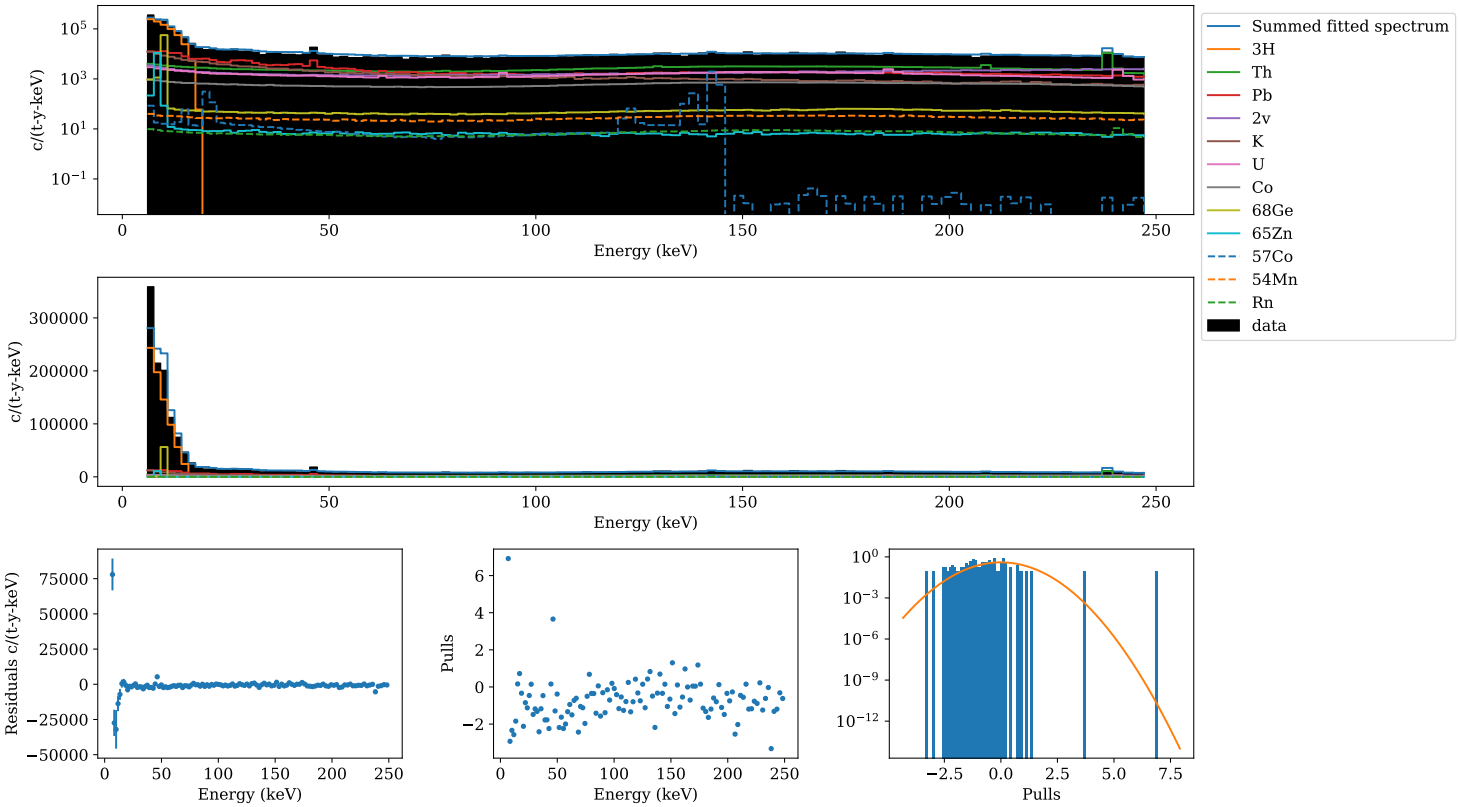

DS12+DS3456, Gran_Psa, M1_Nat+M1_Enr

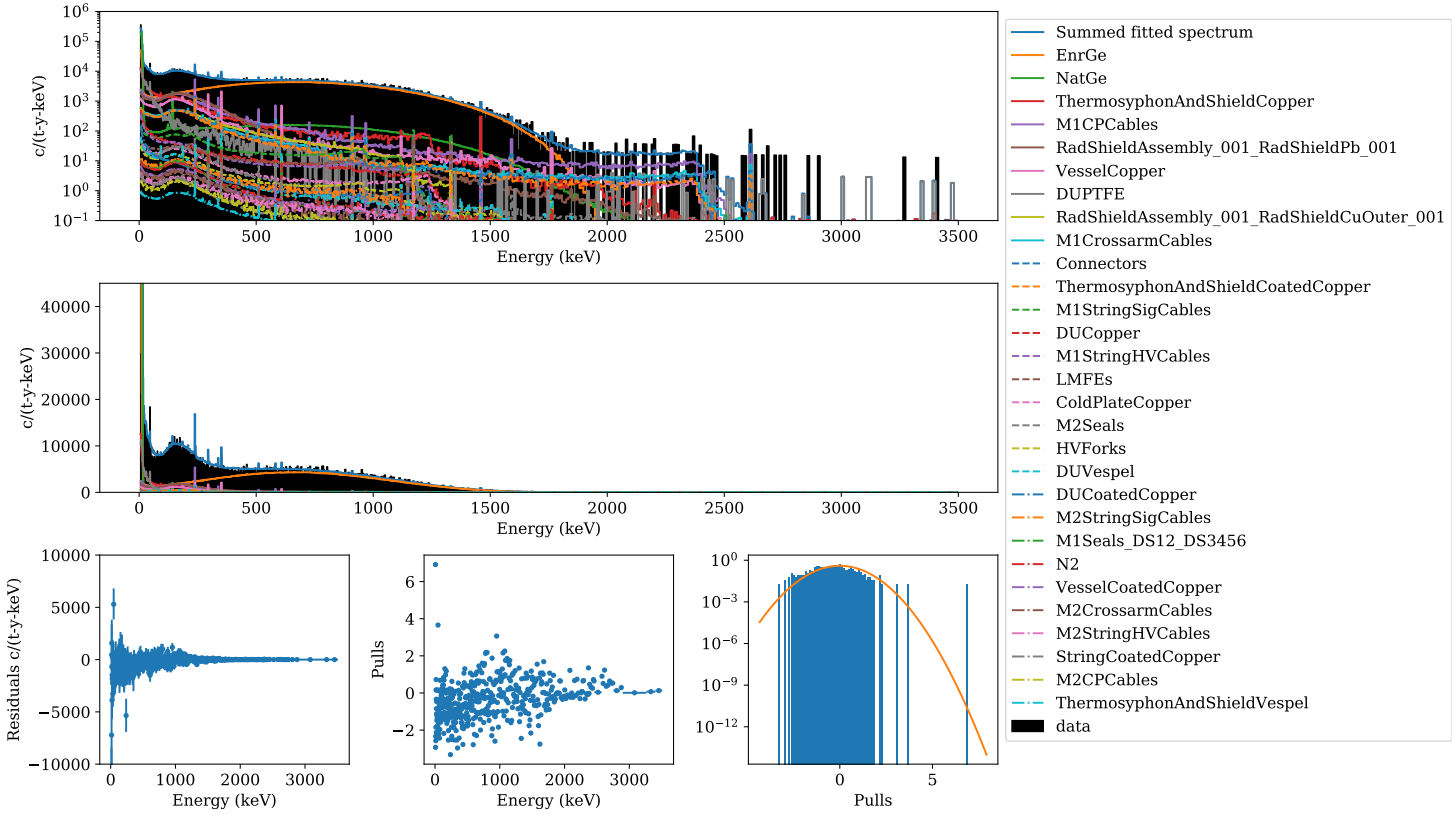

DS12+DS3456, Gran_Psa, M1_Nat+M1_Enr

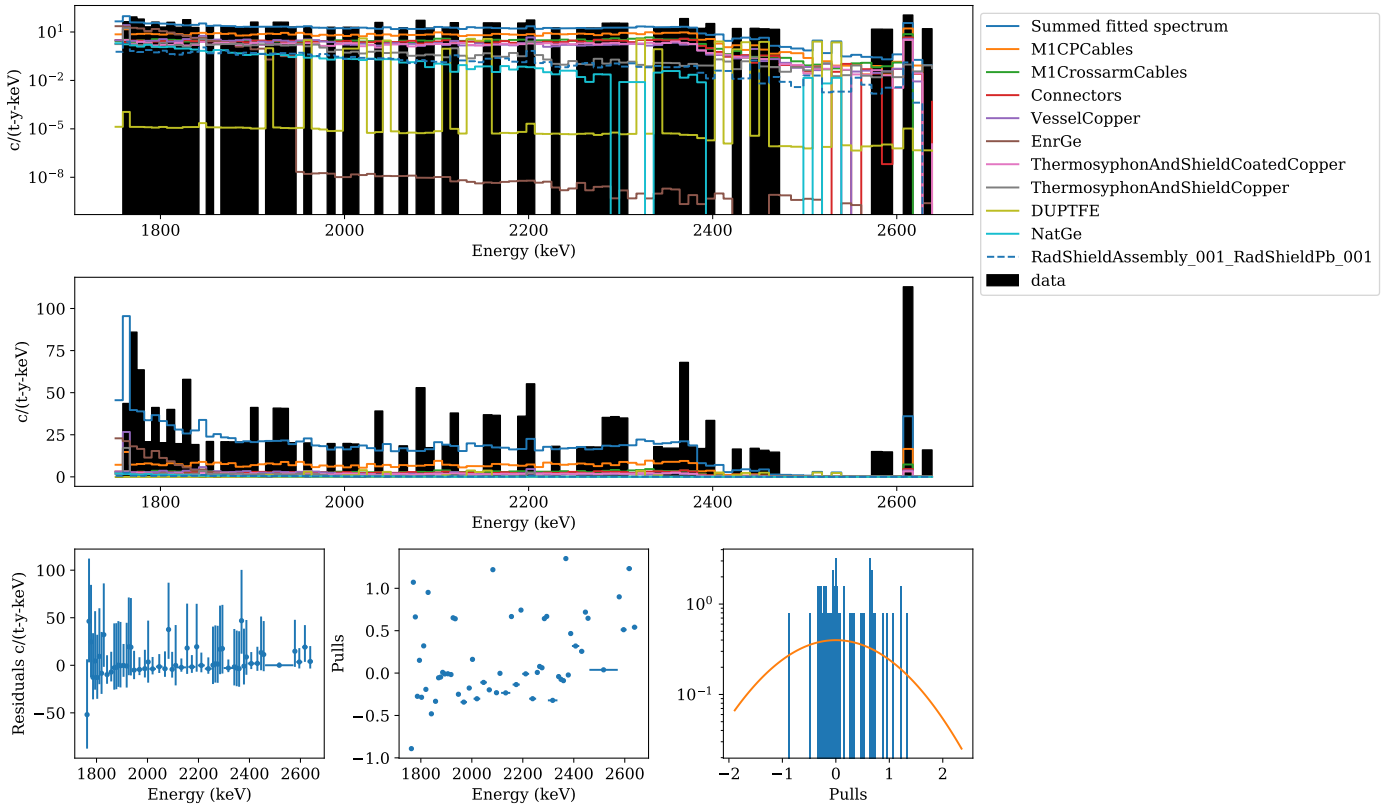

DS12+DS3456, Gran_Psa, M1_Nat+M1_Enr

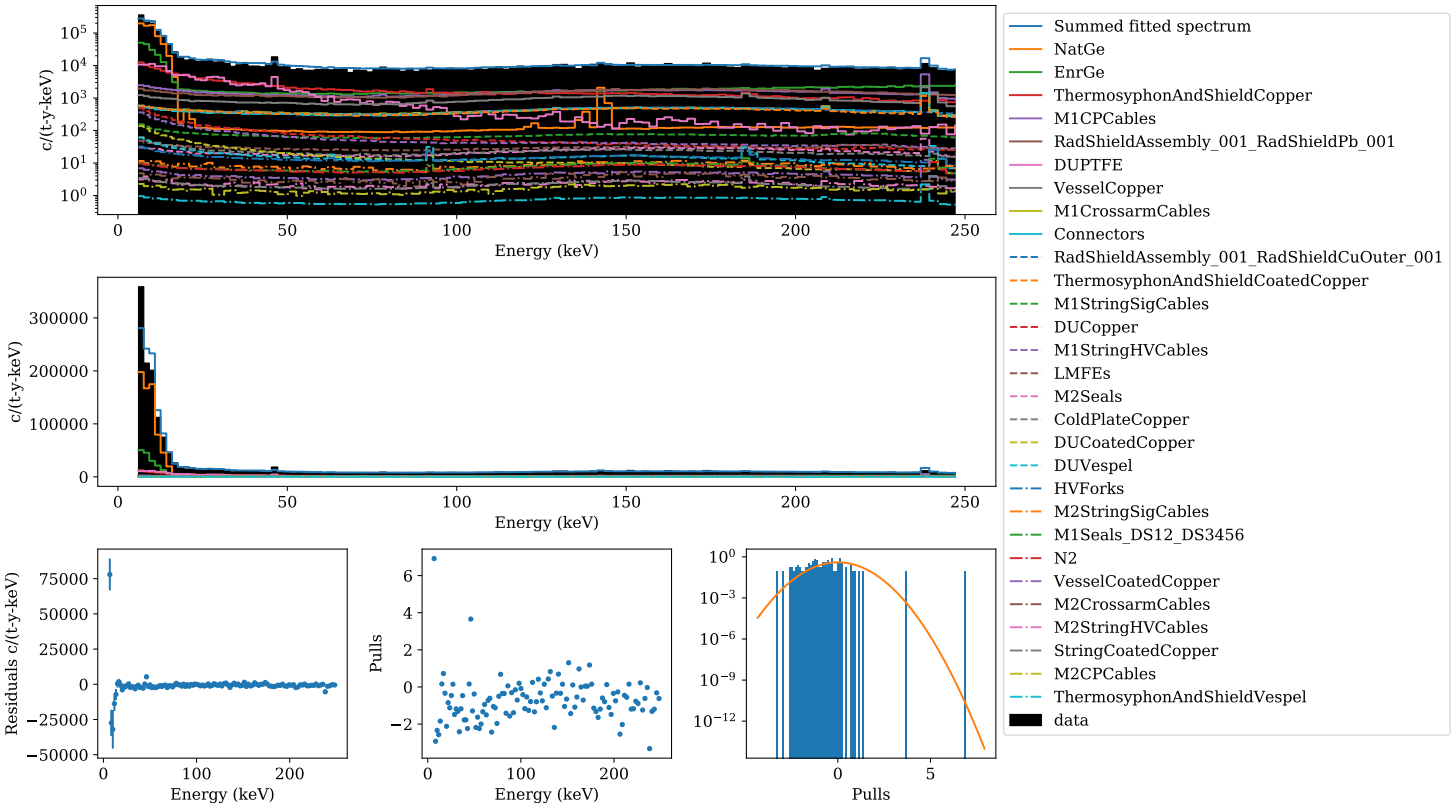

DS12+DS3456, Gran_Psa, M2_Nat+M2_Enr

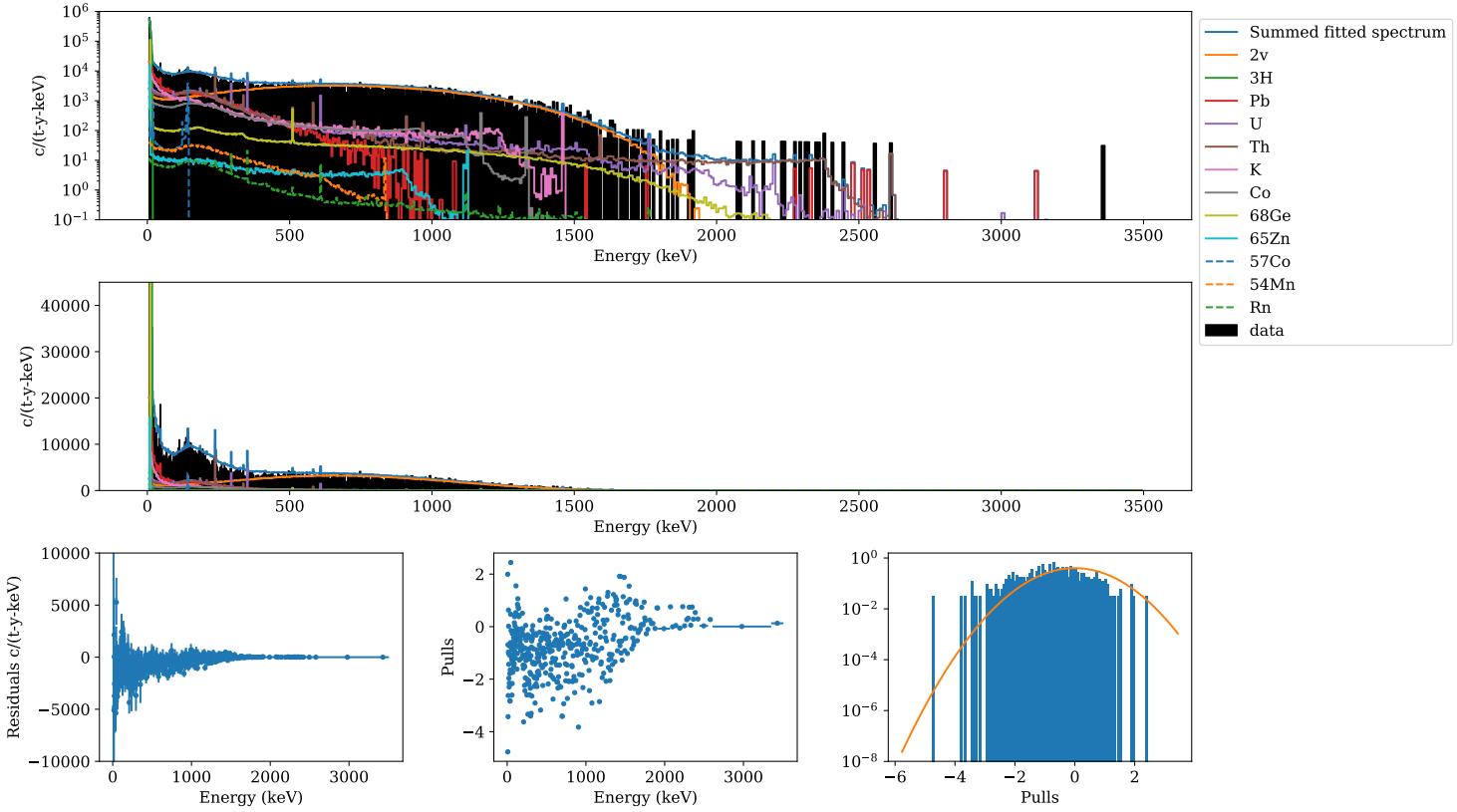

DS12+DS3456, Gran_Psa, M2_Nat+M2_Enr

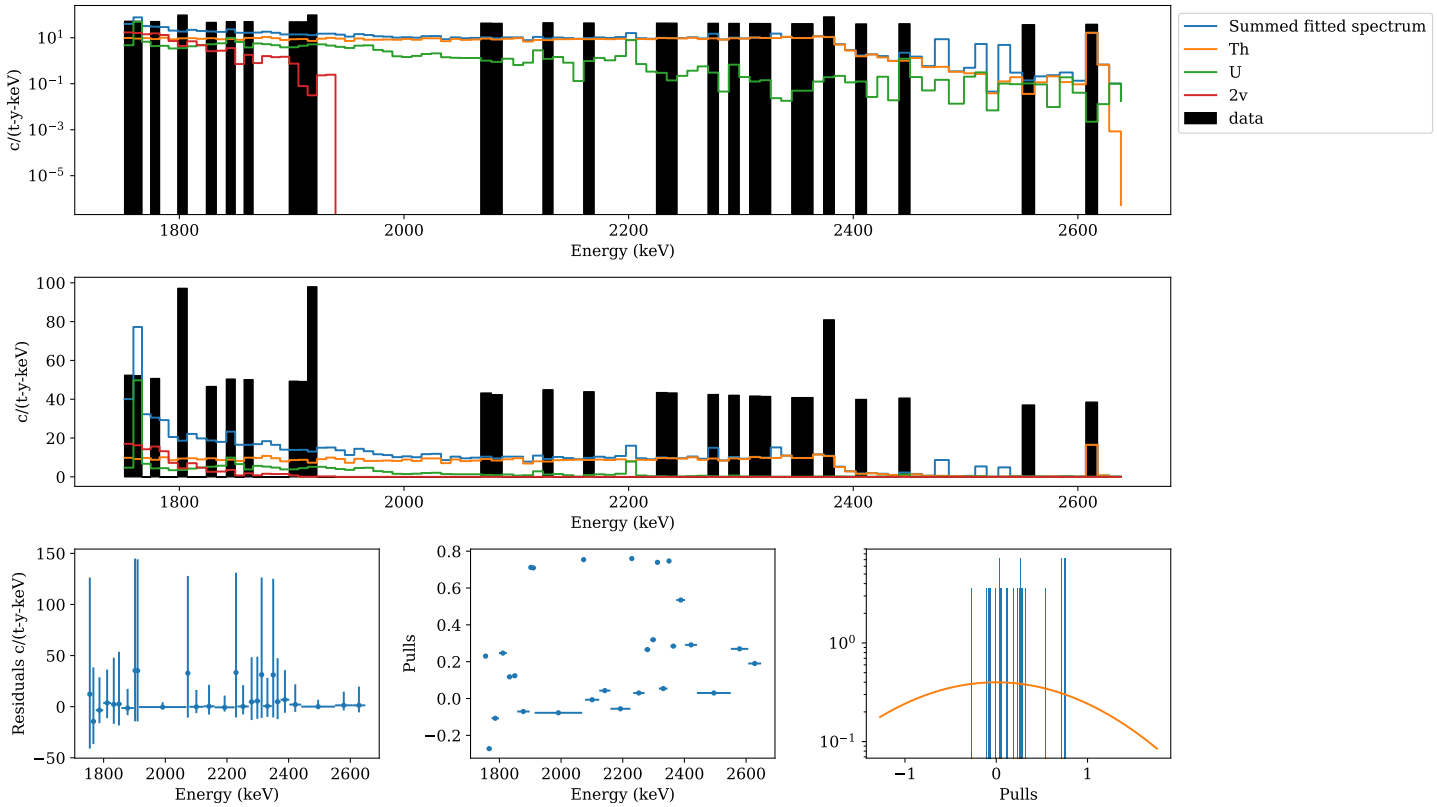

DS12+DS3456, Gran_Psa, M2_Nat+M2_Enr

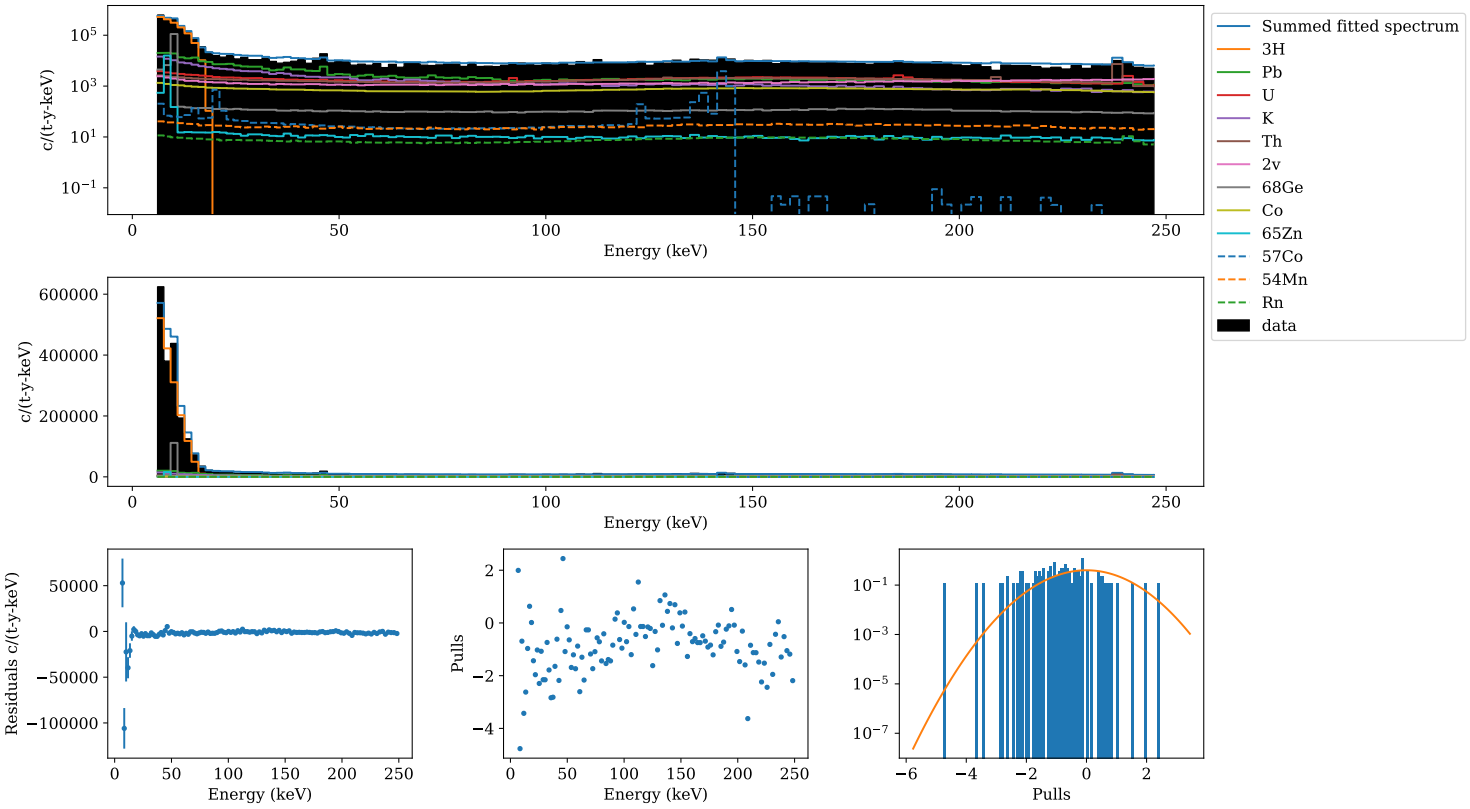

DS12+DS3456, Gran_Psa, M2_Nat+M2_Enr

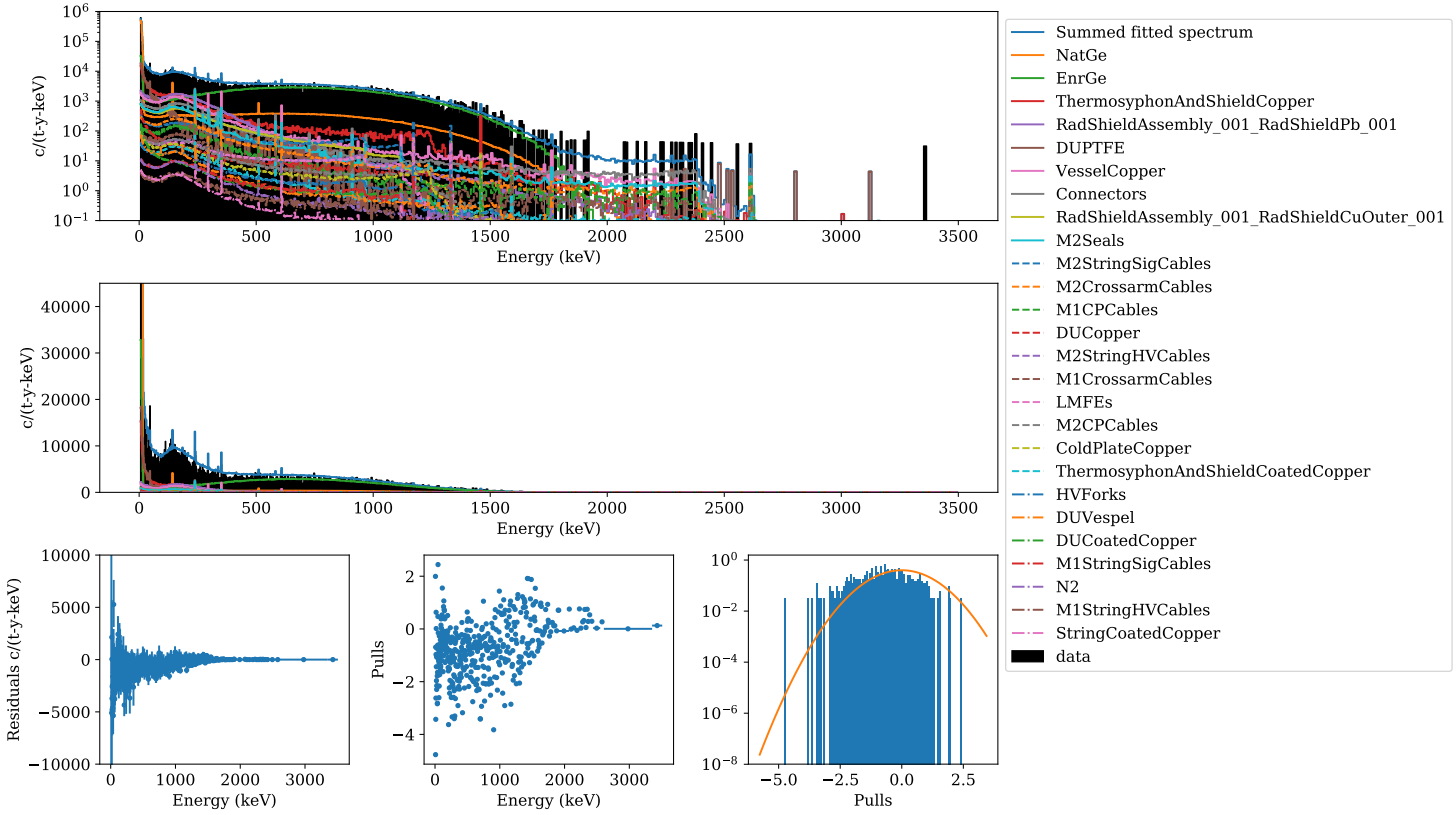

DS12+DS3456, Gran_Psa, M2_Nat+M2_Enr

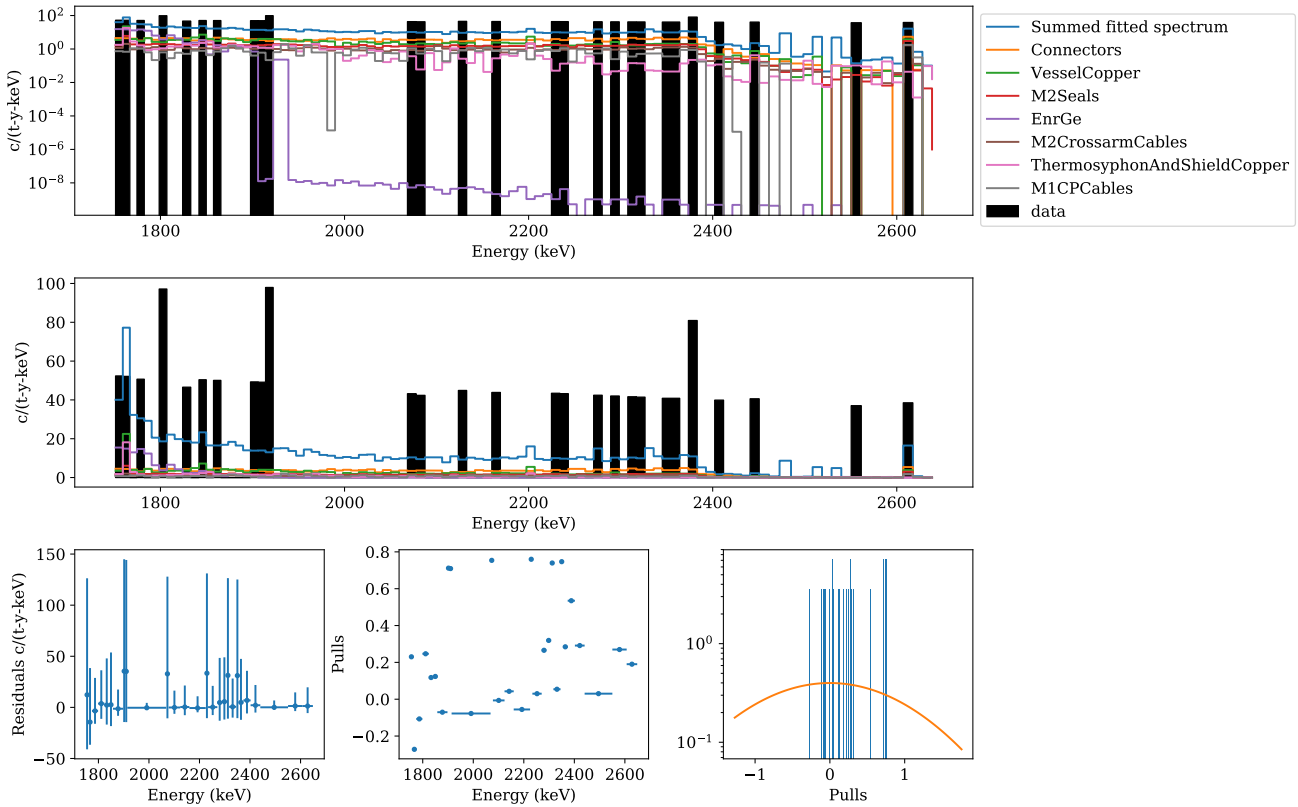

DS12+DS3456, Gran_Psa, M2_Nat+M2_Enr

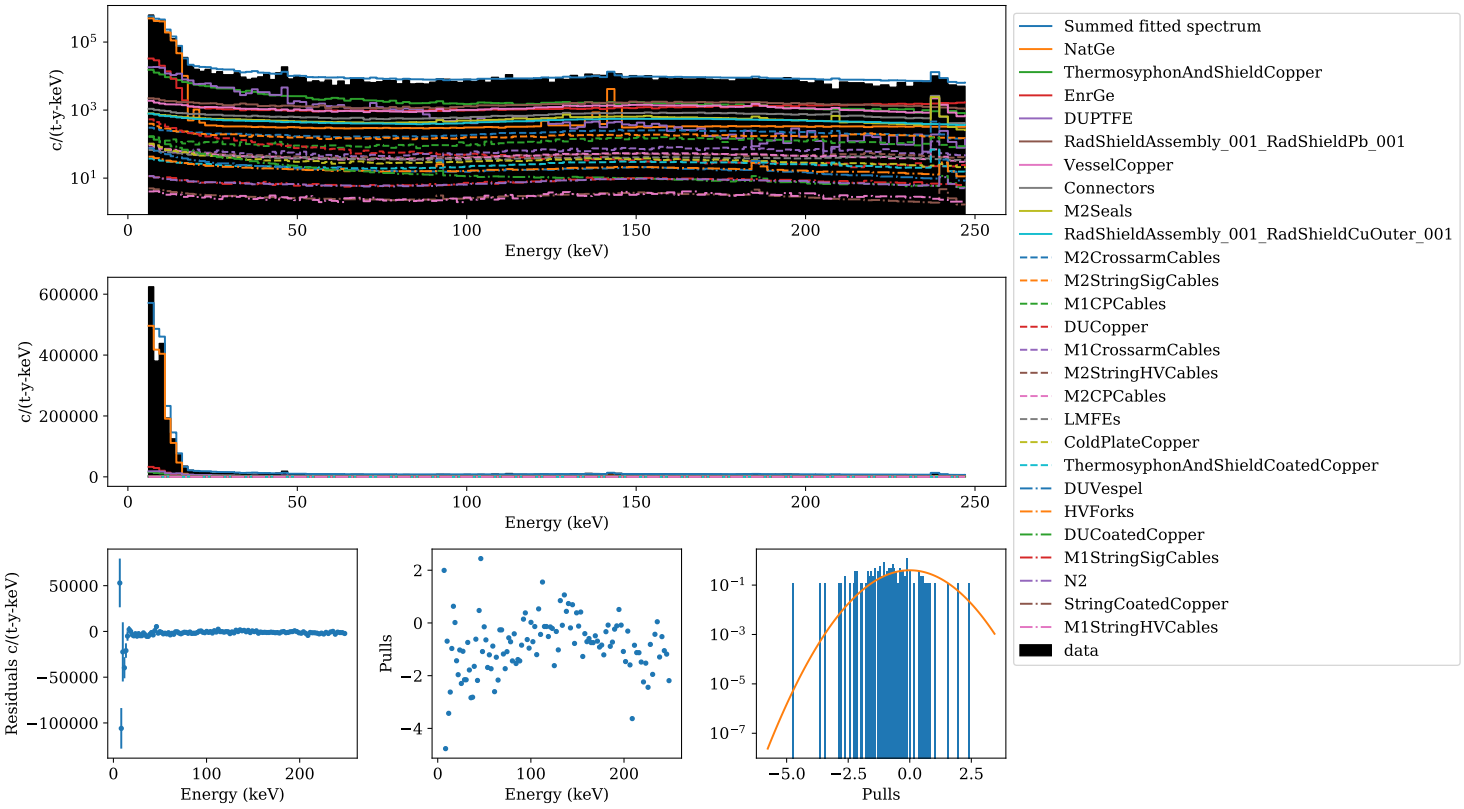

DS0, Gran_Psa, M1_Enr

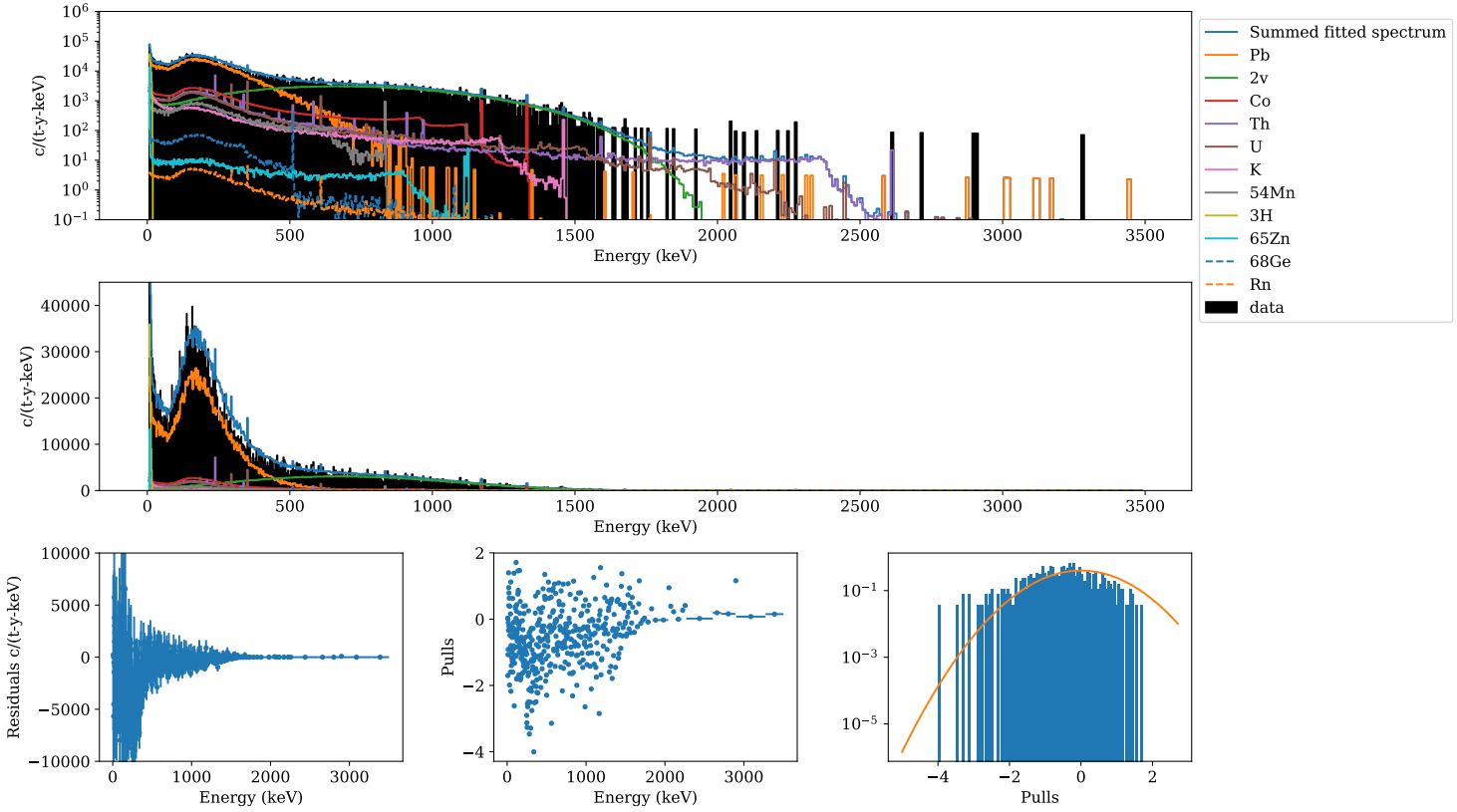

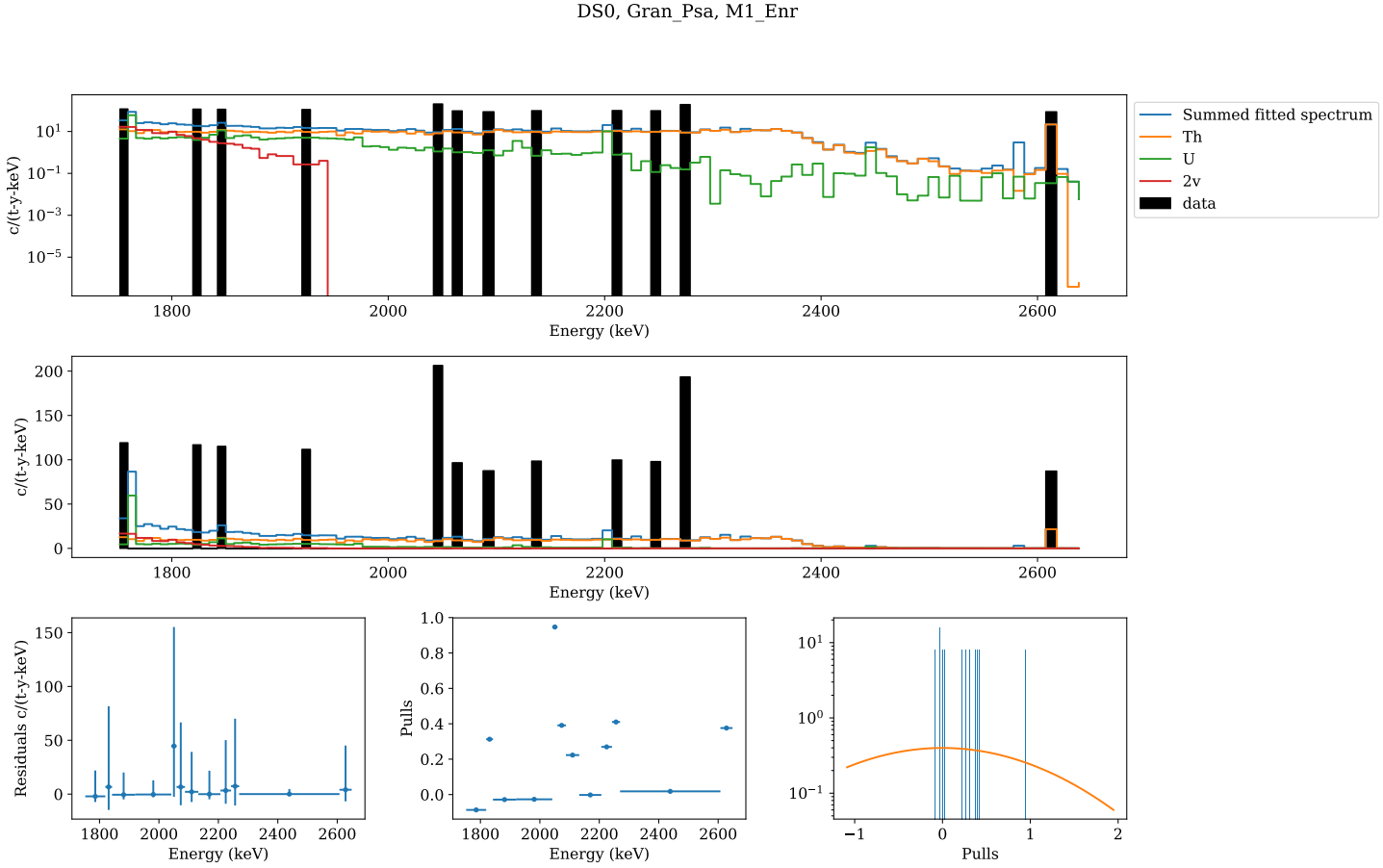
DS0, Gran_Psa, M1_Enr
Summed fitted spectrum
Th
U
2v
data
c/(t-y-keV)
Energy (keV)
Residuals c/(t-y-keV)
Pulls

DS0, Gran_Psa, M1_Enr

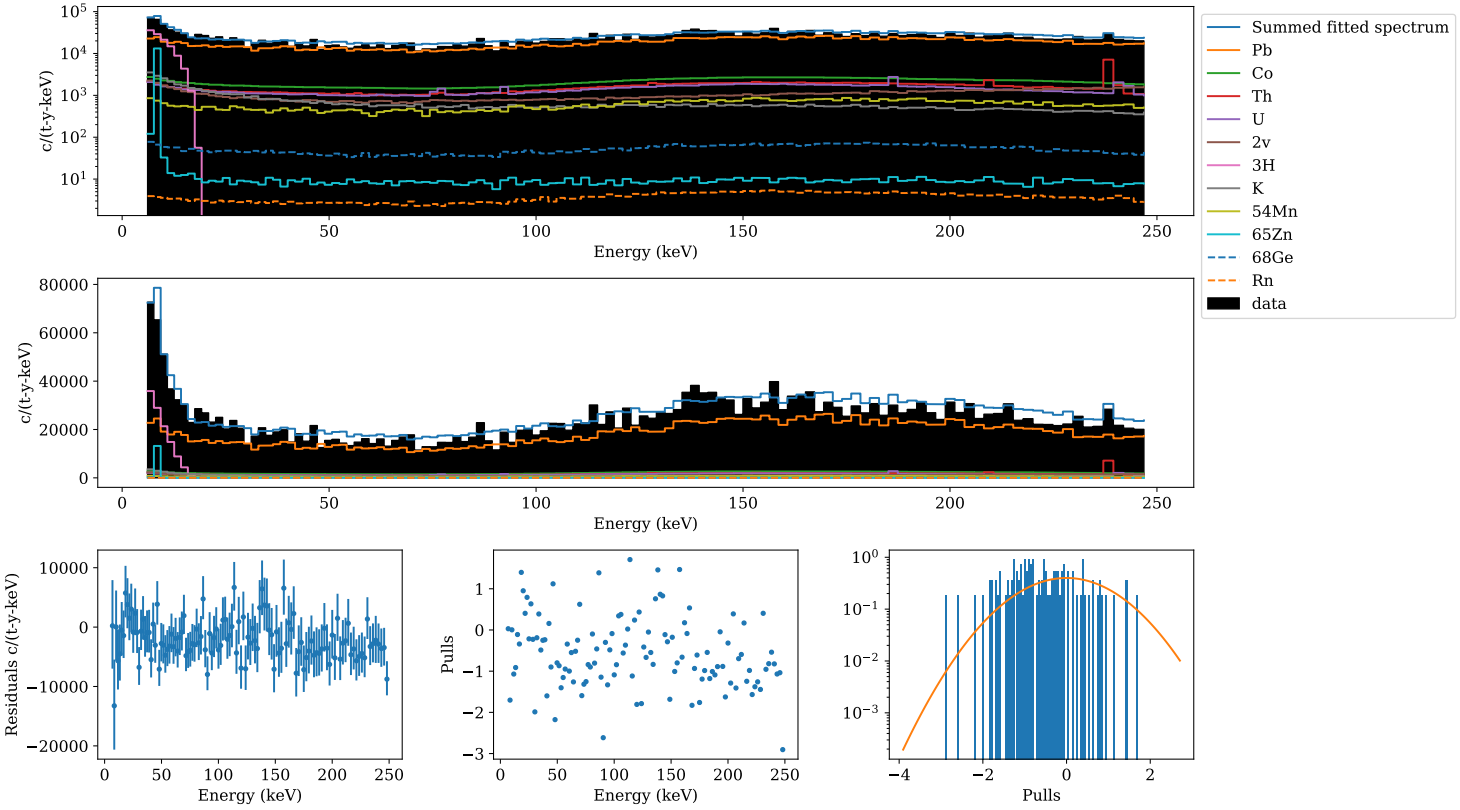

DS0, Gran_Psa, M1_Enr

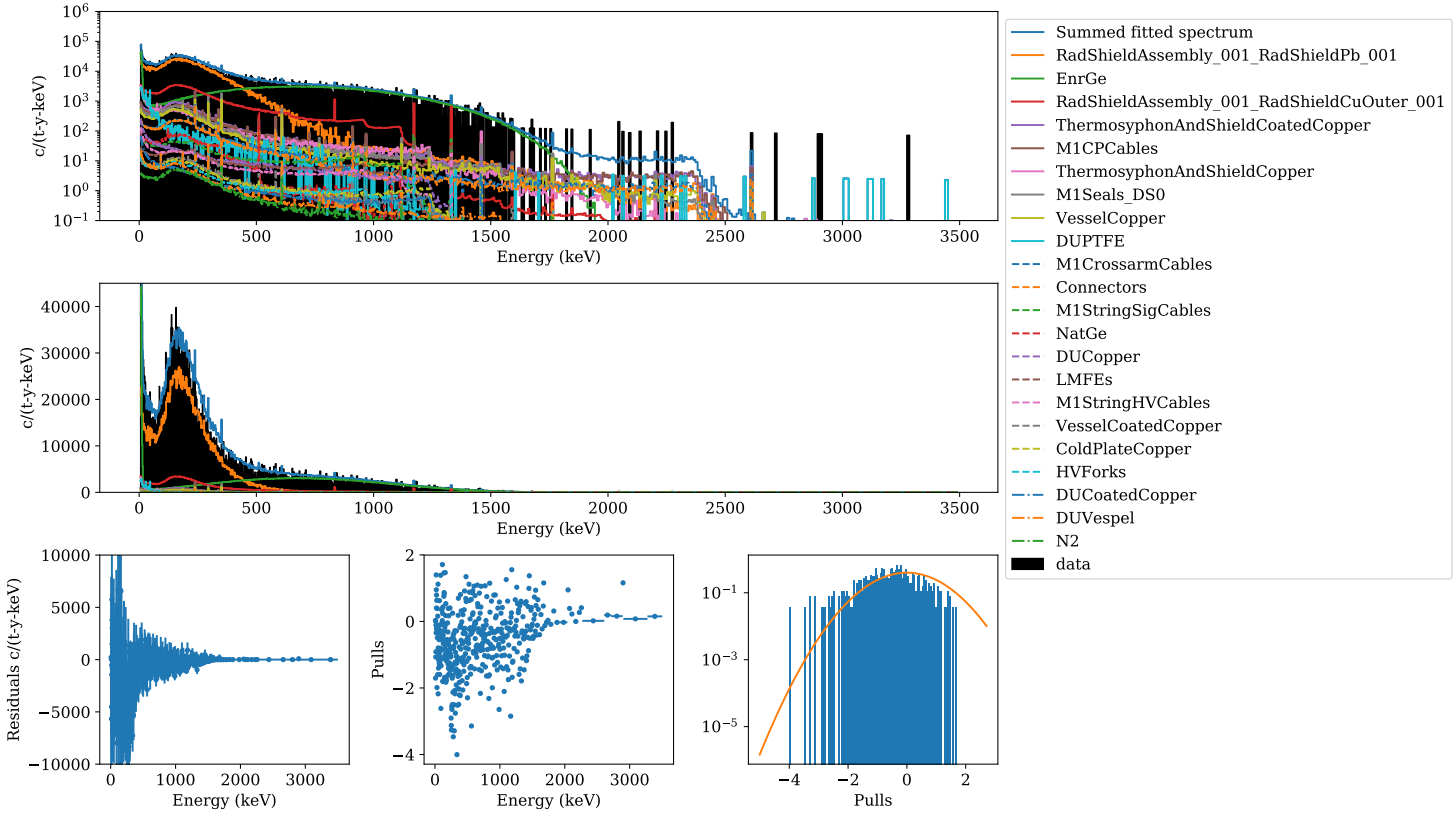

DS0, Gran_Psa, M1_Enr

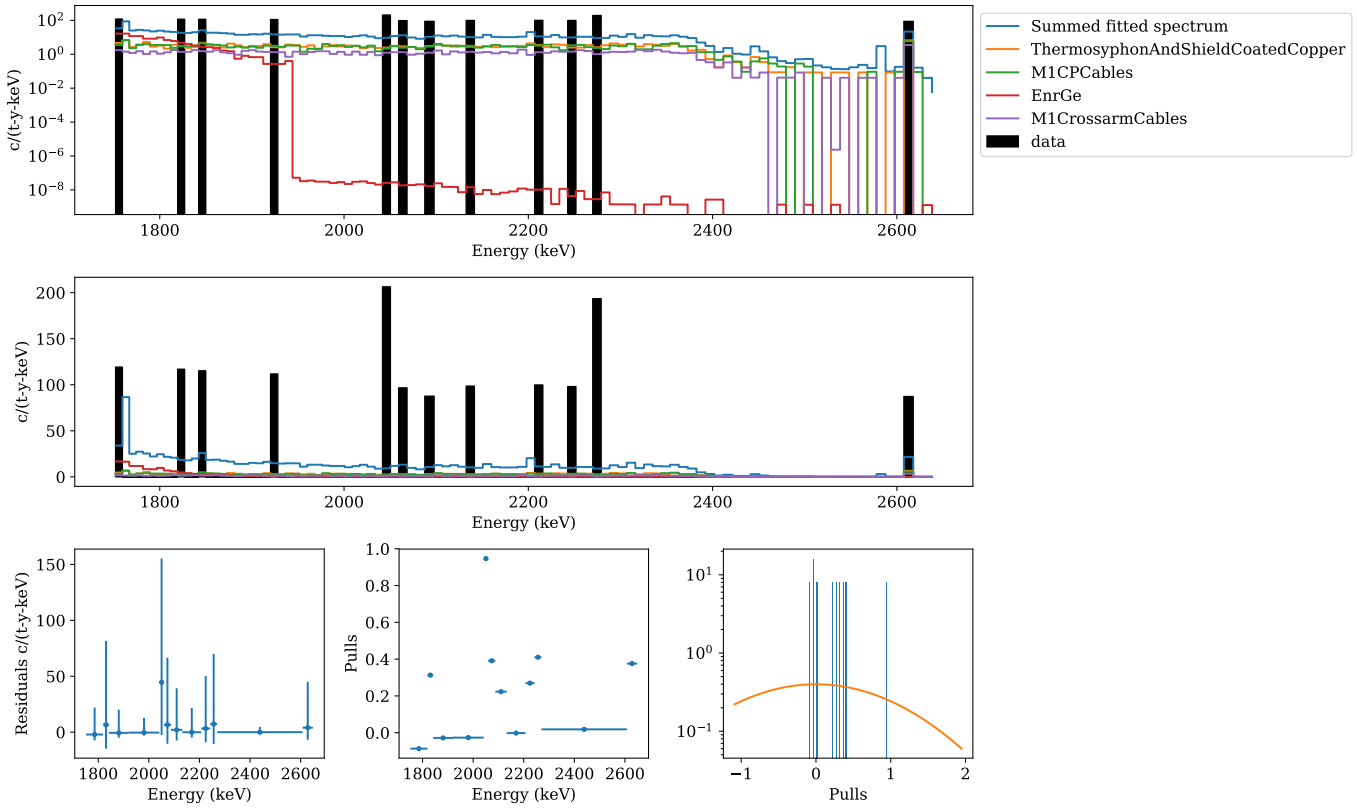

DS0, Gran_Psa, M1_Enr

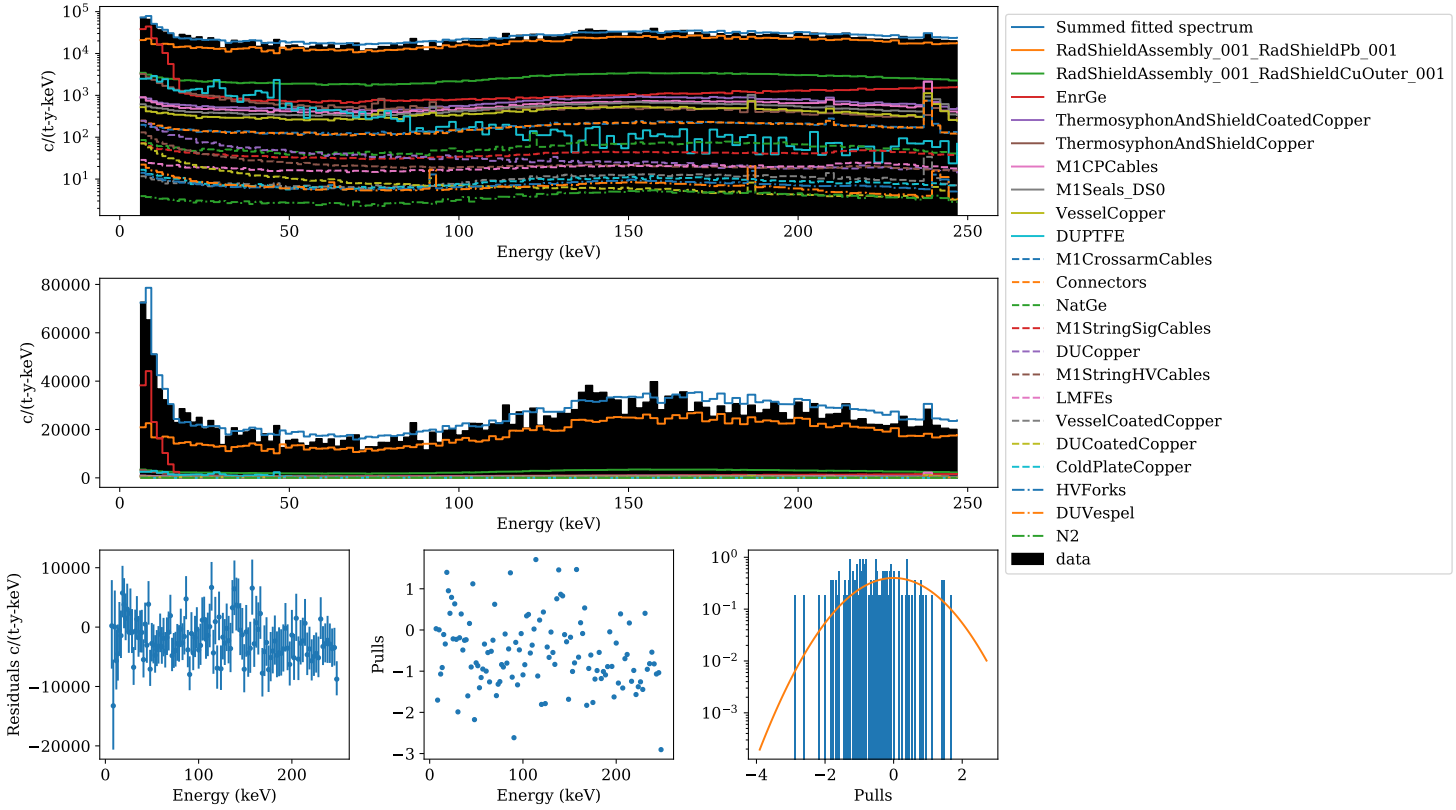

DS12+DS3456, Gran_Psa, M1_Enr+M2_Enr

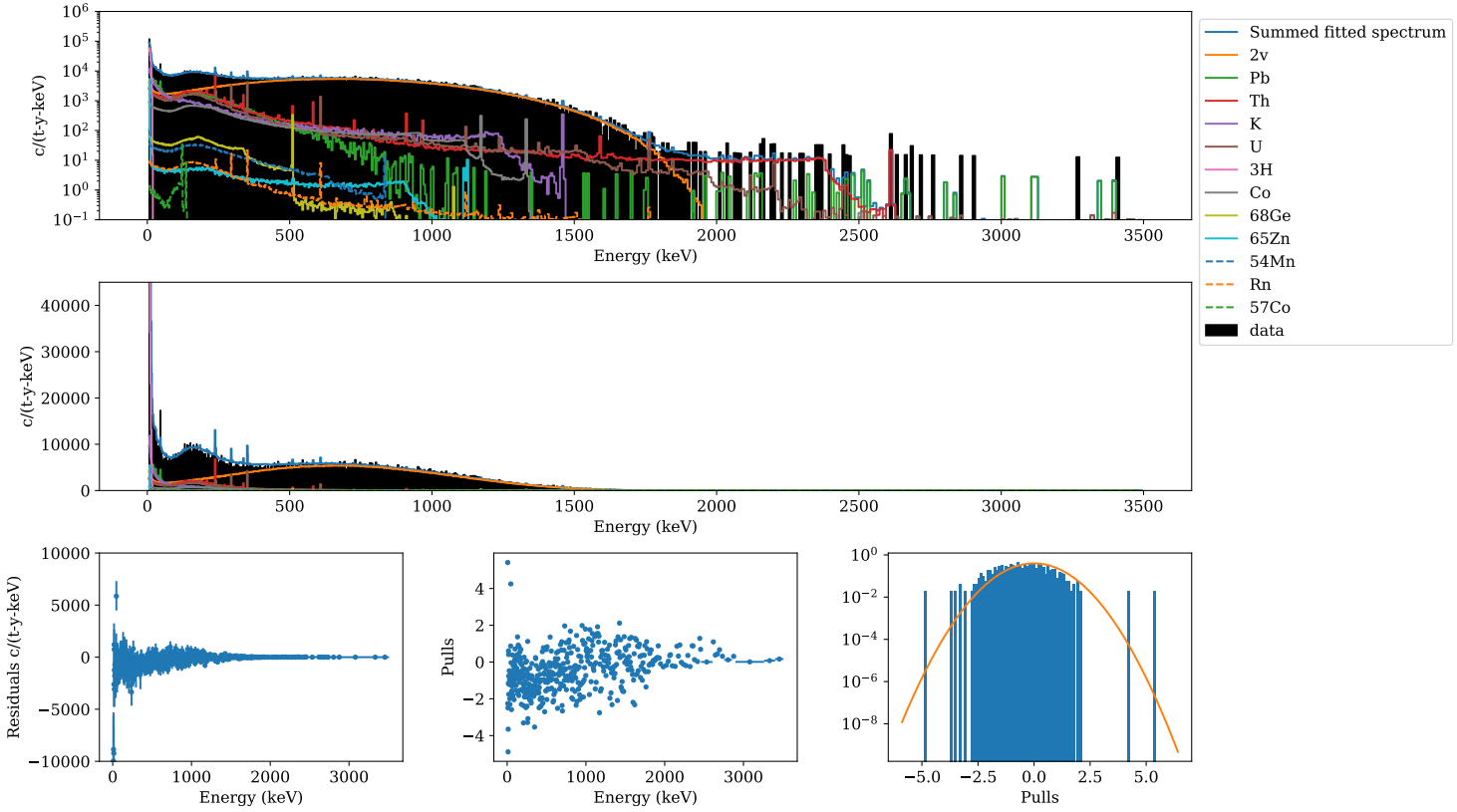

DS12+DS3456, Gran_Psa, M1_Enr+M2_Enr

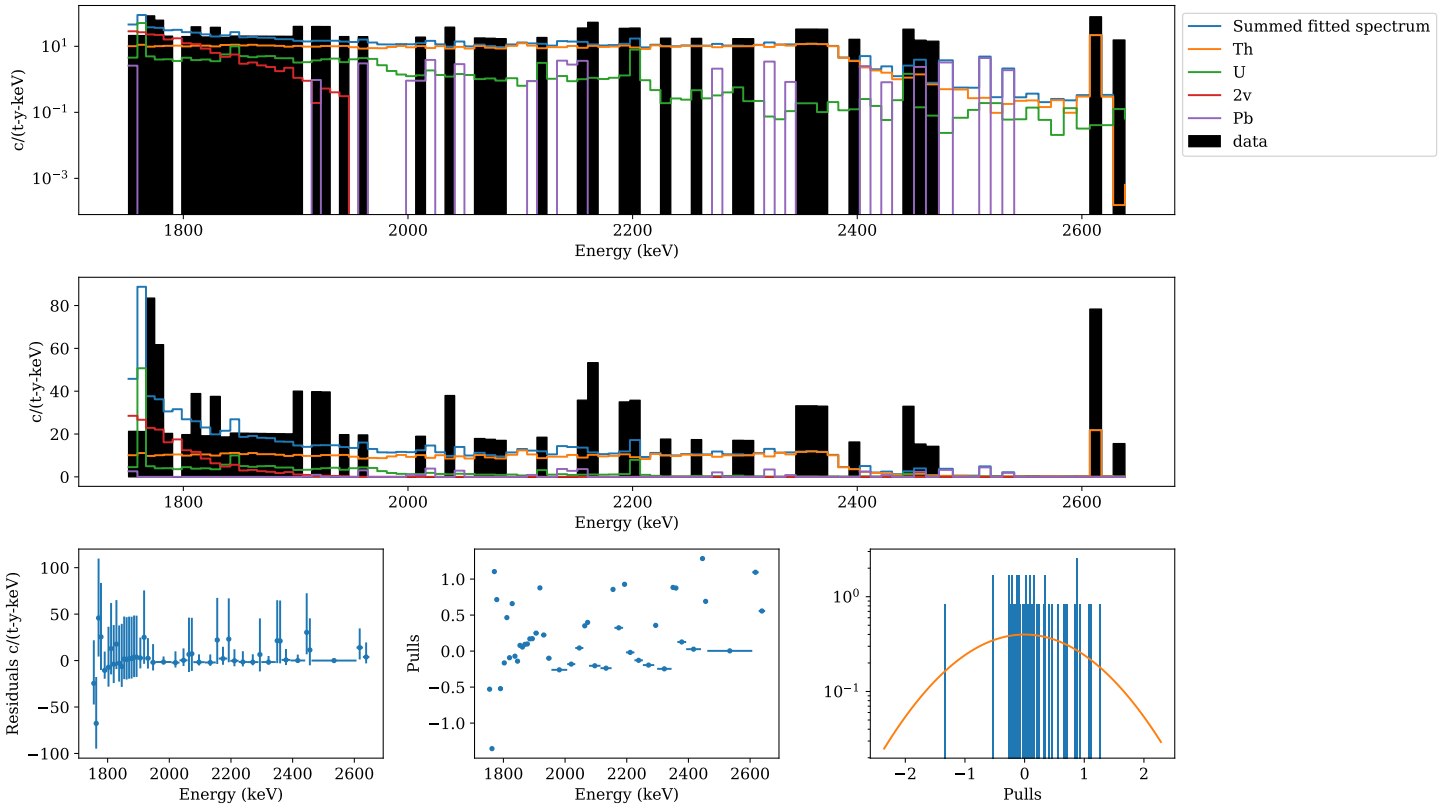

DS12+DS3456, Gran_Psa, M1_Enr+M2_Enr

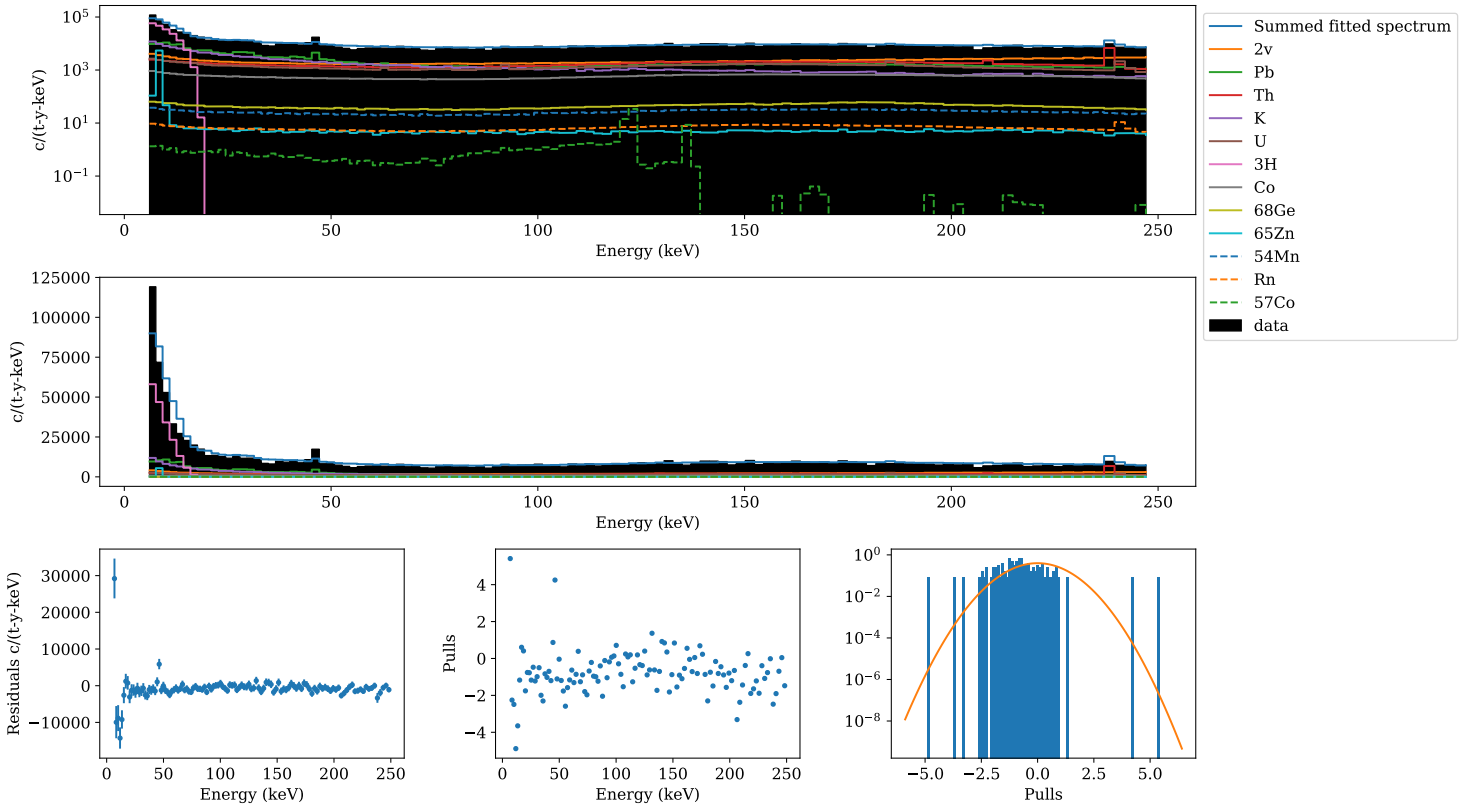

DS12+DS3456, Gran_Psa, M1_Enr+M2_Enr

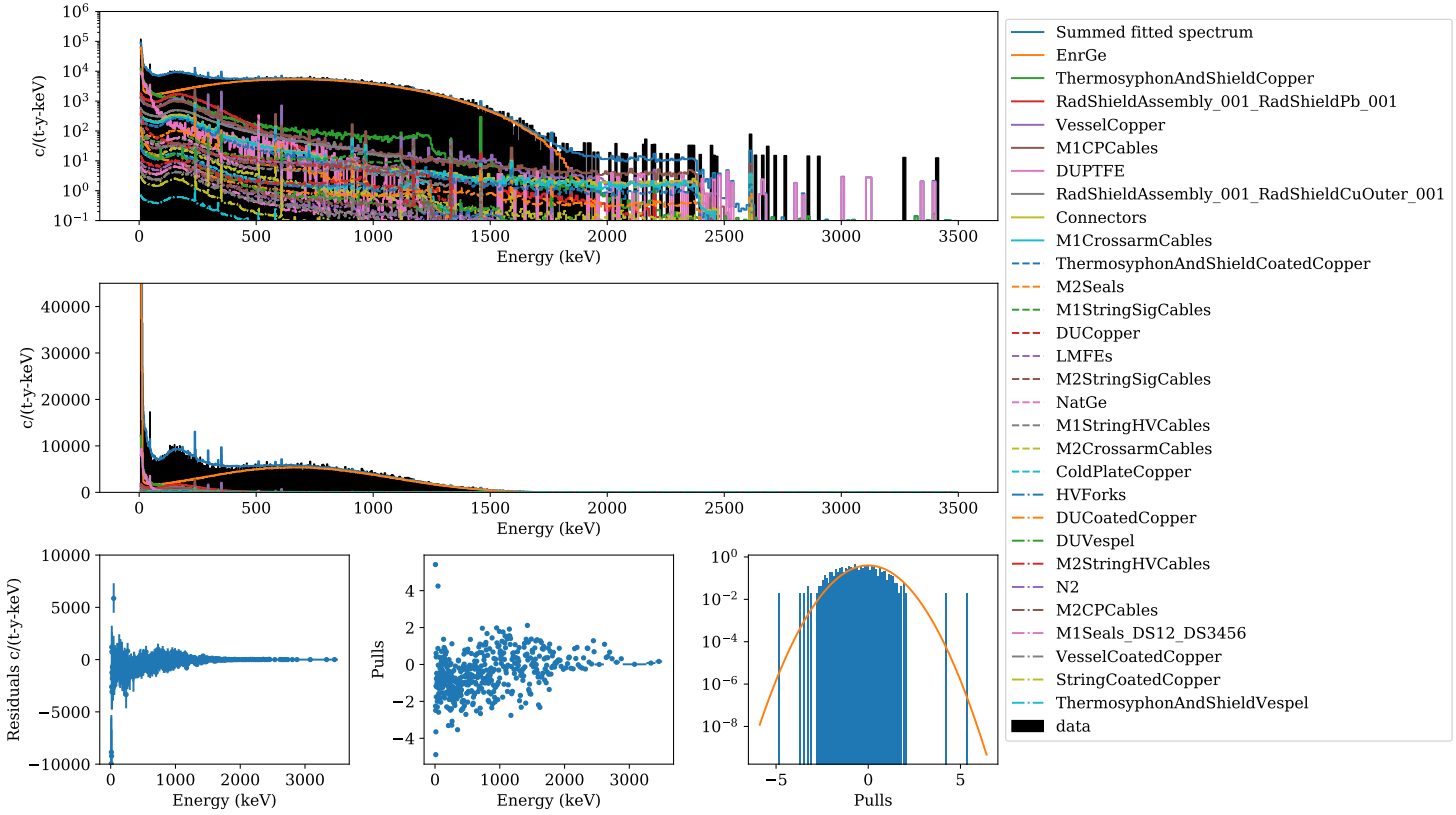

DS12+DS3456, Gran_Psa, M1_Enr+M2_Enr

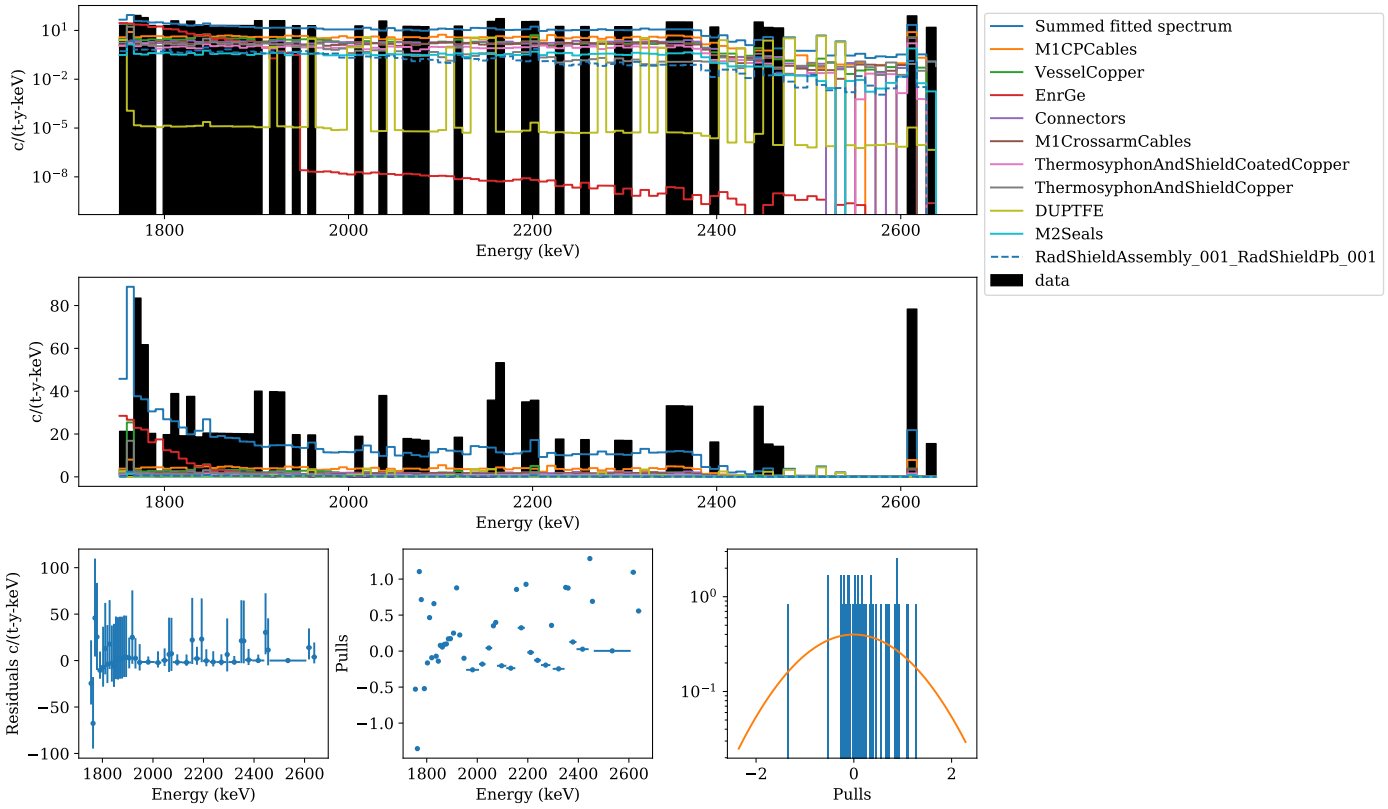

DS12+DS3456, Gran_Psa, M1_Enr+M2_Enr

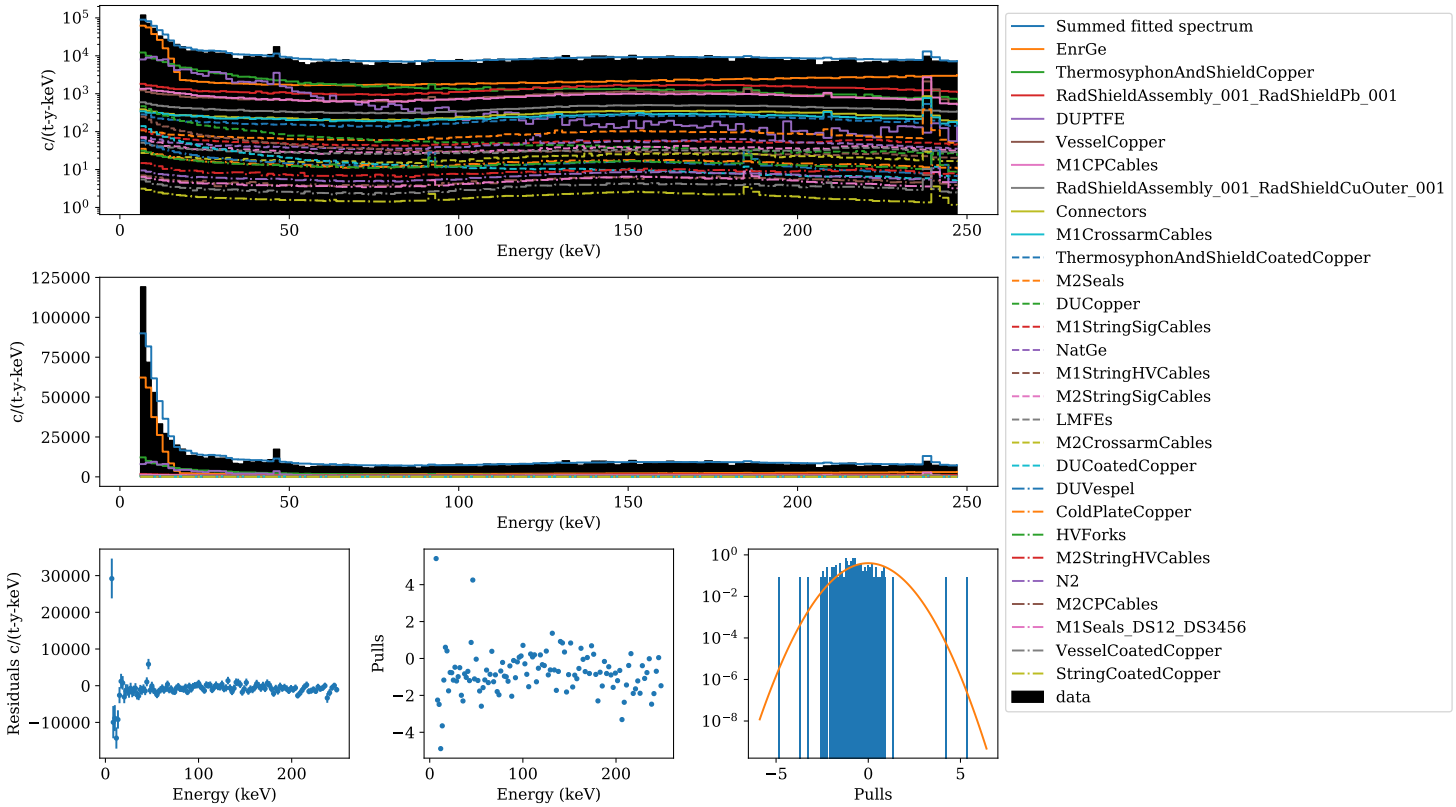

DS0, Gran_Psa, M1_Nat

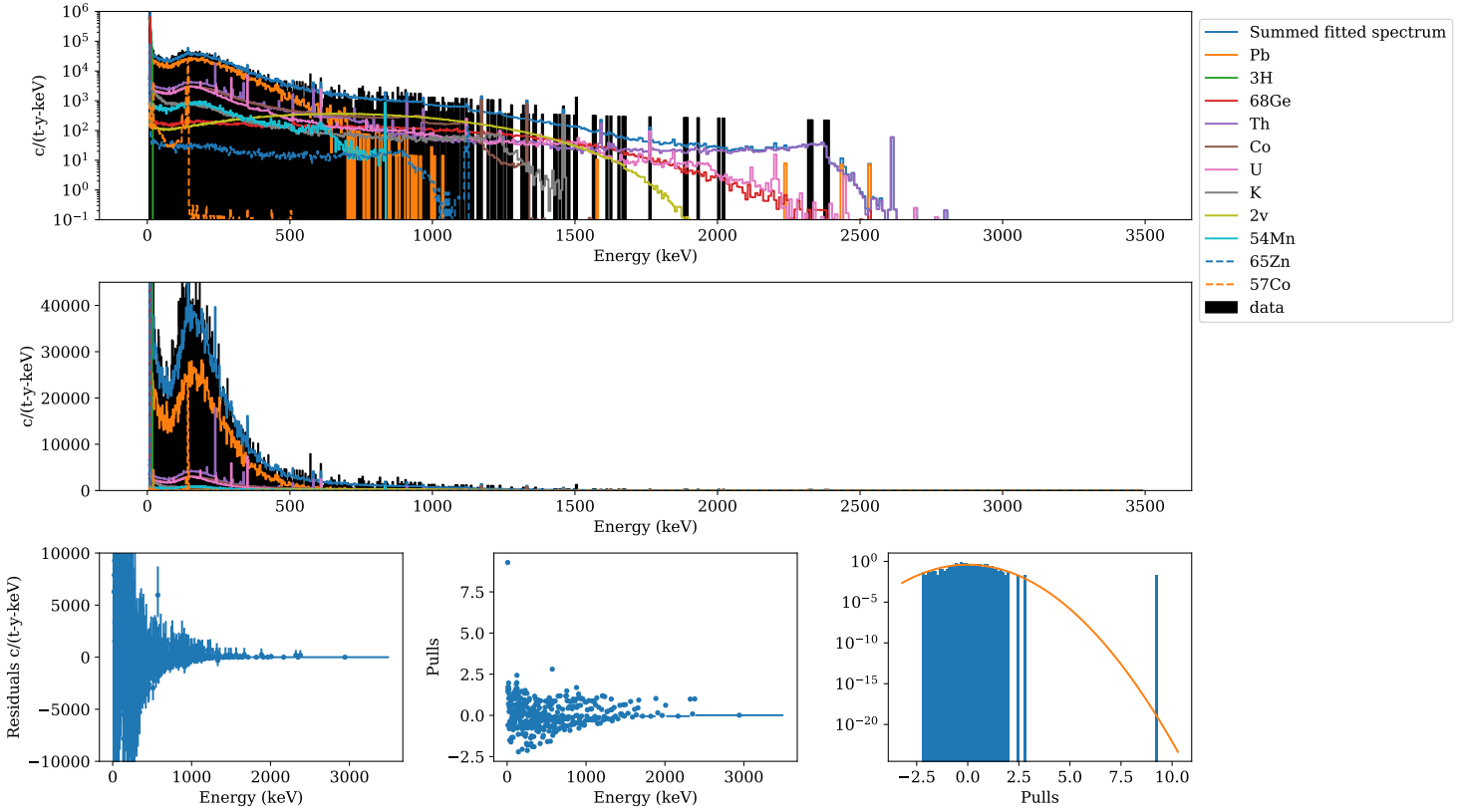

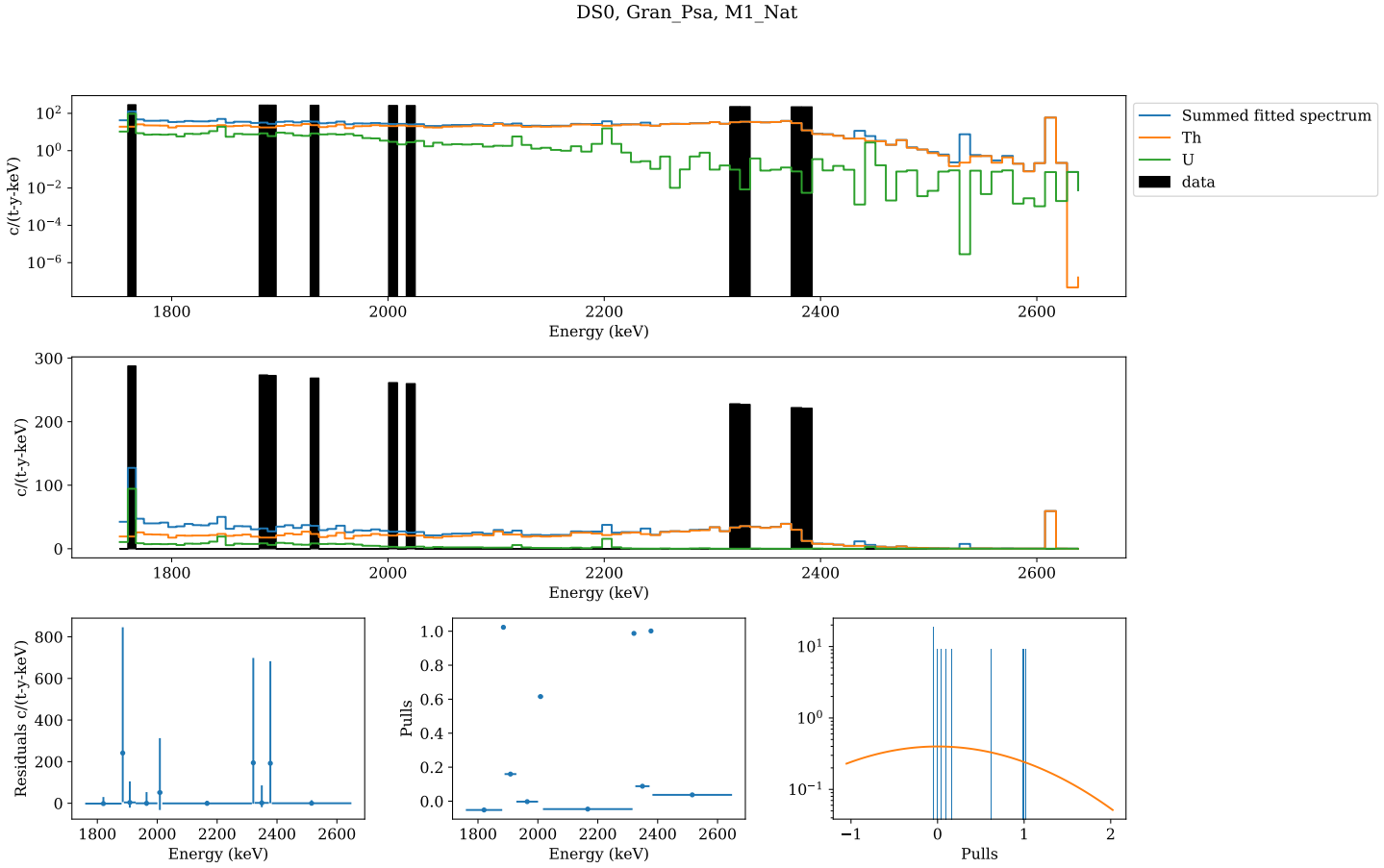
DS0, Gran_Psa, M1_Nat
Summed fitted spectrum
Th
U
data
c/(t-y-keV)
Energy (keV)
Residuals c/(t-y-keV)
Pulls
Energy (keV)
Pulls

DS0, Gran_Psa, M1_Nat

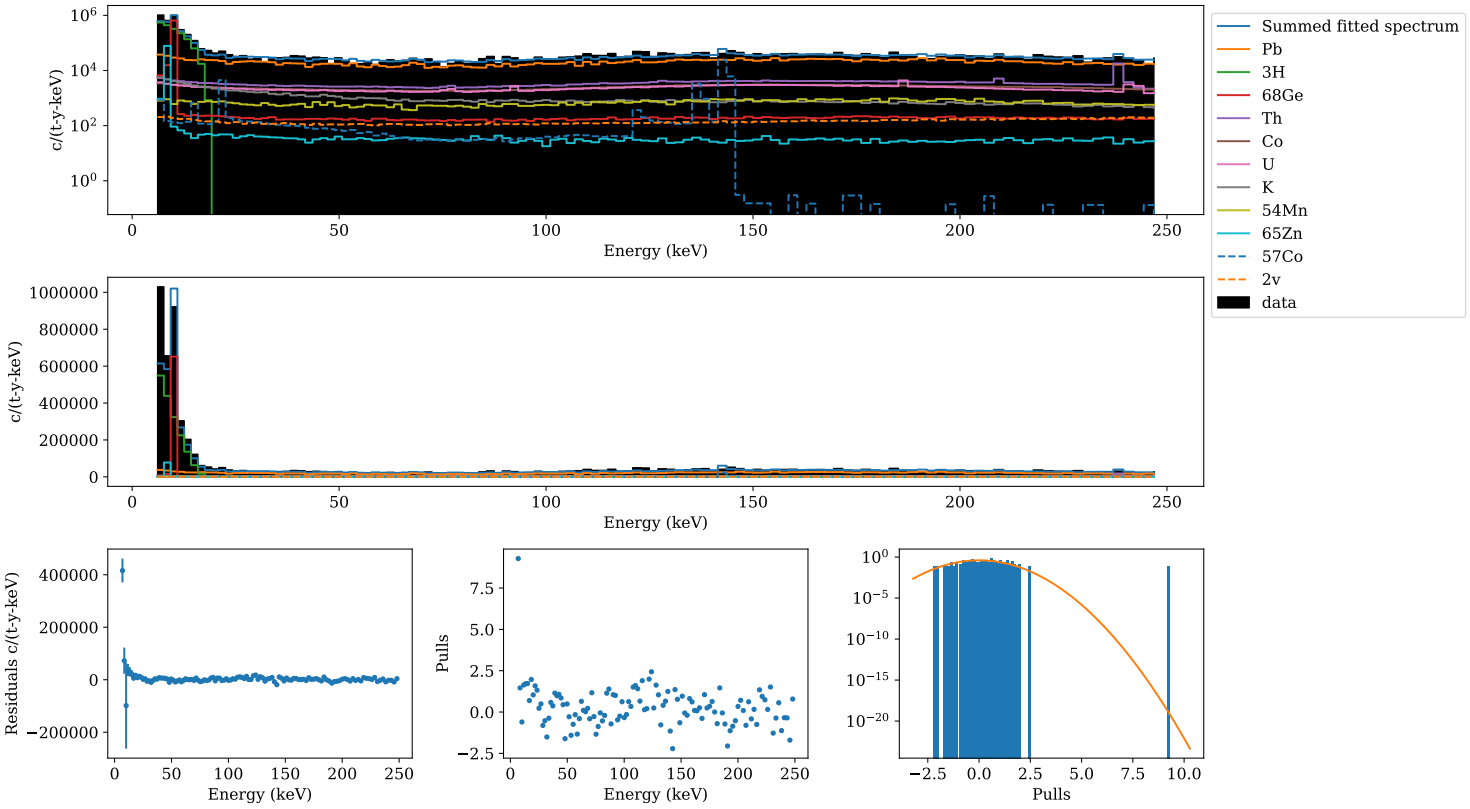

DS0, Gran_Psa, M1_Nat

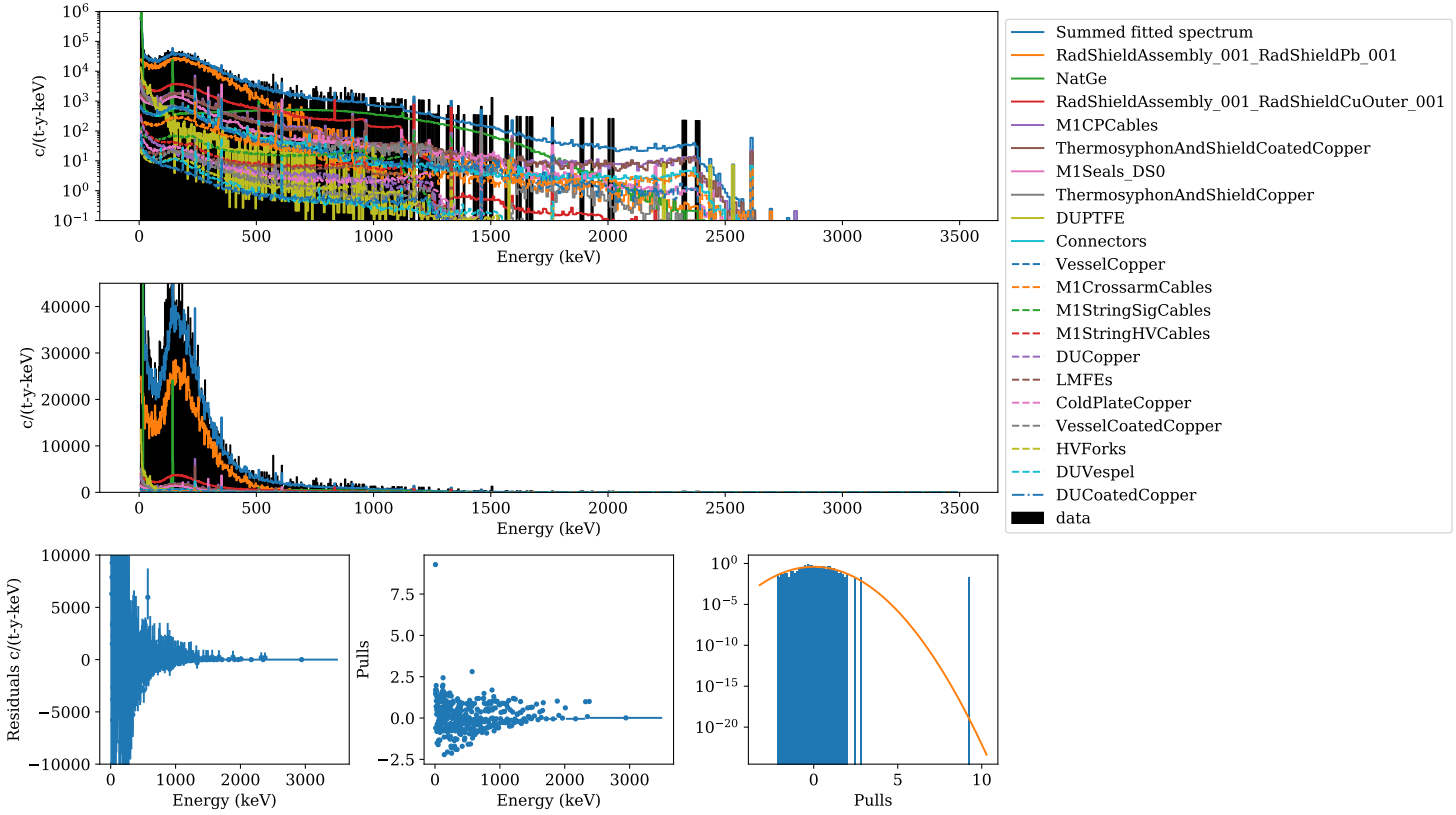

DS0, Gran_Psa, M1_Nat

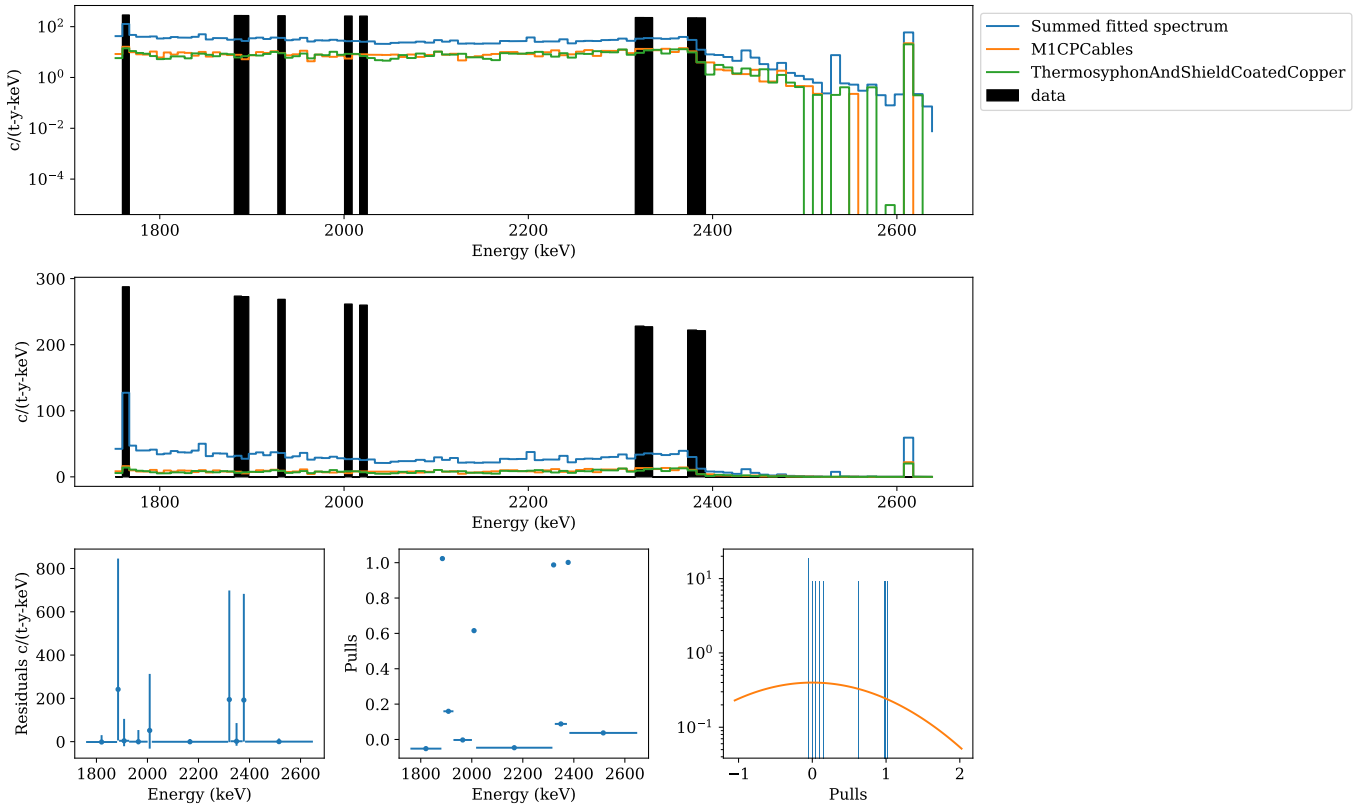

DS0, Gran_Psa, M1_Nat

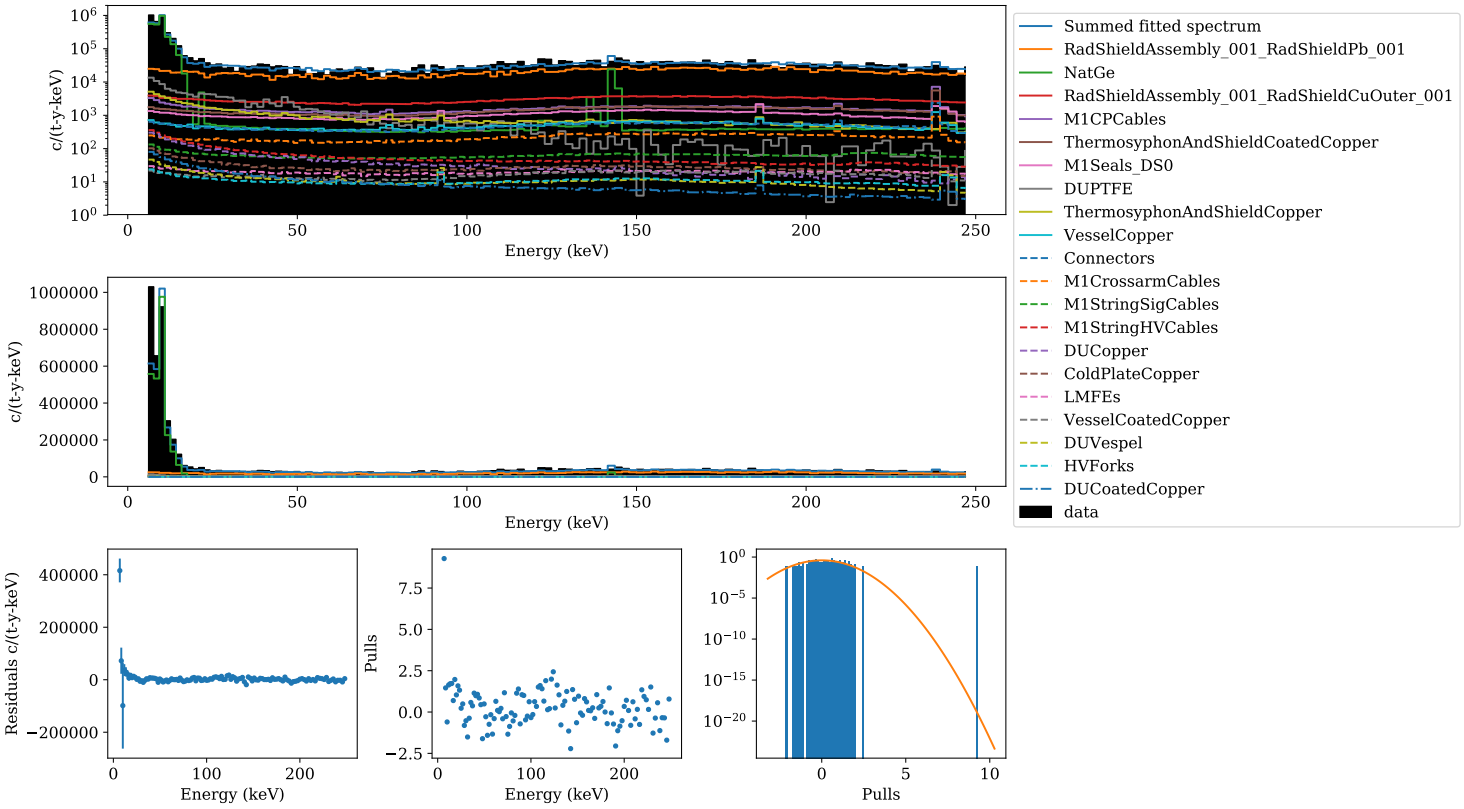

DS12+DS3456, Gran_Psa, M2_Nat+M1_Nat

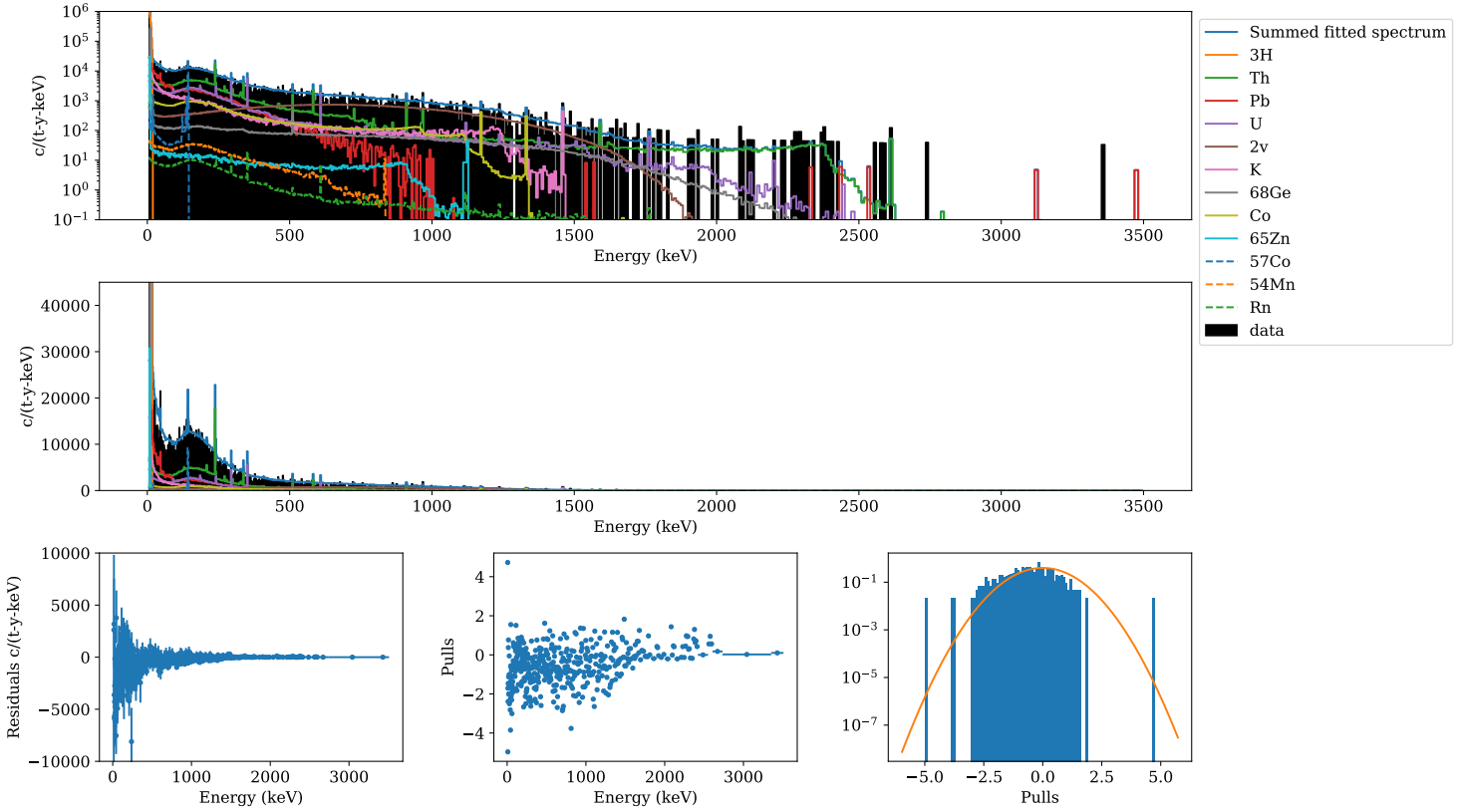

DS12+DS3456, Gran_Psa, M2_Nat+M1_Nat

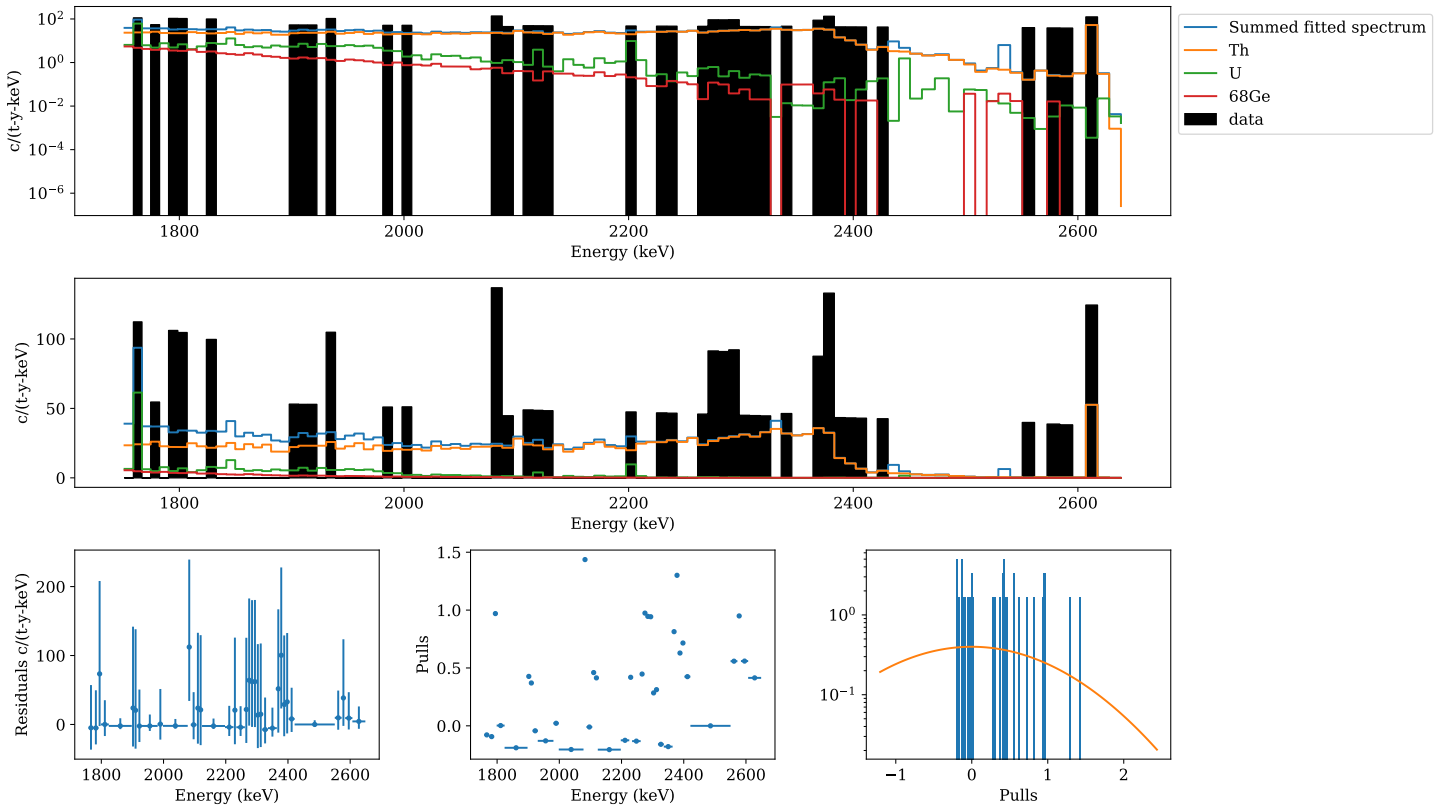

DS12+DS3456, Gran_Psa, M2_Nat+M1_Nat

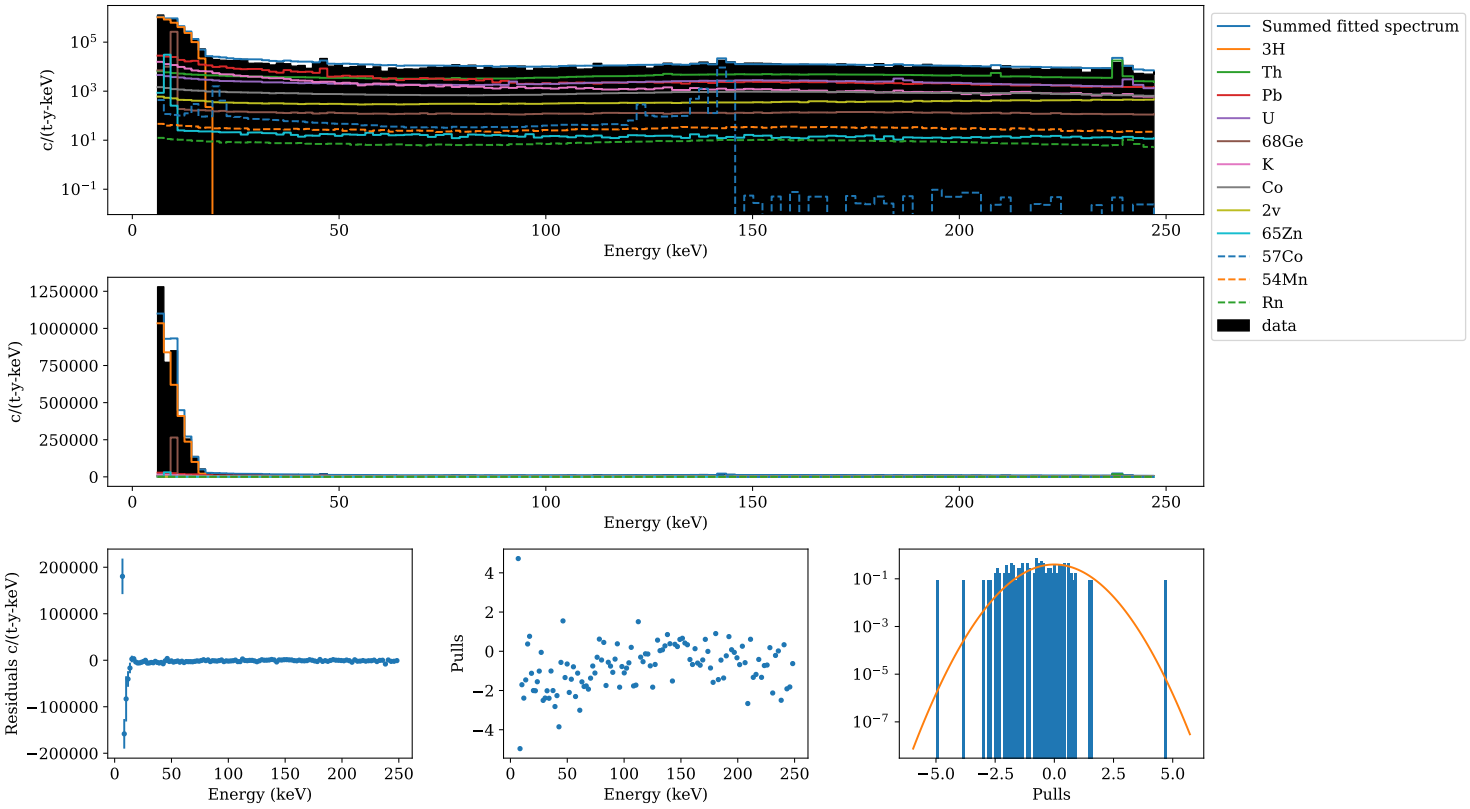

DS12+DS3456, Gran_Psa, M2_Nat+M1_Nat

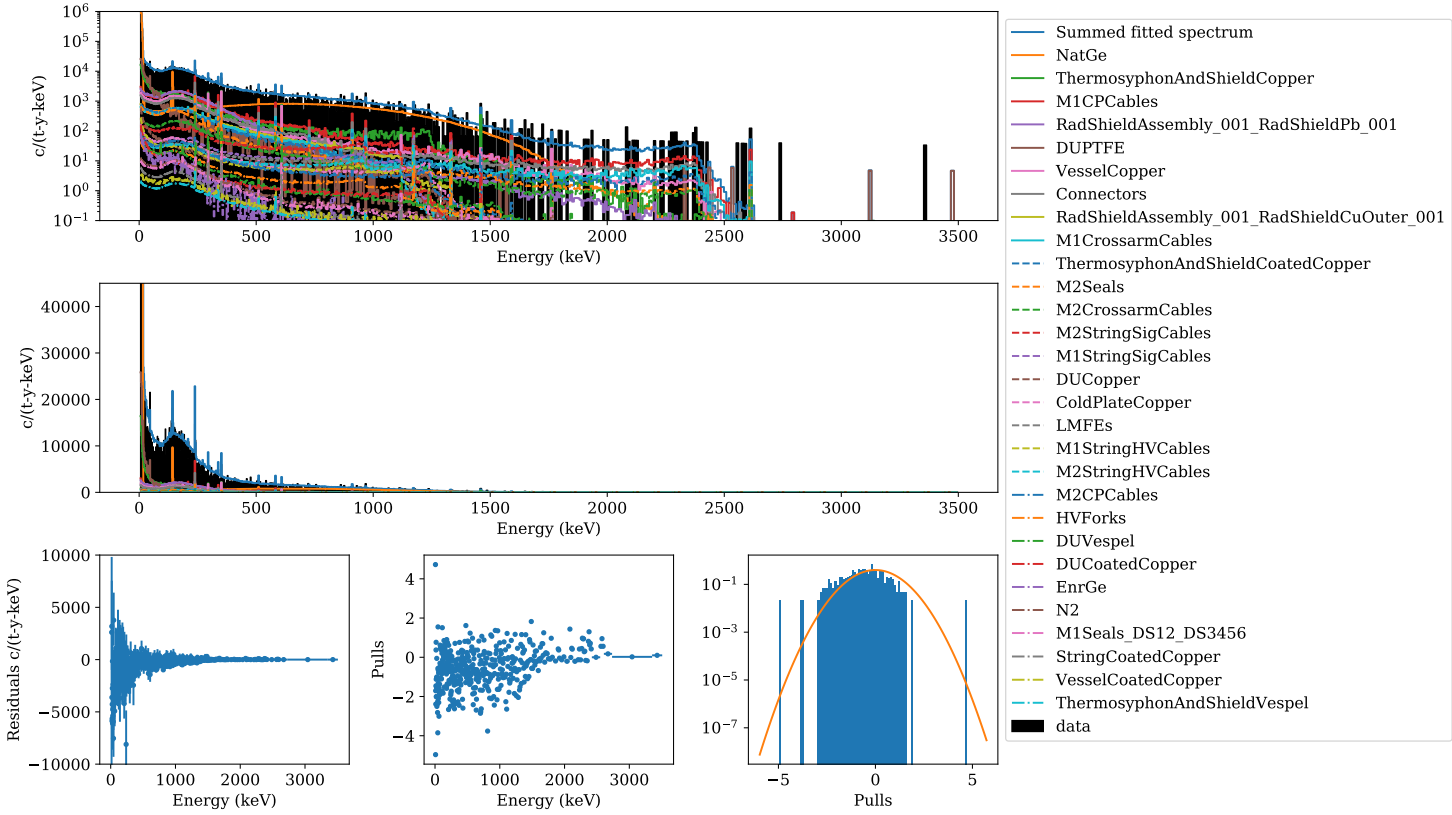

DS12+DS3456, Gran_Psa, M2_Nat+M1_Nat

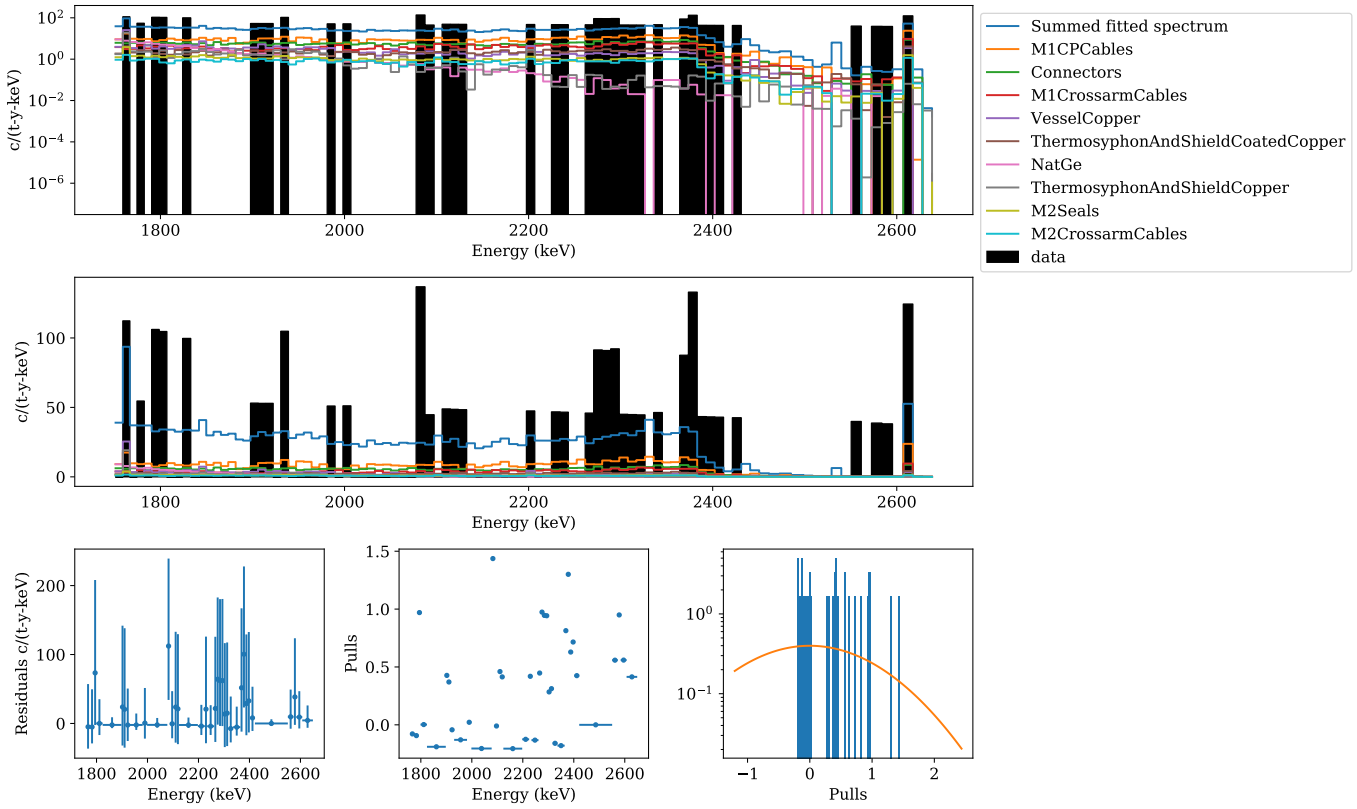

DS12+DS3456, Gran_Psa, M2_Nat+M1_Nat